frontiers | Research Topics

Biogeochemical cycling and depositional processes of critical metals in the deep sea and their constraints on global changes

Edited by
Jiangbo Ren, Yanhui Dong, Xiaodong Jiang and Francisco Javier González

Published in
Frontiers in Marine Science

ISSN 1664-8714
ISBN 978-2-8325-6971-9
DOI 10.3389/978-2-8325-6971-9

Generative AI statement
Any alternative text (Alt text) provided alongside figures in the articles in this ebook has been generated by Frontiers with the support of artificial intelligence and reasonable efforts have been made to ensure accuracy, including review by the authors wherever possible. If you identify any issues, please contact us.

About Frontiers

Frontiers is more than just an open access publisher of scholarly articles: it is a pioneering approach to the world of academia, radically improving the way scholarly research is managed. The grand vision of Frontiers is a world where all people have an equal opportunity to seek, share and generate knowledge. Frontiers provides immediate and permanent online open access to all its publications, but this alone is not enough to realize our grand goals.

Frontiers journal series

The Frontiers journal series is a multi-tier and interdisciplinary set of open-access, online journals, promising a paradigm shift from the current review, selection and dissemination processes in academic publishing. All Frontiers journals are driven by researchers for researchers; therefore, they constitute a service to the scholarly community. At the same time, the *Frontiers journal series* operates on a revolutionary invention, the tiered publishing system, initially addressing specific communities of scholars, and gradually climbing up to broader public understanding, thus serving the interests of the lay society, too.

Dedication to quality

Each Frontiers article is a landmark of the highest quality, thanks to genuinely collaborative interactions between authors and review editors, who include some of the world's best academicians. Research must be certified by peers before entering a stream of knowledge that may eventually reach the public - and shape society; therefore, Frontiers only applies the most rigorous and unbiased reviews. Frontiers revolutionizes research publishing by freely delivering the most outstanding research, evaluated with no bias from both the academic and social point of view. By applying the most advanced information technologies, Frontiers is catapulting scholarly publishing into a new generation.

What are Frontiers Research Topics?

Frontiers Research Topics are very popular trademarks of the *Frontiers journals series*: they are collections of at least ten articles, all centered on a particular subject. With their unique mix of varied contributions from Original Research to Review Articles, Frontiers Research Topics unify the most influential researchers, the latest key findings and historical advances in a hot research area.

Find out more on how to host your own Frontiers Research Topic or contribute to one as an author by contacting the Frontiers editorial office: frontiersin.org/about/contact

Biogeochemical cycling and depositional processes of critical metals in the deep sea and their constraints on global changes

Topic editors

Jiangbo Ren — Guangzhou Marine Geological Survey, China

Yanhui Dong — Second Institute of Oceanography, Ministry of Natural Resources, China

Xiaodong Jiang — Guangdong University of Technology, China

Francisco Javier González — Instituto Geológico y Minero de España (IGME), Spain

Citation

Ren, J., Dong, Y., Jiang, X., González, F. J., eds. (2025). *Biogeochemical cycling and depositional processes of critical metals in the deep sea and their constraints on global changes*. Lausanne: Frontiers Media SA. doi: 10.3389/978-2-8325-6971-9

Table of contents

frontiers | Frontiers in Marine Science

TYPE Editorial
PUBLISHED 25 September 2025
DOI 10.3389/fmars.2025.1702761

OPEN ACCESS

EDITED AND REVIEWED BY
Eric 'Pieter Achterberg,
Helmholtz Association of German Research Centres (HZ), Germany

*CORRESPONDENCE
Jiangbo Ren
dourjb222@163.com

RECEIVED 10 September 2025
ACCEPTED 15 September 2025
PUBLISHED 25 September 2025

CITATION
Ren J, Jiang X, González FJ and Dong Y (2025) Editorial: Biogeochemical cycling and depositional processes of critical metals in the deep sea and their constraints on global changes.
Front. Mar. Sci. 12:1702761.
doi: 10.3389/fmars.2025.1702761

Editorial: Biogeochemical cycling and depositional processes of critical metals in the deep sea and their constraints on global changes

Jiangbo Ren[1]*, Xiaodong Jiang[2], Francisco Javier González[3] and Yanhui Dong[4]

[1]Guangzhou Marine Geological Survey, China Geological Survey, Guangzhou, China, [2]Guangdong University of Technology, Guangzhou, China, [3]Geological Survey of Spain, Madrid, Spain, [4]State Key Laboratory of Submarine Geoscience, Second Institute of Oceanography, Ministry of Natural Resources, Hangzhou, China

KEYWORDS

polymetallic ferromanganese nodules, cobalt-rich ferromanganese crusts, polymetallicsulfides, sediments, seawater, giant diatoms, black shales

Editorial on the Research Topic
Biogeochemical cycling and depositional processes of critical metals in the deep sea and their constraints on global changes

1 Introduction

Critical metals—notably cobalt (Co), nickel (Ni), and rare earth elements (REE)—demonstrate pronounced enrichment in deep-sea sedimentary environments, particularly within polymetallic ferromanganese nodules, Co-rich ferromanganese crusts, and hydrothermal polymetallic sulfide deposits. These metalliferous phases represent strategic resources essential for sustainable technologies and decarbonization economies (Jiang et al., 2023; Sakellariadou et al., 2022). The sediment–water interface functions as a critical biogeochemical reaction front governing metal fluxes between oceanic and sedimentary reservoirs (Ren et al., 2024a; Du et al., 2025). Nevertheless, metal cycling dynamics across this interface are modulated by interconnected environmental forcing: (1) productivity-driven organic matter fluxes, (2) redox oscillations, (3) bottom-current reworking, (4) volcanic-hydrothermal inputs, and (5) climatic-tectonic controls on depositional architectures.

A mechanistic understanding of critical metal transport pathways, enrichment processes in mineral phases, and post-depositional preservation states is fundamental for both elucidating deep-sea ore genesis and reconstructing paleoenvironmental proxies. Integrating metal deposition systems within biogeochemical cycling frameworks under global change scenarios involves two imperatives: advancing earth system science and enabling predictive resource exploration models.

This Research Topic (*Biogeochemical Cycling and Depositional Processes of Critical Metals: Implications for Global Change*) synthesizes 9 pioneering studies examining ferromanganese

nodules, sulfide deposits, giant diatom tests, and black shales across Pacific, Indian, and South China Sea basins and the Yangtze platform continental margin (Figure 1). These findings provide novel insights into metal cycling and paleoceanographic evolution.

2 Summary of Research Topic contributions

Ren et al. investigated Co enrichment in ferromanganese crusts, identifying key controls such as diffusion flux, seawater Co concentration, and MnO_2 dilution. It innovatively integrates these factors into a quantitative model to explain Co variations with water depth, offering a framework for resource assessment. This work highlights the role of biogeochemical processes in deep-sea metal deposition.

He et al. revealed that bacterial communities and biological structures facilitate metal enrichment and mineralization, with regional variations in polymetallic ferromanganese nodule formation linked to redox conditions and productivity. Li et al. demonstrated spatial variability in nodule composition within the Clarion-Clipperton Zone, attributing differences to hydrogenetic vs. diagenetic processes driven by plate motion and Antarctic bottom water dynamics. These studies explore the biogeochemical cycling and depositional processes of critical metals in deep-sea polymetallic nodules, highlighting microbial roles and environmental controls.

Lai et al. investigated microbial driven polymetallic ferromanganese nodule formation in the South China Sea, revealing how heterogeneous marine environments influence metal deposition. An analysis of microbial communities and geochemical conditions across three regions revealed distinct nodule formation mechanisms: diagenesis in suboxic settings and hydrogenesis in oxygen-rich areas. This work highlights microbial roles in metal cycling and nodule genesis, offering novel insights into deep-sea biogeochemical processes and their global implications.

Yang et al. investigated the biogeochemical cycling and deposition of critical metals in the Duanqiao hydrothermal field on the Southwest Indian Ridge. The analysis of mineral textures, trace elements, and $^{230}Th/U$ dating reveals multistage mineralization driven by seawater-hydrothermal fluid interactions. This study identifies enrichment mechanisms for Zn, Pb, As, Ag, and Cd in pyrite, chalcopyrite, and sphalerite, advancing the understanding of metal deposition in ultraslow-spreading ridges.

Yang et al. investigated metal regeneration dynamics in polymetallic nodule areas through *ex-situ* sediment disturbance experiments, revealing synchronized metal behaviors (e.g., Li, V, Co) linked to ferromanganese oxides and sediment texture. Key innovations include quantifying short-term metal release and identifying physicochemical controls, offering critical insights for deep-sea mining ecological risks. Shen et al. explored the middle Pleistocene ventilation history in the Magellan Seamounts via magnetic coercivity, metal enrichment, and grain size, linking weakened ventilation post-430 ka to reduced Antarctic bottom water formation. This work innovatively integrates multiple proxies to disentangle eolian inputs from circulation-driven redox changes, advancing the understanding of deep-sea biogeochemical cycles and their climate connections. Both studies highlight the interplay between metal mobility, sedimentation, and global change.

Lin et al. advanced the understanding of biogeochemical cycling and deep-sea deposition by revealing that Ethmodiscus rex diatom

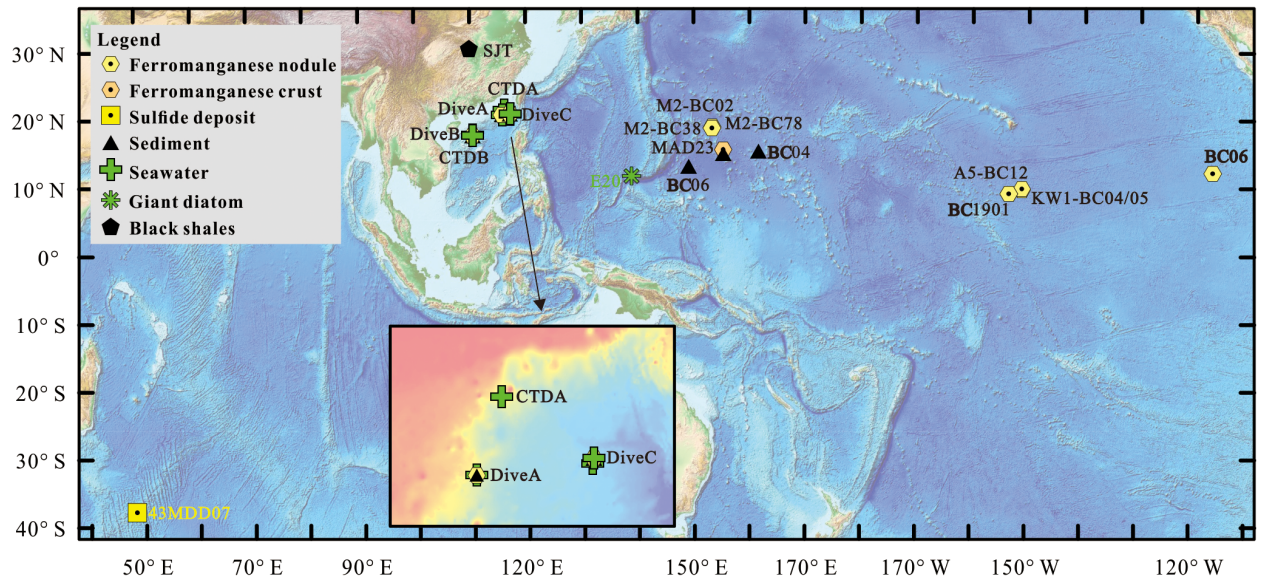

FIGURE 1
Schematic map of sample locations for the 9 studies in the Research Topic. Data sources: Ferromanganese nodules (Lai et al.; Li et al.; He et al.), ferromanganese crusts (Ren et al.), sulfide deposits (Yang et al.), sediments (Lai et al.; Shen et al.; Yang et al.), seawater (Lai et al.), giant diatoms (Lin et al.), and black shales (Wang et al.). The topography dataset available at https://www.ngdc.noaa.gov.

blooms (last glacial maximum to early Holocene) were driven by deep-water upwelling and volcanic nutrient fluxes, not solely eolian dust. Key innovations include linking diatom mat formation to intensified deep currents and topographic upwelling, highlighting the role of deep-ocean processes in carbon sequestration and global climate dynamics. Notably, the Figure 7 in the original publication contained an error, which has been addressed in a subsequent Correction notice (Lin et al.).

Wang et al. investigated the biogeochemical cycling and deposition of critical metals (V, Cr, Ni, U, Sr, Ba) in Cambrian black shales of the Shuijingtuo Formation, highlighting their enrichment mechanisms under anoxic conditions, high productivity, and hydrothermal activity. Key innovations include linking metal enrichment to organic matter affinity, redox-sensitive deposition, and submarine hydrothermal influences, providing insights into paleoenvironmental controls on metal cycling in deep-sea settings.

Author contributions

JR: Conceptualization, Funding acquisition, Visualization, Writing – original draft, Writing – review & editing. XJ: Writing – review & editing. FG: Writing – review & editing. YD: Writing – review & editing.

Funding

The author(s) declare financial support was received for the research and/or publication of this article. This work was supported by the National Natural Science Foundation of China (U2244222), the Project of the Geological Survey of China (DD20240091) and the European Union HORIZON CL4-20022-RESILIANCE-01, TRIDENT Project (101091959).

Acknowledgments

As the topic editors of this Research Topic, we would like to express our sincere gratitude to the Editors-in-Chief, especially Prof. Eric 'Pieter Achterberg, for their expert guidance and the editorial team for their invaluable support throughout the preparation of this Research Topic. We are also deeply grateful to all the reviewers for their time and effort in providing constructive feedback, which has been instrumental in enhancing the quality of the contributions. Our sincere thanks also extend to all the authors for their excellent research papers.

Conflict of interest

The authors declare that the research was conducted in the absence of any commercial or financial relationships that could be construed as potential conflicts of interest.

Generative AI statement

The author(s) declare that no Generative AI was used in the creation of this manuscript.

Any alternative text (alt text) provided alongside figures in this article has been generated by Frontiers with the support of artificial intelligence and reasonable efforts have been made to ensure accuracy, including review by the authors wherever possible. If you identify any issues, please contact us.

Publisher's note

References

Du, J. H., Haley, B. A., McManus, J., Blaser, P., Rickli, J., and Vance, D. (2025). Abyssal seafloor as a key driver of ocean trace-metal biogeochemical cycles. *Nature* 642, 620–627. doi: 10.1038/s41586-025-09038-3

Jiang, S. Y., Wang, W., and Su, H. M. (2023). Super-enrichment mechanisms of strategic critical metal deposits: current understanding and future perspectives. *J. Earth Sci.* 34, 1295–1298. doi: 10.1007/s12583-023-2001-5

Ren, J. B., He, G. W., Yang, Y., Yu, M., Deng, Y. N., Pang, Y. T., et al. (2024a). Ultraselective enrichment of trace elements in seawater by Co-rich ferromanganese nodules. *Global Planetary Change* 239, 104498. doi: 10.1016/j.gloplacha.2024.104498

Sakellariadou, F., Gonzalez, F. J., Hein, J. R., Rincón-Tomás, B., Arvanitidis, N., and Kuhn, T. (2022). Seabed mining and blue growth: exploring the potential of marine mineral deposits as a sustainable source of rare earth elements (MaREEs) (IUPAC Technical Report). *Pure Appl. Chem.* 94 (3), 1–23. doi: 10.1515/pac-2021-0325

frontiers | Frontiers in Marine Science

TYPE Original Research
PUBLISHED 04 October 2024
DOI 10.3389/fmars.2024.1457964

OPEN ACCESS

EDITED BY
Xiaodong Jiang,
Guangdong University of Technology, China

REVIEWED BY
Rui Bao,
Ocean University of China, China
Mabrouk Sami,
United Arab Emirates University,
United Arab Emirates

*CORRESPONDENCE
Jing Li
jingli@cug.edu.cn

RECEIVED 01 July 2024
ACCEPTED 13 September 2024
PUBLISHED 04 October 2024

CITATION
Wang Y, Li J, Lin Y, Zhuang X, Hoang V, Wu P, Luo X, Zhang H and Zhang X (2024) Mineralogy and geochemistry of the Cambrain Shuijingtuo Formation black shales from Western Hubei, China: implications on enrichment of critical metals and paleoenvironment. *Front. Mar. Sci.* 11:1457964. doi: 10.3389/fmars.2024.1457964

Mineralogy and geochemistry of the Cambrain Shuijingtuo Formation black shales from Western Hubei, China: implications on enrichment of critical metals and paleoenvironment

Yuan Wang[1], Jing Li[1]*, Yang Lin[1], Xinguo Zhuang[1], Vanlong Hoang[2], Peng Wu[1], Xin Luo[1], Han Zhang[1] and Xiaoyang Zhang[1]

[1]Key Laboratory of Tectonics and Petroleum Resources of Ministry of Education, China University of Geosciences, Wuhan, China, [2]Exploration & Production Center, Vietnam Petroleum Institute, Hanoi, Vietnam

Black shales have attracted the attention of numerous researchers not only due to their high potential as hydrocarbon source rocks and shale gas reservoirs, but also to the enrichment of critical metal elements in black shale series. Black shale of the Cambrian Shuijingtuo Formation is one of the most important black shales in the Yangtze platform. This paper conducts integrated research on the mineralogical and geochemical characteristics of this black shale from the Luojiacun section in Western Hubei Region, aiming at elaborating the enrichment mechanism of elevated critical metal elements in the Shuijingtuo black shale. Minerals in the Shuijingtuo black shale are predominantly composed of quartz (avg. 43.0%) and clay minerals (avg. 32.5%), with small proportions of calcite, albite, clinochlore, and pyrite. The Shuijingtuo black shale is characterized by high total organic carbon (TOC, avg. 3.9%) content and enriched in V-Ni-Cr-U and Sr-Ba critical metal assemblages. The elevated V, Cr, Ni, and U present dominant organic affinities, while Sr and Ba are closely correlated to calcite and pyrite, respectively. The enrichment of V-Cr-Ni-U critical element assemblages in Shuijingtuo black shale are ascribed to the high primary productivity, anoxic depositional conditions, marine biologic production, and low-temperature hydrothermal activities. The enrichment of Sr and Ba is related to the high primary productivity and anoxic depositional conditions, respectively.

KEYWORDS

critical elements, enrichment mechanism, palaeoredox environment, organic-rich black shale, Shuijingtuo Formation, Western Hubei region

1 Introduction

Black shales are commonly considered as potential hydrocarbon source rocks and shale gas reservoirs because of the high total organic carbon (TOC) content (Gao et al., 2019; Yan et al., 2021), which contribute to large proportions of Proterozoic and Palaeozoic hydrocarbons and play important roles in oil and gas development worldwide (Luning et al., 2000; Wu et al., 2015). Moreover, a variety of important elements, including V, Mn, Ni, Mo, U, Ba, and P are significantly enriched with high grade and large scale in these black shale series in some areas (Ye and Fan, 2000; Fathy et al., 2024), which have a promising economic potential. Consequently, research on black shales is of important economic significance for both hydrocarbon and polymetallic extraction. Furthermore, due to the occurrence of several particular geological events (e.g., mass extinctions, biodiversity change, oceanic anoxia, and continental glaciation) during the deposition process of black shales (Armstrong et al., 2009; Delabroye and Vecoli, 2010; Yan et al., 2010; Sheets et al., 2016; Trela et al., 2016; Pohl et al., 2017), research on black shales is of important theoretical significance as well, which can correspondingly provide valuable information for these geological events (Ghosh and Sarkar, 2010; Dai et al., 2018; Yan et al., 2021).

Black shale of the Niutitang Formation (corresponding to the Shuijingtuo Formation in this paper) is a set of shale with great gas potential in South China. A large number of scholars have carried out studies on the evaluation of pore characteristics and gas potential, sources of organic matter, geochemical characteristics of rare earth elements and restoration of sedimentary environment in the Niutitang Formation black shale (Yin et al., 2017; Wan et al., 2018; Xi et al., 2018; Tian et al., 2019; Liu et al., 2020; Wu et al., 2020; Zhang et al., 2021; Awan et al., 2022; Li et al., 2022; Wei et al., 2022). In particular, research on mineralogical and geochemical characteristics of the Shuijingtuo black shale composition is of crucial significance because they have been widely used as important indicators for ancient seawater chemistry, palaeomarine environment conditions, and source compositions of detrital sediments (Algeo and Maynard, 2004; Algeo and Rowe, 2012; Dai et al., 2013b) due to their predictable behavior during different geological processes (Ghosh and Sarkar, 2010; Dai et al., 2014, 2017).

However, due to the heterogeneity in chemical composition of black shales, the mineralogical and geochemical characterization of these shales remains contentious, let alone the enrichment mechanism of strategic metal elements in black shales (Han et al., 2018). In the current study, the mineralogical and geochemical characteristics of black shales of the Cambrian Shuijingtuo Formation from Western Hubei Region are elaborated, with emphasis on the abundance, occurrence and genesis of potential elevated strategic metals in black shales. This research will provide not only essential mineralogical and geochemical evidences for the provenance composition and depositional paleoenvironment of black shales, but also an objective evaluation on the enrichment of potential strategic metal element resources in black shales.

2 Geological setting

A set of black mudstones and black siliceous rocks with extremely high organic matter content were widely developed and well preserved in the Yangtze platform in the Early Cambrian. The Yangtze platform generally transited from a shallow water platform area to a slope and deep-water basin during the Early Cambrian. Consequently, during this period, the Yangtze platform was roughly divided into four sedimentary facies areas from NW to SE, viz., the inland shelf shallow water platform, the outer shelf depression, the shelf edge upper slope area, and the deep-water basin area (Och et al., 2013; Cremonese et al., 2014; Fu et al., 2016; Zhang et al., 2016).

The western Hubei Region is geotectonically located on the southeast slope of Huangling Uplift in the northwest of the middle of the Yangtze Platform, known as the Yichang slope belt, where the black shales of the Early Cambrian Shuijingtuo Formation are widely distributed (Figure 1A). In the Yichang slope belt, there is a double-layer basement composed of the Kongling complex in the Paleoproterozoic and the intruding Neo-Proterozoic Huangling granite and Xiaofeng basic-ultrabasic rocks, which is held by the western Hubei fold.

The black shales of the Early Cambrian Shuijingtuo Formation were the primary hydrocarbon source rocks and shale gas reservoirs in the studied area, which were mainly deposited in a transitional sedimentary environment from shallow water platform area to the shelf edge upper slope and deep-water basin facies area of the Yangtze platform (Zhu et al., 2015). The Shuijingtuo Formation was lithologically composed of black shales, and unconformably overlay the black mudstones of the Lower Cambrian Yanjiahe Formation (Figure 1B).

3 Sampling and analytical methods

The black shale samples in this study were collected from the lowest part of the Shuijingtuo Formation of the Luojiacun section, which is geographically situated in Zigui county, Yichang city in the Western Hubei Region (Figure 1A). Twenty-six bulk black shale samples were taken with a sampling interval ranging from tens of centimeters to 2 meters (Figure 1B). Each sample was ground to 200 mesh with an agate mortar for mineralogical and geochemical analysis.

The mineral composition of black shale samples was determined by X-ray diffraction analysis (XRD, Bruker D8 A25 Advance), which was carried out on powder diffractometer with monochromatic Cu, Kα radiation. The quantitative content of minerals was subsequently analyzed based on the X-ray diffractograms using Software Jade 6.5.

The morphological characteristics of typical minerals and occurrence of some trace elements in black shales were observed by field emission scanning electron microscope (FE-SEM, FEI Quanta 450 FEG) in conjunction with an energy dispersive X-ray spectrometer (SEM-EDS), which can realize the integrated analysis function of image, composition and structure. SEM images of typical minerals were captured by a retractable solid-state backscatter electron detector.

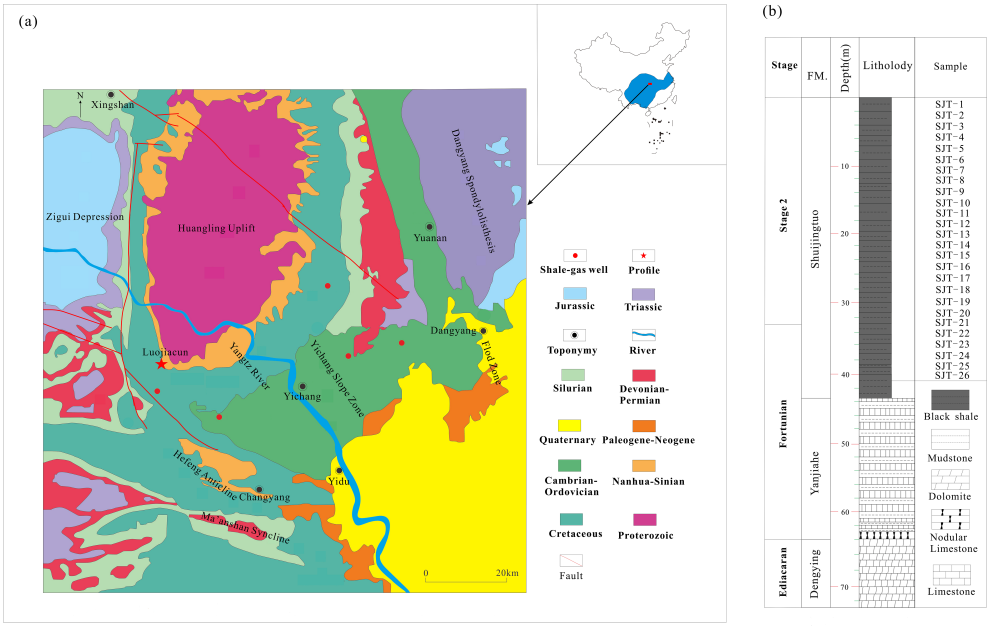

FIGURE 1
(A) Regional geological map of the study area (modified from Chen, 2018); **(B)** sampling column of the Shuingtuo Formation.

The TOC content of black shale samples was determined by a Vario EL III element analyzer with the standard deviation of measurements below ±0.10%. Prior to determination, the black shale samples were first treated by 4 M HCl at 60°C for at least 24 h to remove the carbonate minerals.

The major and trace element concentration of black shale samples was respectively determined by X-ray fluorescence spectrometer (XRF, Primus II) and inductively coupled plasma mass spectrometer (ICP-MS, Agilent 7700e) at the Wuhan Sample Solution Analytical Technology Co., Ltd.

Before XRF analysis, all samples were dried at 105°C for 12 hours, and then no less than 5.0g of each sample was ashed at 815°C using a muffle furnace. The major elements oxides in the sample were determined by the melt plate method. Precision for determination of major elements oxides concentrations is better than 2.5%.

Prior to ICP-MS determination, each black shale sample was acid-digested according to the following process: Dry the samples at 105°C for 12 hours. 50 mg of each sample was digested with 1 ml HNO_3 and 1 ml HF, and heated at 190°C for more than 24 hours. Cool the digestion solution down, and evaporate it at 140°C on an electric heating plate until dry, then digest the residue with 1 ml HNO_3 and evaporate it to dry again. Thereafter, the residue was digested with1 ml HNO_3, 1 ml MQ water and 1 ml of internal standard In (the concentration is 1 μg/g) and heated at 190°C for more than 12 hours. Subsequently, the solution was diluted with 2% HNO_3 for ICP-MS determination. Multi-element standard sample (BHVO-2、BCR-2 and RGM-2) was used for calibration of trace element concentrations. Precision for determination of trace element concentrations is better than 5.0%.

4 Results

4.1 Mineralogical characteristics of black shales

Minerals in the Shuijingtuo black shales from the Luojiacun section are mainly composed of quartz and clay minerals, with small proportions of calcite, albite, clinochlore, and pyrite, as well as traces of siderite and gypsum (Table 1). Quartz is the most abundant mineral (21.1%-68.9%, avg. 43.0%) in the Shuijingtuo black shale. In some cases, quartz occurs with sharp edges and corners and large particles (Figure 2A), indicating a terrigenous origin (Dong et al., 2021; Chen et al., 2022; Ye et al., 2022; Gao et al., 2023). In other cases, quartz occurs as crystals of different sizes with better roundness, which is usually smaller than terrigenous quartz (Figures 2B, I), indicating an authigenic origin. The authigenic quartz was possibly formed from transformation of clay minerals, alteration of clastic minerals (feldspar, mica), dissolution of siliceous biological skeleton, pressure dissolution, or devitrification of volcanic ash (Zhang et al., 2018; Yan et al., 2021).

Illite is the primary clay mineral in the Shuijingtuo black shale (9.7%-52.3%, avg. 29.1% Table 1). Illite occurs in the form of long strips (Figures 2B, C) and pore infillings (Figures 2D, E). The former more likely indicated a terrigenous origin from shallow water shelf or slope sedimentary environment with low TOC content (Zhang et al., 2017). The latter was more likely to represent an authigenic origin, which was probably derived from the alteration of clastic feldspar minerals, the transformation of montmorillonite or mixed layer minerals, or from the precipitation of diagenetic solution (Zhang et al., 2018).

Carbonate minerals in the Shuijingtuo black shale mainly consist of calcite and dolomite, the content of which respectively ranges from 1.0% to 38.0% (avg. 10.8%) and from 1.1% to 6.0% (avg. 3.2%). Calcite

10.3389/fmars.2024.1457964

TABLE 1 Mineral composition and content of black shales of Shujingtuo Formation in Luojiacun, western Hubei Province (%).

Sample	Illite	Clinoch	Quartz	Calcite	Dolomite	Siderite	Pyrite	Gypsum	Albite
SJT-1	29.1	/	68.9	/	1.1	/	0.9	/	/
SJT-2	29.4	/	46.4	9.4	5.1	/	1.9	/	7.7
SJT-3	24.6	/	50.8	4.8	3.8	/	3.9	/	12.2
SJT-4	36.7	/	42.9	3.1	3.7	/	2.5	/	11.2
SJT-5	32.6	/	46.2	3.6	2.5	/	2.4	/	11.9
SJT-6	21.4	/	47.1	3.9	3.6	/	8.7	/	15.2
SJT-7	28.3	/	43.5	6.1	3.9	/	6.0	/	12.2
SJT-8	35.6	/	42.6	6.5	1.5	/	2.5	0.5	10.9
SJT-9	20.6	/	55.2	9.6	2.7	/	2.3	/	9.6
SJT-10	14.4	/	59.6	8.3	4.0	/	3.3	/	10.4
SJT-11	22.2	/	53.0	6.7	3.1	/	3.0	0.7	11.4
SJT-12	31.2	/	48.0	2.7	1.6	/	2.4	1.6	12.6
SJT-13	17.9	/	52.9	11.3	3.1	/	2.5	/	12.3
SJT-14	9.7	/	51.5	18.0	5.0	/	3.8	/	12.1
SJT-15	20.1	/	54.5	12.5	2.0	/	1.8	/	9.1
SJT-16	18.0	/	57.1	10.1	3.2	/	2.2	/	9.5
SJT-17	31.4	0.9	32.8	8.2	3.2	0.6	1.8	/	21.2
SJT-18	32.0	2.6	25.3	16.4	5.0	/	2.6	/	16.1
SJT-19	35.5	4.0	30.8	13.3	1.7	/	1.7	/	12.9
SJT-20	20.0	1.2	29.7	27.6	6.3	/	2.1	/	13.0
SJT-21	30.1	3.8	21.1	38.0	1.9	/	1.2	/	3.9
SJT-22	19.8	7.6	34.6	17.4	2.7	/	1.7	/	16.2
SJT-23	41.9	10.4	28.6	3.6	1.2	/	1.3	/	13.0
SJT-24	29.2	7.5	33.1	10.4	2.7	/	1.3	/	15.7
SJT-25	35.5	8.5	38.7	1.0	1.2	/	1.8	/	13.3
SJT-26	34.6	8.1	22.9	17.7	6.2	/	0.7	/	9.9
MIN	9.7	/	21.1	1.0	1.1	/	0.7	/	3.9
MAX	41.9	10.4	68.9	38.0	6.3	0.6	8.7	1.6	21.2
AVE	27.0	5.4	43.0	10.8	3.1	0.6	2.5	0.9	12.1

mostly exists in the form of fracture- or pore-infillings (Figures 2C, F), while dolomite mainly occurs as single crystals and calcareous cementation (Figure 2C), both indicating an authigenic formation process during the late diagenesis (Shao et al., 1998; Dai et al., 2015).

Pyrite is ubiquitously distributed in the Shuijingtuo black shale (0.7%-8.7%, avg. 2.5%). It mainly occurs in the form of single subhedral crystals (Figure 2H), and framboidal aggregate (Figure 2G), which is indicative of syngenetic origin (Chou, 2012). In a few cases, pyrite also occurs in the form of fracture infillings, filling in cracks of quartz and albite in granular or veinlet form during an epigenetic process (Figures 2A–C).

Albite is the primary feldspar mineral in the Shuijingtuo black shale (3.9%-21.2%, avg. 12.1%), which occurs in the form of long strips (Figure 2H) and subhedral crystals (Figures 2B–E), indicating terrigenous origin and an authigenic origin, respectively. In addition, phosphate minerals, e.g., apatite were also observed under the scanning electron microscope. Apatite is mainly present in the form of authigenic euhedral to subhedral particles (Figures 2A, I).

4.2 Geochemical characteristics of black shales

4.2.1 Major and trace element concentration

Based on the XRF analysis, SiO_2, Al_2O_3 and CaO are the predominant major element oxides in the Shuijingtuo black shale,

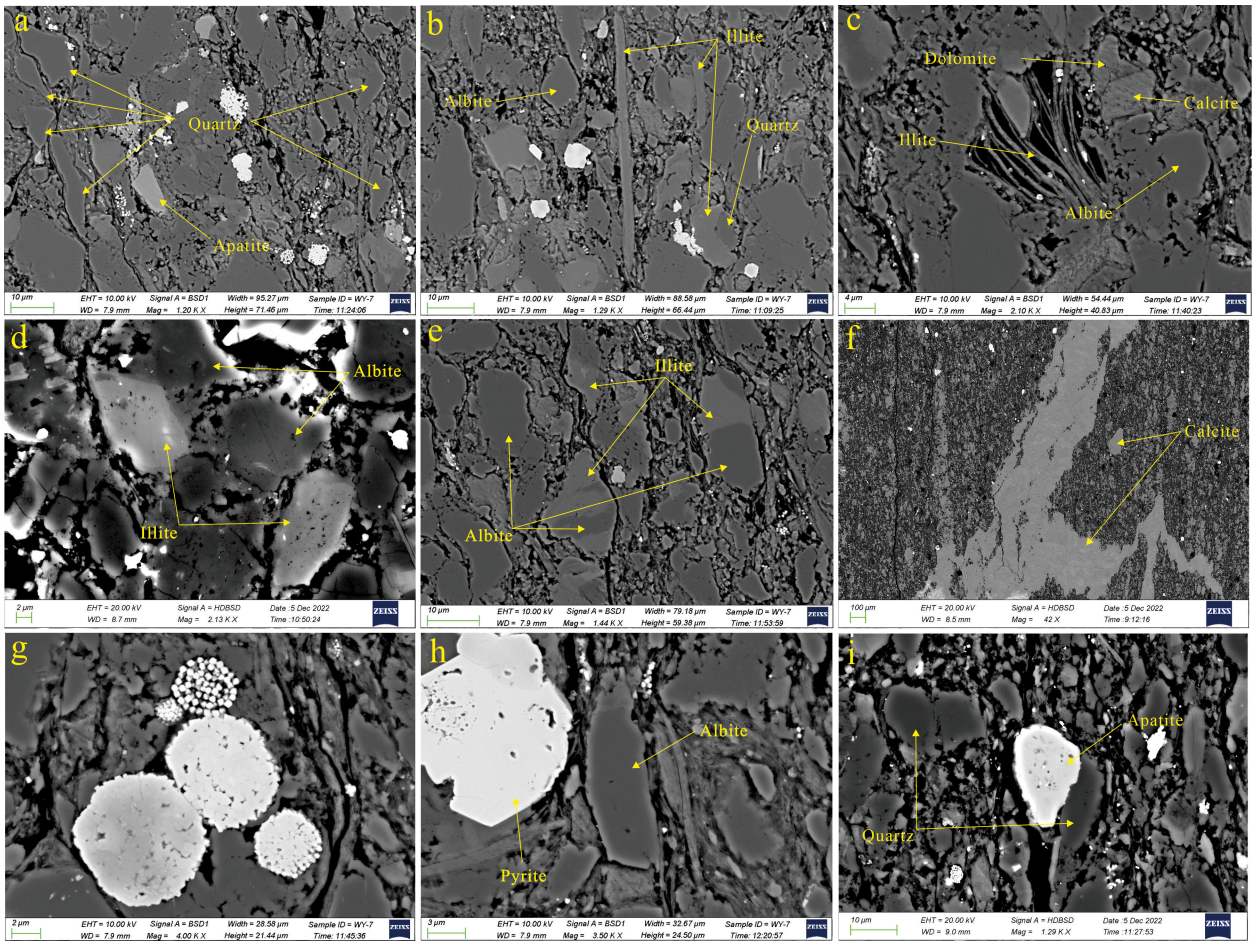

FIGURE 2
Modes of occurrence of minerals in the Shuijingtuo black shale. **(A)** clastic quartz and apatite in sample No.7; **(B)** authigenic quartz, albite and illite in sample No.7; **(C)** illite, albite, calcite and dolomite in sample No.7; **(D)** authigenic illite and albite in sample No.9; **(E)** Mutually metasomatized illite and albite in sample No.7; **(F)** calcite vein in sample No.21; **(G)** framboidal pyrite in sample No.9; **(H)** single subhedral crystals pyrite and albite in sample No.7; **(I)** authigenic quartz, albite and apatite in sample No.7.

followed by Fe_2O_3, K_2O and MgO (Table 2). The content of SiO_2, Al_2O_3 and CaO varies from 37.3% to 65.2% (55.9%), 6.3% to 18.2% (avg. 10.3%), and 1.5% to 22.1% (avg. 8.2%), respectively. Secondarily, the content of Fe_2O_3, K_2O and MgO is respectively 2.3-6.0% (avg. 4.0%), 1.7-4.1% (avg. 2.8%), and 1.1-2.6% (avg. 1.8%). The content of other oxides (TiO_2, Na_2O, MnO and P_2O_5) is less than 1%. Compared with the major element oxide content of North American shale (NASC), CaO content of the Shuijingtuo black shale is slightly enriched (2.26 times higher), while the content of other major elements is similar or depleted. Compared with the average composition of post Archean Australian shale (PAAS), CaO content of the Shuijingtuo black shale is significantly enriched (6.25 times higher), and the content of other major elements is also similar or depleted. The elevated CaO content is ascribed to the relatively high calcite content of the Shuijingtuo black shale.

With respect to the trace elements in the Shuijingtuo black shale, their enrichment degree is evaluated by the concentration coefficient (CC) proposed by Dai et al. (2015). In order to eliminate the influence caused by the change of sedimentary rock composition, the Al-normalized concentration coefficient is used to quantify the enrichment degree of trace elements in this paper (McLennan, 2001a; Piper and Perkins, 2004; Li et al., 2017a, b, c), and the calculation formula is as follows: $CC=(X/Al)_{sample}/(X/Al)_{UCC}$, where X represents a given element in the sample and/or upper crust content (UCC). Compared with the trace element concentration in UCC (Taylor and McLennan, 1995), U is significantly enriched (CC>10), and Ba is enriched (5<CC<10) in the Shuijingtuo black shale (Supplementary Table 1; Figure 3). Uranium and Ba concentration respectively varies from 5.2 μg/g to 68.4 μg/g (avg. 32.4 μg/g) and 708 μg/g to 35156 μg/g (avg. 2846 μg/g). In addition, V, Cr, Ni and Sr are slightly enriched (2<CC<5), the concentration of which respectively ranges from 105 μg/g to 1446 μg/g (avg. 255 μg/g), 97.5 μg/g to 240 μg/g (avg. 165 μg/g), 38.2 μg/g to 216 μg/g (avg. 90.8 μg/g), and 155μg/g to 2583 μg/g (avg. 703 μg/g). The other trace elements (e.g., Li, Be, Sc, Co, Zn, Ga, Rb, Y, Zr, Nb, Sn, Cs, La, Ce, Pr, Nd, Hf, Ta, Tl, Pb and Th) in the Shuijingtuo black shale show similar or depleted concentrations compared to the average concentration of corresponding elements in UCC (CC<2).

The total concentration of rare earth elements (REE) in the Shuijingtuo black shale is 128 μg/g on average (80.9-201 μg/g)

TABLE 2 The content of major element in the blak shales of Shuingtuo Formation in Luojiacun, western Hubei Province (%).

Samples	SiO_2	TiO_2	Al_2O_3	Fe_2O_3	MnO	MgO	CaO	Na_2O	K_2O	P_2O_5	Al_2O_3/TiO_2
SJT-1	61.97	0.57	10.47	3.69	0.02	1.59	4.23	1.01	3.65	0.16	18.31
SJT-2	58.96	0.45	8.39	3.07	0.04	2.05	7.71	0.80	2.88	0.14	18.53
SJT-3	59.45	0.58	10.81	4.14	0.03	1.61	4.56	1.11	3.73	0.14	18.81
SJT-4	60.53	0.62	11.47	4.35	0.04	1.97	4.19	1.11	3.79	0.13	18.62
SJT-5	63.43	0.61	11.21	3.60	0.03	1.52	3.74	1.15	3.68	0.13	18.25
SJT-6	49.82	0.46	8.53	4.73	0.00	1.55	3.72	0.93	2.78	0.16	18.59
SJT-7	62.31	0.54	9.71	3.68	0.04	1.91	4.80	1.03	3.33	0.14	17.91
SJT-8	59.76	0.54	9.57	3.78	0.03	1.28	5.99	0.98	3.24	0.14	17.75
SJT-9	60.95	0.51	9.10	3.14	0.04	1.37	7.06	0.96	2.97	0.16	17.77
SJT-10	63.40	0.54	9.24	3.51	0.03	1.24	5.46	0.99	3.01	0.14	17.15
SJT-11	60.89	0.49	8.66	3.54	0.04	1.54	6.76	0.95	2.80	0.20	17.60
SJT-12	65.16	0.54	9.55	3.49	0.03	1.08	3.65	1.00	3.10	0.22	17.62
SJT-13	59.93	0.45	7.68	3.00	0.05	1.29	8.44	0.86	2.46	0.24	17.27
SJT-14	53.40	0.41	7.30	3.61	0.08	1.67	11.30	0.89	2.28	0.24	17.72
SJT-15	61.97	0.35	6.26	2.28	0.05	1.15	9.16	0.78	1.90	0.16	17.87
SJT-16	61.84	0.38	6.66	2.89	0.07	1.45	8.15	0.85	2.01	0.20	17.75
SJT-17	54.11	0.63	12.46	4.58	0.03	1.82	8.05	1.04	2.77	0.11	19.71
SJT-18	41.73	0.49	10.94	5.10	0.04	2.59	15.15	0.83	2.36	0.10	22.36
SJT-19	48.30	0.55	11.92	4.22	0.04	1.95	12.66	0.87	2.52	0.11	21.83
SJT-20	43.38	0.54	12.23	4.05	0.04	2.49	14.86	0.64	2.74	0.12	22.68
SJT-21	37.33	0.37	8.26	3.49	0.04	1.81	22.12	0.57	1.75	0.12	22.50
SJT-22	50.20	0.51	10.10	5.03	0.05	1.94	12.53	0.85	2.02	0.15	19.89
SJT-23	57.77	0.68	14.23	5.37	0.04	2.18	5.19	1.05	2.97	0.14	20.81
SJT-24	53.15	0.53	10.95	4.79	0.05	2.21	10.63	0.93	2.18	0.13	20.54
SJT-25	56.94	0.81	18.16	6.00	0.03	2.25	1.49	0.80	4.08	0.15	22.42
SJT-26	45.44	0.55	12.65	5.04	0.05	2.52	12.74	0.62	2.70	0.12	22.96
MIN	37.33	0.35	6.26	2.28	0.00	1.08	1.49	0.57	1.75	0.10	/
MAX	65.16	0.81	18.16	6.00	0.08	2.59	22.12	1.15	4.08	0.24	/
AVE	55.85	0.53	10.25	4.01	0.04	1.77	8.24	0.91	2.83	0.15	/
PAAS	63.7	1.01	19.2	7.33	0.1	2.24	1.3	1.21	3.8	0.16	/
NASC	64.9	0.70	16.9	5.67	0.1	2.86	3.6	1.14	4.0	0.13	/
$PASS_N$	0.88	0.52	0.53	0.55	0.35	0.79	6.25	0.75	0.75	0.95	/
$NASC_N$	0.86	0.75	0.61	0.71	0.64	0.62	2.26	0.80	0.71	1.16	/

(Supplementary Table 1), which is lower than that of the UCC (146.4 μg/g), NASC (160.1 μg/g) and PAAS (184.8 μg/g). The total concentration of light rare earth elements (LREE; e.g., La, Ce, Pr, Nd, Sm, Eu, Gd) and heavy rare earth elements (HREE; e.g., Tb, Dy, Ho, Er, Tm, Yb, Lu) respectively ranges from 73.3 μg/g to 190 μg/g (avg. 118 μg/g) and 7.2 μg/g to 14.1 μg/g (avg. 10.3 μg/g), accounting for 92% and 8% of the total REEs. The LREE/HREE ratio ranges from 9.5 to 16.1 (avg. 11.4), higher than that in NASC (9.7), indicating an enrichment of LREE in the Shuijingtuo black shale. Furthermore, according to the chondrite-normalized REE distribution pattern (Figure 4A), the LREE part shows an obvious rightward trend, while the HREE part shows a relatively flat slope, further indicating the high fractionation between LREE and HREE and the enrichment of LREE. When normalized to the REE values of NASC, the Shuijingtuo black shale presents a flat REE distribution pattern (Figure 4B), reflecting a consistent provenance and stable tectonic

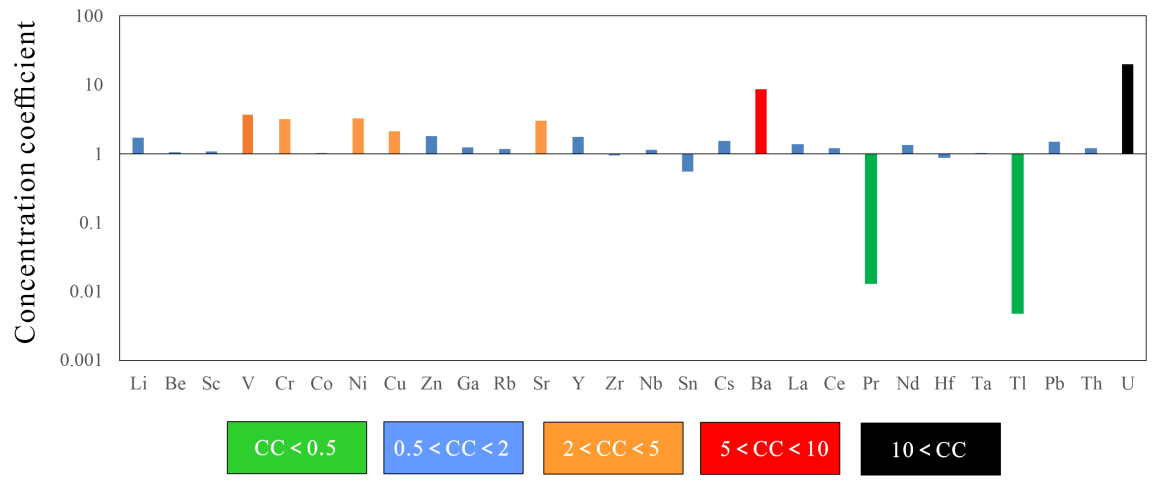

FIGURE 3
Concentration coefficients of trace elements in the Shuijingtuo black shale.

activity (Yan et al., 2021). The NASC-normalized $(La/Sm)_N$ value is 1.13 on average (0.94-1.5), representing a weak fractionation between light rare earth elements.

4.2.2 Distribution and modes of occurrence of elevated elements

According to unary linear regression method, the elevated V, Ni, U and Cr concentration have weak or negative correlation with Al_2O_3 content in the Shuijingtuo black shale (r= -0.07, -0.13, -0.61, -0.39) (Figures 5A–D). Furthermore, it is found that V, Ni, U and Cr concentrations present strong positive correlations with Si_{bio} content in the Shuijingtuo black shale (Figures 5E–H), which indicates that V, Ni, U, and Cr mainly occur in organic form in the Shuijingtuo black shale.

In addition, there is a strong positive correlation between Ba and pyrite in the Shuijingtuo black shale (Figure 5I), indicating that Ba is mainly hosted in pyrite. By contrast, a strong positive correlation between Sr and calcite in the Shuijingtuo black shale indicates that Sr is mainly hosted in calcite (Figure 6).

Vertically, the elevated V and Ni show similar variation characteristics, the contents of which are both higher in the upper portion of the Shuijingtuo black shale from the Luojiacun section (Figure 6). Chromium and U show similar vertical variation characteristics, the content of which are higher in the middle and upper section (Figure 6). Furthermore, Sr content is higher in the lower section and Ba content is higher in the middle section, which presents similar variation to calcite and pyrite content, respectively (Figure 6), furthering indicating the occurrence of Sr with calcite and Ba with pyrite.

5 Discussion

5.1 Tectonic environment

Through outcrop observation, core description, thin section observation, scanning electron microscope observation and geochemical analysis of main and trace elements, it is concluded that the Lower Cambrian sedimentary facies in the Middle Yangtze area is dominated by shallow water shelf - deep water shelf - slope sedimentary facies (Zhang et al., 2019; Zhao et al., 2019; Gao et al., 2020; Ding et al., 2021), among which the western Hubei - Hunan and Guizhou areas belong to deep water shelf - slope sedimentary facies (Zhao et al., 2019). Different tectonic environments have certain characteristics of provenance, and are characterized by specific sedimentary processes, which can be distinguished by several geochemical indexes. Sugisaki et al. (1983) pointed out that the MnO/TiO_2 ratio can be effectively used to distinguish the tectonic environment, with value of 0.5 ~ 3.5 and <0.5 indicative of a deep-sea or trench ocean bottom environment far away from the continent, and a nearshore shallow sea or continental slope environment, respectively. The MnO/TiO_2 ratios of the Shuijingtuo black shale samples range from 0.03 to 0.19 (avg. 0.08), reflecting a nearshore shallow sea or continental slope environment.

Murray (1994) proposed the discrimination diagram of $Al_2O_3/(Al_2O_3+TFe_2O_3)$ - TFe_2O_3/TiO_2 to reflect tectonic environment, in which all the Shuijingtuo black shale samples fall into the continental margin environment (Figure 7A). In the diagram of $Al_2O_3/(Al_2O_3+TFe_2O_3)$ - $(La/Ce)_N$, all the Shuijingtuo black shale samples fall within the continental margin environment as well (Figure 7B). Moreover, the δCe value also can accurately distinguish three tectonic environments near the mid ocean ridge, the pelagic basin and the continental margin. Zhou (2019) proposed that the δCe value of 0.18-0.38, 0.51 ~ 0.61 and 0.74 ~ 0.96 respectively indicates a regional sedimentation near the ocean ridge, the pelagic basin, and the continental margin, and found that the Niutitang (corresponding to the Shuijingtuo) black shale in Northwest Hunan was formed in the deep- to semi deep-water sedimentary environment close to the continental margin. The δCe values of the Shuijingtuo black shale samples in this study range from 0.82 to 1.00 (avg. 0.94), also indicating the normal continental margin environment. Furthermore, SiO_2-log (K_2O/Na_2O) diagram also can

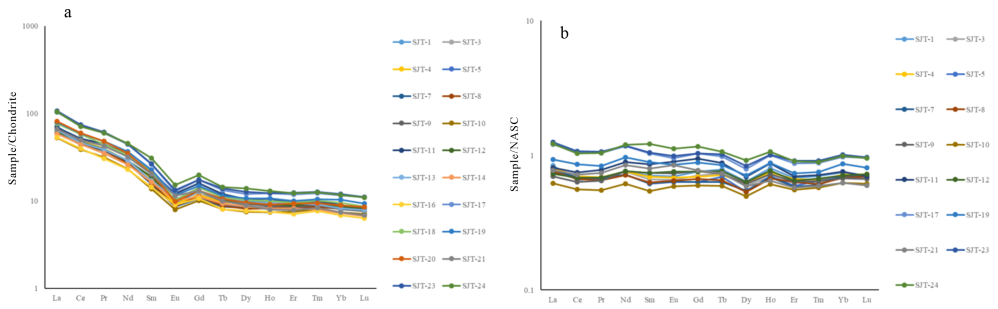

FIGURE 4
REE distribution patterns with chondrite standard **(A)** and NASC standard **(B)** for the Shuijingtuo black shale.

be used to identify the tectonic environment (Roser and Korsch, 1986; Huang et al., 2013). In the diagram of SiO_2-log (K_2O/Na_2O), all the Shuijingtuo black shale samples fall within the passive continental margin (Figure 7C). The normal continental margin includes shallow sea shelf and semi-deep sea slope, which is consistent with the founding that the tectonic location of the Luojiacun profile belongs to shelf margin - upper slope area (Hu, 2019).

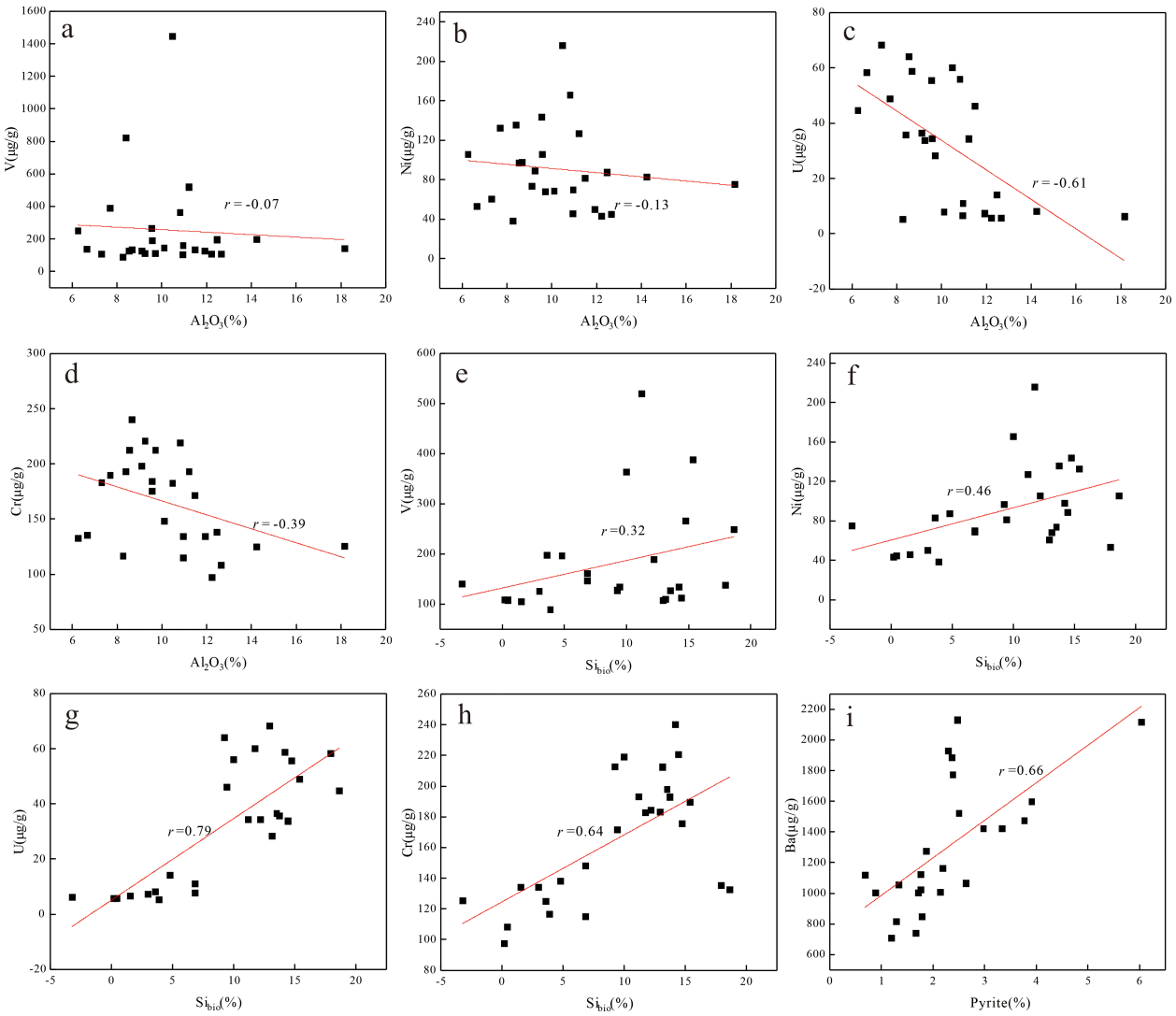

FIGURE 5
Occurrence modes of elevated elements in the Shuijingtuo black shale. **(A)** V vs. Al_2O_3; **(B)** Ni vs. Al_2O_3; **(C)** U vs. Al_2O_3; **(D)** Cr vs. Al_2O_3; **(E)** V vs. Si_{bio}; **(F)** Ni vs. Si_{bio}; **(G)** U vs. Si_{bio}; **(H)** Cr vs. Si_{bio}; **(I)** Ba vs. Pyrite.

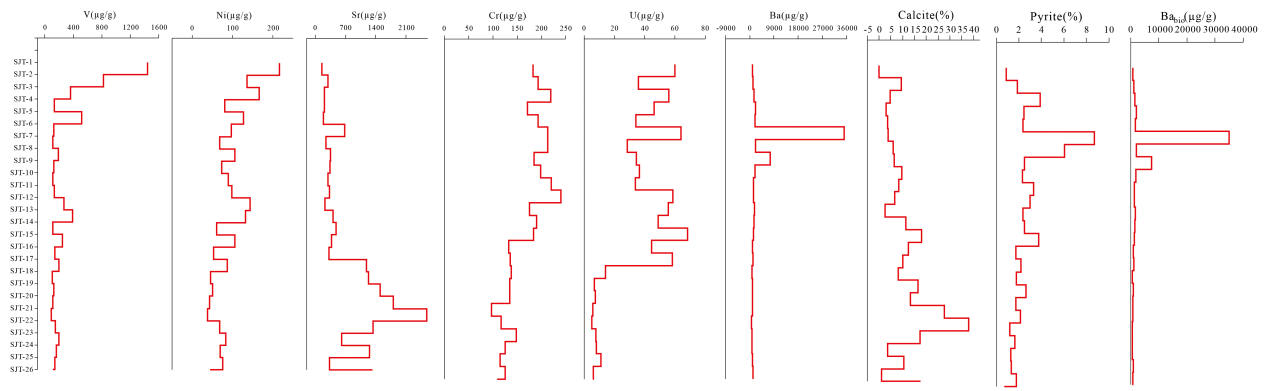

FIGURE 6
Vertical characteristics of enriched trace elements in the Shuijingtuo black shale.

5.2 Sediment provenance

Generally, provenances from sediment source region, marine biological precipitation/recrystallization, and volcanic ash are the dominant sources for black shales and other sediments. The input of terrigenous clastic materials can be manifested by contents and ratios of some elements that are not easily affected by diagenesis and weathering process (Murray, 1994; Murphy et al., 2000; Rachold and Brumsack, 2001; Rimmer, 2004; Tribovillard et al., 2006; Calvert and Pedersen, 2007; Lézin et al., 2013). According to the discriminant indicators of Ti/Al, Th/Al and Zr/Al ratios, the terrigenous clastic input of the Shuijingtuo black shale was of medium degree and remained relatively stable during the deposition process (Yang, 2020). The Al_2O_3/TiO_2 ratio was also widely used as an efficient indicator of the source rock composition, with 3-8, 8-21, and 21-70 respectively of mafic basalt, intermediate

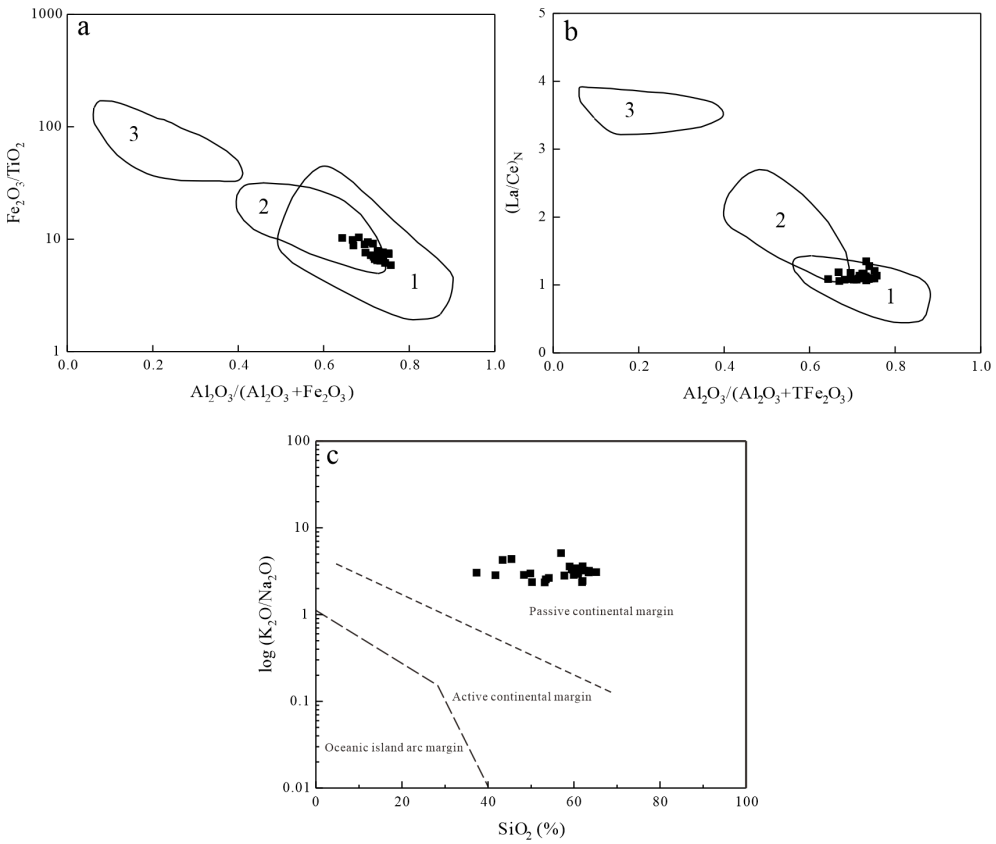

FIGURE 7
Tectonic environment discrimination of Shuijingtuo black shales. **(A)** Diagram of Fe_2O_3/TiO_2 vs. $Al_2O_3/(Al_2O_3+Fe_2O_3)$; **(B)** $(La/Ce)_N$ vs. $(Al_2O_3+TFe_2O_3)$; **(C)** log(K_2O/Na_2O) vs. SiO_2. 1-Continental margin; 2-Pelagic Basin; 3-Mid-oceanic ridge.

granodiorite, and felsic granite source (Hayashi et al., 1997). The Al_2O_3/TiO_2 ratios of the Shuijingtuo black shale in Luojiacun section range from 17.2 to 23.0 (avg. 19.4), predominantly falling within the field of intermediate granodiorite (Figure 8A), which indicates that the terrigenous material source for the Shuijingtuo black shales is of intermediate granodiorite composition. In addition, the TiO_2/Zr ratio of >200, 55-199, and <55 respectively represents a mafic, intermediate, and felsic igneous source rock (Hayashi et al., 1997). The TiO_2/Zr ratios of the Shuijingtuo black shale samples ranges from 38.6 to 56.4, with an average of 44.9, manifesting that the sediment source for the study area is primarily of intermediate to felsic composition (Figure 8B). Moreover, the La–Th–Sc ternary diagram and cross plots of Th/Sc versus Zr/Sc, and La/Th vs. Hf are also reliable indicators of source rock composition (McLennan, 2001b; Vosoughi Moradi et al., 2016; Zhai et al., 2018), according to which the Shuijingtuo black shale samples primarily fall within the field close to felsic and granodiorite source (Figures 8C–E). Based on all these geochemical indexes, it is concluded that the Shuijingtuo black shale from the Luojiacun section were predominantly sourced from intermediate to felsic rocks similar to granodiorite.

Apart from the terrigenous supply, marine biogenic production also contributes as a provenance of the Shuijingtuo black shale from the Luojiacun section. Element Si is often used to reflect the input degree of terrigenous clasts (Murphy et al., 2000; Tribovillard et al., 2006), because Si is generally preserved in quartz and silicate minerals derived from terrigenous clasts (Kidder and Erwin, 2001). However, many studies have shown that marine sediments are usually rich in biogenic silica. The Si/Al ratio of the Shuijingtuo black shale samples ranges from 2.76 to 8.73 (avg. 5.10), which is higher than the average value of terrigenous sediment (3.11, Wedepohl, 1991). This indicates that the excessive Si and the occurrence of authigenic quartz (Figures 2B, I) in the Shuijingtuo black shale may be caused by biogenesis other than terrigenous input (Wojcik-Tabol and Slaczka, 2009). Previous research has also revealed that the provenance for the Early Cambrian black shales in the Yangtze platform was strongly influenced by the marine biogenic production (Wu et al., 2016; Zhu et al., 2021; Xia et al., 2022; Wang et al., 2023; Fu et al., 2023b).

5.3 Palaeoredox conditions

The Palaeoredox environment plays a crucial role in the distribution and evolution of marine organisms, as well as in the circulation, differentiation and enrichment of elements in marine sediments (Chang et al., 2009). It has been confirmed by several research that the early Cambrian black shales in the Yangtze Platform were deposited under an anoxic palaeoredox conditions (Xu et al., 2013; Han et al., 2015; Wu et al., 2016; Zhu et al., 2021; Xia et al., 2022; Wang et al., 2023; Fu et al., 2023b). Correspondingly, several redox sensitive elements and elemental ratios are useful indicators of palaeomarine environment, especially the palaeoredox conditions (Wignall, 1994; Crusius et al., 1996; Algeo, 2004; Algeo and Maynard, 2004; Rimmer, 2004; Rimmer et al., 2004; Tribovillard et al., 2004; Abanda and Hannigan, 2006; Tribovillard et al., 2006; Zhang et al., 2023). For instance, V/(V+Ni) ratio of >0.84, 0.54-0.82, and <0.60 respectively reflects euxinic, anoxic, and dysoxic to oxic conditions, and U/Th ratio of >0.5 is generally indictive of anoxic condition (Jones and Manning, 1994). The U/Th and V/(V+Ni) ratios of the Shuijingtuo black shale samples vary from 0.37 to 10.50 (avg. 4.31) and 0.56 to 0.87 (avg. 0.69), respectively, mostly falling

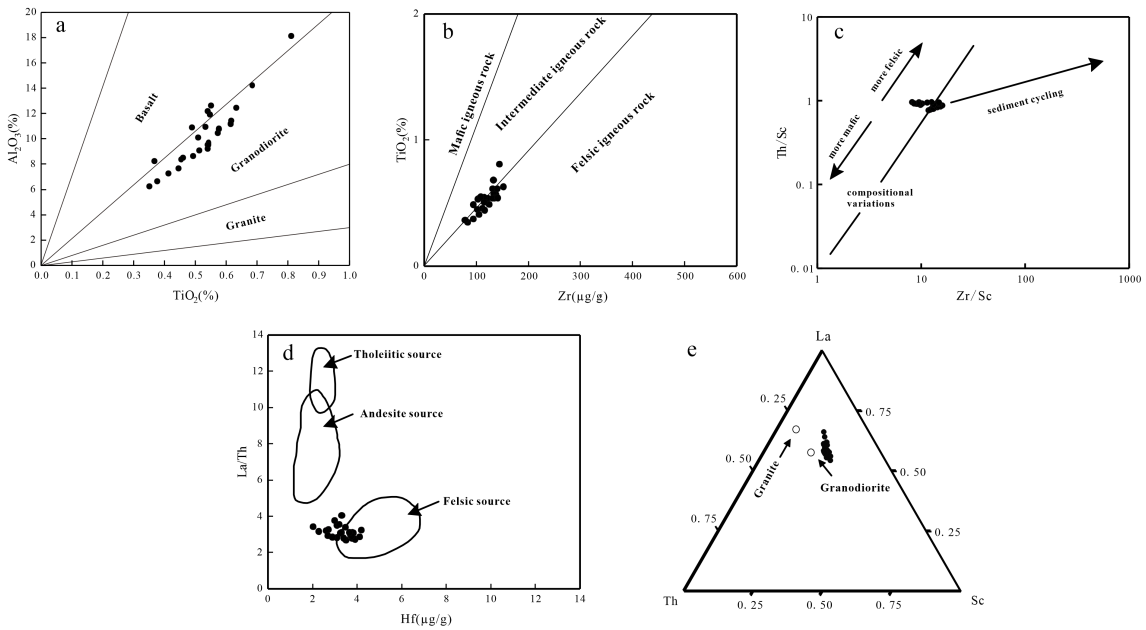

FIGURE 8
Source rock composition of the Shuiijingtuo black shales. **(A)** Cross plots of Al_2O_3 versus TiO_2; **(B)** Cross plot of TiO_2 and Zr; **(C)** Cross plot of Th/Sc versus Zr/Sc; **(D)** La/Th versus Hf bivariate plot; **(E)** La-Th-Sc diagram for the Shuijingtuo black shales.

within the anoxic field in the cross plots of V/(V+Ni) vs. U/Th (Figure 9), indicate that the Shuijingtuo black shale was primarily deposited under anoxic to euxinic conditions. Similarly, Ni/Co ratio of >7, 5-7, and <5 respectively reflects anoxic, dysoxic, and oxic conditions (Jones and Manning, 1994). The Ni/Co ratio of the Shuijingtuo black shale samples vary from 3.24 to 16.62 (avg. 8.18), also indicating deposition of the Shuijingtuo black shale under anoxic conditions.

Furthermore, authigenic uranium (U_a=U_{total}-Th/3) and δU (δU=U/[1/2 (U+Th/3)]) are also commonly used to refer the palaeoredox conditions of sedimentary environment (Wignall, 1994; Wignall and Myers, 1998). The U_a content of less than 5 μg/g generally indicates an oxidizing condition (Jones and Manning, 1994), while δU>1 and <1 respectively indicates an anoxic and normal marine sedimentary environment (Wignall, 1994). The U_a and δU of the Shuijingtuo black shale respectively ranges from 0.6 to 66.2 μg/g (avg. 29.5 μg/g), and 1.05 to 1.94 (avg. 1.68), further manifesting an anoxic sedimentary environment of the Shuijingtuo black shale.

Studies on Ce anomalies in modern seawater show that Ce is a sensitive factor for judging the redox environment (Yang et al., 2008). Generally, under oxidation conditions, Ce^{3+} is oxidized to Ce^{4+}, Ce^{4+} is prone to hydrolysis and precipitation by adsorption of Fe and Mn oxides, which is separated from other rare earth elements, resulting in Ce depletion in seawater. Under anoxic reduction conditions, Fe oxides dissolve and Ce^{4+} is reduced to Ce^{3+}, resulting no obvious Ce anomaly in seawater. Consequently, the variation of δCe value reflects the reduction-oxidation variation of sedimentary environment (DeBaar et al., 1985), and the δCe value of 0.78 is used as the reference value to discriminate the redox conditions of depositional environment (Wright et al., 1987). Coincident with those concluded from the above-mentioned geochemical indexes, the δCe of the Shuijingtuo black shale samples is between 0.82 and 1.00 (avg. 0.94), indicating a relatively anoxic environment as well.

A set of black shales with high organic matter was deposited in the Ordovician-Silurian, and its depositional environment was also anoxic-reductive (Mustafa et al., 2015; Mohammed et al., 2020; Zhou et al., 2021; Yi et al., 2022; Fu et al., 2023a), which is consistent with the depositional environment of the Shuijingtuo Formation in this paper. These results indicate that the shales with high organic matter have a positive correlation with the anoxic environment, which can provide indications for shale gas exploration and paleoenvironmental restoration.

5.4 Palaeomarine productivity

It is widely accepted that apatite is closely related to biological life activities, and has two kinds of formation mechanism. The first is the direct action of biology (Li et al., 2017a), that is, through biological life activities, the dispersed phosphorus in the medium is absorbed and formed into phosphate shell or bone, which is preserved in sediments after biological death, and transformed into apatite during diagenesis. The apatite formed by this mechanism is bioclastic apatite. The second is the indirect effect of biology, which is mainly affected by biomass and redox conditions. The indirect effect of biology is the main form of apatite formation in the early Cambrian. Al_2O_3 is generally considered in geochemistry to be derived only from terrigenous

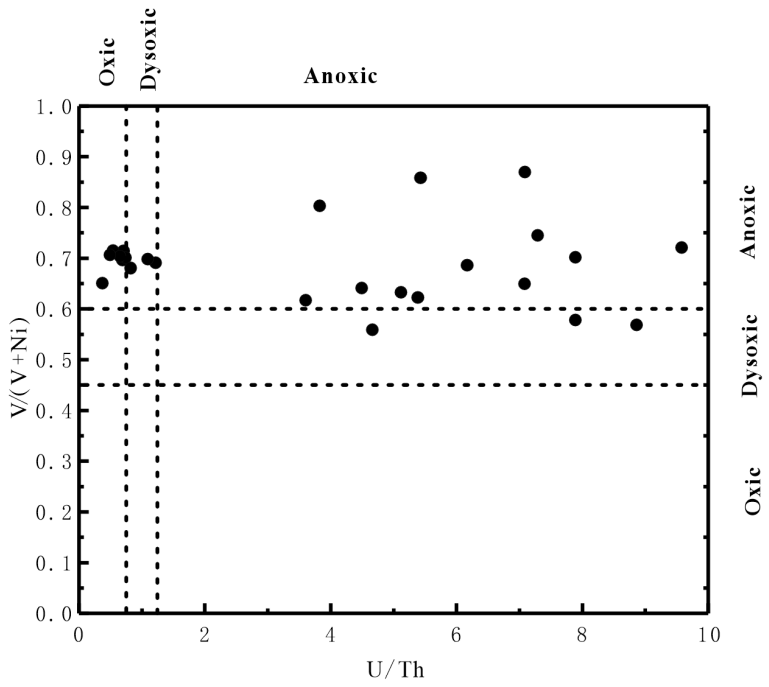

FIGURE 9
Cross plots of U/Th versus V/(V+Ni) of the Shuijingtuo black shale.

clastic inputs (Liu, 2017; Li et al., 2017a). According to unary linear regression method, there is a significant negative correlation between P_2O_5 and Al_2O_3 (Figure 10A), and an obvious positive correlation with TOC (Figure 10B) in the black shale of the Shuijingtuo Formation. Although P is not enriched in the black shale of the Shuijingtuo Formation (Table 2), P is still biogenic and related to higher palaeomarine productivity.

In addition, the content of biological silicon (Si_{bio}) can be used to restore palaemarine productivity, which is quantified by the following formula (Murray and leinen, 1996): $Si_{bio}=Si_{sample} - [(Si/Al)_{average\ shale} \times Al_{sample}]$, where Si_{sample} and Al_{sample} are the total Si and Al content in the studied sample, $(Si/Al)_{average\ shale}$ (3.11) is the Si/Al ratio of average shale (Taylor and Mclennan, 1985). The Si_{bio} content of the Shuijingtuo black shale samples is 9.2% on average, accounting for 35.5% of the total Si. Moreover, the Si_{bio} of the Shuijingtuo black shale is obviously correlated with the TOC (Figure 10I), which is in consistence with previous study that biogenic silicon in marine shale is usually highly correlated with organic carbon content (Luo et al., 2013). The main source of biogenic silicon is various siliceous plankton, such as diatoms, radiolarians and sponge spicule (Aplin and Macquaker, 2011), which is also the primary source of organic matter in marine sediments. The prosperity of plankton is usually accompanied by high organic matter (total organic carbon) content, both of which are responsible for the high paleo productivity. The primary productivity of the Shuijingtuo black shales is relatively high (TOC=1.9-6.5%, avg. 3.9%), manifesting the contribution of biogenic production to black shales.

Furthermore, the element Ba is widely used as a credible indicator for primary productivity of paleo ocean (Dehairs et al., 1987; Dymond et al., 1992; Paytan et al., 1996; Eagle et al., 2003; Tribovillard et al., 2006). The sources of barium in sediments mainly include biogenic barium, barium from terrestrial aluminosilicates, the precipitation of submarine hydrothermal barium and the secretion of some benthic organic organism (Dymond et al., 1992; Gonneea and Paytan, 2006). Only biogenic barium can reflect palaeoproductivity. Barium from biological sources is mainly precipitated in sediments in the form of barium

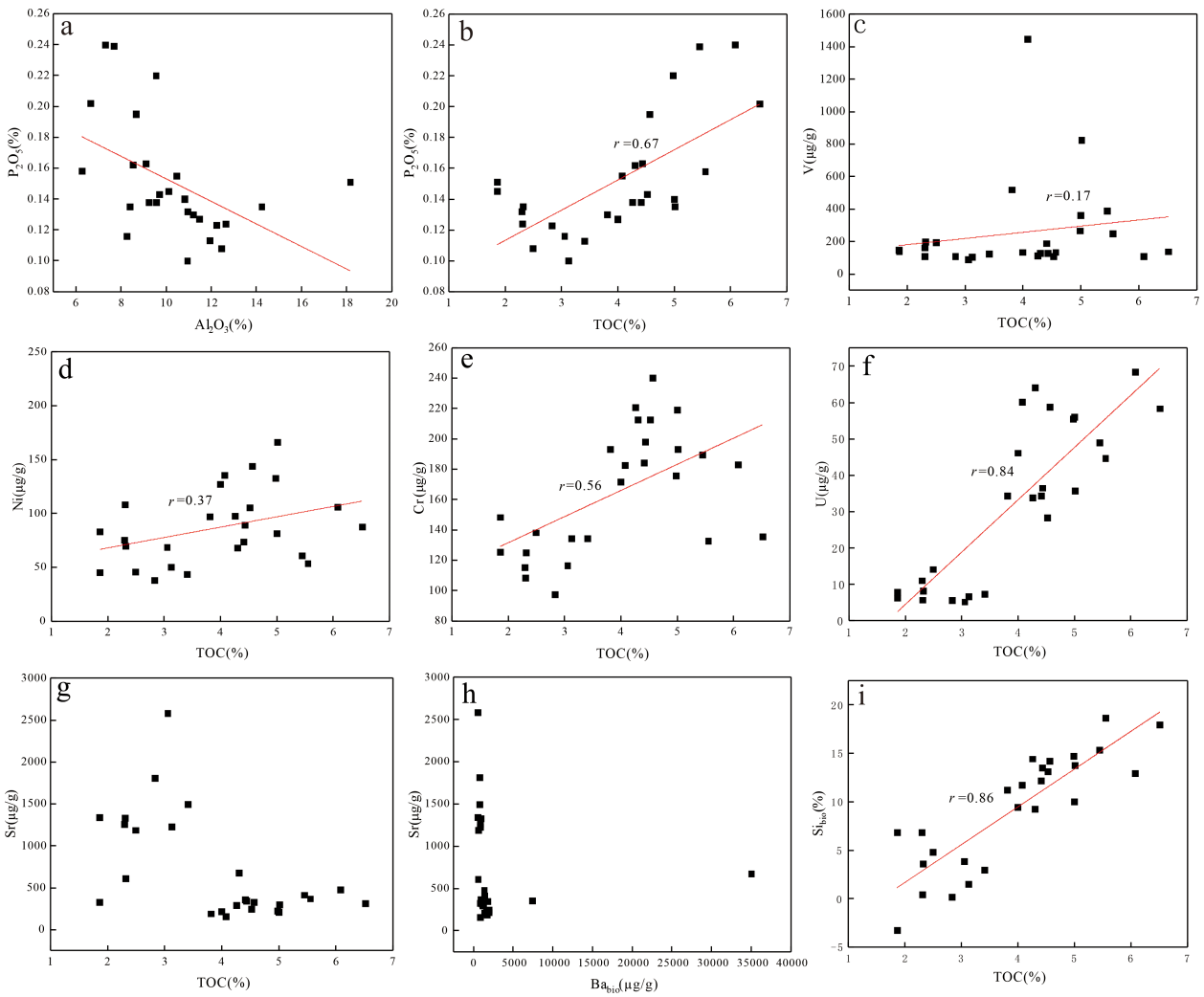

FIGURE 10
Cross plots of P_2O_5 versus Al_2O_3 **(A)** and TOC **(B)**; **(C-F)** TOC versus elevated elements; Sr versus TOC **(G)** and Ba_{bio} **(H)**; **(I)** Si_{bio} versus TOC of the Shuijingtuo black shales.

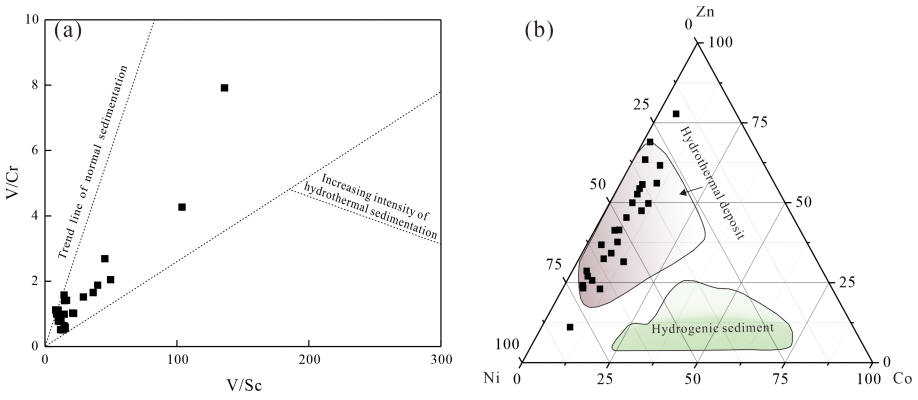

FIGURE 11
(A) Cross plot of V/Cr versus V/Sc; **(B)** Ni-Co-Zn three-phase diagram of the Shuijingtuo black shale.

sulfate (Barite). For the genesis of barium sulfate crystals, the current mainstream view is that there are some SO_4^{2-} ions on the surface of organic matter in the reduction microenvironment of marine diatom cell membrane and some particles, and Ba^{2+} in water will combine with them to form barium sulfate, which will then be deposited on the ocean floor. There is a positive correlation between the amount of barium sulfate crystal precipitation and the amount of organic matter, so the higher the Ba content in the sediment, the higher the primary productivity of the ocean surface.

Currently, it is universally acknowledged that the content of biogenic barium in sediments is 1000 ~ 5000 μg/g, indicating that the Palaeocean surface productivity is high (Murray and Leinen, 1993; Schoepfer et al., 2015). The specific calculation formula is $Ba_{bio}=Ba_{sample} - Al_{sample} \times (Ba/Al)_{clasts}$, where Ba_{sample} and Al_{sample} are the total Ba and Al content in the studied sample, respectively, and $(Ba/Al)_{clasts}$ are the average Ba/Al ratio of crustal rocks (0.0032-0.0046, Taylor and Mclennan, 1985). In this study, the $(Ba/Al)_{clastics}$ value is taken as 0.0032 to calculate the Ba_{bio} content of the Shuijingtuo black shale samples. The Ba_{bio} content of Shuijingtuo black shale samples in Luojiacun profile range from 568 to up to 35011 μg/g (avg. 2672 μg/g), also indicating that the primary productivity of Shuijingtuo black shale in Luojiacun profile is high. The high primary productivity of Shuijingtuo black shale in Luojiacun profile is also consistent with the previous studies (Wu et al., 2016; Zhu et al., 2021; Xia et al., 2022; Wang et al., 2023; Fu et al., 2023b).

5.5 Enrichment mechanism of elevated critical elements

Several productivity- and redox-sensitive elements, such as V, Ni, U, Cr, and Ba have been found enriched in the Shuijingtuo black shale (Yang and Yi, 2012). In the current study, the Shuijingtuo black shale from the Luojiacun section is significantly enriched in U, and enriched in Ba, V, Cr, Ni and Sr.

As stated above, the terrigenous provenance of the Shuijingtuo black shale is primarily of intermediate to felsic composition. However, the contents of U, V, Cr, and Ni in intermediate and felsic rocks are much lower than those in basic and ultrabasic rocks (Vinogradov, 1986), with U, V and Cr content in felsic rocks of 3.5μg/g, 18μg/g, and 8μg/g respectively (Vinogradov, 1986; Condie, 1993). Therefore, the enrichment of these elements in the Shuijingtuo black shale is not ascribed to the intermediate to felsic terrigenous provenance.

Murphy et al. (2000) have found that the strong anoxic condition and slow deposition is responsible for the enrichment of some trace elements, especially those redox sensitive ones in the nutrient-rich upwelling area. Redox sensitive elements such as V, Ni and Cr are prone to enrichment under anoxic conditions in the early diagenetic stage, due to that these redox sensitive elements are generally insoluble and precipitated into insoluble phases under anoxic/euxinic conditions (Sadiq, 1988; Tribovillard et al., 2006). Because the uranium content in open oceans, rivers and upper continental crust is very low, authigenic uranium under anoxic conditions is the main source of uranium in marine sediments. Under anoxic environment, uranium will diffuse in water and deposit in oxygen poor layer to form organometallic ligands and metal complexes (Algeo and Maynard, 2004; Tribovillard et al., 2012). As discussed above, the elevated V, Cr, U, and Ni in the Shuijingtuo black shale show the vertical distribution characteristics (Figure 6). Moreover, V, Ni, Cr, and U have a close correlation with TOC (r=0.17-0.84; Figures 10C–F), indicating that the enrichment of these elements in the black shale is closely related to organic matter by means of complex interaction process under the reduction environment, which needs further investigation.

In addition, the abnormal enrichment of V-Cr-Ni-U element assemblages in organic-rich rocks, e.g., coal and black shale, is often related to hydrothermal activities (Dai et al., 2013a; Jia, 2018). The submarine hydrothermal activity is due to the uplift of the continental crust, which contributes to the intrusion of underground magma along the weak zone, carrying a high content of metal elements into the sedimentary water body. On one hand, the influx of Mo, Ni, U and other elements will form a heavy metal mineral layer in the seawater. On the other hand, the increase of Fe, P and other life elements will provide sufficient nutrients for aquatic organisms, promote the growth of organisms, and produce higher primary productivity. Furthermore, the

occurrence of hydrothermal activities will also locally change the redox conditions of water bodies. A large number of Fe and Mn elements enter the water bodies, forming an H_2S rich anoxic reduction environment at the bottom, resulting in the enrichment of some trace elements (Morforda et al., 2001). Hydrothermal sedimentation will also promote the migration and accumulation of trace elements in sedimentary rocks.

In the current research, the hydrothermal activities is evidenced by geochemical indexes, such as V/Sc and V/Cr ratios, which can be used to distinguish hydrothermal source from normal authigenic element deposition (Yang, 2020). Sc/Cr ratio of <0.120 and >0.144 indicates a hydrothermal sedimentation and normal seawater sedimentation, respectively, while Sc/Cr ratio between 0.120 and 0.144 represents the joint influence of normal seawater sedimentation and hydrothermal sedimentation (Yang, 2020). The Shuijingtuo black shale samples in Luojiacun profile predominantly fall between the trend line of normal sedimentation and the hot water sedimentation line, indicating that the Shuijingtuo black shale was affected by hydrothermal sedimentation (Figure 11A). Additionally, Zn, Ni, Cu and other elements are often enriched due to submarine hydrothermal activities in seawater, while Co is mainly derived from hydrogenic sedimentary environment (Choi and Hariya, 1992). Therefore, the Ni-Co-Zn three-phase diagram is usually used to trace the hydrothermal (Choi and Hariya, 1992). In the Ni-Co-Zn three-phase diagram, the overwhelming majority of the Shuijingtuo black shale samples fall within Hydrothermal deposit area (Figure 11B), further indicating that the Shuijingtuo black shale was affected by hydrothermal sedimentation. Furthermore, calcite is filled in the fracture in the form of veins (Figure 2F), also is an indication of the hydrothermal sedimentation of the Shuijingtuo Formation black shale. Because Luojiacun section was deposited in deep-water continental shelf area, the hydrothermal activity during the deposition process was submarine hydrothermal deposition. Consequently, the submarine hydrothermal fluid accompanying the anoxic condition, high palaeomarine productivity are responsible for the enrichment of U, V, Ni, and Cr in the Shuijingtuo black shale (Figure 12).

With respect to the enrichment of Ba, it is accepted that biogenic process can to some extent give rise to the enrichment of some elements (e.g., Cu, Zn and Ba) by marine organism activity (Breit and Wanty, 1991; Luning et al., 2000; Brumsack, 2006; Tribovillard et al., 2006; Yan et al., 2015; Zhao et al., 2016; Smolarek et al., 2017). The Shuijingtuo black shale of Luojiacun section is characterized by high primary productivity, and occurrence of elevated biological Ba, which indicates that Ba enrichment in Shuijingtuo black shale is mainly the result of higher primary productivity. However, there is no correlation between Sr and TOC (Figure 10G) and Ba_{bio} (Figure 10H) in the Shuijingtuo Formation black shale, indicating that the enrichment of Sr is not related to the biological combination and primary productivity, but mainly related to the anoxic-euxinic sedimentary environment.

6 Conclusion

The Shuijingtuo black shale from the Luojiacun section, Western Hubei Region is characterized by high TOC content and enriched in V-Cr-Ni-U and Sr-Ba elevated critical element assemblages. The elevated V, Cr, Ni, and U present organic affinities, which primarily occur in organic matter in the Shuijingtuo black shale. Strontium is closely correlated to calcite and Ba is closely correlated to pyrite.

The Shuijingtuo black shale was deposited in anoxic conditions in nearshore shallow sea or continental slope environment close to the continental margin, and has a high palaeomarine productivity. Terrigenous provenance of the Shuijingtuo Formation in Luojiacun section is mainly medium-feldspathic granodiorite, which is not

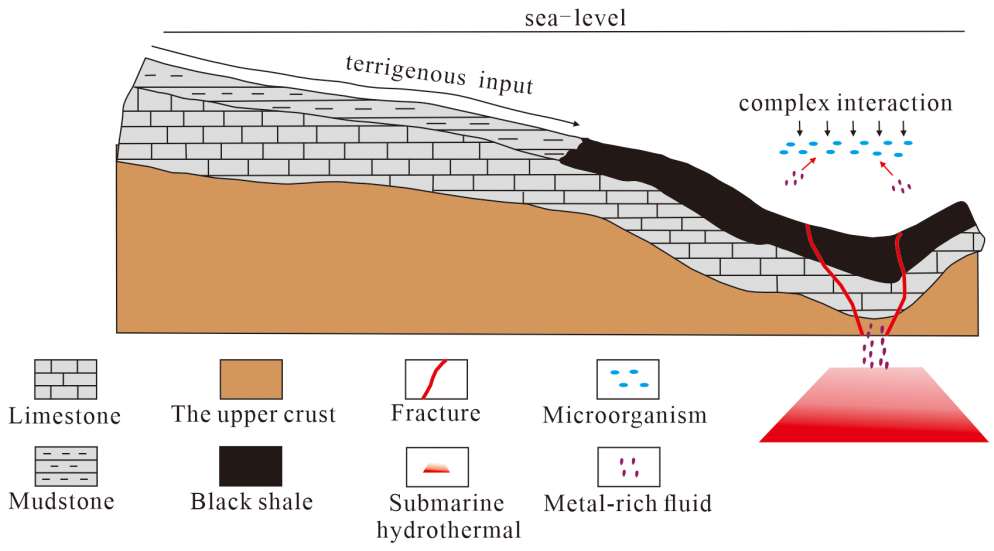

FIGURE 12
Enrichment pattern of elevated elements.

responsible for the enrichment of V-Cr-Ni-U and Sr-Ba critical element assemblages in Shuijingtuo black shale.

The enrichment of U, V, Cr, and Ni in the Shuijingtuo black shale is ascribed to the anoxic condition, high palaeomarine productivity and the submarine hydrothermal solutions. Barium enrichment is predominantly caused by higher primary productivity, while Sr enrichment is primarily ascribed to anoxic depositional conditions.

Data availability statement

The original contributions presented in the study are included in the article/Supplementary Material. Further inquiries can be directed to the corresponding author.

Author contributions

YW: Resources, Writing – original draft, Methodology, Investigation, Conceptualization. JL: Writing – review & editing, Resources, Project administration, Data curation, Conceptualization. YL: Writing – review & editing, Validation. XGZ: Writing – review & editing, Validation. VH: Writing – review & editing. PW: Writing – review & editing. XL: Writing – review & editing, Resources, Investigation. HZ: Writing – review & editing, Resources, Investigation. XYZ: Writing – review & editing, Resources, Investigation.

Funding

The author(s) declare that financial support was received for the research, authorship, and/or publication of this article. This research was funded by the National Key R&D Program of China (No. 2021YFC2902000), the Third Xinjiang Scientific Expedition Program (No. 2023xjkk0100), the Natural Science Foundation of China (Nos. 42372199 and 41972179), the Key State Science and Technology Project of Xinjiang Uygur Autonomous Region (No. 2022A03014-2) and the Foreign Experts Program for The Belt and Road Innovative Talent Exchange (No. DL2023155001L). The authors express great gratitude to the editor and anonymous reviewers for their comments, which greatly improved the manuscript quality.

Conflict of interest

The authors declare that the research was conducted in the absence of any commercial or financial relationships that could be construed as a potential conflict of interest.

Publisher's note

Supplementary material

The Supplementary Material for this article can be found online at: https://www.frontiersin.org/articles/10.3389/fmars.2024.1457964/full#supplementary-material

References

Abanda, P. A., and Hannigan, R. E. (2006). Effect of diagenesis on trace element partitioning in shales. *Chem. Geol.* 230, 42–59. doi: 10.1016/j.chemgeo.2005.11.011

Algeo, T. J. (2004). Can marine anoxic events draw down the trace element inventory of seawater? *Geology* 32, 1057–1060. doi: 10.1130/G20896.1

Algeo, T. J., and Maynard, J. B. (2004). Trace-element behavior and redox facies in core shales of Upper Pennsylvanian Kansas-type cyclothems. *Chem. Geol.* 206, 289–318. doi: 10.1016/j.chemgeo.2003.12.009

Algeo, T. J., and Rowe, H. (2012). Paleoceanographic applications of trace-metal concentration data. *Chem. Geol.* 324-325, 6–18. doi: 10.1016/j.chemgeo.2011.09.002

Aplin, A. C., and Macquaker, J. (2011). Mudstone diversity: Origin and implications for source, seal, and reservoir properties in petroleum systems. *AAPG Bull.* 95, 2031–2059. doi: 10.1306/03281110162

Armstrong, H. A., Abbott, G. D., Turner, B. R., Makhlouf, I. M., Muhammad, A. B., Pedentchouk, N., et al. (2009). Black shale deposition in an Upper Ordovician–Silurian permanently stratified, peri-glacial basin, southern Jordan. *Palaeogeogr. Palaeoclimatol. Palaeoecol.* 273, 368–377. doi: 10.1016/j.palaeo.2008.05.005

Awan, R. S., Liu, C., Feng, D., Zang, Q., Wu, Y., and Ali, S. (2022). Origin of organic matter and depositional characteristics of early Cambrian Niutitang Formation from South China: New insights using molecular fossils. *Geol. J.* 58, 298–314. doi: 10.1002/gj.4593

Breit, G. N., and Wanty, R. B. (1991). Vanadium accumulation in carbonaceous rocks: A review of geochemical controls during deposition and diagenesis. *Chem. Geol.* 91, 83–97. doi: 10.1016/0009-2541(91)90083-4

Brumsack, H.-J. (2006). The trace metal content of recent organic carbon-rich sediments: Implications for Cretaceous black shale formation. *Palaeogeogr. Palaeoclimatol. Palaeoecol.* 232, 344–361. doi: 10.1016/j.palaeo.2005.05.011

Calvert, S. E., and Pedersen, T. F. (2007). Chapter Fourteen Elemental Proxies for Palaeoclimatic and Palaeoceanographic Variability in Marine Sediments: Interpretation and Application. *Develop. Mar. Geol.* 1, 567–644. doi: 10.1016/s1572-5480(07)01019-6

Chang, H., Chu, X., Feng, L., Huang, J., and Zhang, Q. (2009). Redox sensitive trace elements as paleoenvironments proxies. *GEOLOGIC. Rev.* 55, 91–99. doi: 10.16509/j.georeview.2009.01.014

Chen, X., Shi, W., Hu, Q., Hou, Y., Zhai, G., Dong, T., et al. (2022). Origin of authigenic quartz in organic-rich shales of the Niutitang Formation in the northern margin of Sichuan Basin, South China: Implications for pore network development. *Mar. Pet. Geol.* 138, 1–13. doi: 10.1016/j.marpetgeo.2022.105548

Choi, J. H., and Hariya, Y. (1992). Geochemistry and depositional environment of mn oxide deposits in the Tokoro belt, Northeastern Hokkaido, Japan. *Econ. Geol.* 87, 1265–1274. doi: 10.2113/gsecongeo.87.5.1265

Chou, C.-L. (2012). Sulfur in coals: A review of geochemistry and origins. *Int. J. Coal Geol.* 100, 1–13. doi: 10.1016/j.coal.2012.05.009

Condie, K. (1993). Chemical composition and evolution of the upper continental crust: Contrasting results from surface samples and shales. *Chem. Geol.* 104, 1–37. doi: 10.1016/0009-2541(93)90140-E

Cremonese, L., Shields-Zhou, G. A., Struck, U., Ling, H.-F., and Och, L. M. (2014). Nitrogen and organic carbon isotope stratigraphy of the Yangtze Platform during the

Ediacaran–Cambrian transition in South China. *Palaeogeogr. Palaeoclimatol. Palaeoecol.* 398, 165–186. doi: 10.1016/j.palaeo.2013.12.016

Crusius, J., Calvert, S., Pedersen, T., and Sage, D. (1996). Rhenium and molybdenum enrichments in sediments as indicators of oxic, suboxic and sulfidic conditions of deposition. *Earth Planet. Sci. Lett.* 145, 65–78. doi: 10.1016/S0012-821X(96)00204-X

Dai, S., Li, T., Seredin, V. V., Ward, C. R., Hower, J. C., Zhou, Y., et al. (2014). Origin of minerals and elements in the Late Permian coals, tonsteins, and host rocks of the Xinde Mine, Xuanwei, eastern Yunnan, China. *Int. J. Coal Geol.* 121, 53–78. doi: 10.1016/j.coal.2013.11.001

Dai, S., Seredin, V. V., Ward, C. R., Hower, J. C., Xing, Y., Zhang, W., et al. (2015). Enrichment of U–Se–Mo–Re–V in coals preserved within marine carbonate successions: geochemical and mineralogical data from the Late Permian Guiding Coalfield, Guizhou, China. *Miner. Deposita* 50, 159–186. doi: 10.1007/s00126-014-0528-1

Dai, S., Xie, P., Jia, S., Ward, C. R., Hower, J. C., Yan, X., et al. (2017). Enrichment of U-Re-V-Cr-Se and rare earth elements in the Late Permian coals of the Moxinpo Coalfield, Chongqing, China: Genetic implications from geochemical and mineralogical data. *Ore Geol. Rev.* 80, 1–17. doi: 10.1016/j.oregeorev.2016.06.015

Dai, S., Zhang, W., Seredin, V. V., Ward, C. R., Hower, J. C., Song, W., et al. (2013a). Factors controlling geochemical and mineralogical compositions of coals preserved within marine carbonate successions: A case study from the Heshan Coalfield, southern China. *Int. J. Coal Geol.* 109-110, 77–100. doi: 10.1016/j.coal.2013.02.003

Dai, S., Zhang, W., Ward, C. R., Seredin, V. V., Hower, J. C., Li, X., et al. (2013b). Mineralogical and geochemical anomalies of late Permian coals from the Fusui Coalfield, Guangxi Province, Southern China: Influences of terrigenous materials and hydrothermal fluids. *Int. J. Coal Geol.* 105, 60–84. doi: 10.1016/j.coal.2012.12.003

Dai, S., Zheng, X., Wang, X., Finkelman, R. B., Jiang, Y., Ren, D., et al. (2018). Stone coal in China: a review. *Int. Geol. Rev.* 60, 736–753. doi: 10.1080/00206814.2017.1378131

DeBaar, H. J. W., Bacon, M. P., and Brewer, P. G. (1985). Rare earth elements in the Pacific and Atlantic Oceans. *Genchimica Cosmochimica Acta* 49, 1946–1959. doi: 10.1016/0016-7037(85)90089-4

Dehairs, F., Lambert, C. E., Chesselet, R., and Risler, N. (1987). The biological production of marine suspended barite and the barium cycle in the Western Mediterranean Sea. *Biogeochemistry* 4, 119–139. doi: 10.1007/BF02180151

Delabroye, A., and Vecoli, M. (2010). The end-Ordovician glaciation and the Hirnantian Stage: A global review and questions about Late Ordovician event stratigraphy. *Earth Sci. Rev.* 98, 269–282. doi: 10.1016/j.earscirev.2009.10.010

Ding, Y., Li, Z., Liu, S., Song, J., Zhou, X., Sun, W., et al. (2021). Sequence stratigraphy and tectono-depositional evolution of a late Ediacaran epeiric platform in the upper Yangtze area, South China. *Precambrian Res.* 354, 1–24. doi: 10.1016/j.precamres.2020.106077

Dong, T., He, Q., He, S., Zhai, G., Zhang, Y., Wei, S., et al. (2021). Quartz types, origins and organic matter-hosted pore systems in the lower cambrian Niutitang Formation, middle yangtze platform, China. *Mar. Pet. Geol.* 123, 1–21. doi: 10.1016/j.marpetgeo.2020.104739

Dymond, J., Suess, E., and Lyle, M. (1992). Barium in deep-sea sediment: a geochemical proxy for paleoproductivity. *PALEOCEANOGRAPHY* 7, 163–181. doi: 10.1029/92PA00181

Eagle, M., Paytan, A., Arrigo, K. R., van Dijken, G., and Murray, R. W. (2003). A comparison between excess barium and barite as indicators of carbon export. *Paleoceanography* 18, 1–21. doi: 10.1029/2002PA000793

Fathy, D., Baniasad, A., Littke, R., and Sami, M. (2024). Tracing the geochemical imprints of Maastrichtian black shales in southern Tethys, Egypt: Assessing hydrocarbon source potential and environmental signatures. *Int. J. Coal Geol.* 283, 1–17. doi: 10.1016/j.coal.2024.104457

Fu, W., Hu, W., Cai, Q., Wei, S., She, J., Wang, X., et al. (2023a). Sedimentary environment and organic accumulation of the Ordovician–Silurian black shale in Weiyuan, Sichuan Basin, China. *Minerals* 13, 1–19. doi: 10.3390/min13091161

Fu, X., Xu, L., Yan, H., Ye, H., and Ding, J. (2023b). Mineralogy and trace element geochemistry of the early Cambrian black shale-hosted Zhongcun vanadium deposit, southern Qinling, China. *Ore Geol. Rev.* 155, 1–22. doi: 10.1016/j.oregeorev.2023.105371

Fu, Y., Dong, L., Li, C., Qu, W., Pei, H., Qiao, W., et al. (2016). New Re-Os isotopic constrains on the formation of the metalliferous deposits of the Lower Cambrian Niutitang formation. *J. Earth Sci.* 27, 271–281. doi: 10.1007/s12583-016-0606-7

Gao, B., Liu, Z., Shu, Z., Liu, H., Wang, R., Jin, Z., et al. (2020). Reservoir characteristics and exploration of the Lower Cambrian shale gas in the Middle-Upper Yangtze area. *Oil & Gas Geol.* 41, 284–294. doi: 10.11743/ogg20200205

Gao, J., Zhang, J.-k., He, S., Zhao, J.-x., He, Z.-l., Wo, Y.-j., et al. (2019). Overpressure generation and evolution in Lower Paleozoic gas shales of the Jiaoshiba region, China: Implications for shale gas accumulation. *Mar. Pet. Geol.* 102, 844–859. doi: 10.1016/j.marpetgeo.2019.01.032

Gao, P., Xiao, X., Meng, G., Lash, G. G., Li, S., and Han, Y. (2023). Quartz types and origins of the Upper Permian Dalong Formation shale of the Sichuan Basin: Implications for pore preservation in deep shale reservoirs. *Mar. Pet. Geol.* 156, 1–14. doi: 10.1016/j.marpetgeo.2023.106461

Ghosh, S., and Sarkar, S. (2010). Geochemistry of Permo-Triassic mudstone of the Satpura Gondwana basin, central India: Clues for provenance. *Chem. Geol.* 277, 78–100. doi: 10.1016/j.chemgeo.2010.07.012

Gonneea, M. E., and Paytan, A. (2006). Phase associations of barium in marine sediments. *Mar. Chem.* 100, 124–135. doi: 10.1016/j.marchem.2005.12.003

Han, S., Zhang, J., Wang, C., Tang, X., and Chen, Z. Q. (2018). Elemental geochemistry of lower Silurian Longmaxi shale in southeast Sichuan Basin, South China: Constraints for Paleoenvironment. *Geol. J.* 53, 1458–1464. doi: 10.1002/gj.2966

Han, T., Zhu, X., Li, K., Jiang, L., Zhao, C., and Wang, Z. (2015). Metal sources for the polymetallic Ni–Mo–PGE mineralization in the black shales of the Lower Cambrian Niutitang Formation, South China. *Ore Geol. Rev.* 67, 158–169. doi: 10.1016/j.oregeorev.2014.11.020

Hayashi, K.-I., Fujisawa, H., Holland, H. D., and Ohmoto, H. (1997). Geochemistry of ~ 1.9 Ga sedimentary rocks from northeastern Labrador, Canada. *Geochim. Cosmochim. Acta* 61, 4115–4137. doi: 10.1016/S0016-7037(97)00214-7

Hu, J. (2019). Study on geological conditions of shale gas accumulation in the lower Cambrian Shuijing formation of the Huangling domal in western Hubei province. *ChengDu Univ. Technol.* 2020, 1–83. doi: 10.26986/d.cnki.gcdlc.2019.000622

Huang, B., Tian, H., Wilkins, R. W. T., Xiao, X., and Li, L. (2013). Geochemical characteristics, palaeoenvironment and formation model of Eocene organic-rich shales in the Beibuwan Basin, South China Sea. *Mar. Pet. Geol.* 48, 77–89. doi: 10.1016/j.marpetgeo.2013.07.012

Jia, Z. (2018). Geochemistry characteristics of hydrothermal sedimentation in the Lower Cambrian Niutitang Formation in Guizhou. *China Univ. Geosci.* 2022, 1–130. doi: 10.27493/d.cnki.gzdzy.2018.000161

Jones, B., and Manning, D. A. C. (1994). Comparison of geochemical indices used for the interpretation of palaeoredox conditions in ancient mudstones. *Chem. Geol.* 111, 111–129. doi: 10.1016/0009-2541(94)90085-X

Kidder, D. L., and Erwin, D. H. (2001). Secular distribution of biogenic silica through the phanerozoic: comparison of silica-replaced fossils and bedded cherts at the series level. *J. Geology* 109, 509–522. doi: 10.1086/320794

Lézin, C., Andreu, B., Pellenard, P., Bouchez, J.-L., Emmanuel, L., Fauré, P., et al. (2013). Geochemical disturbance and paleoenvironmental changes during the Early Toarcian in NW Europe. *Chem. Geol.* 341, 1–15. doi: 10.1016/j.chemgeo.2013.01.003

Li, T., Gao, H., Wang, C., Cheng, Z., Yang, Y., and Zhan, J. (2022). The accumulation model of organic matters for the Niutitang Formation shale and its control on the pore structure: a case study from Northern Guizhou. *J. Pet. Explor. Prod. Technol.* 12, 2047–2065. doi: 10.1007/s13202-021-01452-3

Li, D., Li, R., Zhu, Z., Wu, X., Cheng, J., Liu, F., et al. (2017a). Origin of organic matter and paleo-sedimentary environment reconstruction of the Triassic oil shale in Tongchuan City, Southern Ordos Basin (China). *Fuel* 208, 223–235. doi: 10.1016/j.fuel.2017.07.008

Li, D., Li, R., Zhu, Z., Wu, X., Liu, F., Zhao, B., et al. (2017b). Elemental characteristics and paleoenvironment reconstruction: a case study of the Triassic lacustrine Zhangjiatan oil shale, southern Ordos Basin, China. *Acta Geochim.* 37, 134–150. doi: 10.1007/s11631-017-0193-z

Li, D., Li, R., Zhu, Z., and Xu, F. (2017c). Elemental characteristics of lacustrine oil shale and its controlling factors of palaeo-sedimentary environment on oil yield: a case from Chang 7 oil layer of Triassic Yanchang Formation in southern Ordos Basin. *Acta Geochim.* 37, 228–243. doi: 10.1007/s11631-017-0206-y

Liu, Q. (2017). Element geochemical characteristics of source rocks in the Shahejie Formation in Well Fangye-1, Dongying sag and their geological significance. *Petrol. Geol. Recovery Efficiency* 24, 40–52. doi: 10.13673/j.cnki.cn37-1359/te.2017.05.006

Liu, Z., Yan, D., and Niu, X. (2020). Insights into pore structure and fractal characteristics of the lower Cambrian niutitang formation shale on the Yangtze platform, South China. *J. Earth Sci.* 31, 169–180. doi: 10.1007/s12583-020-1259-0

Luning, S., Craig, J., Loydell, D. K., Storch, P., and Fitches, B. (2000). Lower Silurian 'hot shales' in North Africa and Arabia: regional distribution and depositional model. *Earth-Sci. Rev.* 49, 121–200. doi: 10.1016/S0012-8252(99)00060-4

Luo, Q., Zhong, N., Zhu, L., Wang, Y., Qin, J., Qi, L., et al. (2013). Correlation of burial organic carbon and paleoproductivity in the mesoproterozoic hongshuizhuang formation, northern north china. *Chin. Sci. Bull.* 58, 1299–1309. doi: 10.1007/s11434-012-5534-z

McLennan, S. M. (2001a). Relationships between the trace element composition of sedimentary rocks and upper continental crust. *Geochem. Geophys. Geosyst.* 2. doi: 10.1029/2000GC000109

McLennan, S. M. (2001b). Relationships between the trace element composition of sedimentary rocks and upper continental crust. *Geochem. Geophys. Geosyst.* 2. doi: 10.1029/2000GC000109

Mohammed, I. Q., Farouk, S., Baioumy, H., Lotfy, N. M., and Al-Hadidy, A. H. (2020). Mineralogical and geochemical characteristics of the Paleozoic source rocks, Akkas gas field, Western Desert of Iraq: Implications for their origin, maturation and Ordovician-Silurian transition. *Mar. Pet. Geol.* 118, 1–18. doi: 10.1016/j.marpetgeo.2020.104432

Morforda, J. L., Russell, A. D., and Emerson, S. (2001). Trace metal evidence for changes in the redox environment associated with the transition from terrigenous clay to diatomaceous sediment, Saanich Inlet, BC. *Mar. Geol.* 174, 355–369. doi: 10.1016/S0025-3227(00)00160-2

Murphy, A. E., Sageman, B. B., Hollander, D. J., Lyons, T. W., and Brett, C. E. (2000). Black shale deposition and faunal overturn in the Devonian Appalachian Basin: Clastic starvation, seasonal water-column mixing, and efficient biolimiting nutrient recycling. *Paleoceanography* 15, 280–291. doi: 10.1029/1999PA000445

Murray, R. W. (1994). Chemical criteria to identify the depositional environment of chert: general principles and applications. *Sediment. Geol.* 90, 213–232. doi: 10.1016/0037-0738(94)90039-6

Murray, R. W., and Leinen, M. (1993). Biogenic flux of al to sediment in the central equatorial pacific ocean: evidence for increased productivity during glacial periods. *PALEOCEANOGRAPHY* 8, 651–670. doi: 10.1029/93PA02195

Murray, R. W., and Leinen, M. (1996). Scavenged excess aluminum and its relationship to bulk titanium in biogenic sediment from the central equatorial pacific ocean. *Geochim. Cosmochim. Acta* 60, 3869–3878. doi: 10.1016/0016-7037(96)00236-0

Mustafa, K. A., Sephton, M. A., Watson, J. S., Spathopoulos, F., and Krzywiec, P. (2015). Organic geochemical characteristics of black shales across the Ordovician–Silurian boundary in the Holy Cross Mountains, central Poland. *Mar. Pet. Geol.* 66, 1042–1055. doi: 10.1016/j.marpetgeo.2015.08.018

Och, L. M., Shields-Zhou, G. A., Poulton, S. W., Manning, C., Thirlwall, M. F., Li, D., et al. (2013). Redox changes in Early Cambrian black shales at Xiaotan section, Yunnan Province, South China. *Precambrian Res.* 225, 166–189. doi: 10.1016/j.precamres.2011.10.005

Paytan, A., Kastner, M., and Chavez, F. P. (1996). Glacial to interglacial fluctuations in productivity in the equatorial pacific as indicated by marine barite. *Science* 274, 1355–1357. doi: 10.1126/science.274.5291.1355

Piper, D. Z., and Perkins, R. B. (2004). A modern vs. Permian black shale—the hydrography, primary productivity, and water-column chemistry of deposition. *Chem. Geol.* 206, 177–197. doi: 10.1016/j.chemgeo.2003.12.006

Pohl, A., Donnadieu, Y., Le Hir, G., and Ferreira, D. (2017). The climatic significance of Late Ordovician-early Silurian black shales. *Paleoceanography* 32, 397–423. doi: 10.1002/2016PA003064

Rachold, V., and Brumsack, H.-J. (2001). Inorganic geochemistry of Albian sediments from the Lower Saxony Basin NW Germany: palaeoenvironmental constraints and orbital cycles. *Palaeogeogr. Palaeoclimatol. Palaeoecol.* 174, 121–143. doi: 10.1016/S0031-0182(01)00290-5

Rimmer, S. M. (2004). Geochemical paleoredox indicators in Devonian–Mississippian black shales, Central Appalachian Basin (USA). *Chem. Geol.* 206, 373–391. doi: 10.1016/j.chemgeo.2003.12.029

Rimmer, S. M., Thompson, J. A., Goodnight, S. A., and Robl, T. L. (2004). Multiple controls on the preservation of organic matter in Devonian–Mississippian marine black shales: geochemical and petrographic evidence. *Palaeogeogr. Palaeoclimatol. Palaeoecol.* 215, 125–154. doi: 10.1016/S0031-0182(04)00466-3

Roser, B., and Korsch, R. (1986). Determination of tectonic setting of sandstone-mudstone suites using SiO2 content and K2O/Na2O ratio. *J. Geol.* 94, 635–650. doi: 10.1086/629071

Sadiq, M. (1988). Thermodynamic solubility relationships of inorganic vanadium in the marine environment. *Mar. Chem.* 23, 87–96. doi: 10.1016/0304-4203(88)90024-2

Schoepfer, S. D., Shen, J., Wei, H., Tyson, R. V., Ingall, E., and Algeo, T. J. (2015). Total organic carbon, organic phosphorus, and biogenic barium fluxes as proxies for paleomarine productivity. *Earth Sci. Rev.* 149, 23–52. doi: 10.1016/j.earscirev.2014.08.017

Shao, L., Zhang, P., Ren, D., and Lei, J. (1998). Late Permian coal-bearing carbonate successions in southern China: coal accumulation on carbonate platforms. *Int. J. Coal Geol.* 37, 235–256. doi: 10.1016/S0166-5162(98)00008-1

Sheets, H. D., Mitchell, C. E., Melchin, M. J., Loxton, J., Storch, P., Carlucci, K. L., et al. (2016). Graptolite community responses to global climate change and the Late Ordovician mass extinction. *Proc. Natl. Acad. Sci. U.S.A.* 113, 8380–8385. doi: 10.1073/pnas.1602102113

Smolarek, J., Marynowski, L., Trela, W., Kujawski, P., and Simoneit, B. R. T. (2017). Redox conditions and marine microbial community changes during the end-Ordovician mass extinction event. *Global Planet. Change* 149, 105–122. doi: 10.1016/j.gloplacha.2017.01.002

Sugisaki, R., Ido, M., Takeda, H., Isobe, Y., Hayashi, Y., Nakamura, N., et al. (1983). Origin of hydrogen and carbon dioxide in fault gases and its relation to fault activity. *J. Geology* 91, 239–258. doi: 10.1086/628769

Taylor, S. R., and McLennan, S. M. (1995). The geochemical evolution of the continental crust. *Rev. Geophys.* 33, 241–265. doi: 10.1029/95RG00262

Taylor, S. R., and McLennan, S. M. (1985). *The continental crust: Its composition and evolution* (Blackwell, Oxford). Available at: https://www.osti.gov/biblio/6582885.

Tian, T., Zhou, S., Fu, D., Yang, F., and Li, J. (2019). Characterization and controlling factors of pores in the Lower Cambrian Niutitang shale of the Micangshan Tectonic Zone, SW China. *Arabian J. Geosci.* 12, 1–14. doi: 10.1007/s12517-019-4407-z

Trela, W., Podhalańska, T., Smolarek, J., and Marynowski, L. (2016). Llandovery green/grey and black mudrock facies of the northern Holy Cross Mountains (Poland) and their relation to early Silurian sea-level changes and benthic oxygen level. *Sediment. Geol.* 342, 66–77. doi: 10.1016/j.sedgeo.2016.06.003

Tribovillard, N., Algeo, T. J., Baudin, F., and Riboulleau, A. (2012). Analysis of marine environmental conditions based onmolybdenum–uranium covariation—Applications to Mesozoic paleoceanography. *Chem. Geol.* 324-325, 46–58. doi: 10.1016/j.chemgeo.2011.09.009

Tribovillard, N., Algeo, T. J., Lyons, T., and Riboulleau, A. (2006). Trace metals as paleoredox and paleoproductivity proxies: An update. *Chem. Geol.* 232, 12–32. doi: 10.1016/j.chemgeo.2006.02.012

Tribovillard, N., Averbuch, O., Devleeschouwer, X., Racki, G., and Riboulleau, A. (2004). Deep-water anoxia over the Frasnian–Famennian boundary (La Serre, France): a tectonically induced oceanic anoxic event? *Terra Nova* 16, 288–295. doi: 10.1111/j.1365-3121.2004.00562.x

Vinogradov, V. (1986). Strontium isotopic composition and problems of genesis of anorthosites. *Izvestiya akademii nauk sssr seriya geologicheskaya*. 8–15.

Vosoughi Moradi, A., Sarı, A., and Akkaya, P. (2016). Geochemistry of the Miocene oil shale (Hançili Formation) in the Çankırı-Çorum Basin, Central Turkey: Implications for Paleoclimate conditions, source–area weathering, provenance and tectonic setting. *Sediment. Geol.* 341, 289–303. doi: 10.1016/j.sedgeo.2016.05.002

Wan, Y., Zhang, S., Tang, S., Pan, Z., and Wu, W. (2018). A comparative study of characterization of lower Palaeozoic Niutitang shale in northwestern Hunan, China. *J. Nat. Gas Sci. Eng.* 53, 284–300. doi: 10.1016/j.jngse.2018.03.015

Wang, Z., Tan, J., Hilton, J., Dick, J., and Wen, Z. (2023). Trace element enrichment mechanisms in black shales during the early cambrian (ca. 521–514 Ma), South China. *Mar. Pet. Geol.* 149, 1–13. doi: 10.1016/j.marpetgeo.2022.106083

Wedepohl, K. (1991). Chemical composition and fractionation of the continental crust. *Geol. Rundsch.* 80, 207–223. doi: 10.1007/BF01829361

Wei, H., Feng, Q., Yu, J., and Chang, S. (2022). Characteristics and sources of organic matter from the early Cambrian niutitang formtion and its preservation environment in Guizhou. *J. Earth Sci.* 33, 933–944. doi: 10.1007/s12583-020-1371-1

Wignall, P. B. (1994). 1.Sequence stratigraphy - applications to basins in Northern England: Leeds, UK. *J. Pet. Geol.* 17, 243–243. doi: 10.1111/j.1747-5457.1994.tb00129.x

Wignall, P. B., and Myers, K. J. (1998). Interpreting benthic oxygen levels in mudrocks: A new approach. *GEOLOGY* 16, 452–455. doi: 10.1130/0091-7613(1988)016<0452:IBOLIM>2.3.CO;2

Wójcik-Tabol, P., and Ślączka, A. (2009). "Provenance and diagenesis of siliciclastic and organic material in the albian-turonian sediments (Silesian nappe, lanckorona, outer carpathians, poland): preliminary studies," in *Annales societatis geologorum poloniae: Polskie towarzystwo geologiczne*, 53–66.

Wright, J., Schrader, H., and holser, W. T. (1987). Paleoredox variations in ancient oceans recorded by rare earth elements in fossil apatite. *Geochim. Cosmochim. Acta* 51, 631–644. doi: 10.1016/0016-7037(87)90075-5

Wu, C., Zhang, L., Zhang, T., Tuo, J., Song, D., Liu, Y., et al. (2020). Reconstruction of paleoceanic redox conditions of the lower Cambrian Niutitang shales in northern Guizhou, Upper Yangtze region. *Palaeogeogr. Palaeoclimatol. Palaeoecol.* 538, 1–11. doi: 10.1016/j.palaeo.2019.109457

Wu, K., Zhang, T., Yang, Y., Sun, Y., and Yuan, D. (2016). Contribution of oxygenic photosynthesis to palaeo-oceanic organic carbon sink fluxes in Early Cambrian Upper Yangtze shallow sea: Evidence from black shale record. *J. Earth Sci.* 27, 211–224. doi: 10.1007/s12583-016-0693-5

Wu, Y., Fan, T., Jiang, S., Yang, X., Ding, H., Meng, M., et al. (2015). Methane adsorption capacities of the lower paleozoic marine shales in the Yangtze platform, South China. *Energy Fuels* 29, 4160–4167. doi: 10.1021/acs.energyfuels.5b00286

Xi, Z., Tang, S., and Wang, J. (2018). The reservoir characterization and shale gas potential of the Niutitang formation: Case study of the SY well in northwest Hunan Province, South China. *J. Petrol. Sci. Eng.* 171, 687–703. doi: 10.1016/j.petrol.2018.08.002

Xia, P., Hao, F., Tian, J., Zhou, W., Fu, Y., Guo, C., et al. (2022). Depositional environment and organic matter enrichment of early Cambrian niutitang black shales in the upper Yangtze Region, China. *Energies* 15, 1–21. doi: 10.3390/en15134551

Xu, L., Lehmann, B., and Mao, J. (2013). Seawater contribution to polymetallic Ni–Mo–PGE–Au mineralization in Early Cambrian black shales of South China: Evidence from Mo isotope, PGE, trace element, and REE geochemistry. *Ore Geol. Rev.* 52, 66–84. doi: 10.1016/j.oregeorev.2012.06.003

Yan, D., Chen, D., Wang, Q., and Wang, J. (2010). Large-scale climatic fluctuations in the latest Ordovician on the Yangtze block, south China. *Geology* 38, 599–602. doi: 10.1130/G30961.1

Yan, D., Li, S., Fu, H., Jasper, D. M., Zhou, S., Yang, X., et al. (2021). Mineralogy and geochemistry of Lower Silurian black shales from the Yangtze platform, South China. *Int. J. Coal Geol.* 237, 1–18. doi: 10.1016/j.coal.2021.103706

Yan, D., Wang, H., Fu, Q., Chen, Z., He, J., and Gao, Z. (2015). Geochemical characteristics in the Longmaxi Formation (Early Silurian) of South China: Implications for organic matter accumulation. *Mar. Pet. Geol.* 65, 290–301. doi: 10.1016/j.marpetgeo.2015.04.016

Yang, J., and Yi, F. (2012). A study on occurrence modes and enrichment patterns of lower Cambrian black shale series in northern Guizhou province, China. *Acta Mineral. Sin.* 32, 281–287. doi: 10.16461/j.cnki.1000-4734.2012.02.022

Yang, X. (2020). Depositional environment and organic matter accumulation of the Lower Cambrian Niutitang Formation shale in northern Guizhou. *China Univ. Geosciences.* 2020, 1–77. doi: 10.27493/d.cnki.gzdzy.2020.000329

Yang, X., Zhu, M., Zhao, Y., Zhang, J., Guo, Q., and Pi, D. (2008). REE geoche mical characteristics of the Ediacaran-Lower cambrian black rock series i n eastern guizhou. *Geological Rev.* 54, 3–15. doi: 10.16509/j.georeview.2008.01.003

Ye, J., and Fan, D. (2000). Characteristics and mineralization of ore deposits related to black shale series. *Bull. Mineral. Petrol. Geochem.* 19, 95–102.

Ye, Y., Tang, S., Xi, Z., Jiang, D., and Duan, Y. (2022). Quartz types in the Wufeng-Longmaxi Formations in southern China: Implications for porosity evolution and shale brittleness. *Mar. Pet. Geol.* 137, 1–15. doi: 10.1016/j.marpetgeo.2021.105479

Yi, X., Ji, X., Huang, Y., Liu, Z., and Meng, J. (2022). Black shale paleo-environmental reconstructions: A geochemical case study of two Ordovician–Silurian boundary sections in middle Yangtze area, China. *Front. Earth Sci.* 10. doi: 10.3389/feart.2022.842752

Yin, L.-M., Borjigin, T., Knoll, A. H., Bian, L.-Z., Xie, X.-M., Bao, F., et al. (2017). Sheet-like microfossils from hydrothermally influenced basinal cherts of the lower Cambrian (Terreneuvian) Niutitang Formation, Guizhou, South China. *Palaeoworld* 26, 1–11. doi: 10.1016/j.palwor.2016.01.005

Zhai, L., Wu, C., Ye, Y., Zhang, S., and Wang, Y. (2018). Fluctuations in chemical weathering on the Yangtze Block during the Ediacaran–Cambrian transition: Implications for paleoclimatic conditions and the marine carbon cycle. *Palaeogeogr. Palaeoclimatol. Palaeoecol.* 490, 280–292. doi: 10.1016/j.palaeo.2017.11.006

Zhang, H., Wu, J., Jin, X., and Li, G. (2018). The genetic type and its geological indication significance of shale minerals in Niutitang Formation. *Coal Geol. Explor.* 46, 61–67. doi: 10.3969/j.issn.1001-1986.2018.02.010

Zhang, J., Xu, H., Zhou, Z., Ren, P., Guo, J., and Wang, Q. (2019). Geological characteristics of shale gas reservoir in Yichang area, western Hubei. *Acta Petrolei Sin.* 40, 887–899. doi: 10.7623/syxb201908001

Zhang, K., Li, X., Wang, Y., Liu, W., Yu, Y., Zhou, L., et al. (2021). Paleo-environments and organic matter enrichment in the shales of the Cambrian Niutitang and Wunitang Formations, south China: Constraints from depositional environments and geochemistry. *Mar. Pet. Geol.* 134, 1–11. doi: 10.1016/j.marpetgeo.2021.105329

Zhang, K., Liu, R., Bai, E., Zhao, Z., Peyrotty, G., Fathy, D., et al. (2023). Biome responses to a hydroclimatic crisis in an Early Cretaceous (Barremian–Aptian) subtropical inland lake ecosystem, Northwest China. *Palaeogeogr. Palaeoclimatol. Palaeoecol.* 622, 1–22. doi: 10.1016/j.palaeo.2023.111596

Zhang, Q., Wang, J., Yu, Q., Wang, X., Zhao, A., and Lei, Z. (2017). Geochemical features and paleoenvironment of shales in longmaxi formation of complicated structure area, Southwestern Sichuan basin. *Xinjiang Petrol. Geol.* 38, 399–406. doi: 10.7657/XJPG20170404

Zhang, Z.-F., Zhang, Z.-L., Li, G.-X., and Holmer, L. E. (2016). The Cambrian brachiopod fauna from the first-trilobite age Shuijingtuo Formation in the Three Gorges area of China. *Palaeoworld* 25, 333–355. doi: 10.1016/j.palwor.2015.10.001

Zhao, J., Jin, Z., Lin, C., Liu, G., Liu, K., Liu, Z., et al. (2019). Sedimentary environment of the Lower Cambrian Qiongzhusi Formation shale in the Upper Yangtze region. *Oil & Gas Geol.* 40, 7.1–715. doi: 10.11743/ogg20190402

Zhao, L., Dai, S., Graham, I. T., Li, X., and Zhang, B. (2016). New insights into the lowest Xuanwei Formation in eastern Yunnan Province, SW China: Implications for Emeishan large igneous province felsic tuff deposition and the cause of the end-Guadalupian mass extinction. *Lithos* 264, 375–391. doi: 10.1016/j.lithos.2016.08.037

Zhou, X., Liu, Y., Cao, H., Zhong, H., and Li, Y. (2021). Responses of oceanic chemistry to climatic perturbations during the Ordovician-Silurian transition: Implications for geochemical proxies and organic accumulations. *Mar. Pet. Geol.* 134, 1–13. doi: 10.1016/j.marpetgeo.2021.105341

Zhou, H. (2019). Geochemical characteristics and geological significance of the lower cambrian black rock series in northwestern hunan. *East China Univ. Technol.* 2020, 1–61.

Zhu, G., Wang, T., Xie, Z., Xie, B., and Liu, K. (2015). Giant gas discovery in the Precambrian deeply buried reservoirs in the Sichuan Basin, China: Implications for gas exploration in old cratonic basins. *Precambrian Res.* 262, 45–66. doi: 10.1016/j.precamres.2015.02.023

Zhu, G., Zhao, K., Li, T., Zhang, Z., Tang, S., and Wang, P. (2021). Anomalously high enrichment of mercury in early Cambrian black shales in South China. *J. Asian Earth Sci.* 216, 1–13. doi: 10.1016/j.jseaes.2021.104794

frontiers | Frontiers in Marine Science

TYPE Original Research
PUBLISHED 11 October 2024
DOI 10.3389/fmars.2024.1470134

OPEN ACCESS

EDITED BY
Xiaodong Jiang,
Guangdong University of Technology, China

REVIEWED BY
Xi Mei,
Qingdao Institute of Marine Geology (QIMG), China
Jianghu Lan,
Chinese Academy of Sciences (CAS), China

*CORRESPONDENCE
Zhongshan Shen
zsshen@mail.iggcas.ac.cn
Haifeng Wang
wanghaifeng112@163.com

RECEIVED 25 July 2024
ACCEPTED 18 September 2024
PUBLISHED 11 October 2024

CITATION
Shen Z, Chen Y, Mikhailik P, Cai Y, Wang H and Yi L (2024) Early diagenesis, sedimentary dynamics and metal enrichment reveal deep-sea ventilation in Magellan Seamounts during the middle Pleistocene.
Front. Mar. Sci. 11:1470134.
doi: 10.3389/fmars.2024.1470134

Early diagenesis, sedimentary dynamics and metal enrichment reveal deep-sea ventilation in Magellan Seamounts during the middle Pleistocene

Zhongshan Shen[1]*, Yanping Chen[2], Pavel Mikhailik[3], Yun Cai[4], Haifeng Wang[5,6]* and Liang Yi[4]

[1]State Key Laboratory of Lithospheric and Environmental Coevolution, Institute of Geology and Geophysics, Chinese Academy of Sciences, Beijing, China, [2]Zhejiang Academy of Marine Sciences, Second Institute of Oceanography, Ministry of Natural Resources, Hangzhou, China, [3]Laboratory of Regional Geology and Tectonic, Far East Geological Institute, Far East Branch of Russian Academy of Sciences, Vladivostok, Russia, [4]State Key Laboratory of Marine Geology, Tongji University, Shanghai, China, [5]Key Laboratory of Marine Mineral Resources, Ministry of Natural Resources, Guangzhou Marine Geological Survey, China Geological Survey, Guangzhou, China, [6]Southern Marine Science and Engineering Guangdong Laboratory (Guangzhou), Guangzhou, China

Seamounts are ubiquitous topographic units in the global oceans, and the Caiwei Guyot in the Magellan Seamounts of the western Pacific is a prime example. In this study, we analyzed a well-dated sediment core using magnetic properties, sediment grain size, and metal enrichment to uncover regional ventilation history during the middle Pleistocene and explore potential linkages to global climate changes. Our principal findings are as follows: (1) The median grain size is 3.3 ± 0.2 μm, and clay and silt particles exhibit minimal variation, with average values of 52.8 ± 1.8% and 38.2 ± 1.6%, respectively, indicating a low-dynamic process; (2) Three grain-size components are identified, characterized by modal patterns of ~3 μm (major one), ~40 μm, and 400–500 μm, respectively; (3) Magnetic coercivity of the deep-sea sediments can be classified into three subgroups, and their coercivity values are 6.1 ± 0.5 mT, 25.7 ± 1.0 mT, and 65.2 ± 2.1 mT. Based on these results, we propose a close linkage between magnetic coercivity and metal enrichment, correlating with changes in deep-sea circulation intensity. Conversely, sediment grain-size changes seem to be more strongly influenced by eolian inputs. Consequently, we suggest that regional ventilation has weakened since ~430 ka, likely linked to a reduction in Antarctic bottom water formation.

KEYWORDS

abyssal ventilation, early diagenesis, magnetic properties, Caiwei (Pako) Guyot, middle Pleistocene, western Pacific

1 Introduction

More than 50,000 seamounts have been identified in the Pacific Ocean, and the Magellan Seamounts, formed by hotspot activity during 120–90 Ma (Wessel, 1997; Wessel and Lyons, 1997; Stepashko, 2008), include the Caiwei, the Vlinder, and the Loah, and are distributed in a northwestward chain (Figure 1). Among them, the Caiwei Guyot, a well-studied deep-sea flat-topped seamount, has water depths of ~1 500–1 600 m at its summit and ~5 500 m at its base. The Caiwei Guyot is situated within the main flow path of the Antarctic bottom water (AABW) and Lower Circumpolar Deep Water (LCDW) as they move toward the North Pacific, and the former, AABW, is considered a potential intermediary in the influence of the Antarctic on global climate change (Talley, 2008; Kawabe and Fujio, 2010). It covers >70% of the ocean-bottom region and represents 30%–40% of the total global water mass (Johnson, 2008). With its high level of dissolved oxygen, the AABW significantly contributes to abyssal ventilation and redox conditions (Gordon, 2001). Furthermore, an anti-cyclonic eddy has been identified over the guyot (Guo et al., 2020), contributing to similar hydrochemical properties around the seamount, such as salinity, pH value, and nitrate, likely influenced by this anti-cyclonic phenomenon (Liu et al., 2019). Previous studies focusing on mineral resources and megafaunal communities (Wang et al., 2016b; Xu et al., 2016) and microorganisms (Liu et al., 2019; Sun et al., 2020; Yang et al., 2020) have proposed that cobalt-rich crusts, carbonate rocks, and calcareous pelagic deposits are the main dominant sediments on the guyot (He et al., 2001; Wei et al., 2017; Zhao et al., 2020). This unique seafloor topography, which rises from the open ocean, also enhances nutrient transport, supporting the local ecosystem (Wang et al., 2024).

Despite these insights, our understanding of the complex deep-sea environment remains incomplete. Cross-validation of different proxies for paleoenvironmental reconstruction has been limited. For example, dissolute-oxygen reconstruction, a key issue in deep-sea environmental inferences, has not been thoroughly examined. In this study, we utilize three widely used proxies, namely early diagenesis, metal enrichment, and sediment grain size, to infer the paleoenvironmental conditions of the Caiwei Guyot, situated in an area strongly influenced by AABW/LCDW circulation (Figure 1). By integrating magnetostratigraphy and authigenic beryllium isotopes ($^{10}Be/^{9}Be$), we have constructed a reliable age-depth model for the studied core. Using this geochronological framework, we discuss the magnetic and grain-size properties in conjunction with metal enrichment in abyssal sediments in this unique region since ~440 ka.

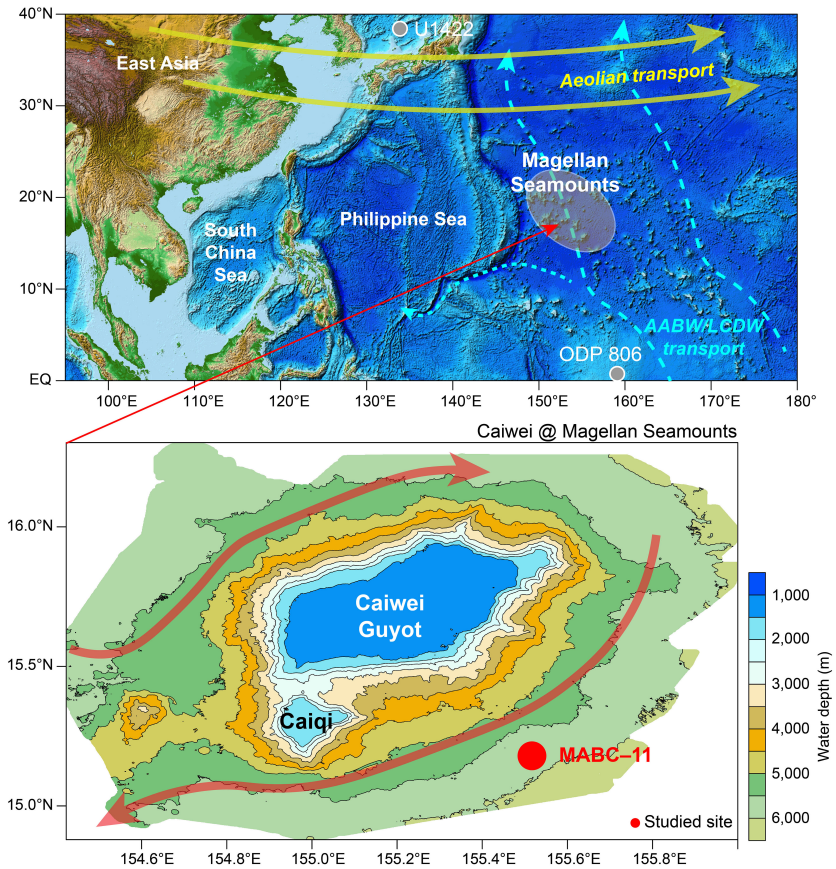

FIGURE 1
Schematic map showing the study site (MABC–11) and oceanographic setting. The flows were modified from previous works (Guo et al., 2020; Kawabe and Fujio, 2010; Zhai and Gu, 2020). AABW, Antarctic bottom water; LCDW, Lower Circumpolar Deep Water. U1422 and ODP 806 are the referenced sites mentioned in the main text.

2 Methods

2.1 The studied core

Core MABC–11 (155.53° E, 15.22° N, 5,840 m water depth) was retrieved from the eastern base of the Caiwei Guyot (Figure 1) using a box corer aboard R/V *Haiyang Liu Hao* in July 2012, with a core length of 59 cm.

The age model of core MABC–11 was developed using magnetostratigraphy and by tuning changes in element Ca intensity (from XRF scanning) with the deep-sea benthic $\delta^{18}O$ stack LR04 (Lisiecki and Raymo, 2005), which reflects global ice volume changes. The resulting average sedimentation rate is 0.73 mm/kyr (Yi et al., 2021a). To further refine the chronology, this age-depth model was adjusted based on $^{10}Be/^{9}Be$ data to integrate deep-sea paleoenvironmental records from the Mariana Trench and Magellan Seamounts (Yi, 2023). For this study, the core was sampled for the depth interval of 7.0–49.5 cm at 5 mm resolution, and 86 subsamples in total were obtained for magnetic and grain-size analyses between 221 and 904 ka (Figure 2).

2.2 Magnetic measurement

Hysteresis loops were conducted on all 86 samples using a Princeton Measurements Inc. MicroMag 3900 Vibrating Sample Magnetometer (VSM). A peak field of 0.3 T was set for hysteresis loops, and saturation magnetization (Ms), saturation remanence (Mrs), coercive force (Bc), and the coercivity of the remanence (Bcr) were determined from the hysteresis loops, after calibration using the data from between 0.25 and 0.30 T. All magnetic measurements were conducted at the Paleomagnetism and Geochronology Lab (PGL), Institute of Geology and Geophysics, Chinese Academy of Sciences.

The mathematical unmixing of hysteresis loops can provide detailed information about different coercivity spectra (Jackson et al., 1990). The polymodal distribution for unmixing in this study is expressed as follows:

$$F = p_1 f_1 + \ldots + p_i f_i;\ \sum_1^n p_i = 1 \tag{1}$$

where f_i represents the function for component i where $i = 1$ to n components, and p_i is the percentage contribution of the components. A series of target functions has been proposed for unmixing (Heslop, 2015); here, we used the normal function to identify the potential end members of magnetic minerals in the sediments (Heslop, 2015; Heslop and Roberts., 2012). The normal function has the following form:

$$F = p_1 \frac{1}{\sqrt{2\pi}\alpha_1} e^{-\left[\frac{(x-\beta_1)^2}{2\alpha_1^2}\right]} + p_2 \frac{1}{\sqrt{2\pi}\alpha_2} e^{-\left[\frac{(x-\beta_2)^2}{2\alpha_2^2}\right]} + p_3 \frac{1}{\sqrt{2\pi}\alpha_3} e^{-\left[\frac{(x-\beta_3)^2}{2\alpha_3^2}\right]} \tag{2}$$

Here, x is the independent variable and represents the magnetic field, and the dependent variables are the second derivatives of the hysteresis loop data, which were first standardized to the interval of

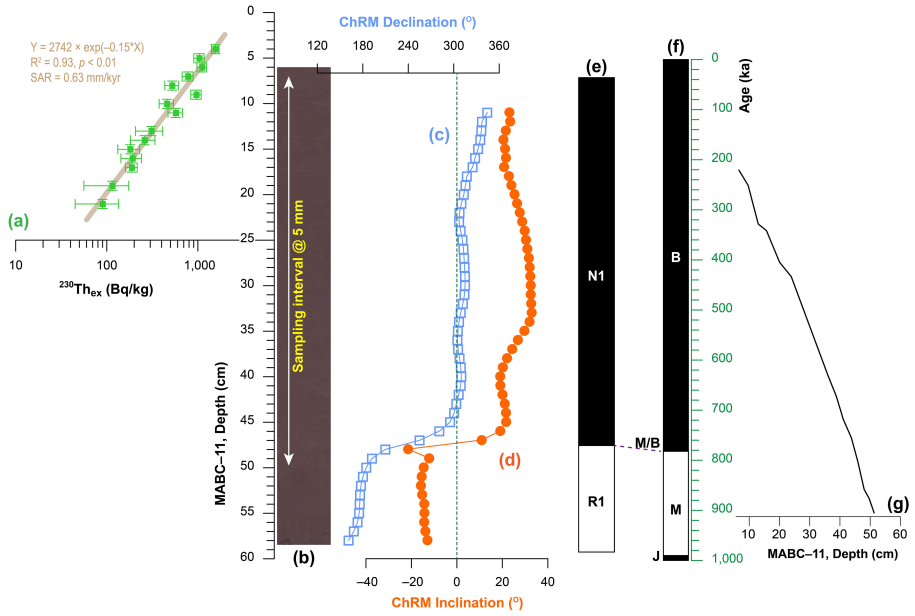

FIGURE 2
Core MABC–11 with the age-depth model during the middle Pleistocene. **(A)** The excess ^{230}Th data and the estimated SAR for the upper part (Yang et al., 2020); **(B)** photo of the core; **(C–E)** ChRM declination and inclination, with the polarity of core MABC–11 (Yi et al., 2021a); **(F)** The geological polarity timescale (GPTS) (Hilgen et al., 2012). B, Brunhes chron; M, Matuyama chron; J, Jaramillo subchron; M/B, the Matuyama/Brunhes boundary. **(G)** The modified age-depth model of core MABC–11 (Yi, 2023).

[0, 4]. The coefficient p represents the relative ratio between three components (namely Cnt1–3), α determines the distribution shape (namely Shp1–3), and β controls the position of the central tendency of the curve, herein, the magnetic coercivity (namely Coe1–3).

2.3 Grain-size measurement

Grain-size samples were placed in an ultrasonic vibrator with sodium hexametaphosphate [$(NaPO_3)_6$] for several minutes to facilitate dispersion and were measured using a Malvern Mastersizer 2000 grain size analyzer in the Key Laboratory of Engineering Oceanography, Second Institute of Oceanography, Ministry of Natural Resources of China.

Fifty grain-size classes between 0.1 and 2000 μm were exported for further analysis. The grain-size distributions were then analyzed by using mathematical methods, including the varimax-rotated principal component analysis (VPCA), environmentally sensitive components, and lognormal-based unmixing (modified from Equation 2), and the common signal of deep-sea dynamics was extracted by a PCA on the studies cores for paleoenvironmental inferences, following the procedures reported in previous studies (e.g., Chen et al., 2021; Paterson and Heslop, 2015; Yi et al., 2022).

3 Results

3.1 Grain-size properties

The median grain-size value (M) of the sediment is 3.3 ± 0.2 μm, indicating a low-dynamic sedimentary environment that remained relatively stable throughout the middle Pleistocene (Figure 3B). The proportions of clay (< 4 μm) and silt (4~63 μm) particles display minimal variation, with average values of 52.8 ± 1.8%, and 38.2 ± 1.6%, respectively, while sand particles (> 63 μm) exhibit greater variability, averaging 9.0 ± 2.6%. Notably, coarse components, likely authigenic micro-nodules (>200 μm), are present in several samples, consistent with slow sediment accumulation in marine environments (Wang et al., 2016a), and are observed in surrounding regions (Yi et al., 2022, 2020).

The grain-size distributions are multi-modal, with modal sizes of approximately 3 μm (dominant), ~40 μm, and 400-500 μm

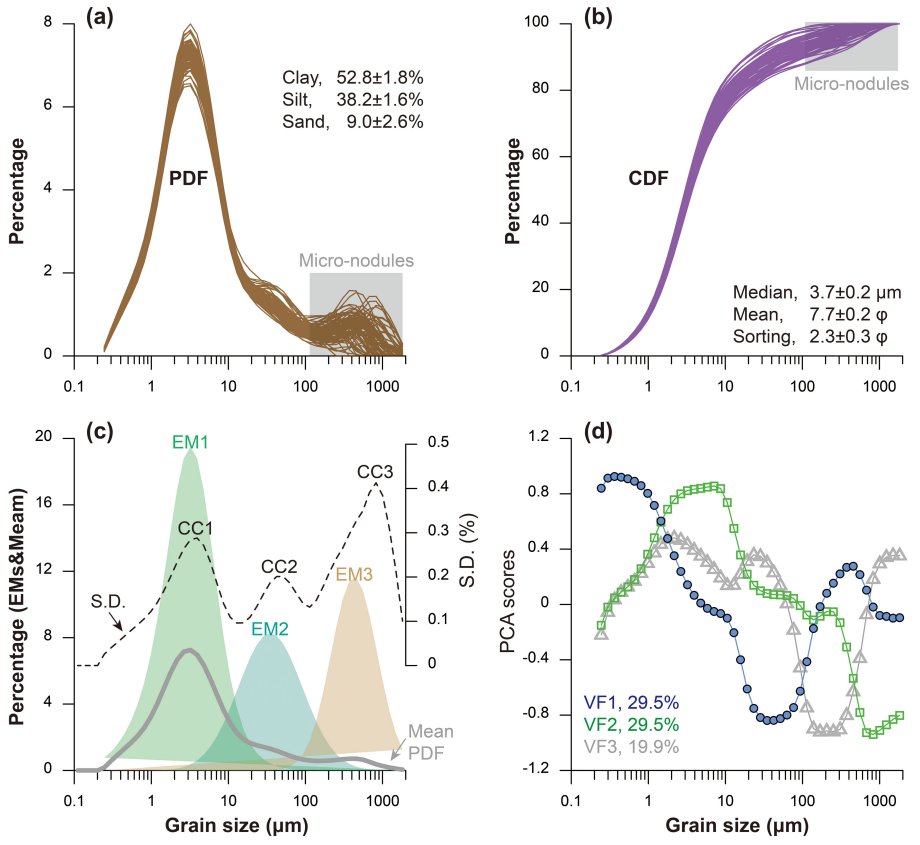

FIGURE 3
Sediment grain-size characteristics of core MABC–11. **(A, B)** Grain-size distribution; PDF, probability density function, CDF, cumulative density function. **(C)** Mathematical unmixing; EMs are the main grain-size components; CCs are the components of the grain-size sensitive fraction; Mean PDF, the average grain-size curve of all samples; S.D., the standard deviation for all samples. **(D)** Principal component analysis (PCA) results; VFs are the leading principal components.

10.3389/fmars.2024.1470134

TABLE 1 Results of the principal component analysis of the sediment grain size of core MABC-11.

Component	Initial Eigenvalues/Extraction Sums of Squared Loadings		
	Total	% of variance	Cumulative %
VF1	13.58	29.5	29.5
VF2	13.56	29.5	59.0
VF3	9.15	19.9	78.9

(Figure 3). Only minor differences were found in the grain-size distributions across different samples, suggesting a stable sedimentary environment during the examined interval. Following the method of Boulay et al. (2003), which has proven effective for identifying sedimentary processes and dynamics (e.g., Hu et al., 2021; Sun et al., 2003), we identified three environmentally sensitive grain-size components (CC1-CC3), with modal sizes of 2.6-4.8 μm, 42.2-51.5 μm, and 676-1000 μm, respectively (Figure 3C).

Polymodal grain-size spectra can be mathematically partitioned (Ashley, 1978), enabling the separation of orthogonal modes (independent grain-size components/factors) to identify potential changes in input functions and/or sedimentary dynamics (e.g., Chen et al., 2020, 2021; Yi et al., 2012b). Using a three-component lognormal function following the method of Paterson and Heslop (2015), which is similar to Equation 2, we obtained three components, EM1, EM2, and EM3 (Figure 3C), with modal sizes of 3.2 μm, 34.6 μm, and 455 μm, respectively. VPCA can also be used to identify the processes controlling sediment grain-size changes and to extract paleoenvironmental signals (e.g., Hu et al., 2021; Yi et al., 2012a). Similarly, the results of VPCA also identify three characteristic components, VF1-VF3 (Figure 3D), accounting for 78.9% in total (Table 1).

Combining all the grain size results, including the environmentally sensitive components (CC1-CC3), lognormal-based unmixing (EM1-EM3), and VPCA results (VF1-VF3), there are three grain-size components similarly identified with a major group (modal sizes at ~3-4 μm), suggesting a single dominant factor controlling sedimentary dynamics in the study area during the depositional interval.

3.2 Magnetic coercivity from unmixing loop curves

Previous studies on magnetic minerals in the Caiwei Guyot sediments, including hysteresis loop, IRM acquisition, and first-order reversal curve analyses, demonstrate that low-coercivity magnetite is the dominant magnetic mineral, with fine grains (Lin et al., 2019; Yi et al., 2021b). Similar mineral properties have been documented at IODP Site U1337 in the eastern Pacific (Yamazaki, 2012), and core XTGC1311 from the middle Pacific (Li et al., 2020).

Hysteresis loop analysis of all 86 samples reveals that the magnetic loops are closed below 200 mT (Figure 4A), indicating a dominance of low-coercivity magnetic minerals. The coercivity values (Bc and Bcr) average 11.4 ± 0.3 mT and 31.5 ± (< 0.05) mT, respectively. On the Day plot (Day et al., 1977), the samples plot within the PSD range, close to the SD field (Figure 4B). Despite minimal variation on the Day plot, a higher Bcr/Bc and Mrs/Ms ratio prior to ~500 ka suggests slightly coarser magnetic grains (Roberts et al., 2018). A three-component lognormal function was applied to mathematically unmix the hysteresis loops (Heslop, 2015; Heslop and Roberts., 2012), yielding coercivity components (Coe1-Coe3) of 6.1 ± 0.5 mT, 25.7 ± 1.0 mT, and 65.2 ± 2.1 mT, respectively (Figure 5). A similar analysis was also applied to unmix the IRM acquisition curves (Maxbauer et al., 2016), and a comparison between hysteresis loop-based and IRM acquisition-based results shows no significant differences (Yi et al., 2021b), and thus is not plotted here.

In a log-normal based unmixing (Equation 2), we employed three parameters to describe a subpopulation of magnetic coercivity, α, β, and p, in which α determines the shape of the distribution (Shp1–Shp3), representing each magnetic type/source/mineral, β controls the position of the central tendency of the curve (Coe1–Coe3), herein representing magnetic coercivity or degree of early diagenesis for each magnetic group, and p indicates the relative

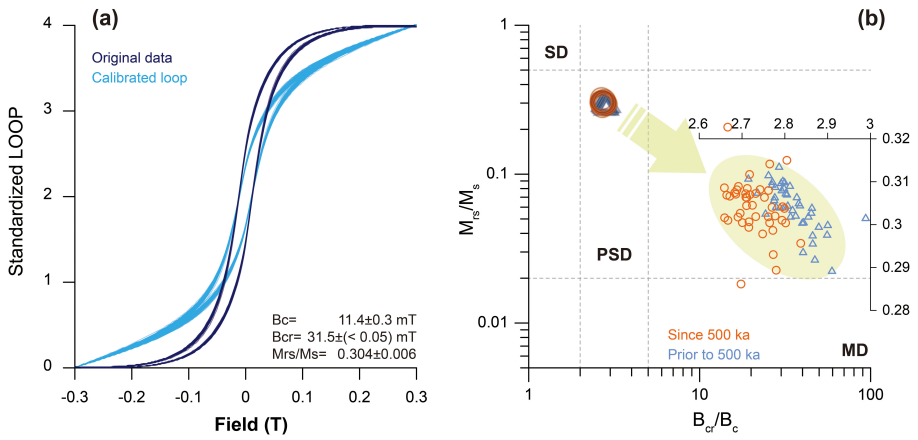

FIGURE 4
Hysteresis loops of all samples in original (blue lines) and calibrated (black lines) forms **(A)**, and Day plot **(B)** of all samples. SD, single domain; PSD, pseudo–single domain; MD, multiple domain.

percentage of each component in a population (Cnt1–Cnt3), representing the ratio of each magnetic group against the total.

Since the source of magnetic minerals in the western Pacific was relatively stable (Chen et al., 2023), the coercivity spectrum can be expressed by these three parameters, and plotting these three parameters together can provide useful information to assess how magnetic minerals changed after deposited (Figure 5). As shown, the major component is Coe2, accounting for about 47%–50% of total magnetic grains in the sediment. Moreover, there is no distinct difference between the pattern of α-β for components Coe2 and Coe3, indicating that these two magnetic groups were linked to a similar source and/or experience similar post-deposition changes (early diagenesis). However, for component Coe1, a more complex relationship between the three magnetic parameters is observed (Figure 5A). Considering all of these observations, together with the close relationship between the derived magnetic components (Figure 5D), component Coe2 was employed for later analysis.

4 Discussion

4.1 Comparison between three ventilation proxies

There are several proxies for studying deep-sea ventilation, including the enrichment of oxygen-sensitive metals (such as Mn, Zn, Ni, and V), sediment grain size, and magnetic coercivity. For instance, element Mn migrates from reducing to oxidizing environments, making it highly sensitive to sedimentary redox changes (Costa et al., 2018; Löwemark et al., 2014; Slemons et al., 2012; Yi et al., 2023). Conversely, sediment grain size reflects the intensity of bottom-water flows, where coarser particles suggest higher sedimentary dynamics and intensified bottom waters, as reported in previous studies (e.g., Hall et al., 2001; Yi et al., 2022). Magnetic properties of deep-sea sediments also offer potential insights into deep-water redox conditions (e.g., Chang et al., 2016; Kissel et al., 2020; Kruiver and Passier, 2001) due to conversions between Fe^{2+} and Fe^{3+} in crystal lattices in the context of oxygen-rich bottom water. However, the exact influence of early diagenesis expressed by changes in magnetic mineral properties may vary between sites because investigations with different oxidation states show that PSD magnetite could be significantly negatively correlated to partial oxidation in a shell-only model, or positively correlated in cases of changing magnetite sizes (Ge et al., 2014; Chen et al., 2023). Hence, considering that the Mn record of core MABC–11 has been cross-validated in previous studies (Yi et al., 2021a; Yi, 2023), we take the Mn record as a reference and compare all of the three proxies to reveal the potential linkages between them (Figures 6–8).

The Mn-enriched sedimentary record from core MABC–11 shows a significant increase in Mn concentration, concurrent with a decrease in sediment median grain size (Figure 6). This observation is contrary to the typical linkage between sediment grain size and bottom-water intensity reported in previous studies (e.g., Hall et al.,

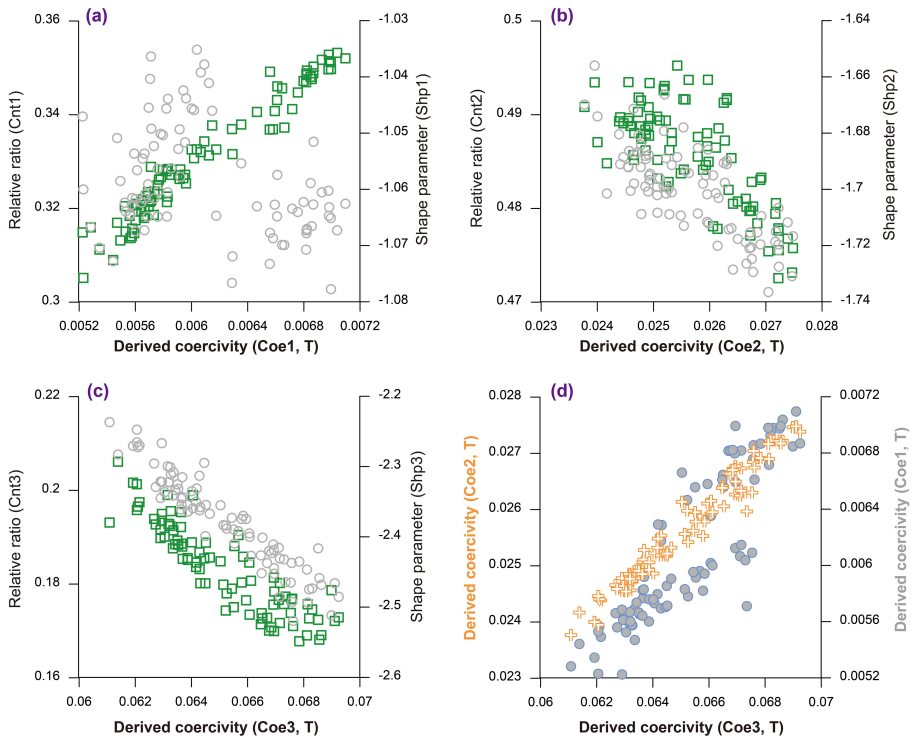

FIGURE 5
Unmixed parameters from hysteresis loops of all samples. **(A–C)** Three magnetic components, **(D)** Coercivity comparison. The relative ratios between the three components were labeled as Cnt1–3, the distribution shapes were labeled as Shp1–3, and the positions of the central tendency of the curve indicating the magnetic coercivity were labeled as Coe1–3.

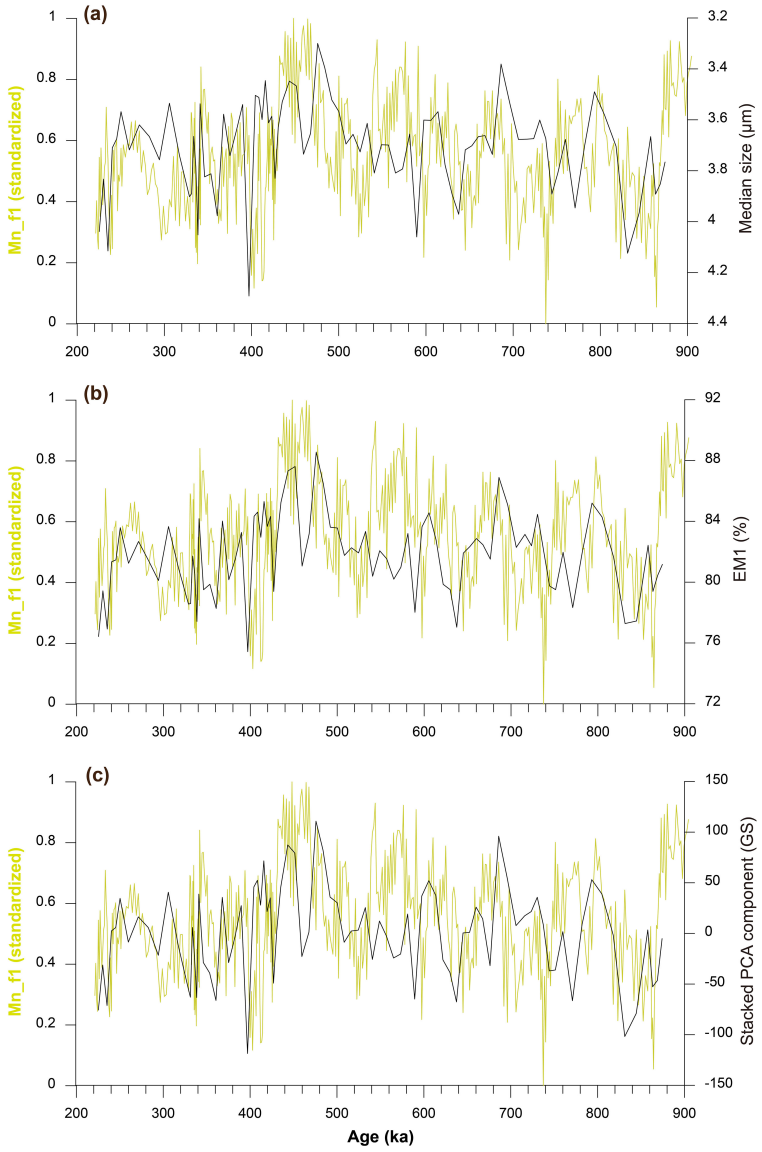

FIGURE 6
Comparison between the sedimentary Mn (Mn_f1) and grain-size variation of core MABC−11 in the middle Pleistocene. **(A)** Median size, **(B)** EM1, **(C)** PCA scores. GS is the integrated record of the three PCA components, namely GS=29.5×VF1 + 29.5×VF2 + 19.9×VF3 (Table 1). Mn−f1 was derived from element ratios of Mn/Cl, Mn/K, Mn/Ca, Mn/Ti, and Mn/Fe, representing the common signal of three cores (MABC-11, J11b, and A25) linked to the regional bottom-water changes (Yi, 2023).

2001; Lamy et al., 2024), suggesting that other processes beyond bottom-water intensity are involved.

Aeolian inputs, which are increasingly recognized as important contributors to deep-sea sedimentation in the western Pacific, may have played a major role, particularly since the middle Pleistocene (Yi et al., 2020, 2022; Yao et al., 2021). The grain-size variation observed in core MABC−11 is generally consistent with records of drying processes in the Asian interior (Figure 7A), inferred from the $\delta^{13}C$ record of the Taklimakan Desert (Liu et al., 2020), and eolian transport to the Japan Sea (Figure 7B), implied from the K content of IODP Site U1422 (Zhang et al., 2018). Fine grains in deep-sea sediments in the North Pacific were mainly carried by the westerlies and/or winter monsoons from the Asian interior (e.g., Rea, 1994; Jiang et al., 2019; Xu et al., 2015), inferring that aridification in inner Asia would result in more eolian particles in deep-sea sediment and a decrease in sediment grain size.

Moreover, seamounts, such as Caiwei Guyot, exert unique influences on regional circulation, vertical mixing, and sediment transport (Bograd et al., 1997; Chen et al., 2015; Yang et al., 2017; Zhang and Boyer, 1993, 1991). For example, a series of complex responses, such as the anticyclonic cap (Lavelle and Mohn, 2010), are generated to modulate regional circulation when currents flow across a seamount (Perfect et al., 2018; Robertson et al., 2017). By studying sediment grain-size properties in the central Philippine Sea, the agreement between deep-sea sedimentary dynamics and ENSO-like changes was highlighted in the Quaternary, suggesting the long-term influence of upwelling and unique submarine topography (Yi et al., 2022). Similarly, in a 3-year monitoring study, a deep anticyclonic cap over the studied guyot was proposed (Guo

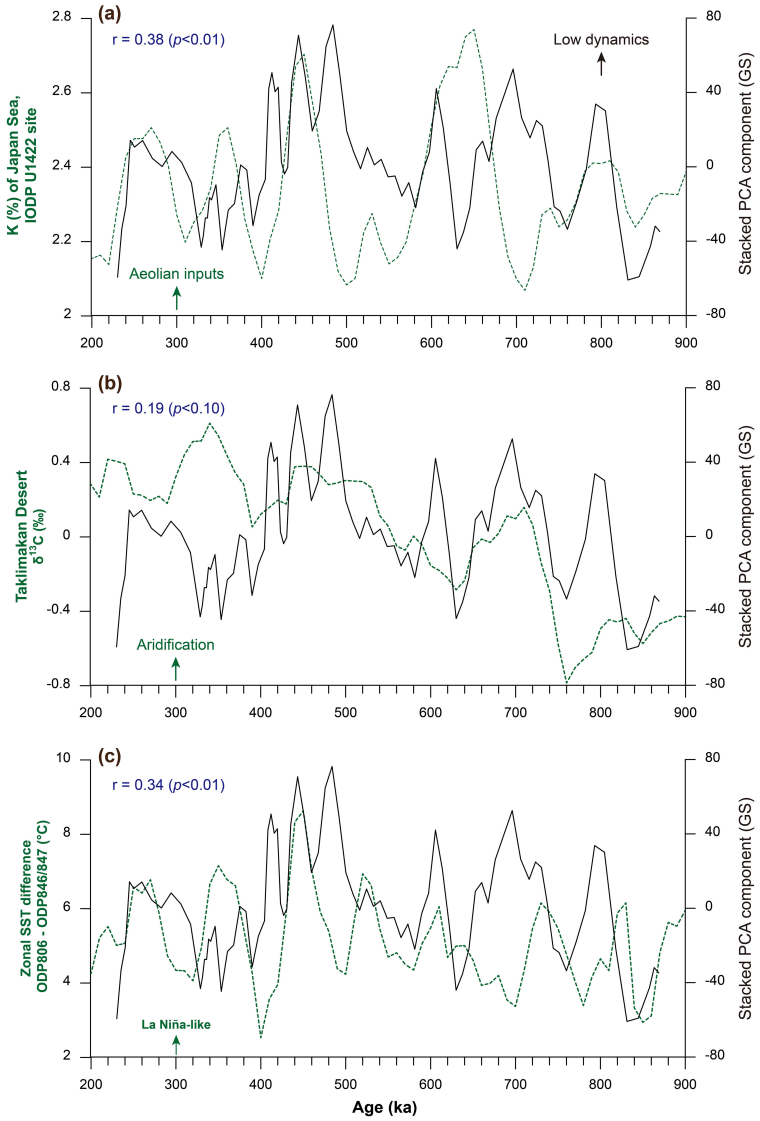

FIGURE 7
Comparison between the grain-size variation of core MABC−11 (GS, 3-point moving average) and various paleoenvironmental proxies in the middle Pleistocene. **(A)** the K content of IODP Site U1422 in the Japan Sea (Zhang et al., 2018), **(B)** the $\delta^{13}C$ record of a sediment core from Lop Nur in the Taklimakan Desert (Liu et al., 2020), and **(C)** the zonal SST difference between ODP Sites 806 and 846/847 (Fedorov et al., 2015). The correlation coefficients in **(A–C)** are r = 0.38 (p<0.01), 0.15 (p<0.10), and 0.34 (p<0.01), respectively. See the aforementioned notes.

et al., 2020), and this topography-induced downwelling could have imparted evident precessional signals into the sedimentary Mn of core MABC–11 (Yi et al., 2021a). Based on this vertical connection in the study area, the downwelling processes could result in more eolian particles being deposited into deep-sea sediments, agreeing with the relationships between the Mn and grain-size records observed in core MABC–11 (Figure 6) and between the zonal SST difference (ENSO-like changes) and MABC–11 grain-size record (Figure 7C). Therefore, it is inferred that eolian inputs may be the dominant factor controlling the sedimentary dynamics in the Caiwei Guyot during the middle Pleistocene.

For magnetic proxies, it is observed that as the Mn contents increase in core MABC–11, the coercivity values of the magnetic components decrease (Figure 8). This inverse relationship between magnetic coercivity and Mn record suggests that redox conditions influenced the preservation and alternations of magnetic minerals in deep-sea sediments.

The relationship between magnetic coercivity and deep-sea redox conditions has been demonstrated using surficial sediments in the Philippine Sea and its surrounding area, and the results show that for PSD magnetite, in higher deep-water oxidation conditions, early diagenesis could result in a lower coercivity of the sediments, and vice versa (Chen et al., 2023). In such a case, prolonged exposure of magnetic minerals to oxygen-rich bottom waters leads to the maghemitization of magnetite grains, which reduces their coercivity. This observation is consistent with experimental studies, in which the partial oxidation of PSD magnetite grains in a core-shell model can decrease the effective diameter of magnetite grains, resulting in a lower coercivity value (Ge et al., 2014; Özdemir and Dunlop, 2010). However, offsets between the Coe2 and Mn_f1 records are also evident (Figure 8),

10.3389/fmars.2024.1470134

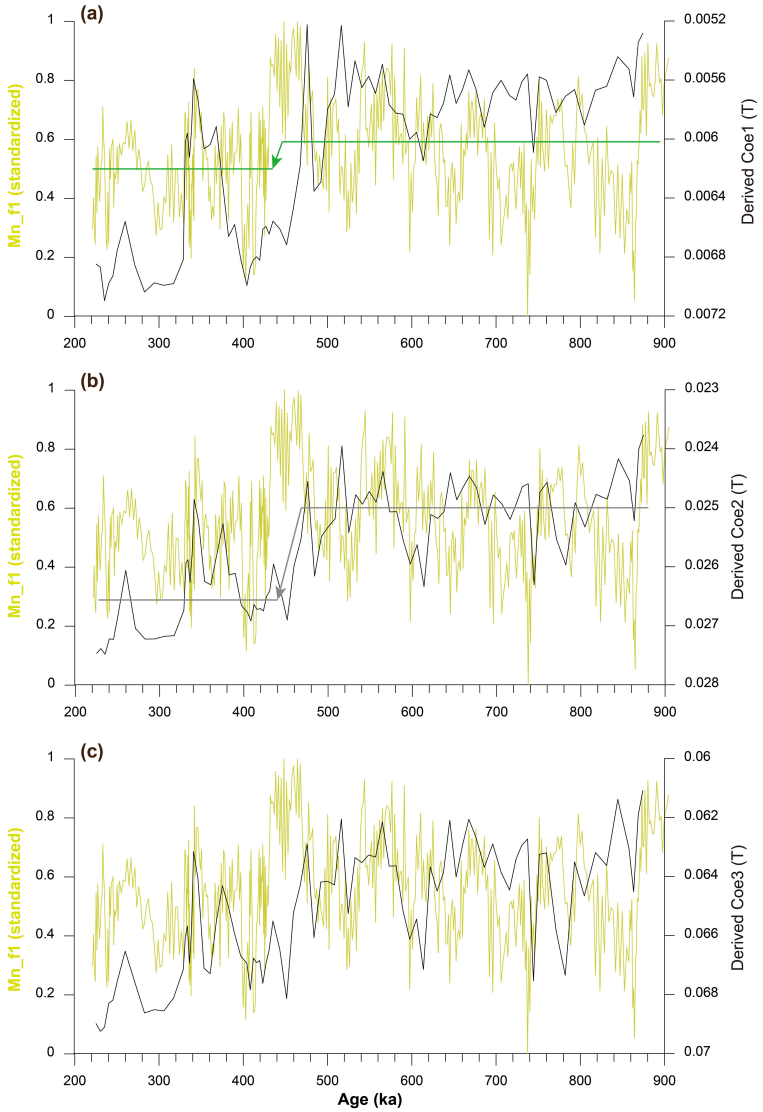

FIGURE 8
Comparison between the sedimentary Mn and magnetic coercivities of core MABC−11 in the middle Pleistocene. **(A–C)** Three coercivity components compared with Mn changes. The arrows in **(A, B)** indicate a significant change across the MBE. The average values of the Coe2 record prior to and post-MBE are 25.0 ± 0.6 mT and 26.5 ± 0.7 mT, respectively. The average values of the Mn_f1 record prior to and post-MBE are 0.50 ± 0.16 and 0.59 ± 0.18, respectively. See the aforementioned notes.

which can be attributed to that the relationship between magnetic coercivity and redox conditions may be influenced by other factors, such as the magnetic grain size, mineralogy, and concentration (Chen et al., 2023). Hence, the observed relationship between magnetic coercivity and sedimentary Mn likely reflects changes in bottom-water oxygenation in the study area and can serve as a proxy for deep-sea ventilation (Figure 9).

4.2 Ventilation history of the Magellan Seamounts

Integrated evidence suggests that significant changes in regional ventilation occurred in the Magellan Seamounts during the middle Pleistocene (Figure 9). To exclude potential dominant influences from marine productivity on abyssal redox conditions, a comparison was conducted between the sedimentary Mn of core MABC−11 and the planktonic $\delta^{13}C$ record from ODP Site 806 (Schmidt et al., 1993). No significant correlation was observed between these records (Yi, 2023), suggesting that ventilation changes were the primary driver of redox conditions rather than changes in productivity in the study area. These proxies reveal a weak but observable in-phase relationship between abyssal ventilation and the LR04 record (Lisiecki and Raymo, 2005), likely indicating intensified deep-sea ventilation during interglacial intervals. This finding aligns with other records from the North Pacific (Jacobel et al., 2017), and further highlights the complex relationship between global glacial-interglacial cycles and deep-sea circulation.

Moreover, glacial intensification of abyssal ventilation is clearly evident during MIS 12, consistent with similar findings in the eastern

10.3389/fmars.2024.1470134

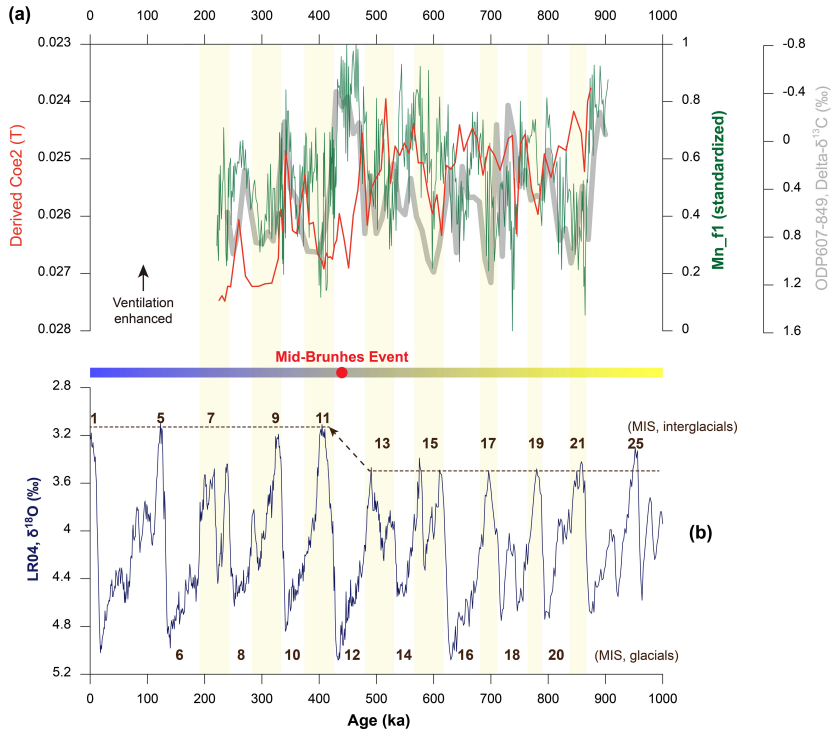

FIGURE 9
Ventilation history of the study region (Caiwei Guyot) in the middle Pleistocene. **(A)** Two proxies of regional ventilation derived from the sediments of core MABC−11 vs. the $\delta^{13}C$ gradient between ODP sites 607 and 849 (Hodell and Venz-Curtis, 2006). **(B)** The benthic $\delta^{18}O$ stack LR04 (Lisiecki and Raymo, 2005). MIS, marine isotope stages, which are labeled as numbers 1–25 at the top. See the aforementioned notes.

Pacific (Yi et al., 2023) and the southwestern Pacific (Hall et al., 2001). The diversity of abyssal ventilation in the study area between glacial and interglacial alternations may be attributed to the redistribution of bottom/deep water masses within the deep Pacific (Yi, 2023), which is worthy of further investigation in the future.

Furthermore, a long-term trend of decreasing abyssal ventilation since ~430 ka (Figure 8) coincides with the Mid-Brunhes Event (MBE), a period characterized by enlarged amplitudes in the glacial-interglacial cycles (Figure 9B). Whether the MBE represents multiple equilibria in the climate system (Jansen et al., 1986; Paillard, 1998), or a transition between two distinct climate states singly responding to astronomical forcing (Tzedakis et al., 2017; Yin, 2013) remains debated. A latitudinal shift of the Southern Hemisphere westerlies inducing CO_2 to respire from the Southern Ocean (Kemp et al., 2010) and/or a slowdown of AABW formation (Yin, 2013) have been proposed to be the potential mechanisms for the MBE. In our study, the reduced ventilation observed in this study is consistent with the predicted slowdown in AABW formation after the MBE, corroborating a recent reconstruction of AABW variability in the eastern Pacific (Yi et al., 2023).

5 Conclusions

By studying core MABC−11, this study reveals significant insights into deep-sea ventilation in the Magellan Seamounts during the middle Pleistocene, specifically through the integration of magnetic coercivity, metal enrichment, and sediment grain size. We have determined that the median value of sediment grain size is 3.3 ± 0.2 μm, with minimal changes in clay and silt contents (average values of 52.8 ± 1.8% and 38.2 ± 1.6%, respectively), and greater variability in sand content (average 9.0 ± 2.6%). The dominant magnetic mineral identified is low-coercivity PSD magnetite, with three distinct coercivity subgroups: 6.1 ± 0.5 mT, 25.7 ± 1.0 mT, and 65.2 ± 2.1 mT. By comparing these proxies with various environmental indicators, we proposed that magnetic coercivity and metal enrichment effectively track the signals of deep-sea circulation intensity, whereas sedimentary grain-size changes are more closely linked to eolian inputs with topography-induced influences on the upper ocean. Furthermore, we confirmed that reginal ventilation weakened since the MBE (~430 ka), which likely reflects the reduced AABW formation. This ventilation decrease aligns with previous reconstructions of AABW in the eastern Pacific, and the observed changes in sedimentary dynamics, magnetic minerals, and geochemical proxies provide valuable insights into the broader implications of the MBE on global deep-sea circulation patterns.

Data availability statement

The datasets presented in this study can be found in online repositories. The names of the repository/repositories and accession number(s) can be found in the article/supplementary material.

Author contributions

ZS: Methodology, Project administration, Funding acquisition, Formal Analysis, Writing – review & editing, Writing – original draft. YC: Funding acquisition, Writing – review & editing, Software, Formal Analysis. PM: Software, Writing – review & editing, Formal Analysis. YC: Writing – review & editing, Formal Analysis, Data curation. HW: Data curation, Writing – review & editing, Supervision, Resources, Investigation. LY: Writing – review & editing, Methodology, Funding acquisition, Conceptualization.

Funding

The author(s) declare that financial support was received for the research, authorship, and/or publication of this article. The work was supported by the National Natural Science Foundation of China (42177422, 41602349, 42304084), the China Postdoctoral Science Foundation (2023M743469), and a state assignment of the Far East Geological Institute, Far East Branch, Russian Academy of Sciences (FEGI FEB RAS).

Conflict of interest

The authors declare that the research was conducted in the absence of any commercial or financial relationships that could be construed as a potential conflict of interest.

Publisher's note

References

Ashley, G. M. (1978). Interpretation of polymodal sediments. *J. Geol.* 86, 411–421. doi: 10.1086/649710

Bograd, S. J., Rabinovich, A. B., LeBlond, P. H., and Shore, J. A. (1997). Observations of seamount-attached eddies in the North Pacific. *J. Geophys. Res. Oceans* 102, 12441–12456. doi: 10.1029/97JC00585

Boulay, S., Colin, C., Trentesaux, A., Pluquet, F., Bertaux, J., and Blamart., D. (2003). Mineralogy and sedimentology of Pleistocene sediment in the South China Sea (ODP Site 1144). *Proc. ODP Sci. Results*, 184, 1-21. doi: 10.2973/odp.proc.sr.184.211.2003

Chang, L., Bolton, C. T., Dekkers, M. J., Hayashida, A., Heslop, D., Krijgsman, W., et al. (2016). Asian monsoon modulation of nonsteady state diagenesis in hemipelagic marine sediments offshore of Japan. *Geochem. Geophy. Geosy.* 17, 4383–4398. doi: 10.1002/2016GC006344

Chen, Y., Li, Y., Lyu, W., Xu, D., Han, X., Fu, T., et al. (2020). A 5000-year sedimentary record of East Asian winter monsoon from the northern muddy area of the east China sea. *Atmosphere* 11, 1376. doi: 10.3390/atmos11121376

Chen, Y., Lyu, W., Fu, T., Li, Y., and Yi., L. (2021). Centennial impacts of the east asian summer monsoon on holocene deltaic evolution of the huanghe river, China. *Appl. Sci.* 11, 2799. doi: 10.3390/app11062799

Chen, G., Wang, D., Dong, C., Zu, T., Xue, H., Shu, Y., et al. (2015). Observed deep energetic eddies by seamount wake. *Sci. Rep.* 5, 17416. doi: 10.1038/srep17416

Chen, Y., Xu, D., Qin, H., Liu, G., Li, Y., Chen, W., et al. (2023). Relationships between abyssal redox conditions and rock magnetic properties of surficial sediments in the western pacific. *J. Mar. Sci. Eng.* 11, (6). doi: 10.3390/jmse11061132

Costa, K. M., Anderson, R. F., McManus, J. F., Winckler, G., Middleton, J. L., and Langmuir, C. H. (2018). Trace element (Mn, Zn, Ni, V) and authigenic uranium (aU) geochemistry reveal sedimentary redox history on the Juan de Fuca Ridge, North Pacific Ocean. *Geochim. Cosmochim. Ac.* 236, 79–98. doi: 10.1016/j.gca.2018.02.016

Day, R., Fuller, M., and Schmidt., V. A. (1977). Hysteresis properties of titanomagnetites: Grain-size and compositional dependence. *Phys. Earth Planet. In.* 13, 260–267. doi: 10.1016/0031-9201(77)90108-X

Fedorov, A. V., Burls, N. J., Lawrence, K. T., and Peterson, L. C. (2015). Tightly linked zonal and meridional sea surface temperature gradients over the past five million years. *Nat. Geosci.* 8, 975–980. doi: 10.1038/ngeo2577

Ge, K., Williams, W., Liu, Q., and Yu., Y. (2014). Effects of the core-shell structure on the magnetic properties of partially oxidized magnetite grains: Experimental and micromagnetic investigations. *Geochem. Geophy. Geosy.* 15, 2021–2038. doi: 10.1002/2014GC005265

Gordon, A. L. (2001). "Bottom water formation," in *Encyclopedia of Ocean Sciences, 2nd ed.* Ed. J. H. Steele (Academic Press, Oxford), 415–421. doi: 10.1016/B978-012374473-9.00006-0

Guo, B., Wang, W., Shu, Y., He, G., Zhang, D., Deng, X., et al. (2020). Observed deep anticyclonic cap over caiwei guyot. *J. Geophys. Res. Oceans* 125, e2020JC016254. doi: 10.1029/2020JC016254

Hall, I. R., McCave, I. N., Shackleton, N. J., Weedon, G. P., and Harris, S. E. (2001). Intensified deep Pacific inflow and ventilation in Pleistocene glacial times. *Nature* 412, 809–812. doi: 10.1038/35090552

He, G., Zhao, Z., and Zhu, K. (2001). *Cobalt-Rich Crust Resources in the West Pacific* (Beijing: Geological Publishing House), 1–92.

Heslop, D. (2015). Numerical strategies for magnetic mineral unmixing. *Earth Sci. Rev.* 150, 256–284. doi: 10.1016/j.earscirev.2015.07.007

Heslop, D., and Roberts., A. P. (2012). A method for unmixing magnetic hysteresis loops. *J. Geophys. Res.-Sol. Ea.* 117, B03103. doi: 10.1029/2011JB008859

Hilgen, F. J., Lourens, L. J., Van Dam, J. A., Beu, A. G., Boyes, A. F., Cooper, R. A., et al. (2012). "Chapter 29 - the neogene period," in *The Geologic Time Scale*. Eds. F. M. Gradstein, J. G. Ogg, M. D. Schmitz and G. M. Ogg (Elsevier, Boston), 923–978.

Hodell, D. A., and Venz-Curtis, K. A. (2006). Late Neogene history of deepwater ventilation in the Southern Ocean. *Geochem. Geophy. Geosy.* 7, Q09001. doi: 10.1029/2005gc001211

Hu, B., Yi, L., Zhao, J., Guo, J., Ding, X., Wang, F., et al. (2021). Magnetostratigraphy of core XT06 and Quaternary sedimentary dynamics of the deep-sea deposits in the West Philippine Basin. *Mar. Geol. Quat. Geol.* 41, 61–74. doi: 10.16562/j.cnki.0256-1492.2020101301

Jackson, M., Worm, H.-U., and Banerjee, S. K. (1990). Fourier analysis of digital hysteresis data: rock magnetic applications. *Phys. Earth Planet. In.* 65, 78–87. doi: 10.1016/0031-9201(90)90077-B

Jacobel, A. W., McManus, J. F., Anderson, R. F., and Winckler., G. (2017). Repeated storage of respired carbon in the equatorial Pacific Ocean over the last three glacial cycles. *Nat. Commun.* 8, 1727. doi: 10.1038/s41467-017-01938-x

Jansen, J. H. F., Kuijpers, A., and Troelstra., S. R. (1986). A mid-brunhes climatic event: long-term changes in global atmosphere and ocean circulation. *Science* 232, 619–622. doi: 10.1126/science.232.4750.619

Jiang, Z., Sun, Z., Liu, Z., Cao, H., Geng, W., Xu, H., et al. (2019). Rare-earth element geochemistry reveals the provenance of sediments on the southwestern margin of the Challenger Deep. *J. Oceanol. Limnol.* 37, 998–1009. doi: 10.1007/s00343-019-8046-8

Johnson, G. C. (2008). Quantifying antarctic bottom water and north atlantic deep water volumes. *J. Geophysical Research: Oceans* 113, C05027. doi: 10.1029/2007jc004477

Kawabe, M., and Fujio, S. (2010). Pacific ocean circulation based on observation. *J. Oceanogr.* 66, 389–403. doi: 10.1007/s10872-010-0034-8

Kemp, A. E. S., Grigorov, I., Pearce, R. B., and Naveira Garabato, A. C. (2010). Migration of the Antarctic Polar Front through the mid-Pleistocene transition: evidence and climatic implications. *Quaternary Sci. Rev.* 29, 1993–2009. doi: 10.1016/j.quascirev.2010.04.027

Kissel, C., Laj, C., Jian, Z., Wang, P., Wandres, C., and Rebolledo-Vieyra., M. (2020). Past environmental and circulation changes in the South China Sea: Input from the magnetic properties of deep-sea sediments. *Quat. Sci. Rev.* 236, 106263. doi: 10.1016/j.quascirev.2020.106263

Kruiver, P. P., and Passier, H. F. (2001). Coercivity analysis of magnetic phases in sapropel S1 related to variations in redox conditions, including an investigation of the S ratio. *Geochem. Geophy. Geosy.* 2, (12). doi: 10.1029/2001GC000181

Lamy, F., Winckler, G., Arz, H. W., Farmer, J. R., Gottschalk, J., Lembke-Jene, L., et al. (2024). Five million years of Antarctic Circumpolar Current strength variability. *Nature* 627, 789–796. doi: 10.1038/s41586-024-07143-3

Lavelle, J. W., and Mohn, C. (2010). Motion, commotion, and biophysical connections at deep ocean seamounts. *Oceanography* 23, 90–103. doi: 10.5670/oceanog.2010.64

Li, J., Liu, Y., Liu, S., Roberts, A. P., Pan, H., Xiao, T., et al. (2020). Classification of a complexly mixed magnetic mineral assemblage in pacific ocean surface sediment by electron microscopy and supervised magnetic unmixing. *Front. Earth Sci.* 8. doi: 10.3389/feart.2020.609058

Lin, Z., Yi, L., Wang, H., Deng, X., Yang, J., Fu, T., et al. (2019). Rock magnetism of deep-sea sediments at Caiwei Guyot, Magellan seamounts of Northwest Pacific and its significance to abyssal environmental changes. *Chin. J. Geophys.* 62, 3067–3077. doi: 10.6038/cjg2019M0526

Lisiecki, L. E., and Raymo, M. E. (2005). A Pliocene-Pleistocene stack of 57 globally distributed benthic $\delta^{18}O$ records. *Paleoceanography* 20, PA1003. doi: 10.1029/2004pa001071

Liu, Q., Huo, Y.-Y., Wu, Y.-H., Bai, Y., Yuan, Y., Chen, M., et al. (2019). Bacterial community on a guyot in the northwest pacific ocean influenced by physical dynamics and environmental variables. *J. Geophys. Res.-Biogeo.* 124, 2883–2897. doi: 10.1029/2019JG005066

Liu, W., Liu, Z., Sun, J., Song, C., Chang, H., Wang, H., et al. (2020). Onset of permanent Taklimakan Desert linked to the mid-Pleistocene transition. *Geology* 48, 782–786. doi: 10.1130/G47406.1

Löwemark, L., März, C., O'Regan, M., and Gyllencreutz., R. (2014). Arctic Ocean Mn-stratigraphy: genesis, synthesis and inter-basin correlation. *Quat. Sci. Rev.* 92, 97–111. doi: 10.1016/j.quascirev.2013.11.018

Maxbauer, D. P., Feinberg, J. M., and Fox, D. L. (2016). MAX UnMix: A web application for unmixing magnetic coercivity distributions. *Comput. Geosci-UK* 95, 140–145. doi: 10.1016/j.cageo.2016.07.009

Özdemir, Ö, and Dunlop, D. J. (2010). Hallmarks of maghemitization in low-temperature remanence cycling of partially oxidized magnetite nanoparticles. *Geophys. Res.-Sol. Ea* 115, B02101. doi: 10.1029/2009JB006756

Paillard, D. (1998). The timing of Pleistocene glaciations from a simple multiple-state climate model. *Nature* 391, 378–381. doi: 10.1038/34891

Paterson, G. A., and Heslop, D. (2015). New methods for unmixing sediment grain size data. *Geochem. Geophy. Geosy.* 16, 4494–4506. doi: 10.1002/2015gc006070

Perfect, B., Kumar, N., and Riley., J. J. (2018). Vortex structures in the wake of an idealized seamount in rotating, stratified flow. *Geophys. Res. Lett.* 45, 9098–9105. doi: 10.1029/2018GL078703

Rea, D. K. (1994). The paleoclimatic record provided by eolian deposition in the deep sea: The geologic history of wind. *Rev. Geophys.* 32, 159–195. doi: 10.1029/93RG03257

Roberts, A. P., Tauxe, L., Heslop, D., Zhao, X., and Jiang, Z. (2018). A critical appraisal of the "Day" Diagram. *J. Geophys. Res.-Sol. Ea.* 123, 2618–2644. doi: 10.1002/2017JB015247

Robertson, R., Dong, J., and Hartlipp, P. (2017). Diurnal critical latitude and the latitude dependence of internal tides, internal waves, and mixing based on barcoo seamount. *J. Geophys. Res. Oceans* 122, 7838–7866. doi: 10.1002/2016JC012591

Schmidt, H., Berger, W., Bickert, T., and Wefer., G. (1993). "Quaternary carbon isotope record of pelagic foraminifers: Site 806, Ontong Java Plateau," in *Proceedings of the Ocean Drilling Program, Scientific Results*. Eds. W. Berger, L. Kroenke, T. Janecek, J. Backman, F. Bassinot and R. Corfield (Ocean Drilling Program, College Station, TX, USA), 397–409.

Slemons, L., Paul, B., Resing, J., and Murray, J. W. (2012). Particulate iron, aluminum, and manganese in the Pacific equatorial undercurrent and low latitude western boundary current sources. *Mar. Chem.* 142-144, 54–67. doi: 10.1016/j.marchem.2012.08.003

Stepashko, A. A. (2008). Spreading cycles in the pacific ocean. *Oceanology* 48, 401–408. doi: 10.1134/S0001437008030120

Sun, Y., Gao, S., and Li, J. (2003). Preliminary analysis of grain-size populations with environmentally sensitive terrigenous components in marginal sea setting. *Chin. Sci. Bull.* 48, 184–187. doi: 10.1360/03tb9038

Sun, Q., Song, J., Li, X., Yuan, H., Ma, J., and Wang, Q. (2020). Bacterial vertical and horizontal variability around a deep seamount in the Tropical Western Pacific Ocean. *Mar. pollut. Bull.* 158, 111419. doi: 10.1016/j.marpolbul.2020.111419

Talley, L. D. (2008). Freshwater transport estimates and the global overturning circulation: Shallow, deep and throughflow components. *Prog. Oceanogr.* 78, 257–303. doi: 10.1016/j.pocean.2008.05.001

Tzedakis, P. C., Crucifix, M., Mitsui, T., and Wolff., E. W. (2017). A simple rule to determine which insolation cycles lead to interglacials. *Nature* 542, 427–432. doi: 10.1038/nature21364

Wang, F., He, G., Wang, H., and Ren, J. (2016a). Geochemistry of rare Earth elements in a core from Mariana Trench and its significance. *Mar. Geol. Quat. Geol.* 36, 67–75. doi: 10.16562/j.cnki.0256-1492.2016.04.008

Wang, X., Li, H., Zhang, J., Chen, J., Xie, X., Xie, W., et al. (2024). Seamounts generate efficient active transport loops to nourish the twilight ecosystem. *Sci. Adv.* 10, eadk6833. doi: 10.1126/sciadv.adk6833

Wang, Y., Zhang, H., Liu, J., Zhang, X., and Zhu, B. (2016b). Abundances and spatial distributions of associated useful elements in Corich crusts from Caiwei Seamount in Magellan Seamounts. *Mar. Geol. Quat. Geol.* 36, 65–74. doi: 10.16562/j.cnki.0256-1492.2016.02.008

Wei, Z., Deng, X., Zhu, K., Yao, H., Yang, Y., and Ren, J. (2017). Characteristic of substrate rocks of Caiwei Seamounts in the west Pacific Ocean. *Mar. Geol. Front.* 33, 1–6. doi: 10.16028/j.1009-2722.2017.12001

Wessel, P. (1997). Sizes and ages of seamounts using remote sensing: implications for intraplate volcanism. *Science* 277, 802–805. doi: 10.1126/science.277.5327.802

Wessel, P., and Lyons, S. (1997). Distribution of large Pacific seamounts from Geosat/ERS-1: Implications for the history of intraplate volcanism. *J. Geophys. Res.-Sol. Ea.* 102, 22459–22475. doi: 10.1029/97JB01588

Xu, Z., Li, T., Clift, P. D., Lim, F., Wan, S., Chen, H., et al. (2015). Quantitative estimates of Asian dust input to the western Philippine Sea in the mid-late Quaternary and its potential significance for paleoenvironment. *Geochem. Geophy. Geosy.* 16, 3182–3196. doi: 10.1002/2015GC005929

Xu, P., Liu, F., Ding, Z., and Wang, C. (2016). A new species of the thorid genus Paralebbeus Bruce & Chace 1986 (Crustacea: Decapoda: Caridea) from the deep sea of the Northwestern Pacific Ocean. *Zootaxa* 4085, 119–126. doi: 10.11646/zootaxa.4085.1.5

Yamazaki, T. (2012). Paleoposition of the Intertropical Convergence Zone in the eastern Pacific inferred from glacial-interglacial changes in terrigenous and biogenic magnetic mineral fractions. *Geology* 40, 151–154. doi: 10.1130/g32646.1

Yang, Z., Qian, Q., Chen, M., Zhang, R., Yang, W., Zheng, M., et al. (2020). Enhanced but highly variable bioturbation around seamounts in the northwest Pacific. *Deep-Sea Res. Part I* 156, 103190. doi: 10.1016/j.dsr.2019.103190

Yang, S., Xing, J., Chen, D., and Chen, S. (2017). A modelling study of eddy-splitting by an island/seamount. *Ocean Sci.* 13, 837–849. doi: 10.5194/os-13-837-2017

Yao, H., Wang, F., Wang, H., Yu, M., Ren, J.-b., He, G., et al. (2021). Pleistocene magnetostratigraphy of four cores in the West Philippian Basin and regional sedimentary shift during the Mid-Pleistocene transition. *Geol. J.* 56, 2919–2929. doi: 10.1002/gj.4082

Yi, L. (2023). Diverse glacial ventilation in deep Pacific: An integrated record from Mariana Trench and Magellan Seamounts over last 1.2 Myr. *Global Planet. Change* 230, 104279. doi: 10.1016/j.gloplacha.2023.104279

Yi, L., Hu, B., Zhao, J., Jiang, X., Shu, Y., Wang, X., et al. (2022). Magnetostratigraphy of abyssal deposits in the central philippine sea and regional sedimentary dynamics during the quaternary. *Paleoceanogr. Paleocl.* 37, e2021PA004365. doi: 10.1029/2021PA004365

Yi, L., Li, Y., Mikhailik, P., Qi, Y., and Deng, C. (2023). Magnetic and geochemical scanning reveals growth history of marine ferromanganese crust on Detroit Seamount, northwest Pacific since the early Miocene. *Quat. Int.* 671, 52–61. doi: 10.1016/j.quaint.2023.08.002

Yi, L., Wang, H., Deng, X., Yuan, H., Xu, D., and Yao, H. (2021a). Geochronology and geochemical properties of mid-pleistocene sediments on the caiwei guyot in the northwest pacific imply a surface-to-deep linkage. *J. Mar. Sci. Eng.* 9, (3). doi: 10.3390/jmse9030253

Yi, L., Wang, H., Liu, G., Chen, Y., Yao, H., and Deng, X. (2021b). Magnetic minerals in Mid-Pleistocene sediments on the Caiwei Guyot, Northwest Pacific and their response to the Mid-Brunhes climate event. *Acta Oceanol. Sini.* 40, 1–11. doi: 10.1007/s13131-021-1872-5

Yi, L., Xu, D., Jiang, X., Ma, X., Ge, Q., Deng, X., et al. (2020). Magnetostratigraphy and authigenic $^{10}Be/^{9}Be$ dating of plio-pleistocene abyssal surficial sediments on the southern slope of mariana trench and sedimentary processes during the mid-pleistocene transition. *J. Geophys. Res. Oceans* 125, e2020JC016250. doi: 10.1029/2020JC016250

Yi, L., Yu, H.-J., Ortiz, J. D., Xu, X.-Y., Chen, S.-L., Ge, J.-Y., et al. (2012a). Late Quaternary linkage of sedimentary records to three astronomical rhythms and the Asian monsoon, inferred from a coastal borehole in the south Bohai Sea, China. *Palaeogeogr. Palaeoclimatol. Palaeoecol.* 329-330, 101–117. doi: 10.1016/j.palaeo.2012.02.020

Yi, L., Yu, H., Ortiz, J. D., Xu, X., Qiang, X., Huang, H., et al. (2012b). A reconstruction of late Pleistocene relative sea level in the south Bohai Sea, China, based on sediment grain-size analysis. *Sediment. Geol.* 281, 88–100. doi: 10.1016/j.sedgeo.2012.08.007

Yin, Q. (2013). Insolation-induced mid-Brunhes transition in Southern Ocean ventilation and deep-ocean temperature. *Nature* 494, 222–225. doi: 10.1038/nature11790

Zhai, F., and Gu, Y. (2020). Abyssal circulation in the Philippine sea. *J. Ocean U. China* 19, 249–262. doi: 10.1007/s11802-020-4241-7

Zhang, X., and Boyer, D. L. (1991). Current deflections in the vicinity of multiple seamounts. *J. Phys. Oceanogr.* 21, 1122–1138. doi: 10.1175/1520-0485(1991)021<1122:CDITVO>2.0.CO;2

Zhang, X., and Boyer, D. L. (1993). Laboratory study of rotating, stratified, oscillatory flow over a seamount. *J. Phys. Oceanogr.* 23, 1122–1141. doi: 10.1175/1520-0485(1993)023<1122:LSORSO>2.0.CO;2

Zhang, W., De Vleeschouwer, D., Shen, J., Zhang, Z., and Zeng, L. (2018). Orbital time scale records of Asian eolian dust from the Sea of Japan since the early Pliocene. *Quat. Sci. Rev.* 187, 157–167. doi: 10.1016/j.quascirev.2018.03.004

Zhao, B., Wei, Z., Yang, Y., He, G., Zhang, H., and Ma, W. (2020). Sedimentary characteristics and the implications of cobalt-rich crusts resources at Caiwei Guyot in the Western Pacific Ocean. *Mar. Georesour. Geotec.* 38, 1037–1045. doi: 10.1080/1064119X.2019.1648615

frontiers | Frontiers in Marine Science

TYPE Original Research
PUBLISHED 24 October 2024
DOI 10.3389/fmars.2024.1480906

OPEN ACCESS

EDITED BY
Jiangbo Ren,
Guangzhou Marine Geological Survey, China

REVIEWED BY
Huan Zhang,
University of Hamburg, Germany
Fenlian Wang,
Guangzhou Marine Geological Survey, China

*CORRESPONDENCE
Juan Yang
yangjuan@cugb.edu.cn

RECEIVED 14 August 2024
ACCEPTED 23 September 2024
PUBLISHED 24 October 2024

CITATION
Yang J, Xing Z, Liu B, Sun D, Wang C, Han L, Xia J, Zhang W and Song C (2024) Metal regeneration during an *ex-situ* disturbance experiment on deep-sea sediments from the polymetallic nodule area of western Pacific. *Front. Mar. Sci.* 11:1480906. doi: 10.3389/fmars.2024.1480906

Metal regeneration during an *ex-situ* disturbance experiment on deep-sea sediments from the polymetallic nodule area of western Pacific

Juan Yang[1,2]*, Zhaohui Xing[1], Baolin Liu[1,2], Dong Sun[3], Chunsheng Wang[3], Luwei Han[1], Jianxin Xia[1,2], Wenquan Zhang[4] and Chengbing Song[4]

[1]School of Ocean Sciences, China University of Geosciences, Beijing, China, [2]Key Laboratory of Polar Geology and Marine Mineral Resource (China University of Geosciences, Beijing), Ministry of Education, Beijing, China, [3]Key Laboratory of Marine Ecosystem and Biogeochemistry, Second Institute of Oceanography, Ministry of Natural Resources, Hangzhou, China, [4]National Deep Sea Center, Qingdao, China

The ecological implications of deep-sea mining, particularly the considerable discharge of suspended sediments during operational processes, have attracted substantial concerns. In order to reveal the metal regeneration dynamics in the polymetallic nodule area of the western Pacific Ocean, *ex-situ* sediment disturbance experiments were conducted on a research vessel. After two levels of regulated stirring disturbance were exerted for half an hour, the concentrations of 12 dissolved metals and physicochemical parameters, including Eh and pH, were monitored continuously in the overlying water for three days. Porewater samples were also collected at the starting and ending time of each experiment to detect the change of dissolved metal profiles within the sediments. The findings revealed that the sediment disturbance led to fluctuations in the concentrations of metals in the overlying water, with manganese exhibiting the most pronounced change at a coefficient of 208%. The temporal patterns of dissolved metal concentrations demonstrated a coherent behavior among certain metals, such as Li, V, Co, Ni, Rb, Mo, and Cs, which displayed an overall increase, ultimately surpassing the initial concentrations in the overlying water. In line with this, the metal concentration profiles in the porewater were also elevated. Spearman correlation analysis confirmed the synchronized behavior of these metals. The results suggested that the metals mobility might be governed by physicochemical factors in the overlying water. Moreover, the sedimentary features, such as grain size composition, and the morphological state of metals in sediments played pivotal roles in the differential responses of metal groups to sediment disturbance across stations. Conversely, the disturbance intensity was found to have a relatively minor impact on the dissolved metal

behavior. The findings from the *ex-situ* experiments provided critical insights for predicting metal regeneration related to deep-sea mining, which are expected to be validated through rigorous monitoring protocols during future *in-situ* mining trials.

KEYWORDS

deep-sea mining, metal regeneration, sediment disturbance, polymetallic nodules, Western Pacific

1 Introduction

Oceanic ferromanganese nodules are typical components of authigenic polymetallic deposits formed by the accretion of hydrated Mn and Fe hydroxide in deep ocean (Ren et al., 2024). They are scattered across the seafloor under diverse and often indistinct geological conditions, which have been identified as a promising alternative for strategic resources, particularly enriched in copper, nickel, and cobalt (Mero, 1965; Glasby, 1977; Amann, 1982; Petersen et al., 2016). Regional mapping showed that hydrogenetic nodules are distributed in the western and southern Pacific at low biological productivity sites, while diagenetic nodules are distributed in the eastern Pacific (Ren et al., 2024). Nonetheless, deep-sea mining operation on these ore deposits has profound impacts on the marine ecosystem (Amos and Roels, 1977; Ozturgut et al., 1978; Nath et al., 2001). The primary disruptions associated with deep-sea mining include (1) the wholesale excavation of surface sediments and the destruction of benthic communities, (2) localized elevations in suspended particulate matter, (3) crushing damage from tailings and overburden, and (4) enhanced toxicity resulting from metal release under high-pressure conditions (Li et al., 2006). When mining activities induce disturbances, elements in both solute and particulate forms may be introduced into the water column through the emergent plume, subsequent dispersal by ocean currents, and ultimate resettlement (Saulnier and Mucci, 2000). Under certain physicochemical conditions, dissolved metal elements may also be scavenged in the particulate or colloidal adsorption processes. These disturbances on bottom sediments can also trigger changes in geochemical attributes and biochemical conditions (Raghukumar et al., 2001), associated with the relocation of metals, which poses latent risks to benthic communities due to their toxicity and resistance to biodegradation (Caroppo et al., 2006; Duman et al., 2007; Varol and Sen, 2012; Drazen et al., 2020). Given the high mobility and bioavailability of these metals, their residence in the water column is critically concerning (Ankley et al., 1996).

Identifying the metal release linked to deep-sea sediment plumes is essential for fostering ecofriendly mining practices. Although the vertical distribution of porewater metals and their diffusion fluxes at the water–sediment interface in the polymetallic nodule area of western Pacific were investigated in our previous study (Yang et al., 2023), their response to sediment disturbance remained elusive. Since the 1970s, numerous experiments simulating deep-sea floor mining or sediment disturbance have been conducted (Burns et al., 1980; Thiel and Tiefsee-Umweltschutz, 2001; Volz et al., 2020), with the majority of research focusing on the impacts of substrate removal or deposition processes. According to the longest recolonization experiment to date, DISCOL, the potential short-term impacts of deep-sea mining activities on the geochemical system included the introduction of oxygen diffusion into previously hypoxic deposits, changes in redox conditions, and the acceleration of metal release and regeneration. The long-term impacts based on the observation over 26 years indicated that the recovery of highly active surface deposits could be protracted for millennia (Volz et al., 2020). However, the current findings are insufficient to provide validated data to evaluate the potential dispersion of toxic chemicals or nutrients associated with sediment disturbance during the mining operation. Recent numerical dispersion models to simulate the dispersion process of plumes during *in-situ* experiments as well as the concentration distribution of sediments over short durations (from several hours to months) suggested that plume dispersion may be limited by factors such as flocculation, background turbidity, and internal tides (Morato et al., 2022; Spearman et al., 2020). Nevertheless, the release and restoration of toxic chemicals in solution due to plume dispersion remain poorly understood.

In general, the increase in metal concentrations in the overlying water following sediment disturbance can be attributed to three primary factors: the release of pre-existing dissolved substances from the sediments, desorption from the sediment matrix, and the dissolution of suspended particles within the water column (Kalnejais et al., 2010). Previous *ex-situ* resuspension experiments conducted on contaminated coastal sediments have suggested that the released metals can be classified into distinct groups according to their properties, such as the dissolved or weakly adsorbed species, those bound within the crystalline lattice of minerals, or those incorporated in various amorphous solid compounds (Calmano et al., 1993). For example, metals with a high affinity for iron oxide [FeOOH(s)] are prone to be desorbed during the reduction of iron oxide. The environmental conditions encountered by suspended particles can also influence the processes of desorption or dissolution, such as scavenging processes during resuspension

(Morin and Morse, 1999; Saulnier and Mucci, 2000; Kalnejais et al., 2010). The properties of overlying water, including salinity, pH, and redox conditions, in conjunction with sedimentation rates, ultimately govern the residence time of these metals in the water column (Martino et al., 2002; Kiratli and Ergin, 1996; Roberts, 2012).

In order to quantify the behavior of dissolved metals throughout the processes of suspension and resettlement, sediment disturbance experiments were conducted on board by using deep-sea sediments and bottom water derived from the polymetallic nodule area in the western Pacific. The study aims to elucidate (1) the short-term response of various metals in the overlying water and sediment porewater after the sediment disturbance and (2) the impacts of physicochemical condition change after the sediment disturbance on the behavior of these metals. The findings are anticipated to provide more definitive evidence to assess the potential ecological risk associated with deep-sea mining.

2 Materials and methods

2.1 Source of sediment samples

Sediments were derived from the undisturbed surface sediments from two box corer sampling stations (BC04 and BC06) during the investigation on the 56th COMRA cruise in September 2019. The stations were located in the intermountain basin of the Marcus-Wake Seamounts Cluster, Northwest Pacific, with information presented in Table 1. Ferromanganese nodules are well developed in the study area (Machida et al., 2016; Ren et al., 2022).

2.2 Procedure of the *ex-situ* sediment disturbance experiments

After over 2 L of overlying water was sampled from the box corer, the rest of the overlying water was removed. Polymetallic nodules were collected before four plastic tubes with sealed holes on the walls were used to collect sediment cores.

The four parallel sediment cores were separated into two groups. One group was used for the sediment disturbance experiments and measurement on the change of overlying water and porewater properties after the disturbance, while the other group was used for the measurement on the porewater and sedimentary properties before the experiment.

As shown in Figure 1, the two parallel sediment cores were fixed and associated with the stirring devices, which were set at different levels of sediment disturbance. In order to minimize the interference of the experimental device, part of the equipment below the surface water level was made of nonmetallic material. The propellers were located 3 cm above the sediment surface to generate turbulence within the sediment tubes. A total of 1 L of the collected overlying water was filtered through 0.45-μm mesh filters and slowly injected into each sediment tube, respectively. Before the stirring began, the two sediment tubes with overlying water were

TABLE 1 Description of the sampling stations.

Station	Location	Depth (m)	Sedimentary description
BC04	161.5724° E, 15.6687° N	5,526	No biological disturbance; brown clay sediment with surficial nodules covered by 40%
BC06	149.7603° E, 13.4624° N	5,914	No biological disturbance; light brown clay sediment with surficial nodules and fragments covered by 15%

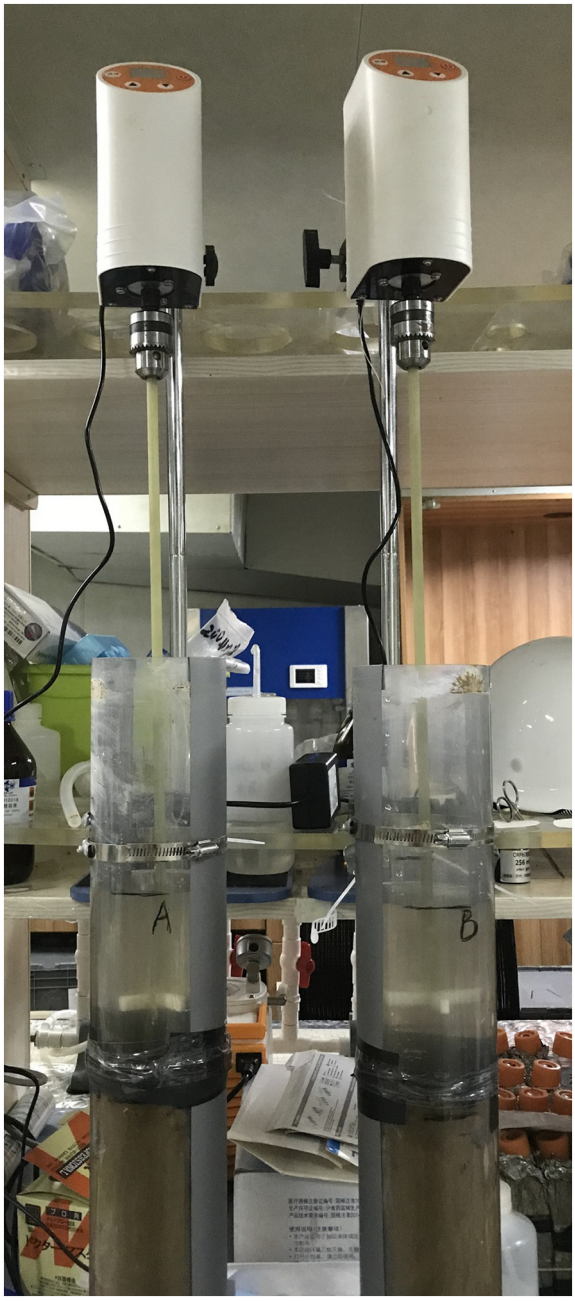

FIGURE 1
Onboard disturbance device.

allowed to stand for 30 min for equilibration. Each set of experiment lasted for 3 days with no more interruption from stormy weather or other induced rocking disturbance in the interim.

Two levels of stirring speed of the propeller working for half an hour at each station were set to simulate the process of sediment disturbance. The experiment was based on the assumption that the shear stress at the sediment–water interface was proportional to the stirring speed, which was 100 ± 5 and 600 ± 5 rpm, respectively, both beyond the erosion threshold of shear stress.

After the regulated disturbance ended and standing for a while, the overlying water was sampled temporally by using a syringe connected with an acid-cleaned hose dipping in the overlying water but 5 cm above the turbid water layer. In the meantime, Eh and pH were doubly measured by using Eh and pH meters (InnoORP 100, InnopH, TWINNO), and the thickness of the turbid water layer was recorded after the propeller stopped. The sampling intervals were before the disturbance and after the disturbance for 15, 30, 60, 2, 6, 12, 24, and 72 h. The volume of each overlying water sample was 10 mL, with a total water volume accounting for approximately 10% of the overlying water volume. The overlying water samples were filtered through a 0.45-μm syringe filter membrane before storing them in acid-cleaned polyethylene centrifuge tubes below -20°C.

After the completion of sampling and monitoring in the overlying water, porewater samples were collected immediately by using Rhizon soil solution collectors (model CSS 5 cm, Rhizosphere), which were inserted into the sampling tube through the sidewall drainage holes for syringe vacuum collection. The sampling depth was approximately 20 cm below the sediment surface, with intervals of 1 cm in the upper layers and 2 to 3 cm in the lower layers. The porewater was pumped in vacuum syringes within 2 to 3 hours. Afterward, they were capped with no air residue and stored at -20°C in a refrigerator. For comparison in the physicochemical properties between stations before the experiments, the porewater was also sampled with one replicated sediment core with no experimental disturbance.

2.3 Sediment and porewater measurement

In the other parallel sediment core with no experimental disturbance, the sediment core was segmented and divided into three parts to measure the morphological partitioning of metals, total organic carbon content (TOC), and grain size composition. Beforehand, the profile of Eh and pH were doubly measured by inserting the probes into the sediments through the sealed holes on the side wall of the plastic tube.

The different extractable fractionations of metals were obtained by using the European Commission-proposed BCR sequential extraction procedure (Rauret et al., 2000). 1 g of sediment sample was placed into 50-mL PE tubes, following the four sequential steps of BCR protocol (Ates et al., 2020). A blank sample with no sediment was carried through the complete procedure with each batch of extraction. Finally, the four extracted states underwent individual measurements by the ICP-MS method. The standard lake sediment, BCR 701 (European Commission, Joint Research Centre), was used to check the accuracy of the fraction analysis. The concentration values of the first three fractions of BCR 701 demonstrated a good consistency with the reference values. In addition, the total recovery with the sequential extraction procedure was calculated, ranging from 93% to 108%. Notably, the weak-acid-soluble state was electrostatically adsorbed onto the surfaces of soil and sediment particles or sequestered within carbonate matrices, facilitating its straightforward release through ion exchange processes. The reducible state, on the other hand, primarily consisted of elements adsorbed by iron oxide, manganese oxide, and similar compounds, with their release contingent upon alterations in redox conditions. Elements in the oxidizable state were predominantly integrated with the active moieties of organic matter or sulfides, capable of being regenerated during oxidative transformations. Lastly, the residual state, unyielded by extraction, housed elements that remained steadfast, predominantly embodied within the silicate lattice (Tessier et al., 1979; Singh et al., 2005; Fan et al., 2002).

The dissolved elements (Li, V, Co, Ni, Rb, Mo, Cs, Cd, Mn, Cu, Zn, and Pb) in porewater samples and those extractable fractionations of metals in sediment samples were determined by using inductively coupled plasma-mass spectrometry (ICP-MS, NexlON300D), following the standard procedure of MNR (Ministry of Natural Resources, 2021). The standard reference solutions were IV-ICPMS-71 A, IV-ICPMS-71 B, and MSLI-10PPM (Inorganic Ventures, Inc.). Four concentration levels (5, 10, 50, and 100 μg/L) of the standard solutions with 2% HNO_3 were used to fit the calibration curves. Repeated measurements on the standard of 10 μg/L were performed to control the relative error within ±5%. The reference materials, including freshwater SLRS-6 and seawater NASS-7, were used for quality control, with recoveries from 85% to 108%.

The total organic carbon content in sediment cores was determined by using the TOC Analyzer (vario TOC cube, Elememtar) according to the standard procedure. After the samples were weighed in silver cups, they were acidified with 1 mol/L HCl to remove carbonate and dried at 45°C before the measurement. The standard material GBW07430 (GSS-16) was used for accuracy control within ±<0.01%.

Grain size analysis for sediment cores was measured by using the Mastersizer 2000 instrument. Before the measurement, 30% (V/V) H_2O_2 was added to remove the organic matter from the sediment sample, and 1 mol/L HCl was added to remove the carbonate (shell fragments). The distribution in a graphic parameter of mean size (Mz) is described based on φ values in Equation (1) (McManus, 1988).

$$\phi = -\log_2^D \quad (1)$$

where D is the particle diameter (unit: μm). The higher the value of φ, the finer the grains in size.

The concentrations of SO_4^{2-} and Cl^- in porewater and overlying water were determined by ion chromatography (En-047). The measurement procedure followed the standard protocol (Ministry of Environmental Protection, 2016). Before the measurement, 1-mL water samples were diluted 10–100-fold with ultrapure water according to the concentration. The ultrapure water for blank samples and the standards were also measured repeatedly to

ensure the accuracy of measurement. NH_4^+ concentration in porewater samples was determined by using a spectrophotometer (HACH DR2800). Based on duplicate measurement, the relative error of analysis was within ±5%.

3 Results

3.1 Comparison of the physicochemical environment properties of the stations

As shown in Table 2, the features of overlying water from the two different stations were similar before sediment disturbance. The Eh of BC04 was slightly lower than that of BC06; however, the pH was slightly higher. The experiments were carried out under room temperature and aerobic conditions.

As shown in Figure 2, the vertical tendencies of Eh and pH at the two stations were similar as well. The pH ranged between 7.26 and 8.24, with the maximum in the overlying water, and remained low in the deep. In contrast, the Eh ranged between 240 and 340 mV, with the minimum in the overlying water and surface sediment.

The vertical trends of Cl^- and SO_4^{2-} and NH_4^+ concentrations in overlying water and porewater fluctuated similarly between stations (see Figure 2). The range was between 0.44 and 0.75 mol/L for Cl^-, between 0.022 and 0.042 mol/L for SO_4^{2-}, and between 6.7 and 10.0 μmol/L for NH_4^+. The maximum concentration of both Cl^- and SO_4^{2-} occurred at 5 cm below the sediment surface.

Figure 2 also shows similar profiles of the TOC in sediments, ranging between 0.28% and 0.47% and decreasing with depth at both stations. The mean grain size (Mz) at station BC04 was coarse in the surface sediment and remained fine below the depth of 2 cm, while the variation in mean grain size (Mz) at station BC06 was more vivid, coarser above the depth of 5 cm as well as below the depth of 17 cm. A more fluctuant hydrodynamic condition was suggested in station BC06 in comparison with station BC04.

The morphological partitioning of metals often reflected the mobility and bioavailability of metals in sediments. Figure 3 shows that the compositions in different states were relatively stable with depths and similar for specific metals at both stations. The predominant state was the residual for Li, V, Rb, Mo, and Cs, with an extremely high proportion (>85%), suggesting very limited mobility and bioavailability of these metals during the resuspension process. Moreover, Li had a relatively higher proportion in the oxidable state, which was potentially bound to organic matter.

Meanwhile, the proportion in the reducible state in sediments was relatively high for Co, Ni, Mn, Cd, Cu, and Pb, with a reducible/oxidable ratio of more than 9:1. The high content of the reducible state, especially for Co, Ni, and Mn, also indicated the potential increase of their mobility and bioavailability with the decrease of redox.

The proportion of the weakly acid soluble in all metals was extremely low. Meanwhile, the slight increase with depth in the residual state proportion for many metals also indicated the decrease of metal immobilization at both stations.

3.2 Temporal variation of physicochemical properties in the overlying water after the sediment disturbance

Similar fluctuating trends of Eh and pH were found under different levels of disturbance at both stations (see Figure 4). After the sediment disturbance terminated, Eh increased in the first 30 min and remained stable before decreasing 12 h later at station BC04. In contrast, the Eh value increased rapidly in the first 15 min and remained stable before decreasing 6 h later at station BC06. At both stations, the Eh values were high, ranging between 230 and 330 mV. Moreover, the Eh after the stirring disturbance under 600 rpm was generally higher than that under 100 rpm.

The trend of the pH values after sediment disturbance was also distinct under different stirring levels but similar at both stations. The variation of pH ranged between 7.8 and 8.2, showing a stronger decrease under the higher level of disturbance but gradually returning to the original level in the end of the experiments. In contrast, the pH at a low level of disturbance remained stable but decreased slightly with time after the disturbance terminated. The final pH values under both levels of disturbance were similar but lower than the initial pH at both stations.

3.3 Concentration variation of dissolved metals in the overlying water after the sediment disturbance

As shown in Figure 5, the concentrations of dissolved metals in the overlying water generally changed with time. According to their response to the disturbance, most metal concentrations increased gradually or fluctuated vividly, with final concentrations in the overlying water higher than the original concentrations. The elevated concentrations were higher under 600 rpm than under 100 rpm, such as Li, V, Co, Ni, Rb, Mo, Cs, and Cd. Other metals, such as Mn and Zn, were characterized as the metal concentrations below the initial concentration after the disturbance, fluctuating and finally returning

TABLE 2 Eh, pH, and temperature of the overlying water before sediment disturbance.

Experiment time	Station	Disturbance level	Eh (mV)	pH	Temperature (°C)
2019-09-22~2019-09-25	BC04	Low (100 rpm, 30min)	264	8.16	23.2
		High (600 rpm, 30min)	260	8.19	23.2
2019-10-05 2019-10-08	BC06	Low (100 rpm, 30min)	280	8.03	22.4
		High (600 rpm, 30min)	277	8.03	22.3

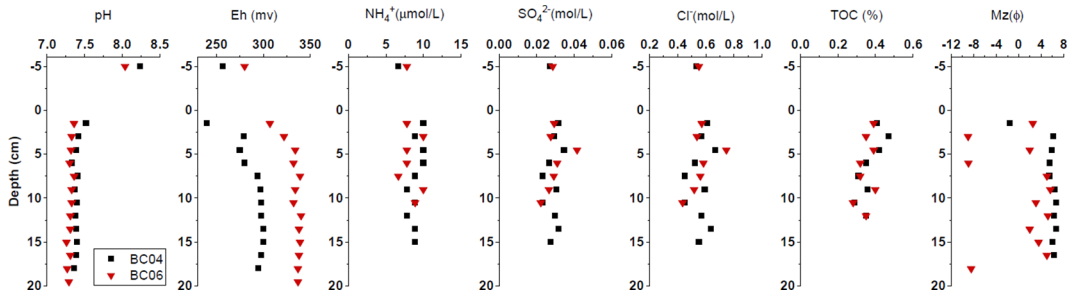

FIGURE 2
Vertical profiles of physicochemical parameters in porewater or sediments at stations BC04 and BC06.

to the initial concentrations. Although Cu and Pb demonstrated to be relatively stable after the disturbance, their concentrations could be also agitated at an early stage with a higher concentration under 600 rpm at station BC04. Moreover, the high scavenging capacity of suspended particles was also confirmed for metals such as Mn, Zn, Cu, and Pb, whose concentrations could decline below pre-disturbance levels or return to the equilibrium rapidly. When considering the resilience to the sediment disturbance, these metals performed better in comparison with the first group of metals.

Spearman correlation analysis on the temporal concentrations of dissolved metals in the overlying water demonstrated that highly positive correlations occurred between metals such as Li, V, Co, Ni, Rb, Mo, Cs, and Cu, especially under 100-rpm disturbance at BC04 and 600-rpm disturbance at BC06 (See Figures 6 and 7). In contrast, metals such as Mn, Zn, and Pb showed an insignificant correlation with the metals above. The exception was Cd, which was positively correlated with the first group of metals under 100-rpm disturbance at BC04 but negatively correlated with them under 100-rpm disturbance at BC06. Moreover, the temporal pH values were significantly negatively correlated with the concentrations of metals such as Li, Rb, Mo, Cs, and Cu under 100-rpm disturbance at BC06 but positively correlated with Cd under 600 rpm at BC04. It is worth noting that the temporal Eh showed an obviously negative correlation with Mn under 100/600-rpm disturbance at BC06, reflecting a high redox sensitivity of Mn.

As shown in Table 3, most variation coefficients were less than 50%, while very few of them could be over 100%, such as Mn and Zn. Those metals, including Li, V, Ni, Rb, Mo, Mn, Cu, Zn, and Pb, demonstrated a higher variation at the BC04 station in comparison with that under the same stirring disturbance level at BC06. The result coincided with the grain size composition of the two stations (see Figure 2). The coarser the mean grain size of the sediments, the less desorption of metals after the disturbance. Moreover, many metals, such as Li, V, Co, Ni, and Mn, demonstrated a higher variation under 100-rpm than that under 600-rpm stirring disturbance at station BC04 but demonstrated a reverse trend at station BC06. Very few metals, such as Rb and Zn, demonstrated a higher variation under lower disturbance levels at both stations, while Mo and Pb demonstrated a reverse trend at both stations. In brief, the impact of the disturbance level on the desorption and dissolution process for different metals is not consistent at different stations.

3.4 Vertical redistribution of dissolved metals in porewater along the depth

As shown in Figure 8, the vertical distributions of most metal concentrations in porewater before the disturbance were similar, with the maximum concentration in the subsurface layer. After the disturbance, almost all metal concentrations in porewater under both disturbance levels increased, and the subsurface peaks disappeared. Due to the continuum between the porewater and overlying water, the redistribution of dissolved metals in porewater, such as Li, V, Co, Ni, Rb, Mo, Cs, and Cd, indicated that metal regeneration could be triggered in sediments. The peak concentrations of many dissolved metals at the depth of 15–20 cm below the sediment surface, especially after the higher level of disturbance, might reflect the activation of metal regeneration in the deep layer.

4 Discussion

4.1 The influence of physicochemical background and disturbance intensity on the geochemical response of metals to the sediment disturbance

Marine sediments serve as both sinks and sources for the exchange of elements with the overlying water column, which can pose significant environmental hazards and elevated ecological risks (Zhong et al., 2006). Despite the release of dissolved metals into the porewater and overlying water being obvious during the experiments, the temporal change of most metal concentrations in the overlying water was concerted and fluctuating for balance in the end of the experiments. Previous research indicated that many external and internal factors have impacts on the element exchange between different phases. For example, sediments are generally categorized into oxic, suboxic, and anoxic based on the diagenetic sequence of terminal electron acceptors. The vertical profiles of Eh exceeding 300 mV, coupled with the predominance of the residual state for many metals in sediments, suggested the oxic sedimentary condition at both stations (see Figure 2). Moreover, the alteration in physicochemical properties, such as pH and Eh after the disturbance, also confirmed the oxic condition in overlying water during the resuspension and resettling processes, which partially accounted for the synchronized metal behaviors.

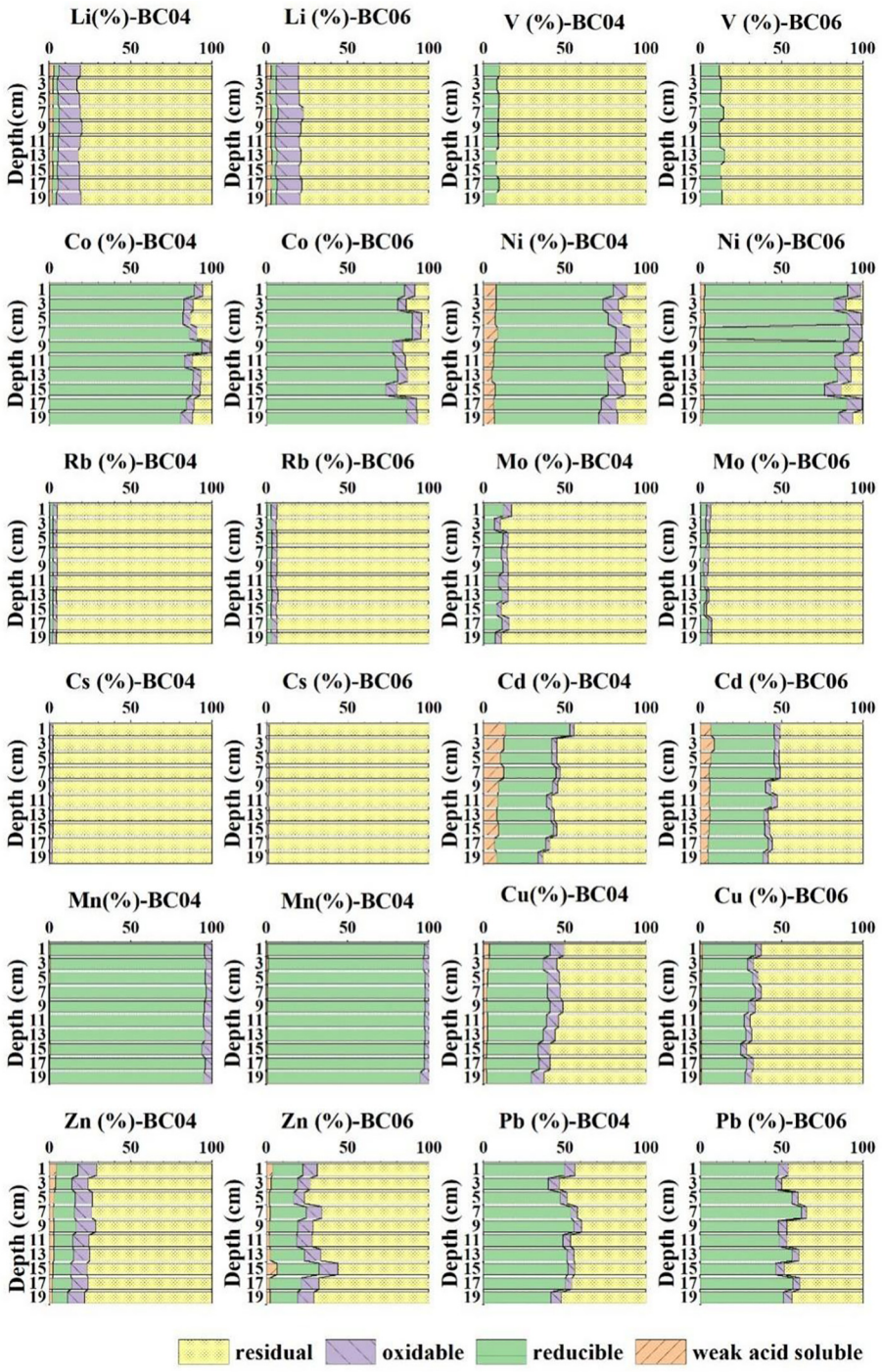

FIGURE 3
Partitioning of metals (Li, V, Co, Ni, Rb, Mo, Cd, Cs, Mn, Cu, Zn, and Pb) in sediments, including weakly acid-soluble, reducible, oxidable, and residual states.

Recent focus on the impacts of deep-sea mining was posed on the release of precipitates like Mn–Fe oxyhydroxides and mobile sediment constituents (Koschinsky et al., 2001; Volz et al., 2018; Stratmann et al., 2018). The mimetic experiments have confirmed that Mn and Fe oxides and oxyhydroxides are pivotal phases in scavenging many dissolved heavy metals (Koschinsky et al., 2003; Grybos et al., 2007). The preferential scavenging order for metals from seawater is typically Mn oxides > Fe oxides > silicate minerals (Takematsu, 1979). Additionally, many laboratory experiments have suggested that the resuspension of oxic to suboxic surface sediments into the bottom water is rapidly followed by the scavenging of dissolved heavy metals through various mechanisms—for example, hydrated cations such as Mn^{2+}, Co^{2+}, and Ni^{2+} are preferentially adsorbed or ion-exchanged onto the

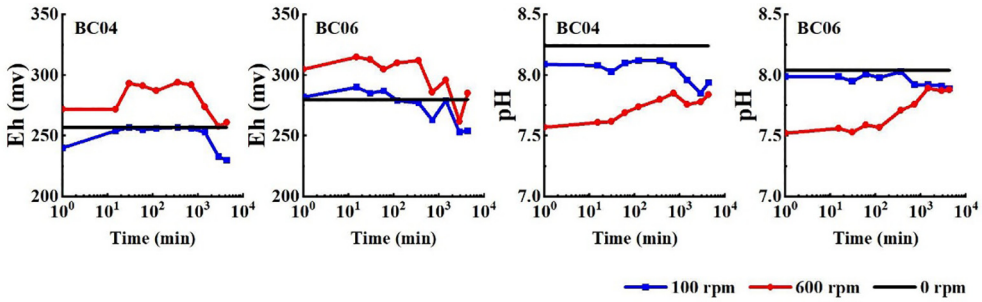

FIGURE 4
Temporal changes in pH and Eh in the overlying water at different disturbance levels and stations. Time intervals include 0 min (before the disturbance started) and 15, 30, 60, 120, 360, 720, 1,440, 2,880, and 4,320 min after the disturbance.

negatively charged surfaces of Mn oxides, whereas oxyanions and neutrally or negatively charged complexes, such as HVO_4^- and MoO_4^-, tend to associate with neutral to slightly positively charged amphoteric Fe oxyhydroxide particles. Other hydrated cations or labile cationic chloro-complexes, such as Cu^{2+}, Zn^{2+}, and $PbCl^+$, can be scavenged in both phases (Koschinsky et al., 2003).

The collective response of metals to the anthropogenic disturbances during the experiments also offered potential insights on their shared characteristics. In terms of their chemical properties, redox-sensitive elements such as V, Mo, and Cd exhibit pronounced responses to variations in oxygen concentrations (Morford and Emerson, 1999). The behavior of Mo, V, Ni, Co, and Cu was also found to be linked to Mn cycling (Paul et al., 2018; Morford et al., 2005), whereas the behavior of Cd was closely associated with Zn (Reddy and DeLaune, 2008; Calmano et al., 1993). Similarly, the concerted behavior among the dissolved metals such as Li, V, Co, Ni, Rb, Mo, and Cs (see Figures 6, 7) also indicated their involvement in similar scavenging processes with Mn and Fe oxides (Koschinsky et al., 2001). In contrast, metals like Cu, Pb, and Zn, with a high proportion of extractable states in sediments, were prone to be released into the overlying water during the resuspension process and rapidly scavenged following the disturbance. It coincided with the breakdown of SEM, which was rapid under oxidizing conditions, coupled with a decrease in pH. However, the rapid recovery of pH also effectively regulated the regeneration of heavy metals (Hong, 2009; Novikau and Lujaniene, 2022; Calmano et al., 1993). Although air exposure likely influenced the behavior of metals in our experimental setup, elements with a high proportion in residual state in sediments, such as V, Mo, Rb, and Cs, demonstrated similar behaviors when subjected to disturbance experiments conducted within a nitrogen-filled glove box (Shi et al., 2023), owing to the prevailing high redox sedimentary condition in both experimental configurations.

In addition, microorganisms can also accelerate the degradation of organic matter and enhance specific metal release during the resuspension process (Lors et al., 2004). The influence of microorganisms was not considered in the experiments owing to the low concentration of TOC in sediments and the short experiment period. However, as regards to a large scale for deep-sea mining, the structure and functional compositions of microbial communities associated with their change in sediments and overlying water must be evaluated in the future for their influence on metal behaviors during the resuspension and resettling processes.

In the context of environmental impacts of commercial deep-sea mining, the particle concentration effect was suggested to be an external factor influencing metal behavior predictions (Jones et al., 2017). The resuspended particles in the overlying water, including their concentration and size distribution, are critical in regulating metal regeneration processes (Trefry et al., 2014; Cantwell et al., 2008; Ma et al., 2019). Most metals have a propensity to resettle within fine particles, which was supported by various experiments and investigations (Ma et al., 2019; Cantwell et al., 2008; Trefry et al., 2014). However, the influence of disturbance intensity on particle concentration effects was not a decisive factor in the metal release process in our study—for instance, larger fluctuations in dissolved metals, such as Mn and Zn, were observed in the overlying water under low disturbance intensity (Table 3). However, a more pronounced fluctuation in metal concentrations within the overlying water was observed at both disturbance levels at station BC04, signifying the influence of sediment composition on metal release across various stations. Furthermore, the distinct temporal patterns in physicochemical characteristics observed under different

TABLE 3 Variation coefficient (%) of metal concentrations in the overlying water under different stirring disturbances at stations BC04 and BC06.

Station	Speed (rpm)	Li	V	Co	Ni	Rb	Mo	Cd	Cs	Mn	Cu	Zn	Pb
BC04	100	19.6	21.0	27.1	28.8	20.2	29.5	48.2	25.9	208.2	33.9	155.9	35.3
	600	15.0	11.4	15.5	10.9	14.2	29.9	50.8	27.1	165.9	45.9	83.5	98.7
BC06	100	7.3	4.7	10.5	4.0	10.8	16.8	64.2	30.1	18.0	8.3	105.1	20.7
	600	9.4	8.1	16.4	9.6	6.4	22.4	24.3	8.6	104.1	5.8	55.6	38.6

The variation coefficient (V) was calculated by using the equation V (%) = $(C_{Max} - C_{Min})/C_{mean} * 100$, where C denotes the temporal metal concentration in the overlying water.

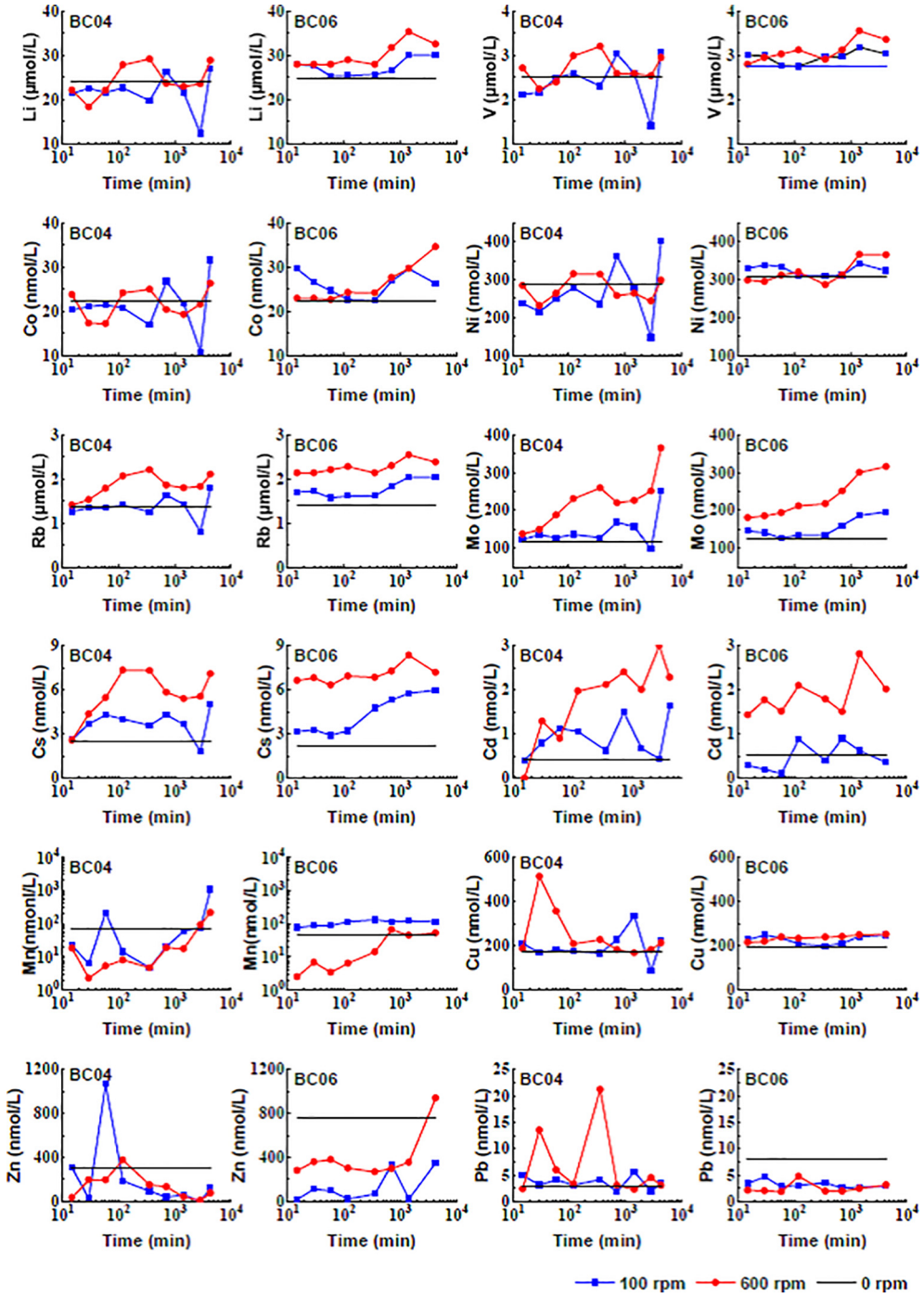

FIGURE 5
Temporal change in concentrations of 12 different metals in the overlying water.

disturbance levels (see Figure 4) provided an explanation for the significantly negative correlation between pH and the concentrations of metals such as Li, Rb, Mo, and Cs at the 100-rpm disturbance level and the significantly positive correlation between pH and metal concentrations including those of Cd, Zn, and Mn at 600 rpm at station BC06. Accordingly, the indirect effects of disturbance intensity on the scavenging capacity of suspended particles were enforced via the media of pH.

4.2 Potential toxic impacts of the dissolved metals after sediment disturbance

Identifying the potential impact of toxic metals released during deep-sea disturbance is a formidable challenge in assessing the ecological risks posed by deep-sea mining activities (Hauton et al., 2017). Benthic organisms take up metals through multiple pathways, including absorption through skin and gills and

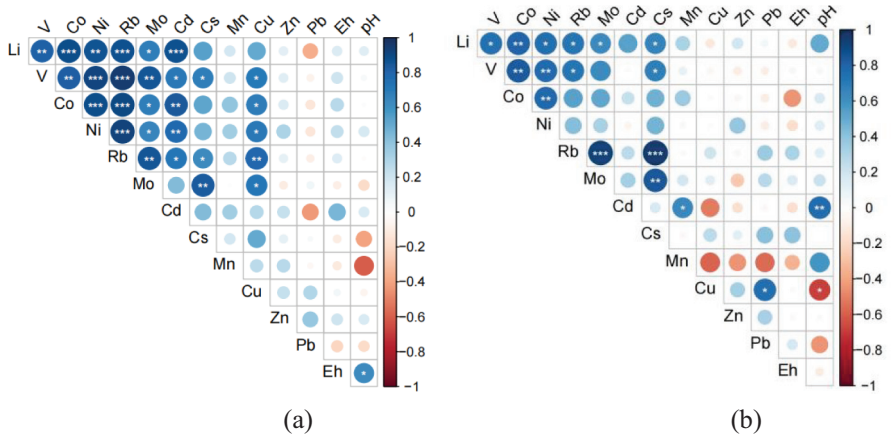

FIGURE 6
Spearman correlations between metal elements of different disturbance intensities at station BC04. **(A)** 100-rpm disturbance, **(B)** 600-rpm disturbance. The number of "*" denotes different significance levels.

ingestion of metal-contaminated sediments or food, yielding both acute and chronic toxic effects (Warren, 1981). The bioavailable metal fraction and the mobility of metals in the environment could be determined by the BCR sequential extraction procedure (Rauret et al., 2000). Thereby, SEM appears to be a good estimate of heavy metal bioavailability, which was applied for a large number of potentially toxic elements over a wide range (Bacon and Davidson, 2008), not only for the prediction of metal behavior under sediment disturbance but also for the potential contamination risk from the human and natural standpoint (Stohs and Bagchi, 1995; Ayala et al., 2014). In our study, Li, V, Rb, Mo, and Cs mainly existed in the residual state, indicating a lower probability of mobility and lower bioavailability and ecological risk. In contrast, those elements, such as Co, Ni, Mn, Cu, and Cd, with a higher fraction in the extractable state in sediments indicated a higher risk of biotoxicity. Moreover, Hauton et al. (2017) reported that redox-active metals, such as Co and Ni, can catalyze the formation of reactive oxygen and nitrogen species that can bind with lipids and cause lipid peroxidation and damage to cell membranes (Stohs and Bagchi, 1995; Ayala et al., 2014). As a large amount of Ni and Co exists in deep seafloor polymetallic nodules on the Northwest Pacific seafloor, the potential environmental risks of metal release during deep-sea mining activities (Hein et al., 1987) should be assessed based on the dissolution of Ni and Co into the water column.

In addition, attention has been given to the potential impacts of metal toxicity changes under deep-sea conditions with high pressure and low temperature during deep-sea mining activities. Scientists used toxicogenomics and the biodynamic model to evaluate metal mixture toxicity and identify associated mechanisms (Rainbow, 2007; Wu et al., 2016). To date, the combined effects of temperature and pressure have rarely been taken into account in modifying the metal tolerance of organisms (Carvalho et al., 1998; Fetters et al., 2016; Hauton et al., 2017), which should be explored based on the potential release of heavy metals, such as Cd, Cu, etc.

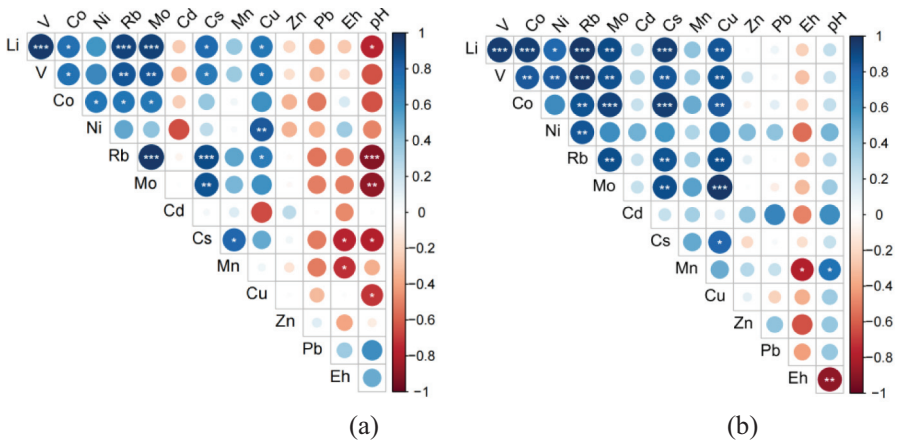

FIGURE 7
Spearman correlations between metal elements of different disturbance intensities at station BC06. **(A)** 100-rpm disturbance, **(B)** 600-rpm disturbance. The number of "*" denotes different significance levels.

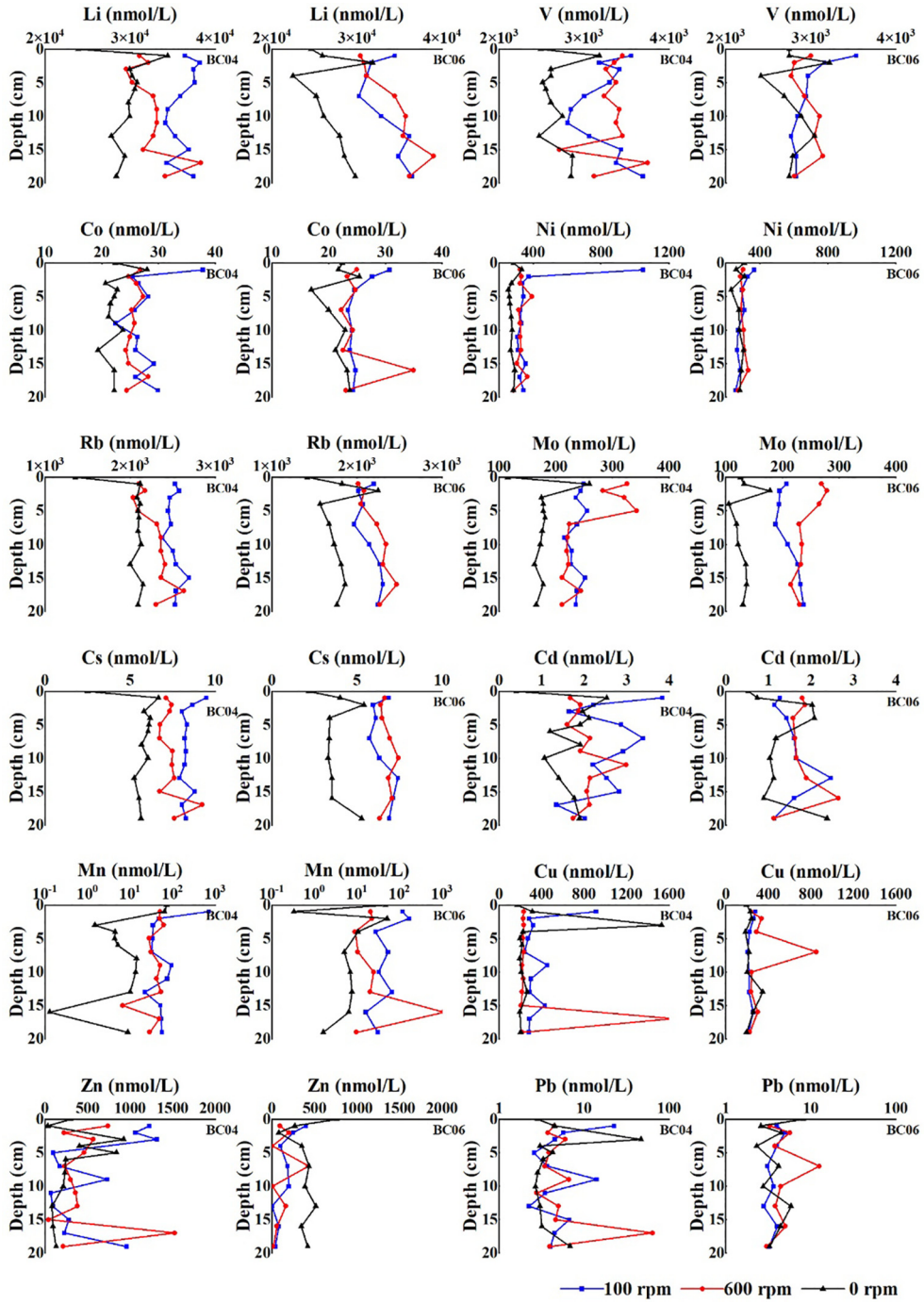

FIGURE 8
Vertical redistribution of dissolved metals in porewater before and after the experiments.

5 Conclusion

Sediment disturbance experiments were carried out to simulate the dissolved metal behavior with plumes aroused by deep-sea mining operations. The concentration of 12 dissolved metals in the overlying water was monitored during the resuspension and resettlement processes. According to their behavior, the 12 metals could be divided into different groups. Most metals, such as Li, V, Co, Ni, Rb, Mo, Cs, and Cd, showed a gradual increase, with the final concentrations being higher than the original concentrations. Others, such as Mn, Cu, Zn, and Pb, fluctuated vividly in the beginning but tended to return to equilibrium in the end of the experiment. Many internal and external factors have impacts on the concerted behavior of metals. The variation coefficients of metal concentration in the overlying water were more influenced by the sediment texture of the stations than by the level of disturbance intensities. Moreover, the concentrations of most metals in the porewater increased following both levels of disturbance, suggesting that the enrichment of those

dissolved metals in the overlying water was partially due to the regeneration of metals within the sediment matrix. The results provide valuable evidence for predicting the concerted behavior of metals under the disturbance of deep-sea mining activities in the polymetallic nodule area of western Pacific. Nevertheless, our current understanding of the environmental impacts of the deep seafloor is far from sufficient. *In-situ* experiments are urgently needed to simulate the resuspension and resettling processes under a larger disturbance scale on the deep seafloor with high pressure, low temperature, and bottom current environments.

Data availability statement

The raw data supporting the conclusions of this article will be made available by the authors, without undue reservation.

Author contributions

JY: Conceptualization, Data curation, Funding acquisition, Investigation, Methodology, Writing – original draft, Writing – review & editing, Validation. ZX: Formal analysis, Validation, Visualization, Writing – original draft. BL: Funding acquisition, Writing – review & editing, Project administration. DS: Data curation, Investigation, Writing – review & editing. CW: Data curation, Funding acquisition, Methodology, Resources, Writing – review & editing. LH: Data curation, Methodology, Writing – review & editing. JX: Funding acquisition, Writing – review & editing. WZ: Data curation, Writing – review & editing, Resources. CS: Data curation, Funding acquisition, Writing – review & editing.

Funding

The author(s) declare financial support was received for the research, authorship, and/or publication of this article. This research work was supported by the National Key R&D Program of China (2022YFC2803902, 2023YFC2811400, and SQ2021YFC2800022) and the China Ocean Mineral Resources Research and Development Association (DY135-E2-2-3).

Acknowledgments

We thank the crews of the 56th cruises of the Chinese Research expedition in the Pacific Ocean for their onboard assistance.

Conflict of interest

The authors declare that the research was conducted in the absence of any commercial or financial relationships that could be construed as a potential conflict of interest.

Publisher's note

References

Amann, H. (1982). Technological trends in ocean mining. *Phil. Trans. R. Soc. Lond. A*. 307, 377–403. doi: 10.1098/rsta.1982.0118

Amos, A. F., and Roels, O. A. (1977). Environmental aspects of manganese nodule mining. *Mar. Policy* 1, 156–163. doi: 10.1016/0308-597X(77)90050-1

Ankley, G., Toro, D. D., Hansen, D., and Berry, W. (1996). Assessing the ecological risk of metals in sediments. *Environ. Toxicol. Chem.* 15, 2053–2055. doi: 10.1002/etc.5620151201

Ates, A., Demirel, H., and Mergul, N. (2020). Risk assessment and chemical fractionation of heavy metals by BCR sequential extraction in soil of the Sapanca Lake Basin, Turk. *Pol. J. Environ. Stud.* 29, 1523–1533. doi: 10.15244/pjoes/101609

Ayala, A., Muñoz, M. F., and Argüelles, S. (2014). Lipid peroxidation: production, metabolism, and signaling mechanisms of malondialdehyde and 4-hydroxy-2-nonenal. *Oxid. Med. Cell. Longevity* 2014, 360438. doi: 10.1155/2014/360438

Bacon, J. R., and Davidson, C. M. (2008). Is there a future for sequential chemical extraction? *Analyst* 133, 25–46. doi: 10.1039/b711896a

Burns, R. E., Erickson, B., Lavelle, J. W., and Ozturgut, E. (1980). *Observations and measurements during the monitoring of deep ocean manganese nodule mining test in the North Pacific, April-May 1978, US Department of Commerce, NOAA technical Memorandum, ERL MESA-47.*

Calmano, W., Hong, J., and Förstner, U. (1993). Binding and mobilization of heavy metals in contaminated sediments affected by pH and redox potential. *Water Sci. Technol.* 28, 223–235. doi: 10.2166/wst.1993.0622

Cantwell, M. G., Burgess, R. M., and King, J. W. (2008). Resuspension of contaminated field and formulated reference sediments Part I: Evaluation of metal release under controlled laboratory conditions. *Chemosphere* 73, 1824–1831. doi: 10.1016/j.chemosphere.2008.08.007

Caroppo, C., Stabili, L., Aresta, M., Corinaldesi, C., and Danovaro, R. (2006). Impact of heavy metals and PCBs on marine picoplankton. *Environ. Toxicol.* 21, 541–551. doi: 10.1002/tox.20215

Carvalho, P. S. M., Zanardi, E., Buratini, S. V., Lamparelli, M. C., and Martins, M. C. (1998). Oxidizing effect on metal remobilization and *daphia similis* toxicity from a Brazilian reservoir sediment suspension. *Water Res.* 32 (1), 193–199. doi: 10.1016/S0043-1354(97)00186-3

Drazen, J. C., Smith, C. R., Gjerde, K. M., Haddock, S. H.D., Carter, G. S., Choy, C.A., et al. (2020). Midwater ecosystems must be considered when evaluating environmental risks of deep-sea mining. *Proc. Natl. Acad. Sci.* 117, 17455–17460. doi: 10.1073/pnas.2011914117

Duman, F., Aksoy, A., and Demirezen, D. (2007). Seasonal variability of heavy metals in surface sediment of lake Sapanca. *Turkey Environ. Monit. Assess.* 133, 277–283. doi: 10.1007/s10661-006-9580-3

Fan, W., Wang, W.-X., Chen, J., Li, X., and Yen, Y.-F. (2002). Cu, Ni, and Pb speciation in surface sediments from a contaminated bay of northern China. *Mar. pollut. Bull.* 44 (8), 820–826. doi: 10.1016/s0025-326x(02)00069-3

Fetters, K. J., Costello, D. M., Hammerschmidt, C. R., and Burton, G. A. Jr (2016). Toxicological effects of short-term resuspension of metal-contaminated freshwater and marine sediments. *Environ. Toxicol. Chem.* 35, 676–686. doi: 10.1002/etc.3225

Glasby, G. P. (1977). "Marine manganese deposits," in *Elsevier oceanography series 15* (Elsevier, Adsterdam), 523 pp.

Grybos, M., Davranche, M., Gruau, G., and Petitjean, P. (2007). Is trace metal release in wetland soils controlled by organic matter mobility or Fe-oxyhydroxides reduction? *J. Colloid Interface Sci.* 314, 490–501. doi: 10.1016/j.jcis.2007.04.062

Hauton, C., Brown, A., Thatje, S. C., Mestre, N. C., Bebianno, M. J., Martins, I., et al. (2017). Identifying toxic impacts of metals potentially released during deep-sea mining—A synthesis of the challenges to quantifying risk. *Front. Mar. Sci.* doi: 10.3389/fmars.2017.00368

Hein, J., Morgenson, L., Clague, D., and Koski, R. (1987), 753–771.

Hong, Y. (2009). *Experimental and mathematical investigation of dynamic availability of metals in sediment* [dissertation], (Austin: The University of Texas at Austin), P 7.

Jones, D. O. B., Kaiser, S., Sweetman, A. K., Smith, C. R., Menot, L., Vink, A., et al. (2017). Biological responses to disturbance from simulated deep-sea polymetallic nodule mining. *PloS One* 12, e0171750. doi: 10.1371/journal.pone.0171750

Kalnejais, L. H., Martin, W. R., and Bothner, M. H. (2010). The release of dissolved nutrients and metals from coastal sediments due to resuspension. *Mar. Chem.* 121, 224–235. doi: 10.1016/j.marchem.2010.05.002

Kiratli, N., and Ergin, M. (1996). Partitioning of heavy metals in surface Black Sea sediments. *Appl. Geochemistry* 11, 775–788. doi: 10.1016/S0883-2927(96)00037-6

Koschinsky, A., Gaye-Haake, B., Arndt, C., Maue, G., Spitzy, A., Winkler, A., et al. (2001). Experiments on the influence of sediment disturbances on the biogeochemistry of the deep-sea environment. *Deep Sea Res. Part II: Topical Stud. Oceanography* 48 (17-18), 3629–3651. doi: 10.1016/S0967-0645(01)00060-1

Koschinsky, A., Winkler, A., and Fritsche, U. (2003). Importance of different types of marine particles for the scavenging of heavy metals in the deep-sea bottom water. *Appl. Geochemistry* 18, 693–710. doi: 10.1016/S0883-2927(02)00161-0

Li, T., Wang, D., Zhang, B., Liu, H., and Tang, H. (2006). Characterization of the phosphate adsorption and morphology of sediment particles under simulative disturbing conditions. *J. Hazardous Materials* 137, 1624–1630. doi: 10.1016/j.jhazmat.2006.04.051

Lors, C., Tiffreau, C., and Laboudigue, A. (2004). Effects of bacterial activities on the release of heavy metals from contaminated dredged sediments. *Chemosphere* 56, 619–630. doi: 10.1016/j.chemosphere.2004.04.009

Ma, T., Sheng, Y., Meng, Y., and Sun, J. (2019). Multistage remediation of heavy metal contaminated river sediments in a mining region based on particle size. *Chemosphere* 225, 83–92. doi: 10.1016/j.chemosphere.2019.03.018

Machida, S., Fujinaga, K., Ishii, T., Nakamura, K., Hirano, N., and Kato, Y. (2016). Geology and geochemistry of ferromanganese nodules in the Japanese Exclusive Economic Zone around Minamitorishima Island. *Geochemical J.* 50, 1–17. doi: 10.2343/geochemj.2.0419

Martino, M., Turner, A., Nimmo, M., and Millward, G. E. (2002). Resuspension, reactivity and recycling of trace metals in the Mersey estuary. *Mar. Chem.* 77, 171–186. doi: 10.1016/S0304-4203(01)00086-X

McManus, J. (1988). Grain size determination and interpretation. *Techniques Sedimentol.*, 63–85.

Mero, J. L. (1965). "The mineral resources of the sea," in *Elsevier Oceanography Series, 1* (Elsevier Publishing Company, Amsterdam/London/New York), 312 pp, ISBN: .

Ministry of Environmental Protection. (2016). "Water quality-determination of inorganic anions (F^-、Cl^-、NO_2^-、Br^-、NO_3^-、PO_4^{3-}、SO_3^{2-}、SO_4^{2-})-ion chromatography," in *National Environmental Protection Standards of the People's Republic of China*. HJ84. (Beijing: China Environmental Science Press).

Ministry of Natural Resources. (1921). "Methods for analysis of groundwater quality—part 80: determination of forty element (lithium,rubidium,cesium, etc) concentrations—by inductively coupled plasma mass spectrometry," in *People's Republic of China, Industry Standards, Geology CN-DZ*, DZ/T 0064.80-2021.

Morato, T., Juliano, M., Pham, C. K., Carreiro-Silva, M., and Martins I and Colaço, A. (2022). Modelling the dispersion of seafloor massive sulphide mining plumes in the mid atlantic ridge around the azores. *Front. Mar. Sci.* 9. doi: 10.3389/fmars.2022.910940

Morford, J. L., and Emerson, S. (1999). The geochemistry of redox sensitive trace metals in sediments. *Geochimica Cosmochimica Acta* 63, 1735–1750. doi: 10.1016/S0016-7037(99)00126-X

Morford, J. L., Emerson, S. R., Breckel, E. J., and Kim, S. H. (2005). Diagenesis of oxyanions (V, U, Re, and Mo) in porewaters and sediments from a continental margin. *Geochimica Cosmochimica Acta* 69, 5021–5032. doi: 10.1016/j.gca.2005.05.015

Morin, J., and Morse, J. W. (1999). Ammonium release from resuspended sediments in the Laguna Madre estuary. *Mar. Chem.* 65, 97–110. doi: 10.1016/S0304-4203(99)00013-4

Nath, B. N., Parthiban, G., and Sankar, S. J. (2001). Sediment redistribution during simulated benthic disturbance and its implications on deep seabed mining. *Deep-Sea Res. Part II* 48, 3363–3380. doi: 10.1016/S0967-0645(01)00046-7

Novikau, R., and Lujaniene, G. (2022). Adsorption behaviour of pollutants: Heavy metals, radionuclides, organic pollutants, on clays and their minerals (raw, modified and treated): A review. *J. Environ. Manage.* 309, 114685. doi: 10.1016/j.jenvman.2022.114685

Ozturgut, E., Anderson, G. C., Burns, R. E., Lavelle, J. W., and Swift, S. A. (1978). "Deep ocean mining of manganese nodules in North Pacific Ocean," in *Pre-mining environmental conditions and anticipated mining effects. NOAA-TM-ERL MESA-33* (National Oceanic and Atmospheric Administration, USA), 138 pp.

Paul, S., Gaye, B., Haeckel, M., Kasten, S., and Koschinsky, A. (2018). Biogeochemical regeneration of a nodule mining disturbance site: trace metals, DOC and amino acids in deep-sea sediments and porewaters. *Front. Mar. Sci.* 5. doi: 10.3389/fmars.2018.00117

Petersen, S., Krätschell, A., Augustin, N., Jamieson, J., Hein, J. R., and Hannington, M. D. (2016). News from the seabed – Geological characteristics and resource potential of deep-sea mineral resources. *Mar. Policy* 70, 175–187. doi: 10.1016/j.marpol.2016.03.012

Raghukumar, C., Bharathi, P. A. L., Ansari, Z. A., Nair, S., Ingole, B., Sheelu, G., et al. (2001). Bacterial standing stock, meiofauna and sediment-nutrient characteristics: Indicators of benthic disturbance in the Central Indian Basin. *Deep-Sea Res. Part II* 48, 3381–3399. doi: 10.1016/S0967-0645(01)00047-9

Rainbow, P. S. (2007). Trace metal bioaccumulation: Models, metabolic availability and toxicity. *Environ. Int.* 33, 576–582. doi: 10.1016/j.envint.2006.05.007

Rauret, G., López-Sánchez, J. F., Sahuquillo, A., Barahona, E., Lachica, M., Ure, A. M., et al. (2000). Application of a modified BCR sequential extraction (three-step) procedure for the determination of extractable trace metal contents in a sewage sludge amended soil reference material (CRM 483), complemented by a three-year stability study of acetic acid and EDTA extractable metal content. *J. Environ. Monit.* 2, 228–233. doi: 10.1039/b001496f

Reddy, K. R., and DeLaune, R. D. (2008). *Biogeochemistry of Wetlands: Science and Applications. 1st ed* (Boca Raton: CRC Press). doi: 10.1201/9780203491454

Ren, J., He, G., Deng, X., Deng, X., Yang, Y., Yao, H., et al. (2022). Metallogenesis of Co-rich ferromanganese nodules in the northwestern Pacific: Selective enrichment of metallic elements from seawater. *Ore Geology Rev.* 143, 104778. doi: 10.1016/j.oregeorev.2022.104778

Ren, J., He, G., Yang, Y., Yu, M., Deng, Y., Pang, Y., et al. (2024). Ultraselective enrichment of trace elements in seawater by Co-rich ferromanganese nodules. *Global Planetary Change* 239, 104498. doi: 10.1016/j.gloplacha.2024.104498

Roberts, D. A. (2012). Causes and ecological effects of resuspended contaminated sediments (RCS) in marine environments. *Environ. Int.* 40, 230–243. doi: 10.1016/j.envint.2011.11.013

Saulnier, I., and Mucci, A. (2000). Trace metal remobilization following the resuspension of estuarine sediments: Saguenay Fjord, Canada. *Appl. Geochemistry* 15, 191–210. doi: 10.1016/S0883-2927(99)00034-7

Shi, P., Yang, J., Sun, D., and Wang, C. (2023). A simulation from offsite disturbance experiments on the metal resuspension process in the seafloor of the western Pacific. *Chemosphere* 311, 137042. doi: 10.1016/j.chemosphere.2022.137042

Singh, K., Mohan, D., Singh, V., and Malik, A. (2005). Studies on distribution and fractionation of heavy metals in Gomti river sediments - A tributary of the Ganges, India. *J. Hydrology* 312, 14–27. doi: 10.1016/j.jhydrol.2005.01.021

Spearman, J., Taylor, J., Crossouard, N., Cooper, A., Turnbull, M., Manning, A., et al. (2020). Measurement and modelling of deep sea sediment plumes and implications for deep sea mining. *Sci. Rep.* 10, 5075. doi: 10.1038/s41598-020-61837-y

Stohs, S. J., and Bagchi, D. (1995). Oxidative mechanisms in the toxicity of metal ions. *Free Radical Biol. Med.* 18, 321–336. doi: 10.1016/0891-5849(94)00159-h

Stratmann, T., Mevenkamp, L., Sweetman, A., Vanreusel, A., and Oevelen, D. (2018). Has phytodetritus processing by an abyssal soft-sediment community recovered 26 years after an experimental disturbance? *Front. Mar. Sci.* 5. doi: 10.3389/fmars.2018.00059

Takematsu, N. (1979). Sorption of transition metals on manganese and iron oxides, and silicate minerals. *J. Oceanographical Soc. Japan* 35, 36–42. doi: 10.1007/BF02108280

Tessier, A., Campbell, P., and Bisson, M. (1979). Sequential extraction procedure for the speciation of particular trace elements. *Environ. Technol.* 15 (7), 844–851. doi: 10.1021/ac50043a017

Thiel, H., and Tiefsee-Umweltschutz, F. (2001). Evaluation of the environmental consequences of polymetallic nodule mining based on the results of the TUSCH Research Association. *Deep-Sea Res. II* 48, 3433–3452. doi: 10.1016/S0967-0645(01)00051-0

Trefry, J. H., Trocine, R. P., Cooper, L. W., and Dunton, K. H. (2014). Trace metals and organic carbon in sediments of the northeastern Chukchi Sea. *Deep Sea Res. Part II: Topical Stud. Oceanography* 102, 18–31. doi: 10.1016/j.dsr2.2013.07.018

Varol, M., and Sen, B. (2012). Assessment of nutrient and heavy metal contamination in surface water and sediments of the upper Tigris River, Turkey. *Catena* 92, 1–10. doi: 10.1016/j.catena.2011.11.011

Volz, J., Haffert, L., Haeckel, M., Koschinsky, A., and Kasten, S. (2020). Impact of small-scale disturbances on geochemical conditions, biogeochemical processes and element fluxes in surface sediments of the eastern Clarion-Clipperton Zone, Pacific Ocean. *Biogeosciences* 17, 1113–1131. doi: 10.5194/bg-17-1113-2020

Volz, J. B., Mogollón, J. M., Geibert, W., Arbizu, P. M., Koschinsky, A., and Kasten, S. (2018). Natural spatial variability of depositional conditions, biogeochemical processes and element fluxes in sediments of the eastern Clarion-Clipperton Zone, Pacific Ocean. *Deep Sea Res. Part I: Oceanographic Res. Papers* 140, 159–172. doi: 10.1016/j.dsr.2018.08.006

Warren, L. J. (1981). Contamination of sediments by lead, zinc and cadmium: A review. *Environ. Pollut. Ser. B Chem. Phys.* 2, 401–436. doi: 10.1016/0143-148X(81)90037-9

Wu, X., Cobbina, S., Mao, G., Xu, H., Zhang, Z., and Yang, L. (2016). A review of toxicity and mechanisms of individual and mixtures of heavy metals in the environment. *Environ. Sci. pollut. Res.* 23, 8244–8259. doi: 10.1007/s11356-016-6333-x

Yang, J., Nie, H., Sun, D., and Wang, C. (2023). Environmental controls on the distribution of metals in porewater and their diffusion fluxes at the sediment-water interface of the western Pacific. *Appl. Geochemistry* 148, 105520. doi: 10.1016/j.apgeochem.2022.105520

Zhong, A., Guo, S., Li, F., Li, G., and Jiang, K. (2006). Impact of anions on the heavy metals release from marine sediments. *J. Environ. Sci.* 18, 1216–1220. doi: 10.1016/S1001-0742(06)60065-X

frontiers | Frontiers in Marine Science

TYPE Original Research
PUBLISHED 11 November 2024
DOI 10.3389/fmars.2024.1430572

OPEN ACCESS

EDITED BY
Francisco Javier González,
Instituto Geológico y Minero de España (IGME), Spain

REVIEWED BY
Chunming Dong,
Third Institute of Oceanography, Ministry of Natural Resources, China
Blanca Rincón-Tomás,
Instituto Geológico y Minero de España (IGME), Spain

*CORRESPONDENCE
Qian Liu
liuqian@sio.org.cn

†These authors have contributed equally to this work and share first authorship

RECEIVED 10 May 2024
ACCEPTED 10 October 2024
PUBLISHED 11 November 2024

CITATION
Lai M, Liu Q, Wang X, Sun D, Ran L, Li X, Yang C, Lu B, Xu X-W and Wang C-S (2024) Heterogeneous marine environments diversify microbial-driven polymetallic nodule formation in the South China Sea.
Front. Mar. Sci. 11:1430572.
doi: 10.3389/fmars.2024.1430572

Heterogeneous marine environments diversify microbial-driven polymetallic nodule formation in the South China Sea

Mingyan Lai[1†], Qian Liu[1,2,3*†], Xiaogu Wang[1], Dong Sun[1], Lihua Ran[1], Xiaohu Li[3,4,5], Chenghao Yang[2], Bo Lu[1], Xue-Wei Xu[6] and Chun-Sheng Wang[1,2,5]

[1]Key Laboratory of Marine Ecosystem Dynamics, Second Institute of Oceanography, Ministry of Natural Resources, Hangzhou, China, [2]State Key Laboratory of Satellite Ocean Environment Dynamics, Second Institute of Oceanography, Ministry of Natural Resources, Hangzhou, China, [3]Ocean College, Zhejiang University, Hangzhou, China, [4]Key Laboratory of Submarine Geoscience, Second Institute of Oceanography, Ministry of Natural Resources, Hangzhou, China, [5]School of Oceanography, Shanghai Jiao Tong University, Shanghai, China, [6]National Deep Sea Center, Ministry of Natural Resources, Qingdao, China

Most studies on the genesis of polymetallic nodules suggested that nodules in the South China Sea (SCS) are hydrogenetic; however, the complexity and the heterogeneity in hydrology and geochemistry of the SCS might cause different processes of nodule formation, impacting their application and economic value. Microbial-mediated ferromanganese deposition is an important process in nodule formation, but the related microbial potentials are still unclear in the SCS. In this study, we sampled in three typical regions (A, B, and C) of the SCS enriched with polymetallic nodules. Firstly, we investigated environmental and microbial characteristics of the water columns to determine the heterogeneity of upper seawater that directly influenced deep-sea environments. Then, microbial compositions and structures in sediment cores, overlying waters, and nodules (inside and outside) collected within the same region were analyzed for inferring features of nodule environments. Microbial interactions between nodules and surrounding environments were estimated with collinear network analysis. The microbial evidence indicated that geochemical characteristics in deep sea of the SCS that were key to the polymetallic nodule formation were severely affected by organic matter flux from upper water column. The sediment in region A was sub-oxic due to the large input of terrigenous and phytoplankton-derived organic matter, potentially enhancing the overflow of reduced metals from the porewater. The intense microbial interaction between nodules and surface sediment reinforced the origin of metals for the ferromanganese deposition from the sediment (diagenetic type). Contrarily, the sediments in regions B and C were relatively rich in oxygen, and metal ions could be majorly supplied from seawater (hydrogenetic type). The large discrepancy in microbial communities between nodule inside and remaining samples suggested that nodules experienced a long-term formation process, consistent with the feature of

hydrogenetic nodules. Overall, distributions and interactions of microbial communities in nodules and surrounding environments significantly contributed to the nodule formation in the SCS by manipulating biogeochemical processes that eventually determined the source and the fate of metal ions.

KEYWORDS

polymetallic nodules, The South China Sea, bacteria, archaea, nodule formation

1 Introduction

Polymetallic nodules are important metal sinks in the ocean, tremendously impacting on global ocean metal chemistry (Hein and Koschinsky, 2014; Shiraishi et al., 2016; Chen et al., 2018). They contain rich Mn, Cu, Ni, Co, rare earth elements, and platinum group elements, being considered as economically significant metal sources (Hein et al., 2013, 2015; Hollingsworth et al., 2021). The nodule formation mechanism has been studied since the 1960s (Ehrlich, 1963). Polymetallic nodules usually form at the water–sediment interface, where the sedimentation rate is low (Jiang et al., 2020). They grow slowly (several to hundreds of mm myr^{-1}) via concentric accumulation of iron and manganese oxides around nuclei (Shiraishi et al., 2016; Jiang et al., 2020). Although inorganic processes are often emphasized with respect to the nodule formation, the evidence for the significance of the microbial role in nodule formation is accumulating (Li et al., 2021). Recent studies on micromorphology and microbial community structure reveal microbial contribution to the nodule formation in marine environments; for example, a high abundance of nodule-specific Mn-cycling bacteria (e.g., *Shewanella*, *Colwellia*, and *Pseudoalteromonas*) were identified in nodules from an abyssal plain (Wu et al., 2013; Blöthe et al., 2015), and the microbial communities of the nodules were significantly distinct from the communities in surrounding sediments (Tully and Heidelberg, 2013). These results provide some clues to the biologically driven metal cycle associated with the nodule formation in the seafloor environment.

Generally, polymetallic nodules are classified based on the source of metal ions in the ocean (Chen et al., 2018). A Mn–(Cu +Co+Ni)–Fe ternary diagram is used to divide ferromanganese deposits into three types: hydrogenetic, diagenetic, and hydrothermal types (Halbach et al., 1981). Nodules are solely hydrogenetic when all constituents are derived from seawater (e.g., Cook Islands; Hein et al., 2015) or solely diagenetic when metal ions originate from sediment porewaters (e.g., Peru Basin; von Stackelberg, 2017). Most nodules acquire metals from both sources (Hein and Koschinsky, 2014). Hydrothermal nodules often precipitate in the vicinity of vent sites from fluids with temperatures higher than ambient bottom waters (González et al., 2016). Polymetallic nodules in the Pacific Ocean have been studied extensively with hydrogenetic type in the north-equatorial region and diagenetic type in the east Pacific. Nodules from the Clarion–Clipperton Zone (CCZ) located in the northeast equatorial Pacific Ocean and Central Indian Ocean Basin represent mixed hydrogenetic–diagenetic nodules (Kuhn et al., 2018; Hein et al., 2020), while those from the Peru Basin are mainly diagenetic origin (von Stackelberg, 1997; Zhong et al., 2017).

Marginal seas have been regarded as unfavorable for the formation of ferromanganese nodules, as the large influx of terrigenous sediments can easily dilute Fe and Mn oxides and bury any potential precipitates that may form polymetallic nodules (Zhang et al., 2013). However, the exploration progress in marginal sea shows enriched nodules and crust distributions, such as Galicia Bank at the northwest Atlantic Iberia margin (González et al., 2016), the Gulf of Cadiz (González et al., 2012), the California continental margin (Hein et al., 2005), and Canary Island Seamount Province (Marino et al., 2017), where Fe–Mn deposits are mostly hydrogenetic. As the third largest marginal sea of the world, the investigation of the metallogenic and exploration potentials of polymetallic nodules in the South China Sea (SCS) has been in progress (Zhang et al., 2013; Guan et al., 2017; Zhong et al., 2020; Ren et al., 2023). Increasing detection of Fe–Mn polymetallic deposits in the central basin of the SCS in recent years (Hang and Wang, 2006; Guan et al., 2017, 2019) has suggested that nodules in the SCS are mainly hydrogenetic in terms of the ore composition and the ratio of iron to manganese (Guan et al., 2017; Ren et al., 2023). However, the recognition of nodule types and formation still remains limited in the SCS due to the shortage of nodule exploration and lack of the understanding of microbial contributions. In this study, we selected three typical regions in the SCS where the nodules were ubiquitously distributed and intended to investigate the impact of environmental heterogeneity on geochemical and biological characteristics at the interface of nodules and surrounding environments to understand the mechanisms of polymetallic nodule formation in the SCS. The hypothesized models of the nodule formation were proposed based on the microbial-derived interactions between nodules and surrounding environments.

2 Methods and materials

2.1 Sample collection

The survey was conducted in the SCS during the cruise DY38 by RV Xiangyanghong 9 from 7 April to 13 May in 2017. We sampled at regions A, B, and C where the nodules were detected (Figures 1A, B; Table 1). Region A was located on the edge of the northern slope, and regions B and C were on seamount slopes in the Xisha Sea area and near the Luzon Strait, respectively (Figure 1A). Within each region, seawater samples were collected from discrete depths of the water column at stations CTDA, CTDB, and CTDC using a conductivity–temperature–depth (CTD, SBE 911plus, Sea-Bird Electronics, Bellevue, Washington, US) rosette sampler equipped with 24 10-L sampling bottles (Table 1). Temperature and salinity were monitored with sensors on CTD. The samples for measuring concentrations of particulate organic carbon (POC), dissolved oxygen (DO), chlorophyll-*a* (Chl-*a*), and dissolved inorganic nutrients (NO_3^-, NO_2^-, and NH_4^+) in the water column were collected on board and analyzed following the standard methods for the specification for marine monitoring (GB 17378-2007). Briefly, DO concentrations in seawater were measured with the Winkler titration method onboard. Water samples (~1 L) for the analysis of Chl-*a* were filtered on 47 mm Whatman GF/C glass fiber filters, and Chl-*a* was extracted into 90% acetone and measured with a Trilogy Laboratory Fluorometer. Approximately 100-mL filtrates were frozen at −20°C for each sample, and [NO_3^-], [NO_2^-], and [NH_4^+] were determined by SmartChem® 600 Automated Discrete Analyzer (KPM Analytics located in Westborough, MA, USA) in the laboratory. Approximately 5 L water was filtered on precombusted Whatman GF/F filter for POC concentration measurement. The filters were frozen at -20°C until analysis. In the laboratory, the filters were dried at 50°C for 48 h and fumigated using HCl (12 mol/L) for 24 h. They were washed by Milli-Q water, dried at 50°C for 48 h, and measured with an elemental analyzer (Flash EA 2000, Thermo Fisher Scientific, Lenexa, KS, USA).

Meanwhile, we selected typical depths (surface, depth of Chl-*a* maximum, bottom of epipelagic zone, mesopelagic zone, oxygen minimum zone, bathypelagic layer, and near bottom depth) for microbial community analysis (Table 1). A total of 5 L of seawater was filtered through 0.22-μm pore size filters, which were stored at −80°C onboard until subsequent analysis. Polymetallic nodules (n=11), sediment column (0–22 cm; n=33), and ~150 ml of overlying water (n=5) of the surface sediment were aseptically sampled from pushcores using the manned submersible "Jiaolong" during dives A–C in regions A–C, respectively

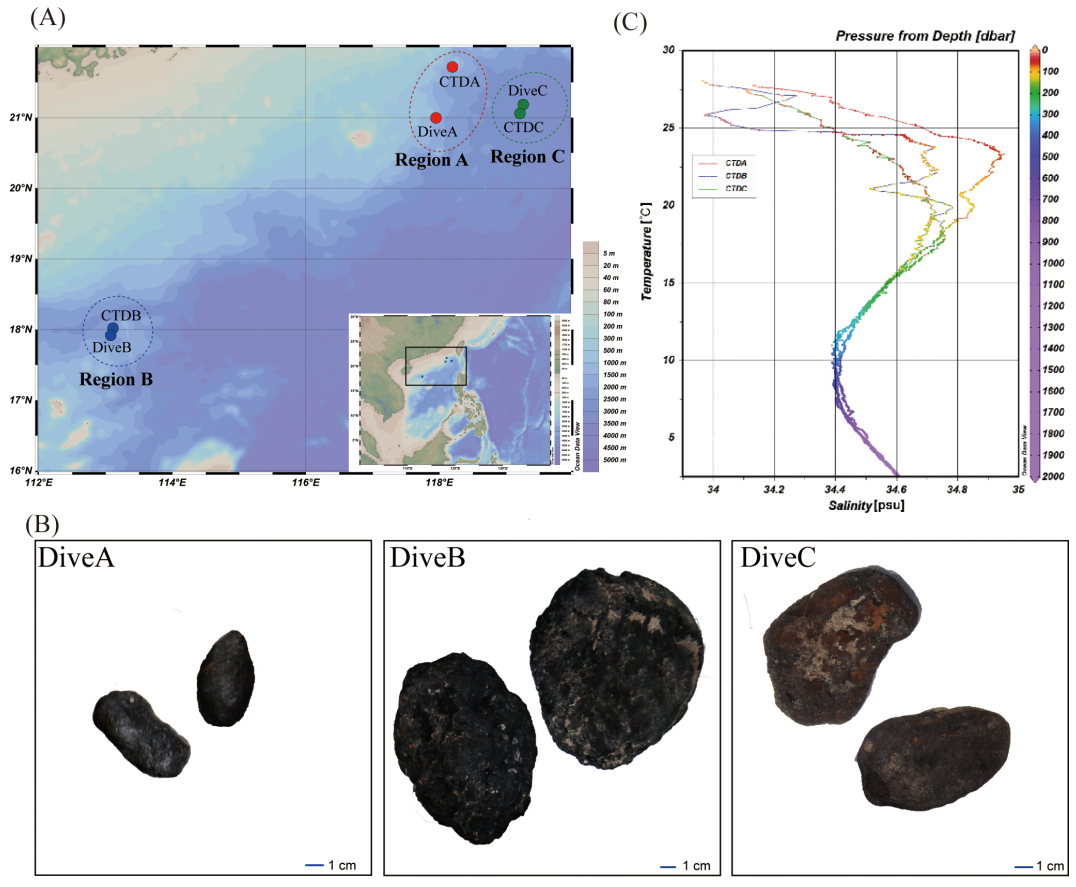

FIGURE 1
Study regions and specific sampling sites in the South China Sea (SCS). **(A)** A map showing the sampling areas of the SCS, including region A (CTDA and DiveA), region B (CTDB and DiveB), and region C (CTDC and DiveC); **(B)** nodules sampled from different dives in the SCS; **(C)** temperature (°C)–salinity diagram (T–S) from all CTD stations in the SCS.

(Table 1; Supplementary Figure 1). On board, a series of sample operations were conducted after removing the samples from the push core. The nodules were gently cleaned with aseptic waters, and small portions (approximately 0.5 g) of surface and interior samples were collected using a sterile chisel and hammer. Sediment samples were sectioned at an interval of 2 cm. Nodule and sediment samples were sealed individually in axenic bags. The overlying water was processed by the same approach as the seawater sample. All samples were stored at −80°C for microbial analyses.

2.2 DNA extraction, PCR amplification, and Illumina sequencing of 16S rRNA genes

DNA was extracted from filtered water samples, 0.5 g of nodules, and sediment samples (n=68; Table 1) with the Fast DNA™ SPIN Kit for Soil (MP Bio, Carlsbad, CA, USA) following the steps recommended by the manufacture, including the bead-beating for additional cell disruption prior to the extraction in nodule and sediment samples (Lindh et al., 2017; Shulse et al., 2017). The DNA concentration and quality were assessed using a NanoDrop ND-2000c Spectrophotometer (Thermo Scientific, Inc., USA). Extracted DNA was stored at − 80°C for downstream sequencing.

The V3–V5 hypervariable regions of archaeal 16S rRNA genes were amplified by the primer pair Arch344F (ACGGGGYGCA GCAGGCGCGA)/Arch915R (GTGCTCCCCCGCCAATTCCT) (Zheng et al., 2013), and the primer pair of 338F (5′-ACTCCTACGGGAGGCAGCA-3′)/806R (5′-GGACTACHVG GGTWTCTAAT-3′) was used to amplify the V3–V4 region of bacterial 16S rRNA genes (Caporaso et al., 2011). The amplicon processing was performed as described in Liu et al. (2023). Negative (no sample) extraction controls were used for PCR amplification to check for the presence of possible environmental contamination (Sheik et al., 2018). Pair-end sequencing was carried out by the Illumina Miseq PE250 platform (Majorbio Bio-Pharm Technology, Shanghai, China).

2.3 Data analysis

Trimmomatic (Bolger et al., 2014) was used for the quality control of raw reads following the criteria reported previously (Liu et al., 2020). Operational taxonomic units (OTUs) were clustered in UPARSE (Edgar, 2013) at a 97% similarity cutoff and taxonomically assigned with the Ribosomal Database Project (RDP) naive–Bayersian classifier against the Silva database Release 138 (http://www.arb-silva.de). A total of 2,684,460 bacterial 16S rRNA gene sequences were obtained from 66 samples and 2,875,089 archaeal sequences from 67 samples (Supplementary Table S1). Specifically, 1,826 bacterial OTUs and 946 archaeal OTUs were recovered from 817,233 bacterial sequences (417 bp average length) and 953,783 archaeal sequences (265 bp average length) of 18 water column samples, respectively, and 6,371 bacterial OTUs and 4254 archaeal OTUs were identified from 1,867,727 bacterial sequences (434 bp average length) and 1,921,306 archaeal sequences (335 bp average length) from samples of sediment, nodules, and overlying water. The rarefaction curves for the observed OTUs from bacteria and archaea showed clear asymptotes (Supplementary Figure S2), indicating a near-complete sampling of the community. OTUs affiliated with chloroplasts and eukaryotes were removed from

TABLE 1 The geographic information of sampling sites in the South China Sea.

Regions	Stations	Longitude (°E)	Latitude (°N)	Total water depth (m)	Sample types	Sampling depths/names
A	CTDA	118.17	21.73	1,304	seawater	0, 10*, 30, 50*, 75, 100*, 125, 150, 200*, 300, 500*, 800, 1000, 1303* m
	DiveA	117.95	20.98	1,397	overlying water	DiveA_OW1; DiveA_OW2
					sediment	0-22 cm b.s.f.
					nodule	DiveA_NO1, DiveA_NO2, DiveA_NO3, DiveA_NI
B	CTDB	113.09	17.96	1,957	seawater	0, 2*, 10, 30*, 50, 85*, 100, 125, 150, 200*, 300, 500, 800*, 1000*, 1500, 1977* m
	DiveB	113.07	17.89	1,733	overlying water	DiveB_OW
					sediment	0-22 cm b.s.f.
					nodule	DiveB_NO1, DiveB_NO2, DiveB_NI1, DiveB_NI2
C	CTDC	119.23	21.09	1,617	seawater	0, 10, 30, 50*, 75, 100*, 125, 150, 200*, 300, 500, 800*, 1100, 1500, 1616* m
	DiveC	119.24	21.14	1,773	overlying water	DiveC_OW1, DiveC_OW2
					sediment	0-22 cm b.s.f.
					nodule	DiveC_NO1, DiveC_NO2, DiveC_NI

*Water samples were selected for microbial analysis.

subsequent analyses. Sequencing depths of water column samples were standardized to 28,429 reads for bacteria and 24,682 reads for archaea. The sequencing depth was normalized to 4,684 reads for the bacterial sample collected from 1,977 m of CTDB due to the low number of reads (Supplementary Table S1); however, since the curve of this sample on the rarefaction curve still showed a clear asymptote (Supplementary Figure S1), the sample was included in the analysis. The sequencing depth of each sample was equalized to 22,351 reads in bacteria and 18,195 reads in archaea corresponding to the lowest sequence number among sediment, nodule, and overlying water samples. The OTU tables were normalized by dividing the number of sequences for each OTU by the total number of sequences in each sample, i.e., normalization to relative abundances. The results of relative abundance were visualized in TBtools (version 0.1098765) software (Chen et al., 2020). Statistical data processing was performed using the Origin 2022 and R (RStudio) 3.6.0 (Kronthaler and Zöllner, 2021).

Based on taxonomic information, statistical analysis of community structure was performed at various taxonomic levels. Alpha-diversity metrics (i.e., Shannon and Chao1 indices) were calculated based on OTU relative abundances for each sample. Beta-diversity across samples was analyzed using the Bray–Curtis distance matrix and visualized using non-metric multidimensional scaling (NMDS, package Phyloseq) and hierarchical clustering tree. Nonparametric analysis of similarities (ANOSIM) was performed on Bray–Curtis community dissimilarities in the R package vegan (Anderson, 2006). Similarity percentage (SIMPER) in PRIMER package V6.0 (Primer-E, UK) was used to identify the taxa that contributed to the dissimilarity between groups (Clarke and Gorley, 2006). The difference in the diversity indices of microbial groups among different samples were analyzed by Kruskal–Wallis H test, and the significant level of the difference (p-value) was evaluated.

We performed collinear network analysis using the NetworkX software (version1.11; Hagberg et al., 2008) based on bacterial and archaeal OTUs, respectively, to identify the interaction of four sample types (nodule outside, nodule inside, surface sediment, and overlying water) and key species at interfacial layers of nodules and surrounding environments. The networks were composed of interconnected nodes, representing the sample node and the species node, and the connection between these two nodes indicated the inclusion of the species in the sample. The number of connections from a node is called the degree of the node. Degree centrality, betweenness centrality, and closeness centrality were studied to obtain the information contained in the network. Degree centrality was measured as the number of direct links that involved a given node (Yuan et al., 2011), and the higher value meant that the node was more central. Closeness centrality is the shortest path between a node and all other reachable nodes (Bröhl and Lehnertz, 2022). Betweenness centrality is a measure of centrality of a node that acts as a bridge along the shortest path between two other nodes (Wasserman and Faust, 1994). Directed networks visualizing the OTU distribution in different samples were generated using the preferred layout algorithm in CYTOSCAPE 3.0 (Shannon et al., 2003).

3 Results

3.1 Environmental characteristics of the water column

The temperature–salinity (T–S) diagram revealed that the upper water masses (<200 m) of stations CTDA, CTDB, and CTDC exhibited different characteristics, while the deep water was relatively homogeneous across all stations (Figure 1C). The water columns of stations CTDA and CTDC exhibited well-developed surface mixed layers (SML) above 16 m and 12 m, respectively, while SML at Sta CTDB was not obvious, approximately at 26 m (Supplementary Figures S3A, B). Nitrate concentrations were below detection limit above 50 m, 75 m, and 25 m at stations CTDA, CTDB, and CTDC, respectively (Figure 2A). The depth of the Chl-*a* maximum (DCM) at Sta CTDB (~85 m) was deeper than that at other two stations (~50 m), and the maximum Chl-*a* concentration (CTDB: 0.45 μg/L) was lower (CTDA: 1.13 μg/L, CTDC: 1.10 μg/L; Figure 2B). The peak of POC concentrations in the water column was in correspondence to that of Chl-*a* except at Sta CTDB, where the highest POC concentration was in surface water. The second peak of POC concentration at Sta CTDA occurred in surface water as well (Figure 2C). The oxygen minimum zone (OMZ) ranged from 800 to 1,000 m at three stations, and stations CTDA and CTDC had a relatively narrow OMZ in comparison to that at Sta CTDB (Figure 2D).

3.2 Microbial community composition and diversity in the water columns

The profiles of Shannon and Chao1 indices showed that the variations in bacterial and archaeal diversity and richness in the water column were similar at stations CTDA and CTDC, while those at Sta CTDB were relatively higher below 200 m (Supplementary Figures S4A, B). The NMDS analyses showed that bacterial and archaeal communities in water column samples of three stations were clearly divided into different groups (Figure 3). The bacterial communities above 100 m were clustered together, while those below 200 m at Sta CTDB were distinctively separated from other two stations (Figure 3A). The archaeal communities from 100 m to 200 m and deep water of three stations (500–1,977 m) were separated except that at 800 m of Sta CTDB (Figure 3B).

A majority of the classified bacterial sequences in water columns of three stations were assigned to Proteobacteria (598 OTUs, 60.9% of total bacterial sequences), followed by Cyanobacteria (9 OTUs, 14.8%), Actinobacteriota (58 OTUs, 5.2%), SAR406 clade (112 OTUs, 4.1%), and Bacteroidota (155 OTUs, 3.5%) (Figures 3A; Supplementary Figure S5). The dominant bacterial groups varied at different depths (Figure 3A). Cyanobacteria were most abundant above the DCM layer (53.3 ± 8.7%), and more than 97% belonged to *Prochlorococcus* MIT9313 and *Synechococcus* CC9902 (Figure 3A). Below the DCM layer, Proteobacteria became dominant, especially at

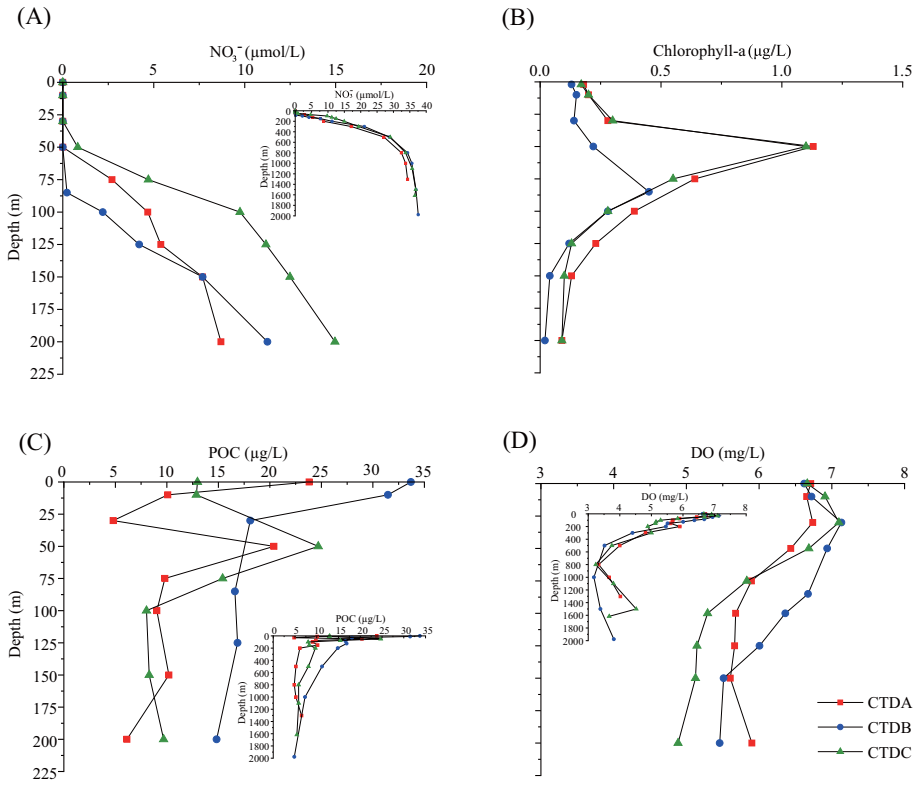

FIGURE 2
The concentrations of **(A)** nitrate, **(B)** chlorophyll *a*, **(C)** particulate organic carbon (POC), and **(D)** dissolve oxygen (DO) in the water column samples of stations CTDA, CTDB, and CTDC in the South China Sea.

stations CTDA and CTDC (>85%), but the composition was different (Figure 3A). *Alteromonas* was the most abundant genus (>45% of Proteobacteria) at 50 m of Sta CTDA, and *Alcanivorax* (25.6 ± 16.3%) and *Marinobacter* (20.3 ± 13.7%) were dominant at depths of 200–1,303 m. At Sta CTDC, a higher proportion of *Salinicola* (20.2 ± 12.7%) was detected below 200 m (Figure 3A). The SIMPER analysis confirmed that *Marinobacter*, *Alcanivorax*, and *Salinicola* contributed to the difference in microbial communities below 200 m between stations CTDA and CTDC (Supplementary Table S2). At Sta CTDB, the relative abundances of the phyla SAR406 clade and SAR324 clade exceeded 10% of total bacterial sequences below 200 m (Figure 3A). The major groups contributing to the difference in bacterial communities below 200 m between CTDB and other two stations included SAR324 clade, SAR406 clade, SAR202 clade, *Marinobacter*, and Sva0996 marine group (Supplementary Table S2).

The archaeal communities were mainly assigned to the phyla Thermoplasmatota and Thaumarchaeota (Figure 3B). Marine group II (MGII) and marine group III (MGIII) of *Thermoplasmatota* were dominant (>50%) through the water column of all stations except 800 m at Sta CTDB (Figure 3B). The relative abundance of Thaumarchaeota increased from 50 m and occupied 29.8 ± 7.5% of total archaeal sequences below 200 m (Figure 3B). *Candidatus* Nitrosopelagicus dominated above 200 m (14.0 ± 10.6%), while the relative abundance of unclassified genera in Nitrosopumilaceae increased below 200 m (CTDA: 18.1 ± 7.3%, CTDB: 31.8 ± 7.9%, CTDC: 18.1 ± 8.1%; Figure 3B). Although there was little variation in archaeal communities in deep water layers (≥200 m) among three stations compared to that of bacterial community (ANOSIM, bacteria: R=0.6212, p-value=0.008; archaea: R=−0.1566, p-value=0.836; Figure 3), the dissimilarity of archaeal community between CTDB and other two stations below 200 m were larger (CTDB vs. CTDA: 30.4%; CTDB vs. CTDC: 29.6%) than that between stations CTDA and CTDC (16.4%; Supplementary Table S2). MGII and MGIII that were relatively more abundant at stations CTDA and CTDC contributed to over 40% of the difference, followed by family Nitrosopumilaceae (~23%) and a group of unidentified archaea (Supplementary Table S2).

3.3 Microbial community composition and diversity in the sediment cores

The bacterial Shannon and Chao1 indices decreased from the surface of three sediment cores collected from DiveA, DiveB, and DiveC (Supplementary Figure S4C), while those of archaea had an opposite trend with a fluctuation below 6 cm (Supplementary Figure S4D). The hierarchical clustering based on Bray–Curtis distance estimation at OTU level showed that the bacterial communities in sediment cores of all dives were divided into three clusters (similarity within each cluster >70%; Supplementary Figure S6A). Cluster I included bacterial communities at depths of 0–2 cm of DiveA, 0–12

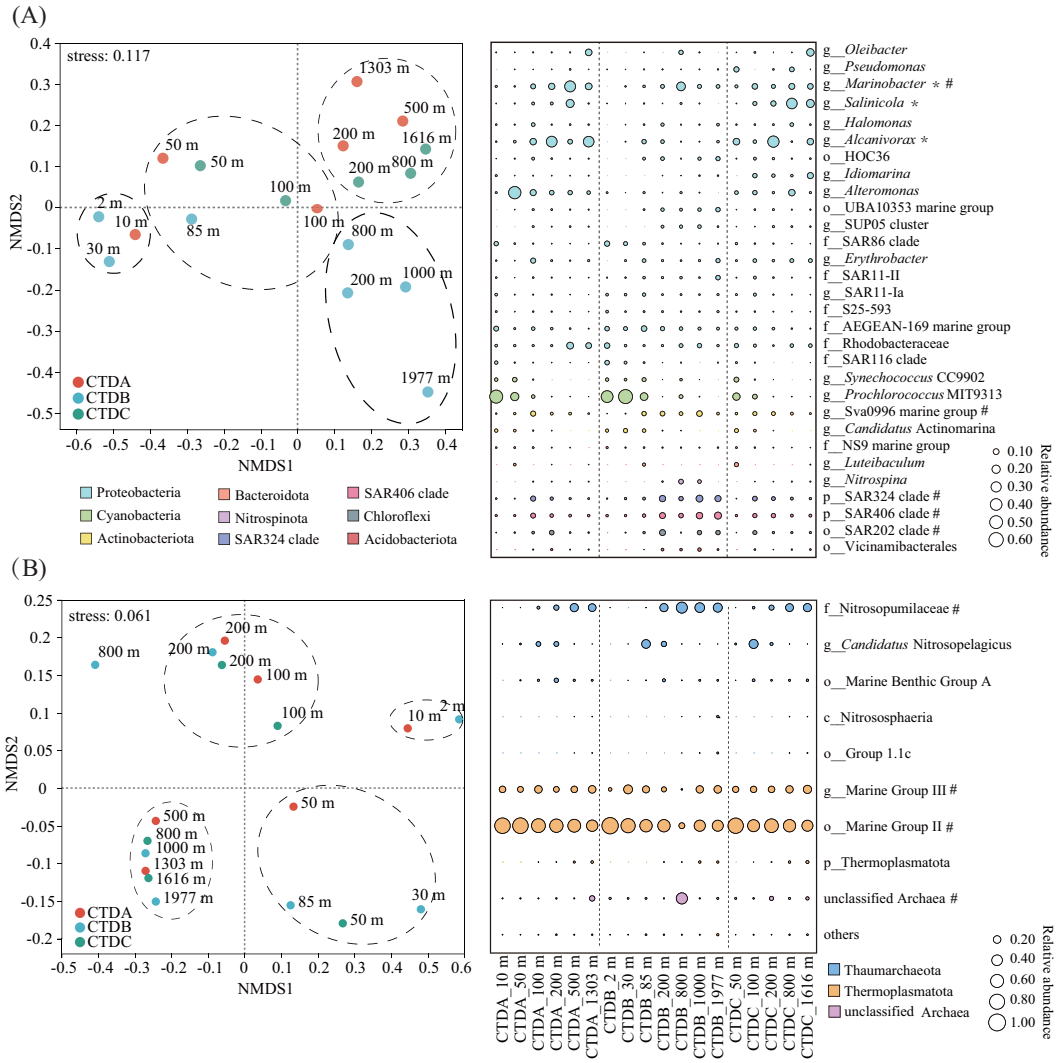

FIGURE 3
Characteristics of microbial communities in water column samples of stations CTDA, CTDB, and CTDC in the South China Sea. **(A)** The NMDS analysis of bacterial community and top 30 bacterial taxa; **(B)** the NMDS analysis of archaeal community and the dominant archaeal taxa (relative abundance>1%). The asterisk and hashtag indicated groups that contributed to differences between microbial communities in water column samples of stations CTDA and CTDC and between those of Sta CTDB and other two stations below 200 m. The black circles in NMDS analyses differentiated the clusters of bacterial and archaeal communities in water column samples of three stations.

cm of DiveB, and 0–6 cm of DiveC. Cluster II was composed of those at 6–22 cm of DiveC, and the remaining ones of DiveA and DiveB were grouped into Cluster III (Supplementary Figure S6A). It also revealed that the bacterial communities in Clusters I and II were closely related (Supplementary Figure S6A). The archaeal community in sediment samples followed a similar pattern of clustering, but it was noted that the archaeal community at 2–4 cm of DiveA was grouped with that at 0–2 cm of the same dive (Supplementary Figure S6B).

The dominant bacterial communities (>3% of total bacterial sequences) in sediment cores were composed of the phyla Chloroflexi (28.1%), Proteobacteria (23%), Acidobacteriota (9.5%), Actinobacteriota (6.1%), Methylomirabilota (4.3%), NB1-j (3.9%), Gemmatimonadota (3.6%), and Planctomycetota (3.4%; Figure 4A). The transition from Cluster I to Cluster III occurred clearly at 2 cm and 12 cm of DiveA and DiveB, respectively (Figure 4A). Most genera from Chloroflexi, such as the unclassified genera from the order S085, family Anaerolineaceae, classes Dehalococcoidia, and JG30-KF-CM66, were mainly distributed in sediments below the transition layer, contributing 28.2% to the difference between Clusters I and III (Figure 4; Supplementary Table S3). Several genera of Proteobacteria also led to more than 15% of the difference (Figure 4B; Supplementary Table S3); for example, a decline in relative abundances of *Woeseia*, *AqS1*, and unclassified genera from family Kiloniellaceae, orders MBMPE27, JTB23, and AT-s2-59, were observed with the increase of the depth (Figure 4A). The genus *Nitrospira* and the phylum NB1-j showed a similar pattern to most Proteobacteria groups and contributed ~8% to the difference between Clusters I and III (Figure 4; Supplementary Table S3). The unclassified genera belonging to the order Aminicenantales of the phylum Acidobacteriota were only present in Cluster III (Figure 4). Other Acidobacteriota, such as the classes Subgroup 21 and Subgroup 22,

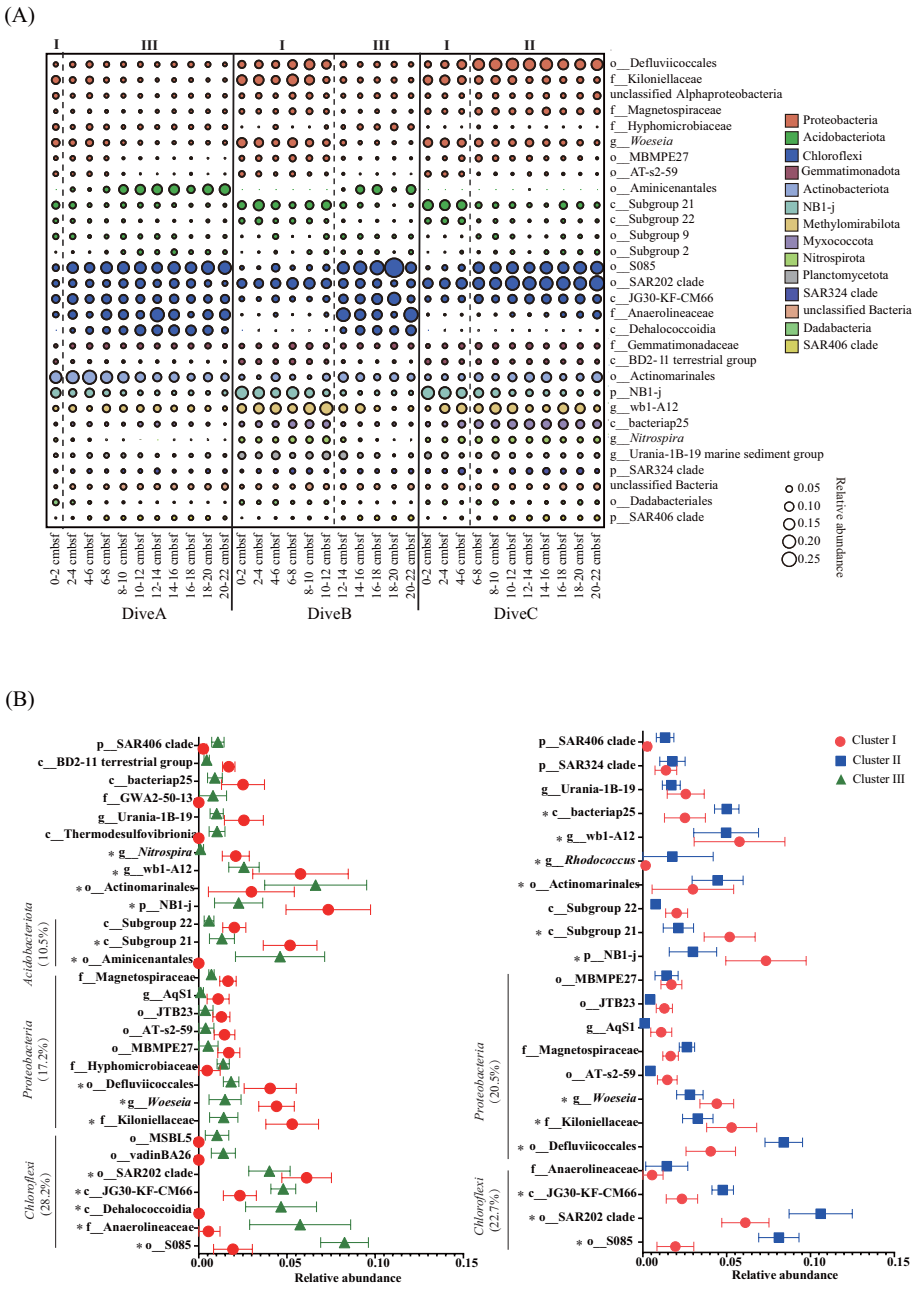

FIGURE 4
Characteristics of bacterial communities in sediment cores of DiveA, DiveB, and DiveC in the South China Sea. **(A)** The distribution of top 30 bacterial taxa in sediment cores of DiveA, DiveB, and DiveC; **(B)** the comparisons of the means of relative abundances of bacterial taxa between Cluster I and Cluster III, and between Cluster I and Cluster II based on β-diversity analysis of bacterial communities shown in Supplementary Figure S6. The asterisks highlighted the taxon that contributed over 2% to the dissimilarity of the bacterial community between two clusters by referring to Supplementary Table S3.

decreased in relative abundances with the increasing depth (Figure 4A). The three groups of Acidobacteriota contributed 10.5% to the difference between Clusters I and III (Figure 4B). Genera from phylum Desulfobacterota, a low-prevalence taxon, were enriched in Cluster III (Supplementary Figure S7). The transition of bacterial community from Cluster I to Cluster II only occurred at 6 cm in DiveC (Supplementary Figure S6A; Figure 4A). The dissimilarity of the bacterial community between Clusters I and II (36.0%) were low in comparison to those between Clusters I and III (55.1%) and Clusters II and III (44.4%; Supplementary Table S3). The genera belonging to the orders Defluviicoccales, S08, SAR202 clade and the class bacteriap25 were enriched at 6–22 cm of DiveC (Cluster II), which contributed more than 18% to the difference between Clusters I and II (SIMPER analysis; Figure 4; Supplementary Table S3).

Thaumarchaeota was the most abundant archaeal group in sediment cores from DiveA, DiveB, and DiveC, and the genera composing Thaumarchaeota showed different distribution patterns among dives (Figure 5). Unidentified genera in family

Nitrosopumilaceae were widely distributed in Clusters I and II (Figure 5A). *Ca.* Nitrosopumilus and *Ca.* Nitrosopelagicus were relatively abundant in Cluster I and sharply declined or disappeared in Clusters II and III (Figure 5). In contrary, Marine Benthic Group A was mainly distributed in Cluster III (Figure 5). The family Nitrosopumilaceae, Marine Benthic Group A, and *Ca.* Nitrosopumilus contributed ~61.5% to the difference between Clusters I and III, while the rest (20.1%) were mainly received from the family Geothermarchaeaceae, classes Lokiarchaeia and Bathyarchaeia, and the order Hydrothermarchaeales, which were mainly present in Cluster III (Figure 5B; Supplementary Table S3). The distinct division between Clusters I and II occurred in DiveC, but again, the dissimilarity was relatively low (36.3%; Supplementary Table S3). The Simper analysis showed that the major groups contributing to the difference (a total of 74.2%) were *Ca.* Nitrosopumilus, the family Nitrosopumilaceae, the order Woesearchaeales, and the class Deep Sea Euryarchaeotic Group (DSEG; Figure 5B; Supplementary Table S3).

3.4 Comparison of microbial communities in polymetallic nodules with surrounding environments

The Shannon indices of bacterial communities in nodules were not different from those in surface sediments (SS) and overlying waters (OW; Kruskal–Wallis H test and *post-hoc* Dunn's test, *p*-value>0.05), but the archaeal community in nodules showed a lower

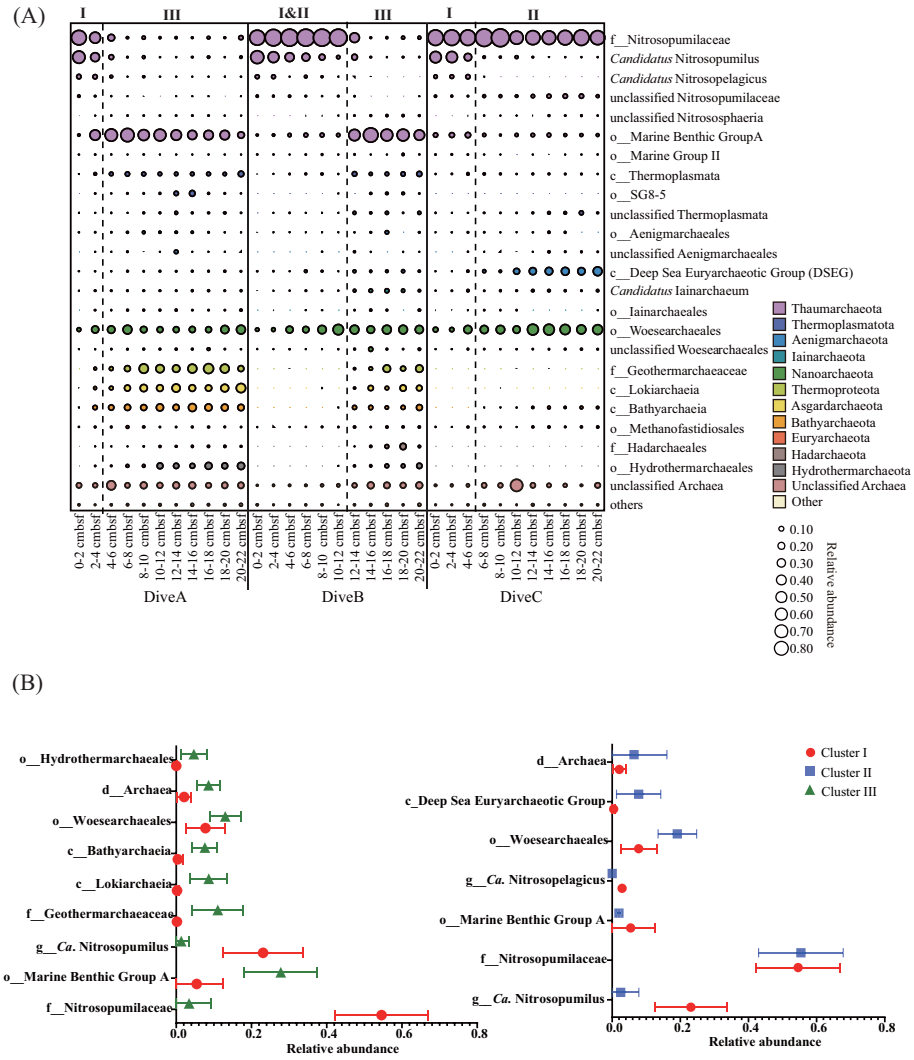

FIGURE 5
Characteristics of archaeal communities in sediment cores of DiveA, DiveB, and DiveC in the South China Sea **(A)** The distribution of the dominant archaeal taxa (relative abundance >1%) in sediment cores of DiveA, DiveB, and DiveC; **(B)** the comparisons of the means of relative abundances of archaeal taxa between Cluster I and Cluster III and between Cluster I and Cluster II based on β-diversity analysis of archaeal communities shown in Supplementary Figure S6. The asterisks highlighted the taxon that contributed over 2% to the dissimilarity of the archaeal community between two clusters by referring to Supplementary Table S3.

10.3389/fmars.2024.1430572

index than that in OW (p-value<0.05). The Chao1 index of the microbial community showed a distinctive variation between nodules and surrounding environments. Bacterial Chao1 indices of NO and NI samples were much lower than that of SS, while the archaeal Chao1 index of NI was lower than those of SS and OW (p-value<0.05). There was no significant difference in bacterial or archaeal Shannon and Chao1 indices between samples of nodule outside (NO) and inside (NI; Supplementary Figures S8A, B). There was a relatively large discrepancy in bacterial communities of OW or NI samples among different dives, while the archaeal community showed large discrepancies in all samples of NO or NI. The microbial communities in SS samples varied rarely among samples (Supplementary Figure S8C). The distance calculated at OTU level among different sample groups (shown by "between") were relatively higher than that within each sample group (ANOSIM; bacteria: R=0.8067, p-value=0.001; archaea: R=0.6462, p-value=0.001; Supplementary Figure S8C). The NMDS analysis also revealed that the sample type was the primary control of microbial community composition in the SCS (Figure 6). Microbial communities at OTU level in nodule samples (NO and NI) were separated from those in SS and OW (Figure 6). The number and the proportion of bacterial or archaeal OTUs shared by

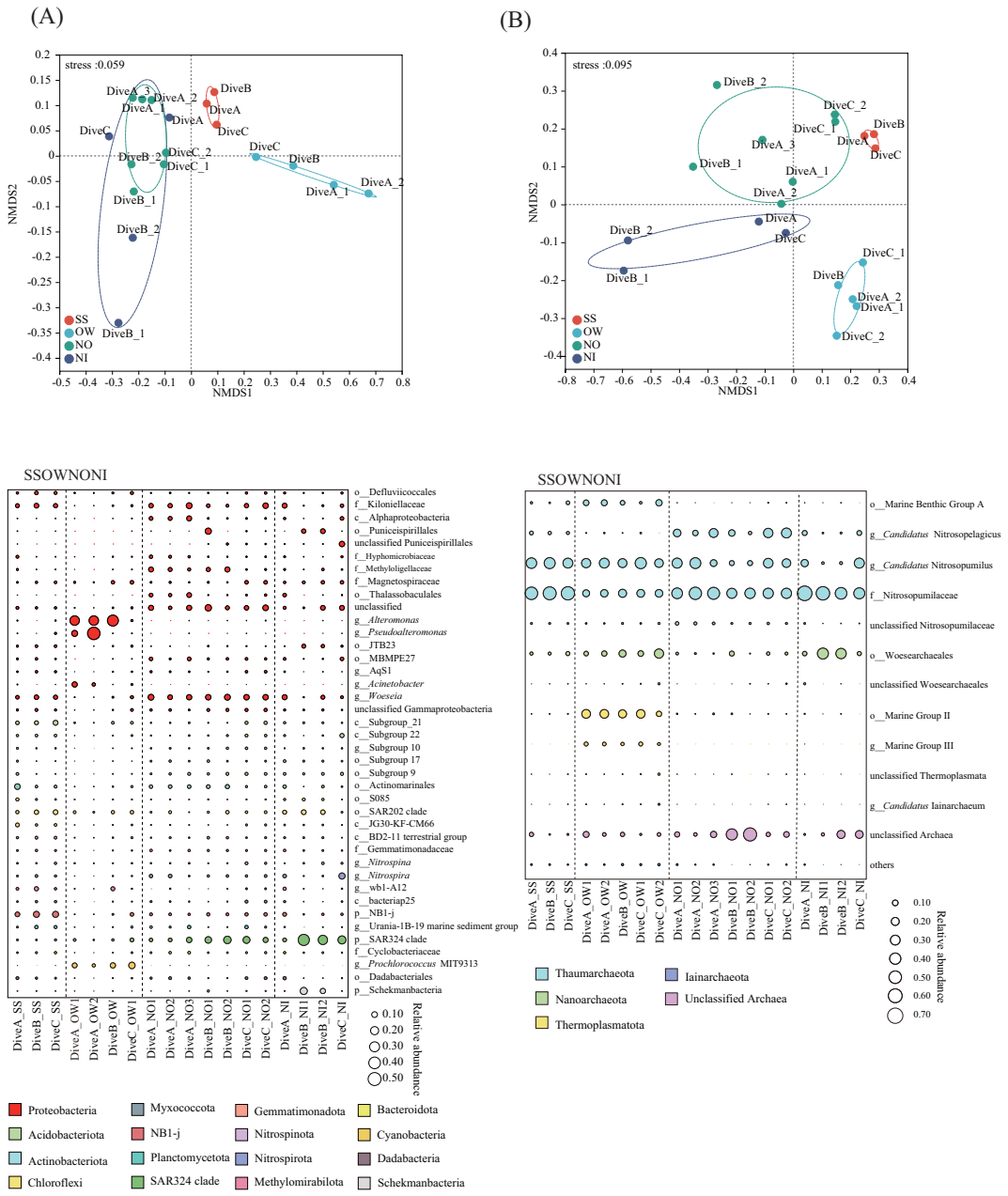

FIGURE 6
Characteristics of microbial communities in samples of surface sediment (SS), overlying water (OW), and nodules (NO, nodule outside; NI, nodule inside). **(A)** The NMDS analysis and top 30 bacterial taxa of the bacterial community; **(B)** the NMDS analysis and the dominant archaeal taxa (relative abundance >1%) of the archaeal community.

nodules and surrounding environments (OW and SS) or either one were highest in samples of DiveA (Supplementary Figure S9).

SAR324 clade was the dominant group in all nodule samples, especially at DiveB and DiveC (Figure 6A). The Proteobacteria linages showed an enrichment in NO samples. The genus *Woeseia* and the family Kiloniellaceae, which were abundant in SS, were also dominant in NO of all dives and NI of DiveA (Figure 6A). The family Hyphomicrobiaceae was shared by samples of NO and SS of DiveA (Figure 6A). Bacterial communities in OW were dominated by the phyla Proteobacteria and Cyanobacteria, representing over 60% of bacterial sequences. *Prochlorococcus* MIT9313 was the most dominant cyanobacterial group, mainly distributed in OW of DiveC and DiveB (Figure 6A). *Alteromonas* of Proteobacteria was enriched at DiveA and DiveB, while *Pseudoalteromonas* occupied abundantly only in OW of DiveA. The dominant genera *Halomonas*, *Pseudoalteromonas*, *Acinetobacter*, *Oleibacter*, and *Marinobacter* in OW of DiveA were relatively low in nodule and SS samples (Figure 6A; Supplementary Figure S10). Taxa from family Magnetospiraceae were mainly distributed in OW and nodules of DiveC, and OW and NI of DiveB (Figure 6A).

Thaumarchaeota was also a major group in nodule samples that both *Ca.* Nitrosopelagicus and *Ca.* Nitrosopumilus were enriched in nodules of DiveA and DiveC. At DiveB, the order *Woesearchaeale* in the phylum *Nanoarchaeotas* were relatively abundant in NI (Figure 6B). In addition, it was noteworthy that a large number of unidentified archaea were found in nodule samples of DiveB (Figure 6B). The archaeal communities in OW were similar among different dives and dominated by Thaumarchaeota, Thermoplasmatota, and Nanoarchaeota (Figure 6B). Marine Benthic Group A of Thaumarchaeota and MGII and MGIII of Thermoplasmatota were almost exclusively distributed in OW (Figure 6B).

3.5 Collinear network analysis of microbial communities from polymetallic nodules and surrounding environments

The collinear network was performed at bacterial OTU level with all samples (SS, OW, NO, and NI) for each dive (Figure 7). The network contained 3,361 effective nodes in DiveA, more than those in DiveB (3,021) and DiveC (3,164). The network centralization was 0.647, 0.624, and 0.653 in networks of DiveA, DiveB, and DiveC, respectively. In DiveA, the SS sample had 2,175 degrees, followed by samples of NO (1,589), NI (1,382), and OW (1,252; Supplementary Table S4). Similarly, the values of degree centrality, betweenness centrality, and closeness centrality were highest in samples of SS and NO (Supplementary Table S4). There were 63 dominant OTUs (after the filtration with the total OTU abundance at one station >200) that had the highest centrality measurement, most of which were prevalent in both SS and nodule samples, such as OTUs identified as the class Subgroup 21; the orders Subgroup 17, MBMPE27, and Actinomarinales; the families Hyphomicrobiaceae, Kiloniellaceae, and Methyloligellaceae; and the genera *Woeseia*, wb1-A12, *Nitrospira*, and AqS1 (Supplementary Table S5). In networks of DiveB and DiveC, the highest degree was also found in SS samples,

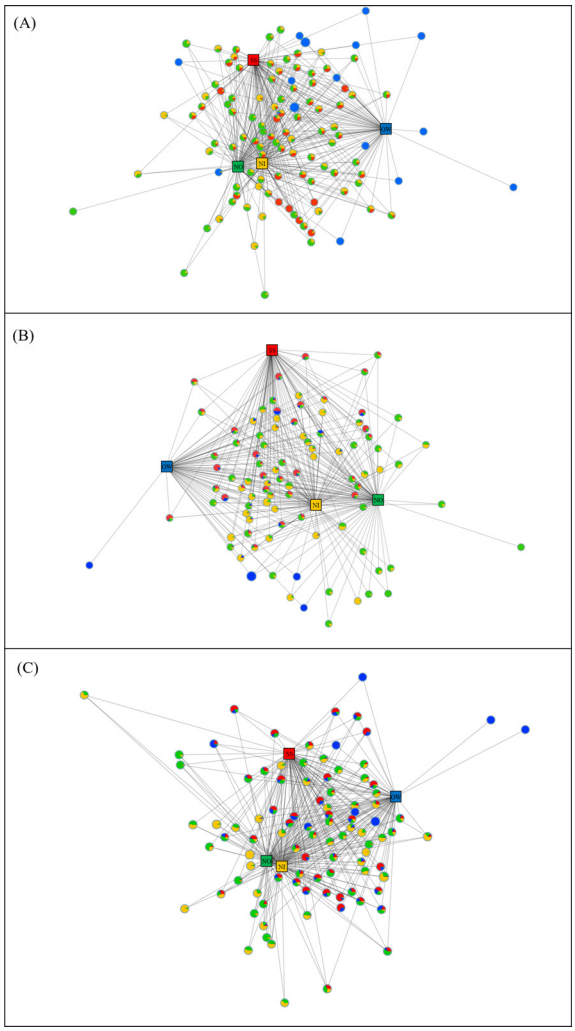

FIGURE 7
Collinear network analysis at bacterial OTU level on samples of surface sediment (SS), overlying water (OW), and nodules (NO, nodule outside; NI, nodule inside) for **(A)** DiveA, **(B)** DiveB, and **(C)** DiveC. Networks were analyzed based on all OTUs of each dive, but only those with the number beyond 200 were displayed. The square nodes represent sample types (red, SS; blue, OW; green, NO; yellow, NI) as source nodes, and the circle nodes are key OTUs as target nodes. The proportion of colors in the circle means the relative abundances of the OTU in the corresponding sources.

but the degree of OW exceeded those of nodules (Supplementary Tables S6, S7). Degree centrality, betweenness centrality, and closeness centrality exhibited similar trends (Supplementary Table S4). The numbers of dominant OTUs characterized by the highest centrality were 65 and 67 in networks of DiveB and DiveC, respectively (Supplementary Tables S6, S7). In DiveB, the taxa belonging to the class Subgroup 21 and the genus wb1-A12 were the key species mostly abundant in SS and OW. The classes BD2-11 terrestrial group and Gammaproteobacteria, the orders Actinomarinales and MBMPE27, the family Magnetospiraceae, and the genera Woeseia and Nitrospira were enriched in both SS and nodule samples (Supplementary Table S6). Few OTUs occurred in large numbers in nodules and OW simultaneously (Supplementary Figure S9; Supplementary Table S6). OTU from the family Hyphomicrobiaceae were mainly distributed in

OW and NO (Supplementary Table S6). In DiveC, NO, SS, and OW shared more OTUs compared to other dives, including those belonging to the classes Subgroup 21, Gammaproteobacteria, and BD2-11 terrestrial group, and the genera *Woeseia* and AqS1 (Supplementary Figure S9; Supplementary Table S7). The order MBMPE27, the families Magnetospiraceae and Kiloniellaceae, and the genera *Woeseia* and *Nitrospira* were prevalent in SS and nodule samples (Supplementary Table S7).

The numbers of effective nodes of the collinear networks based on archaeal OTUs were 1,379, 1,490, and B8 in DiveA, DiveB, and DiveC, respectively, with the network centralization of 0.632, 0.584, and 0.447 (Supplementary Figure S11). Both degree and centrality measurements of OW were highest among samples for each dive, followed by SS (DiveA) or NO (DiveB and DiveC; Supplementary Table S4). The dominant OTUs with highest centrality measurements (DiveA: 44 OTUs, DiveB: 35 OTUs, and DiveC: 32 OTUs) majorly belonged to the orders MGII and Marine Benthic Group A, family Nitrosopumilaceae, and the genera *Ca.* Nitrosopumilus and *Ca.* Nitrosopelagicus in all dives, and specifically the order Woesearchaeales in DiveC (Supplementary Tables S8–S10). *Ca.* Nitrosopelagicus (OTU1026) was mainly distributed in SS and nodule samples. OTUs from *Ca.* Nitrosopumilus were prevalent in OW and SS of all dives but abundant in nodules of DiveA and DiveC (Supplementary Tables S8–S10).

4 Discussion

4.1 Heterogeneous environments surrounding polymetallic nodules in the SCS

The South China Sea is hydrologically and geologically complex and is subject to a large terrestrial input and metal flux from continental shelf to the central deep-sea basin. It also experiences seasonal upwelling, high primary productivity, and a well-developed oxygen minimum zone (Guan et al., 2017; Zhong et al., 2017). Polymetallic nodules were mostly explored in the central basin of the SCS with low sedimentation rate (Zhong et al., 2017); however, in this study, we detected a wide and dense distribution of nodules in region A on the continental slope, with the morphology different from those collected from regions B and C (Figure 1B). It implied different formation mechanisms that could be affected by surrounding environments.

We found that POC flux from the upper water column and redox states in sediments were distinct among three regions, which could determine the scavenging of metals from seawater and porewater (Zhong et al., 2017). The quality and quantity of POC transported from the epipelagic layer to the deep ocean were key to determine the deep-sea sedimentary environments (Mestre et al., 2018). Although POC concentrations near the bottom of three stations were within the similar range (Figure 2C), the differences in POC sources could affect their fluxes and bioavailability in deep sea of three stations, potentially influencing the oxygen concentration and biogeochemical cycling. POC at Sta CTDB could be largely derived from terrestrial input (Figure 2C). The microbial composition and structure verified that SAR406 clade, SAR324 clade, and SAR202, which have been considered as free-living microbial groups adapted to oligotrophic environments (Boeuf et al., 2021; Geller-McGrath et al., 2023), were widely distributed below 200 m at Sta CTDB (Figure 3A). SAR406 clade and SAR202 clade indicated the refractory property of organic carbon at Sta CTDB because they were associated with the degradation of recalcitrant compounds (Thrash et al., 2017) and semi-labile alicyclic alkanes (Landry et al., 2017), respectively. SAR324 clade has been considered as particle-associated bacteria (PA) in epipelagic environment and FL in deep waters. The intense cluster of dominant SAR324 clade below 200 m (OTU1357) of Sta CTDB with deep-sea FL clades (Supplementary Figure S12) suggested that SAR324 clade were in FL mode and autotrophs (Swan et al., 2011; Boeuf et al., 2021). In contrast, nearly half of bathypelagic microbiome at stations CTDA and CTDC were dominated by PA lifestyle communities (Figure 3), including *Marinobacter* (23.8%) in the order Alteromonadales (Holtzapple and Schmidt-Dannert, 2007) and *Alcanivorax* (6.4-34.2%) and *Salinicola* (19.4-33.1%) in the order Oceanospirillales (Mason et al., 2012; Sebastián et al., 2021), all of which could rapidly utilize aliphatic hydrocarbons in the deep sea. In addition, higher proportions of *Oleibacter* in deep waters of stations CTDA and CTDC (Figure 3; Supplementary Table S2) indicated abundant aliphatic hydrocarbon (i.e., alkane; Liu et al., 2019). Thus, it implied that organic carbon could be more bioavailable in the deep sea of stations CTDA and CTDC, corresponding to the contribution of high proportion of phytoplankton-derived organic matter to total POC (Figure 2C). The relatively higher [NH_4^+] at the bottom of Sta CTDA (Supplementary Figure S3C) and rapid consumption of DO in the sediment core of DiveA (discussed below) indicated that organic carbon sinking to the deep water of Region A could be more abundant or labile.

The redox potential in the sediment core played a key role in mediating biogeochemical element cycling and manipulating deep-sea environment as a feedback (Zakem et al., 2020). Although our study did not directly measure or infer redox potential from geochemical parameters, we could use the microbial community in the sediment core as an index of the redox potential based on their well-established relationship (Wang et al., 2022) and the intense association of microbial and environmental properties in the water column of this study. The relative abundances of anaerobic microbial taxa, such as unidentified genera in orders Aminicenantales (Booker et al., 2023) and Marine Benthic Group A, the class Dehalococcoidia (Kaster et al., 2014; Yang et al., 2020), and the family Anaerolineae (Cai et al., 2021) of Chloroflexi, increased in sediment cores below 2 cm and 12 cm of DiveA and DiveB, respectively (Figures 4, 5). Aminicenantales dominated in anoxic ocean crust and were able to use organic carbon to drive sulfur oxides or extracellular iron oxyhydroxide reduction (Booker et al., 2023). Marine Benthic Group A was known to be found where nitrate was depleted (Durbin and Teske, 2011). It suggested a rapid depletion of oxygen and nitrate in top 2 cm of DiveA and 12 cm of DiveB. The relatively large numbers of two nitrifiers *Nitrospira* and Nitrosopumilaceae above the two layers could be active by receiving the substrate from nitrate reduction, since they have been detected

in anaerobic marine environment (Chen et al., 2017; Kraft et al., 2022; Martens-Habbena and Qin, 2022). Thus, the decrease in nitrifiers below the layers also suggested the depletion of nitrate (Figures 4, 5). The co-occurrence of Desulfobacterota and Lokiarchaeota observed at depths of 2–22 cm of DiveA and 12–22 cm of DiveB (Figure 5; Supplementary Figure S7) implied the initiation of sulfate reduction and iron oxide reduction, which were generally tightly linked (Jorgensen et al., 2012; Li et al., 2021). In the sediment core of DiveC, the increase in anaerobic groups from 4 cm (i.e., the class bacteriap25 of the phylum Myxococcota and the class DSEG of the phylum Aenigmarchaeota; Figure 4A; Cleary et al., 2023; Durbin and Teske, 2011) indicated the lack of oxygen starting at ~4 cm. DSEG was used to be detected before nitrate depletion (Durbin and Teske, 2011), suggesting enriched nitrate below 4 cm despite oxygen deficiency. The abundant Nitrosopumilaceae through the sediment core and consistent increase in *Nitrospira* from the surface layer likely revealed the supply of nitrate from nitrification process (Figures 4, 5; Hodgskiss et al., 2023; Garritano et al., 2023).

Overall, in terms of characteristics of microbial distribution and compositions in water columns and sediment cores of three regions, the geochemical environments at the bottom of the SCS were highly heterogeneous. As a consequence, the elemental fluxes, biogeochemical cycling, mineral precipitation, and geological features could be diverse and contributed to the alteration of redox conditions at interfaces of waters, sediments, and nodules, affecting the fate of elements involved in nodule formation.

4.2 Microbial interaction between polymetallic nodules and surrounding environments

The distinction of compositions and structures of the nodule communities from those in SS and OW in each region of the SCS (Figure 6; Supplementary Figures S8, S9) suggested that the nodule community was indigenous and not attributed to the simple accumulation from surrounding environments; however, the large discrepancy of microbial community in nodules among dives (Supplementary Figure S8) and the shared clusters with SS or OW in the corresponding dive (Figure 7; Supplementary Figures S9, S11; Supplementary Tables S5–S10) indicated the link of nodules and surrounding environments. Thus, the heterogeneous characteristics of deep-sea environments of three regions could eventually lead to the diversity in the formation of ferromanganese deposits in the SCS (Shulga et al., 2022).

The network based on bacterial communities in samples of DiveA showed an intense interaction between nodules (both NO and NI) and SS (Figure 7A; Supplementary Tables S4, S5). As discussed above, the deep sedimentary environment at DiveA likely received the most adequate supply of organic carbon among three regions. The high sedimentation rate and slow bottom current (monthly average < 1 cm/s; unpublished data) might create a stable and sub-oxic bottom environment for nodule growth, as indicated by the microbial composition in the sediment core. As discussed in *Section 4.1*, the activated reduction in Mn^{4+} and Fe^{3+} in shallow sediment layers could induce fluxes of Mn^{2+} and Fe^{2+} to the surface through the porewater (Hein et al., 2020; Shulga et al., 2022). The relatively abundant methanotrophs (i.e., Methyloligellaceae; Supplementary Figure S7; Knief, 2015) and methanogens (e.g., Methanofastidiosales; Figure 4A; Wang et al., 2021) present through the sediment core of DiveA, especially Methyloligeliaceae in SS, suggested that CH_4 oxidation could sustain sufficient reduced metals at the surface (González et al., 2012). Thus, the intense link between nodules and SS of DiveA in the network implied the sediment as the major sources of minerals for nodule formation in Region A. The families Magnetospiraceae, Kiloniellaceae, and Hyphomicrobiaceae associated with metal cycling were mostly shared by nodules and SS of DiveA, contributing significantly to the interaction between SS and nodules (Figure 6A; Supplementary Table S5). Hyphomicrobiaceae was functional in Mn oxidation (Tang et al., 2016), suggesting that the sediment-originated Mn was a major source to Fe–Mn deposits of DiveA. The NI shared most abundant OTUs with NO, SS, and OW at DiveA (Supplementary Figure S9), probably being caused by poor crystallization and a rapid growth of Mn-enriched nodules (Zhang C. et al., 2023). This was consistent with the characteristics of diagenetic Mn-enriched nodules in a stable growth environment (Zhong et al., 2017; Ren et al., 2023). The genus *Woeseia* and nitrifiers *Nitrospira*, *Nitrosomonas*, *AqS1* of Nitrosococcaceae, and Nitrosopumiliceae that had been enriched in Fe-rich deposit (Shulga et al., 2022) were abundant in SS and nodules, and the key groups in bacterial network of DiveA (Figure 6; Supplementary Table S5), implying the enrichment of Fe oxides in both niches. A more pronounced selection for Fe reducers (i.e., the family Magnetospiraceae; Matsunaga, 1991) in nodules and SS also reflected a higher content of an amorphous state of Fe minerals in a sub-oxic environment (Vereshchagin et al., 2019). Fe (i.e., pyrite, FeS_2) could originate from the upper water column through a large input of terrigenous materials in Region A (Figure 2C). We found a large number of symbiotic bacteria shared by SS and nodules, such as Kiloniellaceae and Subgroup21 (Schauer et al., 2010; Molari et al., 2020), which were associated with deep-sea benthic fauna (i.e., sponge, foraminifera; Cleary et al., 2023; Hori et al., 2013). It has been investigated that agglutinated foraminifera play a crucial role in nodule formation (Graham and Cooper, 1959; Greenslate, 1974). Thus, biological debris entrapped in nodules could be a mechanism of metal precipitation at DiveA (Molari et al., 2020; Wiese et al., 2020). Family Kiloniellaceae also owned potential of iron acquisition (Wang et al., 2015).

Different from DiveA, the microbial interaction between nodules and SS became weaker at DiveB and DiveC (Figures 7B, C; Supplementary Figures S11B, C; Supplementary Tables S6, S7, S9, S10), possibly a result of the variation in the redox state in sediments. The reduced metals might be oxidized before fluxing to the surface sediment (McKay et al., 2007). At DiveB, the bacterial network centrality was lowest among three regions and the archaeal one was lower than that of DiveA (Supplementary Table S4), suggesting the low association of nodules with surrounding environments in comparison to DiveA. Organic carbon was considered as refractory at DiveB due to much input of terrigenous components (Figure 2C); however, it could bring Fe-

rich waters to the deep ocean (Ziegler et al., 2008). The occurrence of large abundance of *Woeseia* again suggested enriched Fe in nodules (Figure 6A). Most of key bacterial OTUs in the network of DiveB belonged to SAR324 clade and SAR202 clade (Supplementary Table S6), which were abundant in nodule samples. It indicated that the nodule environment was in shortage of bioavailable carbon (see *Section 4.1*). SAR324 clade was also dominant in nodules from oligotrophic ocean, i.e., the South Pacific Gyre (Shiraishi et al., 2016) and the CCZ (Zhang C. et al., 2023). The accumulation of Fe deposit from upper water layers could be used as an energy source for autotrophic activity (Boeuf et al., 2021) or recalcitrant organic carbon degradation (Landry et al., 2017). SAR324 clade contained *nifH* gene encoding nitrogenase iron protein (Zhang D. et al., 2023), indicating the potential for N_2 fixation in nodules. It could provide nutrients for benthic organisms and enhance nitrogen cycling with enriched nitrifiers, i.e., *Nitrospira*, *Nitrospina*, *Ca.* Nitrosoplegicus, and family Nitrosopumilaceae (Figure 6). They all acquired iron as energy sources (Shafiee et al., 2021). The metal-cycling-related groups, such as families Kiloniellaceae and Hyphomicrobiaceae, did not share large numbers of OTUs among SS, OW, and nodules (Supplementary Table S6), suggesting that microbial mineralization was not the main process at interfaces of nodules. Family Magnetospiraceae (OTU1248) related to Fe cycle was mainly distributed in NI (Supplementary Table S6), revealing high contents of iron mineral in the nodule. The co-occurrence of sponge-associated bacteria Schekmanbacteria that were involved in sulfur cycling (Cleary et al., 2023) indicated the intense coupling of Fe–S cycling. Similarly, the order Puniceispirillales of SAR116 clade involved in Fe–S cycling was also detected ubiquitously in nodules of DiveB. They were mostly detected in eutrophic zone either in FL status or being associated with sponges or corals (Cleary et al., 2023; Roda-Garcia et al., 2023), implying that the nodule composition at DiveB (i.e., Fe) was affected by materials transported from the shallow waters. The detection of symbiotic bacteria also gave a hint that nodules collected at DiveB entrapped coral or sponge debris as the core of the nodule for subsequential formation. The decrease in shared OTUs between NI and other microbial niches (Supplementary Figure S9) and the distanced NI and NO in the networks (Figure 7B; Supplementary Figure S11B) revealed a large discrepancy of microbial community of NI from other environments. The nodule formation could be a long-term process, consistent with the record of slow growth of hydrogenetic nodules in the northwestern SCS (Zhong et al., 2017).

The highest bacterial network centrality of DiveC indicated an intense connectivity between nodules and surrounding environments (Figure 7C; Supplementary Table S4). SS and OW might co-affect the biogenic formation of nodules because they shared most bacterial or archaeal OTUs with NO (Supplementary Figure S9). It has been said the SCS nodules above the seamounts contained abundant hematite (Fe_2O_3) due to a narrowed oxygen minimum zone (OMZ; Zhong et al., 2019). A narrow OMZ was detected at Sta CTDC because the relatively high concentration of Chl-*a* could cause a rapid remineralization with a sharp consumption of oxygen at the mesopelagic zone (Figure 2D). Thus, the nodules at DiveC could be enriched with Fe oxides. Fe-scavenging family Magnetospiraceae was prevalent in both NI and NO (Matsunaga, 1991), confirming a high content and an amorphous state of Fe^{3+} minerals in nodules of DiveC (Vereshchagin et al., 2019; Ren et al., 2023). The presence of SAR324 clade in NO and NI indicated a low flux of organic carbon to the seafloor due to most degradation occurring in the

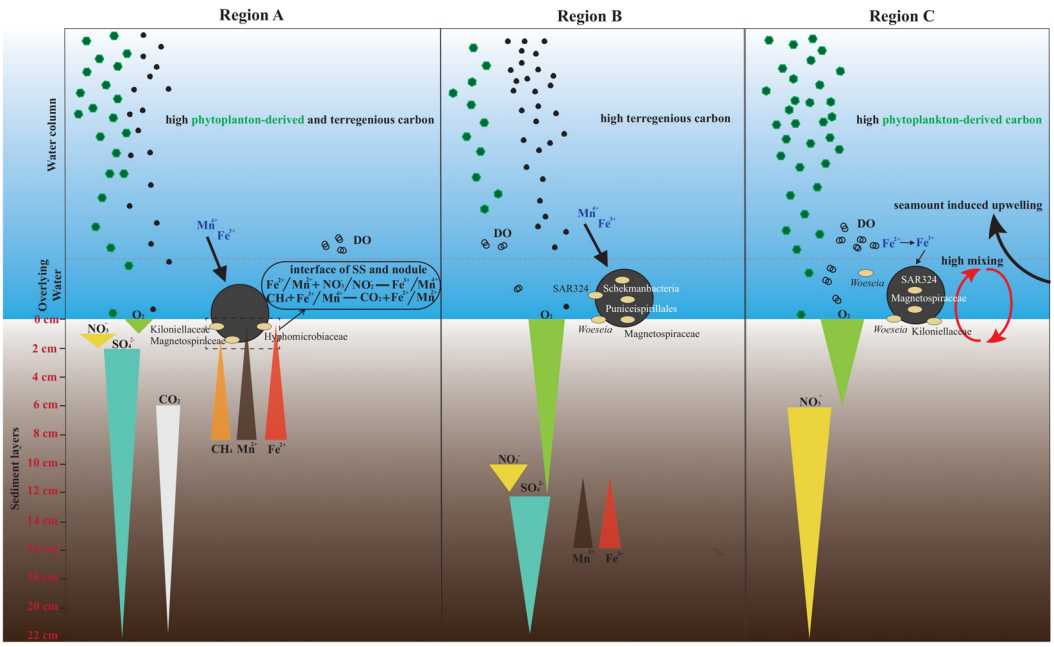

FIGURE 8
The hypothesized model of polymetallic nodule formation in three regions **(A–C)**. SS, surface sediment; DO, dissolved oxygen.

water column. The low Woesearchaeales and the high nitrifier (e.g., *Nitrospira* and Thaumarchaeota) abundances (Figure 6) suggested that NI was microaerobic, which could be a result of slow and loose formation under the condition of low sedimentation rate (Yang et al., 2024). The large divergence of microbial communities between NI and other three niches (Figure 6; Supplementary Figure S9) also suggested that the nodules were formed in a long process.

4.3 Potential mechanisms of polymetallic nodule formation

The nodule morphology at DiveA (Figure 1B) were similar to that collected in the northeastern SCS where the nodules were formed by early diagenesis and hydrogenetic growth according to the low Mn/Fe ratio and trace metal contents (Zhong et al., 2017). In our study, the hypothesized nodule formation at DiveA deduced from microbial compositions, functions in metal metabolisms, and microbial interactions between nodules and surrounding environments was consistent with previous results based on the analysis of elemental compositions. The shallow redox boundary (<2 cm) indicated by the microbial distribution in the sediment core reflected the sources of Fe–Mn deposits from the sediment, while a high input of terrigenous matter and relatively abundant Fe-utilizing microbes suggested the origin of Fe from seawaters (Figure 8). Although the nodules from DiveB and DiveC were inferred to be hydrogenetic, the source of metal ions could be different. At DiveB, the terrigenous matter fluxing into the deep-water could contribute to Fe–Mn deposits, and the debris of fauna from eutrophic zone of shelf waters or benthic environments enhanced the formation of nodules. At DiveC, the narrow OMZ induced by the intense degradation of phytoplankton-derived organic matter caused a low concentration of organic matter and rich oxygen in deep water, where Fe oxides were formed and enriched (Figure 8). Overall, relatively low sedimentation rates and strong bottom currents (monthly average < 3 cm/s and < 6 cm/s in regions B and C, respectively; unpublished data) induced by either coastal fluxes or upwelling and mixing at DiveB and DiveC could lead to a slow formation of the nodules.

5 Conclusion

In this study, we combined the investigations of hydrological properties and microbial communities of upper water columns, sediment cores, overlying waters, and polymetallic nodules for understanding the impact of environmental heterogeneity of the SCS on the formation of polymetallic nodules. In the water column, we found that the spatial variations of microbial communities and environmental characteristics in seawaters of three regions were consistent, suggesting that the distribution of microbial composition and diversity was a great indicator of the environment. The redox states in sediment cores inferred from microbial communities were diverse among three regions, potentially being affected by organic matter fluxes and physical dynamics in deep waters. The dissolved oxygen concentration in surface sediment of DiveA could be extremely low, which is beneficial for the overflow of reduced metals from the porewater for diagenetic formation of polymetallic nodules. Differently, polymetallic nodules at DiveB and DiveC, where bottom currents were relatively strong and sediments were more oxidized, could receive nodule constitutes from upper water layers (i.e., terrigenous-originated Fe at DiveB and Fe oxides from upper layer of seamount of DiveC). Overall, this study focused on microbe-mediated nodule formation process and provided a new perspective for understanding nodule formation mechanisms.

Data availability statement

The original contributions presented in the study are included in the article. Bacterial and archaeal 16S gene sequences have been deposited in the NCBI Sequence Read Archive under BioProject ID PRJNA1147917.

Author contributions

ML: Writing – review & editing, Writing – original draft, Visualization, Validation, Software, Methodology, Investigation, Formal analysis, Data curation. QL: Writing – review & editing, Writing – original draft, Visualization, Validation, Supervision, Software, Resources, Project administration, Methodology, Investigation, Funding acquisition, Formal analysis, Data curation, Conceptualization. XW: Writing – review & editing, Resources, Investigation, Data curation. DS: Writing – review & editing, Resources, Investigation, Data curation. LR: Writing – review & editing, Methodology, Investigation, Data curation. XL: Writing – review & editing, Investigation, Funding acquisition. CY: Writing – review & editing, Resources, Investigation, Data curation. BL: Writing – review & editing, Resources, Investigation. X-WX: Writing – review & editing, Supervision, Resources, Funding acquisition. C-SW: Writing – review & editing, Supervision, Project administration, Funding acquisition.

Funding

The author(s) declare financial support was received for the research, authorship, and/or publication of this article. This work was financially supported by the National Natural Science Foundation of China (no. 42176038), Scientific Research Fund of the Second Institute of Oceanography, MNR (no. SZ2401), the Project of State Key Laboratory of Satellite Ocean Environment Dynamics, Second Institute of Oceanography (no. SOEDZZ2204), and Science Foundation of Donghai Laboratory (no. DH-2022KF0211).

Conflict of interest

The authors declare that the research was conducted in the absence of any commercial or financial relationships that could be construed as a potential conflict of interest.

Publisher's note

Supplementary material

The Supplementary Material for this article can be found online at: https://www.frontiersin.org/articles/10.3389/fmars.2024.1430572/full#supplementary-material

SUPPLEMENTARY FIGURE 1
The images of polymetallic nodules on the seabed of DiveB in Region B and DiveC in Region C. The image was not successfully obtained by the camera mounted on the manned submersible 'Jiaolong' during DiveA in Region A.

SUPPLEMENTARY FIGURE 2
The rarefaction curves based on the Shannon index for the observed bacterial and archaeal OTUs from samples of **(A)** water columns and **(B)** sediment cores, nodules and overlying waters in all regions.

SUPPLEMENTARY FIGURE 3
Vertical distributions of **(A)** temperature, **(B)** salinity and **(C)** ammonium concentrations from 0-200 m (top row) and from 0-2000 m (bottom row).

SUPPLEMENTARY FIGURE 4
Shannon and Chao1 indices calculated for **(A)** bacterial and **(B)** archaeal communities in water column samples of stations CTDA, CTDB and CTDC, and **(C)** bacterial and **(D)** archaeal communities in sediment cores of DiveA, DiveB and DiveC in the South China Sea.

SUPPLEMENTARY FIGURE 5
Bacterial groups ranking 31-60 in the relative abundance in water column samples of stations CTDA, CTDB and CTDC in the South China Sea. The relative abundances of these groups were >0.01.

SUPPLEMENTARY FIGURE 6
β-diversity analysis of **(A)** bacterial and **(B)** archaeal communities in sediment cores of DiveA, DiveB and DiveC.

SUPPLEMENTARY FIGURE 7
Bacterial groups ranking 31-60 in the relative abundance in sediment cores of DiveA, DiveB and DiveC. The relative abundances of these groups were >0.01.

SUPPLEMENTARY FIGURE 8
(A) The comparisons of the means of **(A)** Shannon and **(B)** Chao1 indices of bacterial and archaeal communities of surface sediment (SS), overlying water (OW), nodule outside (NO) and nodule inside (NI) from all dives. $*p < 0.05$, $** p < 0.01$, $*** p < 0.001$. **(C)** ANOSIM analysis for bacterial and archaeal communities of SS, OW, NO and NI from all dives. The boxes of 'SS', 'OW', 'NO' and 'NI' represented the distance values within samples of the same sample type. The boxes of 'Between' represented the distance values between all samples.

SUPPLEMENTARY FIGURE 9
Venn analysis on OTU level. The numbers and the proportions of the common **(A)** bacterial OTUs or **(B)** archaeal OTUs shared by surface sediments (SS), overlying waters (OW) and nodules (NO, nodule outside; NI, nodule inside) were shown for DiveA, DiveB and DiveC.

SUPPLEMENTARY FIGURE 10
Bacterial groups ranking 31-60 in the relative abundance in surface sediments (SS), overlying waters (OW), nodules (NO, nodule outside; NI, nodule inside) of DiveA, DiveB and DiveC. The relative abundances of these groups were >0.01.

SUPPLEMENTARY FIGURE 11
Collinear network analysis at archaeal OTU level on samples of surface sediment (SS), overlying water (OW) and nodules (NO, nodule outside; NI, nodule inside) for **(A)** DiveA, **(B)** DiveB and **(C)** DiveC. Networks were analyzed based on all OTUs of each dive, but only those with the number beyond 200 were displayed.

SUPPLEMENTARY FIGURE 12
Maximum Likelihood phylogenetic tree was constructed for SAR324 OTUs obtained from water column samples of stations CTDA, CTDB and CTDC. The reference sequences were obtained by NCBI 'blast' alignment. The pie charts showed the distribution of OTUs at different water depths.

References

Anderson, M. J. (2006). Distance-based tests for homogeneity of multivariate dispersions. *Biometrics* 62, 245–253. doi: 10.1111/j.1541-0420.2005.00440.x

Blöthe, M., Wegorzewski, A., Müller, C., Simon, F., Kuhn, T., and Schippers, A. (2015). Manganese-cycling microbial communities inside deep-sea manganese nodules. *Environ. Sci. Technol.* 49, 7692–7700. doi: 10.1021/es504930v

Boeuf, D., Eppley, J. M., Mende, D. R., Malmstrom, R. R., Woyke, T., and DeLong, E. F. (2021). Metapangenomics reveals depth-dependent shifts in metabolic potential for the ubiquitous marine bacterial SAR324 lineage. *Microbiome* 9, 172. doi: 10.1186/s40168-021-01119-5

Bolger, A. M., Lohse, M., and Usadel, B. (2014). Trimmomatic: a flexible trimmer for Illumina sequence data. *Bioinformatics* 30, 2114–2120. doi: 10.1093/bioinformatics/btu170

Booker, A. E., D'Angelo, T., Adams-Beyea, A., Brown, J. M., Nigro, O., Rappé, M. S., et al. (2023). Life strategies for *Aminicenantia* in subseafloor oceanic crust. *ISME J.* 17, 1406–1415. doi: 10.1038/s41396-023-01454-5

Bröhl, T., and Lehnertz, K. (2022). A straightforward edge centrality concept derived from generalizing degree and strength. *Sci. Rep.* 12, 4407. doi: 10.1038/s41598-022-08254-5

Cai, C., Li, L., Hua, Y., Liu, H., and Dai, X. (2021). Ferroferric oxide promotes metabolism in Anaerolineae other than microbial syntrophy in anaerobic methanogenesis of antibiotic fermentation residue. *Sci. Total Environ.* 758, 143601. doi: 10.1016/j.scitotenv.2020.143601

Caporaso, J. G., Lauber, C. L., Walters, W. A., Berg-Lyons, D., Lozupone, C. A., Turnbaugh, P. J., et al. (2011). Global patterns of 16S rRNA diversity at a depth of millions of sequences per sample. *Proc. Natl. Acad. Sci. U.S.A.* 108, 4516–4522. doi: 10.1073/pnas.1000080107

Chen, C., Chen, H., Zhang, Y., Thomas, H. R., Frank, M. H., He, Y., et al. (2020). TBtools: an integrative toolkit developed for interactive analyses of big biological data. *Mol. Plant* 13, 1194–1202. doi: 10.1016/j.molp.2020.06.009

Chen, S., Yin, X., Wang, X., Huang, X., Ma, Y., Guo, K., et al. (2018). The geochemistry and formation of ferromanganese oxides on the eastern flank of the Gagua Ridge. *Ore Geology Rev.* 95, 118–130. doi: 10.1016/j.oregeorev.2018.02.026

Chen, Y., Liu, Y., and Wang, X. (2017). Spatiotemporal variation of bacterial and archaeal communities in sediments of a drinking reservoir, Beijing, China. *Appl. Microbiol. Biotechnol.* 101, 3379–3391. doi: 10.1007/s00253-016-8019-1

Clarke, K., and Gorley, R. N. (2006). *Primer v6: user manual/tutorial* (Plymouth: PRIMER-E).

Cleary, D. F. R., Oliveira, V., Gomes, N. C. M., Bialecki, A., and de Voogd, N. J. (2023). A comparison of free-living and sponge-associated bacterial communities from

a remote oceanic island with a focus on calcareous sponges. *FEMS Microbiol. Ecol.* 99, fiad014. doi: 10.1093/femsec/fiad014

Durbin, A. M., and Teske, A. (2011). Microbial diversity and stratification of South Pacific abyssal marine sediments. *Environ. Microbiol.* 13, 3219–3234. doi: 10.1111/j.1462-2920.2011.02544.x

Edgar, R. C. (2013). UPARSE: highly accurate OTU sequences from microbial amplicon reads. *Nat. Methods* 10, 996–998. doi: 10.1038/nmeth.2604

Ehrlich, H. L. (1963). Bacteriology of manganese nodules: I. Bacterial action on manganese in nodule enrichments. *Appl. Microbiol.* 11, 15–19. doi: 10.1128/am.11.1.15-19.1963

Garritano, A. N., Majzoub, M. E., Ribeiro, B., Damasceno, T., Modolon, F., Messias, C., et al. (2023). Species-specific relationships between deep sea sponges and their symbiotic *Nitrosopumilaceae*. *ISME J.* 17, 1517–1519. doi: 10.1038/s41396-023-01439-4

Geller-McGrath, D., Mara, P., Taylor, G. T., Suter, E., Edgcomb, V., and Pachiadaki, M. (2023). Diverse secondary metabolites are expressed in particle-associated and free-living microorganisms of the permanently anoxic Cariaco Basin. *Nat. Commun.* 14, 656. doi: 10.1038/s41467-023-36026-w

González, F. J., Somoza, L., Hein, J. R., Medialdea, T., León, R., Urgorri, V., et al. (2016). Phosphorites, Co-rich Mn nodules, and Fe-Mn crusts from Galicia Bank, NE Atlantic: Reflections of Cenozoic tectonics and paleoceanography: MINERALIZATIONS FROM GALICIA BANK. *Geochem. Geophys. Geosyst.* 17, 346–374. doi: 10.1002/2015GC005861

González, F. J., Somoza, L., León, R., Medialdea, T., de Torres, T., Ortiz, J. E., et al. (2012). Ferromanganese nodules and micro-hardgrounds associated with the Cadiz Contourite Channel (NE Atlantic): Palaeoenvironmental records of fluid venting and bottom currents. *Chem. Geology* 310–311, 56–78. doi: 10.1016/j.chemgeo.2012.03.030

Graham, J. W., and Cooper, S. C. (1959). Biological origin of manganese-rich deposits of the sea floor. *Nature* 183, 1050–1051. doi: 10.1038/1831050a0

Greenslate, J. (1974). Microorganisms participate in the construction of manganese nodules. *Nature* 249, 181–183. doi: 10.1038/249181a0

Guan, Y., Ren, Y., Sun, X., Xiao, Z., Wu, Z., Liao, J., et al. (2019). Fine scale study of major and trace elements in the Fe-Mn nodules from the South China Sea and their metallogenic constraints. *Mar. Geology* 416, 105978. doi: 10.1016/j.margeo.2019.105978

Guan, Y., Sun, X., Ren, Y., and Jiang, X. (2017). Mineralogy, geochemistry and genesis of the polymetallic crusts and nodules from the South China Sea. *Ore Geology Rev.* 89, 206–227. doi: 10.1016/j.oregeorev.2017.06.020

Hang, W., and Wang, P. (2006). Sediment mass and distribution in the south china sea since the oligocene. *Sci. China Ser. D Earth Sci.* 49, 1147–1155.

Hagberg, A. A., Schult, D. A., and Swart, P. J. (2008). "Exploring network structure, dynamics, and function using NetworkX," in Gäel Varoquaux, Travis Vaught and Jarrod Millman (Eds). *Proceeding of the 7th Python in Science Conference (SciPy2008)*, 11–15 (Pasadena, CA USA).

Halbach, P., Hebisch, U., and Scherhag, C. (1981). Geochemical variations of ferromanganese nodules and crusts from different provinces of the Pacific Ocean and their genetic control. *Chem. Geology* 34, 3–17. doi: 10.1016/0009-2541(81)90067-X

Hein, J. R., and Koschinsky, A. (2014). *Deep-ocean ferromanganese crusts and nodules, in: treatise on geochemistry* (Amsterdam: Elsevier), 273–291. doi: 10.1016/B978-0-08-095975-7.01111-6

Hein, J. R., Koschinsky, A., and Kuhn, T. (2020). Deep-ocean polymetallic nodules as a resource for critical materials. *Nat. Rev. Earth Environ.* 1, 158–169. doi: 10.1038/s43017-020-0027-0

Hein, J. R., Koschinsky, A., and McIntyre, B. R. (2005). Mercury- and silver-rich ferromanganese oxides, southern california borderland: deposit model and environmental implications. *Economic Geology* 100, 1151–1168. doi: 10.2113/gsecongeo.100.6.1151

Hein, J. R., Mizell, K., Koschinsky, A., and Conrad, T. A. (2013). Deep-ocean mineral deposits as a source of critical metals for high- and green-technology applications: Comparison with land-based resources. *Ore Geology Rev.* 51, 1–14. doi: 10.1016/j.oregeorev.2012.12.001

Hein, J. R., Spinardi, F., Okamoto, N., Mizell, K., Thorburn, D., and Tawake, A. (2015). Critical metals in manganese nodules from the Cook Islands EEZ, abundances and distributions. *Ore Geology Rev.* 68, 97–116. doi: 10.1016/j.oregeorev.2014.12.011

Hodgskiss, L. H., Melcher, M., Kerou, M., Chen, W., Ponce-Toledo, R. I., Savvides, S. N., et al. (2023). Unexpected complexity of the ammonia monooxygenase in archaea. *ISME J.* 17, 588–599. doi: 10.1038/s41396-023-01367-3

Hollingsworth, A. L., Jones, D. O. B., and Young, C. R. (2021). Spatial variability of abyssal nitrifying microbes in the north-eastern clarion-clipperton zone. *Front. Mar. Sci.* 8. doi: 10.3389/fmars.2021.663420

Holtzapple, E., and Schmidt-Dannert, C. (2007). Biosynthesis of isoprenoid wax ester in marinobacter hydrocarbonoclasticus DSM 8798: identification and characterization of isoprenoid coenzyme A synthetase and wax ester synthases. *J. Bacteriol* 189, 3804–3812. doi: 10.1128/JB.01932-06

Hori, S., Tsuchiya, M., Nishi, S., Arai, W., Yoshida, T., and Takami, H. (2013). Active bacterial flora surrounding foraminifera (Xenophyophorea) living on the deep-sea floor. *Bioscience Biotechnology Biochem.* 77, 381–384. doi: 10.1271/bbb.120663

Jiang, X. D., Zhao, X., Chou, Y. M., Liu, Q. S., Roberts, A. P., Ren, J. B., et al. (2020). Characterization and quantification of magnetofossils within abyssal manganese nodules from the western pacific ocean and implications for nodule formation. *Geochem. Geophys. Geosyst* 21. doi: 10.1029/2019GC008811

Kaster, A., Mayer-Blackwell, K., Pasarelli, B., and Spormann, A. M. (2014). Single cell genomic study of Dehalococcoidetes species from deep-sea sediments of the Peruvian margin. *ISME J.* 8, 1831–1842.

Jorgensen, S. L., Hannisdal, B., Lanzen, A., Baumberger, T., Flesland, K., Fonseca, R., et al. (2012). Correlating microbial community profiles with geochemical data in highly stratified sediments from the arctic mid-ocean ridge. *Proc. Nalt. Acad. Sci. U. S. A.* 109, 16764–16765.

Knief, C. (2015). Diversity and habitat preferences of cultivated and uncultivated aerobic methanotrophic bacteria evaluated based on pmoA as molecular marker. *Front. Microbiol.* 6. doi: 10.3389/fmicb.2015.01346

Kraft, B., Jehmlich, N., Larsen, M., Bristow, L. A., Könneke, M., Thamdrup, B., et al. (2022). Oxygen and nitrogen production by an ammonia-oxidizing archaeon. *Science* 375, 97–100. doi: 10.1126/science.abe6733

Kronthaler, F., and Zöllner, S. (2021). *R and RStudio, in: data analysis with RStudio* (Berlin, Heidelberg: Springer Berlin Heidelberg), 1–12. doi: 10.1007/978-3-662-62518-7_1

Kuhn, T., Wegorzewski, A., Rühlemann, C., and Vink, A. (2018). Correction to: composition, formation, and occurrence of polymetallic nodules, Chapter 2 in *Deep-Sea Mining*, R. Sharma (ed.). Springer International Publishing, Cham). doi: 10.1007/978-3-319-52557-0_19

Landry, Z., Swan, B. K., Herndl, G. J., Stepanauskas, R., and Giovannoni, S. J. (2017). SAR202 genomes from the dark ocean predict pathways for the oxidation of recalcitrant dissolved organic matter. *mBio* 8, e00413–e00417. doi: 10.1128/mBio.00413-17

Li, J., Li, L., Bai, S., Chen, S., Xu, H., Ta, K., et al. (2021). Geochemical and molecular characteristics of ferromanganese deposits and surrounding sediments in the Mariana Trench: An Implication for the geochemical Mn cycle in sedimentary environments of the trench zone. *Geochimica Cosmochimica Acta* 310, 155–168. doi: 10.1016/j.gca.2021.07.018

Lindh, M. V., Maillot, B. M., Shulse, C. N., Gooday, A. J., Amon, D. J., Smith, C. R., et al. (2017). From the surface to the deep-sea: bacterial distributions across polymetallic nodule fields in the clarion-clipperton zone of the pacific ocean. *Front. Microbiol.* 8. doi: 10.3389/fmicb.2017.01696

Liu, J., Huang, F., Liu, J., Liu, X., Lin, R., Zhong, X., et al. (2023). Phylotype resolved spatial variation and association patterns of planktonic Thaumarchaeota in eastern Chinese marginal seas. *Mar. Life Sci. Technol.* 5, 257–270. doi: 10.1007/s42995-023-00169-y

Liu, J., Zheng, Y., Lin, H., Wang, X., Li, M., Liu, Y., et al. (2019). Proliferation of hydrocarbon-degrading microbes at the bottom of the Mariana Trench. *Microbiome* 7, 47. doi: 10.1186/s40168-019-0652-3

Liu, J., Zhu, S., Liu, X., Yao, P., Ge, T., and Zhang, X.-H. (2020). Spatiotemporal dynamics of the archaeal community in coastal sediments: assembly process and co-occurrence relationship. *ISME J.* 14, 1463–1478. doi: 10.1038/s41396-020-0621-7

Marino, E., González, F. J., Somoza, L., Lunar, R., Ortega, L., Vázquez, J. T., et al. (2017). Strategic and rare elements in Cretaceous-Cenozoic cobalt-rich ferromanganese crusts from seamounts in the Canary Island Seamount Province (northeastern tropical Atlantic). *Ore Geology Rev.* 87, 41–61. doi: 10.1016/j.oregeorev.2016.10.005

Martens-Habbena, W., and Qin, W. (2022). Archaeal nitrification without oxygen. *Science* 375, 27–28. doi: 10.1126/science.abn0373

Mason, O. U., Hazen, T. C., Borglin, S., Chain, P. S. G., Dubinsky, E. A., Fortney, J. L., et al. (2012). Metagenome, metatranscriptome and single-cell sequencing reveal microbial response to Deepwater Horizon oil spill. *ISME J.* 6, 1715–1727. doi: 10.1038/ismej.2012.59

Matsunaga, T., Sakaguchi, T., and Tadakoro, F. (1991). Magnetite formation by a magnetic bacterium capable of growing aerobically. *Appl. Microb. Biotechnol.* 35, 651–655.

McKay, J. L., Pedersen, T. F., and Mucci, A. (2007). Sedimentary redox conditions in continental margin sediments (N.E. Pacific)—Influence on the accumulation of redox-sensitive trace metals. *Chem. Geology* 238, 180–196. doi: 10.1016/j.chemgeo.2006.11.008

Mestre, M., Ruiz-González, C., Logares, R., Duarte, C. M., Gasol, J. M., and Sala, M. M. (2018). Sinking particles promote vertical connectivity in the ocean microbiome. *Proc. Natl. Acad. Sci. U.S.A.* 115, E6799–E6807. doi: 10.1073/pnas.1802470115

Molari, M., Janssen, F., Vonnahme, T. R., Wenzhöfer, F., and Boetius, A. (2020). The contribution of microbial communities in polymetallic nodules to the diversity of the deep-sea microbiome of the Peru Basin (4130–4198 m depth). *Biogeosciences* 17, 3203–3222. doi: 10.5194/bg-17-3203-2020

Ren, Y., Guan, Y., Sun, X., Xu, L., Xiao, Z., Deng, Y., et al. (2023). Nano-mineralogy and growth environment of Fe-Mn polymetallic crusts and nodules from the South China Sea. *Front. Mar. Sci.* 10. doi: 10.3389/fmars.2023.1141926

Roda-Garcia, J. J., Haro-Moreno, J. M., and López-Pérez, M. (2023). Evolutionary pathways for deep-sea adaptation in marine planktonic Actinobacteriota. *Front. Microbiol.* 14. doi: 10.3389/fmicb.2023.1159270

Schauer, R., Bienhold, C., Ramette, A., and Harder, J. (2010). Bacterial diversity and biogeography in deep-sea surface sediments of the South Atlantic Ocean. *ISME J.* 4, 159–170. doi: 10.1038/ismej.2009.106

Sebastián, M., Sánchez, P., Salazar, G., Álvarez-Salgado, X. A., Reche, I., Morán, X. A. G., et al. (2021). The quality of dissolved organic matter shapes the biogeography of the active bathypelagic microbiome. *bioRxiv*. [preprint]. doi: 10.1101/2021.05.14.444136

Shafiee, R. T., Diver, P. J., Snow, J. T., Zhang, Q., and Rickaby, R. E. M. (2021). Marine ammonia-oxidising archaea and bacteria occupy distinct iron and copper niches. *ISME Commun.* 1, 1. doi: 10.1038/s43705-021-00001-7

Shannon, P., Markiel, A., Ozier, O., Baliga, N. S., Wang, J. T., Ramage, D., et al. (2003). Cytoscape: a software environment for integrated models of biomolecular interaction networks. *Genome Res.* 13, 2498–2504.

Sheik, C. S., Reese, B. K., Twing, K. I., Sylvan, J. B., Grim, S. L., Schrenk, M. O., et al. (2018). Identification and removal of contaminant sequences from ribosomal gene databases: lessons from the census of deep life. *Front. Microbiol.* 9. doi: 10.3389/fmicb.2018.00840

Shiraishi, F., Mitsunobu, S., Suzuki, K., Hoshino, T., Morono, Y., and Inagaki, F. (2016). Dense microbial community on a ferromanganese nodule from the ultra-oligotrophic South Pacific Gyre: Implications for biogeochemical cycles. *Earth Planetary Sci. Lett.* 447, 10–20. doi: 10.1016/j.epsl.2016.04.021

Shulga, N., Abramov, S., Klyukina, A., Ryazantsev, K., and Gavrilov, S. (2022). Fast-growing Arctic Fe–Mn deposits from the Kara Sea as the refuges for cosmopolitan marine microorganisms. *Sci. Rep.* 12, 21967. doi: 10.1038/s41598-022-23449-6

Shulse, C. N., Maillot, B., Smith, C. R., and Church, M. J. (2017). Polymetallic nodules, sediments, and deep waters in the equatorial North Pacific exhibit highly diverse and distinct bacterial, archaeal, and microeukaryotic communities. *MicrobiologyOpen* 6, e00428. doi: 10.1002/mbo3.428

Swan, B. K., Martinez-Garcia, M., Preston, C. M., Sczyrba, A., Woyke, T., Lamy, D., et al. (2011). Potential for chemolithoautotrophy among ubiquitous bacteria lineages in the dark ocean. *Science* 333, 1296–1300. doi: 10.1126/science.1203690

Tang, W., Gong, J., Wu, L., Li, Y., Zhang, M., and Zeng, X. (2016). DGGE diversity of manganese mine samples and isolation of a Lysinibacillus sp. efficient in removal of high Mn (II) concentrations. *Chemosphere* 165, 277–283. doi: 10.1016/j.chemosphere.2016.08.134

Thrash, J. C., Seitz, K. W., Baker, B. J., Temperton, B., Gillies, L. E., Rabalais, N. N., et al. (2017). Metabolic roles of uncultivated bacterioplankton lineages in the northern gulf of Mexico "Dead zone. *mBio* 8, e01017–e01017. doi: 10.1128/mBio.01017-17

Tully, B. J., and Heidelberg, J. F. (2013). Microbial communities associated with ferromanganese nodules and the surrounding sediments. *Front. Microbiol.* 4. doi: 10.3389/fmicb.2013.00161

Vereshchagin, O. S., Perova, E. N., Brusnitsyn, A. I., Ershova, V. B., Khudoley, A. K., Shilovskikh, V. V., et al. (2019). Ferro-manganese nodules from the Kara Sea: Mineralogy, geochemistry and genesis. *Ore Geology Rev.* 106, 192–204. doi: 10.1016/j.oregeorev.2019.01.023

von Stackelberg, U. (1997). Growth history of manganese nodules and crusts of the Peru Basin. *SP* 119, 153–176. doi: 10.1144/GSL.SP.1997.119.01.11

von Stackelberg, U. (2017). "Manganese nodules of the Peru basin," in *Handbook of marine mineral deposits*. Ed. D. S. Cronan (New York: Routledge), 197–238. doi: 10.1201/9780203752760-8

Wang, L., Li, X., Lai, Q., and Shao, Z. (2015). Kiloniella litopenaei sp. nov., isolated from the gut microflora of Pacific white shrimp, Litopenaeus vannamei. *Antonie van Leeuwenhoek* 108, 1293–1299. doi: 10.1007/s10482-015-0581-5

Wang, Y., Wegener, G., Williams, T. A., Xie, R., Hou, J., Tian, C., et al. (2021). A methylotrophic origin of methanogenesis and early divergence of anaerobic multicarbon alkane metabolism. *Sci. Adv.* 7, eabj1453. doi: 10.1126/sciadv.abj1453

Wang, Z., Liu, F., Li, E., Yuan, Y., Yang, Y., Xu, M., et al. (2022). Network analysis reveals microbe-mediated impacts of aeration on deep sediment layer microbial communities. *Front. Microbiol.* 13. doi: 10.3389/fmicb.2022.931585

Wasserman, S., and Faust, K. (1994). *Social network analysis: methods and applications, 1st ed* (Cambridge: Cambridge University Press). doi: 10.1017/CBO9780511815478

Wiese, J., Imhoff, J. F., Horn, H., Borchert, E., Kyrpides, N. C., Göker, M., et al. (2020). Genome analysis of the marine bacterium Kiloniella laminariae and first insights into comparative genomics with related Kiloniella species. *Arch. Microbiol.* 202, 815–824. doi: 10.1007/s00203-019-01791-0

Wu, Y.-H., Liao, L., Wang, C.-S., Ma, W.-L., Meng, F.-X., Wu, M., et al. (2013). A comparison of microbial communities in deep-sea polymetallic nodules and the surrounding sediments in the Pacific Ocean. *Deep Sea Res. Part I: Oceanographic Res. Papers* 79, 40–49. doi: 10.1016/j.dsr.2013.05.004

Yang, K., Dong, Y., Li, Z., Wang, H., Ma, W., Qiu, Z., et al. (2024). Geochemistry of buried polymetallic nodules from the eastern Pacific Ocean: Implication for the depth-controlled alteration process. *Mar. Geology* 467, 107190. doi: 10.1016/j.margeo.2023.107190

Yang, Y., Sanford, R., Yan, J., Chen, G., Cápiro, N. L., Li, X., et al. (2020). Roles of organohalide-respiring dehalococcoidia in carbon cycling. *mSystems* 5, e00757–e00719. doi: 10.1128/mSystems.00757-19

Yuan, Y. C., Rickard, L. N., Xia, L., and Scherer, C. (2011). The interplay between interpersonal and electronic resources in knowledge seeking among co-located and distributed employees. *J. Am. Soc Inf. Sci.* 62, 535–549. doi: 10.1002/asi.21472

Zakem, E. J., Polz, M. F., and Follows, M. J. (2020). Redox-informed models of global biogeochemical cycles. *Nat. Commun.* 11, 5680. doi: 10.1038/s41467-020-19454-w

Zhang, C., Liu, X., Shi, L.-D., Li, J., Xiao, X., Shao, Z., et al. (2023). Unexpected genetic and microbial diversity for arsenic cycling in deep sea cold seep sediments. *NPJ Biofilms Microbiomes* 9, 13. doi: 10.1038/s41522-023-00382-8

Zhang, D., Li, X., Wu, Y., Xu, X., Liu, Y., Shi, B., et al. (2023). Microbe-driven elemental cycling enables microbial adaptation to deep-sea ferromanganese nodule sediment fields. *Microbiome* 11, 160. doi: 10.1186/s40168-023-01601-2

Zhang, Z., Du, Y., Wu, C., Fang, N., Yang, S., Liu, J., et al. (2013). Growth of a polymetallic nodule from the northwestern continental margin of the South China Sea and its response to changes in the paleoceanographical environment of the Late Cenozoic. *Sci. China Earth Sci.* 56, 453–463. doi: 10.1007/s11430-012-4535-8

Zheng, X., Su, Y., Li, X., Xiao, N., Wang, D., and Chen, Y. (2013). Pyrosequencing reveals the key microorganisms involved in sludge alkaline fermentation for efficient short-chain fatty acids production. *Environ. Sci. Technol.* 47, 4262–4268. doi: 10.1021/es400210v

Zhong, Y., Chen, Z., González, F. J., Hein, J. R., Zheng, X., Li, G., et al. (2017). Composition and genesis of ferromanganese deposits from the northern South China Sea. *J. Asian Earth Sci.* 138, 110–128. doi: 10.1016/j.jseaes.2017.02.015

Zhong, Y., Chen, Z., Hein, J. R., González, F. J., Jiang, Z., Yang, X., et al. (2020). Evolution of a deep-water ferromanganese nodule in the South China Sea in response to Pacific deep-water circulation and continental weathering during the Plio-Pleistocene. *Quaternary Sci. Rev.* 229, 106106. doi: 10.1016/j.quascirev.2019.106106

Zhong, Y., Liu, Q., Chen, Z., González, F. J., Hein, J. R., Zhang, J., et al. (2019). Tectonic and paleoceanographic conditions during the formation of ferromanganese nodules from the northern South China Sea based on the high-resolution geochemistry, mineralogy and isotopes. *Mar. Geology* 410, 146–163. doi: 10.1016/j.margeo.2018.12.006

Ziegler, C. L., Murray, R. W., Plank, T., and Hemming, S. R. (2008). Sources of fe to the equatorial pacific ocean from the holocene to miocene. *Earth Planetary Sci. Lett.* 270, 258–270. doi: 10.1016/j.epsl.2008.03.044

frontiers | Frontiers in Marine Science

TYPE Original Research
PUBLISHED 19 December 2024
DOI 10.3389/fmars.2024.1489943

OPEN ACCESS

EDITED BY
Francisco Javier González,
Instituto Geológico y Minero de España (IGME), Spain

REVIEWED BY
Egidio Marino,
Instituto Geológico y Minero de España (IGME), Spain
Jiangbo Ren,
Guangzhou Marine Geological Survey, China

*CORRESPONDENCE
Xiangwen Ren
renxiangwen@163.com

RECEIVED 02 September 2024
ACCEPTED 28 November 2024
PUBLISHED 19 December 2024

CITATION
Ren X, Hein JR, Yang Z, Xing N and Zhu A (2024) Controls on cobalt concentrations in ferromanganese crusts from the Magellan seamounts, west Pacific. *Front. Mar. Sci.* 11:1489943. doi: 10.3389/fmars.2024.1489943

Controls on cobalt concentrations in ferromanganese crusts from the Magellan seamounts, west Pacific

Xiangwen Ren[1,2]*, James R. Hein[3], Zanzhong Yang[4], Na Xing[5] and Aimei Zhu[1]

[1]Key Laboratory of Marine Geology and Metallogeny, First Institute of Oceanography, Ministry of Natural Resources, Qingdao, China, [2]Laboratory for Marine Geology, Laoshan Laboratory, Qingdao, China, [3]Retired, Soquel, CA, United States, [4]School of Materials Science and Engineering, Shandong University of Technology, Zibo, Shandong, China, [5]Lab of Isotope Marine Chemistry, Xiamen University, Xiamen, Fujian, China

Introduction: Cobalt is the most important critical element in ferromanganese crusts. Co concentration in the Fe-Mn crusts is one of the key parameters for determination of the Co resource. Thus, it is essential to clarify the controls on the variations of Co concentration of ferromanganese crusts.

Methods: To clarify the controls on Co concentration of hydrogenetic nonphosphatized ferromanganese crusts, an equation was deduced based on Fick's First Law: $Co(\%) = Mn0_2(\%) \cdot D_{sw} \cdot \frac{C_{sw}}{\delta} \cdot \frac{z}{GR} \cdot S_{sp}$, and eight potential controls were gleaned from this equation, including dilution, diffusivity of Co ions in seawater (D_{sw}), temperature which controls the D_{sw}, Co ion concentration in seawater (C_{sw}), the diffusion distance of Co ions near the interface of seawater and Fe-Mn crusts (δ), thickness of one molecular layer (z), growth rate (GR), and specific surface area of Fe-Mn crusts (S_{sp}). To constrain the value of Co ion diffusion gradients ($\overline{C_{sw}}/\delta$) and consequently verify the proposed equation, we determined the Co concentrations, growth rates, and specific surface area of the outermost layer of Fe-Mn crusts, and calculated diffusivity of Co^{2+}.

Results: The $\overline{C_{sw}}/\delta$ for the Fe-Mn crusts from Caiwei seamount (Magellan seamounts) was determined to be 295-496 pM/mm, which are reasonable for the Co ion concentrations and seawater mixing in the deep ocean.

Discussion: According to the equation established in this study, the trend of decreasing Co concentrations in Fe-Mn crusts with increasing water depth is controlled mainly by dilution and to a lesser extent by seawater Co ion concentration, temperature of seawater, and consequently the diffusivity of Co ions in seawater.

KEYWORDS

ferromanganese crusts, Magellan seamounts, cobalt, diffusivity, Pacific

1 Introduction

Cobalt (Co) is the most important critical element in ferromanganese crusts (Fe-Mn crusts) due to the high concentrations, economic value, and application in the manufacture of hybrid and electric car batteries, storage of solar energy, magnetic recording media, high-T super-alloys, supermagnets, and smart phones (Hein et al., 2013). Relative to 2020, it's estimated by the International Energy Agency that a 21-fold Co supply will be needed by 2040 to achieve the clean energy transition (IEA, 2021). Compared to the land-based reserve of Co, 11 million tons (U. S. Geological Survey, 2024), the tonnage of in place Co in Fe-Mn crusts from the Pacific Prime Crust Zone (PPCZ) is as high as 50 million tons (Hein and Koschinsky, 2014). Land-based Co ores mainly occur in the West African copper belt (D.R. Congo), with a reserve of 6 million tons, which is 55% of the land-based Co reserves (U. S. Geological Survey, 2024). The average grade of the Co ores in the West African copper belt is 0.12% (Milesi et al., 2006). In contrast, the average Co concentration in Fe-Mn crusts in PPCZ is 0.67% (Hein et al., 2013). Although the mining of Fe-Mn crusts is not currently feasible for technological and economic reasons, Fe-Mn crusts are promising future Co ores.

For determination of the Co resource both before and during mining, Co concentration (grade) in the Fe-Mn crusts is one of the key parameters. However, the Co concentrations in Fe-Mn crusts show regional, local, and stratigraphic (depth in the crusts) variations. The average Co concentrations of Fe-Mn crusts from the seamounts in the Pacific range from 0.3% to 0.8% (Hein et al., 2000). Cobalt concentrations of Fe-Mn crusts show a negative correlation with water depth (Cronan, 1977; Halbach et al., 1983; Manheim, 1986; Andreev and Gramberg, 2002; Benites et al., 2023), and the data show a wide range of variations (Andreev and Gramberg, 2002). The average Co concentrations of the stratigraphic sections of the Fe-Mn crusts from the Magellan seamounts range from 0.32% to 0.65% (Melnikov and Pletnev, 2013). Thus, it is essential to clarify the controls on the variations of Co concentration of Fe-Mn crusts to develop criteria for exploration and extraction.

Halbach et al. (1983) suggested that Co-flux is constant over one order of magnitude of Fe-Mn crust growth rates, and consequently concluded that extremely slow growth rates and high Mn concentrations result in high Co concentrations. Based on the growth rate and chemical compositions of Fe-Mn crusts from the mid-Pacific, Manheim (1986) proposed that Co fluxes were roughly constant regardless of the water depth, which indicates that slow growth rates will result in high Co concentration in Fe-Mn crusts. Ren et al.(2022, 2024) proposed that oxidizing deep-water, oligotrophic bottom currents, and low sedimentation rates are optimal for west Pacific Co-rich Fe-Mn nodule formations (similar to Fe-Mn crusts in chemistry and mineralogy) to enrich multiple elements from seawater, including Co. Hein et al. (2000) suggested that the dominant controls on the concentration of elements (including Co) in Fe-Mn crusts include the concentration of the elements in seawater, element-particle reactivity, element residence time in seawater, the absolute and relative amounts of Fe and Mn in Fe-Mn crusts, dilution from detrital and diagenetic minerals, the colloid surface charge and types of complexing agents, the value of x in MnO_{2-x}, dissolved O_2 and pH of seawater, specific surface area, and growth rate.

In this work, we analyze the potential controls for Co concentrations in Fe-Mn crusts from the Magellan seamounts, and propose an equation that unites all the factors.

2 Samples and methods

2.1 Sample description

Fe-Mn crusts from two sites are used here. Fe-Mn crust DY31-III-JL-Dive70C (hereafter Fe-Mn crust DY31) was collected by the Chinese submersible *Jiaolong* in 2013 on Caiwei seamount (Magellan seamounts) (155.5492° E, 15.9246° N) at a water depth of 2270 m. Fe-Mn crust MAD23 was collected by dredge on the *R. V. Dayang Yihao* in 2006 from Caiwei seamount (155.5284° E, 15.9124° N) at a water depth between 1904 m and 1885 m (Figure 1). Fe-Mn crust DY31 is about 6 cm thick, and the stratigraphic section can be divided into three distinct layers called II-1, II-2 and III (Figure 2). Layer II-1 is the lowermost layer, 1 cm thick, and shows a dendritic texture with dendrite orientation indicating that layer II-1 is an older crust that was turned over before layers II-2 and III were accreted on to it. The overlying layer II-2 is about 2 cm thick, black, and dense, with a dendritic texture composed of short dendrites oriented in the opposite direction to those in layer II-1. Layer III is about 3 cm thick, composed of long, black dendrites. The substrate rock was not recovered. Fe-Mn crust MAD23 is 6.6 cm thick, and the stratigraphic section is divided into three distinct layers from the bottom to the surface: I-1, II and III. Layer I-1 is 1.2 cm thick, dense, and black, with a laminated texture; layer II is 3.2 cm thick, dendritic, and varies from the compact to friable; layer III is 2.2 cm thick, black, and compact, with a dendritic texture (Figure 2).

2.2 Analytical methods for major elements, ^{230}Th isotope, and specific surface area of Fe-Mn crusts

In order to characterize the chemical composition, 20 samples were taken along the stratigraphic section of Fe-Mn crust DY31 (13 for layer III, 6 for layer II-2, and 1 for layer II-1); 21 samples were taken for Fe-Mn crust MAD23 (11 for layer III, 7 for layer II, and 3 for layer I-1) (Table 1). The outermost layers (youngest), 2.5 mm for Fe-Mn crust DY31 and 3.6 mm for Fe-Mn crust MAD23, are used in this study to investigate the controls on Co concentrations in Fe-Mn crusts. The samples were ground to a <74 μm powder in an agate mortar and pestle. The samples were then digested following the procedure described by Ren et al. (2010), and analyzed by Inductively Coupled Plasma Optical Emission Spectrometer (ICP-OES, Thermal iCAP6300 instrument) for Al_2O_3, CaO, TFe, K_2O, MgO, MnO_2, Na_2O, P_2O_5, TiO_2, Co, Cu, Ni, Ba, Sr, and Pb. Standards GSMC-1and GSMC-2 were analyzed together with Fe-Mn crust samples to monitor accuracy.

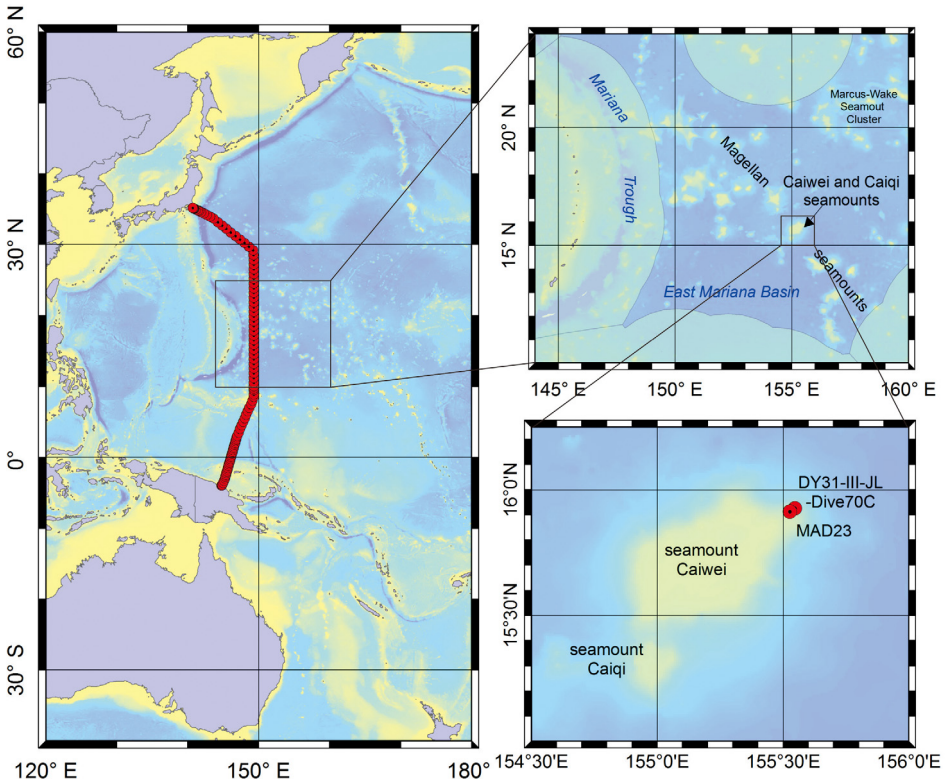

FIGURE 1
Left map, location of World Ocean Circulation Experiment (WOCE) P10 transect (red line); right top map, location of Caiwei seamount; and right bottom map, sampling sites of Fe-Mn crusts (red circles).

For determination of $^{230}Th_{ex}$ growth rates of the outermost layers of the Fe-Mn crusts, ten (DY31) and eight (MAD23) samples were scraped layer by layer with surgical blades from the outermost approximately 2 mm of crust (based on decay of ^{230}Th in Fe-Mn crusts and the detection limit). The sampling intervals d (mm) were calculated with the formula: $d(mm) = \frac{10 \times w(g)}{\rho(g/cm^3) \times A(cm^2)}$, where w is the weight of each sample; ρ is the density of Fe-Mn crusts (1.6 g/cm^3, Halbach et al., 1983), and A is the sampling area. The error of d is estimated to be ±20% (Ku et al., 1979). The samples were ground in an agate mortar and pestle and then dried at 110 ° C. Then the

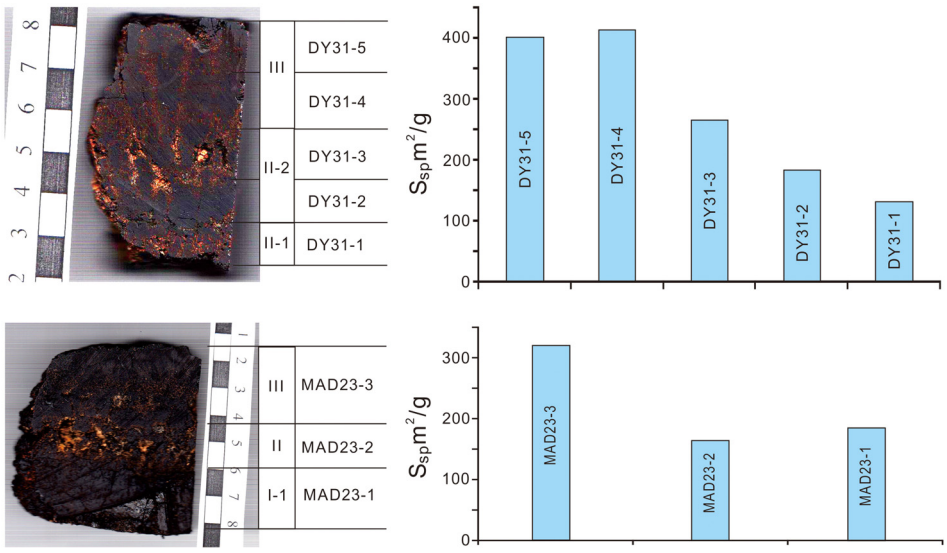

FIGURE 2
Variation of specific surface area in the stratigraphic sections of Fe-Mn crusts from Caiwei seamount; note the scale bars in cm divisions.

TABLE 1 Major element concentrations through stratigraphic sections of Fe-Mn crusts from Caiwei seamount of the Magellan seamounts.

Sample No.	Interval		Al_2O_3	CaO	TFe	K_2O	MgO	MnO_2	Na_2O	P_2O_5	TiO_2	Co	Cu	Ni	Ba	Sr	Pb
	mm		%														
DY31-III-JL-Dive70C: Layer III																	
Dive70C-(1)	0.0	2.5	2.4	2.9	15.9	0.77	1.95	34.5	2.23	0.84	2.2	0.67	0.24	0.49	0.20	0.14	0.17
Dive70C-(2)	2.5	4.7	1.5	3.4	17.5	0.56	1.68	32.2	2.13	0.86	1.6	0.68	0.06	0.33	0.13	0.14	0.16
Dive70C-(3)	4.7	7.1	1.5	3.0	17.8	0.56	1.69	31.5	2.16	0.81	1.6	0.63	0.07	0.33	0.14	0.15	0.16
Dive70C-(4)	7.1	9.1	1.5	2.9	17.5	0.55	1.63	32.0	2.15	0.79	1.6	0.62	0.08	0.34	0.14	0.14	0.15
Dive70C-(5)	9.1	11.6	1.4	2.8	17.2	0.55	1.61	32.9	2.17	0.80	1.6	0.64	0.09	0.36	0.14	0.14	0.15
Dive70C-(6)	11.6	14.1	1.5	3.0	16.7	0.59	1.69	32.9	2.17	0.76	1.8	0.61	0.11	0.37	0.14	0.15	0.15
Dive70C-(7)	14.1	15.6	1.5	3.0	16.3	0.57	1.64	33.2	2.15	0.76	1.8	0.59	0.13	0.39	0.15	0.14	0.15
Dive70C-(8)	15.6	18.2	1.7	3.0	17.8	0.62	1.75	36.3	2.38	0.85	2.1	0.62	0.16	0.44	0.16	0.15	0.16
Dive70C-(9)	18.2	20.8	1.6	2.9	15.7	0.59	1.63	31.8	2.00	0.71	1.9	0.47	0.14	0.37	0.15	0.14	0.18
Dive70C-(10)	20.8	22.5	1.8	3.0	17.0	0.63	1.67	32.2	2.12	0.73	2.0	0.45	0.16	0.37	0.16	0.15	0.14
Dive70C-(11)	22.5	25.1	2.1	2.9	18.7	0.63	1.64	30.3	2.10	0.78	2.0	0.43	0.16	0.33	0.17	0.15	0.15
Dive70C-(12)	25.1	27.2	2.3	2.8	18.6	0.64	1.61	29.6	2.08	0.77	1.8	0.44	0.17	0.32	0.17	0.14	0.14
Dive70C-(13)	27.2	30.8	2.4	2.9	17.3	0.71	1.76	31.0	2.12	0.73	1.9	0.52	0.18	0.36	0.17	0.14	0.13
DY31-III-JL-Dive70C: Layer II-2																	
Dive70C-(14)	30.8	33.8	2.7	3.0	15.0	0.83	1.98	34.0	2.15	0.70	2.1	0.64	0.22	0.47	0.17	0.14	0.11
DiIve70C-(15)	33.8	37.2	2.4	3.2	15.3	0.80	1.97	33.8	2.08	0.75	2.3	0.59	0.22	0.45	0.19	0.14	0.12
Dive70C-(16)	37.2	40.8	2.3	3.1	15.9	0.73	1.92	34.3	2.06	0.82	1.9	0.53	0.23	0.49	0.19	0.14	0.11
Dive70C-(17)	40.8	44.6	2.4	3.2	15.5	0.77	2.03	35.3	2.12	0.79	1.8	0.52	0.24	0.54	0.19	0.14	0.10
Dive70C-(18)	44.6	48.6	1.8	3.4	14.3	0.74	2.07	38.3	2.18	0.69	1.8	0.51	0.25	0.63	0.20	0.14	0.12
Dive70C-(19)	48.6	51.6	1.8	3.3	13.6	0.73	2.08	38.7	2.27	0.75	1.6	0.52	0.25	0.74	0.20	0.14	0.12
DY31-III-JL-Dive70C: Layer II-1																	
Dive70C-(20)	51.6	60.8	2.3	3.2	16.5	0.68	1.96	35.2	2.28	0.84	1.6	0.65	0.12	0.51	0.14	0.14	0.14
MAD23: Layer III																	
MAD23-(1)	0.0	3.6	5.5	3.5	18.8	0.63	1.92	29.7	2.62	1.03	1.4	0.53	0.04	0.32	0.12	0.14	0.15
MAD23-(2)	3.6	4.4	1.9	3.0	18.7	0.60	1.80	30.5	2.54	0.94	1.5	0.56	0.04	0.31	0.12	0.14	0.16
MAD23-(3)	4.4	5.2	1.8	2.9	18.7	0.61	1.78	30.4	2.46	0.95	1.5	0.59	0.05	0.31	0.12	0.14	0.16
MAD23-(4)	5.2	6.6	1.7	2.9	18.8	0.61	1.78	31.6	2.46	0.92	1.5	0.62	0.05	0.34	0.13	0.14	0.16
MAD23-(5)	6.6	9.0	1.6	3.0	17.9	0.62	1.83	32.3	2.47	0.83	1.6	0.68	0.06	0.38	0.14	0.15	0.15
MAD23-(6)	9.0	10.9	1.8	2.8	17.8	0.62	1.73	31.8	2.49	0.81	1.6	0.69	0.07	0.38	0.14	0.14	0.15
MAD23-(7)	10.9	13.5	2.0	2.8	17.2	0.64	1.70	31.7	2.54	0.79	1.6	0.71	0.07	0.39	0.14	0.13	0.15
MAD23-(8)	13.5	14.8	2.1	2.8	16.8	0.68	1.66	31.5	2.55	0.77	1.6	0.66	0.08	0.37	0.14	0.13	0.14
MAD23-(9)	14.8	17.6	1.9	3.0	16.9	0.68	1.74	32.3	2.49	0.76	1.8	0.63	0.09	0.37	0.14	0.14	0.14
MAD23-(10)	17.6	19.6	1.5	3.1	16.8	0.58	1.72	34.8	2.42	0.81	2.0	0.65	0.11	0.42	0.16	0.15	0.15
MAD23-(11)	19.6	22.6	1.3	3.2	16.8	0.58	1.77	36.1	2.42	0.77	2.1	0.62	0.13	0.44	0.17	0.16	0.16

(Continued)

10.3389/fmars.2024.1489943

TABLE 1 Continued

Sample No.	Interval		Al_2O_3	CaO	TFe	K_2O	MgO	MnO_2	Na_2O	P_2O_5	TiO_2	Co	Cu	Ni	Ba	Sr	Pb
	mm		%														
MAD23: Layer II																	
MAD23-(12)	22.6	23.0	1.6	3.1	17.5	0.63	1.82	33.8	2.36	0.77	2.1	0.56	0.14	0.42	0.18	0.15	0.16
MAD23-(13)	23.0	33.0	2.4	3.0	17.8	0.81	1.89	31.8	2.33	0.74	2.0	0.56	0.16	0.39	0.18	0.14	0.14
MAD23-(14)	33.0	39.0	2.5	3.2	16.6	0.85	2.01	34.1	2.27	0.84	2.3	0.61	0.18	0.44	0.21	0.14	0.12
MAD23-(15)	39.0	43.0	2.4	3.2	16.8	0.80	2.00	33.6	2.25	0.84	2.0	0.53	0.19	0.47	0.21	0.14	0.12
MAD23-(16)	43.0	45.5	1.6	3.4	15.6	0.68	1.98	37.9	2.36	0.76	2.0	0.56	0.21	0.57	0.21	0.15	0.13
MAD23-(17)	45.5	49.0	1.5	3.7	14.7	0.72	2.07	39.5	2.48	0.90	1.8	0.51	0.23	0.68	0.22	0.15	0.12
MAD23-(18)	49.0	53.8	1.9	4.2	15.9	0.71	1.92	36.5	2.44	1.41	1.6	0.37	0.20	0.55	0.23	0.15	0.14
MAD23: Layer I-1																	
MAD23-(19)	53.8	56.7	1.6	6.0	16.4	0.65	1.79	34.4	2.32	2.54	1.8	0.34	0.18	0.44	0.26	0.16	0.15
MAD23-(20)	56.7	59.4	1.3	10.3	13.8	0.60	1.70	33.7	2.27	5.19	1.8	0.39	0.18	0.46	0.26	0.17	0.14
MAD23-(21)	59.4	66.2	0.9	15.0	12.5	0.46	1.44	30.7	2.15	8.46	1.8	0.40	0.16	0.38	0.25	0.17	0.14

samples were digested following the procedure described by Hu et al. (2002). The digested samples were separated and purified using the procedure of Luo et al. (1986). U and Th isotopes were determined by alpha spectrometry (Octete ^{TM} PC).

To determine variations in specific surface area, eight samples were taken along the stratigraphic section of the Fe-Mn crusts in this study: five samples from Fe-Mn crust DY31 (two for layer III, two for layer II-2, and one for layer II-1) and three samples from layer III, II, and I-1 of Fe-Mn crust MAD23 (Figure 2). The samples were crashed to grains of about 1 mm in diameter, and then dried at 110 ° C. The specific surface areas were determined by N_2 adsorption using the BET method using a Belsorp-max instrument, in September 2014.

3 Results

3.1 Fe-Mn crusts cobalt and transition metals

The concentrations of Mn, Fe, Co, Ni, and Cu of Fe-Mn crusts DY31 and MAD23 show the same variations as those of other hydrogenetic Fe-Mn deposits (Table 1; Figure 3, right panel). The Co concentration of the outermost layer (2.5 mm) of DY31 is 0.67%, and MnO_2 concentration is 34.5%. The Co concentrations of layer III (0-30.8 mm) of this Fe-Mn crust range from 0.43% to 0.68% with a mean value of 0.57%. The Co concentrations of layer II-2 (30.8-51.6 mm) range from 0.51% to 0.64% with a mean value of 0.55%, and the Co concentration of layer II-1 (51.6-60.8 mm) is 0.65%. The Co concentration of the outermost layer (3.6 mm) of MAD23 is 0.53%, and MnO_2 concentration is 29.7%. The Co concentrations through the stratigraphic section of Fe-Mn crust MAD23 vary between 0.71% and 0.34%. The ranges of Co concentrations in MAD23 crust layer III (0-22.6 mm), II (22.6-53.8 mm), and I-1 (53.8-66.2 mm) are 0.53-0.71%, 0.37-0.61%, and 0.34-0.40% respectively. The average Co concentrations for crust MAD23 decreases from 0.63% in layer III, to 0.53% of layer II, to 0.38% of layer I-1 (Figure 3, left panel).

3.2 Growth rates of outermost layers of the Fe-Mn crusts

The $^{230}Th_{ex}$ and ratios of $^{230}Th_{ex}/^{232}Th$ of the Fe-Mn crusts show exponential decreases with depth (age) (Table 2). The growth rates (GR) were estimated by fitting the depth distributions of $^{230}Th_{ex}$ and $^{230}Th_{ex}/^{232}Th$ with the isotope decay equations $^{230}Th_{ex})_d = {}^{230}Th_{ex})_0 \cdot e - \frac{\lambda_{230}}{GR} d$ and $^{230}Th_{ex}/^{232}Th)_d = {}^{230}Th_{ex}/^{232}Th)_0 \cdot e - \frac{\lambda_{230}}{GR} d$, where d is sampling depth in the stratigraphic sections and λ_{230} is the decay constant of ^{230}Th (9.19×10^{-6} a^{-1}) (Figure 4).

The decay curve of $^{230}Th_{ex}$ of Fe-Mn crust DY31 shows a deflection at 0.74 mm (around 420 ka). The GR of this Fe-Mn crust derived from $^{230}Th_{ex}$ are 1.75 ± 0.13 mm/Myr between 0.00 mm and 0.74 mm, and 5.90 ± 0.83 mm/Myr between 0.74 mm and 1.99 mm in the stratigraphic section, whereas the GR of this Fe-Mn crust derived from $^{230}Th_{ex}/^{232}Th$ are slightly higher between 0 mm and 0.74 mm, 2.03 ± 0.17 mm/Myr, and the same within error between 0.74 mm and 1.99 mm, 5.22 ± 0.45 mm/Myr. In contrast, the growth rates of Fe-Mn crust MAD23 are constant between 0 mm to 1.9 mm, 2.82 ± 0.13 mm/Myr by $^{230}Th_{ex}$ and 2.77 ± 0.23 mm/Myr by $^{230}Th_{ex}/^{232}Th$.

3.3 Specific surface area of Fe-Mn crusts from Caiwei seamount

The specific surface area decreases with depth (age) through the stratigraphic sections of the two Fe-Mn crusts (Table 3; Figure 2).

10.3389/fmars.2024.1489943

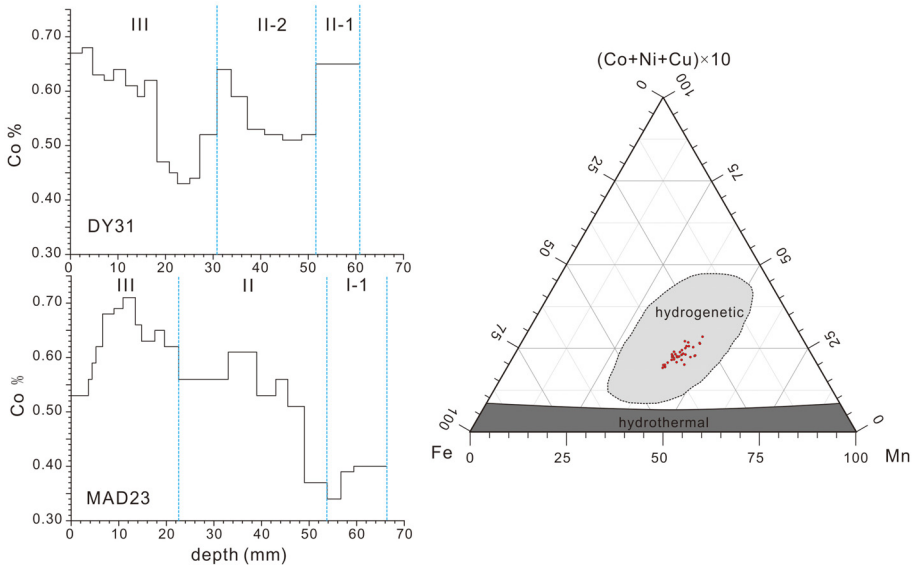

FIGURE 3
Left panel, Co concentrations of Fe-Mn crusts DY31 and MAD23 through the stratigraphic sections; right panel, ternary diagram of Mn, Fe, and (Cu +Co+Ni)×10 following Bonatti et al. (1972) for samples analyzed in this study.

TABLE 2 ^{238}U, ^{234}U, ^{230}Th, ^{232}Th, and $^{230}Th_{ex}$ specific activity, and the ratios $^{230}Th_{ex}/^{232}Th$ of Fe-Mn crusts from Caiwei seamount.

Sample No.	interval	Average depth	^{238}U	^{234}U	^{230}Th	^{232}Th	$^{230}Th_{ex}$	$^{230}Th_{ex}/^{232}Th$
	(mm)	(mm)	10^{-2} Bq/g					
DY31-III-JL-Dive70C								
Dive 70C-1	0-0.16	0.08	16.92 ± 1.48	18.55 ± 1.56	1207.20 ± 43.05	13.28 ± 0.87	1188.64 ± 43.08	89.50 ± 6.70
Dive 70C-2	0.16-0.34	0.25	15.71 ± 1.31	17.93 ± 1.42	468.43 ± 18.80	12.56 ± 0.89	450.50 ± 18.85	35.86 ± 2.96
Dive 70C-3	0.34-0.53	0.44	15.01 ± 1.10	15.74 ± 1.14	182.62 ± 7.80	9.77 ± 0.76	166.88 ± 7.89	17.08 ± 1.55
Dive 70C-4	0.53-0.74	0.63	14.54 ± 1.22	15.74 ± 1.29	105.83 ± 7.91	9.88 ± 1.21	90.09 ± 8.02	9.11 ± 1.38
Dive 70C-5	0.74-0.96	0.85	15.39 ± 1.24	15.79 ± 1.27	88.05 ± 6.79	11.04 ± 1.32	72.26 ± 6.91	6.54 ± 1.00
Dive 70C-6	0.96-1.15	1.05	15.82 ± 1.20	17.89 ± 1.31	95.63 ± 4.91	13.36 ± 1.01	77.74 ± 5.09	5.82 ± 0.58
Dive 70C-7	1.15-1.35	1.25	13.37 ± 1.25	16.67 ± 1.45	54.97 ± 3.20	12.66 ± 1.03	38.30 ± 3.52	3.02 ± 0.37
Dive 70C-8	1.35-1.56	1.45	17.56 ± 1.54	17.51 ± 1.54	39.77 ± 2.24	11.54 ± 0.89	22.26 ± 2.73	1.93 ± 0.28
Dive 70C-9	1.56-1.78	1.67	15.86 ± 1.30	14.01 ± 1.20	31.85 ± 1.95	13.25 ± 1.01	17.84 ± 2.29	1.35 ± 0.20
Dive 70C-10	1.78-1.99	1.89	13.26 ± 1.15	14.71 ± 1.22	28.83 ± 1.90	10.97 ± 0.93	14.12 ± 2.26	1.29 ± 0.23
MAD23								
MAD23-2-1	0-0.18	0.09	13.79 ± 0.99	21.85 ± 1.33	748.61 ± 21.60	10.21 ± 0.59	726.76 ± 21.65	71.21 ± 4.62
MAD23-2-2	0.18-0.42	0.3	16.58 ± 1.11	20.27 ± 1.27	376.73 ± 12.21	12.75 ± 0.73	356.47 ± 12.28	27.97 ± 1.87
MAD23-2-3	0.42-0.78	0.6	12.60 ± 0.97	17.22 ± 1.19	155.74 ± 5.06	9.98 ± 0.52	138.52 ± 5.20	13.88 ± 0.90
MAD23-2-4	0.78-1.04	0.91	13.13 ± 0.79	16.80 ± 0.92	55.34 ± 2.03	10.32 ± 0.57	38.53 ± 2.24	3.73 ± 0.30
MAD23-2-5	1.04-1.29	1.16	12.03 ± 0.69	12.21 ± 0.70	47.46 ± 2.48	10.90 ± 0.72	35.25 ± 2.57	3.23 ± 0.32
MAD23-2-6	1.29-1.56	1.42	12.19 ± 0.79	14.08 ± 0.88	25.07 ± 1.34	9.39 ± 0.61	11.00 ± 1.66	1.17 ± 0.19
MAD23-2-7	1.56-1.71	1.64	18.17 ± 1.35	18.90 ± 1.39	–	–	–	–
MAD23-2-8	1.71-1.90	1.81	15.04 ± 1.01	16.60 ± 1.08	–	–	–	–

"-" means below detection limit.

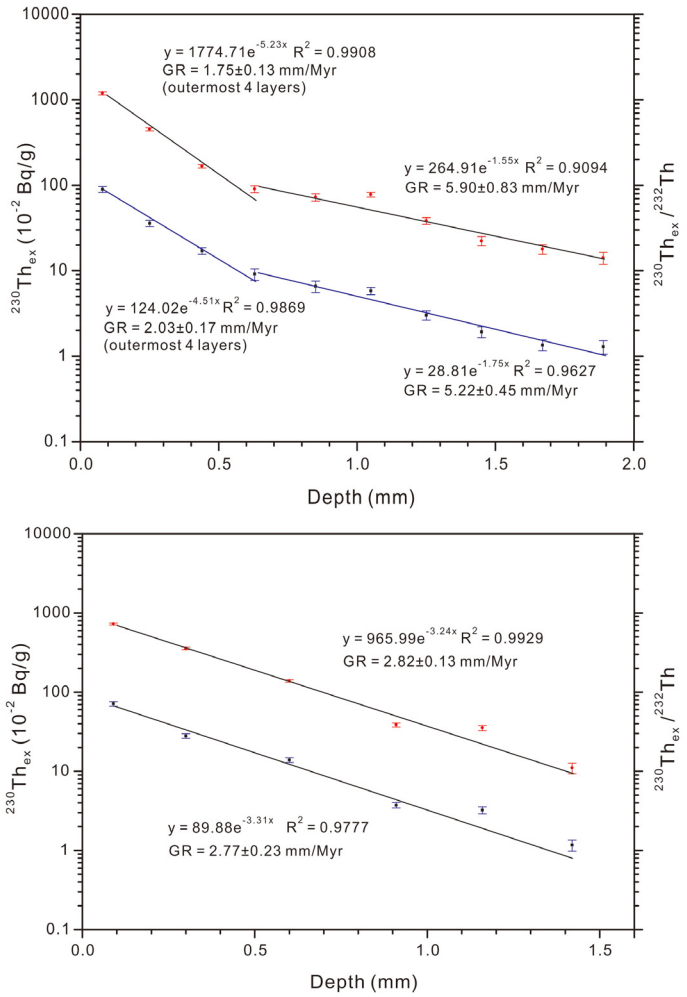

FIGURE 4
Fe-Mn crusts DY31 (top panel) and MAD23 (bottom panel) from Caiwei seamount, decay profiles of $^{230}Th_{ex}$ activities (upper curves, red dots in each panel) and $^{230}Th_{ex}/^{232}Th$ activities (lower curve, blue dots in each panel), error bars are shown for each datum.

The specific surface areas of DY31 decrease from 401 m^2/g and 414 m^2/g in the upper and lower parts of layer III respectively, to 266 m^2/g and 185 m^2/g in the upper and lower parts of layer II-2, to 132 m^2/g in layer II-1 (Figure 2, top panel). The specific surface areas of MAD23 decrease from 321 m^2/g in layer III, to 165 m^2/g in layer II, and about the same in layer I-1, 185 m^2/g (Figure 2, bottom panel). Fe-Mn crust DY31 was kept moist after recovery from Caiwei seamount, and determined one year after recovery, while Fe-Mn crust MAD23 was stored dry and analyzed 8 years after recovery. The Fe-Mn crust analyzed soon after collection has higher specific surface areas relative to those analyzed later.

4 Discussion

4.1 Theoretical model for the controls of cobalt in Fe-Mn crusts

Almost all of the Co in seawater from the western North Pacific is dissolved rather than particulate (Nakatsuka et al., 2009). The two main species of dissolved Co in seawater are Co^{2+} (65%) and $CoCl^+$ (14%) (Byrne, 2002). Those Co ions are transported with bottom currents and diffuse onto the surface of Fe-Mn crusts, where Co^{2+} ions are adsorbed by δ-MnO_2 (98-99%; Koschinsky and Hein, 2003) and oxidized to Co^{3+}, initially proposed by Murray and Dillard (1979). In this Co enrichment process, diffusion is the critical step because of the low diffusion flux relative to its oxidation rate by δ-MnO_2. Halbach et al. (1983) estimated that the fluxes of Co into Fe-Mn crusts from the Line Islands are 2.4-4.0 μg cm^{-2} kyr^{-1}; in their calculation, the high specific surface area of Fe-Mn crusts (average 300 m^2/g; Hein et al., 2000) was not incorporated, which can decrease the Co flux. Kanungo et al. (2004) carried out adsorption experiments of Co on hydrous manganese dioxide from complex electrolyte solutions resembling seawater in major ion concentrations, and the results show that δ-MnO_2 adsorbed 2.4 mmole/g Co in 72 hours at pH 7.25 and temperature of 300 K. The specific surface areas of δ-MnO_2 used in that study range from 2.64 m^2/g to 94.22 m^2/g (Parida et al., 1981). Consequently, we calculated the maximum adsorption flux of Co on the surface of δ-MnO_2 to be about 1.62×10^6 μg cm^{-2} kyr^{-1}, which is much higher

TABLE 3 Specific surface area of stratigraphic sections of Fe-Mn crusts from Caiwei seamount.

Aliquot No.	Stratigraphic layer	Sampling interval	Specific surface area	Total volume
		mm	m^2/g	cm^3/g
DY31-III-JL-Dive70C (155.5492°E, 15.9246°N; water depth 2270 m; sampling date: September 4, 2013)				
DY31-III-JL-DIve70C-5	III	1.2	401.08	0.1966
DY31-III-JL-DIve70C-4	III	1.3	414.94	0.2041
DY31-III-JL-DIve70C-3	II-2	1.2	266.26	0.1415
DY31-III-JL-DIve70C-2	II-2	1.3	184.75	0.0917
DY31-III-JL-DIve70C-1	II-1	0.6	131.81	0.0710
MAD23 (155.5294°E, 15.9102°N; water depth 1895 m;, sampling date: June 6, 2006)				
MAD23-3	III	3.0	321.15	0.1579
MAD23-2	II	1.3	165.15	0.0816
MAD23-1	I-1	2.7	185.49	0.0915

than the Co fluxes on Fe-Mn crusts in the natural seawater system. This difference in Co flux may result mainly from the different Co concentrations in the laboratory solution and in seawater. Nevertheless, the adsorption experiment shows the great potential of Fe-Mn crusts to adsorb Co. Therefore, based on flux data and adsorption capacity, it is reasonable to conclude that the diffusion of Co in seawater is the critical step in the Co enrichment process from seawater to Fe-Mn crusts.

Assuming that all the Co ions that diffused to the surface of the Fe-Mn crusts were adsorbed and eventually captured through surface oxidation by the Fe-Mn crusts, the concentrations of Co in the Fe-Mn crusts (C_{cr}, assuming that the concentration of δ-MnO_2 in Fe-Mn crusts is equal to the percentage of MnO_2; Co concentration in Fe-Mn crusts normalized to MnO_2 = 100% to eliminate dilution mainly from detrital minerals and FeOOH) can be given by

$$C_{cr} = J \cdot S_{sp} \cdot \int_0^t dt \quad (1)$$

Where J = diffusion flux of Co, S_{sp} = specific surface area of the Fe-Mn crusts, and $\int_0^t dt$ = duration for the growth of one molecular layer.

When J is the function of time t, Equation 1 should be rewritten as

$$C_{cr} = \int_0^t J \cdot S_{sp} dt \quad (2)$$

For a semi-infinite medium with constant surface concentration, the concentration can be derived from Albarede (1995) as

$$C = (C_0 - C_{int}) erf \frac{x}{2\sqrt{Dt}} + C_{int} \quad (3)$$

Where C = concentration in a semi-infinite medium, $C_{int} = C$ at $x = 0$, $C_0 = C$ at $x = \infty$, D = diffusivity. Based on Equation 3, the response time and gradient of concentration C to the surface concentration C_{int} can be estimated for Co diffusion in deep-sea water in a diffusion layer of 5 mm as shown in Figure 5, where C_{int} = 34.1 pM, $C_0 = 0$, $D = 3.626\times10^{-6}$ cm^2/s for this research (shown in section 4.2.2 and 4.2.3). Figure 5 shows that the gradient of the concentration of Co in the diffusion layer is nearly constant when time t = 1000 s, which indicates that the response time of Co concentration in the diffusion layer is rather short. In this case with a constant gradient of concentration Co, the diffusion can be described by Fick's First Law. Since deep seawater is a dissipative system, it is reasonable to assume that the Co concentration in ambient seawater of seamounts vary slowly relative to the short response time of the diffusion layer. Hence, we can use Fick's First Law to describe Co diffusion near the ferromanganese crusts on seamounts concisely.

Based on Fick's First Law, the diffusion flux of Co (J) from seawater to the Fe-Mn crusts can be given by

$$J = -D_{sw} \cdot \frac{dC_{sw}}{dx} \quad (4)$$

Where D_{sw} = diffusivity of Co ion in seawater, C_{sw} = Co ion concentration in seawater at time t, $\frac{dC_{sw}}{dx}$= diffusion gradient of Co ions. D_{sw} can be estimated by $D_{sw} = (m_0 + m_1 T)\times10^{-6}$ cm^2/s, where m_0 = 3.31, m_1 = 0.158, and T is temperature in Celsius (Boudreau, 1997). Assuming that the Co concentration in seawater near the interface of seawater and Fe-Mn crusts is 0 and the diffusion distance of Co ions near the interface is δ, then the $\frac{dC_{sw}}{dx} = -\frac{C_{sw}}{\delta}$.

The duration for the growth of one molecular layer of Fe-Mn crust t can be given by

$$t = \frac{z}{GR} \quad (5)$$

Where z = the thickness of one molecular layer of Fe-Mn crust (4.7Å, Manheim, 1986), GR = growth rate.

When the Equations 2, 4, and 5 are combined, the concentration of Co in Fe-Mn crusts (C_{cr}) can be given by

$$C_{cr} = \int_0^{\frac{z}{GR}} D_{sw} \cdot \frac{C_{sw}}{\delta} \cdot S_{sp} \cdot dt \quad (6)$$

Where C_{sw} is not constant in the duration for the growth of one molecular layer and varies with time t.

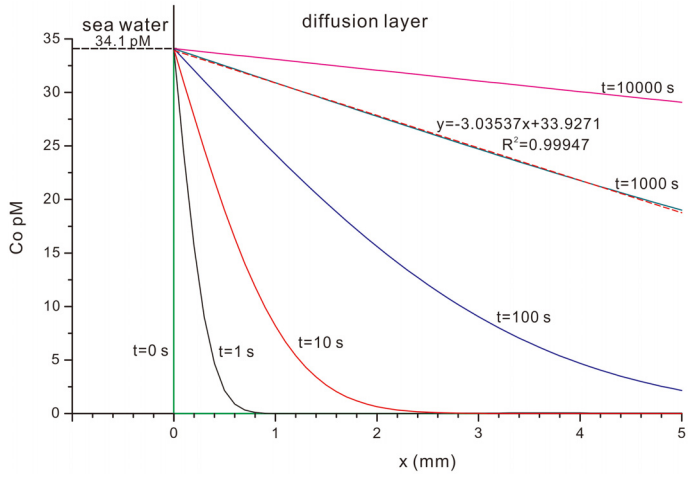

FIGURE 5
Response time and gradient of Co concentrations in the diffusion layer to the surface concentration.

When C_{sw} is constant in the duration for the growth of one molecular layer, Equation 4 can be rewritten as

$$C_{cr} = D_{sw} \cdot \frac{C_{sw}}{\delta} \cdot S_{sp} \cdot \frac{z}{GR} \quad (7)$$

When C_{sw} is not constant in the duration for the growth of one molecular layer, Equation 4 can be rewritten as

$$\overline{C_{cr}} = D_{sw} \cdot \frac{\overline{C_{sw}}}{\delta} \cdot S_{sp} \cdot \frac{z}{GR} \quad (8)$$

Where $\overline{C_{sw}}$ is the averaged C_{sw} weighted by time t, and $\overline{C_{cr}}$ is the averaged Co concentration derived from $\overline{C_{sw}}$.

Equations 5, 6 indicate that the controls on the Co concentrations in Fe-Mn crusts include diffusivity of Co ions in seawater (D_{sw}), temperature which controls the D_{sw}, Co ion concentration in seawater (C_{sw} or $\overline{C_{sw}}$), the diffusion distance of Co ions near the interface of seawater and Fe-Mn crusts (δ), growth rate (GR), and specific surface area of Fe-Mn crusts (S_{sp}).

4.2 Estimation of parameters

In Equations 7, 8, the diffusion distance of Co ions near the interface of seawater and Fe-Mn crusts (δ) cannot be measured directly. Therefore, we calculated δ for the Fe-Mn crusts from Caiwei seamount based on Co concentrations, growth rates, and specific surface area of the outermost layer of the Fe-Mn crusts, diffusivity of Co^{2+}, and Co concentration in the seawater.

4.2.1 Major elements

The sequential leaching experiments (Koschinsky and Halbach, 1995; Koschinsky and Hein, 2003) and X-ray absorption near-edge structure data (Takahashi et al., 2007) show that the Co in Fe-Mn crusts resides in vernadite (δ-MnO_2). Consequently, the other minerals in Fe-Mn crusts, such as aluminosilicates, phosphates, and FeOOH dilute the Co concentration of Fe-Mn crusts. In order to eliminate the dilution parameter, we normalized the Co concentration to 100%MnO_2. The normalized Co concentrations of the outermost layers of DY31 (2.5 mm) and MAD23 (3.6 mm) are 2.14% and 1.79% respectively.

4.2.2 Diffusivity of Co ions in seawater (D_{sw})

The modern seawater temperature is 2°C at 2000 m water depth around Caiwei seamount (Figure 6). The diffusivity of Co ions in seawater is estimated to be 3.626×10^{-6} cm^2/s by $D_{sw} = (m_0 + m_1T)\times10^{-6}$ cm^2/s, where m_0 = 3.31, m_1 = 0.158, and T is in Celsius (Boudreau, 1997).

4.2.3 Specific surface area

In Equations 7, 8, the specific surface area of δ-MnO_2 should be used to calculate δ. However, the specific surface area of δ-MnO_2 is difficult to determine separately from FeOOH, which is epitaxially intergrown. The vernadite (δ-MnO_2) in Fe-Mn crusts from the western Pacific are sheets as thin as 1 nm determined by Aberration-corrected FEG-STEM, and ferrihydrite (FeOOH) is typically 10 nm or less in diameter (Hochella, 2008), both of which coexist at a less than 1 micron scale as shown by EPMA with a spot diameter of 1 μm, which can detect the X-ray signals from Mn and Fe simultaneously (e.g. Ren et al., 2011).

The specific surface areas (S_{sp}) in this study were determined for Fe-Mn crusts, which predominantly reflect δ-MnO_2 and FeOOH. The specific surface areas of surface samples (≤ 1 mm sampling depth) and volume samples (≤ 5-6 mm sampling depth) of Fe-Mn crusts from Karin Ridge of the Mid-Pacific Mountains vary from 250 m^2/g to 381 m^2/g, and decreased up to 20% and 40% during the first four weeks and the eight weeks respectively after collection (Hein et al., 1994). The specific surface area along the section of a Fe-Mn crust from Marshall Islands range from 373 m^2/g to 530 m^2/g for the younger generation, and from 84 m^2/g to 178 m^2/g for the older generation (Xue, 2007). The specific surface areas for Fe-Mn crusts DY31 and MAD23 in this study show the same variations as those obtained by Hein et al. (1994) and Xue (2007). The specific surface

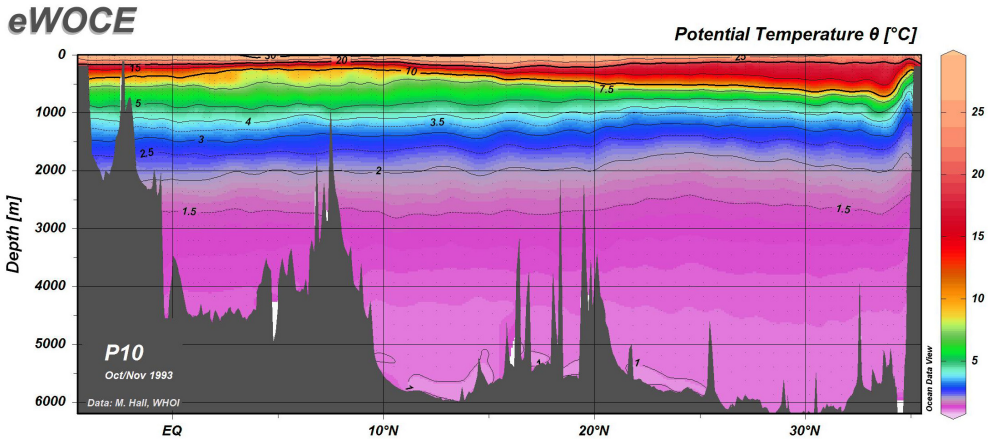

FIGURE 6
Profile of seawater temperature, west Pacific (location is shown in left map of Figure 1; modified with permission after http://www.ewoce.org/gallery/P10_TPOT.gif, Schlitzer, Reiner, Electronic Atlas of WOCE Hydrographic and Tracer Data Now Available, Eos Trans. AGU, 81(5), 45, 2000).

areas of the younger generations are greater than those of the older generation; the specific surface areas of MAD23 8-years after collection are lower than those measured 1 year after collection (Figure 7). The variation of specific surface areas reflects differences in stratigraphy and preservation. From these data, we infer that only the well-preserved outermost layers of Fe-Mn crusts can be used to obtain specific surface areas that may closely reflect those existing under *in situ* conditions. Specific surface area shows a nearly perfect positive correlation (r = 0.997) with pore volume, with an intercept close to zero (Figure 7), which indicates that the same characteristic or process may control both, such as particle size. These considerations indicate that it is most appropriate to use the S_{sp} of the outermost layer of crust DY31 to estimate the δ in Equations 7, 8.

4.2.4 Growth rate by $^{230}Th_{ex}$

The plots of $^{230}Th_{ex}$ and $^{230}Th_{ex}/^{232}Th$ versus depth show constant exponential decay curves for Fe-Mn crusts DY31 (0-0.74 mm) and MAD23 (0-1.99 mm), indicating that the growth rates were constant during the growth of these outermost layers for each crust. Therefore, we assume that the growth rates for modern Fe-Mn crusts are the same as those that define the growth rates of the outermost layers approximately 0.74 mm and 2 mm for DY31 and MAD23 respectively. Here we use 1.75 mm/Myr ($^{230}Th_{ex}$) and 2.03 mm/Myr ($^{230}Th_{ex}/^{232}Th$) for Fe-Mn crust DY31, and 2.82 mm/Myr ($^{230}Th_{ex}$) and 2.77 mm/Myr ($^{230}Th_{ex}/^{232}Th$) for Fe-Mn crust MAD23 to estimate δ in Equations 7, 8.

4.2.5 Estimation of diffusion gradients of Co ions ($\overline{C_{sw}}/\delta$)

Using the above parameters, the diffusion gradients of Co ions ($\overline{C_{sw}}/\delta$) can be estimated (Table 4). Based on the parameters for Fe-Mn crust DY31, the diffusion gradient of Co ions ranges from 295 pM/mm to 342 pM/mm. The gradient calculated for Fe-Mn crust MAD23 is greater than for DY31, ranging from 487 pM/mm to 496

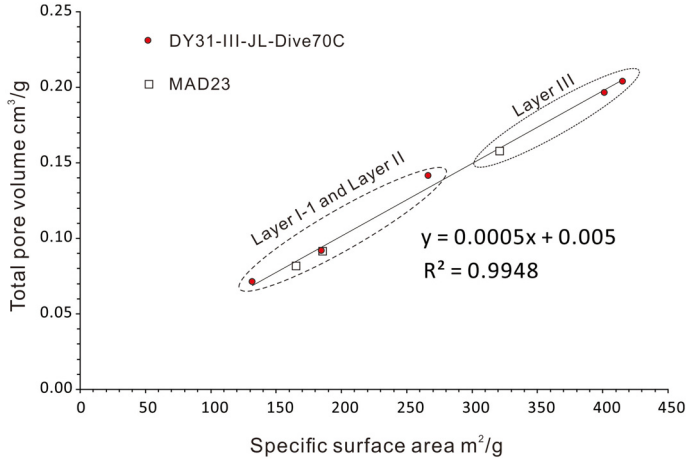

FIGURE 7
Regression of specific surface area versus total pore volume.

TABLE 4 Parameters used for calculation of diffusion gradients of Co ions $(\overline{C_{sw}}/\delta)$.

		DY31	MAD23	
Water depth	m	2270	1895	sampling water depth of Fe-Mn crusts
Thickness	mm	2.5	3.6	thickness of outermost layers in this study
MnO_2	%	35.48	29.69	MnO_2 concentration of Fe-Mn crust
Co	%	0.76	0.53	Co concentration of Fe-Mn crust
$\overline{C_{cr}}$	%	2.14	1.79	Co concentration, normalized to MnO_2 = 100%
S_{sp}	m^2/g	401.08	321.15	layer III
GR_1	mm/Myr	1.75	2.82	growth rate of outermost layer, determined by $^{230}Th_{ex}$
GR_2	mm/Myr	2.03	2.77	growth rate of outermost layer, $^{230}Th_{ex}/^{232}Th$
z	Å	4.7	4.7	thickness of one molecular layer
D_{sw}	10^{-6} cm^2/s	3.626	3.626	diffusivity of Co ions in seawater
$\overline{C_{sw}}/\delta$	pM/mm	295	496	using GR_1
	pM/mm	342	487	using GR_2

pM/mm. Given the bottom currents and mixing generated by the impact of water masses on seamounts (e.g., Lueck and Mudge, 1997), and the Co ion concentrations of seawater below 2000 m in the Pacific ranging from approximately 30 pM to 40 pM, the diffusion gradients of Co ions obtained in this study are reasonable.

4.3 Controls on the decreased Co concentrations with water depth

The Co concentrations of Fe-Mn crusts decrease with water depth. For example, the Co concentrations of Fe-Mn crusts from Line Islands decrease by 69% with increasing water depth, from 2.0% at 1120 m to 0.62% at 3280 m (Halbach et al., 1983). Data from Cronan (1977) also show that Co concentrations of Fe-Mn crusts decrease by more than 50% from 1000 m to 3000 m. The average Co concentrations of Fe-Mn crusts from the global ocean (Andreev and Gramberg, 2002) decrease from around 0.75% at 1000 m to 0.25% at 4000 m, a 66% decrease.

According to Equation 8, the Co concentration in Fe-Mn crusts can be given by

$$\mathrm{Co}(\%) = \mathrm{MnO_2}(\%) \cdot \mathrm{D_{sw}} \cdot \frac{\mathrm{C_{sw}}}{\delta} \cdot \frac{\mathrm{z}}{\mathrm{GR}} \cdot \mathrm{S_{sp}} \qquad (9)$$

The statistical data show that no significant correlation exists between water depth and growth rates of surface samples of Fe-Mn crusts (Hein et al., 2000). The specific surface areas of Fe-Mn crusts from Karin Ridge of the central Pacific do not show a significant correlation with water depth (Hein et al., 1994). Furthermore, z and δ are constant in Equation 9. So in this study we only consider the D_{sw}, C_{sw} and MnO_2 concentration (dilution effects).

The seawater Co concentrations (C_{sw}) decrease from around 38 pM at 2000 m to around 32 pM at 4000 m, a decrease of 16% (Biller and Bruland, 2012); the Co diffusivity (D_{sw}) decreases from 3.626×10^{-6} cm^2/s (2000 m and 2°C) to 3.468×10^{-6} cm^2/s (around 4500 m and 1°C), a decrease of 4.4%. So, integration of the decreases of D_{sw} and C_{sw} can decrease Co concentration of Fe-Mn crusts by 20% of the original value from shallow water to deep water, which is not enough to account for the measured deceases of Co concentrations of Fe-Mn crusts with increasing water depth. Therefore, we infer that the decrease of MnO_2 concentration through dilution from aluminosilicates and FeOOH should be the major control, which is consistent with the conclusions of other studies. Halbach and Puteanus (1984) attributed the high Co concentration in the Fe-Mn crusts from shallow water (1500-1000 m) to the lower carbonate dissolution rates and correspondingly lower Fe supply to the crusts.

Equation 9 defines the controls on Co concentrations in the layers of Fe-Mn crusts as they were accreted. However, in most cases, only bulk Co concentrations in Fe-Mn crusts are available to quantify resources. The bulk Co concentrations are mathematically equal to the weighted average of those in various layers of Fe-Mn crusts, which can be affected by absence of some layers that were eroded as noted before by Hein et al. (2000). Bulk concentrations may also be influenced by the subsidence and migration of seamounts, which can change the ambient seawater chemical conditions around seamounts, even if the seawater chemistry was constant (as in the present oceans) during the growth of Fe-Mn crusts through the Cenozoic. Nevertheless, based on Equation 9, it is possible to ascertain the sensitivity of Co concentration to those potential influences for each stratigraphic interval. The controls including dilution effect from incorporation of detrital minerals (Kim et al., 2006) or dissolution of carbonate (Halbach and Puteanus, 1984), seawater Co concentrations (C_{sw}), and diffusivity (D_{sw}) vary continuously in the region of a seamount. When the Co concentrations in Fe-Mn crusts from a seamount are sensitive to those controls, Equation 9 can constitute the theoretical foundation for the application of Kriging to interpolate Co grade values and estimate the resources for each stratigraphic generation.

5 Summary and conclusions

Eight controls on Co concentrations in nonphosphatized Fe-Mn crusts are evaluated, including dilution effects, diffusivity of Co ions in seawater (D_{sw}), temperature which controls the D_{sw}, Co ion concentration in seawater (C_{sw}), the diffusion distance of Co ions near the interface of seawater and Fe-Mn crusts (δ), the thickness of one molecular layer of Fe-Mn crusts (z), growth rate (GR), and specific surface area of Fe-Mn crusts (S_{sp}). Those controls are integrated in the equation: $C_{cr} = D_{sw} \cdot \frac{C_{sw}}{\delta} \cdot \frac{z}{GR} \cdot S_{sp}$. Based on Co concentrations, growth rates, and specific surface area of the outermost layer of the Fe-Mn crusts, and diffusivity of Co^{2+}, the Co diffusion gradients ($\overline{C_{sw}}/\delta$) for the Fe-Mn crusts from Caiwei seamount is estimated to be 295-496 pM/mm. According to the model developed here, the decrease of Co concentration in Fe-Mn crusts with increasing water depth is controlled mainly by dilution of MnO_2, the main Co host-, and to a lesser extent seawater Co ion concentration, temperature, and consequently the diffusivity of Co ions in seawater.

Data availability statement

The raw data supporting the conclusions of this article will be made available by the authors, without undue reservation.

Author contributions

XR: Conceptualization, Funding acquisition, Investigation, Project administration, Visualization, Writing – original draft, Writing – review & editing. JH: Writing – review & editing. ZY: Methodology, Writing – review & editing. NX: Methodology, Writing – review & editing. AZ: Methodology, Writing – review & editing.

Funding

The author(s) declare financial support was received for the research, authorship, and/or publication of this article. This work was supported by the Marine S&T Fund of Shandong Province for Laoshan Laboratory (grant number: LSKJ202203600-2), by the China Ocean Mineral Resources R&D Association (COMRA) project (grant number: DY135-N2-1-04), and by the National Natural Science Foundation of China (grant number: 40806027).

Conflict of interest

The authors declare that the research was conducted in the absence of any commercial or financial relationships that could be construed as a potential conflict of interest.

Publisher's note

References

Albarede, F. (1995). *Introduction to geochemical modeling* (Cambridge: Cambridge University Press). doi: 10.1017/CBO9780511622960.010

Andreev, S. I., and Gramberg, I. S. (2002). *Cobalt-rich ores of the world ocean* (St. Petersburg: VNIIOkeageologia).

Benites, M., González, F. J., Hein, J., Marino, E., Reyes, J., Millo, C., et al. (2023). Controls on the chemical composition of ferromanganese crusts from deep-water to the summit of the Rio Grande Rise, South Atlantic Ocean. *Mar. Geol.* 462, 107094. doi: 10.1016/j.margeo.2023.107094

Biller, D. V., and Bruland, K. W. (2012). Analysis of Mn, Fe, Co, Ni, Cu, Zn, Cd, and Pb in seawater using the Nobias-chelate PA1 resin and magnetic sector inductively couples plasma mass spectrometry (ICP-MS). *Mar. Chem.* 130-131, 12–20. doi: 10.1016/j.marchem.2011.12.001

Bonatti, E., Kraemer, T., and Rydell, H. S. (1972). "Classification and genesis of submarine iron-manganese deposits," in *Ferromanganese Deposits on the Ocean Floor*. Ed. D. R. Horn (Washington, D. C.: Columbia University), 149–166.

Boudreau, B. P. (1997). *Diagenetic models and their implementation* (Berlin: Springer). doi: 10.1007/978-3-642-60421-8

Byrne, R. H. (2002). Inorganic speciation of dissolved elements in seawater: the influence of pH on concentration ratios. *Geochem. Trans.* 3, 11–16. doi: 10.1186/1467-4866-3-11

Cronan, D. S. (1977). "Deep-sea nodules: Distribution and geochemistry," in *Marine Manganese Deposits*. Ed. G. P. Glasby (Elsevier, Amsterdam), 11–44. doi: 10.1016/s0422-9894(08)71016-x

Halbach, P., and Puteanus, D. (1984). The influence of the carbonate dissolution rate on the growth and composition of Co-rich ferromanganese crusts from Central Pacific seamount areas. *Earth Planet. Sci. Lett.* 68, 73–87. doi: 10.1016/0012-821x(84)90141-9

Halbach, P., Segl, M., Puteanus, D., and Mangini, A. (1983). Co-flux and growth rates in ferromanganese deposits from central Pacific seamount areas. *Nature* 304, 716–719. doi: 10.1038/304716a0

Hein, J. R., Bychkov, A. S., and Gibbs, A. E. (1994). *Data and results from R.V. Aleksandr Vinogradov cruises 91-AV-19/1, North Pacific hydrochemistry transect; 91-av-19/2, North Equatorial Pacific Karin Ridge Fe-Mn crust studies; and 91-AV-19/4, Northwest Pacific and Bering sea sediment geochemistry and paleoceanographic studiest*. U.S. Geological Survey Open File Report Washington D.C.: Department of the Interior, 94–230. doi: 10.3133/ofr94230

Hein, J. R., and Koschinsky, A. (2014). "Deep-ocean ferromanganese crusts and nodules," in *Treatise on geochemistry, second edition, V. 13, Chapter 11*. Eds. H. D. Holland and K. K. Turekian (Oxford: Elsevier Ltd.), 273–291. doi: 10.1016/b978-0-08-095975-7.01111-6

Hein, J. R., Koschinsky, A., Bau, M., Manheim, F. T., Kang, J.-K., and Roberts, L. (2000). "Cobalt-rich ferromanganese crusts in the pacific," in *Handbook of Marine Mineral Deposits*. Ed. D. S. Cronan (CRC Press, Boca Raton, Florida), 239–279. doi: 10.1201/9780203752760-9

Hein, J. R., Mizell, K., Koschinsky, A., and Conrad, T. A. (2013). Deep-ocean mineral deposits as a source of critical metals for high- and green-technology applications: Comparison with land-based resources. *Ore. Geol. Rev.* 51, 1–14. doi: 10.1016/j.oregeorev.2012.12.001

Hochella, M. F. J. (2008). Nanogeoscience: From origins to cutting-edge application. *Elements* 4, 373–379. doi: 10.2113/gselements.4.6.373

Hu, G. L., Cai, Y. H., Yang, C. Y., Zhuang, Z. X., Wang, X. R., and Huang, Y. P. (2002). Determination of 27 elements in two polymetallic nodule reference samples from the Pacific Ocean by ICP-MS. *Acta Oceanol. Sin.* 24, 47–52. doi: 10.1007/s11670-002-0022-7

IEA (2021). *The Role of Critical Minerals in Clean Energy Transitions* (Paris: IEA). Available at: https://www.iea.org/reports/the-role-of-critical-minerals-in-clean-energy-transitions (Accessed November 13, 2023).

Kanungo, S. B., Tripathy, S. S., and Rajeev, (2004). Adsorption of Co, Ni, Cu, and Zn on hydrous manganese dioxide from complex electrolyte solutions resembling sea water in major ion content. *J. Colloid. Interface Sci.* 269, 1–10. doi: 10.1016/s0021-9797(03)00464-8

Kim, J., Hyeong, K., Jung, H., Moon, J., and Kim, K. (2006). Southward shift of the Intertropical Convergence Zone in the western Pacific during the late Tertiary: Evidence from ferromanganese crusts on seamounts west of the Marshall Islands. *Paleoceanography* 21, PA4218. doi: 10.1029/2006pa001291

Koschinsky, A., and Halbach, P. (1995). Sequential leaching of marine ferromanganese precipitates: Genetic implications. *Geochim. Cosmochim. Acta* 59, 5113–5132. doi: 10.1016/0016-7037(95)00358-4

Koschinsky, A., and Hein, J. R. (2003). Uptake of elements from seawater by ferromanganese crusts: solid-phase associations and seawater speciation. *Mar. Geol.* 198, 331–351. doi: 10.1016/S0025-3227(03)00122-1

Ku, T. L., Omura, A., and Chen, P. S. (1979). "Be^{10} and U-series isotopes in Mn nodules from the central North Pacific," in *Marine Geology and Oceanography of the Pacific Manganese Nodule Province*. Eds. J. L. Bishop and Z. Piper (Plenum, New York), 791–814. doi: 10.1007/978-1-4684-3518-4_26

Lueck, R. G., and Mudge, T. D. (1997). Topographically induced mixing around a shallow seamount. *Science* 276, 831–833. doi: 10.1126/science.276.5320.1831

Luo, S. D., Shi, W. Y., Chen, Z., and Huang, Y. P. (1986). Study on a new method for Separation and determination of U and Th in deep sea manganese nodules. *Acta Oceanol. Sin.* 8 (3), 324–330. Available at: http://www.hyxbocean.cn//cn/article/pdf/preview/19860309.pdf (Accessed August 2, 2024).

Manheim, F. T. (1986). Marine cobalt resources. *Science* 232, 600–608. doi: 10.1126/science.232.4750.600

Melnikov, M. E., and Pletnev, S. P. (2013). Age and formation conditions of the Co-rich manganese crust on guyots of the Magellan seamounts. *Lithol. Miner. Resour.* 48, 3–16. doi: 10.1134/s0024490212050057

Milesi, J.-P., Toteu, S. F., Deschamps, Y., Feybesse, J. L., Catherine, L., Cocherie, A., et al. (2006). An overview of the geology and major ore deposits of Central Africa: Explanatory note for the 1:4,000,000 map "Geology and major ore deposits of Central Africa. *J. Afr. Earth Sci.* 44, 571–595. doi: 10.1016/j.jafrearsci.2005.10.016

Murray, J. W., and Dillard, J. G. (1979). The oxidation of cobalt (II) adsorbed on manganese dioxide. *Geochim. Cosmochim. Acta* 43, 781–787. doi: 10.1016/0016-7037(79)90261-8

Nakatsuka, S., Okamura, K., Takeda, S., Nishioka, J., Firdaus, M., Norisuye, K., et al. (2009). Behaviors of dissolved and particulate Co, Ni, Cu, Zn, Cd and Pb during a mesoscale Fe-enrichment experiment (SEEDS II) in the western North Pacific. *Deep-Sea. Res. II.* 56, 2822–2838. doi: 10.1016/j.dsr2.2009.06.008

Parida, K. M., Kanungo, S. B., and Sant, B. R. (1981). Studies on MnO_2-I. chemical composition, microstructure and other characteristics of some synthetic MnO_2 of various crystalline modifications. *Electrochim. Acta* 26, 435–443. doi: 10.1016/0013-4686(81)85033-5

Ren, J. B., He, G. W., Deng, X. G., Deng, X. Z., Yang, Y., Yao, H. Q., et al. (2022). Metallogenesis of Co-rich ferromanganese nodules in the northwestern Pacific: Selective enrichment of metallic elements from seawater. *Ore. Geol. Rev.* 143, 104778. doi: 10.1016/j.oregeorev.2022.104778

Ren, J. B., He, G. W., Yang, Y., Yu, M., Deng, Y. N., Pang, Y. T., et al. (2024). Ultraselective enrichment of trace elements in seawater by Co-rich ferromanganese nodules. *Global Planet. Change* 239, 104498. doi: 10.1016/j.gloplacha.2024.104498

Ren, X. W., Liu, J. H., Cui, Y. C., Shi, X. F., and Yin, J. W. (2011). Effects of phosphatization on enrichment of cobalt in the Co-rich Fe-Mn crusts from seamount MP2 of the Line Islands in the central Pacific. *Adv. Mar. Sci.* 29, 323–329. doi: 10.3969/j.issn.1671-6647.2011.03.008

Ren, X. W., Shi, X. F., Zhu, A. M., Liu, J. H., and Fang, X. S. (2010). Controlling factors on enrichment of cerium in Co-rich Fe-Mn crusts from Magellan Seamount Cluster. *J. Chin. Rare. Earth Soc.* 28 (4), 489–494. Available at: https://www.docin.com/p-1186041205.html (Accessed August 2, 2024).

Takahashi, Y., Manceau, A., Geoffroy, N., Marcus, M. A., and Usui, A. (2007). Chemical and structural control of the partitioning of Co, Ce, and Pb in marine ferromanganese oxides. *Geochim. Cosmochim. Acta* 71, 984–1008. doi: 10.1016/j.gca.2006.11.016

U. S. Geological Survey (2024). "Cobalt," in *Mineral Commodity Summaries 2024* (Washington D.C.: Department of the Interior), 62–63. doi: 10.3133/mineral2024

Xue, T. (2007). *Geochemical characters and ore-forming elements enrichment mechanism of ferromanganese crusts from Pacific Ocean*. Ph.D. dissertation (Guangzhou: Sun Yat-Sen University) (in Chinese with English abstract).

frontiers | Frontiers in Marine Science

TYPE Original Research
PUBLISHED 19 December 2024
DOI 10.3389/fmars.2024.1489184

OPEN ACCESS

EDITED BY
Jiangbo Ren,
Guangzhou Marine Geological Survey, China

REVIEWED BY
Kiho Yang,
Pusan National University, Republic of Korea
Jun Hu,
Ocean University of China, China

*CORRESPONDENCE
Jie Li
lijie@sio.org.cn
Xiaohu Li
xhli@sio.org.cn

RECEIVED 31 August 2024
ACCEPTED 25 November 2024
PUBLISHED 19 December 2024

CITATION
Li J, Jin Y, Wang H, Yang K, Zhu Z, Meng X and Li X (2024) *In-situ* analysis of polymetallic nodules from the clarion-Clipperton zone, Pacific Ocean: implication for controlling on chemical composition variability. *Front. Mar. Sci.* 11:1489184. doi: 10.3389/fmars.2024.1489184

In-situ analysis of polymetallic nodules from the clarion-Clipperton zone, Pacific Ocean: implication for controlling on chemical composition variability

Jie Li[1]*, Yinjia Jin[2], Hao Wang[1], Kehong Yang[1], Zhimin Zhu[1], Xingwei Meng[1] and Xiaohu Li[1]*

[1]Key Laboratory of Submarine Geosciences, Second Institute of Oceanography, Ministry of Natural Resources, Hangzhou, China, [2]Huadian Electric Power Research Institute Co., LTD., Hangzhou, China

Polymetallic ferromanganese nodules (PMNs) in the Clarion-Clipperton Zone (CCZ) exhibit significant spatial variability in chemical composition, which complicates exploration efforts and increases associated costs. The primary factors driving this spatial variability remain unclear due to limited understanding of the growth history of these nodules. This study investigated the internal structure and elemental distributions of PMNs from both the eastern and western CCZ using a range of *in-situ* techniques, including high-resolution element mapping and chemical analysis, to characterize the compositional differences and growth processes of the nodules. Analysis of Nodule BC06 from the eastern CCZ reveals a decreasing Mn/Fe ratio from the inner part (Layer I) to the outer part (Layer II). In contrast, Nodule BC1901 from the western CCZ consists of three layers, with the Mn/Fe ratio increasing from Layer I to Layer II and then decreasing from Layer II to Layer III. Discrimination diagrams indicate that both nodules formed through hydrogenetic and diagenetic processes, with Nodule BC06 showing stronger diagenetic influences. Variations in diagenetic effects from core to rim suggest different geochemical controls in the two regions. In the eastern CCZ, compositional changes are mainly driven by the movement of PMNs away from the equatorial high-productivity zone. In the western CCZ, the variability in deep-water ventilation and the intensity of Antarctic Bottom Water are the key factors influencing nodule composition. These findings enhance our understanding of the growth history and spatial variability of PMNs in the CCZ and provide valuable insights for future resource evaluation.

KEYWORDS

micro-layers, ferromanganese nodule, spatial variability, *in-situ* analysis, clarion-Clipperton zone

1 Introduction

Polymetallic manganese (or ferromanganese) nodules (PMNs) contain high concentrations of nickel, copper, and cobalt, as well as other metals such as molybdenum, rare earth elements, and lithium, all of which are critical to high-tech industries and hold significant economic value (Hein et al., 2020). Additionally, the extremely slow accumulation rates of these nodules, combined with their continuous adsorption of dissolved metals from seawater, allow them to record changes in the seawater composition over time (e.g., Glasby, 2006; Kuhn et al., 2017). As a result, studying these PMNs is vital for both exploring critical metal resources in the marine environment and for understanding the environmental changes of seawater (Ren et al., 2024).

Nodule deposits are found throughout the global oceans, but they typically form on the surfaces of abyssal plains at depths of 4,000 to 6,000 m below sea level (Hein and Koschinsky, 2014). Among these, the Clarion-Clipperton Zone (CCZ) is the most prominent nodule field and hosts the largest known nodule resources in the ocean. Currently, 17 out of 19 exploration contract areas for polymetallic nodules, granted by the International Seabed Authority, are located in the CCZ (http://www.isa.org.jm) (Figure 1). Extensive research has been conducted on PMNs in the CCZ for many years, and the chemical composition of bulk PMNs in this region is well-documented (e.g., Menendez et al., 2019; Wegorzewski et al., 2015; Wegorzewski and Kuhn, 2014). In general, PMNs from the CCZ are classified as mixed type, with both hydrogenetic and diagenetic origins (e.g. Hein et al., 2020; Bau et al., 2014; Von Stackelberg, 1997). However, covering an area of approximately 4.5 million km^2 and stretching about 7,240 km in length, the chemical compositions of PMNs in the CCZ vary regionally. The manganese and copper contents of the PMNs increase markedly towards the southeast, while the nickel and cobalt contents exhibit a partial trend along the central axis of the CCZ (ISA, 2010). Despite extensive research, relatively little attention has been given to the reasons behind the spatial variations in the compositions of Mn-nodules within the CCZ. With the current demand for deep-sea PMN exploration, the process remains challenging and costly. Therefore, efficiently identifying promising locations requires a theoretical understanding of nodule formation and spatial variability.

The varying populations of PMNs in different locations can be attributed to several factors, including the seafloor topography, bottom current activity, and the activity of benthic organisms (Zhong et al., 2019; Wang et al., 2015; Pan and Hua, 1996). While these parameters can be readily measured under modern seafloor conditions, obtaining historical data is significantly more challenging. Since PMNs typically grow over several million years, changes in the geological environment during such a long growth process have a profound impact on their composition. To better understand the factors influencing the chemical composition of PMNs in the CCZ, it is crucial to study their growth history. Numerous studies have examined the individual growth layers of PMNs worldwide. For example, Menendez et al. (2019) conducted an integrated study of the chemical compositions of micro-layers in PMNs from the UK contract area and Areas of Particular Environmental Interest (APEI-6) in northeastern CCZ. It was concluded that the compositional changes in the nodules in these areas are related to plate motion as the PMNs move from high to low productivity zones due to northwestward plate movement. Thus, primary productivity, associated with the activity of benthic organisms, has been identified as the primary factor controlling chemical variations in the study area. However, Menendez et al. (2019) only addressed the vertical variations in the chemical compositions of PMNs in the eastern CCZ. It remains unclear whether lateral variations in the nodule composition across the CCZ can also be ascribed to plate motion, and if this is not determined, the primary factors controlling the differences in the chemical compositions of nodules in the eastern and western parts of the CCZ are still not well understood. A comprehensive understanding of nodule formation requires studying their micro-features. Because individual growth layers of PMNs can serve as an archive of changes in environmental conditions during their formation, they are considered one of the best recorders of geological history.

Therefore, to improve our understanding of lateral variations in the CCZ, in this study, PMNs were collected from both the eastern and western regions. Various *in-situ* analytical techniques were utilized to investigate the element distributions and mineralogy within the PMNs. We focused on three key aspects: (i) micrographic variations and mineral assemblages during nodule growth; (ii) changes in environmental conditions during nodule development; and (iii) the primary factors influencing the nodule formation process. Understanding the spatial distribution of individual growth layers with varying chemical and mineralogical compositions in PMNs provides valuable insights into the geochemical processes involved in their formation (Park et al., 2023).

2 Geologic setting and samples

The CCZ, located in the Central Eastern Pacific Ocean, north of the equatorial high productivity zone (Antoine et al., 1996), extends from approximately 5°N to 20°N and from 120°W to 160°W. CCZ is bounded by the Clarion Fracture Zone to the north and the Clipperton Fracture Zone to the South, with a total length of approximately 7,240 km and an area of 4.5 million km^2 (Figure 1). The fractures trend southwest–northeast in response to the northwestward motion of the Pacific Plate (Von Stackelberg and Beiersdorf, 1991). This area contains one of the largest nodule fields in the ocean and hosts several contract areas for the exploration of polymetallic nodules (e.g., Halbach et al., 1988). The sedimentation rates in the western CCZ are 0.15–0.4 cm ka^{-1} (Müller and Mangini, 1980), while those in the eastern CCZ are slightly higher (0.20–1.15 cm ka^{-1}) (Mewes et al., 2014; Mogollón et al., 2016; Volz et al., 2018). The study areas are located below the carbonate compensation depth (CCD), which is located at depth of approximately 4,500 m below sea level (Johnson, 1972; Lyle, 2003). The oxygen penetration depths (OPDs) in the eastern CCZ are 1–4.5 m (Mewes et al., 2014; Mogollón et al., 2016; Volz et al., 2018). The sediment in the study areas is mainly siliceous clay (ISA, 2010).

10.3389/fmars.2024.1489184

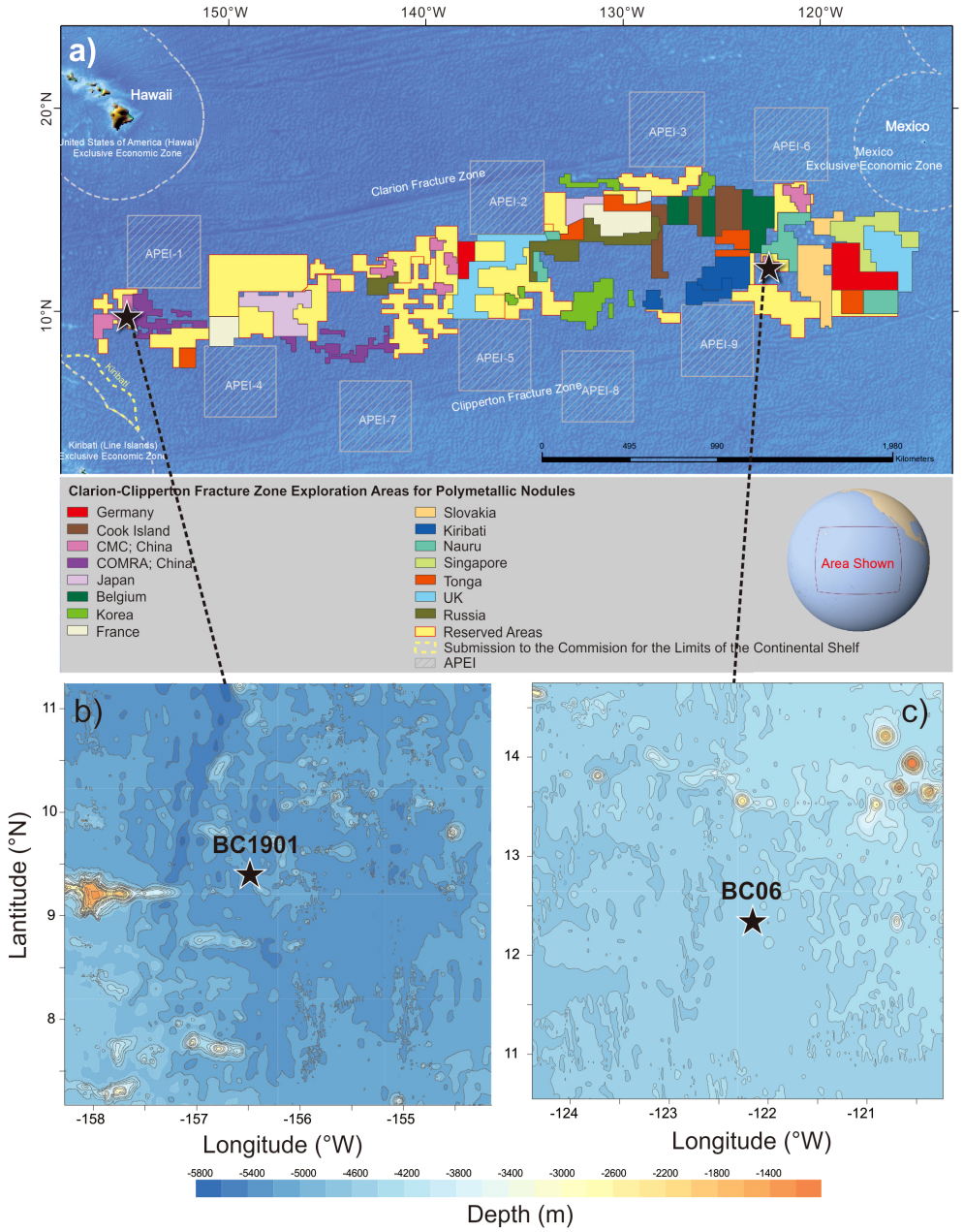

FIGURE 1
The locations of **(A)** contract areas for ferromanganese nodule exploration and areas of particular environmental interest (APEI) in the Clarion-Clipperton Zone (CCZ) (modified from the website of the International Seabed Authority (ISA); http://www.isa.org.jm); **(B, C)** Bathymetric maps showing the locations of the sampling sites in the eastern and western CCZ. The sampling locations are depicted by the red stars.

The present-day primary productivity decreases slightly from east to west across the CCZ (Glasby, 2006).

The nodules used in this study were collected from box cores obtained during the cruise of the *R/V Xiangyanghong 10* in 2019. Site BC06 (122.16°W, 12.34°N) and Site BC1901 (156.50°W, 9.38° N) are located in the eastern and western CCZ, respectively, and have a water depth of ~5000 m. Although considerable variations exist in the morphology and size of the PMNs at these two stations, previous research has reported that morphology and size have minimal impacts on the compositions of the PMNs (DY54 cruise report, 2020). Therefore, in this study, we selected one PMN from each site to represent the sites in the study area (Figure 2). As most of the PMNs from Site BC06 had rough surfaces, we also selected a PMN with a rough surface from Site BC1901 for comparison. The selected PMNs were cut vertically into two equal parts. One part was adhered to glass slides using epoxy resins. After polishing, 300 µm thick thin sections were prepared for *in-situ* geochemical analysis. Additionally, five subsamples of individual layers were subsequently drilled from the other part, which were used to determine the mineralogical composition.

10.3389/fmars.2024.1489184

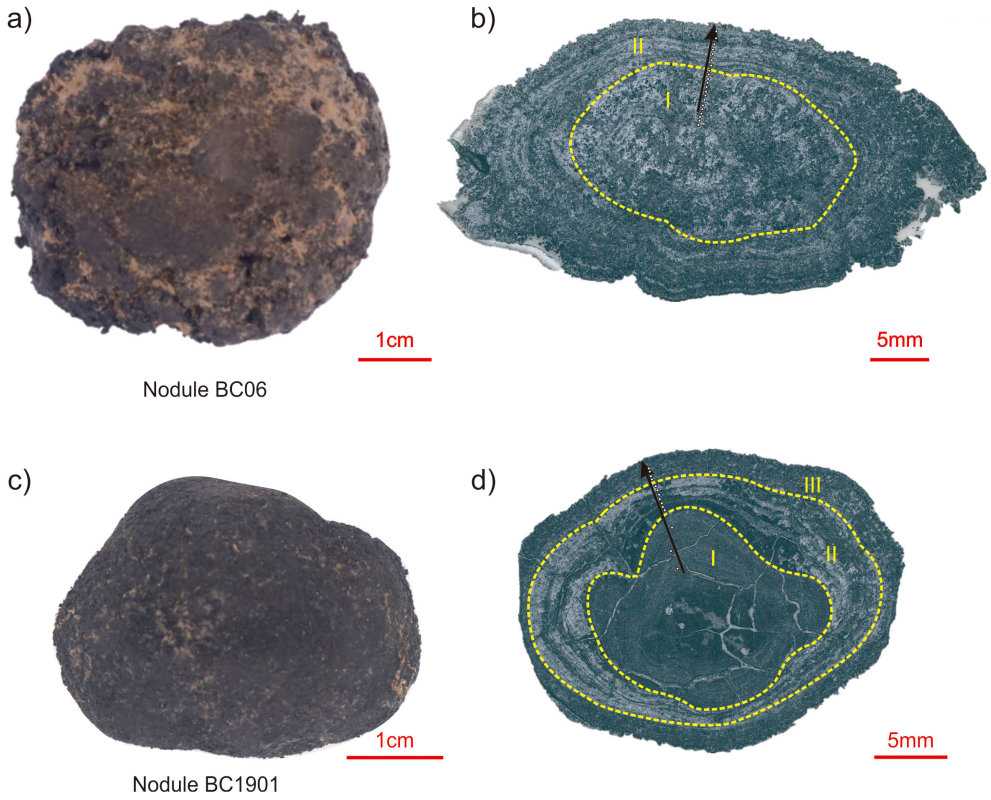

FIGURE 2
(A, C) Photographs of hand specimens, and **(B, D)** reflected light microscope images of selected samples. The yellow dotted lines denote the boundaries between the layers. The locations of the LA-ICP-MS line analyses are denoted by the black arrows. The locations of the LA-ICP-MS spot analyses are denoted by the white circles on the lines.

3 Methods

3.1 BSE images

Back-scattered electron (BSE) imaging was performed at the Key Laboratory of Submarine Geosciences, Second Institute of Oceanography, Ministry of Natural Resources, Hangzhou, China. An 8100 electron probe micro-analysis instrument(EPMA, JEOL Corporation, Japan) was utilized to conduct the analysis. The analytical conditions were an acceleration voltage of 10 kV and a probe current of 20 nA. The samples were carbon-coated and observed using the EPMA to examine their micro-textures and structures.

3.2 LA-ICP-MS spot and line analyses

In-situ major and trace element analysis of the individual microlayers within the PMNs was conducted via laser ablation-inductively coupled plasma mass spectrometry (LA-ICP-MS) at the Hefei University of Technology, Hefei, China. A 193 nm ArF excimer laser system (GeoLasPro) was coupled with an Agilent 7900 × ICP-MS instrument. For each analysis, a 50 µm spot size, an energy density of 5 J/cm^2, and a repetition rate of 5 Hz were used. At the ablation site, 20 seconds of background measurement were conducted followed by 45 seconds of data acquisition. The chemical compositions of the PMNs were calibrated against fused glass chips of multiple external standards, namely, NIST SRM 610, NIST SRM 612, and BCR-2G. The raw data calculations were conducted offline using an Excel-based software (ICPMS DataCal). A total content normalization strategy without the use of internal standards was employed (Liu et al., 2008). The accuracy and reproducibility of the measurements were assessed using the United States Geological Survey standard nodule NOD-A-1 for quality control. The NOD-A-1 powder was pressed into pellets to more closely resemble the nodule samples. The external reproducibility of the analysis calculated using NOD-A-1 was better than ±10% for most of the major elements and the rare earth elements plus Y (REY), which is in good agreement with the recommended values (Supplementary Table S1). The results for a total of 35 data points on the studied samples are presented in Supplementary Table S2.

Line analysis of the PMNs via LA-ICP-MS was performed at Tuoyan Testing Technology Co., Ltd., Guangzhou, China. A 193 nm ArF Excimer laser ablation system (NWR 193) coupled with a Thermo Fisher iCAP RQ and a dual concentric injector (DCI) plasma torch integrated with a two-volume ablation cell were used. The operating conditions for the laser ablation system and the ICP-MS instrument were as follows: a beam size of 20 µm, an energy density of 4 J/cm^2, and a repetition rate of 20 Hz. The laser scan speed was 5 µm/s. Line analysis was performed on selected areas of

the PMNs, and these areas covered the micro-layers from the core to the rim (Figure 2). The raw data were calibrated using the Iolite software following the methods of Paton et al. (2011) and Zhu et al. (2017). All of the element concentrations were converted to ppm values from Iolite to Excel and the data were saved as csv files.

3.3 Micro X-ray fluorescence mapping

Major element mapping was conducted using a Bruker M4 plus Tornado micro-X-ray fluorescence (XRF) energy dispersive spectrometer (μ-XRF) at the Tuoyan Testing Technology Co., Ltd., Guangzhou, China. The instrument was equipped with a Rh X-ray tube and two XFlash silicon drift X-ray detectors. A single polished thin section was mapped to obtain the element abundances and phase proportions. The analytical parameters were 50 kV, 300 μA, a spacing of ~20 μm, and a dwell time of 5 ms. After the test was completed, the M4 Tornado V1.6.614.0 software was used to calibrate the raw data, resolve the spectral peaks, and export the element maps.

3.4 X-ray diffraction analysis

The mineralogical compositions of the subsamples were analyzed using a Rigaku SmartLab diffractometer at Westlake University. The X-ray diffraction (XRD) was conducted using Cu-Kα generated at 45 kV and 100 mA. Powder subsamples were scanned from 0° to 80° 2θ at a rate of 2°/min and a step size of 0.03°. The results were analyzed using the Jade 6.5 software. The mineral compositions were determined by comparing the test results with the Crystallography Open Database (COD). Todorokite (or buserite II) and buserite I have peaks at ~10 Å. The peak of unstable buserite I shifts to 7 Å birnessite upon heating to 105°C for 24 hours. Therefore, a heating experiment was conducted to distinguish between the different types of 10 Å manganates (Manceau et al., 2014; Wegorzewski et al., 2015; Reykhard and Shulga, 2019).

4 Results

4.1 Structure

As shown in Figures 2 and 3, both of the studied PMNs exhibited relatively symmetrical structures. The layers grew concentrically around a single nucleus. However, the internal structures of the PMNs were observed to differ under the optical microscope and the electron microscope. The BSE images revealed that the internal structures of the PMNs consisted of areas with medium to high brightness and dark gray regions. The dark/light areas exhibited a variety of different textures, i.e., laminated, dendritic, massive, and detrital (Figure 3). Various textures were present within an individual nodule, and their extents varied among the different PMNs. Nodule BC06 contained two layers, and Nodule BC1901 contained three layers. Specifically, in Nodule BC06, the inner part (Layer I) exhibited a detritic texture, which was characterized by rounded, bulbous, discontinuous layers with pore spaces between circular growths. This texture was unique to Nodule BC06 from the eastern CCZ (Figures 3A, B). The outer part (Layer II) exhibited a highly porous texture and apparently dendritic features (Figures 3C, D). In contrast, Nodule BC1901 exhibited three types of textures, i.e., massive, dendritic, and laminated. The inner part (Layer I) of the nodule exhibited a massive texture with some detrital minerals (Figure 3E). The middle part (Layer II) exhibited a laminated morphology of alternating dark/light layers of the similar thickness (Figure 3F). The outer part (Layer III) predominantly exhibited dendritic textures and was less porous (Figures 3G, H). The manganese oxide minerals exhibited a finely layered, coliform structure with a porous texture (i.e., stromatolitic). Overall, the inner structure of Nodule BC06 was more porous than that of Nodule BC1901.

4.2 Element mapping

μ-XRF maps of the PMNs' cross-sections are displayed in Figures 4 and 5, which show the qualitative distributions of the major elements (including Fe, Mn, Cu, Ni, and Co) in the nodules. In both PMNs, Mn and Fe are negatively correlated. The distributions of Ni, Cu, and Mn are generally similar and opposite to that of Fe. The current μ-XRF results show that Mn is considerably more abundant than Fe in the overall region of Nodule BC06, except for the nuclei and some very thin Fe-rich microlayers in Layer II. Compared with Layer I, Layer II of Nodule BC06 has lower Cu and Ni contents and higher amounts of Fe (Figure 4). For Nodule BC1901, Fe is considerably more abundant than Mn in the overall region of Nodule BC1901. The areas with higher Mn, Ni, and Cu contents are mostly located in the middle of the nodule (Layer II) compared to the outer and inner parts. The inner and outer parts contain larger amounts of Fe (Figure 5). Among all of the microlayers in both PMNs, Co is predominantly enriched in some of the thin Fe-rich layers and the nucleus.

4.3 Individual layers

Quantitative analysis was conducted via LA-ICP-MS. The results are presented in Supplementary Table S1. Parts of the PMNs have relatively high Mn contents (up to 35.97 wt.%), with corresponding Cu and Ni contents of up to 2.52 wt.% and 2.87 wt.%, respectively. The Mn-rich layers also tend to have relatively low Fe and Co contents (as low as 0.74 wt.% and 0.01 wt.%, respectively) and high Mn/Fe ratios (up to 44.79). Compared with Nodule BC06 (Fe = 3.84 wt.%, Co =0.17 wt.%), Nodule BC1901 from the western CCZ tends to contain layers with higher Fe and Co contents (8.40 wt.% and 0.19 wt.% on average, respectively). Moreover, these layers have lower Cu and Ni contents (average values of 1.15 wt.% and 1.13 wt.%) compared to those in Nodule BC1901 (Figures 6A–C). The REY contents of the individual layers are also highly variable, with ΣREY values of ~211 μg/g to ~1448 μg/g. On Post-Archean Australian Shale (PAAS) normalized REY plots (Figure 7), the PMNs from both sites exhibit negative Y

10.3389/fmars.2024.1489184

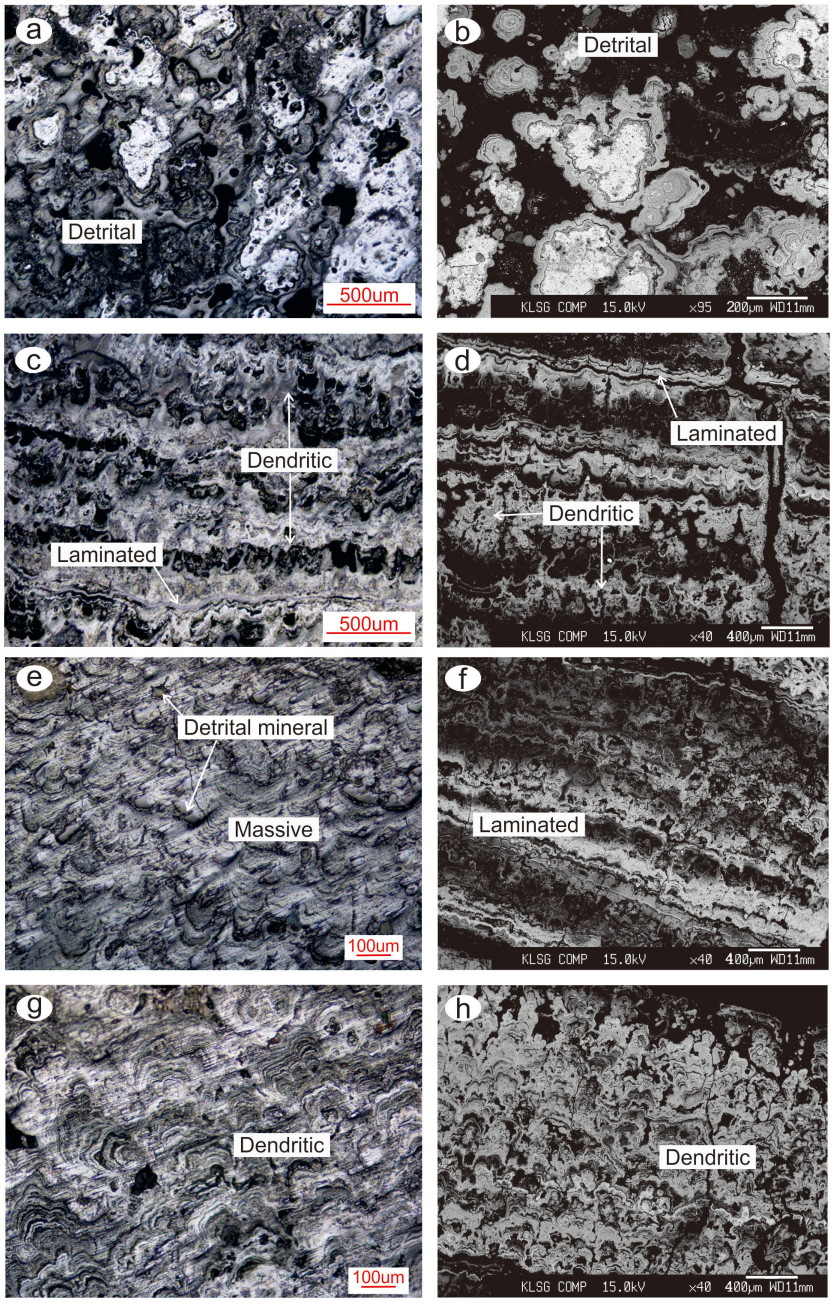

FIGURE 3
Microphotographs showing the growth textures of the polymetallic nodules analyzed in this study. **(A, B)** Layer I and **(C, D)** Layer II of Nodule BC06; **(E)** Layer I and **(F)** Layer II of Nodule BC1901; and **(G, H)** Layer III of Nodule BC1901. The left column contains micro-photographs under reflected light. The right column contains backscattered electron (BSE) images of the two nodules.

anomalies. Nodule BC06 from the eastern CCZ has lower δCe values (0.38–1.70) and Y_N/Ho_N ratios (0.41–0.74) compared to those of Nodule BC1901 from the western CCZ (δCe = 1.07–1.92; Y_N/Ho_N = 0.59–0.84) (Figures 6, 7). The PMNs from both stations exhibit weak positive Eu anomalies, with δEu values of 1.08–1.34. Generally, the low ΣREY contents are associated with small positive or even negative Ce anomalies (as low as ~0.39). These layers are more abundant in Nodule BC06 from the eastern CCZ than in Nodule BC1901. Nodule BC06 has a larger number of layers with low ΣREY contents (average of 462 μg/g), negative Ce anomalies (average of 1.03), and generally lower LREE contents (average of 356 μg/g) compared to Nodule BC1901 (Figure 7). However, both PMNs exhibit light rare earth element (LREE) enrichment (by a factor of 3–4) compared to the heavy rare earth elements (HREEs) (Figure 6F).

Vertical profiles of the Mn/Fe and Co/(Cu+Ni) ratios of the studied PMNs are shown in Supplementary Figure S1. The results are consistent with the element mapping data The Mn-rich layer is located close to the nuclei of Nodule BC06, whereas the middle part of Nodule BC1901 contains a greater proportion of Mn-rich layers

10.3389/fmars.2024.1489184

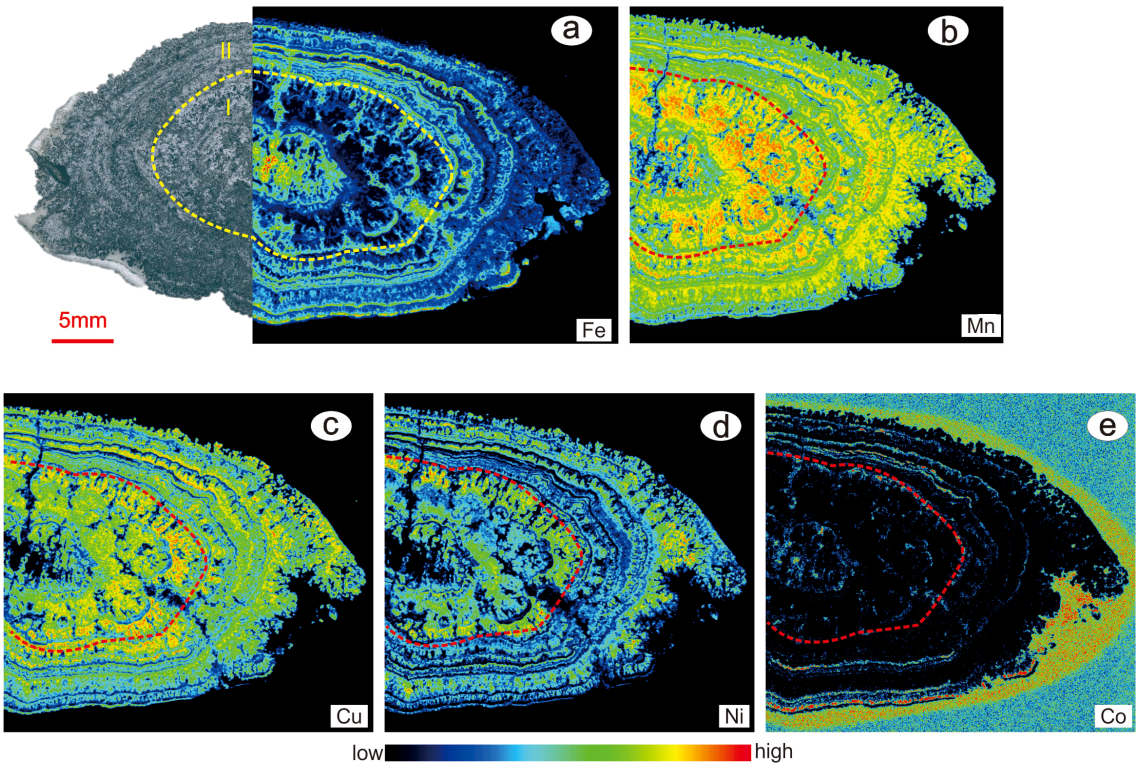

FIGURE 4
μ-XRF map images of the thin section of Nodule BC06showing the element distributions: **(A)** Fe; **(B)** Mn; **(C)** Cu; **(D)** Ni; and **(E)** Co. The microphotograph under reflected light in a) is the same as that in Figure 2B.

than the outer and inner parts. Overall, the Mn/Fe ratio of Nodule BC06 is much higher than that of Nodule BC1901 (Figure 8A). With respect to the Co/(Cu+Ni) ratios, Nodule BC06 has a lower Co/(Cu+Ni) ratio than Nodule BC1901 (Figure 8B). Regarding the individual layers, the median values of the layers generally exhibit a trend that is opposite to that of the Mn/Fe ratio. In Nodule BC06, these values increase from Layer I to Layer II, while in Nodule BC1901 they decrease from Layer I to Layer II and then increase from Layer II to Layer III. In both samples, the Ba content consistently decreases from the core to the rim (Figure 8C).

4.4 XRD patterns

Figure 9 presents the XRD patterns for powdered samples of various layers within Nodules BC06 and BC1901. The XRD patterns contain prominent diffraction peaks at approximately 10 Å (attributed to the 001 reflection) and 5 Å (the 002 reflection of the same mineral). Additionally, there are weaker peaks at around 7 Å, indicative of a different mineral. Notably, the 7 Å reflection is nearly undetectable in Layer I of Nodule BC06. Comparative analysis shows that the 10 Å peaks are more intense and distinct in Nodule BC06 than in Nodule BC1901, and the 10 Å peak is not present in Layer I of Nodule BC1901. For Nodule BC06, the ~10 Å peak is sharpest in Layer I, whereas in Nodule BC1901, it is sharpest in Layer II, indicating a well-ordered mineral structure in these layers. Conversely, Layer III in Nodule BC1901 contains a moderate peak, and Layer I had the broadest peak, indicating a less-ordered arrangement. Two hk bands at approximately 2.45 Å and 1.42 Å are also discernible in all of the samples. The other significant peaks correspond to the diffraction patterns of various minerals, including quartz and phillipsite.

After drying the samples at 105°C, the ~10 Å peak decreased to varying extents, while the 7 Å peak intensified. Specifically, in Layers I and III of Nodule BC1901 and Layer II of Nodule BC06, the ~10 Å peak became less pronounced than the ~7 Å peak. In contrast, after heating, in Layer II of Nodule BC1901 and Layer I of Nodule BC06, the ~10 Å peak significantly decreased but remained more distinct than the ~7 Å peak. Furthermore, some reflections near ~10 Å shifted to lower angle regions (9–9.6 Å) after drying, e.g., in Layer III of Nodule BC1901.

5 Discussion

5.1 Reliability of LA-ICP-MS line-scan analysis

The LA-ICP-MS technique is a powerful tool for geochemical analysis of PMNs and has distinct advantages over traditional EPMA. Unlike EPMA, which has been the standard for major element analysis for some time, LA-ICP-MS can simultaneously acquire both major and trace element data. This capability eliminates the discrepancies that often arise between the major

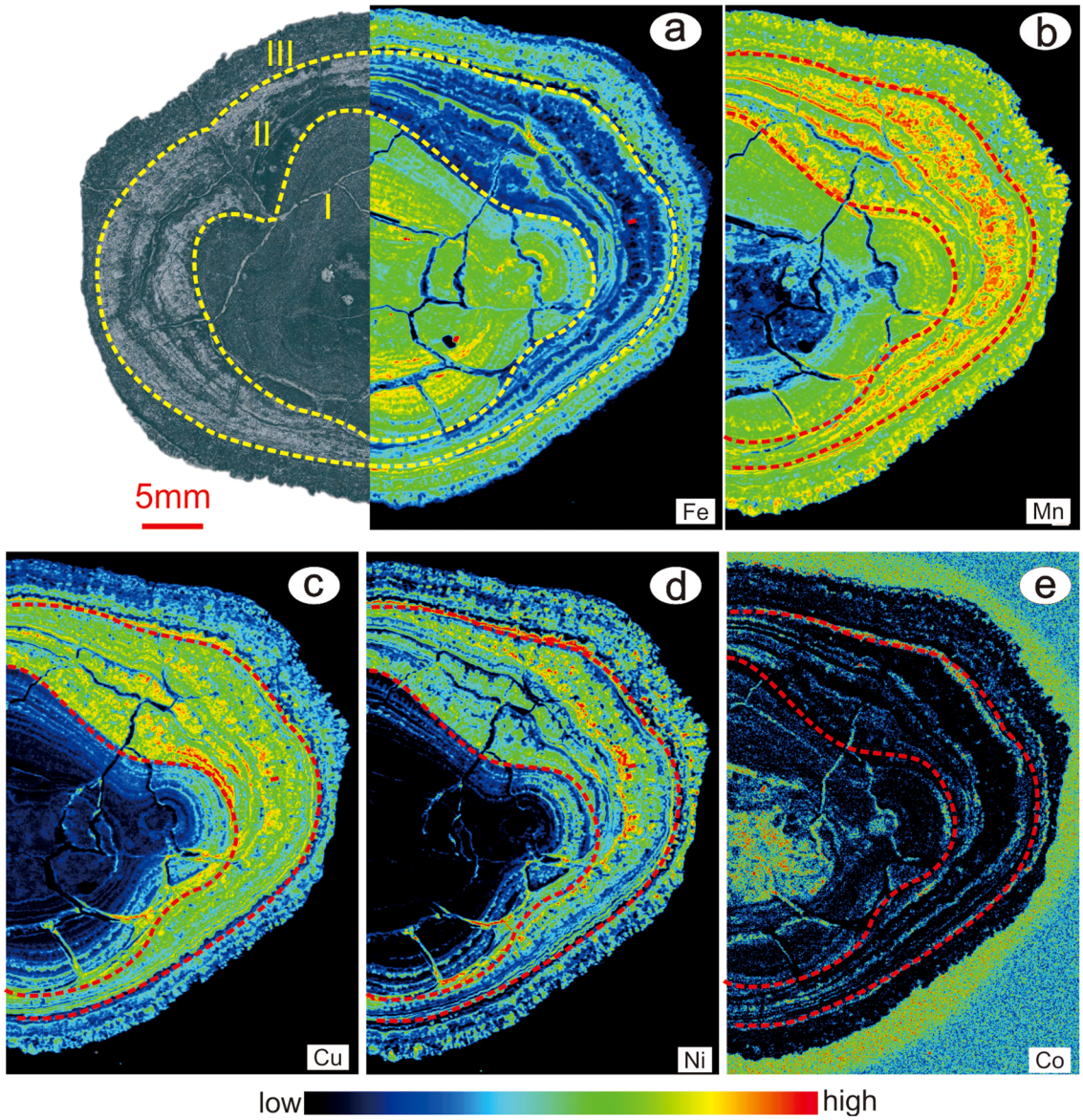

FIGURE 5
μ-XRF map images of the thin section of Nodule BC1901showing elemental distributions: **(A)** Fe; **(B)** Mn; **(C)** Cu; **(D)** Ni; and **(E)** Co. The microphotograph under reflected light in **(A)** is the same as that in Figure 2D.

and trace element compositions determined using different analytical methods, especially for PMNs containing micro/nano-layers. Furthermore, LA-ICP-MS provides a more rapid and sensitive determination of the element composition, leading to significant reductions in both time and cost. Advances in this technology have significantly broadened the scope of geochemical investigations, as demonstrated by Menendez et al. (2019), who successfully utilized LA-ICP-MS to conduct simultaneous major and trace element analysis of PMNs. Additionally, the application of the Iolite software by Zhu et al. (2017) and Li et al. (2020) for data reduction has streamlined the process of converting raw line-scan and mapping data into meaningful element concentrations.

The present study further validated the reliability of LA-ICP-MS line-scan analysis. We found that the element concentration ranges obtained via line-scan analysis were in close agreement with those obtained via spot analysis, suggesting that LA-ICP-MS can effectively be used for both line and mapping compositional statistics. This provides a more comprehensive and detailed view of a nodule's composition. The consistency of the trends of the contents of elements such as Mn, Fe, Co, Ni, Cu, and REY obtained via line-scan analysis and spot analysis (Figure 6) underscores the reliability of using LA-ICP-MS in geochemical investigations.

Although the precision and accuracy of LA-ICP-MS may be influenced by certain limitations, its ability to offer detailed element distributions across a sample's surface is invaluable. This level of detail is crucial for attaining a nuanced understanding of the geochemical processes occurring during the formation of PMNs. Therefore, when used with careful interpretation and validation

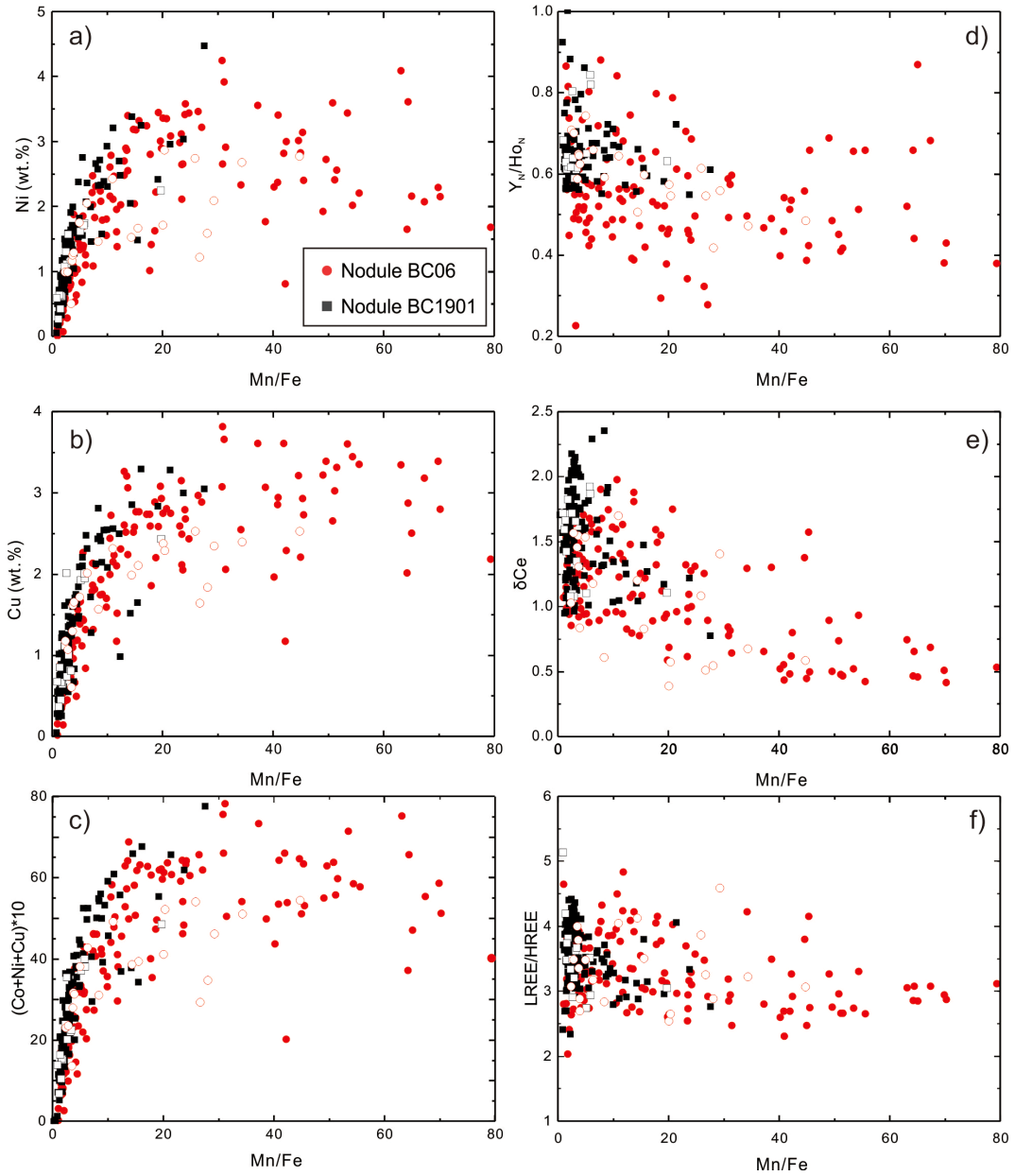

FIGURE 6
Plots of Mn/Fe vs. **(A)** Ni; **(B)** Cu; **(C)** (Co+Ni+Cu)x10; **(D)** Y_N/Ho_N; **(E)** δCe; and **(F)** LREE/HREE for Nodule BC06 and Nodule BC1901. $\delta Ce = Ce_N/(0.5La_N + 0.5Pr_N)$. All of the elements (Ce, La, Pr, Y and Ho) are normalized to Post-Archean Average Shale (PAAS). The values for PAAS are from McLennan (1989). The open and solid symbols denote data obtained via LA-ICP-MS spot and line analyses.

against established standards and techniques, LA-ICP-MS line-scan analysis is a robust and reliable method for geochemical analysis of Mn-PMNs.

5.2 Genesis of PMNs

Marine PMNs can be categorized into three groups based on their origin: hydrogenetic, diagenetic, and hydrothermal PMNs (Josso et al., 2017; Bau et al., 2014; Bonatti et al., 1972). These groups are generally distinguished by their different mineral compositions and geochemical compositions. The following discussion explores the genesis of the different layers of the nodules analyzed in this study. We focus on variations in their mineralogy and chemical compositions.

5.2.1 Mineralogy

Hydrogenetic PMNs, which precipitate directly from seawater, are predominantly composed of Fe-rich vernadite, a poorly crystalline form of δ-MnO_2. This mineral is intricately interwoven with poorly ordered or amorphous iron oxyhydroxide (δ-FeOOH) and exists in the form of nanoparticles (Koschinsky et al., 2010). Despite their high iron contents, hydrogenetic PMNs typically lack distinct X-ray reflections for Fe-phase minerals due to the poor

10.3389/fmars.2024.1489184

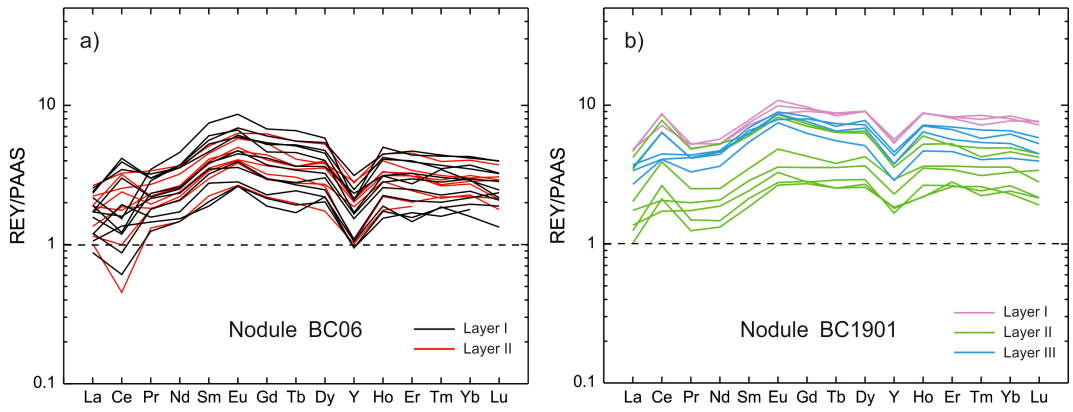

FIGURE 7
PAAS-normalized REY patterns of ferromanganese nodules. **(A)** REY patterns of Nodule BC06 from the eastern CCZ; and **(B)** REY patterns of Nodule BC1901 from the western CCZ.

crystallinity or X-ray amorphous nature of iron oxides/hydroxides. For instance, for Layer I of Nodule BC1901, the XRD pattern lacks sharp reflections, displaying only weak ~7 Å and ~10 Å peaks. In combination with the elevated Fe content, this supports the identification of Fe-bearing vernadite as the primary manganese mineral, which is indicative of a predominant hydrogenetic process (Hein et al., 2013, 2016).

In contrast, diagenetic PMNs form through pore-fluid precipitation, yielding phyllomanganates such as birnessite (~7 Å) and buserite (~10 Å), as well as tectomanganates such as todorokite. Todorokite, buserite I, and II, which are characterized by a ~10 Å peak. However, buserite I is prone to transformation into birnessite after heating at 105°C for 24 hours, while buserite II, which has a high interlayer cation content, exhibits greater thermal stability.

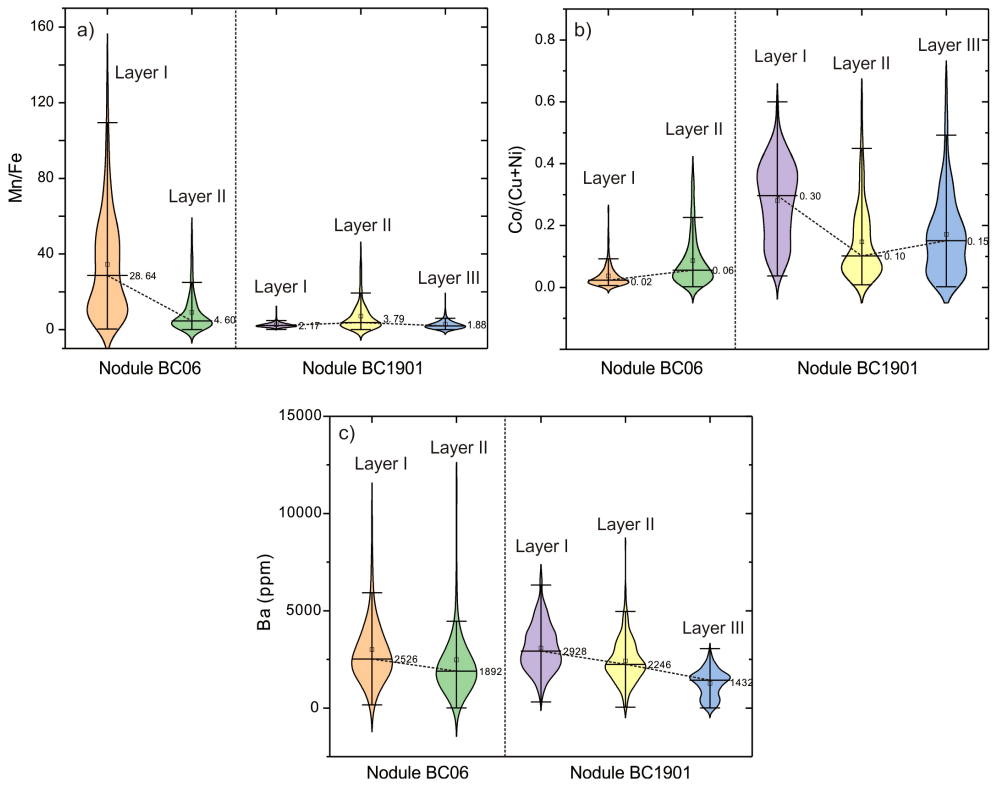

FIGURE 8
Violin plots of the **(A)** Mn/Fe ratio; **(B)** Co/(Cu+Ni) ratio, and **(C)** Ba content for the different layers of the studied nodules. The lower and upper lines on the violins denote the lower quartile and upper quartile values, respectively. The open squares denote the median values for each layer. The numbers to the right of the violins are the median values.

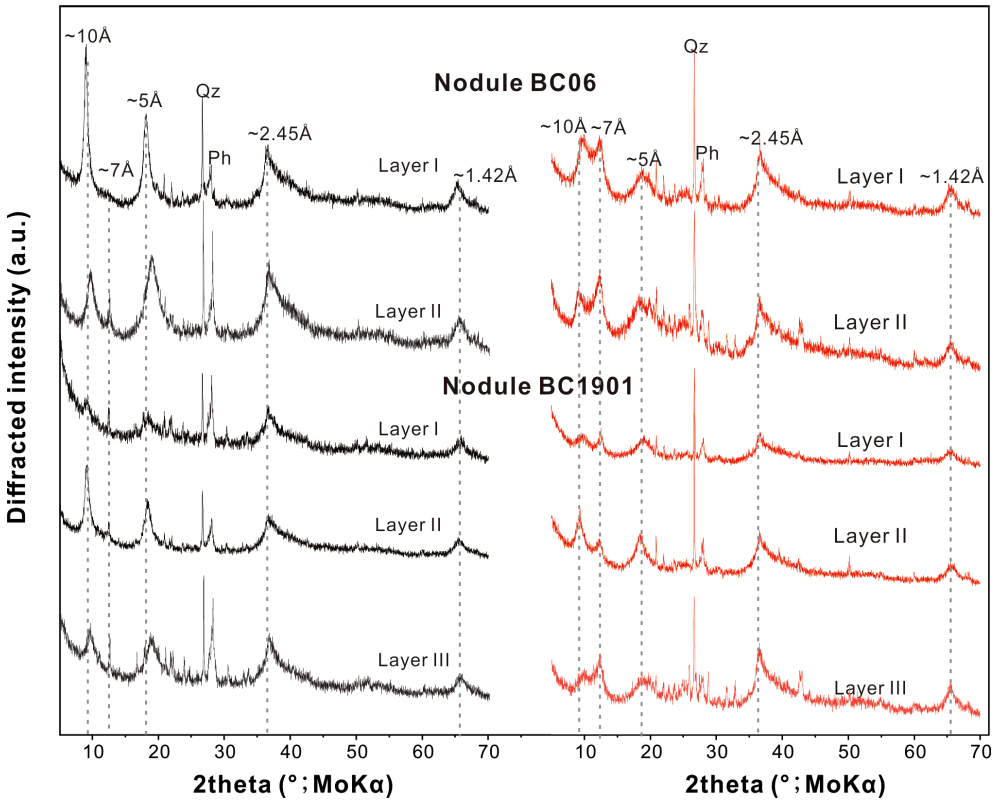

FIGURE 9
XRD patterns of PMNs analyzed in this study. All of the subsamples were analyzed at room temperature (black pattern) after drying at 105°C (red pattern). The peaks at ~7 Å correspond to 7 Å phyllomanganate. The reflections at ~2.45 Å and ~1.42 Å are typical of Fe-rich vernadite. The broad peaks at ~10 Å and ~5 Å at room temperature correspond to 10 Å Mn-phases (10 Å phyllomanganate/todorokite). The 10 Å and ~5 Å peaks that are still present after heating are characteristic of a stable 10 Å manganite (todorokite/buserite II) phase. The intensified peaks at ~7 Å are indicative of an unstable 10 Å –manganese phase (buserite I), which collapses upon heating at 105°C. Qz = quartz and Ph = phillipsite.

The cations in buserite II resist the structural collapse to the 7 Å spacing observed in less stable buserite I after heating (Manceau et al., 2014). Thus, heating experiments are a valuable tool for distinguishing between different 10 Å manganates. In this study, the XRD patterns of all of our samples exhibited a notable reduction in the ~10 Å peak after heating at 105°C, and the ~10 Å peak was predominantly transformed into a ~7 Å peak, suggesting that the original 10 Å phase was predominantly buserite I. The remaining ~10 Å peak was likely caused by a stable manganate phase, such as buserite II or todorokite.

Previous research has revealed that 10 Å phyllomanganates can incorporate more Ni and Cu than todorokite, which typically contains less than 2 wt% of these elements (Bodeï et al., 2007). Our analysis of Nodule BC06, which has high Mn/Fe ratios and Ni +Cu contents of greater than 2 wt%, suggests that the layers in this nodule are predominantly composed of buserite II, rather than todorokite. This conclusion is consistent with that of Wegorzewski et al. (2015), who suggested that unstable 10 Å phyllomanganates are the dominant Mn-phase, the stable 10 Å Mn-phase constitutes subordinate mineral components, and todorokite is absent in the central Pacific Ocean.

Unlike Fe-rich vernadite, buserite has a high crystallinity and produces clear X-ray reflections. In Nodule BC06, Layer I exhibits a more pronounced ~10 Å peak compared to Layer II, indicating a higher concentration of buserite and the significant influence of diagenetic processes. Similarly, Layer II of Nodule BC1901 also exhibits a strong ~10 Å peak, indicating a higher concentration of buserite and a more substantial contribution of diagenetic precipitates compared to the other two layers.

5.2.2 Chemical composition

Marine PMNs can be distinguished through analysis of specific element ratios and trace element contents. Discrimination between hydrogenetic, diagenetic, and hydrothermal PMNs can be achieved using the Mn/Fe ratio, (Co+Ni+Cu)×10 value, and trace element compositions (Bonatti et al., 1972; Bau et al., 2014; Josso et al., 2017).

Hydrogenetic PMNs, which precipitate from seawater, are characterized by high Fe concentrations, typically exceeding 10%, Mn/Fe ratios of less than 2.5, and a significant Co concentration, which has been reported for PMNs in the northwestern Pacific and Cook Islands-Penrhyn Basin (Hein et al., 2020; Ren et al., 2022, 2023). In contrast, diagenetic PMNs are distinguished by higher Cu, Ni, and Mn contents compared to their hydrogenetic counterparts. Mixed hydrogenetic-diagenetic PMNs exhibit additional Cu enrichment, while hydrothermal deposits have variable Fe and Mn contents and lower (Co+Ni+Cu) contents than hydrogenetic PMNs (Hein et al., 2020).

10.3389/fmars.2024.1489184

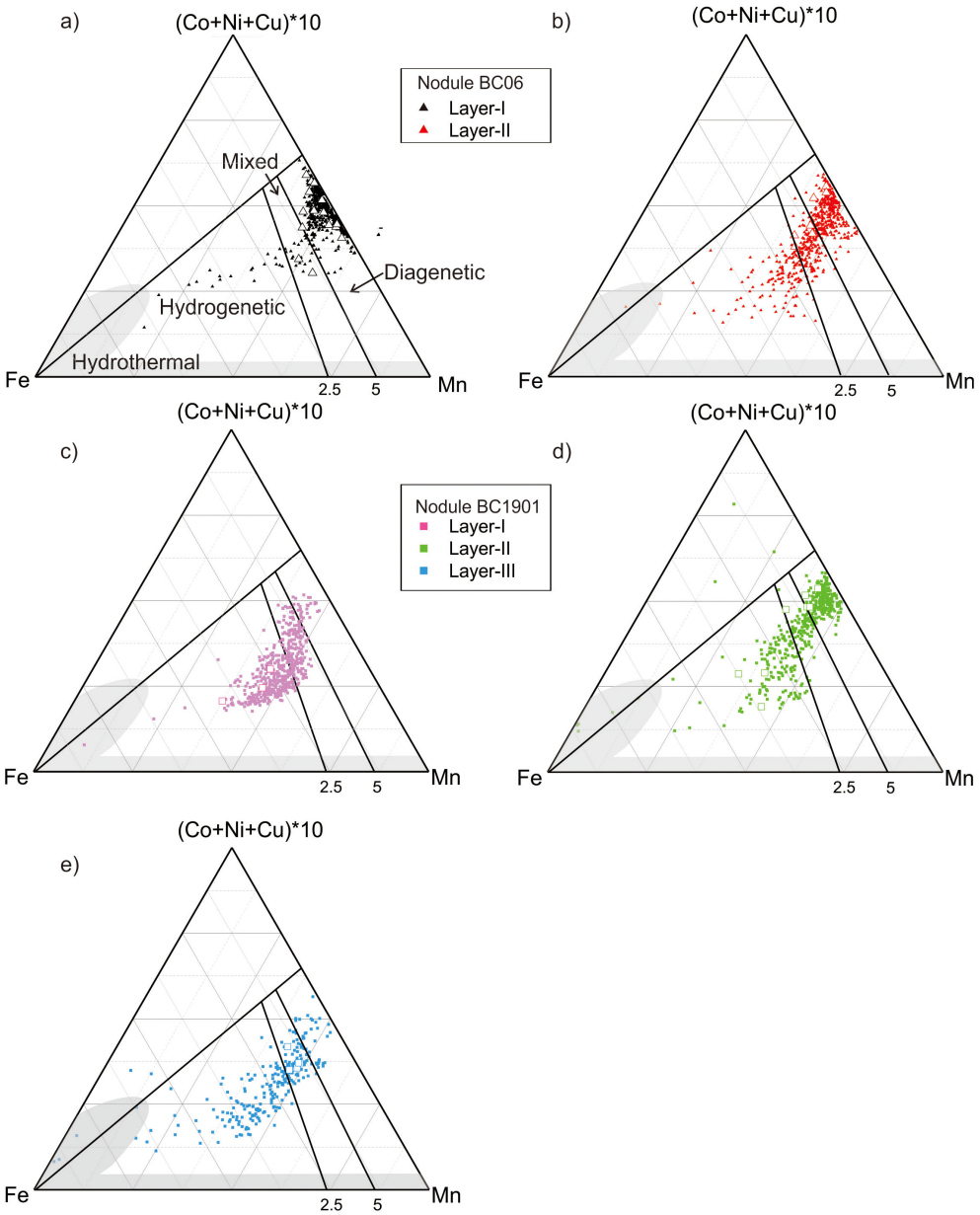

FIGURE 10
Chemical characteristics of the studied nodules. Nodule BC06: **(A)** Layer I and **(B)** Layer II; Nodule BC1901: **(C)** Layer I, **(D)** Layer II and **(E)** Layer III. Ternary diagram of Fe, Mn, and (Cu + Ni) × 10 is following Bonatti et al. (1972). The samples with Mn/Fe ratios of > 2.5 (some refer to 5) indicate a influence by early diagenetic processes. The open and filled symbols denote data obtained via LA-ICP-MS spot and line analyses. The grey shaded area denotes a hydrothermal origin.

In this study, the significant variations in the Mn/Fe ratios and (Co+Ni+Cu)×10 values of the analyzed nodules suggest that their growth was influenced by both hydrogenetic and diagenetic processes, while hydrothermal processes only had a slight impact (Figure 10). Layer I of Nodule BC06, which exhibits a detrital texture and is Mn-rich, has the highest Mn/Fe ratio (44.78) and Ni +Cu contents (reaching 5.30 wt.%). This is indicative of the occurrence of diagenetic processes. Although the μ-XRF mapping results indicate that Layer II is dominated by Mn-rich minerals, characterized by dendritic and laminated textures, the Mn/Fe ratio of this layer (determined via LA-ICP-MS) is lower than that of Layer I. This places Layer II closer to the mixed hydrogenetic-diagenetic field on the genesis discrimination diagram (Figure 10B), suggesting a reduction of the influence of diagenetic processes.

Nodule BC1901 generally exhibits higher Fe contents and lower Mn/Fe ratios compared to Nodule BC06, and its Fe-rich layers likely consist of Fe-bearing vernadite. These layers form via precipitation of hydrated Mn and Fe oxide colloids from oxic seawater, as well as metal enrichment via adsorption, complexation, and oxidation (Koschinsky and Hein, 2003; Hein et al., 2013). Typical characteristics of nodules formed via a hydrogenetic formation mechanism are Mn/Fe ratios of up to ~3, low (Ni + Cu) and Ba concentrations, and notably high Co and Ti concentrations (Wegorzewski and Kuhn, 2014). In the case of Nodule BC1901, the

10.3389/fmars.2024.1489184

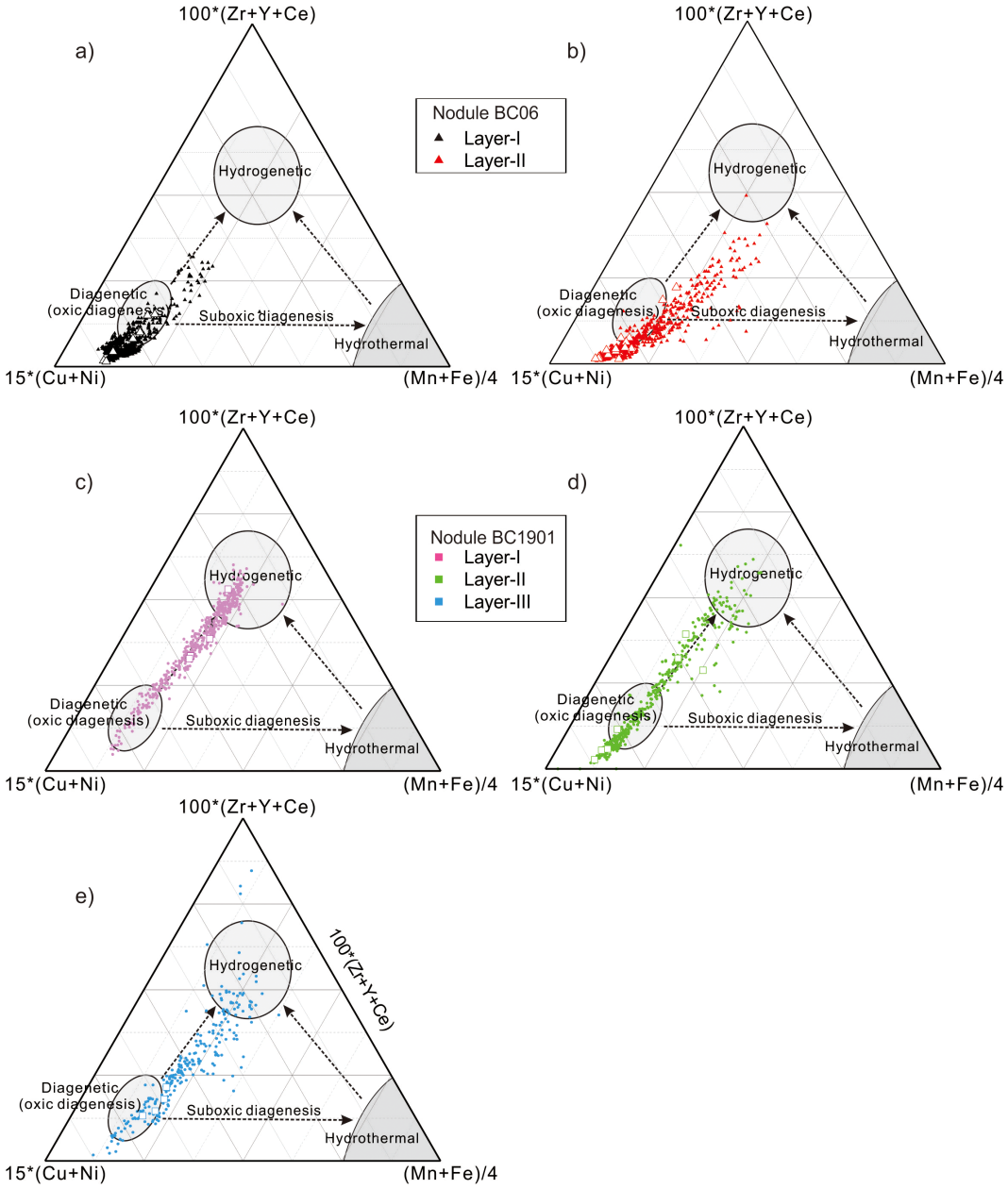

FIGURE 11
15×(Cu+Ni)−(Mn+Fe)/4−(Zr+Y+Ce)×100 ternary diagram [after Josso et al. (2017)]. Nodule BC06: **(A)** Layer I and **(B)** Layer II; Nodule BC1901: **(C)** Layer I, **(D)** Layer II and **(E)** Layer III. The legend is the same as in Figures 6 and 10. The open and filled symbols denote data obtained via spot and line analyses, respectively.

highest Mn/Fe ratio determined for Layer I via LA-ICP-MS is 1.82. The μ-XRF mapping results revealed that the Fe is mainly concentrated in Layer I. Combined with its geochemical characteristics, this supports the conclusion that this layer has a predominantly hydrogenetic origin. This is also evident on the ternary discrimination plot, on which the data for Layer I predominantly plot within the hydrogenetic field (Figure 10C). In contrast to Layer I, Layer II and Layer III of Nodule BC1901 plot within both the hydrogenetic and diagenetic fields this discrimination diagram (Figures 10C–E). This distribution suggests that while these layers primarily acquired metals from seawater, they also incorporated metals from sediment pore water. Notably, Layer II has the highest average and maximum Mn/Fe ratios among the layers of Nodule BC1901, indicating that the diagenetic processes had a greater influence. However, this diagenetic signature is weaker in the outer parts of the nodule, suggesting a gradient of the contribution of diagenetic metal enrichment.

In addition to major element data, REY and trace element data provide further insights into the genesis of Mn-nodules. Hydrogenetic layers tend to have high (Zr+Ce+Y) contents and positive δCe values. Whereas fast-growing suboxic diagenetic phases usually have lower (Zr+Ce+Y) contents and negative δCe values (Kuhn et al., 1998; Ohta et al., 1999). In Figures 11 and 12, Layer I of Nodule BC06 plots in the diagenetic field on the

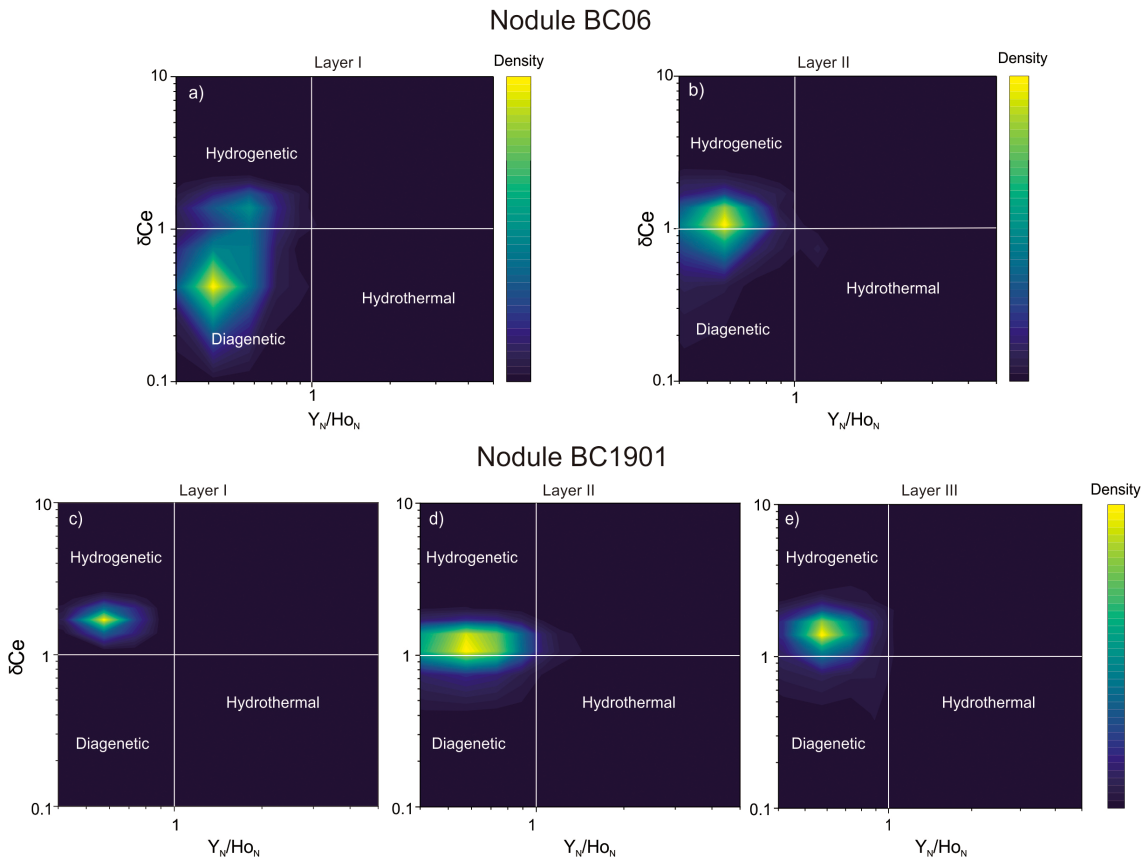

FIGURE 12
Plots showing the density of the individual layers in the studied nodules. Nodule BC06: **(A)** Layer I and **(B)** Layer II; Nodule BC1901: **(C)** Layer I, **(D)** Layer II and **(E)** Layer III. $\delta Ce = Ce_N/(0.5La_N + 0.5Pr_N)$. All of the elements (Ce, La, Pr, Y, and Ho) are normalized to PAAS (McLennan, 1989). The white lines are based on the discriminate diagram of Bau et al. (2014).

discrimination plots created by Josso et al. (2017) and Bau et al. (2014). In contrast, Layer II plots in the mixed diagentic-hydrogenetic field and has higher δCe values and (Zr+Ce+Y) contents. The data for Nodule BC1901 plot in the mixed and hydrogenetic fields and have positive Ce anomalies when normalized to PAAS (average δCe of 1.52, n = 15). The δCe value decreases from Layer I to Layer II and then increases from Layer II to Layer III.

There are two explanations for the variations in the Ce anomaly value. One hypothesis suggests that these variations are associated with the redox conditions, under which PMNs selectively absorb tetravalent Ce from seawater. During diagenesis, under suboxic to anoxic conditions, Ce is reduced from insoluble Ce^{4+} to soluble Ce^{3+}, leading to diagenetic phases having negative Ce anomalies (Bau et al., 1997; Pattan et al., 2005; Bau et al., 2014). An alternative explanation is that these variations are related to the growth rate of the PMN. A slow growth rate results in prolonged contact with seawater, facilitating Ce enrichment and leading to a positive Ce anomaly. These results indicate that the redox conditions may not be the dominant factor controlling the Ce anomaly, thus the δCe values are positive for PMNs with a diagenetic or hydrogenetic source (Cheng et al., 2023; Su et al., 2022). However, in this study, we found that the δCe value is negatively correlated with the Mn/Fe ratio (Figure 6E). Layers with lower δCe values tend to plot closer to the diagenetic field on the ternary discrimination plots compared to layers with higher δCe values (Figures 10, 11). We propose that the lower Ce anomaly values are likely indicative of a greater input from diagenetic precipitation.

In conclusion, Nodule BC06from the eastern CCZ predominantly exhibit characteristics indicative of intensification of diagenetic influences from the core to the rim. In contrast, Nodule BC1901from the western CCZ characteristics indicative of initial intensification of diagenetic processes followed by a trend of weakening of diagenetic processes towards the outer layers. This suggests the occurrence of complex interplay between hydrogenetic and diagenetic processes.

5.3 Major factors controlling the growth of individual layers

Our findings indicate that Nodule BC06 is primarily of diagenetic origin. The decrease in the Mn/Fe ratio (Figure 8) and increase in the δCe value from Layer I to Layer II (Figures 10C, D) suggest a transition from a sub-oxic environment to a more oxic environment. Previous studies have suggested that a reduction of the supply of organic matter to the seafloor can induce a shift in the redox environment (Wegorzewski and Kuhn, 2014). When biological productivity is high enough to increase the amount of

organic matter that reaches the seafloor, aerobic respiration decreases the amount of dissolved oxygen in the sediment pore fluid (Kuhn et al., 2017), causing a rapid decrease in the oxygen content and forming a shallower oxic/suboxic front (OSF). Consequently, Layer I likely precipitated when the flux of organic material to the sediments was higher than that during the formation of Layer II (e.g., Halbach et al., 1988). This is further supported by the decrease in the Ba content from Layer I to Layer II (Figure 8C) as the variation in Ba within the PMN reflects fluctuations in the primary biological productivity (Dymond et al., 1984; Hein et al., 1997). During the decomposition of organic matter, Ba is released into the water column and is incorporated into the PMNs. Currently, the high productivity zone is located to the south of our sampling sites. The flux of organic matter to the sediments is likely highest within this high productivity zone, providing optimal conditions for PMN growth via diagenetic processes. According to the movement of the tectonic plates, the Pacific Plate has moved northwestward by 0.3° latitude per million years since 43 Ma (Wessel and Kroenke, 1998). Therefore, the initial location of the site at which Nodule BC06 was collected may have been closer to the equatorial high-productivity zone than it is today. As the Pacific Plate moved, this site likely moved away from this zone. A decrease in the surface primary productivity would have led to oxidizing conditions, causing the OSF to retreat deeper into the sediment. As a result, the diagenetic formation weakened towards the outer parts of the nodule (Figure 13A). Polymetallic nodules from the nearby UK contract area also exhibit this pattern, suggesting it is a regional phenomenon rather than an isolated case (Menendez et al., 2019).

In contrast, Nodule BC1901 from the western CCZ initially grew in an oxic environment. The diagenetic processes intensified during the formation of Layer II and then weakened during the formation of the outer layers. This growth history is also supported by the trends of the Mn/Fe ratio and δCe value (Figures 8, 12). If this phenomenon was also driven by plate movement, it would imply that the site from which Nodule BC1901 was collected must have migrated from south of the equator and passed through the high productivity zone before reaching its current location. Based on the present-day distribution of the primary productivity, this site would need to have moved from approximately ~3°S to its current position (~9°N). Because the Pacific Plate moved northwestward by 0.3° latitude/Ma after 43 Ma (Wessel and Kroenke, 1998), the estimated age of nodule is ~40 Ma. However, our estimate of the age of Nodule C1901 is up to ~4.22 Ma obtained via Co chronology (Supplementary Table S2). This is consistent with the estimated age

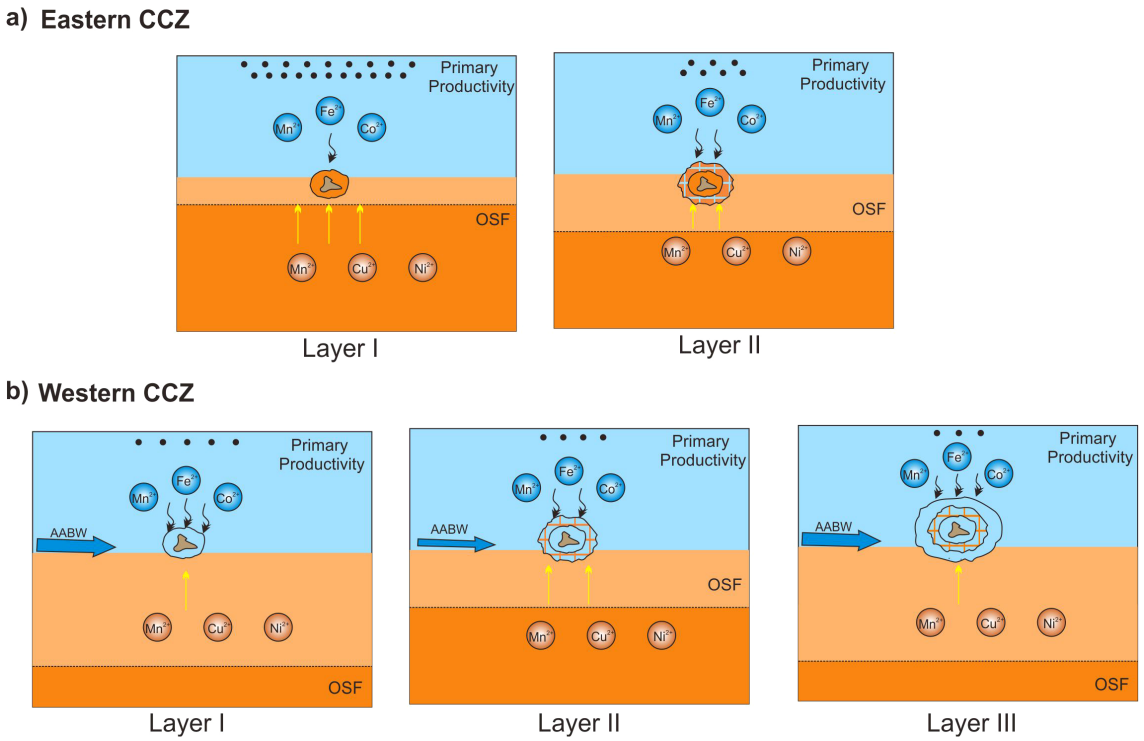

FIGURE 13
Schematic models illustrating the environmental changes during the formation of the PMNs in the eastern and western CCZ. **(A)** Nodule BC06 from the eastern CCZ consists of two layers. As the nodule moved away from the equatorial high productivity zone due to tectonic movement of the Pacific Plate, the redox conditions changed from sub-oxic to more oxic. The metal elements were primarily sourced from the pore water, especially during the growth of Layer I. **(B)** Nodule BC1901 from the western CCZ is composed of three layers. During the growth of Layer I, the nodule began to form on the seafloor under oxic conditions as a result of strengthening of the AABW. The metal elements were mainly sourced from the seawater. As global climate change weakened the bottom currents, the OSF moved closer to the surface of the sediments. The formation mechanism shifted from hydrogenetic to diagenetic, and the metal elements were increasingly sourced from the pore water (Layer II). Subsequently, the strengthening of the AABW led to more oxidizing conditions, causing the OSF to retreat deeper into the sediment. This provided optimal conditions for hydrogenetic formation (Layer III). The yellow arrows represent pore water, and the black arrows represent seawater. The blue and orange colors in the PMNs represent diagenetic and hydrogenetic precipitates, respectively.

of PMNs with similar sizes and morphologies in this region reported by Yi et al. (2020), who estimated the age of PMNs in this area (10.05°N, 154.32°W) to be ~4.70 Ma (Early Pliocene) using comprehensive methods, including magnetic scanning, $^{10}Be/^{9}Be$ dating, and Co chronometers. The substantial discrepancy between these estimated ages suggests that the change in the formation mechanism cannot be solely explained by the movement of the Pacific Plate.

Another factor that may have contributed to the fluctuations of the diagenetic formation processes is the variability of the oxygen-rich Antarctic Bottom Water (AABW). When the AABW weakens, the oxygen content in the sediment decreases, causing the OSF to become shallower, thereby intensifying diagenesis (Park et al., 2023). Previous studies have shown that deep-sea ventilation linked to the formation of AABW and its variability is a key factor controlling the ventilation (i.e., the redox conditions) beneath the Eastern Tropical Pacific (Yi et al., 2023). Additional support for this interpretation comes from the lower Co/(Cu+Ni) ratios of Layer II compared to Layers I and III (Figure 8B), which is a proxy for deep-water ventilation conditions (Zhong et al., 2020). Thus, the intensified diagenesis during the formation of Layer II of Nodule BC1901 may have been associated with weakening of the AABW (Figure 13B). According to previous research, Earth experienced a transition from ice-free conditions in the Northern Hemisphere to extensive glaciation due to the onset of Northern Hemisphere glaciation (NHG) at around 3.6 Ma (Studer et al., 2012; Mudelsee and Raymo, 2005). Following the expansion of sea ice, the AABW weakened, creating strongly reducing conditions that caused the OSF to move toward the sediment-water interface. The inferred change in the formation mechanism may be related to these changes in the environment. While the current evidence strongly supports this interpretation, future studies that utilize more precise dating techniques could provide further validation and deeper insights into the timing and dynamics of these changes.

In summary, movement of the Pacific Plate was only a secondary factor influencing the nodule growth in the western CCZ. Instead, variations in the AABW were likely the primary factor controlling the growth of Nodule BC1901. Initially, Nodule BC1901 began to form on the seafloor in an oxic environment with greater deep-water ventilation and stronger AABW. As global climate change led to diminished bottom currents, the nodule formation mechanism shifted from hydrogenetic to diagenetic. Subsequently, intensification of the AABW led to more oxidizing conditions, causing the OSF to retreat deeper into the sediment. Under the new oxygenated bottom water conditions, hydrogenetic growth of PMNs was favored (Figure 13B).

5.4 Implications for spatial variability within the CCZ

As the largest nodule field found on the deep-sea floor of all oceans worldwide, the CCZ contains PMNs with varying chemical compositions. This variability reflects differences in the nodule growth mechanisms within the CCZ. The polymetallic nodules in the eastern CCZ were primarily precipitated from suboxic sediment pore water; whereas, although they also contain diagenetic layers, the polymetallic nodules in the western CCZ were principally formed via hydrogenous precipitation. The Fe oxyhydroxide and Mn oxide colloids formed via hydrogenetic precipitation attracted dissolved Co^{2+} from the seawater onto the surfaces of the PMNs. At the same time, metal ions (such as Cu^{2+} and Ni^{2+}) were released via dissolution of Mn oxides, diffused upward into the pore-water, and re-precipitated around the accreting PMNs (Hein et al., 2020; Manceau et al., 2014). Consequently, compared to those in the western CCZ, the PMNs in the eastern CCZ are enriched in Mn and Cu and depleted in Co (ISA, 2010). The formation of this geochemical composition requires spatial variability of the depositional and geochemical conditions, which control the growth mechanisms of the PMNs. In the past, the PMNs in the eastern CCZ were located closer to the equatorial high productivity zone. Although plate motion has moved them to an area with lower productivity, the initial diagenetic layers, which are enriched in Mn and Cu, continue to significantly influence the bulk composition of the PMNs. Furthermore, at present, the primary productivity in the eastern CCZ is still higher than that in the western CCZ, creating conditions suitable for the formation of more diagenetic microlayers with higher Mn and Cu contents in the eastern CCZ. In contrast, the PMNs in the western CCZ have always been located outside the equatorial high productivity zone, making the western CCZ an ideal environment for the formation of Fe-rich layers via hydrogenetic processes.

As a result, the Mn and Cu contents of PMNs increase towards the eastern CCZ. However, the reason for the trend of Ni along the central axis of the CCZ remains elusive. Therefore, future studies are needed to obtain a more detailed characterization of PMNs from different regions within the CCZ, which would be beneficial to exploration efforts. Nonetheless, the results of this study underscore the importance of the growth history of PMNs in explaining the spatial variability of their element distributions.

6 Conclusions

Based on the analysis of the mineralogical and geochemical compositions of polymetallic nodules from the eastern and western CCZ in the Pacific Ocean, we reached the following conclusions.

1. Based on careful interpretation and validation against established standards and techniques, LA-ICP-MS line-scan analysis yielded reliable geochemical data for PMNs.
2. Polymetallic nodules from the eastern and western CCZ had different textures, mineralogical compositions, and chemical distributions. The nodule collected from the eastern CCZ was primarily influenced by diagenetic processes, whereas the nodule collected from western CCZ was influenced by both hydrogenetic and diagenetic processes.
3. The growth history of Nodule BC06 from the eastern CCZ was divided into two periods. The movement of the nodule away from the equatorial high-= productivity zone as a result of plate motion was the principle reason for the change in the growth mechanism. The growth history of

Nodule BC1901 from the western CCZ was divided into three periods. Variations in the deep-water ventilation and AABW were the major controlling factors.

4. Studying the growth history of PMNs could help to explain the spatial varieties of some elements in PMNs in the eastern and western CCZ. Therefore, future studies are needed to obtain a more detailed characterization of PMNs in different regions in the CCZ.

Data availability statement

The datasets presented in this study can be found in online repositories. The names of the repository/repositories and accession number(s) can be found in the article/Supplementary Material.

Author contributions

JL: Writing – review & editing, Writing – original draft, Conceptualization. YJ: Writing – review & editing, Methodology, Investigation. HW: Writing – original draft, Methodology, Investigation, Conceptualization. KY: Writing – review & editing, Methodology. ZZ: Writing – review & editing, Investigation, Formal Analysis. XM: Writing – review & editing. XL: Writing – review & editing, Project administration, Funding acquisition.

Funding

The author(s) declare that financial support was received for the research, authorship, and/or publication of this article. This work was supported by the National Key R&D Program of China (Grant No. 2023YFC2811305) and the Chinese Natural Science Foundation (Project 42076084, U2244222).

Conflict of interest

Author YJ was employed by the company Huadian Electric Power Research Institute Co., LTD.

The remaining authors declare that the research was conducted in the absence of any commercial or financial relationships that could be constructed as a potential conflict of interest.

Publisher's note

Supplementary material

The Supplementary Material for this article can be found online at: https://www.frontiersin.org/articles/10.3389/fmars.2024.1489184/full#supplementary-material

SUPPLEMENTARY FIGURE 1
LA-ICP-MS line analysis results for PMNs in this study. Variability of **(A, B)** Mn/Fe ratio; **(C, D)** Co/(Cu+Ni) ratio; and **(E, F)** Ba content, along the chemical measurement line, i.e., along the growth direction. The grey lines denote the original data; and the red lines denote the 9-point moving average. The thin black dashed lines in Layers I–III denote distinct textural zones (see Section 4.1 in text and photos under microscope in Figure 2).

References

Antoine, D., André, J.-M., and Morel, A. (1996). Oceanic primary production: 2. Estimation at global scale from satellite (coastal zone color scanner) chlorophyll. *Global Biogeochem. Cycles* 10, 57–69. doi: 10.1029/95GB02832

Bau, M., Möller, P., and Dulski, P. (1997). Yttrium and lanthanides in eastern Mediterranean seawater and their fractionation during redox-cycling. *Mar. Chem.* 56, 123–131. doi: 10.1016/S0304-4203(96)00091-6

Bau, M., Schmidt, K., Koschinsky, A., Hein, J., Kuhn, T., and Usui, A. (2014). Discriminating between different genetic types of marine ferro-manganese crusts and nodules based on rare earth elements and yttrium. *Chem. Geol.* 381, 1–9. doi: 10.1016/j.chemgeo.2014.05.004

Bodeï, S., Manceau, A., Geoffroy, N., Baronnet, A., and Buatier, M. (2007). Formation of todorokite from vernadite in Ni-rich hemipelagic sediments. *Geochim. Cosmochim. Acta* 71, 5698–5716. doi: 10.1016/j.gca.2007.07.020

Bonatti, E., Kraemer, T., and Rydell, H. (1972). "Classification and genesis of submarine iron-manganese deposits," in *Ferromanganese deposits on the ocean floor (1st edition)*. Ed. D. R. Horn (Washington: National Science Foundation), 149–166.

Cheng, Y., Xu, Y., Yi, L., Li, D., Lin, F., Yin, X., et al. (2023). Chronology and critical metals enrichment mechanism of ferromanganese nodules from the Parece Vela Basin, Philippine Sea. *Chem. Geol.* 630, 121494. doi: 10.1016/j.chemgeo.2023.121494

Dymond, J., Lyle, M., Finney, B., Piper, D.Z., Murphy, K., Conard, R., et al. (1984). Ferromanganese nodules from MANOP sites H, S and R — control of mineralogical and chemical composition by multiple accretionary processes. *Geochim. Cosmochim. Acta* 48, 931–949. doi: 10.1016/0016-7037(84)90186-8

Glasby, G. ,. P. (2006). "Manganese: Predominant role of nodules and crusts," in *Marine geochemistry*. Eds. H. D. Schulz and M. Zabel (Springer Berlin Heidelberg, Berlin, Heidelberg), 371–427. doi: 10.1007/3-540-32144-6_11

Halbach, P. E., Friedrich, G., and von Stackelberg, U. (1988). "The manganese nodule belt of the Pacific Ocean," in *Geological environment, nodule formation, and mining aspects* (Ferdinand Enke Verlag, Stuttgart), 1–254.

Hein, J.R., Koschinsky, A., Halbach, P., Manheim, F. T., Bau, M., Kang, J.-K., et al. (1997). Iron and manganese oxide mineralization in the Pacific. *Manganese Mineralization: Geochemistry and Mineralogy of Terrestrial and Marine Deposits*. Eds. K. Nicholson, J.R. Hein, B. Bühn and S. Dasgupta. London: Geological Society, 123–138.

Hein, J. R., Koschinsky, A., and Kuhn, T. (2020). Deep-ocean polymetallic nodules as a resource for critical materials. *Nat. Rev. Earth Environ.* 1, 158–169. doi: 10.1038/s43017-020-0027-0

Hein, J. R., Mizell, K., Koschinsky, A., and Conrad, T. A. (2013). Deep-ocean mineral deposits as a source of critical metals for high- and green-technology applications: Comparison with land-based resources. *Ore Geol. Rev.* 51, 1–14. doi: 10.1016/j.oregeorev.2012.12.001

Hein, J.R., and Koschinsky, A. (2014). Deep-ocean ferromanganese crusts and nodules. In: *Treatise on Geochemistry (2nd edition)*. Eds. H.D. Holland and K.K. Turekian. Amsterdam: Elsevier, 273–291.

Hein, J. R., Conrad, T., Mizell, K., Banakar, V. K., Frey, F.A., and Sager, W. W. (2016). Controls on ferromanganese crust composition and reconnaissance resource potential, Ninetyeast Ridge, Indian Ocean. *Deep Sea Research Part I: Oceanographic Research Papers* 110, 1–19.

ISA (International Seabed Authority) (2010). *A Geological Model of Polymetallic Nodule Deposits in the Clarion-Clipperton Fracture Zone and Prospector's Guide for Polymetallic Nodule Deposits in the Clarion-Clipperton Fracture Zone* (Kingston: International Seabed Authority Technical Study: No. 6) 210-211, ISBN: .

Johnson, D. A. (1972). Ocean-floor erosion in the aquatorial Pacific. *Geol. Soc. Am. Bull.* 83, 3121–3144. doi: 10.1130/0016-7606(1972)83[3121:OEITEP]2.0.CO;2

Josso, P., Pelleter, E., Pourret, O., Fouquet, Y., Etoubleau, J., Cheron, S., et al. (2017). A new discrimination scheme for oceanic ferromanganese deposits using high field strength and rare earth elements. *Ore Geol. Rev.* 87, 3–15. doi: 10.1016/j.oregeorev.2016.09.003

Koschinsky, A., and Hein, J. R. (2003). Uptake of elements from seawater by ferromanganese crusts: solid-phase associations and seawater speciation. *Mar. Geol.* 198, 331–351. doi: 10.1016/S0025-3227(03)00122-1

Koschinsky, A., Hein, J.R., Schmidt, K., Alexander, B., and Bau, M. (2010). Rare and valuable metals for high-tech applications found in marine ferromanganese nodules and crusts: relationships to genetic endmembers. In: *Toward the Sustainable Development of Marine Minerals: Geological, Technological and Economic Aspects*. Gelendzhik, Russia: Underwater Mining Institute, 1–13.

Kuhn, T., Bau, M., Blum, N., and Halbach, P. (1998). Origin of negative Ce anomalies in mixed hydrothermal-hydrogenetic Fe-Mn crusts from the Central Indian Ridge. *Earth Planet. Sci. Lett.* 163, 207–220. doi: 10.1016/S0012-821X(98)00188-5

Kuhn, T., Wegorzewski, A., Ruhlemann, C., and Vink, A. (2017). "Composition, formation, and occurrence of polymetallic nodules," in *Deep Sea Mining: Resource Potential, Technical and Environmental Considerations*. Ed. R. Sharma (Cham: Springer International Publishing), 23–63.

Li, D. F., Fu, Y., Sun, X. M., and Wei, Z. Q. (2020). Critical metal enrichment mechanism of deep-sea hydrogenetic nodules: Insights from mineralogy and element mobility. *Ore Geol. Rev.* 118, 103371. doi: 10.1016/j.oregeorev.2020.103371

Liu, Y. S., Hu, Z. C., Gao, S., Günther, D., and Xu, J. (2008). *In situ* analysis of major and trace elements of anhydrous minerals by LA-ICP-MS without applying an internal standard. *Chem. Geol.* 257, 1–2, 34–43. doi: 10.1016/j.chemgeo.2008.08.004

Lyle, M. (2003). Neogene carbonate burial in the Pacific Ocean. *Paleoceanogr. Paleoclimatol.* 18, 1-9. doi: 10.1029/2002PA000777

Manceau, A., Lanson, M., and Takahashi, Y. (2014). Mineralogy and crystal chemistry of Mn, Fe, Co, Ni, and Cu in a deep-sea Pacific polymetallic nodule. *Am. Mineralogist* 99, 2068–2083. doi: 10.2138/am-2014-4742

McLennan, S. (1989). Rare earth elements in sedimentary rocks; influence of provenance and sedimentary processes. *Rev. Mineral. Geochem.* 21, 169–200.

Menendez, A., James, R. H., Lichtschlag, A., Connelly, D., and Peel, K. (2019). Controls on the chemical composition of ferromanganese nodules in the Clarion-Clipperton Fracture Zone, eastern equatorial Pacific. *Mar. Geol.* 409, 1–14. doi: 10.1016/j.margeo.2018.12.004

Mewes, K., Mogollón, J. M., Picard, A., Rühlemann, C., Kuhn, T., Nöthen, K., et al. (2014). Impact of depositional and biogeochemical processes on small scale variations in nodule abundance in the Clarion-Clipperton Fracture Zone. *Deep Sea Res. Part I: Oceanogr. Res. Papers* 91, 125–141. doi: 10.1016/j.dsr.2014.06.001

Mogollón, J. M., Mewes, K., and Kasten, S. (2016). Quantifying manganese and nitrogen cycle coupling in manganese-rich, organic carbon-starved marine sediments: examples from the Clarion-Clipperton fracture zone. *Geophys. Res. Lett.* 43, 7114–7123. doi: 10.1002/2016GL069117

Mudelsee, M., and Raymo, M. E. (2005). Slow dynamics of the northern hemisphere glaciation. *Paleoceanography* 20, PA4022. doi: 10.1029/2005PA001153

Müller, P. J., and Mangini, A. (1980). Organic carbon decomposition rates in sediments of the pacific manganese nodule belt dated by ^{230}Th and ^{231}Pa. *Earth Planet. Sci. Lett.* 51, 94–114. doi: 10.1016/0012-821X(80)90259-9

Ohta, A., Ishii, S., Sakakibara, M., Mizuno, A., and Kawabe, I. (1999). Systematic correlation of the Ce anomaly with the Co/(Ni+Cu) ratio and Y fractionation from Ho in distinct types of Pacific deep-sea nodules. *Geochem. J.* 33, 399–417. doi: 10.2343/geochemj.33.399

Pan, G. F., and Hua, Z. G. (1996). Distribution of manganese nodules and its relation to geologic and geographic environment in the Clarion-Clipperton Zone. *Oceanol. Limnol. Sin.* 27, 405–413.

Park, J., Jung, J., Ko, Y., Lee, Y., and Yang, K. (2023). Reconstruction of the paleo-ocean environment using mineralogical and geochemical analyses of mixed-type ferromanganese nodules from the tabletop of western Pacific Magellan Seamount. *Geochem. Geophys. Geosyst.* 24, e2022GC010768. doi: 10.1029/2022GC010768

Paton, C., Hellstrom, J., Paul, B., Woodhead, J., and Hergt, J. (2011). Iolite: Freeware for the visualisation and processing of mass spectrometric data. *J. Anal. At. Spectrom.* 26 (12), 2508-2518. doi: 10.1039/c1ja10172b

Pattan, J. N., Pearce, N. J. G., and Mislankar, P. G. (2005). Constraints in using Cerium-anomaly of bulk sediments as an indicator of paleo bottom water redox environment: a case study from the Central Indian Ocean Basin. *Chem. Geol.* 221, 260–278. doi: 10.1016/j.chemgeo.2005.06.009

Ren, J. B., He, G. W., Deng, X. G., Deng, X. Z., Yang, Y., Yao, H. Q., et al. (2022). Metallogenesis of Co-rich ferromanganese nodules in the northwestern Pacific: Selective enrichment of metallic elements from seawater. *Ore Geol. Rev.* 143, 104778. doi: 10.1016/j.oregeorev.2022.104778

Ren, J. B., He, G. W., Yang, Y., Yu, M., Deng, Y. N., Pang, Y. T., et al. (2024). Ultraselective enrichment of trace elements in seawater by Co-rich ferromanganese nodules. *Global Planet. Change* 239, 104498. doi: 10.1016/j.gloplacha.2024.104498

Ren, J. B., Yao, H. Q., Yang, Y., Wang, L. X., He, G. W., Lai, P. X., et al. (2023). Critical metal enrichment in atypical hydrogenetic ferromanganese nodules: A case study in the Central Basin Ridge of the West Philippine Basin. *Chem. Geol.* 615, 121224. doi: 10.1016/j.chemgeo.2022.121224

Reykhard, L. Y., and Shulga, N. A. (2019). Fe-Mn nodule morphotypes from the NE Clarion-Clipperton Fracture Zone, Pacific Ocean: Comparison of mineralogy, geochemistry and genesis. *Ore Geol. Rev.* 110, 102933. doi: 10.1016/j.oregeorev.2019.102933

Studer, A. S., Martinez-Garcia, A., Jaccard, S. L., Girault, F. E., Sigman, D. M., and Haug, G. H. (2012). Enhanced stratification and seasonality in the Subarctic Pacific upon Northern Hemisphere Glaciatione-New evidence from diatom-bound nitrogen isotopes, alkenones and archaeal tetraethers. *Earth Planet. Sci. Lett.* 351–352, 84–94. doi: 10.1016/j.epsl.2012.07.029

Su, R., Sun, F. Y., Li, X. H., Chu, F. Y., Sun, G. S., Li, J., et al. (2022). Diverse early diagenetic processes of ferromanganese nodules from the eastern Pacific Ocean: evidence from mineralogy and *in-situ* geochemistry. *Int. Geol. Rev.* 65 (13), 2131–2147. doi: 10.1080/00206814.2022.2122087

Volz, J. B., Mogollón, J. M., Geibert, W., Arbizu, P. M., Koschinsky, A., and Kasten, S. (2018). Natural spatial variability of depositional conditions, biogeochemical processes and element fluxes in sediments of the eastern Clarion-Clipperton Zone, Pacific Ocean. *Deep Sea Res. Part I: Oceanogr. Res. Papers* 140, 159–172. doi: 10.1016/j.dsr.2018.08.006

Von Stackelberg, U. (1997). Growth history of manganese nodules and crusts of the Peru Basin. In: *Manganese Mineralization: Geochemistry and Mineralogy of Terrestrial and Marine Deposits*. Eds. K. Nicholson, J.R. Hein, B. Bühn and S. Dasgupta. London: Geological Society, 153–176.

Von Stackelberg, U., and Beiersdorf, H. (1991). The formation of manganese nodules between the Clarion and Clipperton fracture zones southeast of Hawaii. *Mar. Geol.* 98, 411–423. doi: 10.1016/0025-3227(91)90113-I

Wang, H. F., Liu, Y. G., and Zhu, K. C. (2015). Polymetallic nodules distribution in the basin and comparison with nodules in China pioneer area, CC zone. *Mar. Geol. Quaternary Geol.* 35, 73–79. doi: 10.3724/SP.J.1140.2015.02073

Wegorzewski, A. V., and Kuhn, T. (2014). The influence of suboxic diagenesis on the formation of manganese nodules in the Clarion Clipperton nodule belt of the Pacific Ocean. *Mar. Geol.* 357, 123–138. doi: 10.1016/j.margeo.2014.07.004

Wegorzewski, A. V., Kuhn, T., Dohrmann, R., Wirth, R., and Grangeon, S. (2015). Mineralogical characterization of individual growth structures of Mn-nodules with different Ni+Cu content from the central Pacific Ocean. *Am. Mineralogist* 100, 2497–2508. doi: 10.2138/am-2015-5122

Wessel, P., and Kroenke, L. K. (1998). The geometric relationship between hot spots and seamounts: Implications for Pacific hot spots. *Earth Planet. Sci. Lett.* 158, 1–18. doi: 10.1016/S0012-821X(98)00043-0

Yi, L., Medina-Elizalde, M., Kletetschka, G., Yao, H., Simon, Q., Paterson, G.A., et al. (2020). The Potential of Marine Ferromanganese Nodules From Eastern Pacific as Recorders of Earth's Magnetic Field Changes During the Past 4.7Myr: A Geochronological Study by Magnetic Scanning and Authigenic 10Be/9Be Dating. *Journal of Geophysical Research: Solid Earth* 125 (7), 1–15. doi: 10.1029/2019JB018639

Yi, L., Medina-Elizalde, M., Tan, L., Kemp, D.B., Li, Y., Kletetschka, G., et al. (2023). Plio-Pleistocene deep-sea ventilation in the eastern Pacific and potential linkages with Northern Hemisphere glaciation. *Science Advances* 9 (8), 1–10. doi: 10.1126/sciadv.add1467

Zhong, Y., Liu, Q., Chen, Z., González, F. J., Hein, J. R., Zhang, J., et al. (2019). Tectonic and paleoceanographic conditions during the formation of ferromanganese nodules from the northern South China Sea based on the high-resolution geochemistry, mineralogy and isotopes. *Mar. Geol.* 410, 146–163. doi: 10.1016/j.margeo.2018.12.006

Zhong, Y., Chen, Z., Hein, J.R., González, F.J., Jiang, Z., Yang, X., et al. (2020). Evolution of a deep-water ferromanganese nodule in the South China Sea in response to Pacific deep-water circulation and continental weathering during the Plio-Pleistocene. *Quaternary Science Reviews* 229, 106106. doi: 10.1016/j.quascirev.2019.106106

Zhu, B., Zhu, Z. Y., Lv, M., and Yang, T. (2017). Application of Iolite in data reduction of laser ablation-inductively coupled plasma-mass spectrometry line-scan analysis. *Rock Mineral Anal.* 36, 14–21. doi: 10.15898/j.cnki.11-2131/td.2017.01.003

frontiers | Frontiers in Marine Science

TYPE Original Research
PUBLISHED 14 January 2025
DOI 10.3389/fmars.2024.1538022

OPEN ACCESS

EDITED BY
Jiangbo Ren,
Guangzhou Marine Geological Survey, China

REVIEWED BY
Sun Ki Choi,
Korea Institute of Ocean Science and Technology (KIOST), Republic of Korea
Bing Li,
First Institute of Oceanography, China

*CORRESPONDENCE
Chunhui Tao
taochunhuimail@163.com

RECEIVED 02 December 2024
ACCEPTED 23 December 2024
PUBLISHED 14 January 2025

CITATION
Yang W, Tao C, Liao S, Zhang H, Zhu C, Li W, Zhang G, Wang X and Wang L (2025) Evolution of a seafloor massive sulfide deposit on axial volcanic ridges: a case study of the Duanqiao hydrothermal field, Southwest Indian Ridge. *Front. Mar. Sci.* 11:1538022. doi: 10.3389/fmars.2024.1538022

Evolution of a seafloor massive sulfide deposit on axial volcanic ridges: a case study of the Duanqiao hydrothermal field, Southwest Indian Ridge

Weifang Yang[1], Chunhui Tao[1,2]*, Shili Liao[1], Huichao Zhang[1,3], Chuanwei Zhu[4], Wei Li[1], Guoyin Zhang[1], Xuefeng Wang[5] and Lisheng Wang[5]

[1]Key Laboratory of Submarine Geosciences, Second Institute of Oceanography, Ministry of Natural Resources, Hangzhou, China, [2]School of Oceanography, Shanghai Jiaotong University, Shanghai, China, [3]Institute of Marine Geology, College of Oceanography, Hohai University, Nanjing, China, [4]State Key Laboratory of Ore Deposit Geochemistry, Institute of Geochemistry, Chinese Academy of Sciences, Guiyang, China, [5]Key Laboratory of Cenozoic Geology and Environment, Institute of Geology and Geophysics, Chinese Academy of Sciences, Beijing, China

The mineralization process below the surface of the seafloor in a hydrothermal field has an important influence on the distribution and enrichment of elements. The Duanqiao hydrothermal field (DHF) is located on the new axial volcanic ridge of the ultraslow-spreading Southwest Indian Ridge. Owing to the limited surface sulfide samples, the metallogenic processes occurring below the seafloor surface such as the element enrichment mechanism and the temporal evolution of the sulfide deposits remain unclear. In this study, we conducted mineral texture, geochemical, ^{230}Th/U dating, and laser ablation inductively coupled plasma mass spectrometer analyses of a drill core containing shallow sulfide deposits to study their evolution process. The results revealed that pyrite is enriched in Mn, Co, As, Mo, Ag, Cd, Sb, Tl, and Pb, chalcopyrite is characterized by high concentrations of Se, Sn, In, As, Ag and Pb, and sphalerite is enriched in Co, Ga, Ge, As, Ag, Cd, Sb, and Pb. The ^{230}Th/U dating data suggested five different mineralization periods during 4,552–2,297 years. Apart from the top and bottom, the core exhibited obvious characteristics of gradual accumulation of mineralization. Results revealed that the variations in the elemental contents of different layers and different types of pyrite were controlled by the interaction of seawater and hydrothermal fluids within the sulfide mound over five different mineralization periods. Compared with other hydrothermal fields on other mid-ocean ridges, DHF pyrite is generally enriched in Zn, Pb, As, Ag, Cd, Mo, and Sb, which might reflect shallow subsurface mixing during different periods of hydrothermal activity.

KEYWORDS

sulfide drill core, trace metal geochemistry, ^{230}Th/U dating, evolution process, Southwest Indian ridge

1 Introduction

Submarine hydrothermal sulfide deposits have been discovered in different tectonic settings, including mid-ocean ridges, back-arc spreading centers and volcanic arcs (Hannington et al., 2005). Approximately 57% of such hydrothermal sulfide deposits are formed in mid-ocean ridge environments (https://vents-data.interridge.org). The scale of the distribution of hydrothermal sulfide deposits is greater on the slow and ultraslow spreading ridges because of the longer duration of hydrothermal activity, deeper magma chambers, and development of detachment faults (Fouquet et al., 1997; Hannington et al., 2011; Petersen and Hein, 2013; Tao et al., 2020). Since 2011, a series of cruises have been conducted by the China Ocean Mineral Resources Research & Development Association to collect samples and data from the Southwest Indian Ridge (SWIR). The geochemical characteristics of ore-forming elements, sources of ore-forming materials, forms of occurrence of precious metals, precipitation mechanisms, and physicochemical conditions of ore formation have been studied using surface sulfide samples obtained from the SWIR (Münch et al., 2001; Tao et al., 2011; Nayak et al., 2014; Zeng et al., 2017; Liao et al., 2018; Cao et al., 2021; Yuan et al., 2018a, Yuan et al., 2018b).

The Duanqiao hydrothermal field (DHF) is located on the new axial volcanic ridges of the ultraslow spreading SWIR. Hydrothermal fields on axial volcanic ridges generally contain only small-scale sulfide deposits, but preliminary exploration of the DHF has revealed that its scale of distribution is larger than that of most hydrothermal fields on either fast- or slow- spreading ridge axis (Hannington et al., 2011; German et al., 2016; Yang et al., 2023). However, its potential mineral resources are lower than those of some ore deposits developed on the northern Mid-Atlantic Ridge, e.g., s Puy des Folles, and Krasnov hydrothermal fields (Cherkashov et al., 2023). Previous studies have demonstrated that a sufficient heat source, stable channels, and alternating intensity of magma supply on a ridge axis might explain the large-scale mineralization in the DHF (Li et al., 2015; Jian et al., 2017; Tao et al., 2020; Chen et al., 2021). Earlier analyses revealed that the contents of Pb (263-2630 ppm), As (234-726 ppm), Sb (7.32-44.3 ppm), and Ag (35.2 to >100 ppm) in the DHF surface sulfides are relatively high, and substantially higher than those of the Longqi, Yuhuang, and Tianzuo hydrothermal fields on the SWIR and those of most magmatic hydrothermal fields on slow- spreading ridge axis (Fouquet et al., 2010; Yang et al., 2023). The current understanding of sulfide mineralization associated with the SWIR is based on the analysis of surface samples, but the metallogenic processes occurring below the seafloor surface have yet to be investigated.

Through analysis of sulfide drilling samples collected by the International Ocean Discovery Program and Blue Mining programs, the three-dimensional structure and composition of sulfide deposits can be obtained. The mineralization process occurring below the surface of the seafloor in a hydrothermal field has an important influence on the distribution and enrichment of elements. Current research on drilling samples is limited to the TAG and Snake Pit hydrothermal fields of the Mid-Atlantic Ridge, and the Bent Hill hydrothermal zone of the Middle Valley (Petersen et al., 1998, Petersen et al., 2000; You and Bickle, 1998;Zierenberg et al., 1998). The internal structure of the Semenov-5 hydrothermal field has also been studied through mineralogical and chemical analyses of different parts of the sulfide deposits (Firstova et al., 2022). The formation of submarine hydrothermal sulfide proceeded via periodic mineralization, and its accumulation process included chimney growth, collapse accumulation, and hydrothermal fluid filling and metasomatism in open spaces (Humphris et al., 1995; Zierenberg et al., 1998; Graber et al., 2020). In recent years, the application of *in situ* and high-spatial-resolution mineral chemical analysis techniques has led to important advances in both elucidation of element migration and enrichment mechanisms, and determination of the mode of occurrence of modern and ancient seafloor hydrothermal sulfides (Butler and Nesbitt, 1999; Choi et al., 2023; Cook et al., 2009; Keith et al., 2016a; Li et al., 2018, Li et al., 2024; Ren et al., 2021; Wohlgemuth-Ueberwasser et al., 2015; Wang et al., 2017; Yuan et al., 2018a, Yuan et al., 2018b). The study of hydrothermal sulfide chronology is vitally important in determining the history of the formation and evolution, mineralization scale, accumulation rate, and hydrothermal activity of sulfide deposits (Lalou and Brichet, 1982, Lalou and Brichet, 1987; Lalou et al., 1993, Lalou et al., 1996; Kuznetsov et al., 2015; Cherkashov et al., 2017; Jamieson et al., 2014, Jamieson et al., 2023).

This study used drill cores of surface sulfide mounds collected from the DHF to systematically analyze the sulfide mineralogy, bulk geochemistry, and *in situ* geochemical compositions of pyrite, chalcopyrite, and sphalerite and to perform ^{230}Th/U dating. Based on the results, the mineralization characteristics and the controlling factors on trace elements were investigated. The findings of this study support systematic comprehension of both the metallogenic element enrichment mechanism and the evolution process of the DHF from a spatiotemporal perspective.

2 Geological setting

The SWIR extends from the Bouvet Triple Junction in the South Atlantic Ocean to the Rodrigues Triple Junction in the Indian Ocean (Figure 1A). It is characterized by ultraslow spreading, with a full spreading rate of 1.4–1.8 cm/yr (Dick et al., 2003). The DHF is located between the Indomed and Gallina transfer faults, with the central volcano at 50°28′ E in segment#27 (Figure 1B) (Cannat et al., 1999). The SWIR is expanding symmetrically, and the oceanic crust is 9.5–10.2 km thick, i.e., approximately 3 km thicker than the average thickness of oceanic crust (Li et al., 2015; Jian et al., 2017; Liu and Buck, 2018). The DHF is on the axial ridge high at a depth of approximately 1,700 m (Tao et al., 2012). It is a typical magma-supply type hydrothermal field, evidently different from the Longqi and Yuhuang hydrothermal fields that have poor magma supply and are controlled by detachment faults (Tao et al., 2012; Tao et al., 2020; Yu et al., 2021). The sufficient magma supply, alternating intensity of magmatic activity, and large numbers of normal faults and tectonic fractures suggest that the DHF is well suited to the development of sulfide deposits.

The DHF was discovered in 2009 during the DY20 cruise. Since then, several subsequent cruises conducted in this area have

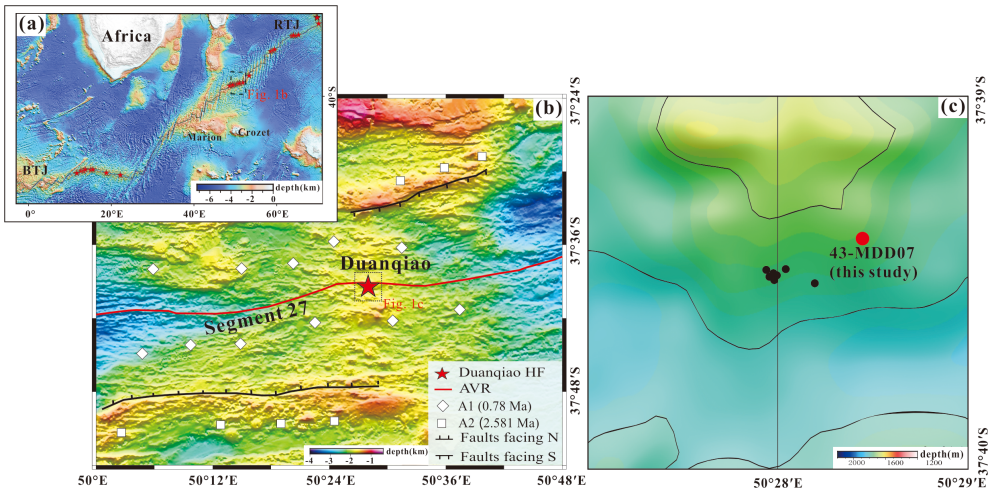

FIGURE 1
Geological setting and bathymetry of the study area. **(A)** Geotectonic setting and topography of the SWIR. **(B)** Shipboard bathymetric map of the segment #27 of the SWIR (Revised form Yang et al., 2023). **(C)** The sulfide drilling locations. The black and red dots represent all the drilling locations. The red dot represents the sample station discussed in this paper. All the normal fault line and the age of ocean crust in panel **(B)** are from Chen et al. (2021). The red stars in panel **(A)** represent the hydrothermal fields along the SWIR. Abbreviations: BTJ, Bouvet Triple Junction; RTJ, Ridge Triple junction, AVR, Axial volcano ridge.

collected abundant geological samples that include basalts, sulfides, and opals (Tao et al., 2012). Preliminary studies of the DHF sulfide distribution revealed that it consists of two main areas of sulfide deposition.

Massive sulfides and relict chimney fragments are found on the surface or adjacent to the mound. The host rocks are basalts and basaltic breccias, whereas sediments are distributed along slopes or in areas of low terrain (Yang et al., 2023). During the DY30, DY34, DY43 and DY65 cruises, sulfide drilling sampling was performed and eight drilling cores were obtained (Figure 1C). The maximum drilling depth was 10 m, which initially revealed the mineralized zonation characteristics of the sulfide in the area.

3 Samples and analytical methods

3.1 Sample collection and description

The representative DHF sulfide samples (from drill core 43-MDD07) used in this study were collected from the sulfide mound using shallow drilling equipment during the DY43 cruise of R/V *Xiayanghong* 10 in 2017. The entire core used in this study comprises Fe-rich sulfides. The drilling depth was 2 m, but the obtained sample length was 99 cm, the core recovery was 49.5%. Owing to core collapse, only an 8-cm sample of sulfide breccia was obtained from the top 1m. And 91-cm sample of sulfides was obtained from the bottom 1m (Figure 2A). Of the bottom 1 m, the uppermost part of the drill core comprises sulfide breccias of pyrite, marcasite, sphalerite, amorphous silica and chalcopyrite. The underlying mineralized sulfide comprises zones of massive pyrite – marcasite – sphalerite – silica (108-117 cm), massive pyrite – chalcopyrite – sphalerite – marcasite – silica (117-151 cm), massive pyrite – chalcopyrite – sphalerite – silica (151-173 cm), massive pyrite – sphalerite – marcasite – silica (173-193 cm), massive pyrite – silica – marcasite (193-199 cm) (Figures 2B–F).

3.2 Analytical methods

Mineral and textural analyses were conducted at the Key Laboratory of Submarine Geosciences (Ministry of Natural Resources, Hangzhou, China). All samples were examined as polished thin sections using a reflected and transmitted light polarizing microscope (Zeiss AXIO Scope A1).

Micro-drilling was also conducted at the Key Laboratory of Submarine Geosciences using Proxxon MICROMOT drilling equipment to obtain geochemical and chronological subsamples. Thirteen micro-drilled subsamples were selected for determination of bulk geochemical concentrations at the ALS Laboratory in Guangzhou (China). Trace elements were analyzed using an inductively coupled plasma mass spectrometer (ICP-MS; POEMS III ICP-MS, Thermo Jarrell Ash Ltd., USA). The analytical error of the trace elements data was <0.05%.

Trace element concentrations of pyrite, sphalerite and chalcopyrite from the DHF were determined with a laser ablation (LA)-ICP-MS at Nanjing FocuMS Technology (China), using a Teledyne Cetac Technologies Analyte Excite LA system (Bozeman, Montana, USA) coupled to an Agilent Technologies 7700x quadrupole ICP-MS (Hachioji, Tokyo, Japan). A 193 nm ArF excimer laser, homogenized by a set of beam delivery systems, was focused on mineral surface with a fluence of 6.06J/cm^2. The ablation protocol employed a spot diameter of 40 μm at a 6-Hz repetition rate for 40 s (equating to 280 pulses). Further details of the operating conditions and methods used can be found in Hou et al. (2009) and Gao et al. (2013). The United States Geological Survey polymetallic sulfide pressed pellet *MASS-1* and synthetic

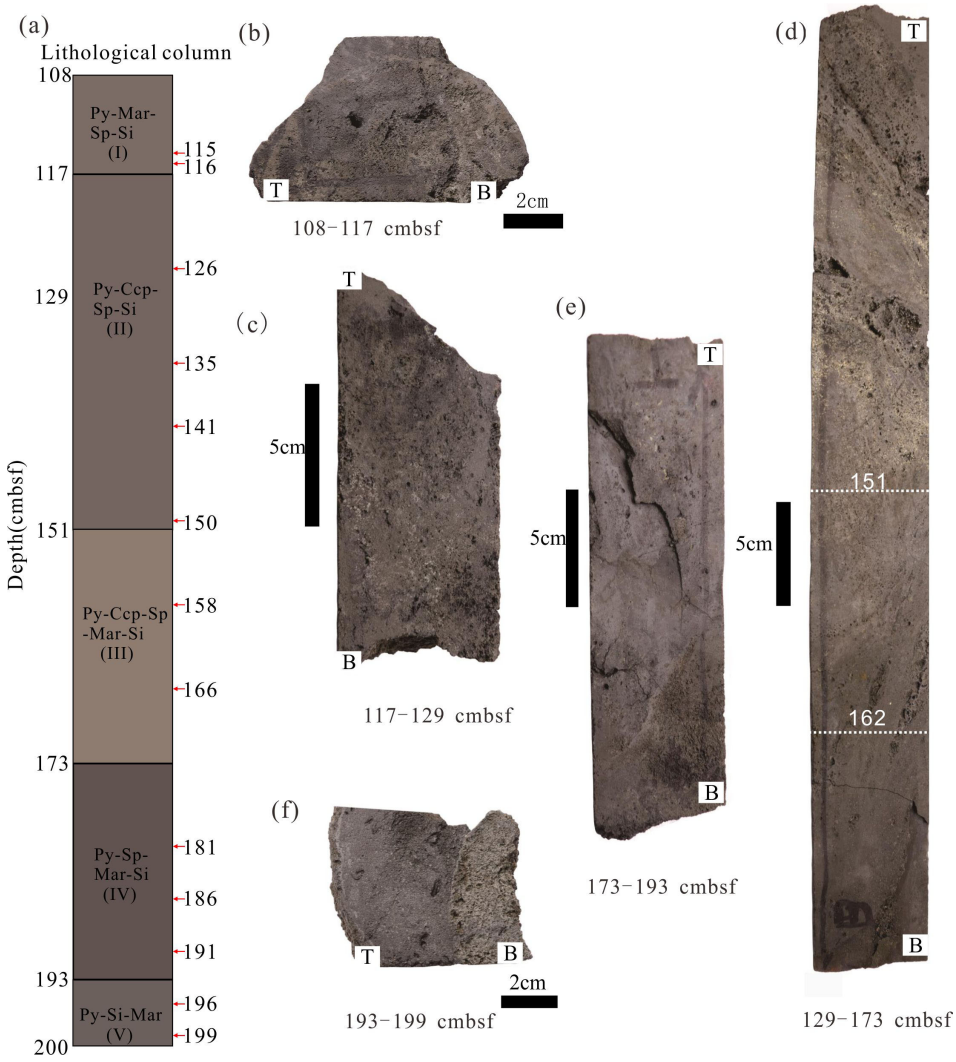

FIGURE 2
Photographs of cross sections of drill core (43-MDD07) from the DHF and original samples used for analysis. **(A)** the lithological column of the core (unit: cm); **(B)** massive pyrite – marcasite – sphalerite – silica; **(C)** massive pyrite – chalcopyrite – sphalerite – marcasite – silica; **(D)** massive pyrite – chalcopyrite – sphalerite – marcasite – silica and massive pyrite – chalcopyrite – sphalerite – silica; **(E)** massive pyrite – sphalerite – marcasite – silica; **(F)** massive pyrite – silica – marcasite. bsf: below seafloor. The red arrow in Figure a represents the sampling location for bulk chemistry and chronology analysis. T and B in Figure b-f represents top and bottom respectively. Mineral abbreviations: Py, pyrite; Ccp, chalcopyrite; Sp, sphalerite; Mar, Marcasite; Si, silica.

basaltic glasses *GSE-1G* were used as standards to calibrate the elements contents of the sulfides. Raw data reduction was performed offline by ICPMSDataCal software using a 100%-normalization strategy without applying an internal standard (Liu et al., 2008). Precision and accuracy were better than ± 10%.

Seven micro-drilled subsamples were selected for ^{230}Th/U dating. The chemical separation of U and Th, together with the MS analysis, were performed at the Uranium Series Chronology Laboratory of the Institute of Geology and Geophysics, Chinese Academy of Sciences. The chemical separation procedures and MS analysis adopted were similar to those described in Yang et al. (2017) and Wang et al. (2021). A standard (GBW04412) was analyzed to verify the accuracy and precision of the ^{230}Th/U dating, providing precision better than 95%. The best age accuracy can be better than 5‰ (Cheng et al., 2013). All the results were within 2σ uncertainty, unless indicated otherwise.

4 Results

4.1 Mineralogy and paragenesis of sulfides

From the microscopically observed characteristics of the drilling core in different mineralized zones, it was determined that the core comprised mainly Fe-rich sulfide, and that the mineral assemblage was pyrite, sphalerite, chalcopyrite, marcasite, and amorphous silica. Among those minerals, pyrite was most abundant, although sphalerite and chalcopyrite were also common.

Pyrite was found present throughout the core. Four paragenetic types with distinct textures were recognized: granular pyrite (Py1), late overgrowths of coarse granular pyrite (Py2), colloform and/or dendritic pyrite (Py3), and euhedral pyrite (Py4). Granular Py1 and colloform Py3 were common through the core. Granular Py1, coarse-grained Py2 and chalcopyrite particles were found in the inner wall of the hydrothermal channel, and the pyrite shows obvious growth zoning (Figure 3A). Colloform Py3 and marcasite were also common in the top and the bottom parts of the core. Colloform Py3 was often associated with marcasite (Figure 3G). Colloform Py3 also often surrounded by

Sphalerite in the massive Py-Sp layer of the core (129–151 cmbsf) (Figure 3E). Dendritic pyrite, which generally occurred because of sphalerite intergrowth, was common in the silicified Py layer (173–193 cmbsf) (Figure 3G). Early granular Py1 was replaced by late recrystallized coarse granular Py2 and disseminated with globular Py3 in amorphous silica (173–193 cmbsf) (Figure 3H). Euhedral Py4 exhibited sharp, well-defined crystal boundaries and discrete well-formed euhedral shapes, and it was commonly replaced by chalcopyrite in the massive Py-Sp layer of the core (162–173 cmbsf) (Figure 3F).

Sphalerite often occurred with massive textures in most samples of the core. In the upper part and the lower-middle part of the core, the content of sphalerite was obviously higher than that in the central part. Sphalerite (Sp2) surrounding pyrite indicates a precipitation after pyrite and can occur as laminated colloform textures in the inner wall of the fluid conduit in the middle part of the core (151–162 cmbsf) (Figure 3E). In the top of the core (108–117 cmbsf), massive sphalerite (Sp1) is commonly associated with colloform Py3 (Figure 3C). Massive sphalerite often replaced chalcopyrite and pyrite (Figure 3I) and was found to have a mutual replacement relationship with pyrite (Figure 3G) in the middle and bottom of the core.

Chalcopyrite was often found with granular textures, and it occurred mainly as a replacement of sphalerite and pyrite (Figures 3D, E, I). Chalcopyrite was also often found in the inner wall of the fluid conduit in the top of the core (Figure 3A). In the central part of the core, the content of chalcopyrite was higher than that in the in the upper and lower parts of the core.

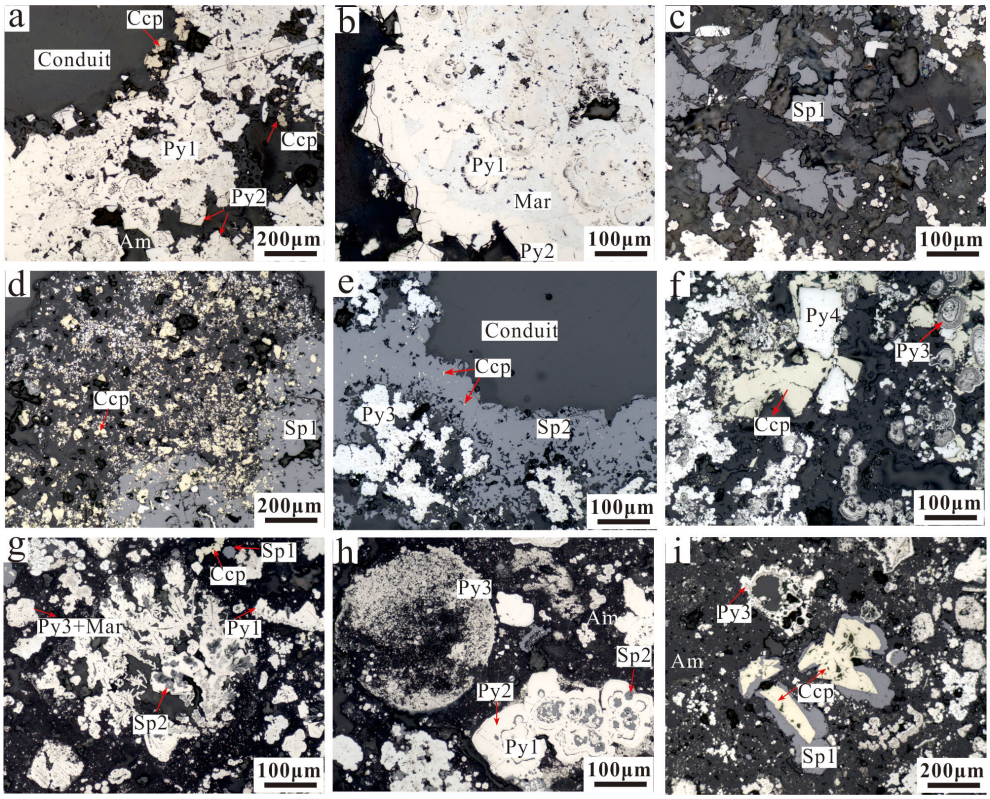

FIGURE 3
Representative photomicrographs of the sulfide core samples of the DHF. **(A)** The coarse-grained pyrite and chalcopyrite particles were found in the inner wall of the hydrothermal channel, the pyrite multiple generations of grained Py1 and Py2 (108– 117 cmbsf); **(B)** Marcasite was often associated with grained Py1 and Py2 (108–117 cmbsf); **(C)** Massive sphalerite (108–117 cmbsf); **(D)** Chalcopyrite was dispersed in massive sphalerite (Sp1) and pyrite (129–151 cmbsf); **(E)** Sphalerite was distributed around the hydrothermal channel and associated with pyrite 3 (151–162 cmbsf). **(F)** Chalcopyrite was filled in the gap of colloform pyrite (Py3) and replaced euhedral pyrite (Py4) (162–173cmbsf); **(G)** Dendritic pyrite (Py3) generally occurred as colloform sphalerite (Sp2) replacement structure (173–193 cmbsf); **(H)** Early colloform pyrite was replaced by late recrystallized pyrite and disseminated with globular pyrite in amorphous silica (173–193 cmbsf); **(I)** Massive sphalerite (Sp1) replaced chalcopyrite and recrystallized pyrite replaced early colloform pyrite (Py3) (173–193 cmbsf). Mineral abbreviations: Py, pyrite; Ccp, chalcopyrite; Sp, sphalerite; Mar, marcasite; Am, amorphous silica.

Marcasite was often associated with grained Py1, Py2 and colloform Py3 in the upper and bottom layer of the core (Figures 3B, G).

4.2 Bulk chemistry

The geochemical compositions of the samples, presented in Table 1, were found characterized by high Fe content (19.31-41.75 wt.%, avg. 26.23 wt.%, n=13) and variable Zn content (0.47–19.54 wt.%, avg. 5.17 wt.%). The Zn content in the 126- and 186-cm layers was evidently higher than that in other layers. Compared with Fe and Zn, the content of Cu was low (0.11–8.69 wt.%, avg. 2.02 wt.%, n=13). The Pb, As, and Cd contents were 142.45–755.24 ppm (avg. 235.17 ppm), 150.13–797.20 ppm (avg. 314.38 ppm), and 25.17–920.01 ppm (avg. 212.09 ppm), respectively. The Co, Mo, and Mn contents were 21.25–213.68 ppm (avg. 87.06 ppm), 37.53–161.24 ppm (avg. 79.77 ppm), and 25.17–124.76 ppm (avg. 65.03 ppm), respectively. In contrast, the contents of Ag (1.83–50.35 ppm, avg. 18.73 ppm, n = 9), Sb (17.00–85.36 ppm, avg. 34.46, n = 8), Ni (4.71–14.25 ppm, avg. 8.10 ppm, n =11), and Se (20.85–43.08 ppm, avg. 30.14 ppm, n = 5) were relatively low compared with those of Pb, As, and Cd. The contents of trace elements showed considerable variation with depth. It is evident from Figure 4 that the variations trend in the contents of Cu and Co were similar. And the Fe, Pb, Ag, and As presented the same variations trend. However, it is notable that at the bottom of the core, the Fe content exhibited a maximum, the Cu and Co contents were markedly reduced, and the Pb, Ag, and As contents were particularly high (Table 1).

4.3 LA-ICP-MS data

4.3.1 Pyrite

A total of 144 spot analyses were performed on different types of pyrite at different depths within the core. The range of trace element concentrations was found to fall into five main groups: <1, 1–10, 10–100, 100–1000, and >1000 ppm (Table 2). Elements found to have the highest concentration were Cu (avg. 1,237 ppm) and Zn (avg. 4,486 ppm). The average contents of Co, As, and Pb (i.e., 151, 417, and 992 ppm, respectively) were in the range 100–1,000 ppm with notable outliers (up to 1,669 ppm Co, 3,998 ppm As, and 6,862 ppm Pb). The average contents of Mn, Mo, Ag, Cd, Sb, and Tl were in the range 10–100 ppm with notable outliers (up to 1027 ppm Mn, 572 ppm Mo, 474 ppm Ag, 1283 ppm Cd and 884 ppm Tl). The average contents of V, Cr, Ni, Ga, Ge, Se and In were in the range 1–10 ppm (up to 257 ppm Ga, 376 ppm Ge and 144 ppm Se). The average contents of Ti, Te, Ba, W, Au and Bi were all <1 ppm.

The contents and compositions of the trace elements in different types of pyrite at different depths within the core were evidently different (Supplementary Table S1). The downhole distribution of selected trace elements is shown in Figure 5. The average values of Co, Se, As, Pb, and Cd of pyrite showed a trend of gradual decline. However, the contents of Co and Se were relatively high in the 162–173 cmbsf layer, whereas the content of Cd was relatively high in the 173–193 cmbsf layer. The average values of Ag in the pyrite showed a trend of gradual increase, whereas those of Mo and Au showed a tendency to first increase and then decline.

4.3.2 Chalcopyrite

Twenty-three spot analyses were conducted on the granular chalcopyrite selected from different depths within the core (Supplementary Table S2). The element with the highest concentration was Zn (avg. 840 ppm). The average contents of Ag (avg. 149 ppm, up to 258 ppm) and Cd (avg. 129 ppm, up to 2,055 ppm) were in the range 100–1000 ppm. The average contents of Ga, Ge, As, Se, In, Sb, and Pb were in the range 10–100 ppm. The Pb content was mostly low, ranging from below the detection limit to 74.1 ppm, however, some individual points showed that Pb enrichments to 172 and 698 ppm. The average contents of Ti, Cr, Mn, Co, Mo, Sn, and W were in the range 1–10. The average contents of V, Ni, Te, Ba, Au, Tl, and Bi were all <1 ppm (Table 2).

4.3.3 Sphalerite

Thirty-six sphalerite grains (including 4 colloform sphalerite and 32 massive sphalerite) were analyzed to identity the trace elements (Supplementary Table S3, Table 2). Elements with the highest concentrations were Cu (avg. 5,494 ppm) and Fe (24,461 ppm). Additionally, sphalerite was highly enriched in Cd (avg. 2,961 ppm, up to 13,272 ppm) and Pb (avg. 1,221 ppm, up to 13,272 ppm). The average contents of Ga (avg. 303 ppm, up to 1317 ppm), Ge (avg. 201 ppm, up to 596 ppm), As (avg.162 ppm, up to 890 ppm), Ag (avg. 219 ppm, up to 1044 ppm), Sb (avg. 241 ppm, up to 1006 ppm) were in the range 100–1000 ppm. The average contents of Mn and Co were in the range 10–100 ppm, and the average contents of Se, Mo, and In were in the range 1–10 ppm. The average contents of V, Cr, Ni, Sn, Te, Ba, W, Au, Tl, and Bi were all <1 ppm. Compared with pyrite and chalcopyrite, sphalerite was found more enriched in Ga, Ge, Cd, Ag, Sb, and Pb (Table 2).

4.4 *U-Th isotope ratios and U-Th ages*

The U–Th isotope systematics of the samples are presented in Table 3. The U concentrations ranged from 237 to 1871 ppb, with an average of 723.9 ppb. The Th concentrations ranged from 300 to 5795 ppt, with an average of 1732.4 ppt. The U content was extremely high in 186cm layer of the core (1841 ± 4.2 ppb). The measured $\delta^{234}U$ values ranged between 86.6 ± 2.0 and 142.4 ± 2.4 and the corrected $\delta^{234}U_{initial}$ ranged between 108 ± 3 and 144 ± 2 (Table 3). The formation age of the whole core was found to be relatively young. The corrected ^{230}Th age varied from 2297 ± 52 to 4552 ± 60 yrs. The metallogenic age of the core exhibited a trend of gradual increase from the surface to the bottom (Figure 6A). The age distribution bar chart is presented in Figure 6B.

5 Discussion

5.1 Paragenesis and spatial variation of mineralization

The microscope observations and mineralization zonation sequence of the core revealed substantial differences in the

TABLE 1 Bulk chemistry of sulfide drilling samples from the DHF.

Elements	Fe	Cu	Zn	S	Pb	Co	Ag	As	Cd	Mo	Mn	Sb	Ni	Se	Tl	V	Ga	Hg
Unit	%	%	%	%	ppm	ppm	ppm	ppm	ppm	ppm	ppm	ppm	ppm	ppm	ppm	ppm	ppm	ppm
Detection limit	0.01	0.01	0.01	0.01	0.02	0.01	0.004	0.01	0.01	0.01	0.01	0.04	0.01	0.05	0.1	0.01	0.05	0.02
Sample depth (cmbsf)																		
115	32.52	0.31	4.50	36.21	197.51	69.50	1.83	296.27	168.25	120.70	102.41	21.95	7.32	–	73.15	7.32	25.60	7.32
116	25.31	0.15	7.66	27.76	134.49	134.49	–	259.37	393.85	57.64	62.44	33.62	9.61	–	48.03	–	62.44	–
126	23.53	0.11	16.29	25.70	145.83	40.23	–	226.28	502.85	45.26	50.28	35.20	–	–	50.28	–	30.17	10.06
135	28.21	1.29	1.02	31.95	170.40	85.20	29.35	402.34	28.40	52.07	42.60	–	4.73	33.13	47.33	23.67	–	–
141	27.26	8.69	0.47	29.30	142.45	213.68	2.85	218.42	33.24	71.23	33.24	–	14.25	28.49	–	47.48	–	–
150	25.22	5.03	0.61	28.03	163.64	155.24	2.94	151.05	25.17	142.66	25.17	20.98	12.59	25.17	–	58.74	–	–
158	30.52	1.34	0.95	34.47	170.02	21.25	5.95	573.82	29.75	72.26	51.01	17.00	8.50	–	42.50	46.76	–	–
166	21.40	0.93	2.26	25.82	259.12	76.78	27.35	148.75	62.38	47.98	124.76	–	4.80	–	95.97	4.80	–	–
181	19.31	0.79	3.01	22.02	191.83	66.72	5.84	150.13	112.59	37.53	100.08	–	8.34	20.85	83.40	4.17	–	–
186	20.25	2.75	19.54	22.05	218.15	–	–	360.42	920.01	161.24	37.94	85.36	4.74	–	–	61.65	109.07	9.48
191	22.28	3.96	8.38	24.58	221.35	–	–	273.16	390.89	127.16	42.39	37.68	4.71	–	–	47.10	61.22	9.42
196	23.45	0.61	1.28	26.32	287.17	52.65	42.12	229.74	47.86	38.29	110.08	23.93	9.57	43.08	47.86	14.36	–	–
199	41.75	0.34	1.29	46.57	755.24	41.96	50.35	797.20	41.96	62.94	62.94	–	–	–	–	–	–	–

cmbsf. cm below seafloor.

10.3389/fmars.2024.1538022

10.3389/fmars.2024.1538022

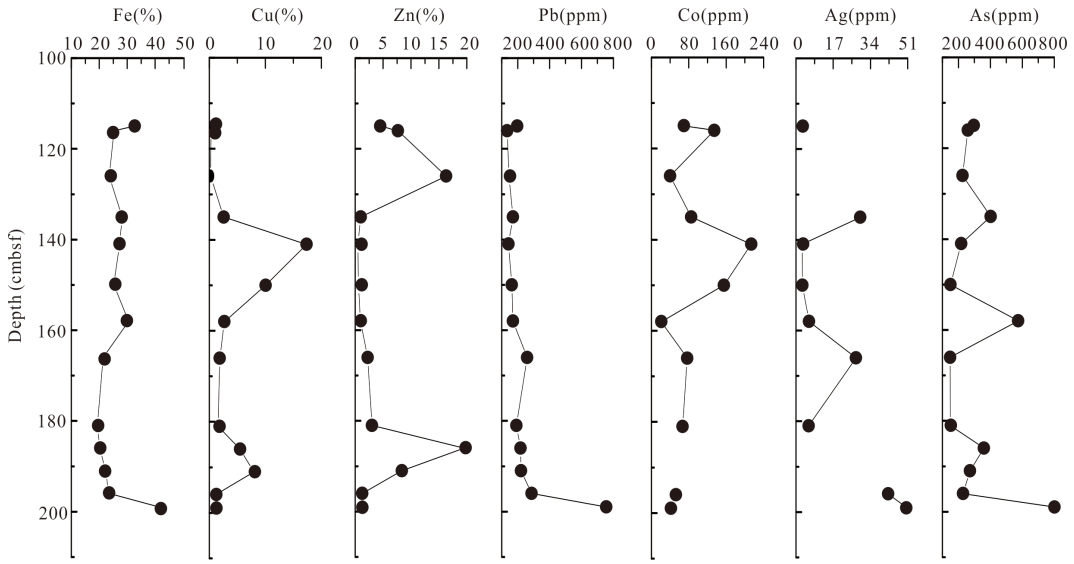

FIGURE 4
The element contents distribution of the drill core of 43-MDD07 (cmbsf: below seafloor).

TABLE 2 Summary of LA-ICP-MS data (in ppm) for samples in this study.

All data in ppm	Ti	V	Cr	Mn	Fe	Co	Ni	Cu	Zn	Ga	Ge	As	Se
Pyrite													
Minimum	0.001	0.118	0.013	0.074	na	0.090	0.005	11.6	0.799	0.001	0.767	6.22	0.002
Maximum	10.4	28.5	23.4	1027	na	1670	15.4	10814	25302	257	376	3998	144
N	141	144	123	143	na	143	140	139	141	142	144	144	144
Mean	0.932	3.67	1.89	94.4	na	151	3.30	1237	4486	4.89	8.615	417	9.71
Median	0.621	1.75	1.07	63.0	na	42.6	2.87	649	2309	0.71	3.574	257	1.45
Chalcopyrite													
Minimum	0.114	0.019	0.087	0.162	na	1.981	0.128	na	71.4	0.133	0.071	0.375	5.01
Maximum	24.1	0.686	4.61	16.5	na	53.588	2.929	na	5857	363.446	118.487	296.014	111
N	19	19	14	19		23	13		20	23	22	17	23
Mean	2.43	0.167	2.18	2.77	na	8.823	0.669	na	840	27.597	13.741	48.476	37.2
Median	1.20	0.141	1.87	1.184	na	7.104	0.425	na	146	2.631	2.394	13.535	30.1
Sphalerite													
Minimum	0.017	0.002	0.047	3.39	3598	0.003	0.004	192	na	0.002	5.86	2.71	0.014
Maximum	1.40	0.687	1.518	140	131063	294	0.707	57202	na	1317	569	890	7.23
N	35	33	21	36	36	31	25	36		36	36	36	36
Mean	0.548	0.106	0.528	31.8	24461	22.7	0.148	5494	na	304	201	162	1.85
Median	0.497	0.859	0.480	17.4	10168	0.201	0.079	3126	na	133	171	73.9	1.53
	Mo	Ag	Cd	In	Sn	Sb	Te	Ba	W	Au	Tl	Bi	Pb
Pyrite													
Minimum	0.231	0.008	0.006	0.001	0.006	0.045	0.005	0.003	0.002	0.004	0.001	0.001	0.049

(Continued)

10.3389/fmars.2024.1538022

TABLE 2 Continued

All data in ppm	Ti	V	Cr	Mn	Fe	Co	Ni	Cu	Zn	Ga	Ge	As	Se
Pyrite													
Maximum	572	474	1283	38.9	24.4	121	0.437	12.4	9.77	4.60	884	0.253	6862
N	144	144	138	136	128	143	73	131	141	136	134	81	144
Mean	64.1	91.3	34.3	1.25	1.31	14.9	0.102	0.373	0.607	0.572	98.2	0.010	992
Median	57.1	51.0	5.956	0.09	0.314	4.36	0.082	0.126	0.233	0.222	60.7	0.004	657
Chalcopyrite													
Minimum	0.001	30.9	0.256	5.16	0.815	0.001	0.127	0.014	0.027	0.001	0.009	0.001	0.007
Maximum	29.0	258	2055	53.5	20.7	116	0.969	1.00	16.6	0.128	2.94	0.116	689
N	20	23	23	23	23	18	9	13	21	18	14	15	20
Mean	2.46	149	129	16.6	5.84	13.1	0.520	0.31	1.21	0.052	0.39	0.023	58.0
Median	0.516	147	1.334	11.4	4.01	1.30	0.503	0.148	0.206	0.042	0.061	0.020	11.1
Sphalerite													
Minimum	0.005	12.3	152	0.001	0.056	1.55	0.016	0.004	0.004	0.008	0.003	0.001	26.5
Maximum	16.2	1044	13272	19.4	3.56	1007	0.999	0.351	1.58	1.52	14.0	0.051	5918
N	32	36	36	33	33	36	20	27	34	32	34	25	36
Mean	1.45	220	2961	1.76	0.701	241	0.120	0.059	0.149	0.197	0.689	0.009	1221
Median	0.132	138	2700	0.052	0.263	179	0.079	0.023	0.047	0.061	0.043	0.004	607

'na' indicates data is not applicable. Data are in ppm.

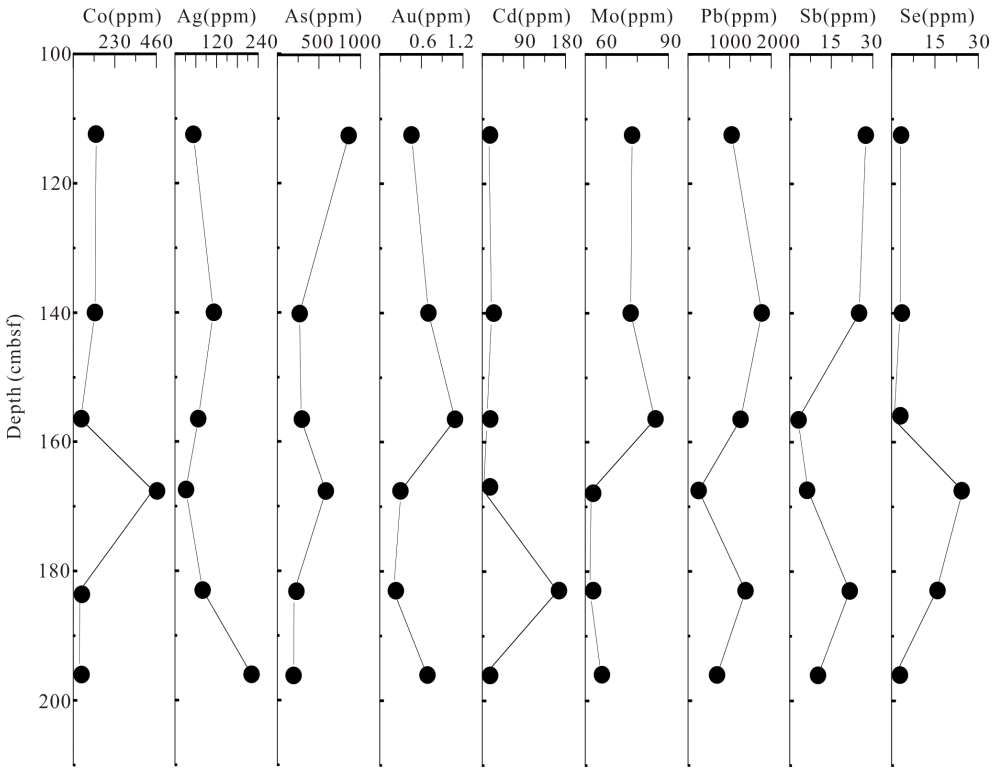

FIGURE 5
Downhole plots of the average concentrations of selected trace elements in all types of pyrite from the core.

10.3389/fmars.2024.1538022

TABLE 3 U and Th and ^{230}Th ages for sulfide drilling samples from the DHF.

Sample Number	^{238}U (ppb)		^{232}Th (ppt)		^{230}Th/^{232}Th (atomic x10^{-6})		d^{234}U* (measured)		^{230}Th/^{238}U (activity)		^{230}Th Age (yr) (uncorrected)		^{230}Th Age (yr) (corrected)		d$^{234}U_{initial}$** (corrected)		^{230}Th Age (yr BP)*** (corrected)	
115	237.0	± 0.0	1253	± 25	91.0	± 2.9	120.7	± 2.0	0.0315	± 0.0007	3104	± 70	2967	± 120	122	± 2	2949	± 120
126	375.0	± 0.5	300	± 6	485.8	± 14.6	109.9	± 2.1	0.0235	± 0.0005	2337	± 50	2316	± 52	111	± 2	2297	± 52
135	517.0	± 0.8	419	± 9	482.6	± 12.9	112.3	± 2.0	0.0237	± 0.0004	2350	± 40	2328	± 43	113	± 2	2309	± 43
150	272.8	± 0.3	733	± 15	204.0	± 7.5	106.7	± 2.4	0.0332	± 0.0010	3325	± 103	3254	± 114	108	± 2	3235	± 114
158	407	± 1	2148	± 43	115.0	± 5.0	106.6	± 4.3	0.0368	± 0.0014	3683	± 150	3545	± 179	108	± 4	3525	± 179
186	1871.0	± 4.2	5795	± 117	254.1	± 5.2	142.4	± 2.1	0.0477	± 0.0002	4650	± 23	4571	± 60	144	± 2	4552	± 60
196	1388	± 2	1479	± 30	405.5	± 11.0	109.3	± 2.1	0.0262	± 0.0005	2606	± 48	2578	± 52	110	± 2	2558	± 52
GBW04412	10278	± 14	5821	± 117	31226.7	± 631.2	852.4	± 2.2	1.0726	± 0.0021	87046	± 294	87038	± 294	1090	± 3	87017	± 294

*$\delta^{234}U = ([^{234}U/^{238}U]_{activity} - 1) \times 1000$. **$\delta^{234}U_{initial}$ was calculated based on ^{230}Th age (T), i.e., $\delta^{234}U_{initial} = \delta 234U_{measured} \times e^{\lambda 234 \times T}$. Corrected ^{230}Th ages assume the initial $^{230}Th/^{232}Th$ atomic ratio of 4.4 ±2.2 ×10-6. Those are the values for a material at secular equilibrium, with the bulk earth $^{232}Th/^{238}U$ value of 3.8. The errors are arbitrarily assumed to be 50%.
***B.P. stands for "Before Present" where the "Present" is defined as the year 2000 A.D.

mineralization features between the upper, middle, and bottom parts of the core (Figure 7). The upper part of the core (layer I) is dominated by granular pyrite, containing a small amount of colloform pyrite and late granular pyrite. The central part of the core (layer III) is dominated by euhedral pyrite, although the lower part is dominated by granular pyrite. The bottom of the core (layer V) is dominated by colloform pyrite. The marcasite content is relatively high, whereas the sphalerite content is low at the bottom of the core (layer V). The following paragenetic associations are apparent through the core: chalcopyrite + euhedral pyrite (Py4) → chalcopyrite + granular pyrite (Py1) + massive sphalerite (Sp1) → marcasite + coarse-grained pyrite (Py2) + massive sphalerite (Sp1) → later recrystallized pyrite (Py2) + colloform sphalerite (Sp2) → colloform pyrite (Py3) + marcasite → amorphous silica. Compared with the lower-middle part of the core, the upper-middle part of the core is notably enriched copper-rich minerals such as chalcopyrite, which might suggest a sustained influence by high-temperature hydrothermal activity (Hannington et al., 1995).

In the early stage, large quantities of high-temperature minerals formed, which included chalcopyrite and associated euhedral pyrite and euhedral sphalerite. The second stage and the low-temperature stage comprised the main ore-forming period of the core, when a large quantity of massive pyrite formed. The late stage is characterized by silicification caused by cooling of the hydrothermal fluids, resulting in precipitation of high quantities of amorphous silica.

5.2 Controlling factors on trace elements

5.2.1 Controls on trace elements in pyrite

Time-resolved LA-ICP-MS analytical signals revealed a uniform distribution of most elements such as Pb, Zn, Cu, Co, As, Sb, Mo, and Ag (Figures 8A, B) in the granular and colloform pyrite, indicating that these elements are present mainly in lattice substitutions rather than as inclusions of other sulfides. However, in the euhedral pyrite, the distribution trend of Cu revealed by the analytical signals was different from that of most other elements, suggesting that chalcopyrite inclusions might be present (Figure 8C).

Pyrite is widely distributed within hydrothermal deposits (Cook et al., 2009; Deditius et al., 2014; Keith et al., 2016a); it is the most common sulfide phase in seafloor massive sulfides and its precipitation can effectively control the distribution of many trace elements (Hannington, 2014; Keith et al., 2016a; Large et al., 2009; Maslennikov et al., 2009).Previous studies suggested that pyrites have crystallized at low temperatures are rich in Pb, As, Mn, Tl, Ag and Cd (Metz and Trefry, 2000; Maslennikov et al., 2009). Pyrites have crystallized at high temperatures are rich in Co, Se, Sn and Ni (Keith et al., 2016a; Maslennikov et al., 2009; Meng et al., 2020). Pyrite in the studied core is characterized by high contents of Mn, Co, As, Mo, Ag, Cd, Sb, Tl and Pb, and low contents of Ti, Ga, In, Sn, Ni, Se, Ba, W and Au (Table 2). This might suggest that the formation of the sulfide mound underwent a combined process of low-temperature and high-temperature mineralization.

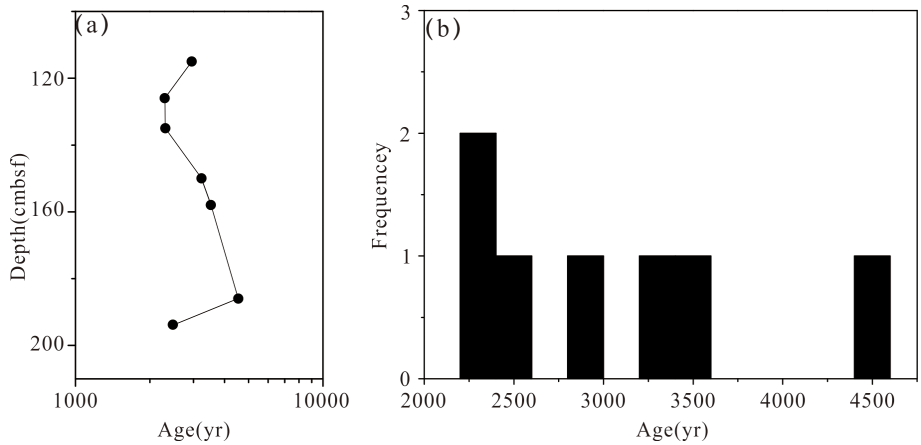

FIGURE 6
Age distribution of hydrothermal sulfide samples from the DHF, **(A)** The age distribution of the drill core of 43-MDD07 (cmbsf: below seafloor) **(B)** Age error bar chart frequency-age diagram.

The source of the relatively enriched As in pyrite is primarily the hydrothermal fluids, and a low-temperature environment is favorable for its occurrence (Huston et al., 1995; Metz and Trefry, 2000; Maslennikov et al., 2009; Wohlgemuth-Ueberwasser et al., 2015). The As contents in the granular pyrites in layer I are higher than other layers and there are no significant differences in As content among the pyrite types. The positive correlation found between As and Sb in the pyrite is possibly because metals such As and Sb are derived via sphalerite reactivation and might be influenced by zonal refining (Keith et al., 2016a). Thus, zone refining was likely a key factor controlling As and Sb behavior. At medium–high temperatures and in a reducing hydrothermal fluid, Mn has high solubility (Large et al., 2007; Maslennikov et al., 2009; Grant et al., 2018), the high concentrations of Mn in the granular pyrite of layer IV might reflect low fluid temperature and a relatively oxidized seawater environment. Although the low-temperature mineral galena was not detected in the DHF, the highest Pb content observed in granular pyrite replaced by sphalerite suggests the potential presence of Pb-mineral inclusions (Figure 8; Smith and Huston, 1992). This is because Pb is unlikely to substitute directly into the sulfide lattice due to its large ionic radius (George et al., 2018; Grant et al., 2018).

The range of concentration of Tl is large (0.001–884 ppm) with the maximum content found in the granular pyrite of the bottom layer of the core (Supplementary Table S1). Usually, Tl is preferentially enriched in sulfide under low-temperature conditions (approximately 100–250°C) and it has high solubility in high-temperature hydrothermal fluids (Huston et al., 1995; Wang et al., 2017; Maslennikov et al., 2009). Mo is mainly derived from seawater and its solubility in high-temperature fluid decreases sharply (Von Damm, 1995; Douville et al., 2002; Metz and Trefry, 2000). The solubility of Mo derived mainly from seawater is markedly reduced in a high-temperature fluid (Keith et al., 2016a). The range of concentration of Mo is very wide with the maximum content (572ppm) found in the granular pyrite in layer I (Supplementary Table S1) which suggests that this layer is formed under strong hydrothermal-fluid-seawater mixing conditions.

The Ag content is enriched in the colloform pyrite at the bottom of the core, whereas it is relatively low in the euhedral pyrite (Supplementary Table S1). The distribution of Ag might be related to seawater–hydrothermal fluid mixing front as Ag solubility decreases with increasing pH and decreasing temperature (Butler and Nesbitt, 1999; Wang et al., 2017). The Ni contents are very low in all types of pyrite. The depletion of Ni may also reflect the influence of fluid-seawater mixing (i.e., sub-seafloor mixing) (Gini et al., 2024). Consequently, the pronounced variation in the concentrations of Pb, Tl, Mn, As, Se, Ag, Sb, and Ni in pyrite throughout the core indicates that seawater mixing may have played a crucial role in fluctuating the physicochemical conditions of the hydrothermal fluid during the mineralization process.

5.2.2 Controls on trace elements in chalcopyrite

The ablation profiles of Cr, Mn, Co, Zn, Ge, As, Se, In, Sn, and Pb were relatively uniform (Figure 8D), indicating that these elements are present mainly as substitutions in the mineral lattice (e.g., In for Cu; Co and Sn for Fe, Huston et al., 1995). The ablation profile of Ag was different from that of other elements, and the appearance of sharp peaks might indicate that the effect of mineral inclusions containing the element of Ag (Huston et al., 1995; Grant et al., 2015; George et al., 2016).

Previous studies revealed that chalcopyrite is generally a relatively poor carrier of trace elements (Cook et al., 2011; George et al., 2016; Keith et al., 2016b). Compared with the contents of Sb, Co, Au, and Sn in chalcopyrite, those of Ag, Pb, Cd, and Se are relatively high. The Au content exhibits no correlations with Ag, Pb and Sb (Figures 9A–C). Typically, Au is common in medium-temperature associations, whereas Pb is common in lower-temperature associations (Halbach et al., 2003). The precipitation of Ag in chalcopyrite is sensitive to increasing pH (Tivey et al., 1999), and lower-temperature and stronger oxidation conditions

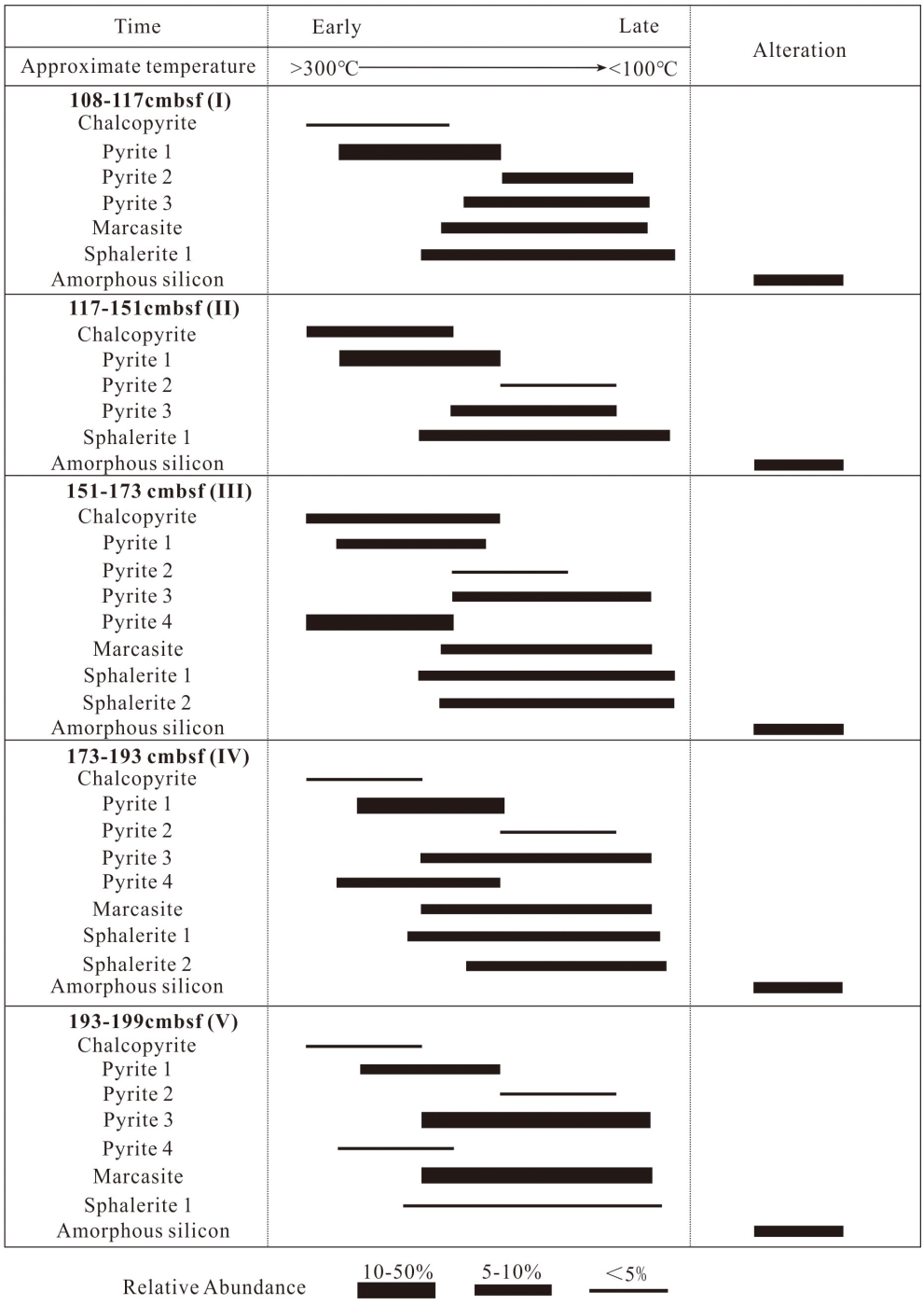

FIGURE 7
Paragenetic sequences of mineralization in sulfides from the DHF.

are conducive to Ag precipitation in micro- inclusions; conversely, high-temperature reducing conditions are conducive to Ag entering chalcopyrite in the form of lattice substitution (Huston et al., 1995; Grant et al., 2015).

The maximum content of Zn in the chalcopyrite reached 0.33 wt.%, and no Zn-bearing inclusions were observed (Shalaby et al., 2004; Helmy et al., 2014). Therefore, we conclude that Zn in the chalcopyrite exists mainly in solid solution. This is supported by the fact that Cd, a typical element in sphalerite, shows a positive correlation with Zn (Figure 9D). Meanwhile, Co and Se are indicators of fluid with high temperatures (Herzig et al., 1998; Grant et al., 2018). The Co contents are much lower than the average contents of seafloor sulfides (236 ppm, Hannington et al., 2005) and ferromanganese nodules on their surfaces (Ren et al., 2022, Ren et al., 2024). The Se content has no correlation with both Co and Sn (Figures 9E, F). Previous studies suggested that the content of Se can be controlled by the temperature of precipitation, with Se-rich and Se-poor chalcopyrite precipitating at high and

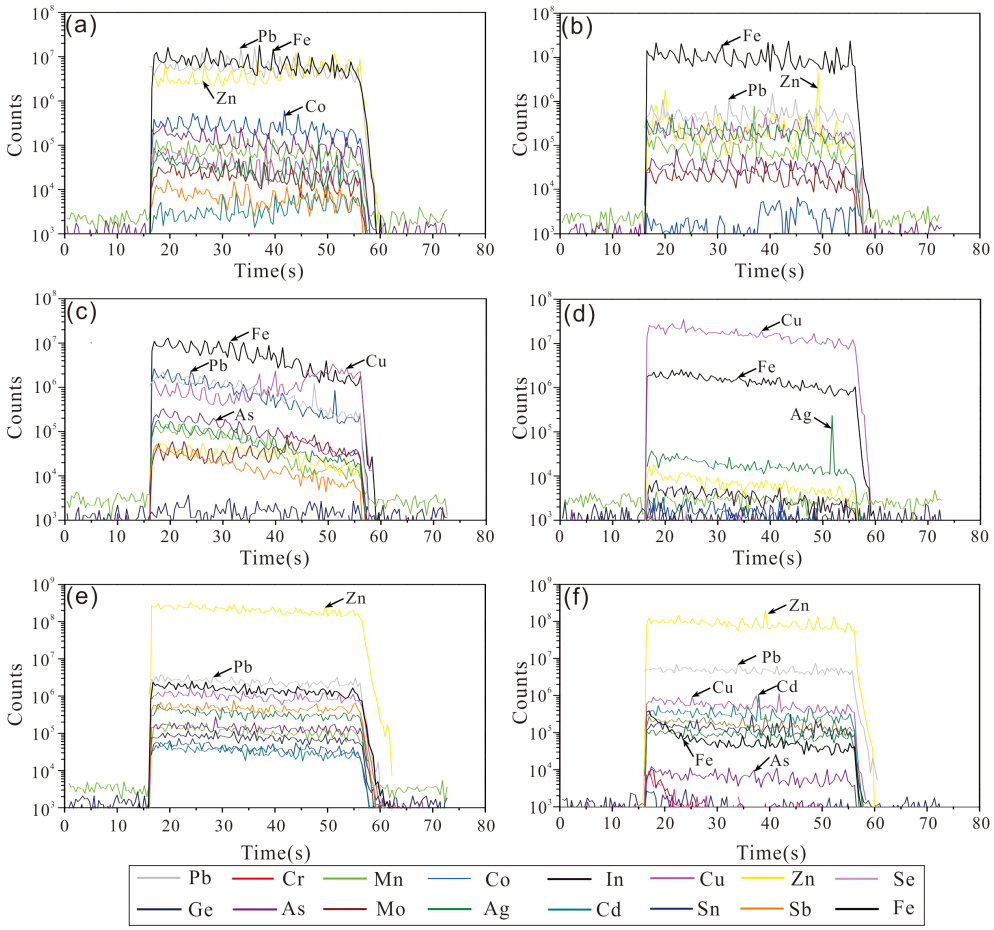

FIGURE 8
Examples of LA-ICP-MS profiles (time-resolved) for sulfides in the DHF field. **(A)** Ablation profile for granular Py of 129-151cmbsf; **(B)** Ablation profile for colloform Py of 193-199cmbsf; **(C)** Ablation profile for euhedral Py replaced by Ccp of 162-173 cmbsf; **(D)** Ablation profile for granular Ccp of 162-173 cmbsf; **(E)** Ablation profile for grained Sph of 151-162 cmbsf; **(F)** Ablation profile for colloform Sph of 108-117 cmbsf. Mineral abbreviations: Py, pyrite; Ccp, chalcopyrite; Sp, sphalerite.

medium-low temperatures, respectively (Auclair et al., 1987; Rouxel et al., 2004). The wide range of Se contents (5.81–112 ppm) can be interpreted as reflecting variable degrees of fluid-seawater mixing. Owing to the structure of stannite (Cu_2FeSnS_4) being very similar to that of $CuFeS_2$, chalcopyrite can incorporate Sn at high temperatures (300–500°C) (Maslennikov et al., 2009). The chalcopyrite in our study area has a relatively low Sn content which indicate that a complex mineralization process indeed occurred.

5.2.3 Controls on trace elements in sphalerite

The ablation profiles of Pb, Ag, Sb, Mn, Co, and Cd in both the granular and the colloform sphalerite were relatively smooth, indicating that these elements might occur as lattice substitution in minerals (Figures 8E, F). Lack of correlation between Fe and Cu indicated that submicroscopic chalcopyrite inclusions were not involved in the analyses. However, Pb, Ag, Ga, and Sn in the colloform sphalerite occasionally exhibited irregular undulating spectral lines, suggesting that these elements might be present as nanoscale inclusions (Figure 8F).

The concentrations of Cd, Pb, Ag, Cr, Mn, As, Sn, Ga, and Ge in sphalerite are higher than those in pyrite and chalcopyrite. Sphalerite precipitates under a range of temperature, pressure, sulfur fugacity, and oxygen fugacity conditions (e.g., Keith et al., 2014). When the ore-forming fluid is at or below 250 °C, Zn is preferentially precipitated in the form of sphalerite (Metz and Trefry, 2000; Hannington et al., 2005; Hannington, 2014). A high concentration of Pb (avg. 1,221 ppm) was found in all samples of sphalerite, likely indicating the presence of Pb-bearing mineral inclusions formed under medium–low temperature and moderately reducing conditions (Grant et al., 2018). Positive correlation (coefficient of determination R^2 = 0.73) between As and Pb can best be interpreted in terms of nanoscale inclusions of galena or sulfosalts (Figure 10A).

High Cd concentrations (up to 13,272 ppm) are also found in all the studied samples. The most common mineral of Cd is sphalerite, and the high concentrations of Cd are caused by the replacement of Cd^{2+} for Zn^{2+} (Cook et al., 2009). Variations in the Cd and Sn contents of sphalerite might reflect fluctuating fluid chemistry and deposition temperature (Scott and Barnes, 1972). In high-

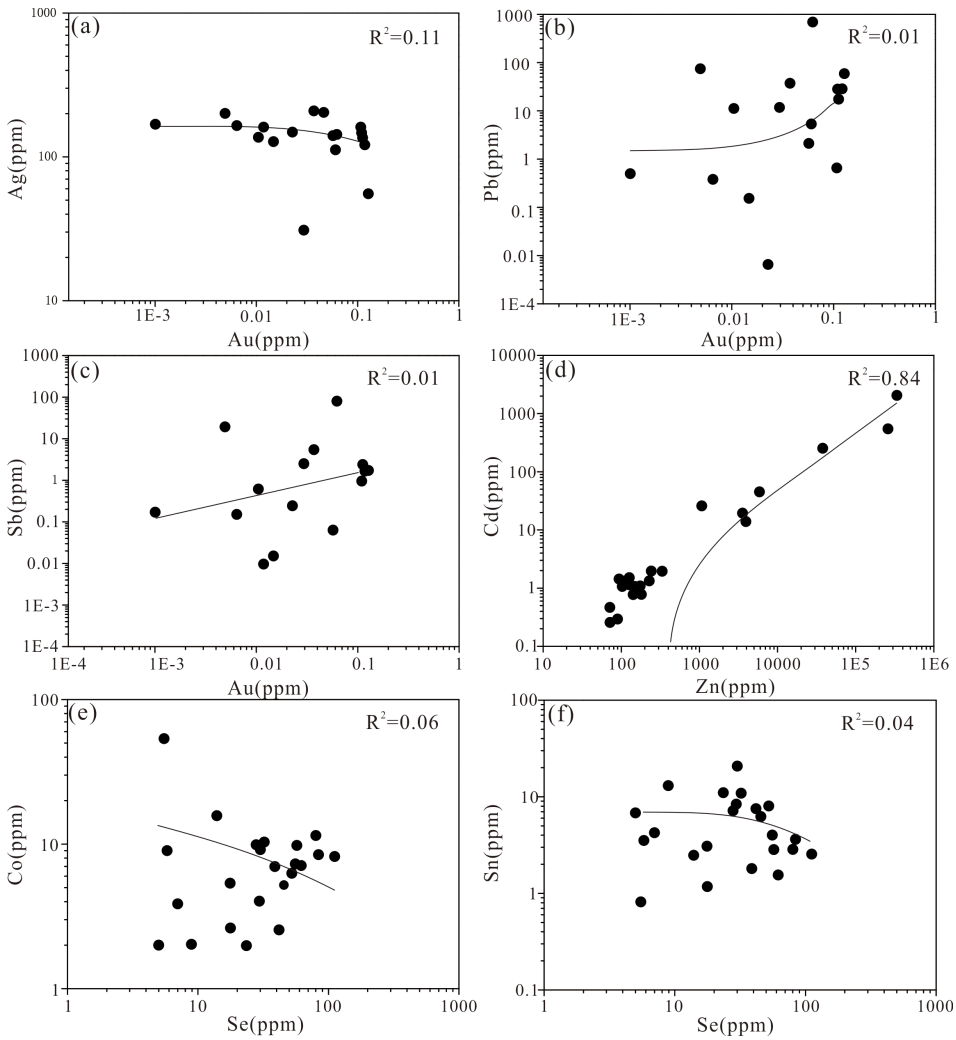

FIGURE 9
Correlation plots of **(A)** Au-Ag; **(B)** Au-Pb; **(C)** Au-Sb; **(D)** Zn-Cd; **(E)** Se-Co; **(F)** Se-Sn in chalcopyrite from the DHF.

temperature, acidic, reducing hydrothermal solutions, Sn can be transported as the Sn(II) aqueous complex, such as $SnCl_2$ (Heinrich and Eadington, 1986). Given the low Sn content and its lack of correlation with Cd in this study, the substitution of Sn^{2+} for Zn^{2+} in ZnS can be expected (Figure 10B; Maslennikov et al., 2009).

The high Ag concentration in sphalerite might be caused by periodic reduction in temperature and rapid precipitation of Ag from the original high temperature, strongly reducing fluid (Maslennikov et al., 2009). The sphalerite samples contain high concentrations of Sb (up to 1,006 ppm). The weak correlation between Ag and Sb (R^2 = 0.23) (Figure 10C) suggests a limited degree of $2Zn^{2+} \leftrightarrow Ag^{+} + Sb^{3+}$ substitution and the inclusion of Ag—Sb bearing minerals (Cook et al., 2009). These trace elements commonly precipitate under lower temperature conditions. All the samples show enrichment in Ga and Ge but there is no evident correlation between Ga and Ge (Figure 10D). The transport of Ga in sphalerite is dominated by neutral to weakly charged hydroxyl complexes, even in a hydrothermal solution containing reduced sulfur (Wood and Samson, 2006). Consequently, the high contents of Ga and Ge in the sphalerite might explained by coupled substitution rather than direct substitution for Zn (II) (Cook et al., 2009).

5.3 Distribution of trace elements in pyrite with depth below the seafloor

The distribution of ages within the surface of the DHF sulfide mound indicates a complex evolution process. The relatively intense hydrothermal activity over the past 4,552 years can be broadly divided into five different mineralization periods: 2,949 years (108–117 cmbsf), 2,307–2,297 years (117–151 cmbsf), 3,523–3,253 years (151–173 cmbsf), 4,552 years (173–193 cmbsf), and 2,558 years (193–199 cmbsf) (Table 3, Figure 6A). Apart from the top and the bottom, the core has obvious characteristics of gradual accumulation of mineralization. At the bottom and top, it is considered that hydrothermal seepage and metasomatic mineralization occurred continuously in the interior of the mound.

The distributions of Co, Ag, As, Au, Cd, Mo, Pb, Sb, and Se in the pyrite with depth below the seafloor are shown in Figures 11A–I.

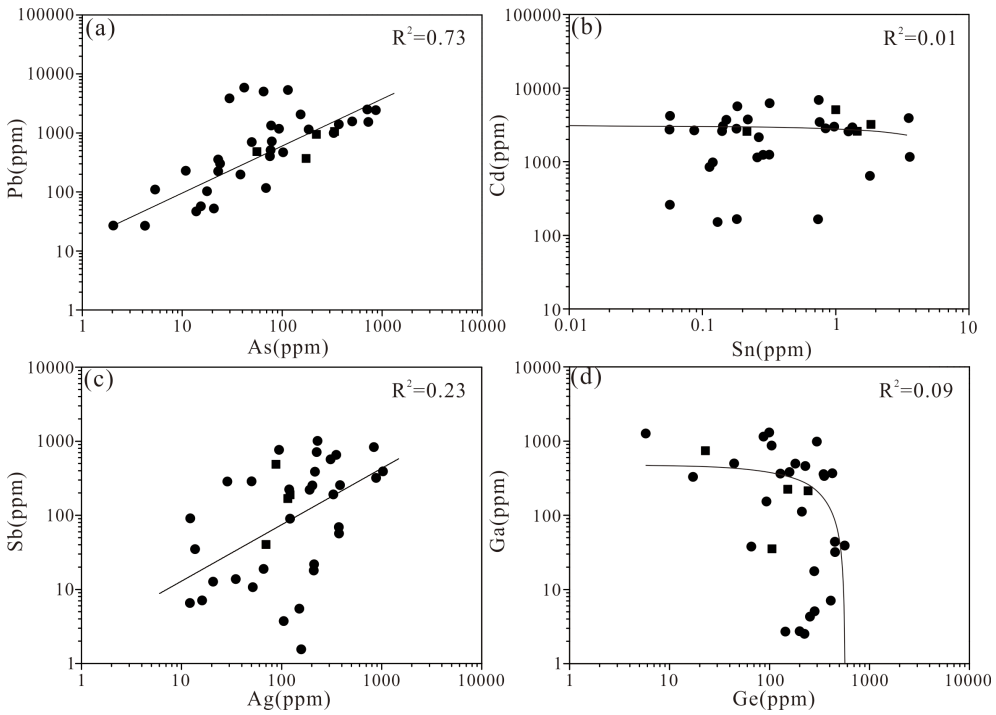

FIGURE 10
Correlation plots of **(A)** As vs. Pb, **(B)** Sn vs. Cd, **(C)** Ag vs. Sb, and **(D)** Ga vs. Ge in sphalerite from DHF. The dots and the boxes represent the grained sphalerite and colloform sphalerite respectively.

Pyrite in the DHF is generally enriched in Pb, As, Ag, Cd, Mo, and Sb and relatively depleted in Co, Se, and Au. The Se content is relatively low in most of the pyrites except the euhedral pyrites in the central part of the core. The As content of the granular pyrite was higher than that of the colloform pyrite, which might reflect direct precipitation from As-rich hydrothermal fluids (Huston et al., 1995; Kristall et al., 2006). The granular pyrite at layer I is enriched in Ag, As, Mo, Pb, and Sb compared with other types of pyrite at other layers. The granular pyrite and late recrystallized pyrite at layer II are enriched in Ag, Mo, Pb, and Se. The euhedral pyrite at layer III is enriched in Co, As, Se, Sb and Pb. The enrichment of Co and Se in euhedral pyrite suggests high-temperature mineralization (Metz and Trefry, 2000; Martin et al., 2023). This is in reasonable agreement with the mineralogical observations that euhedral pyrite is often associated with chalcopyrite or distributed in the inner wall of the hydrothermal channel. The granular pyrite at layer IV is enriched in Cd, Ag, Au and Pb. The colloform pyrite at layer V is enriched in Ag, Pb and depleted in Co and Se.

According to the chronological model, the shallow sulfide mound reflects a superposition process. Pyrites of different layers and different periods show obvious metasomatism. The variation in the elemental contents in different layers and types of pyrite is controlled by the evolution of physicochemical conditions of the hydrothermal fluid attributable to the interaction of seawater and hydrothermal fluids within the sulfide mound. The shallow sulfide mound underwent a mineralization process of precipitation followed by multiple metasomatic precipitation episodes over a short period. Owing to the limitations of the current domestic drilling rig used in the collection of the sulfide samples, further technological advances are required to enable deeper sulfide sampling. It is also necessary to refine the chronological evolution to the point where individual episodes can be resolved with confidence.

5.4 Comparison with trace elements in pyrites from other hydrothermal fields along the mid-ocean ridges

Compared with other hydrothermal fields along the mid-ocean ridges (e.g., Longqi, Tianzuo, and East Longjing on the SWIR, Wocan on the Northwest Indian Ridge, Edmond, Meso zone, and Kairei on the Central Indian Ridge, and TAG, 5°S and Logatchev on the Mid-Atlantic Ridge) (Yuan et al., 2018b; Liao et al., 2021; Ding et al., 2022; Wang et al., 2017; Zhang et al., 2023; Keith et al., 2016a), all types of pyrite in the DHF are generally enriched in Zn, Pb, As, Ag, Cd, Mo and Sb and relatively depleted in Co and Se (Figure 12). Pb shows positive correlations with Zn, Ag, Cd, Mo, and Sb with coefficients of determination of 0.87, 0.80, 0.79, 0.41, and 0.62, respectively (Figures 12A, C, D, F, H). Correlations between Pb and As, Pb and Co, and Pb and Se, are weak (Figures 12B, E, G). This contrasts with the enrichment of Zn, Pb, Ag, Cd, Mo, and Sb in back-arc basin deposits, which is partly attributed to the influence of felsic rocks and/or thick terrigenous sediments (Herzig et al., 1993; Keith et al., 2016a; Yeats et al., 2017). Moreover, some pyrite grains from the sediment-starved mid-ocean ridges such as 5°S and the Meso zone also show enrichment in Zn and Cd, which in some

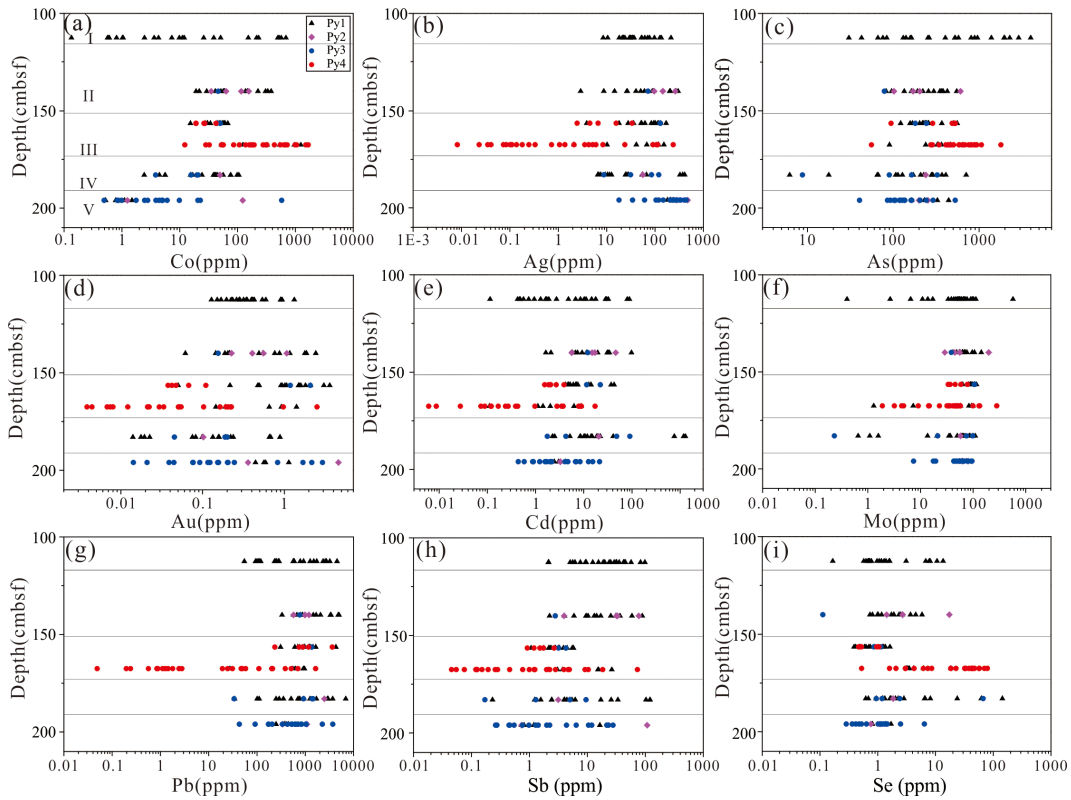

FIGURE 11
The distribution of trace elements in pyrite from different layers in the DHF. **(A–I)** represent the distribution of Co, Ag, As, Au, Cd, Mo, Pb, Sb, and Se respectively. All layers are calculated at intermediate depth. Py1: granular pyrite, Py2: late overgrowths coarse granular pyrite, Py3: colloform pyrite, Py4: euhedral pyrite. Layer I to V corresponds to 2,949 years (108–117 cmbsf), 2,307–2,297 years (117–151 cmbsf), 3,523-3253 years (151–173 cmbsf), 4,552 years (173–193 cmbsf) and 2,558 years (193–199 cmbsf) respectively.

cases might reflect the precipitation processes rather than a sediment related metal source (Keith et al., 2016a).

Previous studies suggested that fluid boiling can enhance the enrichment of As, Cu, Pb, Ag, and Au while depleting Co and Ni in pyrite from various active seafloor and continental hydrothermal systems (Román et al., 2019; Wang et al., 2022; Dang et al., 2023). This is primarily because fluid boiling significantly impacts the physicochemical conditions of hydrothermal fluids, including temperature, chloride concentration, pH, and oxygen fugacity which consequently causes abrupt alterations in the solubility and distribution of these elements (Keith et al., 2014, Keith et al., 2016a; Tivey et al., 1999). In contrast, the concentrations of As, Cu, and Pb in DHF pyrite are significantly lower compared to those precipitated in association with the aforementioned fluid boiling (Table 2; Román et al., 2019; Wang et al., 2022; Dang et al., 2023). This can be attributed to the absence of fluid boiling in DHF, as confirmed by results from phase-separation simulations conducted using the salt-water ($NaCl$-H_2O) Equation of State software (https://www.xthermal.info/en/index.html).

The enrichment of As, Sb, Ag, Pb and lower contents of Co and Se in the pyrite of the Brothers hydrothermal system can be explained by seawater mixing during shallow recharge (Martin et al., 2023). Additionally, these elements have the common characteristic that they tend to precipitate at low temperatures; consequently, the unique mineralization process of particular deposits might play an important role in the enrichment of such elements. Bulk geochemical results of massive sulfide collected by TV grabs in this area showed that these sulfides have high contents of Pb, As, Cd, and Ag. Because of the frequent magma activities, extremely low spreading rate at the DHF, long duration hydrothermal activity, multi-stage mineralization, early precipitated Ag, Sb, Pb, As and Cd in subseafloor sulfide would be remobilized in the following episode of hydrothermal activity (Yang et al., 2023). The bulk chemistry of the core analyzed in this study exhibits the same feature. Therefore, the DHF, as a typical axial volcanic ridge sediment-starved hydrothermal field, exhibits trace element compositions that have obvious particularity compared with other mid-ocean ridge hydrothermal fields. This is further supported by multistage mineralization, as evidenced by varying ages determined through ^{230}Th/U dating (Figure 6). The chalcopyrite and sphalerite in the DHF are also enriched in As, Sb, Ag, and Pb. Ascending hydrothermal fluid undergoes mixing and cooling within seawater, causing pronounced change in the fluid temperature and deposition of pyrite, chalcopyrite and sphalerite with high contents of As, Sb, Ag, and Pb. The enrichment of As, Sb, Ag, and Pb and the lower contents of Co and Se in the pyrite are best explained by shallow subsurface mixing during different periods of hydrothermal activity.

10.3389/fmars.2024.1538022

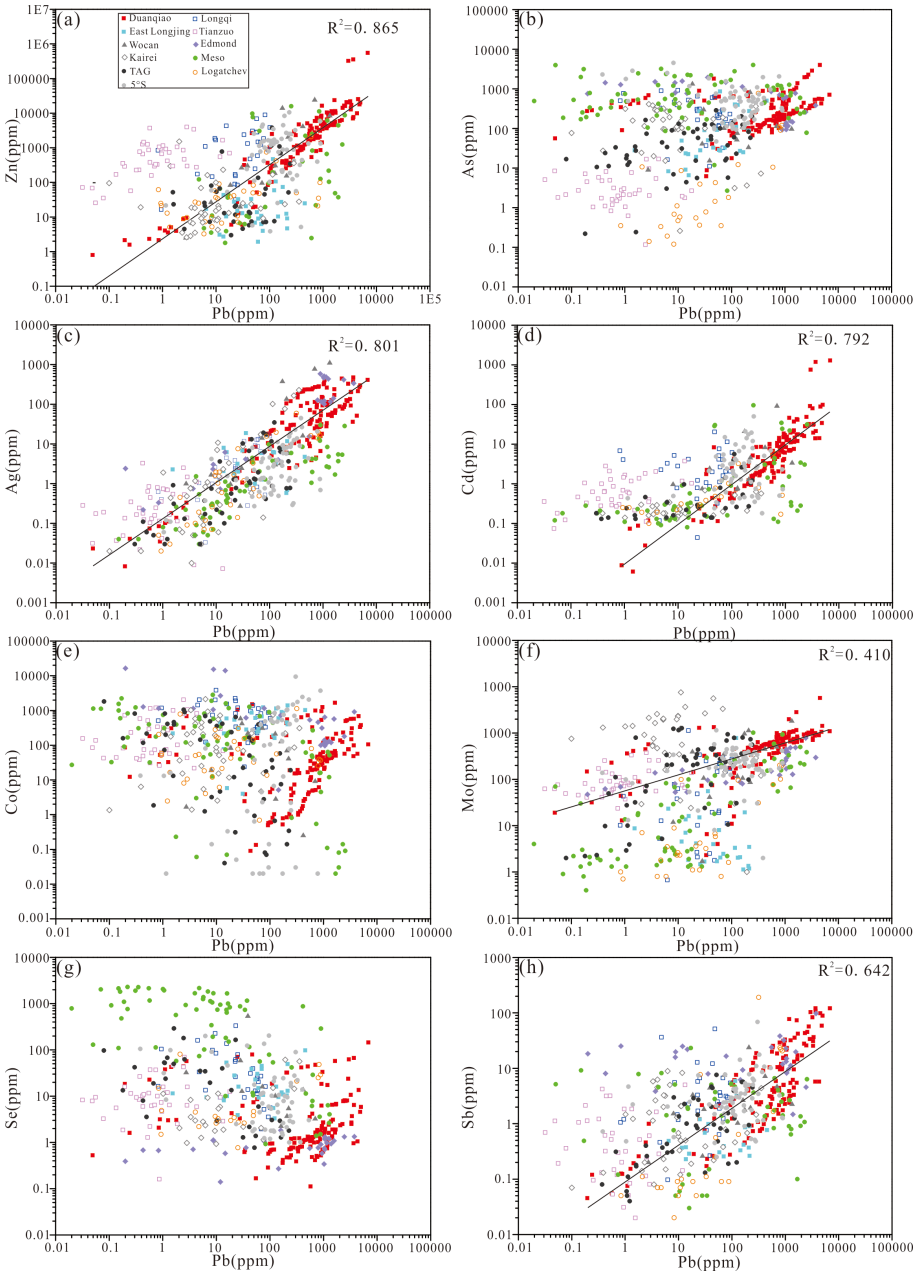

FIGURE 12
Concentrations of **(A)** Zn, **(B)** As, **(C)** Ag, **(D)** Cd, **(E)** Co, **(F)** Mo, **(G)** Se and **(H)** Sb vs. Pb in pyrite from various hydrothermal fields along the mid-ocean ridges. Longqi (Yuan et al., 2018b), East Longjing (Liao et al., 2021), Tianzuo (Ding et al., 2022), Wocan (Wang et al., 2017), Edmond (Zhang et al., 2023), Karei, Meso, TAG, Logatchev and 5°S (Keith et al., 2016a). Filled symbols and empty symbols represent the basalts-hosted and ultramafic-hosted hydrothermal fields respectively.

6 Conclusion

A sulfide drill core recovered from the DHF on the ultraslow spreading SWIR was studied in detail to understand the mineralization conditions, enrichment mechanism of metallogenic elements, and the associated evolution process. Analysis revealed that granular pyrite dominated the upper part of the core, euhedral pyrite dominated the central part of the core and colloform pyrite dominated the bottom of the core.

Pyrite is characterized by high Mn, Co, As, Mo, Ag, Cd, Sb, Tl and Pb contents, and is characterized by low Ti, Ga, In, Sn, Ni, Se, Ba, W and Au contents. Chalcopyrite is characterized by high concentrations of Se, Sn, In, As, Ag and Pb and sphalerite is characterized by high concentrations of Co, Ga, Ge, As, Ag, Cd, Sb and Pb. The ^{230}Th/U dating data suggests five different mineralization periods, and the core has obvious characteristics of gradual accumulation of mineralization during 4,552–2,297 years. The variations in the elemental contents of the different layers and the different types of pyrite were controlled by

the evolution of the physicochemical conditions of the hydrothermal fluid caused by the interaction of seawater and hydrothermal fluids within the sulfide mound.

Compared with other hydrothermal fields along other mid-ocean ridges, the pyrite in the DHF is generally enriched in Zn, Pb, As, Ag, Cd, Mo, and Sb, which might be attributed to shallow subsurface mixing during different periods of hydrothermal activity. This work provides the first documentation of the evolution process of a shallow sulfide mound on the SWIR.

Data availability statement

The original contributions presented in the study are included in the article/supplementary material. Further inquiries can be directed to the corresponding author.

Author contributions

WY: Conceptualization, Data curation, Formal analysis, Writing – original draft, Methodology. CT: Funding acquisition, Writing – review & editing, Resources. SL: Methodology, Writing – review & editing. HZ: Writing – review & editing, Data curation. CZ: Methodology, Data curation, Writing – review & editing. WL: Data curation, Writing – review & editing. GZ: Software, Writing – review & editing. XW: Methodology, Writing – review & editing. LW: Methodology, Writing – review & editing.

Funding

The author(s) declare that financial support was received for the research, authorship, and/or publication of this article. This work was supported by the National Natural Science Foundation of China (Grant No. 42127807), Natural Science Foundation of China (Grant No. 42406226), National Key Research and Development Project of China (2023YFC2811100), COMAR (China Ocean Mineral Resources R & D Association) Project (Grant No. DY135-S1-1-01, DY135-S1-1-02).

Conflict of interest

The authors declare that the research was conducted in the absence of any commercial or financial relationships that could be construed as a potential conflict of interest.

Generative AI statement

The author(s) declare that no Generative AI was used in the creation of this manuscript.

Publisher's note

Supplementary material

The Supplementary Material for this article can be found online at: https://www.frontiersin.org/articles/10.3389/fmars.2024.1538022/full#supplementary-material

References

Auclair, G., Fouquet, Y., and Bohn, M. (1987). Distribution of selenium in high-temperature hydrothermal sulfide deposits at 13° North, East Pacific Rise. *Can. Mineralogist* 25, 577–5872-s2.0-0023588769

Butler, I. B., and Nesbitt, R. W. (1999). Trace element distributions in the chalcopyrite wall of a black smoker chimney: insights from laser ablation inductively coupled plasma mass spectrometry (LA–ICP–MS). *Earth Planetary Sci. Lett.* 167, 335–345. doi: 10.1016/S0012-821X(99)00038-2

Cannat, M., Rommevaux-Jestin, C., Sauter, D., Deplus, C., and Mendel, V. (1999). Formation of the axial relief at the very slow spreading Southwest Indian Ridge (49° to 69°E). *J. Geophysical Research: Solid Earth* 104, 22825–22843. doi: 10.1029/1999jb900195

Cao, H., Sun, Z. L., Jiang, Z. K., Dong, A. G., Geng, W., Zhang, X. L., et al. (2021). Source origin and ore-controlling factors of hydrothermal sulfides from the Tianzuo hydrothermal field, southwest Indian ridge. *Ore Geology Rev. 134* 8), 104168. doi: 10.1016/j.oregeorev.2021.104168

Chen, J., Cannat, M., Tao, C. H., Sauter, D., and Munschy, M. (2021). 780 thousand years of upper-Crustal construction at a melt-rich segment of the ultraslow spreading southwest Indian ridge 50°28′E. *J. Geophysical Research: Solid Earth* 126, e2021JB022152. doi: 10.1029/2021JB022152

Cheng, H., Edwards, R. L., Shen, C. C., Woodhead, J., Hellstrom, J, Wang, Y. J., et al. (2013). Improvements in 230Th dating, 230Th and 234U half-life values, and U–Th isotopic measurements by multi-collector inductively coupled plasma mass spectrometry. *Earth Planet Sci Lett.* 371–372, 82–91. doi: 10.1016/j.epsl.2013.04.006

Cherkashov, G. A., Firstova, A. V., Bich, A. S., Kuksa, K. A., Sukhanova, A. A., Yakovenko, E. S., et al. (2023). Geochronological study of hydrothermal precipitates in the northern equatorial area of the mid-atlantic ridge. *Geotectonics* 57, S69–S83. doi: 10.1134/S001685212307004X

Cherkashov, G., Kuznetsov, V., Kuksa, K., Tabuns, E., Maksimov, F., and BeĽtenev, V. (2017). Sulfide geochronology along the Northern Equatorial Mid-Atlantic Ridge. *Ore Geology Rev.* 87, 147–154. doi: 10.1016/j.oregeorev.2016.10.015

Choi, S. K., Pak, S. J., Park, J. W., Kim, H. S., Kim, J. K., and Choi, S. H. (2023). Trace –element distribution and ore–forming processes in Au-Ag–rich hydrothermal chimneys and mounds in the TA25 West vent field of the Tonga Arc. *Mineralium Deposita* 58, 135–160. doi: 10.1007/s00126-022-01136-w

Cook, N. J., Ciobanu, C. L., Danyushevsky, L. V., and Gilbert, S. (2011). Minor and trace elements in bornite and associated Cu–(Fe)-sulphides: A LA-ICP-MS study. *Geochimica Cosmochimica Acta* 75, 6473–6496. doi: 10.1016/J.GCA.2011.08.021

Cook, N. J., Ciobanu, C. L., Pring, A., Skinner, W., Shimizu, M., Danyushevsky, L., et al. (2009). Trace and minor elements in sphalerite: A LA-ICPMS study. *Geochimica Cosmochimica Acta* 73, 4761–4791. doi: 10.1016/j.gca.2009.05.045

Dang, Y., Li, C. S., Shi, X. F., Wang, S., Ye, J., Li, B., et al. (2023). Metallogenetic process of Xunmei hydrothermal field (26°S), South Mid-Atlantic Ridge: Constraints

from *in-situ* sulfur isotope and trace elements of sulfides. *Mar. Geology* 466, 107182. doi: 10.1016/j.margeo.2023.107182

Deditius, A. P., Reich, M., Kesler, S. E., Utsunomiya, S., Chryssoulis, S. L., Walshe, J., et al. (2014). The coupled geochemistry of Au and As in pyrite from hydrothermal ore deposits. *Geochimica Cosmochimica Acta* 140, 644–670. doi: 10.1016/j.gca.2014.05.045

Dick, H. J. B., Lin, J., and Schouten, H. (2003). An ultraslow-spreading class of ocean ridge. *Nature* 426, 405–412. doi: 10.1038/nature02128

Ding, T., Wang, J., Tao, C. H., Dias, Á.A., Liang, J., Wang, Y., et al. (2022). Trace-element compositions of sulfides from inactive Tianzuo hydrothermal field, Southwest Indian Ridge: Implications for ultramafic rocks hosting mineralization. *Ore Geology Rev.* 140, 104421. doi: 10.1016/j.oregeorev.2021.104421

Douville, E., Charlou, J. L., Oelkers, E. H., Bienvenu, P., Jove Colon, C. F., Donval, J. P., et al. (2002). The rainbow vent fluids (36°14′N, MAR): the influence ofultramafic rocks and phase separation on trace metal content inMid-Atlantic Ridge hydrothermal fluids. *Chem. Geology* 184, 37–48. doi: 10.1016/S0009-2541(01)00351-5

Firstova, A., Cherkashov, G., Stepanova, T., Sukhanova., A., and Poroshina, I. (2022). New data for the internal structure of ultramafic hosted seafloor massive sulfides (SMS) deposits: case study of the semenov-5 hydrothermal field (13°31′ N, MAR). *Minerals* 12, 1–24. doi: 10.3390/min12121593

Fouquet, Y., Cambon, P., Etoubleau, J., Charlou, J. L., Ondr′eas, H., Barriga, F. J., et al. (2010). "Geodiversity of hydrothermal processes along the Mid-Atlantic Ridge–Ultramafic-hosted mineralization: A new type of oceanic Cu-Zn-Co-Au volcanogenic massive sulfide deposit," in *Diversity of hydrothermal systems on slow spreading ocean ridges*, vol. 321 . Eds. P. A. Rona, C. W. Devey, J. Dyment and B. J. Murton (American Geophysical Union, Washington DC), 367. doi: 10.1029/2008GM000746

Fouquet, Y., Charlou, J. L., Ondréas, H., Radford-Knoery, J., Donval, J. P., Douville, E., et al. (1997). Discovery and first submersible investigations on the Rainbow Hydrothermal Field on the MAR (36°14′N), Eos, Transactions, American Geophysical Union 78, 832. (abstract).

Gao, J. F., Zhou, M. F., Lightfoot, P. C., Wang, C. Y., Qi, L., and Sun, M. (2013). Sulfide saturation and magma emplacement in the formation of the Permian Huangshandong Ni-Cu Sulfide Deposit, Xinjiang, Northwestern China. *Economic Geology* 108, 1833–1848. doi: 10.2113/econgeo.108.8.1833

George, L. L., Cook, N. J., and Ciobanu, C. L. (2016). Partitioning of trace elements in co-crystallized sphalerite-Galena–Chalcopyrite hydrothermal ores. *Ore Geology Rev.* 77, 97–116. doi: 10.1016/j.oregeorev.2016.02.009

George, L. L., Cook, N. J., Crowe, B. B. P., and Ciobanu, C. L. (2018). Trace elements in hydrothermal chalcopyrite. *Mineral Magazine* 82, 59–88. doi: 10.1180/minmag.2017.081.021

German, C. R., Petersen, S., and Hannington, M. D. (2016). Hydrothermal exploration of mid-ocean ridges: where might the largest sulfide deposits be forming? *Chem. Geology* 420, 114–126. doi: 10.1016/j.chemgeo.2015.11.006

Gini, C., Jamieson, J. W., Reeves, E. P., Gartman, A., Barreyre, T., Babechuk, M. G., et al. (2024). Iron oxyhydroxide-rich hydrothermal deposits at the high temperature Fåvne vent field, Mohns Ridge. *Geochemistry Geophysics Geosystems* 25, e2024GC011481. doi: 10.1029/2024GC011481

Graber, S., Petersen, S., Yeo, I., Florent Szitkar, F., Klischies, M., Jamieson, J., et al. (2020). Structural control, evolution, and accumulation rates of massive sulfides in the TAG hydrothermal field. *Geochemistry Geophysics Geosystems* 21, e2020GC009185. doi: 10.1029/2020GC009185

Grant, H. L. J., Hannington, M. D., Pertersen, S., Frische, M., and Fuchs, S. H. (2018). Constraints on the behavior of trace elements in the activity-forming tag deposit, mid-atlantic ridge, based on la-icp-ms analysis. *Chem. Geology* 498, 45–471. doi: 10.1016/j.chemgeo.2018.08.019

Grant, H. L. J., Layton-Matthews, D., and Peter, J. M. (2015). Distribution and controls on silver mineralization in the Hackett River Main Zone, Nunavut, Canada: an Ag- and Pbenriched Archean volcanogenic massive sulfide deposit. *Economic Geology* 110, 943–982. doi: 10.2113/econgeo.110.4.943

Halbach, P., Fouquet, Y., and Herzig, P. (2003). "Mineralization compositional patterns in deep-sea hydrothermal systems," in *Energy mass transfer in marine hydrothermal systems* (Dahlem university press), 85–122. doi: cir.nii.ac.jp/crid/1572543025765604480

Hannington, M. D. (2014). Volcanogenic massive sulfide deposits,in *Treatise on geochemistry*, *2nd ed.* Eds. H. D. Holland and K. K. Turekian (Elsevier, Oxford), 463–488. doi: 10.1016/B978-0-08-095975-7.01120-7

Hannington, M. D., de Ronde, C. E. J., and Petersen, S. (2005). Sea-floor tectonics and submarine hydrothermal systems. *Economic Geology 100th Anniversary* 1905, 111–141. doi: 10.5382/av100.06

Hannington, M., Jamieson, J., Monecke, T., Petersen, S., and Beaulieu, S. (2011). The abundance of seafloor massive sulfide deposits. *Geology* 39, 1155–1158. doi: 10.1130/G32468.1

Hannington, M. D., Jonasson, I. R., Herzig, P. M., and Petersen, S. (1995). "Physical and chemical processes of seafloor mineralization at Mid-Ocean Ridges," in *Seafloor hydrothermal systems: physical, chemical, biological, and geological interactions*. Eds. S. E. Humphris, R. A. Zierenberg, L. S. Mullineaux and R. E. Thomson (American Geophysical Union, Washington DC), 115–157. doi: 10.1029/GM091p0115

Heinrich, C. A., and Eadington, P. J. (1986). Thermodynamic predictions of the hydrothermal chemistry of arsenic and their significance for the paragenetic sequence of some cassiteritearsenopyrite- base metal sulfide deposits. *Economic Geology* 81, 511–529. doi: 10.2113/gsecongeo.81.3.511

Helmy, H. M., Shalaby, I. M., and Rahman, H. A. (2014). Large-scale metal zoning in a late-Precambrian skarn type mineralization, Wadi Kid, SE Sinai, Egypt. *J. Afr. Earth Sci.* 90, 77–86. doi: 10.1016/j.jafrearsci.2013.11.015

Herzig, P. M., Hannington, M. D., and Arribas, A. (1998). Sulfur isotopic composition of hydrothermal precipitates from the Lau back-arc: implications for magmatic contributions to seafloor hydrothermal systems. *Mineralium Deposita* 33, 226–237. doi: 10.1007/s001260050143

Herzig, P. M., Hannington, M. D., Fouquet, Y., von Stackelberg, U., and Petersen, S. (1993). Goldrich sulfides from the Lau Back arc and implications for the geochemistry of gold in sea-floor hydrothermal systems of the Southwest Pacific. *Economic Geology* 88, 2182–2209. doi: 10.2113/gsecongeo.88.8.2182

Hou, K. J., Li, Y. H., and Ye, T. R. (2009). In-situ U-Pb zircon dating laser ablation-multi iron counting-ICP-MS. *Mineral Deposits* 28, 481–492. doi: 10.1360/972008-2143

Humphris, S. E., Herzig, P. M., Miller, D. J., Alt, J. C., Becker, K., Brown, D., et al. (1995). The internal structure of an active sea-floor massive sulfide deposit. *Nature* 377, 713–716. doi: 10.1038/377713a0

Huston, D. L., Sie, S.-H., Suter, G. F., and Cooke, D. R. (1995). Trace elements in sulfide minerals from eastern Australian volcanic-hosted massive sulfide deposits: part I. Proton microprobe analyses of pyrite, chalcopyrite, and sphalerite, and part II. Selenium levels in pyrite: comparison with $\delta^{34}S$ values and implications for the source of sulfur in volcanogenic hydrothermal systems. *Economic Geology* 90, 1167–1196. doi: 10.2113/gsecongeo.90.5.1167

Jamieson, J. W., Clague, D. A., and Hannington, M. D. (2014). Hydrothermal sulfide accumulation along the Endeavour Segment, Juan de Fuca Ridge. *Earth Planetary Sci. Lett.* 395, 136–148. doi: 10.1016/j.epsl.2014.03.035

Jamieson, J. W., Galley, C., McNeil, N., and Mora, D. S. (2023). Evaluating episodicity of high-temperature venting within seafloor hydrothermal vent fields. *Earth Planetary Sci. Lett.* 606, 118051. doi: 10.1016/j.epsl.2023.118051

Jian, H. C., Singh, S. C., Chen, Y. J., and Li, J. B. (2017). Evidence of an axial magma chamber beneath the ultraslow-spreading Southwest Indian Ridge. *Geology* 45, G38351–G38356. doi: 10.1130/G38356.1

Keith, M., Haase, K. M., Klemd, R., Stefan Krumm, S., and Strauss, H. (2016b). Systematic variations of trace element and sulfur isotope compositions in pyrite with stratigraphic depth in the Skouriotissa volcanic-hosted massive sulfide deposit, Troodos ophiolite, Cyprus. *Chem. Geology* 423, 7–18. doi: 10.1080/03717453.2016.1166643

Keith, M., Haase, K. M., Schwarz-Schampera, U., Klemd, R., Petersen, S., and Bach, W. (2014). Effects of temperature, sulfur, and oxygen fugacity on the composition of sphalerite from submarine hydrothermal vents. *Geology* 42, 699–702. doi: 10.1130/G35655.1

Keith, M., Häckel, F., Haase, K. M., Schwarz-Schampera, U., and Klemd, R. (2016a). Trace element systematics of pyrite from submarine hydrothermal vents. *Ore Geology Rev.* 72, 728–745. doi: 10.1016/j.oregeorev.2015.07.012

Kristall, B., Kelly, D., Hannington, M. K., and Deleaney, J. R. (2006). Growth history of a diffusely venting sulfide structure from the Juan de Fuca Ridge: A petrological and geochemical study. *Geochemistry Geophysics Geosystems* 7, 1–30. doi: 10.1029/2005GC001166

Kuznetsov, V., Tabuns, E., Kuksa, K., Cherkashov, G., Maksimov, F., BeĽtenev, V., et al. (2015). The oldest seafloor massive sulfide deposits at the Mid-Atlantic ridge: ^{230}Th/U chronology and composition. *Geochronometria* 42, 100–106. doi: 10.1515/geochr-2015-0009

Lalou, C., and Brichet, E. (1982). Ages and implications of East Pacific Rise sulphide deposits 21°N. *Nature* 300, 169–171. doi: 10.1038/300169a0

Lalou, C., and Brichet, E. (1987). On the isotopic chronology of submarine hydrothermal deposits. *Chem. Geology: Isotope Geosci. Section* 65, 197–207. doi: 10.1016/0168-9622(87)90003-0

Lalou, C., Reyss, J. L., Brichet, E., Arnoldm, M., Thompson, G., Fouquet, Y., et al. (1993). New age data for Mid-Atlantic Ridge hydrothermal sites: TAG and Snakepit chronology revisited. *J. Geophysical Research: Solid Earth* 98, 9705–9713. doi: 10.1029/92JB01898

Lalou, C., Reyss, J. L., Brichet, E., Krasnov, S., Stepanova, T., Cherkashev, G., et al. (1996). Initial chronology of a recently discovered hydrothermal field at 14°45′N, Mid-Atlantic Ridge. *Earth Planetary Sci. Lett.* 144, 483–490. doi: 10.1016/S0012-821X(96)00190-2

Large, R. R., Danyushevsky, L., Hollit, C., Maslennikov, V., Meffre, S., Gilbert, S., et al. (2009). Gold and trace element zonation in pyrite using a laser imaging technique: implications for the timing of gold in orogenic and Carlin-style sediment-hosted deposits. *Economic Geology* 104, 635–668. doi: 10.2113/gsecongeo.104.5.635

Large, R. R., Maslennikov, V. V., Robert, F., Danyushevsky, L. V., and Chang, Z. (2007). Multistage sedimentary and metamorphic origin of pyrite and gold in the Giant Sukhoi log deposit, Lena Gold Province, Russia. *Economic Geology* 102, 1233–1267. doi: 10.2113/gsecongeo.102.7.1233

Li, J. B., Jian, H. C., Chen, Y. S. J., Singh, S. C., Ruan, A. G., Qiu, X. L., et al. (2015). Seismic observation of an extremely magmatic accretion at the ultraslow spreading Southwest Indian ridge. *Geophysical Res. Lett.* 42, 2563–2663. doi: 10.1002/2014GL062521

Li, B., Shi, X. F., Li, C. S., Wang, S., Fan, L., Ye, J., et al. (2024). Subseafloor hydrothermal mineralization in a non-transform offset: Mineralogy and LA-ICP-MS study of sulfide from the Taiji-2 hydrothermal field, Southern Mid-Atlantic Ridge. *Ore Geology Rev.* 167, 105975. doi: 10.1016/j.oregeorev.2024.105975

Li, B., Shi, X. F., Wang, J. X., Yan, Q. S., Liu, C. G., and the DY- Leg, DY- Legs – and DY- Leg Science Parties (2018). Tectonic environments and local geologic controls of potential hydrothermal fields along the southern mid-atlantic ridge (12–14°s). *J. Mar. Syst.* 181, 1–13. doi: 10.1016/j.jmarsys.2018.02.003

Liao, S. L., Tao, C. H., Li, H. M., Barriga, J. A. S. F., Liang, J., Yang, W. F., et al. (2018). Bulk geochemistry, sulfur isotope characteristics of the Yuhuang-1 hydrothermal field on the ultraslow-spreading Southwest Indian Ridge. *Ore Geology Rev.* 96, 13–27. doi: 10.1016/j.oregeorev.2018.04.007

Liao, S. L., Zhu, C. W., Zhou, J. P., Liu, W. ,. Y., iang, J., Yang, W. F., et al. (2021). Distal axis sulfide mineralization on the ultraslow-spreading Southwest Indian Ridge: an LA-ICP-MS study of pyrite from the East Longjing-2 hydrothermal field. *Acta Oceanologica Sin.* 40, 105–113. doi: 10.1007/s13131-020-1681-2

Liu, Z. L., and Buck, W. R. (2018). Magmatic controls on axial relief and faulting at mid-ocean ridges. *Earth Planetary Sci. Lett.* 491, 226–237. doi: 10.1016/j.epsl.2018.03.045

Liu, Y. S., Hu, Z. C., Gao, S., Günther, D., Xu, J., Gao, C. G., et al. (2008). *In situ* analysis of major and trace elements of anhydrous minerals by LA-ICP-MS without applying an internal standard. *Chem. Geology* 257, 34–43. doi: 10.1016/j.chemgeo.2008.08.004

Martin, A. J., Jamieson, J. W., de Ronde, C. E. J., Humphris, S. E., McDonald, I., Layne, G. D., et al. (2023). Trace metal and sulfur cycling in a hydrothermally active arc volcano: deep–sea drilling of the Brothers volcano, Kermadec arc, New Zealand. *Mineralium Deposita* 58, 403–425. doi: 10.1007/s00126-022-01135-x

Maslennikov, V. V., Maslennikova, S. P. M., Large, R. R., and Danyushevsky, L. V. D. (2009). Study of trace element zonation in vent chimneys from the Silurian Yaman-kasy volcanic-hosted massive sulfide deposit (Southern Urals, Russia) using laser ablation-inductively coupled plasma mass spectrometry (LA-ICP-MS). *Economic Geology* 104, 1111–1141. doi: 10.2113/gsecongeo.104.8.1111

Meng, X., Li, X., Chu, F., Zhu, J., Lei, J., Li, Z., et al. (2020). Trace element and sulfur isotope compositions for pyrite across the mineralization zones of a sulfide chimney from the East Pacific rise (1–2°S). *Ore Geology Rev.* 116, 103209. doi: 10.1016/j.oregeorev.2019.103209

Metz, S., and Trefry, J. H. (2000). Chemical and mineralogical influences on concentrations of trace metals in hydrothermal fluids. *Geochimica Cosmochimica Acta* 64, 2267–2279. doi: 10.1016/S0016-7037(00)00354-9

Münch, U., Lalou, C., Halbach, P., and Fujimoto, H. (2001). Relict hydrothermal events along the super-slow Southwest Indian spreading ridge near 63°56′E-mineralogy, chemistry and chronology of sulfide samples. *Chem. Geology* 177, 341–349. doi: 10.1016/S0009-2541(00)00418-6

Nayak, B., Halbach, P., Pracejus, B., and Münch, U. (2014). Massive sulfides of Mount Jourdanne along the super-slow spreading Southwest Indian Ridge and their genesis. *Ore Geology Rev.* 63, 115–128. doi: 10.1016/j.oregeorev.2014.05.004

Petersen, S., and Hein, J. R. (2013). The Geology of Sea-Floor Massive Sulphides [M]//Deep Sea Minerals: Sea-Floor Massive Sulphides, A physical, biological, environmental, and technical review. *Secretariat of the pacific community (SPC), GRID-Arendal, 1A*, 7–18.978-82-7701-119-6

Petersen, S., Herzig, P. M., and Hannington, M. D. (1998). "Fluid inclusion studies as a guide to the temperature regime within the TAG hydrothermal mound, 26°N, Mid-Atlantic Ridge," in *Proc ODP 158, scientific results*. Eds. P. M. Herzig, S. E. Humphris, D. J. Miller and R. A. Zierenberg(College Station, TX) Ocean Drilling Program, 163–178. doi: 10.2973/ODP.PROC.SR.158.210.1998

Petersen, S., Herzig, P. M., and Hannington, M. D. (2000). Third dimension of a presently forming VMS deposit: TAG hydrothermal mound, Mid-Atlantic Ridge, 26°N. *Mineralium Deposita* 35, 233–259. doi: 10.1007/s001260050018

Ren, J. B., He, G. W., Deng, X. G., Deng, X. Z., Yang, Y., and Yao, H. Q. (2022). Metallogenesis of Co-rich ferromanganese nodules in the northwestern Pacific: Selective enrichment of metallic elements from seawater. *Ore Geol Rev.* 143, 104778. doi: 10.1016/j.oregeorev.2022.104778

Ren, J. B., He, G. W., Yang, Y., Yu, M., Deng, Y. N., and Pang, Y. T. (2024). Ultraselective enrichment of trace elements in seawater by Co-rich ferromanganese nodules. *Global Planetary Change* 239, 104498. doi: 10.1016/j.gloplacha.2024.104498

Ren, Y. Q., Wohlgemuth-Ueberwasser, C. C., Huang, F., Shi, X. F., Li, B., Oelze, M., et al. (2021). Distribution of trace elements in sulfides from Deyin hydrothermal field, Mid-Atlantic Ridge – Implications for its mineralizing processes. *Ore Geology Rev.* 128, 103911. doi: 10.1016/j.oregeorev.2020.103911

Román, N., Reich, M., Leisen, M., Morata, D., Barra, F., and Deditius, A. P. (2019). Geochemical and micro-textural fingerprints of boiling in pyrite. *Geochimica Cosmochimica Acta* 246, 60–85. doi: 10.1016/j.gca.2018.11.034

Rouxel, O., Fouquet, Y., and Ludden, J. N. (2004). Subsurface processes at the Lucky Strike hydrothermal field, Mid-Atlantic Ridge: Evidence from sulfur, selenium, and iron isotopes. *Geochimica Cosmochimica Acta* 68, 2295–2311. doi: 10.1016/j.gca.2003.11.029

Scott, S. D., and Barnes, H. L. (1972). Sphalerite-wurtzite equilibria and stoichiometry. *Geochimica Cosmochimica Acta* 36, 1275–1295. doi: 10.1016/0016-7037(72)90049-X

Shalaby, I. M., Stumpfl, E., Helmy, H. M., El Mahallawi, M. M., and Kamel, O. A. (2004). Silver and silver-bearing minerals at the Um Samiuki volcanogenic massive sulphide deposit, Eastern Desert, Egypt. *Mineralium Deposita* 39, 608–621. doi: 10.1007/s00126-004-0427-y

Smith, R. N., and Huston, D. L. (1992). Distribution and association of selected trace elements at the Rosebery Deposit, Tasmania. *Economic Geology* 87, 706–719. doi: 10.2113/gsecongeo.87.3.706

Tao, C. H., Li, H. M., Huang, W., Han, X. Q., Wu, G. H., Su, X., et al. (2011). Mineralogical and geochemical features of sulfide chimneys from the 49°39′ E hydrothermal field on the Southwest Indian Ridge and their geological inferences. *Chin. Sci. Bull.* 56, 2828–2838. doi: 10.1007/s11434-011-4619-4

Tao, C. H., Lin, J., Guo, S. Q., Chen, Y. S. J., Wu, G. H., Han, X. Q., et al. (2012). First active hydrothermal vents on an ultraslow-spreading center: Southwest Indian Ridge. *Geology* 40, 47–50. doi: 10.1130/G32389.1

Tao, C. H., Seyfried, W. E. Jr., Lowell, R. P., Liu, Y. L., Liang, J., Guo, Z. K., et al. (2020). Deep high-temperature hydrothermal circulation in a detachment faulting system on the ultra-slow spreading Ridge. *Nat. Communication* 11, 1300. doi: 10.1038/s41467-020-15062-w

Tivey, M. K., Stakes, D. S., Cook, T. L., Hannington, M. D., and Petersen, S. (1999). A model for growth of steep-sided vent structures on the Endeavour Segment of the Juan de Fuca Ridge: Results of a petrologic and geochemical study. *J. Geophysical Res.* 104, 22859–22883. doi: 10.1029/1999JB900107

Von Damm, K. L. (1995). "Controls on the chemistry and temporal variability of fluids," in Seafloor hydrothermal systems, physical, chemical, biological, and geological interactions. *Geophysical monograph series, The America Geophysical Union* 91, 222–2473. doi: 10.1029/GM091

Wang, Y. J., Han, X. Q., Petersen, S., Frische, M., Qiu, Z. Y., Li, H. M., et al. (2017). Mineralogy and trace element geochemistry of sulfide minerals from the Wocan Hydrothermal Field on the slow-spreading Carlsberg Ridge, Indian Ocean. *Ore Geology Rev.* 84, 1–19. doi: 10.1016/j.oregeorev.2016.12.020

Wang, S., Li, C. S., Li, B., Dang, Y., Ye, J., Zhu, Z. W., et al. (2022). Constraints on fluid evolution and growth processes of black smoker chimneys by pyrite geochemistry: A case study of the Tongguan hydrothermal field, South Mid-Atlantic Ridge. *Ore Geology Rev.* 140, 10440. doi: 10.1016/j.oregeorev.2021.104410

Wang, L. S., Sun, Z. L., Cao, H., Li, H. C., Wang, X. F., Liu, Y. H., et al. (2021). A new method for the U–Th dating of a carbonate chimney deposited during the last glaciation in the northern Okinawa Trough, east China sea. *Quaternary Geochronology* 66, 101199. doi: 10.1016/j.quageo.2021.101199

Wohlgemuth-Ueberwasser, C. C., Viljoen, F., Petersen, S., and Vorster, C. (2015). Distribution and solubility limits of trace elements in hydrothermal black smoker sulfides: An *in-situ* LA-ICP-MS study. *Geochimica Cosmochimica Acta* 159, 16–41. doi: 10.1016/j.gca.2015.03.020

Wood, S. A., and Samson, I. M. (2006). The aqueous geochemistry of gallium, germanium, indium and scandium. *Ore Geology Rev.* 28, 57–102. doi: 10.1016/j.oregeorev.2003.06.002

Yang, W. F., Liao, S. L., Dias, Á., Liang, J., Li, W., Ding, T., et al. (2023). Geochemistry, sulfur and lead isotopic composition of hydrothermal sulfide from the Duanqiao hydrothermal field on the Southwest Indian Ridge: Implications for ore genesis. *Int. Geology Rev.* 65, 883–899. doi: 10.1080/00206814.2022.2081937

Yang, W. F., Tao, C. H., Li, H. M., Liang, J., Liao, S. L., Long, J. P., et al. (2017). $^{230}Th/^{238}U$ dating of hydrothermal sulfides from Duanqiao hydrothermal field, Southwest Indian Ridge. *Mar. Geophysical Res.* 38, 71–83. doi: 10.1007/s11001-016-9279-y

Yeats, C. J., Holli, S. P., Halfpenny, A., Corona, J. C., LaFlamme, C., Southam, G., et al. (2017). Actively forming Kuroko-type volcanic-hosted massive sulfide (VHMS) mineralization at Iheya North, Okinawa Trough, Japan. *Ore Geology Rev.* 84, 20–41. doi: 10.1016/j.oregeorev.2016.12.014

You, C. F., and Bickle, M. J. (1998). Evolution of an active sea-floor massive sulphide deposit. *Nature* 394, 668–671. doi: 10.1038/29279

Yu, J. Y., Tao, C. H., Liao, S. L., Dias, Á.A., Liang, J., Yang, W. F., et al. (2021). Resource estimation of the sulfide-rich deposits of the Yuhuang-1 hydrothermal field on the ultraslow-spreading Southwest Indian Ridge. *Ore Geology Rev.* 134, 104169. doi: 10.1016/j.oregeorev.2021.104169

Yuan, B., Yang, Y. M., Yu, H. J., Zhao, Y. X., Ding, Q. F., Yang, J. C., et al. (2018a). Geochemistry of pyrite and chalcopyrite from an active black smoker in 49.6°E Southwest Indian Ridge. *Mar. Geophysical Res.* 39, 441–461. doi: 10.1007/s11001-017-9324-5

Yuan, B., Yu, H. J., Yang, Y. M., Zhao, Y. X., Yang, J. C., Xu, Y., et al. (2018b). Zone refinement related to the mineralization process as evidenced by mineralogy and element geochemistry in a chimney fragment from the Southwest Indian Ridge at 49.6° E. *Chem. Geology* 482, 46–60. doi: 10.1016/j.chemgeo.2018.01.024

Zeng, Z. G., Ma, Y., Chen, S., Selby, D., Wang, X. Y., and Yin, X. B. (2017). Sulfur and lead isotopic compositions of massive sulfides from deep-sea hydrothermal systems: Implications for ore genesis and fluid circulation. *Ore Geololy Rev.* 87, 155–171. doi: 10.1016/j.oregeorev.2016.10.014

Zhang, H. C., Chen, K., Tao, C. H., Dias, Á., Liang, J., Yang, W. F., et al. (2023). Occurrence and precipitation mechanism of silver in pyrite from chimney fragments in the Edmond hydrothermal field, Central Indian Ridge. *Ore Geology Rev.* 158, 105471. doi: 10.1016/j.oregeorev.2023.105471

Zierenberg, R. A., Fouquet, Y., Miller, D. J., Bahr, J. M., Baker, P. A., Bjerkgård, T., et al. (1998). The deep structure of a sea-floor hydrothermal deposit. *Nature* 392, 485–488. doi: 10.1038/33126

frontiers | Frontiers in Marine Science

TYPE Original Research
PUBLISHED 03 March 2025
DOI 10.3389/fmars.2025.1533654

OPEN ACCESS

EDITED BY
Xiaodong Jiang,
Guangdong University of Technology, China

REVIEWED BY
Ruiyong Zhang,
Chinese Academy of Sciences (CAS), China
Yan Liu,
Chinese Academy of Sciences (CAS), China

*CORRESPONDENCE
Xiaohu Li
xhli@sio.org.cn

RECEIVED 24 November 2024
ACCEPTED 03 February 2025
PUBLISHED 03 March 2025

CITATION
He X, Liu Q, Li X, Li Z, Wang H, Zhu Z, Dong Y, Li J and Li H (2025) Bacterial contributions to the formation of polymetallic nodules in the Pacific Ocean.
Front. Mar. Sci. 12:1533654.
doi: 10.3389/fmars.2025.1533654

Bacterial contributions to the formation of polymetallic nodules in the Pacific Ocean

Xinyi He[1,2,3,4], Qian Liu[5], Xiaohu Li[1,2,3]*, Zhenggang Li[1,2], Hao Wang[1,2], Zhimin Zhu[1,2], Yanhui Dong[1,2], Jie Li[1,2] and Huaiming Li[1,2]

[1]State Key Laboratory of Submarine Geoscience, Hangzhou, China, [2]Second Institute of Oceanography, Ministry of Natural Resources, Hangzhou, China, [3]School of Oceanography, Shanghai Jiao Tong University, Shanghai, China, [4]Bureau of Marine Development, Qingdao West Coast New Area, Qingdao, China, [5]Key Laboratory of Marine Ecosystem Dynamics, Second Institute of Oceanography, Ministry of Natural Resources, Hangzhou, China

Polymetallic nodules, widely distributed in the deep seafloor of the Pacific Ocean, are characterized by their abundance of diverse metal elements and considerable economic value. Previous studies have suggested a partial biogenic origin of these nodules. This study investigated the role of microorganisms in nodule formation by examining biological-like structures and bacterial communities within nodules and sediments. Scanning electron microscopy revealed bacteria-like microspheres, skeleton-like structures and extracellular polymeric substances-like structures in the nodules. Energy dispersive spectroscopy showed that these biological-like structures facilitated metal enrichment, enabling subsequent mineral precipitation. *Shewanella*, *Colwellia*, *Leptospirillum*, *Sulfitobacter*, and other bacteria may possess mineralization potential due to their Mn or Fe oxidation capabilities. Differences in internal structures and bacterial community composition between nodules from the western and eastern Pacific Ocean could potentially suggest that growth environment factors may contribute to nodule formation variation. These findings highlight the involvement of microorganisms in nodule formation and contribute to a better understanding of the biogenic mineralization process.

KEYWORDS

polymetallic nodules, sediment, bacterial composition, biomineralization, scanning electron microscope, Pacific Ocean

1 Introduction

Polymetallic nodules, also known as ferromanganese nodules, are widespread mineral resources in the deep seafloor. They are rich in Fe, Mn, Ni, Co, Cu, rare earth elements (REEs), and other metal elements, such as Ti, Mo, Zr, Li, and Y (Hein et al., 2020). These elements occupy crucial positions in various economic sectors, including the automotive, aerospace, and renewable energy industries (Hein et al., 2013). The substantial reserves of

nodules are found primarily in the Clarion-Clipperton Fracture Zone (CCZ) in the eastern Pacific Ocean (Hein et al., 2013).

Initially, it was widely believed that nodule formation was primarily driven by physicochemical interactions (Takematsu et al., 1989; Roy, 1992). This process was thought to be dominated by water-rock interactions and precipitation dynamics, with iron and manganese oxides precipitating under redox gradient conditions as the main mineralization driver (Goldberg and G.O.S, 1958; Crerar and Barnes, 1974).

Nodules that form through the continuous precipitation of Fe and Mn minerals from oxygen-rich near-bottom waters are known as "hydrogenetic nodules." These nodules typically exhibit a Fe/Mn ratio of approximately 1 in bulk analyses and are enriched in elements such as Fe and Co (Hein et al., 2013). In contrast, nodules that precipitate from oxygenated or suboxic sediment pore waters are referred to as "diagenetic nodules," which typically have an Mn/Fe ratio > 5 and are enriched in elements such as Mn and Cu (Halbach et al., 1988). Additionally, nodules that exhibit a mixture of diagenetic and hydrogenetic origin are called "mixed-type nodules" (Halbach et al., 1981).

Since Graham and Cooper (1959) suggested that manganese-rich deposits on the seafloor may result from biological processes, research into the role of microorganisms in nodule mineralization has steadily gained attention. Subsequent studies employing techniques such as scanning electron microscopy (SEM) and transmission electron microscopy (TEM) have further highlighted the independent relationships between microorganisms and the metals and minerals within the nodules (Burnett and Nealson, 1983; Hu et al., 2000; Wang and Müller, 2009; Nayak et al., 2013). The involvement of microorganisms in nodule formation has become an increasingly acknowledged and explored topic within the field.

Nodules exhibit distinct distribution patterns in various marine regions and are significantly influenced by the underlying environments (Glasby, 1976; Cochonat et al., 1992; Molari et al., 2020). The western Pacific contains one of the oldest oceanic crusts (Glasby et al., 1982) and the seafloor is coated with red clay (Glasby et al., 1987). The CCZ mainly develops on the smooth relief of abyssal hills (Halbach et al., 1981), and the seafloor is covered by rather thick, extensive layers of siliceous oozes (Margolis and Burns, 1976). Furthermore, the western Pacific mainly produces hydrogenetic nodules (Jiang et al., 2020b), while nodules from the CCZ are mostly of diagenetic or mixed-type origin (Wegorzewski and Kuhn, 2014; Hollingsworth et al., 2021).

In recent years, microorganisms within nodules have been acknowledged to significantly contribute to the process of nodule formation (Jiang et al., 2020a). Microorganisms significantly contribute to the cycling and mineralization of metals, utilizing their metabolic activities to influence nucleation and crystallization processes (Banfield and Nealson, 2018). By altering microenvironments such as pH and redox conditions, they facilitate mineral precipitation and shape mineral compositions (Konhauser, 1997). The deposition of minerals is crucial for the formation and growth of nodules, and microorganisms may exhibit a promoting effect on nodule formation due to their ability to mediate mineral formation and deposition (Hoffmann et al., 2021). Moreover, microbial mineralization activities are also associated with the rough surface structure and the growth of internal laminae in the nodules (Akai et al., 2013; Jiang et al., 2017).

However, the current understanding of microbial communities and their biomineralization functions in nodules in different regions of the Pacific Ocean remains limited. Comprehensive assessments of the variations in environmental conditions, nodule types, and abundance, as well as benthic organism activities across different regions, are challenging. Further research is needed to provide a more in-depth and comprehensive understanding.

In this study, we analyzed elemental composition of nodules and applied scanning electron microscopy coupled with energy dispersive X-ray spectroscopy (SEM-EDS) to analyze biological structures and surface elemental composition in nodules from the western and eastern Pacific. Furthermore, full-length 16S rRNA gene analysis was conducted to examine bacterial community composition within the nodules and underlying sediments, aiming to uncover potential bacterial mineralization processes and their role in the formation of mineralized structures in nodules.

2 Materials and methods

2.1 Sample collection

Samples of nodules and underlying sediments were collected using a multicorer at depths of 5302-5562 m from zone M2 (MC02, BC38A, and BC78) in the western Pacific during August and September 2022 aboard the research vessel *Dayangyihao* on voyage 75 (Figure 1, Table 1). The M2 area in the northern Magellan Seamounts of the western Pacific is a geologically stable region with limited volcanic and tectonic activity (Hein et al., 1997). The surface sediments are mainly composed of brownish-yellow clay. The study area represents a typical tropical oligotrophic environment, with low surface productivity (Jiang et al., 2020a), moderately high bottom water oxygen concentrations (175–200 mmol/m^3) (Dutkiewicz et al., 2020; Ren et al., 2022), and a bottom seawater temperature of approximately 1.5°C and salinity of around 34.6. The nodules in this area are primarily formed through hydrogenic processes, characterized by Co enrichment and a spheroidal morphology.

Samples were also collected using a multicorer at depths of 5177-5267 m from zone KW1 (MC04 and BC05) and zone A5 (BC12) in the eastern Pacific during voyage 73 of the research vessel *Dayanghao* within the same timeframe (Figure 1, Table 1). KW1 and A5 are adjacent blocks, both located in the western part of the CCZ in the eastern Pacific. The feature surface sediments with a brown hue, is primarily consisting of siliceous oozes. The dissolved oxygen concentration in the bottom seawater is approximately 150 mmol/m^3 (Dutkiewicz et al., 2020), with a temperature of 1.5°C and salinity around 34.7 (Washburn et al., 2021). The nodules are predominantly poly-nodules and have a hydrogenetic or mixed-type origin (Reyss et al., 1985).

The collected nodules and sediments were stored at −80°C and transported on dry ice to the laboratory.

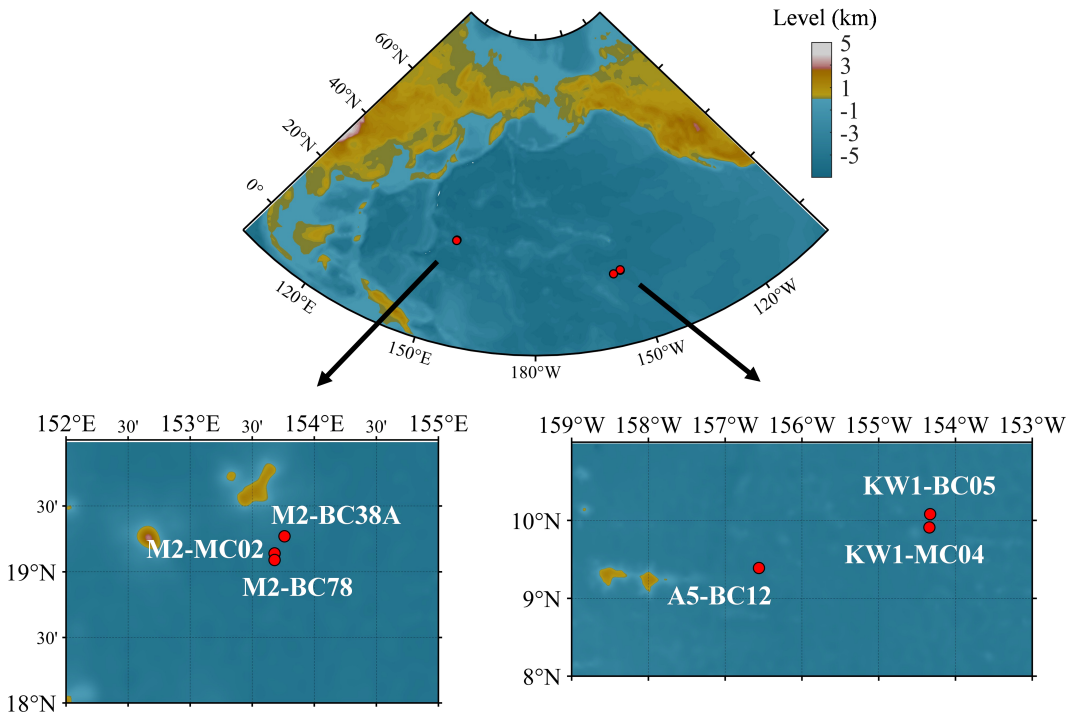

FIGURE 1
Locations of nodules and sediments sampling sites.

2.2 Elemental composition analysis

The polymetallic nodules were dried, crushed, weighed (5 g) and then ground into a homogeneous powder of 200 mesh size using an agate pestle and mortar. Elemental analyses were conducted at the Key Laboratory of Submarine Geosciences, Second Institute of Oceanography, Ministry of Natural Resources. The major elements in the nodules and sediments were determined using X-ray fluorescence spectroscopy (XRF, AxiosMAX, PANalytical, Netherlands). The trace elements in the nodules and sediments were determined using inductively coupled plasma-mass spectrometry(ICP-MS, Elan DRC-e, Perkin Elmer). All measured concentrations exceeded detection limits, with a relative standard deviation of laboratory precision less than 10%.

TABLE 1 Description of the polymetallic nodules and surrounding sediments sampled at six sites in the Pacific Ocean.

	Western Pacific			Eastern Pacific		
Site	M2-MC02	M2-BC38A	M2-BC78	KW1-MC04	KW1-BC05	A5-BC12
Longitude	153.68°E	153.76°E	153.68°E	154.34°W	154.33°W	156.56°W
Latitude	19.14°N	19.27°N	19.09°N	9.91°N	10.08°N	9.39°N
Depth	5519 m	5302 m	5562 m	5219 m	5177 m	5267 m
Sampling Method	Multicorer	Multicorer	Multicorer	Multicorer	Multicorer	Multicorer
Sample Type (Symbol)	Nodule (WNA) Sediment (WSA)	Nodule (SA)	Nodule (SB)	Nodule (ENB) Sediment (ESB)	Nodule (SC)	Nodule (SD)
Nodule Morphology	Spheroidal	Spheroidal	Spheroidal	Poly nuclei	Poly nuclei	Poly nuclei
Type of Sediment	Siliceous clay	Siliceous clay	Siliceous clay	Siliceous oozes	Siliceous oozes	Siliceous oozes
Technology	16S rRNA sequencing	SEM-EDS	SEM-EDS	16S rRNA sequencing	SEM-EDS	SEM-EDS

2.3 Scanning electron microscopy and energy dispersive X-ray spectroscopy

The nodules were mounted to epoxy and then cut in along the maximum axis to make thin sections. SEM images were performed using a TESCAN MIRA3 field-emission scanning electron microprobe (FE-SEM) at the Testing Center, Tuoyan Analytical Technology Co. Ltd. (Guangzhou, China). After the samples were carbon-coated, SEM images were acquired under an acceleration voltage of 20 kV, a beam current of 15 nA and a magnification of 300–500×. The surface elemental composition of carbon coated sample was characterized by energy dispersive X-ray analysis (SEM-EDAX) EDS detector (EDAX Element EDS detector) device attached to an SEM operating at 20 kV. Observing SEM images provides information about the internal structures within nodules, and further analysis can be conducted by combining the corresponding EDS results.

2.4 Full-length 16S rRNA gene sequence analysis

Under sterile conditions, the surface deposits adhering to the nodules were scraped away. The nodules were then fragmented using a chisel and then ground with a mortar. The nodules and surrounding sediments were individually weighed to 0.5 g. DNA was extracted using an Advanced Soil DNA Kit (MOBIO, Solana Beach, USA) according to the instructions.

The extracted DNA was used as a template for amplifying the V1-V9 regions with the primer set 27 F (5'-AGRGTTY GATYMTGGCTCAG-3') and 1492 R (5'-RGYTACCTTGTT ACGACTT-3'). Polymerase chain reaction (PCR) was conducted using the BioRad (S1000, Bio-Rad Laboratories, USA). Each sample was run in triplicate, and the PCR products from the same sample were pooled. Library preparation followed the 16S Amplification SMRTbell® Library Preparation protocol, and sequencing of the amplicon library was performed by Guangzhou Meige Biotechnology Co., Ltd., utilizing the PacBio Sequel II platform (PacBio, USA).

Fastp (v0.14.1) removed sequences over 2000 bp, and Cutadapt (v1.14) eliminated primers, resulting in valid fragments. Uparse defined operational taxonomic units (OTUs) at a 97% similarity threshold, with a confidence level of 0.8. Usearch-sintax (v10.0.240) aligned OTU representative sequences against the Silva v132 database.

Alpha diversity indices, including abundance-based coverage estimator (ACE) and Shannon, were calculated using usearch-alpha div (v10) based on the relative abundances of OTUs in each sample. Rarefaction curves were drawn by usearch-alpha div rare (v10) based on a richness index to estimate the sampling efforts. Community compositions were performed using R software.

3 Results

3.1 Morphologies and structures of nodules

Disparities were observed in the external morphological characteristics and internal structures of polymetallic nodules from the western and eastern Pacific (Figure 2). The nodules from the western Pacific were near-spherical (Figure 2A), with a homogeneous texture and no distinct core (Figure 2B). In contrast, nodules from the eastern Pacific were primarily poly-nodules containing more than three nuclei, exhibiting rough surfaces (Figure 2C) and distinct cores, which were encased by surrounding conduits (Figure 2D).

3.2 Elemental compositions

Nodules exhibited a significant enrichment of metal elements such as Mn, Fe, Ti, Co, Cu and Ni compared to the sediments (Table 2). Mn, Cu and Ni were generally more enriched in nodules from the eastern Pacific, while Fe, Ti and Co were more enriched in nodules from the western Pacific. Based on the Mn/Fe ratio, nodules from the western Pacific were indicative of a pronounced hydrogenetic origin (Mn/Fe ≈ 1) (Verlaan et al., 2004; Hein and Koschinsky, 2014), whereas nodules from eastern Pacific generally show a mixture of diagenetic and hydrogenetic origin, with a predominantly diagenetic input (2.09-2.77) (Wegorzewski and Kuhn, 2014; Hein et al., 2020).

3.3 Internal structures in nodules

Both western and eastern Pacific nodules exhibit regularly arranged laminated structures (Figure 3). The nodules from the western Pacific are characterized by laminated and concentric rims (He et al., in press), where compact layers (brighter) and loose layers (darker) alternate in a ring-like pattern, forming a rhythmic structure (Figures 3A–C). In contrast, nodules from the eastern Pacific predominantly display stromatolite-like rims with a loose texture and abundant pores (darker areas) distributed irregularly (Figures 3D–F). The compact structures in both regions show clear Mn enrichment on their surfaces, identified from the Mn elemental mapping, where lighter purple areas indicate higher Mn concentrations (Figures 3C, F). This is based on qualitative EDS analysis. The Mn distribution follows a rhythmic pattern, corresponding to concentric or stromatolite-like laminations.

Furthermore, many biological-like structures were observed from the fissures and cavities in the thin sections. For example, some bacteria-like microspheres (Figures 4A) exhibited a ring-like arrangement, with morphologies similar to those considered bacteria by Jiang et al. (2019) and Reykhard and Shulga (2019). Additionally, another type of bacteria-like microsphere, characterized by a flattened, centrally concave shape, was densely distributed within the channels (Figure 4B). Larger biological-like structures (>20 μm), including porous spheroidal (Figure 4C) and annular (Figures 4D, E) structures were also observed. Furthermore, a transparent and highly reflective extracellular polymeric substance (EPS)-like structure (Figure 4F) (Ren and Jones, 2021).

To further elucidate the elemental composition of these structures, qualitative EDS analysis was performed. Higher peak intensities indicate greater element enrichment (Figure 4). Mn, Fe, and Ti are the primary metals that exhibit substantial enrichment

10.3389/fmars.2025.1533654

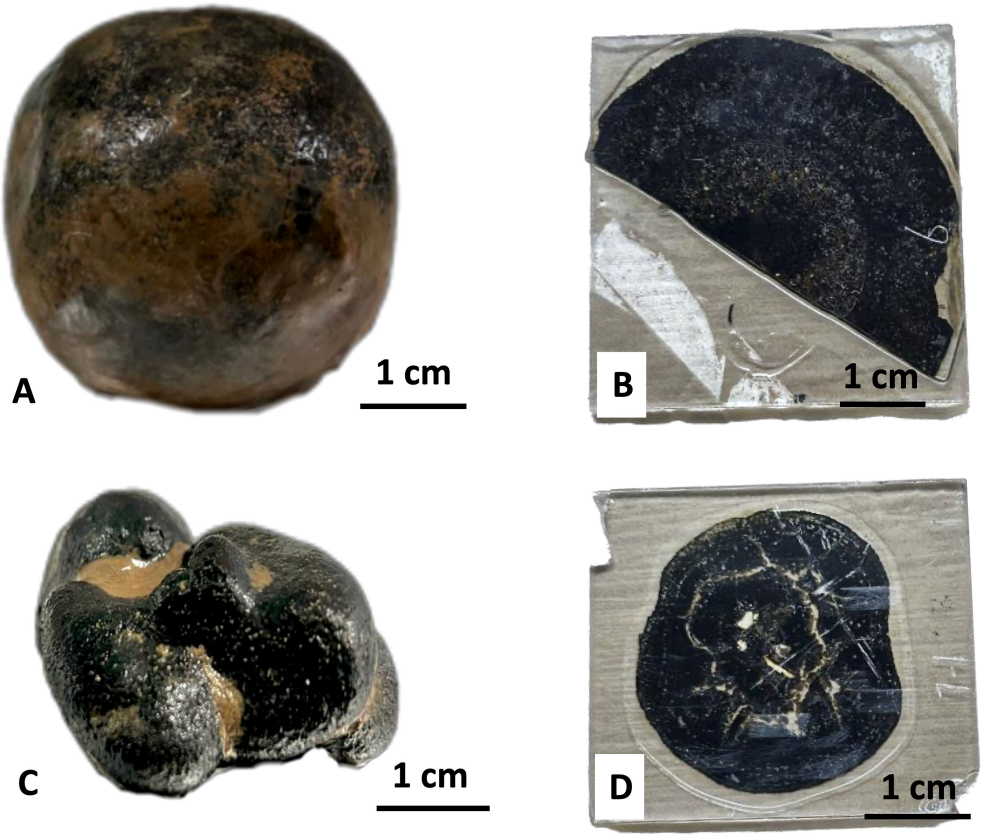

FIGURE 2
Photographs of hand-specimen and thin sections of representative nodules from the Pacific Ocean, captured by digital camera: **(A)** A near-spherical nodule from the western Pacific; **(B)** A thin section of a nodule from the western Pacific; **(C)** A typical coalesced nodule from the eastern Pacific; **(D)** A thin section of a nodule from the eastern Pacific.

TABLE 2 Partial major and trace element compositions of the nodules and sediments. Co, Cu, and Ni in ppm; Mn/Fe dimensionless; others in wt.%.

	Western Pacific				Eastern Pacific			
	Nodule (WNA)	Sediment (WSA)	Nodule (SA)	Nodules (SB)	Nodule (ENB)	Sediment (ESB)	Nodule (SC)	Nodule (SD)
Mn	17.47	0.65	17.50	17.27	23.54	0.50	23.81	25.43
Fe	18.57	6.19	17.98	15.86	11.28	4.52	11.20	9.19
Si	7.84	24.08	7.80	8.84	6.67	25.43	6.86	6.83
Al	3.10	9.21	2.90	3.59	2.58	6.66	2.56	2.89
Mg	1.30	2.13	1.22	1.46	1.34	1.93	1.09	1.86
Ca	1.77	1.49	1.82	1.84	1.87	0.93	1.90	1.73
Na	1.44	2.80	1.45	1.51	1.74	4.65	1.71	1.90
K	0.67	2.66	0.67	0.83	0.85	2.22	0.88	0.86
Ti	1.39	0.53	1.37	1.12	0.84	0.44	0.92	0.63
Co	3906	88	4148	3191	3271	95	3105	2549
Cu	2229	217	2168	3349	4974	364	5669	8582
Ni	3702	205	4018	4753	8159	188	9113	11157
Mn/Fe	0.94	0.11	0.97	1.09	2.09	0.11	2.13	2.77

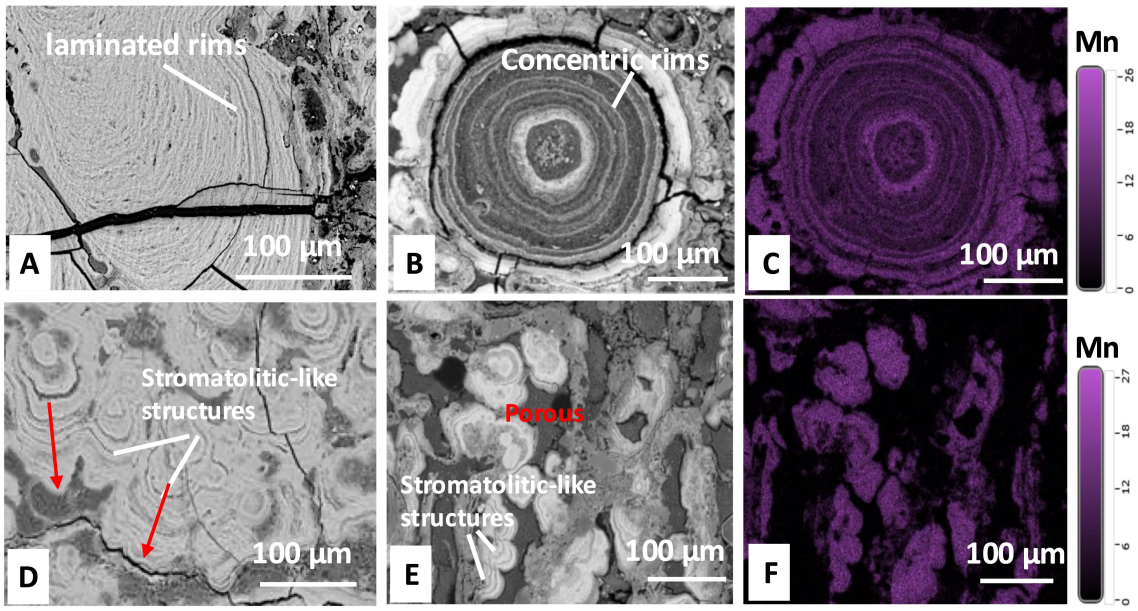

FIGURE 3
Images of internal structures in thin sections captured by SEM **(A, B, D, E)** and Mn distribution by EDS **(C, F)**: **(A, B)** Internal structures of nodules from the western Pacific, with **(A)** densely distributed laminated rims and **(B)** Concentric rims growing around a micro-core; **(C)** Mn distribution map of the structure shown in **(B)**; **(D, E)** Stromatolitic-like structures in nodules from the eastern Pacific; **(F)** Mn distribution map of the structure shown in **(E)**. Lighter purple areas indicate higher Mn concentrations.

within the nodules, and due to their considerable economic value, they have been the subject of extensive research (Hein et al., 2020). Furthermore, Mn and Fe play pivotal roles in cellular processes such as development, metabolism, and enzymatic activity (Bruins et al., 2000; Helmann, 2014), and are also known to facilitate the formation of bacterial biofilms (Avidan et al., 2010; Mhatre et al., 2016). Of particular interest, Mn, Fe, and Ti are also found to exhibit markedly high concentrations on the microstructural surfaces, which warrants further attention. The surfaces of microspheres exhibited the ability to enrich metals (Mn, Fe, Ti), particularly Mn (Figures 4A, B). Surfaces of other types of structures have similar elemental enrichments (Fe, Mn, Ti), particularly Fe (Figures 4C–E). EPS-like structure displayed comparable levels of enrichment for both Mn and Fe (Figure 4F).

3.4 Microbial community composition

The sequencing depth was sufficient, capturing most of the community diversity with a rich variety of bacterial taxa (Supplementary Figure S1; Figure 5) (He et al., in press). Proteobacteria (38.2%-46.9%) was predominant across the samples, with the dominance of the class Gammaproteobacteria (18.1% to 32.3%). *Woeseia* exhibited dominance in WNA (12.26%) and WSA (9.56%), while *Arcicella* was the dominant genus in ENB (28.02%) and ESB (22.22%).

The experiment identified some unique genera that appeared to be exclusive to specific samples (Table 3; Supplementary Table S1). For example, *Leptospirillum* and *Lentisphaera* were found only in western Pacific samples (WNA, WSA), while *Psychrobium* and *Sulfitobacter* were detected exclusively in eastern Pacific samples (ENB, ESB). *Halomonas* was enriched in ENB but was not detected in WNA. Similarly, *wb1-A12*, *Blastocatella*, and *IS-44* were enriched in sediment samples (WSA, ESB) and were not identified in WNA. However, reliance on relative abundances alone was insufficient to definitively confirm the presence or absence of these genera, though it suggests the possibility of such patterns. It is important to note that these results are based on sequencing data from a single sample, highlighting the need for further replicates to robustly assess microbial enrichment preferences across different sample types.

The 16S full-length sequencing technique enabled species identification 29 species were detected from the nodule samples. Excluding the unsigned and uncultured species, 9 species could be identified (Table 4). These species, belonging to the Gamma or Alpha classes of Proteobacteria, were from various genera (Supplementary Table S2), indicating potential variations in their physiological characteristics and functions. It is also noteworthy that the occurrence of these species may be influenced by experimental factors, which may hinder the definitive determination of their exclusivity to a specific sample. Consequently, the zero abundances observed (Table 4) cannot be conclusively interpreted as the absence of these species but instead represent the potential for these species to be unique to certain samples.

4 Discussion

4.1 Biological structures potentially involved in nodule formation

Previous studies utilizing SEM-EDS have identified manganese-oxidizing bacteria (MOB) and biological structures involved in

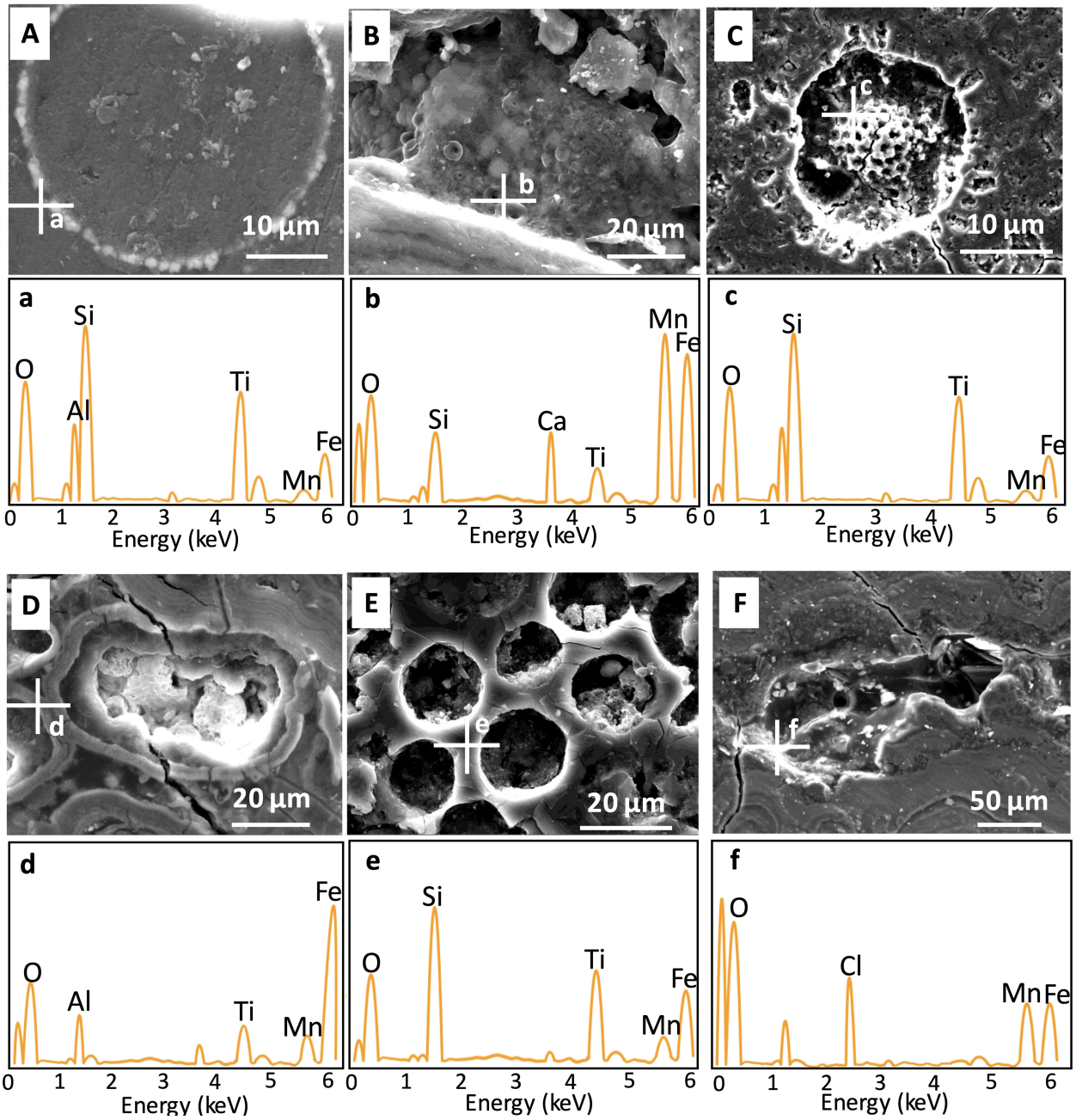

FIGURE 4
Images of biological-like structures in nodules from the western Pacific **(A-C)** and the eastern Pacific **(D-F)** captured using SEM-EDS: **(A)** Microspheres arranged in a ring on a platform; **(B)** Multiple flattened microspheroidal structures with central concavities; **(C)** A porous spheroidal structure; **(D, F)** Annular structures of varying shapes; **(E, F)** EPS-like structures coating tunnel surfaces. White crosses indicate analysis points. a-f indicate the regions in the images **(A–F)** where elemental analysis was performed using EDS.

nodule mineralization (Wang and Müller, 2009; Jiang et al., 2020a; Shulga et al., 2022). In this study, metal-enriched biological-like structures were observed, including bacteria-like structures (Figures 4A, B) and other biomophs (Figures 4C–F), which are also likely involved in the mineralization process. SEM-EDS may have resolution limitations in analyzing biological structures, which can hinder accurate characterization of fine biological features and trace element distributions, making these findings speculative in the absence of direct evidence for their biological origin. However, careful comparisons with similar structures reported in the literature were made during the SEM-EDS analysis.

In addition to the microspheres potentially representing mineralizing bacteria (Figures 4A, B), other biomorphs that may contribute to the mineralization process include porous structures, likely remnants of radiolarian skeletons, characterized by high Si content and features such as spines or spine-like openings (Figure 4C) (Jiang et al., 2019);annular, skeleton-like structures resembling the solid shells produced by coccolithophores

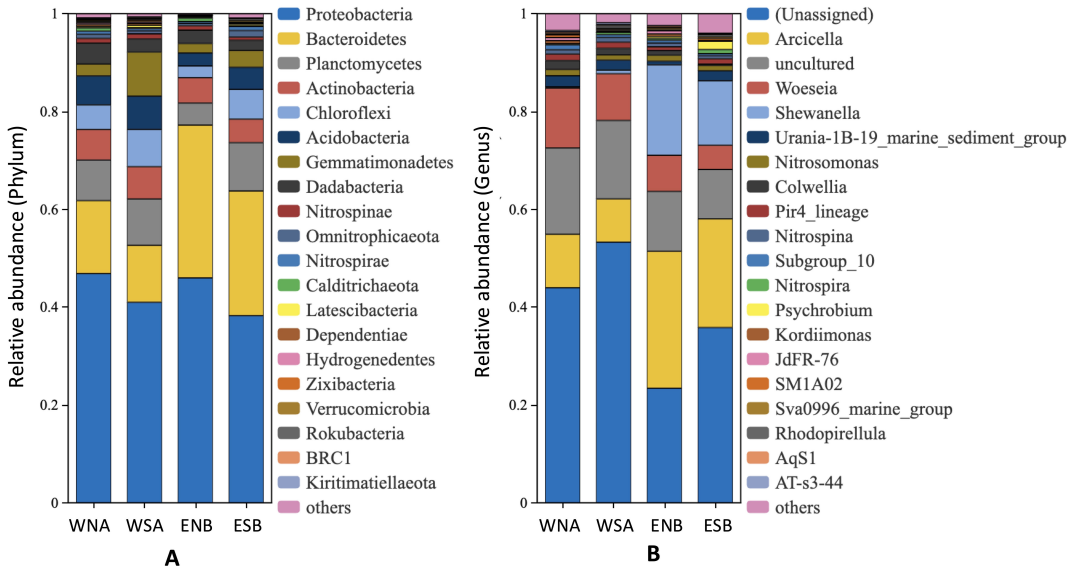

FIGURE 5
Bacterial community compositions in the nodules and underlying sediments (He et al., in press): **(A)** The relative abundance of bacteria at the phylum level (top 20); **(B)** The relative abundance of bacteria at the genus level (top 20). WNA and WSA represent the western Pacific samples, with WNA referring to the nodule and WSA referring to the sediment; ENB and ESB represent the eastern Pacific samples, with ENB referring to the nodule and ESB referring to the sediment.

(Figures 4D, E), as proposed by Wang et al. (2012); and transparent, highly reflective structures capable of enriching Mn and Fe, similar to extracellular polymeric substances (EPS) (Figure 4F) (Ren and Jones, 2021).The surfaces of these structures seem to serve as sites for the precipitation of metal oxides, resulting in the accumulation of Fe and Mn minerals (Jiang et al., 2019), which fall under the category of biologically induced mineralization (BIM). BIM occurs when organisms secrete metabolites that react with ions or compounds in the environment, leading to the growth and deposition of mineral particles (Frankel and Bazylinski, 2003). Jiang et al. (2019) suggested that these biomorphs can induce mineralization processes through surface enrichment and proposed a mineralization process of mixed colloids of Mn- and Fe-oxide-hydroxides through biological-induced oxidation of Mn(II) and Fe(II) on the surfaces of biological structures. The significant enrichment of metals observed on the surfaces of biological structures in the present study provides further evidence for this idea (Figures 4).

However, it is crucial to acknowledge that the proposed biological structures are primarily qualitative interpretations based on the literature, rather than quantitative determinations. As such, their identification remains speculative, with EDS serving only as a supplementary tool. Consequently, the possibility of non-biological processes contributing to the observed morphological features cannot be excluded. For example, abiotic processes such as mineral precipitation or physical deposition could produce structures that resemble those associated with biological mineralization, complicating the interpretation of the results (Ren and Jones, 2021; Zhang et al., 2024). Moreover, the relationship between biological forms and mineral types in BIM remains unclear. Therefore, further research should aim to establish a more definitive link between specific biological structures and the minerals they may induce, with a focus on acquiring direct evidence of biological processes, while also critically considering the potential role of abiotic mechanisms in shaping these structures.

TABLE 3 Unique genera that not fully present in all samples (top 10, n.d: not detected).

Unique genera	Relative abundance (%)			
	Nodule (WNA)	Sediment (WSA)	Nodule (ENB)	Sediment (ESB)
Psychrobium	n.d	n.d	0.38	1.69
Sulfitobacter	n.d	n.d	0.15	1.01
Moritella	0.26	n.d	0.07	0.28
Halomonas	n.d	0.01	0.43	0.04
wb1-A12	n.d	0.23	0.02	0.39
Leptospirillum	0.40	n.d	n.d	n.d
Blastocatella	n.d	0.18	0.04	0.13
Ulvibacter	0.16	0.07	n.d	0.04
IS-44	n.d	0.14	0.01	0.13
Lentisphaera	0.11	0.03	n.d	n.d

4.2 Potentials of bacterial community in mineralization

4.2.1 Main bacterial communities with mineralization potential

Previous studies have suggested that mineralizing bacteria, especially manganese-mineralizing bacteria, are present in

TABLE 4 Specific species in nodules and the surrounding sediments (removing unsigned and uncultured species).

Species	Relative abundance (%)			
	Nodule (WNA)	Sediment (WSA)	Nodule (ENB)	Sediment (ESB)
Halomonas sp. 148Z-13	0.00	0.01	0.42	0.04
Halomonas sp. CSM-2	0.00	0.00	0.02	0.00
Alcanivorax marinus	0.00	0.00	0.01	0.06
Moritella sp. BSw20747	0.09	0.00	0.03	0.10
Pseudoalteromonas sp. 520P1 No. 423	0.00	0.00	0.03	0.06
Pseudomonas pachastrellae	0.00	0.00	0.02	0.01
Roseovarius sp. TM1035	0.00	0.00	0.01	0.01
Bradyrhizobium japonicum	0.00	0.00	0.02	0.00

nodules and actively contribute to the mineralization process (Blöthe et al., 2015; Reykhard and Shulga, 2019; Jiang et al., 2020b). SEM-EDS analysis has indicated the potential involvement of biological components, including bacteria, in mineralization (He et al., in press). Advances in sequencing technologies could further elucidate the mineralization functions of different bacterial species.

For example, members of the Magnetospiraceae and Hyphomicrobiaceae have been identified as playing significant roles in the iron cycle (Matsunaga et al., 1991; Shulga et al., 2022). The Magnetospiraceae group, characterized by magnetotaxis, also exhibits a unique iron-capturing ability that influences the distribution and migration of iron in the environment (Molari et al., 2020). Meanwhile, the Hyphomicrobiaceae group, as iron-oxidizing bacteria, alters the chemical form and reactivity of iron, thereby affecting its solubility, mobility, and bioavailability. This group may also indirectly impact the cycling of other metal elements (Molari et al., 2020). Additionally, Shewanella and Colwellia are known to participate in manganese reduction processes (Blöthe et al., 2015). Several Shewanella strains are also capable of oxidizing manganese to form manganese oxide nanoparticles (Omoike and Chorover, 2006; Bräuer et al., 2011; Wright et al., 2016). In addition, *Shewanella* may also participate in the Fe cycle, exemplified by *Shewanella oneidensis MR-1*, which is considered a model strain for dissimilatory iron reduction and is capable of mediating metal reduction through the production of EPS (Yan et al., 2021). EPS, composed of polysaccharides, proteins, and lipids, are biopolymers that serve as a prerequisite for biofilm formation (Liu et al., 2020) and act as carriers for biogeochemical processes such as cell adhesion, mineralization, and microbial metal redox cycling (Zheng et al., 2019). It should be noted that 16S rRNA sequencing has limitations in resolution and sensitivity, which may hinder accurate representation of the actual bacterial community composition (Poretsky et al., 2014). Future studies could employ metagenomics for a more comprehensive characterization of microbial community structure and functional traits (Arıkan and Muth, 2023; Satya et al., 2024).

4.2.2 Unique bacteria with mineralization potential

Several genera, which were temporarily detected only in specific samples, also exhibit mineralization potential. For instance, *Leptospirillum*, which was detected exclusively in western Pacific nodule samples, possesses the ability for obligate Fe(II) oxidation and is widely distributed in metal-rich environments, suggesting its potential role in mineralization (Barrie Johnson, 2015). *Lentisphaera*, which was detected exclusively in western Pacific samples, has multiple strains capable of secreting transparent exopolymers, potentially facilitating metal adsorption on the bacterial surface and subsequent precipitation (Choi et al., 2013).

Similarly, several genera, including *Sulfitobacter* (Templeton et al., 2005), *Halomonas* (Templeton et al., 2005), *Marinobacter* (Handley and Lloyd, 2013), *Pseudoalteromonas* (Wu et al., 2013), and *Marinomonas* (Xuezheng et al., 2008), have been temporarily detected exclusively in nodules from the eastern Pacific (Supplementary Table S1) (He et al., in press). Strains of these manganese-oxidizing bacteria have been successfully isolated and cultured under laboratory conditions, demonstrating their ability to oxidize Mn(II) (Templeton et al., 2005; Zhang et al., 2019). Among these, *Pseudoalteromona* has received considerable attention for its production of extracellular organic compounds (Bowman, 2007), with EPS serving as effective carriers for inducing or controlling mineralization processes. For example, the strain *Pseudoalteromonas* TG12 has been reported to produce EPS capable of binding metals in sediments (Gutierrez et al., 2008). In addition, *Marinobacter* and *Alcanivorax*, both exclusively detected in eastern Pacific samples, have shown the ability to oxidize Fe(II) (Handley et al., 2009; Sudek et al., 2009; Smith et al., 2011). Beyond iron and manganese, some bacteria from eastern samples can also facilitate the oxidation of other metals. For instance, *Acinetobacter* has been found to oxidize Cr (Zakaria et al., 2007), while *Marinobacter* can oxidize As (Handley et al., 2009). While this does not diminish the discussion on bacterial roles in mineralization, the limitations of sequencing methods necessitate further evidence to definitively

confirm the presence or absence of bacterial taxa across samples (Mainali et al., 2017).

4.2.3 Mineralization potentials of specific bacterial species

Moreover, by utilizing the BIOCYC database (Caspi et al., 2015, 2016), several species with the potential for Mn(II)-oxidizing have been identified among species detected (Table 4): *Roseovarius* sp. TM1035, *Pseudoalteromonas* sp. 520P1 No. 423, and *Bradyrhizobium japonicum* were all found exclusively in nodules from the eastern Pacific. The enrichment of these species with Mn (II) oxidation capabilities may correlate with the higher Mn content in the nodule from the eastern Pacific (Table 2). However, the specific oxidation pathways and enzymes involved in the Mn oxidation process of these species still require further clarification.

Besides, *Roseovarius* sp. TM1035 can produce biofilm to adapt to changes in the underlying environment (Kent et al., 2018). Biofilm, an EPS containing embedded bacteria, aids in bacterial resistance against adverse environmental stresses and also provides sites on its surface for metal oxidation, mineral aggregation, and precipitation, potentially facilitating the mineralization process (Wang and Müller, 2009; Decho, 2010). Some strains of *Pseudoalteromonas* can also generate biofilms for the removal of Pb(II), Cr(VI), and Cd(II) (Priyadarshanee and Das, 2021), and some strains of *Bradyrhizobium* has been found to employ an EPS-mediated defense mechanism for metal precipitation (Santamaría et al., 2003). However, given our experimental results, more precise functional analysis or prediction of key genes may be required to further enhance our understanding of the mineralization functions of the aforementioned bacteria. It's also important to recognize that the relative abundance data alone may not conclusively indicate the exclusive presence of certain bacterial taxa in specific samples, given potential variations arising from factors like limited sequencing depth and methodological biases.

4.3 Potential discrepancies in the nodule growth environment

The growth environments of polymetallic nodules in the western and eastern Pacific may differ. In the western Pacific, polymetallic nodules are thought to be primarily hydrogenetic (Mn/Fe ~ 1), with metals precipitating from oxygen-rich near-bottom seawater, enriching Fe and Co, while nodules from the eastern Pacific appear to be more significantly influenced by diagenetic processes, with metal precipitation occurring in sediment pore spaces, enriching Mn, Cu, and Ni (Halbach et al., 1981, 1988). The elemental composition of nodules is likely influenced by factors such as surface primary productivity, organic carbon content in the seafloor, and redox conditions. In the western Pacific, low primary productivity and high dissolved oxygen in bottom waters may contribute to the rapid oxidation of Fe and Co to stable +3 oxidation states (Liu and Millero, 2002; Dutkiewicz et al., 2020; Jiang et al., 2020a). In contrast, in the eastern Pacific, higher primary productivity and organic carbon content in sediments may promote the formation of metal-organic complexes, potentially enriching Mn, Cu, and Ni in the sediments (Verlaan et al., 2004). As organic matter degrades, reducing conditions at the seafloor may release Mn and other elements in their 2+ states into pore waters, which could further contribute to the enrichment of these elements in the nodules (Jorgensen, 2001; Arndt et al., 2013).

The differing genesis of polymetallic nodules may also suggest variations in the hydrodynamic and geological conditions under which the nodules form. Nodules of hydrogenetic origin in the western Pacific typically develop in relatively stable aquatic and geological environments, facilitating the growth of near-spherical nodules characterized by rhythmic, dense, and uniform laminae (Figure 2A, Figures 3A, B) (Li et al., 2020). In contrast, nodules from the eastern Pacific are predominantly influenced by diagenetic processes, displaying stromatolitic-like growth structures with broader fissures and pores (Figure 2D, Figures 3D, E). These features indicate that nodule growth in this region was influenced by ongoing environmental modifications, including seafloor bioturbation and bottom currents (Veillette et al., 2007; Wegorzewski and Kuhn, 2014).

Furthermore, the differences in microbial community composition across nodule fields in different marine regions may also reflect variations in the environmental conditions. For example, notable distinctions were observed when comparing the bacterial communities identified in this study with those from other Mn nodule fields, Such as the Korea Deep Ocean Study (KODOS) (Cho et al., 2018) and the German license area (Blöthe et al., 2015) in the Clarion-Clipperton Fracture Zone (CCFZ), as well as the Kara Sea (Vereshchagin et al., 2019)and the South Pacific Gyre (Shiraishi et al., 2016). For instance, *Marinobacter* and *Idiomarina*, two genera that are mostly strictly aerobic, were abundant in the KODOS area (Ivanova et al., 2000; Green et al., 2006). However, they were not detected in samples from the western Pacific in this study, and their abundances in samples from the eastern Pacific were extremely low (<0.2%), potentially linked to variations in environmental oxygen levels. Moreover, *Shewanella* and *Colwellia*, as potentially important genera in the nodule formation in this study, were not detected in the KODOS area and were only found in nodules from the German license area. However, *Colwellia* exhibited widespread enrichment in sediments from the Kara Sea (2%) and the South Pacific Gyre (>50%). Both of these two regions are characterized by extremely low surface primary productivity (D'Hondt et al., 2009; Demidov et al., 2017), suggesting that *Colwellia* may accumulate in environments with exceptionally low carbon content due to its capability to degrade recalcitrant substances (Tully and Heidelberg, 2013). The acquisition of more detailed environmental data in future studies may provide further empirical support for our hypothesis.

5 Conclusion

This study provides valuable insights into the relationship between microorganisms and polymetallic nodule formation in the Pacific Ocean. Through SEM-EDS analysis, we discovered various biological-like structures capable of enriching metal elements on their surfaces, indicating their potential role in promoting nodule formation and growth. Several bacteria-like microspheres may suggest the

presence of mineralizing bacteria within the nodules. Furthermore, 16S rRNA gene sequencing identified several bacteria with mineralization potential. These bacteria were found to be involved in metal redox cycles through physiological metabolism or by facilitating mineral deposition through the production of biofilms or EPS. Additionally, differences in elemental compositions, internal structures, and bacterial community compositions may indicate variations in the growth environments of nodules across different regions. In the results and discussion, we drew upon literature to clarify the bio-analogous types and the functions of bacteria (especially potential mineralization functions). Further research is needed to explore the specific mechanisms of interaction between microorganisms and minerals, and to investigate the potential applications of these findings in areas such as deep-sea mining and environmental management.

Data availability statement

The raw data supporting the conclusions of this article will be made available by the authors, without undue reservation.

Author contributions

XH: Conceptualization, Data curation, Formal Analysis, Investigation, Methodology, Software, Writing – original draft, Writing – review & editing. QL: Conceptualization, Formal Analysis, Methodology, Supervision, Writing – review & editing. XL: Conceptualization, Funding acquisition, Project administration, Resources, Supervision, Writing – review & editing. ZL: Data curation, Methodology, Resources, Writing – review & editing. HW: Methodology, Resources, Writing – review & editing. ZZ: Methodology, Resources, Writing – review & editing. YD: Methodology, Resources, Writing – review & editing. JL: Methodology, Resources, Writing – review & editing. HL: Methodology, Resources, Writing – review & editing.

Funding

The author(s) declare that financial support was received for the research, authorship, and/or publication of this article. This work was funded by the National Key R&D Program of China (Grant No. 2023YFC2811305, 2023YFC2811205-01, 2022YFC2806601 and 2022YFC2806602), the National Natural Science Foundation of China (U2244222).

Acknowledgments

We thank the captain, crew, and scientists for their assistance during the Dayangyihao and Dayanghao research cruise. We would like to express our appreciation to the technical staff, especially Zedong Fan, Yurong Qian, Mingyan Lai and Ziang Li for their helpful advice and suggestions with experimental operations.

Conflict of interest

The authors declare that the research was conducted in the absence of any commercial or financial relationships that could be construed as a potential conflict of interest.

Generative AI statement

The author(s) declare that no Generative AI was used in the creation of this manuscript.

Publisher's note

Supplementary material

The Supplementary Material for this article can be found online at: https://www.frontiersin.org/articles/10.3389/fmars.2025.1533654/full#supplementary-material

References

Akai, J., Akiyama, S., Tsuchiyama, A., and Akai, K. (2013). Ocean manganese nodules as stromatolite with a fractal like-signature. *Phys. Chem. Earth Parts A/B/C* 58-60, 42–48. doi: 10.1016/j.pce.2013.04.004

Arıkan, M., and Muth, T. (2023). Integrated multi-omics analyses of microbial communities: a review of the current state and future directions. *Mol. Omics*. doi: 10.1039/D3MO00089C

Arndt, S., Jørgensen, B. B., LaRowe, D. E., Middelburg, J. J., Pancost, R. D., and Regnier, P. (2013). Quantifying the degradation of organic matter in marine sediments: A review and synthesis. *Earth-Science Rev.* 123, 53–86. doi: 10.1016/j.earscirev.2013.02.008

Avidan, O., Satanower, S., and Banin, E. (2010). "Iron and bacterial biofilm development," in *Microbial Mats: Modern and Ancient Microorganisms in Stratified Systems* (Dordrecht: Springer), 359–383.

Banfield, J. F., and Nealson, K. H. (2018). *Geomicrobiology: Interactions between microbes and minerals* (Berlin: Walter de Gruyter GmbH & Co KG).

Barrie Johnson, D. (2015). "Leptospirillum," in *Bergey's Manual of Systematics of Archaea and Bacteria* (Wiley, Hoboken, NJ), 1–8.

Blöthe, M., Wegorzewski, A., Muller, C., Simon, F., Kuhn, T., and Schippers, A. (2015). Manganese-cycling microbial communities inside deep-dea manganese nodules. *Environ. Sci. Technol.* 49, 7692–7700. doi: 10.1021/es504930v

Bowman, J. P. (2007). Bioactive compound synthetic capacity and ecological significance of marine bacterial genus *Pseudoalteromonas*. *Mar. Drugs* 5, 220–241. doi: 10.3390/md504220

Bräuer, S. L., Adams, C., Kranzler, K., Murphy, D., Xu, M., Zuber, P., et al. (2011). Culturable *Rhodobacter* and *Shewanella* species are abundant in estuarine turbidity maxima of the Columbia river. *Environ. Microbiol.* 13, 589–603. doi: 10.1111/j.1462-2920.2010.02360.x

Bruins, M. R., Kapil, S., and Oehme, F. W. (2000). Microbial resistance to metals in the environment. *Ecotoxicology Environ. Saf.* 45, 198–207. doi: 10.1006/eesa.1999.1860

Burnett, B. R., and Nealson, K. H. (1983). Energy dispersive X-ray analysis of the surface of a deep-sea ferromanganese nodule. *Mar. Geology* 53, 313–329. doi: 10.1016/0025-3227(83)90048-8

Caspi, R., Billington, R., Ferrer, L., Foerster, H., Fulcher, C. A., Keseler, I. M., et al. (2015). The MetaCyc database of metabolic pathways and enzymes and the BioCyc collection of pathway/genome databases. *Nucleic Acids Res.* 44, D471–D480. doi: 10.1093/nar/gkv1164

Caspi, R., Billington, R., Foerster, H., Fulcher, C. A., Keseler, I., Kothari, A., et al. (2016). BioCyc: online resource for genome and metabolic pathway analysis. *FASEB J.* 30, lb192–lb192. doi: 10.1096/fasebj.30.1_supplement.lb192

Cho, H., Kim, K.-H., Son, S. K., and Hyun, J.-H. (2018). Fine-scale microbial communities associated with manganese nodules in deep-sea sediment of the Korea deep ocean study area in the northeast equatorial pacific. *Ocean Sci. J.* 53, 337–353. doi: 10.1007/s12601-018-0032-0

Choi, A., Yang, S.-J., Rhee, K.-H., and Cho, J.-C. (2013). *Lentisphaera* marina sp. nov., and emended description of the genus *Lentisphaera*. *Int. J. Systematic Evolutionary Microbiol.* 63, 1540–1544. doi: 10.1099/ijs.0.046433-0

Cochonat, P., Le Suavé, R., Charles, C., Greger, B., Hoffert, M., Lenoble, J. P., et al. (1992). First *in situ* studies of nodule distribution and geotechnical measurements of associated deep-sea clay (Northeastern pacific ocean). *Mar. Geology* 103 (1), 373–380. doi: 10.1016/0025-3227(92)90027-F

Crerar, D. A., and Barnes, H. L. (1974). Deposition of deep-sea manganese nodules. *Geochimica Cosmochimica Acta* 38, 279–300. doi: 10.1016/0016-7037(74)90111-2

D'Hondt, S., Spivack, A. J., Pockalny, R., Ferdelman, T. G., Fischer, J. P., Kallmeyer, J., et al. (2009). Subseafloor sedimentary life in the South Pacific Gyre. *Proc. Natl. Acad. Sci.* 106, 11651–11656. doi: 10.1073/pnas.0811793106

Decho, A. W. (2010). Overview of biopolymer-induced mineralization: What goes on in biofilms? *Ecol. Eng.* 36, 137–144. doi: 10.1016/j.ecoleng.2009.01.003

Demidov, A. B., Kopelevich, O. V., Mosharov, S. A., Sheberstov, S. V., and Vazyulya, S. V. (2017). Modelling Kara Sea phytoplankton primary production: Development and skill assessment of regional algorithms. *J. Sea Res.* 125, 1–17. doi: 10.1016/j.seares.2017.05.004

Dutkiewicz, A., Judge, A., and Müller, R. D. (2020). Environmental predictors of deep-sea polymetallic nodule occurrence in the global ocean. *Geology* 48, 293–297. doi: 10.1130/g46836.1

Frankel, R. B., and Bazylinski, D. A. (2003). Biologically induced mineralization by bacteria. *Rev. Mineralogy Geochemistry* 54, 95–114. doi: 10.2113/0540095

Glasby, G. P. (1976). Manganese nodules in the south pacific: A review. *New Z. J. Geology Geophysics* 19 (5), 707–736. doi: 10.1080/00288306.1976.10426315

Glasby, G. P., Gwozdz, R., Kunzendorf, H., Friedrich, G., and Thijssen, T. (1987). The distribution of rare earth and minor elements in manganese nodules and sediments from the equatorial and S.W. pacific. *Lithos* 20 (2), 97–113. doi: 10.1016/0024-4937(87)90001-6

Glasby, G. P., Stoffers, P., Sioulas, A., Thijssen, T., and Friedrich, G. (1982). Manganese nodule formation in the pacific ocean: a general theory. *Geo-Marine Lett.* 2 (1), 47–53. doi: 10.1007/BF02462799

Goldberg, E. D., and G.O.S, A. (1958). Chemistry of Pacific pelagic sediments. *Geochimica cosmochimica Acta* 13, 153–212. doi: 10.1016/0016-7037(58)90046-2

Graham, J. W., and Cooper, S. C. (1959). Biological origin of manganese-rich deposits of the sea floor. *Nature* 183, 1050–1051. doi: 10.1038/1831050a0

Green, D. H., Bowman, J. P., Smith, E. A., Gutierrez, T., and Bolch, C. J. S. (2006). *Marinobacter algicola* sp. nov., isolated from laboratory cultures of paralytic shellfish toxin-producing dinoflagellates. *Int. J. Systematic Evolutionary Microbiol.* 56, 523–527. doi: 10.1099/ijs.0.63447-0

Gutierrez, T., Shimmield, T., Haidon, C., Black, K., and Green, D. H. (2008). Emulsifying and metal ion binding activity of a glycoprotein exopolymer produced by *Pseudoalteromonas* sp. strain TG12. *Appl. Environ. Microbiol.* 74, 4867–4876. doi: 10.1128/AEM.00316-08

Halbach, P., Friedrich, G., and von Stackelberg, U. (1988). *The manganese nodule belt of the Pacific Ocean: geological environment, nodule formation, and mining aspects* (Germany: F. Enke Stuttgart).

Halbach, P., Scherhag, C., Hebisch, U., and Marchig, V. (1981). Geochemical and mineralogical control of different genetic types of deep-sea nodules from the Pacific Ocean. *Mineralium Deposita* 16, 59–84. doi: 10.1007/BF00206455

Handley, K. M., Héry, M., and Lloyd, J. R. (2009). Redox cycling of arsenic by the hydrothermal marine bacterium Marinobacter santoriniensis. *Environ. Microbiol.* 11, 1601–1611. doi: 10.1111/j.1462-2920.2009.01890.x

Handley, K., and Lloyd, J. (2013). Biogeochemical implications of the ubiquitous colonization of marine habitats and redox gradients by *Marinobacter* species. *Front. Microbiol.* 4. doi: 10.3389/fmicb.2013.00136

He, X., Liu, Q., Li, X., Li, Z., Wang, H., Zhu, Z., et al. (in press). Preliminary study on microbial community structure and function in deep-sea polymetallic nodules and surrounding sediments. *J. Mar. Sci.* 43 (1).

Hein, J. R., and Koschinsky, A. (2014). "Deep-ocean ferromanganese crusts and nodules," in *Treatise on Geochemistry*, *2nd ed.* (Elsevier, Newnes), 273–291.

Hein, J. R., Koschinsky, A., Halbach, P., Manheim, F. T., Bau, M., Kang, J.-K., et al. (1997). Iron and manganese oxide mineralization in the Pacific. *Geological Society London Special Publications* 119, 123–138. doi: 10.1144/GSL.SP.1997.119.01.09

Hein, J. R., Koschinsky, A., and Kuhn, T. (2020). Deep-ocean polymetallic nodules as a resource for critical materials. *Nat. Rev. Earth Environ.* 1, 158–169. doi: 10.1038/s43017-020-0027-0

Hein, J. R., Mizell, K., Koschinsky, A., and Conrad, T. A. (2013). Deep-ocean mineral deposits as a source of critical metals for high- and green-technology applications: comparison with land-based resources. *Ore Geology Rev.* 51, 1–14. doi: 10.1016/j.oregeorev.2012.12.001

Helmann, J. D. (2014). Specificity of metal sensing: iron and manganese homeostasis in Bacillus subtilis. *J. Biol. Chem.* 289, 28112–28120. doi: 10.1074/jbc.R114.587071

Hoffmann, T. D., Reeksting, B. J., and Gebhard, S. (2021). Bacteria-induced mineral precipitation: a mechanistic review. *Microbiology* 167 (4), 1–13. doi: 10.1099/mic.0.001049

Hollingsworth, A. L., Jones, D. O. B., and Young, C. R. (2021). Spatial variability of abyssal nitrifying microbes in the north-eastern clarion-clipperton zone. *Front. Mar. Sci.* 8. doi: 10.3389/fmars.2021.663420

Hu, W., Zhou, H., Gu, L., Zhang, W., Lu, X., Fu, Q., et al. (2000). New evidence of microbe origin for ferromanganese nodules from the East Pacific deep sea floor. *Sci. China Ser. D: Earth Sci.* 43, 187–192. doi: 10.1007/bf02878148

Ivanova, E. P., Romanenko, L. A., Chun, J., Matte, M. H., Matte, G. R., Mikhailov, V. V., et al. (2000). *Idiomarina* gen. nov., comprising novel indigenous deep-sea bacteria from the Pacific Ocean, including descriptions of two species, Idiomarina abyssalis sp. nov. and *Idiomarina zobellii* sp. nov. *Int. J. Systematic Evolutionary Microbiol.* 50, 901–907. doi: 10.1099/00207713-50-2-901

Jiang, X.-D., Gong, J.-L., Ren, J.-B., Liu, Q.-S., Zhang, J., and Chou, Y.-M. (2020a). An interdependent relationship between microbial ecosystems and ferromanganese nodules from the Western Pacific Ocean. *Sedimentary Geology* 398, 1–18. doi: 10.1016/j.sedgeo.2019.105588

Jiang, X. D., Sun, X. M., and Guan, Y. (2019). Biogenic mineralization in the ferromanganese nodules and crusts from the South China Sea. *J. Asian Earth Sci.* 171, 46–59. doi: 10.1016/j.jseaes.2017.07.050

Jiang, X.-D., Sun, X.-M., Guan, Y., Gong, J.-L., Lu, Y., Lu, R.-F., et al. (2017). Biomineralisation of the ferromanganese crusts in the Western Pacific Ocean. *J. Asian Earth Sci.* 136, 58–67. doi: 10.1016/j.jseaes.2017.01.025

Jiang, X. D., Zhao, X., Chou, Y. M., Liu, Q. S., Roberts, A. P., Ren, J. B., et al. (2020b). Characterization and quantification of magnetofossils within abyssal manganese nodules from the western Pacific ocean and implications for nodule formation. *Geochemistry Geophysics Geosystems* 21, e2019GC008811. doi: 10.1029/2019GC008811

Jorgensen, B. (2001). "Diagenesis and sediment-water exchange," in *The Benthic Boundary Layer. Transport Processes and Biogeochemistry* (New York: Oxford University Press), 211–244.

Kent, A. G., Garcia, C. A., and Martiny, A. C. (2018). Increased biofilm formation due to high-temperature adaptation in marine Roseobacter. *Nat. Microbiol.* 3, 989–995. doi: 10.1038/s41564-018-0213-8

Konhauser, K. O. (1997). Bacterial iron biomineralisation in nature. *FEMS Microbiol. Rev.* 20, 315–326. doi: 10.1111/j.1574-6976.1997.tb00317.x

Li, D., Fu, Y., Sun, X., and Wei, Z. (2020). Critical metal enrichment mechanism of deep-sea hydrogenetic nodules: Insights from mineralogy and element mobility. *Ore Geology Rev.* 118, 103371. doi: 10.1016/j.oregeorev.2020.103371

Liu, H., Li, P., Wang, H., Qing, C., Tan, T., Shi, B., et al. (2020). Arsenic mobilization affected by extracellular polymeric substances (EPS) of the dissimilatory iron reducing bacteria isolated from high arsenic groundwater. *Sci. Total Environ.* 735, 139501. doi: 10.1016/j.scitotenv.2020.139501

Liu, X., and Millero, F. J. (2002). The solubility of iron in seawater. *Mar. Chem.* 77, 43–54. doi: 10.1016/S0304-4203(01)00074-3

Mainali, K. P., Bewick, S., Thielen, P., Mehoke, T., Breitwieser, F. P., Paudel, S., et al. (2017). Statistical analysis of co-occurrence patterns in microbial presence-absence datasets. *PloS One* 12, e0187132. doi: 10.1371/journal.pone.0187132

Margolis, S. V., and Burns, R. G. (1976). Pacific deep-sea maganese nodules-their distribution, composition, and origin. *Annu. Rev. Earth Planetary Sci.* 4, 229–263.

Matsunaga, T., Sakaguchi, T., and Tadokoro, F. (1991). Magnetite formation by a magnetic bacterium capable of growing aerobically. doi: 10.1007/BF00169632

Mhatre, E., Troszok, A., Gallegos-Monterrosa, R., Lindstädt, S., Hölscher, T., Kuipers, O. P., et al. (2016). The impact of manganese on biofilm development of Bacillus subtilis. *Microbiology* 162, 1468–1478. doi: 10.1099/mic.0.000320

Molari, M., Janssen, F., Vonnahme, T. R., Wenzhöfer, F., and Boetius, A. (2020). The contribution of microbial communities in polymetallic nodules to the diversity of the deep-sea microbiome of the Peru Basin, (4130–4198 m depth). *Biogeosciences* 17, 3203–3222. doi: 10.5194/bg-17-3203-2020

Nayak, B., Das, S. K., and Munda, P. (2013). Biogenic signature and ultra microfossils in ferromanganese nodules of the Central Indian Ocean Basin. *J. Asian Earth Sci.* 73, 296–305. doi: 10.1016/j.jseaes.2013.03.032

Omoike, A., and Chorover, J. (2006). Adsorption to goethite of extracellular polymeric substances from *Bacillus subtilis*. *Geochimica Cosmochimica Acta* 70, 827–838. doi: 10.1016/j.gca.2005.10.012

Poretsky, R., Rodriguez-R, L. M., Luo, C., Tsementzi, D., and Konstantinidis, K. T. (2014). Strengths and limitations of 16S rRNA gene amplicon sequencing in revealing temporal microbial community dynamics. *PloS One* 9, e93827. doi: 10.1371/journal.pone.0093827

Priyadarshanee, M., and Das, S. (2021). Bioremediation potential of biofilm forming multi-metal resistant marine bacterium Pseudomonas chengduensis PPSS-4 isolated from contaminated site of Paradip Port, Odisha. *J. Earth System Sci.* 130, 125. doi: 10.1007/s12040-021-01627-w

Ren, J., He, G., Deng, X., Deng, X., Yang, Y., Yao, H., et al. (2022). Metallogenesis of Co-rich ferromanganese nodules in the northwestern Pacific: Selective enrichment of metallic elements from seawater. *Ore Geology Rev.* 143, 104778. doi: 10.1016/j.oregeorev.2022.104778

Ren, M., and Jones, B. (2021). Modern authigenic amorphous and crystalline iron oxyhydroxides in subsurface Ordovician dolostones (Jinan, North China Block): Biomineralization and crystal morphology. *Sedimentary Geology* 426, 106044. doi: 10.1016/j.sedgeo.2021.106044

Reykhard, L. Y., and Shulga, N. A. (2019). Fe-Mn nodule morphotypes from the NE Clarion-Clipperton Fracture zone, Pacific ocean: comparison of mineralogy, geochemistry and genesis. *Ore Geology Rev.* 110, 1–15. doi: 10.1016/j.oregeorev.2019.102933

Reyss, J., Lemaitre, N., Ku, T., Marchig, V., Southon, J., Nelson, D., et al. (1985). Growth of a manganese nodule from Peru Basin: A radiochemical anatomy. *Geochimica Cosmochimica Acta* 49, 2401–2408. doi: 10.1016/0016-7037(85)90240-6

Roy, S. (1992). Environments and processes of manganese deposition. *Economic Geology* 87, 1218–1236. doi: 10.2113/gsecongeo.87.5.1218

Santamaría, M., Díaz-Marrero, A. R., Hernández, J., Gutiérrez-Navarro, A. M., and Corzo, J. (2003). Effect of thorium on the growth and capsule morphology of Bradyrhizobium. *Environ. Microbiol.* 5, 916–924. doi: 10.1046/j.1462-2920.2003.00487.x

Satya, S., Sharma, S., Choudhary, G., and Kaushik, G. (2024). "Advances in environmental microbiology: A multi-omic perspective," in *Microbial Omics in Environment and Health*. Eds. M. Kesheri, S. Kanchan, T. B. Salisbury and R. P. Sinha (Springer Nature Singapore, Singapore), 175–204.

Shiraishi, F., Mitsunobu, S., Suzuki, K., Hoshino, T., Morono, Y., and Inagaki, F. (2016). Dense microbial community on a ferromanganese nodule from the ultra-oligotrophic South Pacific Gyre: Implications for biogeochemical cycles. *Earth Planetary Sci. Lett.* 447, 10–20. doi: 10.1016/j.epsl.2016.04.021

Shulga, N., Abramov, S., Klyukina, A., Ryazantsev, K., and Gavrilov, S. (2022). Fast-growing Arctic Fe–Mn deposits from the Kara Sea as the refuges for cosmopolitan marine microorganisms. *Sci. Rep.* 12, 21967. doi: 10.1038/s41598-022-23449-6

Smith, A., Popa, R., Fisk, M., Nielsen, M., Wheat, C. G., Jannasch, H. W., et al. (2011). *In situ* enrichment of ocean crust microbes on igneous minerals and glasses using an osmotic flow-through device. *Geochemistry Geophysics Geosystems* 12, Q06007. doi: 10.1029/2010GC003424

Sudek, L. A., Templeton, A. S., Tebo, B. M., and Staudigel, H. (2009). Microbial ecology of Fe (hydr)oxide mats and basaltic rock from Vailulu'u seamount, American Samoa. *Geomicrobiology J.* 26, 581–596. doi: 10.1080/01490450903263400

Takematsu, N., Sato, Y., and Okabe, S. (1989). Factors controlling the chemical composition of marine manganese nodules and crusts: a review and synthesis. *Mar. Chem.* 26, 41–56. doi: 10.1016/0304-4203(89)90063-7

Templeton, A. S., Staudigel, H., and Tebo, B. M. (2005). Diverse Mn(II)-oxidizing bacteria isolated from submarine basalts at Loihi seamount. *Geomicrobiology J.* 22, 127–139. doi: 10.1080/01490450590945951

Tully, B. J., and Heidelberg, J. F. (2013). Microbial communities associated with ferromanganese nodules and the surrounding sediments. *Front. Microbiol.* 4. doi: 10.3389/fmicb.2013.00161

Veillette, J., Sarrazin, J., Gooday, A. J., Galéron, J., Caprais, J.-C., Vangriesheim, A., et al. (2007). Ferromanganese nodule fauna in the Tropical North Pacific Ocean: Species richness, faunal cover and spatial distribution. *Deep Sea Res. Part I: Oceanographic Res. Papers* 54, 1912–1935. doi: 10.1016/j.dsr.2007.06.011

Vereshchagin, O. S., Perova, E. N., Brusnitsyn, A. I., Ershova, V. B., Khudoley, A. K., Shilovskikh, V. V., et al. (2019). Ferro-manganese nodules from the Kara Sea: Mineralogy, geochemistry and genesis. *Ore Geology Rev.* 106, 192–204. doi: 10.1016/j.oregeorev.2019.01.023

Verlaan, P. A., Cronan, D. S., and Morgan, C. L. (2004). A comparative analysis of compositional variations in and between marine ferromanganese nodules and crusts in the South Pacific and their environmental controls. *Prog. Oceanography* 63, 125–158. doi: 10.1016/j.pocean.2004.11.001

Wang, X., and Müller, W. E. (2009). Marine biominerals: perspectives and challenges for polymetallic nodules and crusts. *Trends Biotechnol.* 27, 375–383. doi: 10.1016/j.tibtech.2009.03.004

Wang, X.-H., Schloßmacher, U., Wang, S.-F., Schröder, H. C., Wiens, M., Batel, R., et al. (2012). From nanoparticles via microtemplates and milliparticles to deep-sea nodules: biogenically driven mineral formation. *Front. Materials Sci.* 6, 97–115. doi: 10.1007/s11706-012-0164-6

Washburn, T. W., Jones, D. O. B., Wei, C.-L., and Smith, C. R. (2021). Environmental heterogeneity throughout the clarion-clipperton zone and the potential representativity of the APEI network. *Front. Mar. Sci.* 8. doi: 10.3389/fmars.2021.661685

Wegorzewski, A. V., and Kuhn, T. (2014). The influence of suboxic diagenesis on the formation of manganese nodules in the Clarion Clipperton nodule belt of the Pacific Ocean. *Mar. Geology* 357, 123–138. doi: 10.1016/j.margeo.2014.07.004

Wright, M. H., Farooqui, S. M., White, A. R., and Greene, A. C. (2016). Production of manganese oxide nanoparticles by *Shewanella* species. *Appl. Environ. Microbiol.* 82, 5402–5409. doi: 10.1128/AEM.00663-16

Wu, Y.-H., Liao, L., Wang, C.-S., Ma, W.-L., Meng, F.-X., Wu, M., et al. (2013). A comparison of microbial communities in deep-sea polymetallic nodules and the surrounding sediments in the Pacific Ocean. *Deep Sea Res. Part I: Oceanographic Res. Papers* 79, 40–49. doi: 10.1016/j.dsr.2013.05.004

Xuezheng, L., Aiguo, G., and Haowen, C. (2008). Isolation and phylogenetic analysis of cultivable manganese bacteria in sediments from the Arctic Ocean. *Acta Ecologica Sin.* 28, 6364–6370. doi: 10.1016/S1872-2032(09)60017-2

Yan, W., Guo, W., Wang, L., and Jing, C. (2021). Extracellular polymeric substances from Shewanella oneidensis MR-1 biofilms mediate the transformation of Ferrihydrite. *Sci. Total Environ.* 784, 147245. doi: 10.1016/j.scitotenv.2021.147245

Zakaria, Z. A., Zakaria, Z., Surif, S., and Ahmad, W. A. (2007). Hexavalent chromium reduction by *Acinetobacter haemolyticus* isolated from heavy-metal contaminated wastewater. *J. Hazardous Materials* 146, 30–38. doi: 10.1016/j.jhazmat.2006.11.052

Zhang, J., Wang, C., Han, J.-R., Chen, G.-J., and Du, Z.-J. (2019). *Alteromonas flava* sp. nov. and *Alteromonas facilis* sp. nov., two novel copper tolerating bacteria isolated from a sea cucumber culture pond in China. *Systematic Appl. Microbiol.* 42, 217–222. doi: 10.1016/j.syapm.2018.11.006

Zhang, C., Yang, K., Li, F., and Zhou, J. (2024). The roles of amorphous phase on Ca–Mg carbonate mineralization under the action of bacteria and EPS. *J. Crystal Growth* 644, 127841. doi: 10.1016/j.jcrysgro.2024.127841

Zheng, S., Zhou, Q., Chen, C., Yang, F., Cai, Z., Li, D., et al. (2019). Role of extracellular polymeric substances on the behavior and toxicity of silver nanoparticles and ions to green algae Chlorella vulgaris. *Sci. Total Environ.* 660, 1182–1190. doi: 10.1016/j.scitotenv.2019.01.067

frontiers | Frontiers in Marine Science

TYPE Hypothesis and Theory
PUBLISHED 14 May 2025
DOI 10.3389/fmars.2025.1556799

OPEN ACCESS

EDITED BY
Xiaodong Jiang,
Guangdong University of Technology, China

REVIEWED BY
Xiting Liu,
Ocean University of China, China
Hongrui Zhang,
Tongji University, China

*CORRESPONDENCE
Dong Xu
xudong@sio.org.cn

RECEIVED 07 January 2025
ACCEPTED 24 April 2025
PUBLISHED 14 May 2025
CORRECTED 28 August 2025

CITATION
Lin J, Xu D, Li Y, Ye L, Ge Q, Bian Y, Han X, Zhang W and Cheng S (2025) Giant diatom blooms driven by deep water upwelling since late MIS3? Evidence from the rim of the Mariana Trench. *Front. Mar. Sci.* 12:1556799. doi: 10.3389/fmars.2025.1556799

Giant diatom blooms driven by deep water upwelling since late MIS3? Evidence from the rim of the Mariana Trench

Junyu Lin[1,2], Dong Xu[1,2]*, Yue Li[2], Liming Ye[1,2], Qian Ge[1,2], Yeping Bian[1,2], Xibin Han[1,2], Weiyan Zhang[1,2] and Shenghui Cheng[1,2]

[1]State Key Laboratory of Submarine Geoscience, Hangzhou, China, [2]Second Institute of Oceanography, Ministry of Natural Resources, Hangzhou, China

Laminated Diatom Mats (LDMs) in the low-latitude Western Pacific provide key insights into global climate and carbon cycling. While *Ethmodiscus rex* (*E. rex*) LDMs research has advanced, two critical aspects remain to be elucidated: (1) the precise chronology of LDMs formation, and (2) its relationship with oceanic circulation patterns and associated nutrient flux variations. In this study, we employed AMS ^{14}C dating coupled with carbonate content variations to constrain the formation age of LDMs, complemented by comprehensive geochemical and clay mineral analyses of core E20, we found: (1) Diatom blooms occurred mainly from Last Glacial Maximum (LGM) to early Holocene; (2) Sediments are mostly volcanic, with increased material in *E. rex* layers suggesting stronger deep currents transported volcanic debris; (3) Blooms weren't solely caused by Asian dust-derived nutrients. We propose deep current intensification and topographic upwelling drove diatom growth, highlighting deep ocean processes' role in surface productivity and LDMs formation. This advances understanding of their climate and carbon cycle significance.

KEYWORDS

last glacial period, Western Pacific, Mariana Trench, laminated diatom mats, *Ethmodiscus rex*

1 Introduction

The low-latitude Western Pacific is a pivotal region for global sea-air interactions, with its interannual variability exerting a substantial influence on global climate dynamics (Yan et al., 1992; Webster et al., 1998; Hollstein et al., 2018; Bowman et al., 2023). Studies have demonstrated the low-latitude Western Pacific's capacity for atmospheric CO_2 sequestration during glacial periods (Bradtmiller et al., 2006; Xiong et al., 2013; Xu et al., 2020). Recent discoveries of extensive Laminated Diatom Mats (LDMs) in the low-latitude

Western Pacific have significantly enhanced our understanding of global climate dynamics and carbon cycling processes (Xiong et al., 2013; Luo et al., 2018a, 2018b; Tang et al., 2024).

Diatoms, which contribute approximately 40% of marine primary productivity (Nelson et al., 1995), play a crucial role in the biological pump, exhibiting higher carbon sequestration efficiencies compared to calcareous organisms (Harrison, 2000). Diatom mats typically form through the bloom of 'giant' or 'shade' diatoms, which are rapidly buried and preserved as laminated sediments (Kemp and Baldauf, 1993; Zhai et al., 2009). These mats deliver significant quantities of organic carbon and biogenic silica to the seafloor, thereby influencing atmospheric CO_2 partial pressure regulation and playing a pivotal role in the global carbon cycle and silica cycle (Kemp and Villareal, 2013). To date, diatom mats have been documented in the Pacific, Atlantic, Indian, and Southern Oceans (Kemp et al., 2006). The Western Pacific's predominant mat-forming diatom species, *Ethmodiscus rex* (*E. rex*), exhibits unique ecological adaptations, including the capacity to thrive in oligotrophic, stratified subsurface waters and perform vertical migrations (Kemp and Baldauf, 1993; Yoder et al., 1994; Kemp et al., 2010). *E. rex* LDMs are found across various geomorphological units in the Western Pacific, including trenches (hadal zones) (Luo et al., 2017; Zhang et al., 2019; Huang et al., 2020; Lai et al., 2023; Tang et al., 2024), basins (Zhai et al., 2009; Xiong et al., 2010; Shen et al., 2017; Zhang et al., 2021), ridges (Shibamoto and Harada, 2010; Cai, 2019; Li et al., 2021). Most *E. rex* LDMs have been dated to the Last Glacial Maximum (LGM) (Zhai et al., 2009; Xiong et al., 2010) and the Last Deglaciation (LD) (Tang et al., 2024), with a limited number of studies reporting Holocene diatom mats (Zhang et al., 2024).

Three primary hypotheses have been proposed to explain the formation mechanism of *E. rex* diatom mats in the Western Pacific during the LGM: (1) The Silica Ventilation Hypothesis (Zhai et al., 2009), this hypothesis proposes that the northward expansion of silica-rich Antarctic Intermediate Water (AAIW) during the last glacial period could have stimulated diatom blooms. (2) The Eolian-Silicon-Induced Bloom Hypothesis (Xiong et al., 2013, 2015), this mechanism suggests that diatom blooms were fueled by nutrients (Si and Fe) derived from Asian dust. These blooms occurred in stratified seawater environments, with diatoms subsequently deposited on the seafloor through a process termed 'fall dumping'. (3) The Middle-Deep Water Upwelling Stimulation Hypothesis (Zhang et al., 2021), this hypothesis proposes that diatom blooms were triggered by a reduction in seawater stratification and the upwelling of nutrient-rich waters from mid and deep layers. Additionally, the thermohaline circulation of surface seawater played a critical role in this process. Although widely recognized, the "Silicon-Induced Bloom Hypothesis" still faces challenges in explaining certain phenomena, including:1)*E. rex* LDMs have not been reported in the northwestern corner of the Philippine Basin (northwest of core WPS1/2, see Figure 1), which is closer to the eolian dust source. Instead, *E. rex* LDMs are more commonly found around the Mariana-Yap Trench, a region farther from the dust source (Luo et al., 2017; Zhang et al., 2019, 2024; Huang et al., 2020; Lai et al., 2023). 2) Although substantial eolian dust deposition occurred in the Western Pacific during marine oxygen isotope stage (MIS) 4 and 6 (Han et al., 2002; Maeda et al., 2002; Xu et al., 2015), no *E. rex* LDMs have been documented in these periods, despite reported increases in opal mass accumulation rates (MAR) during MIS6 and MIS4 (Maeda et al., 2002). Recently, Xiong et al. (2022) refined their hypothesis, suggesting that strong aridity during the LGM prevented the formation of a subsurface barrier layer, allowing deep key nutrients (nitrate and/or phosphate) to reach surface waters, thereby stimulating blooms of *E. rex* and the subsequent formation of LDMs in the Indo-Pacific Warm Pool (IPWP).

A review of current research on *E. rex* LDMs in the Western Pacific reveals some key limitations, including but not limited to: (1) Uncertainty in the age of LDMs. The chronological framework of LDMs remains contentious, particularly regarding the reliability of AMS ^{14}C dating applied to diatom-rich samples (Xiong et al., 2013; Zhang et al., 2021); (2) Numerous cores containing *E. rex*-rich layers have been recovered from submarine high-relief topography. Researchers have investigated the relationship between the formation of these *E. rex*-rich layers and changes in current dynamics (and nutrient supply), as documented in cores from the Bermuda Rise in the North Atlantic (Hendry et al., 2014), the 23-33° S section of the Mid-Atlantic Ridge (Romero and Schmieder, 2006), and the 90°E Ridge in the Indian Ocean (Broecker et al., 2000). However, in the Western Pacific, LDMs records are predominantly derived from deep-water environments, with a conspicuous scarcity of cores collected from submarine high-relief topography (Cai, 2019; Li et al., 2021). Furthermore, the influence of current systems has received remarkably little attention; (3) The lack of geochemical criteria for classifying LDM or diatomaceous clay (DC) presents another limitation. For instance, there are no established thresholds for total SiO_2 or opal content in sediments to definitively categorize deposits as either LDM or DC. This knowledge gap hinders robust assessment of diatom bloom intensity in the Western Pacific and obscures the mechanisms underlying their formation.

This study presents a comprehensive analysis of the geochemical signatures and clay mineral assemblages in core E20 from the Mariana Arc, which exhibits alternating *E. rex* LDMs and calcareous clay sequences. Through integrated analysis of LDMs distribution patterns, seabed topography, and deep current dynamics during the last glacial period, we propose a new mechanistic framework for LDMs formation in the low-latitude Western Pacific.

2 Materials and methods

2.1 Study area

The study area is situated primarily within the Mariana subduction zone, a classic example of an ocean-ocean subduction zone formed by the westward subduction of the Pacific plate beneath the Philippine plate. This region features a complex trench-arc-basin system, with the Mariana Island Arc, the Parece

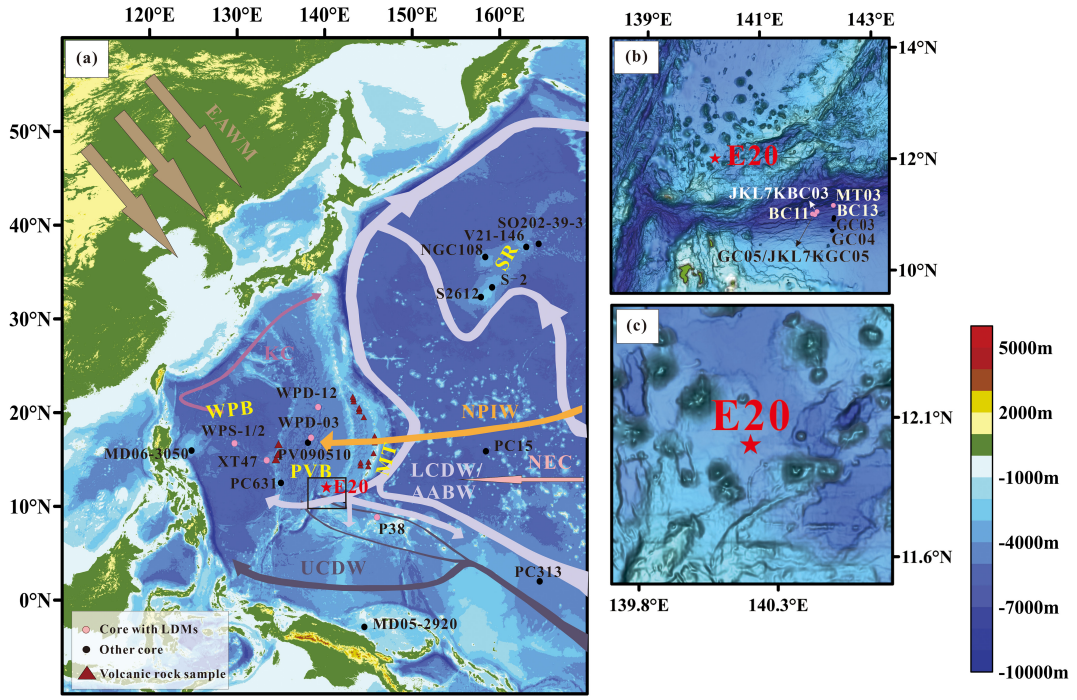

FIGURE 1
Sketch map of the study area and the core sites. **(a)** Current distribution in the study area (modified after Hu et al., 2015; Hu and Piotrowski, 2018; Xiao et al., 2020; Tang et al., 2024). **(b)** The black boxed area in panel **(a)**. **(c)** Seafloor topography around core E20. WPB, West Philippine Basin; PVB, Parece Vela Basin; MT, Mariana Trench; SR, Shatsky Rise; AABW, Antarctic Bottom Water; LCDW, Lower Circumpolar Deep Water; UCDW, Upper Circumpolar Deep Water; NEC, North Equatorial Current; NPIW, North Pacific Intermediate Water; KC, Kuroshio Current; EAWM, East Asian Winter Monsoon. Valcanic rock samples (red triangles): Marianan Arc and Marianan Trench (Ikeda et al., 2016); Palau-Kyushu Ridge (Lelikov et al., 2018; Ishizuka et al., 2011). Cores with LDMs (pink dots): BC11, BC13, GC03, GC04 and GC05 (Luo et al., 2017, 2018); JL7KGC05 (Zhang et al., 2019); JL7KBC03 (Zhang et al., 2024); MT03 (Lai et al., 2023); WPD-12, WPD-03 (Xiong et al., 2013); XT47 (Zhang et al., 2021); WPS-1/2 (Tang et al., 2024); P38 (Cai, 2019). Other cores (black dot): PC313 (Khim et al., 2012); MD05-2920 (Tachikawa et al., 2011); MD06-3050 (Sun et al., 2017); S-2 (Yamane, 2003); PC15 (Wang et al., 2021); PC631 (Seo et al., 2014); PV090510 (Ming et al., 2014); V21-146 (Han et al., 2002); SO202-39-3 (Korff et al., 2016); S2612 and NGC108 (Maeda et al., 2002).

Vela Basin, the Kyushu-Palau Ridge, and the West Philippine Basin developing sequentially from east to west. The deep-sea basins near island arcs and ridges accumulate sediments comprising both distal sources, such as Asian inland dust transported by the East Asian winter monsoon, and proximal sources, including materials from ridge (seamount) erosion and volcanic activities (Scott and Kroenke, 1980; Seo et al., 2014). Recent studies have revealed that the *E. rex* LDMs in western Pacific are predominantly located in low-lying basins, rifts, and trenches (hadal zones) due to the "funnel effect": the variations in seafloor topography can cause some stations to block lateral transport by bottom currents, allowing deposited diatom mat fragments to accumulate and preserve, while others are carried away by current flushing (Tang et al., 2024).

The study area is located within the oligotrophic North Pacific Subtropical Gyre, where strong stratification significantly inhibits vertical mixing between surface waters and the deeper ocean (Dai et al., 2023). The deep water in this area is influenced by the Circumpolar Deep Water (CDW), a component of the Antarctic Bottom Water (AABW) (Lumpkin and Speer, 2007), which can be further divided into Lower Circumpolar Deep Water (LCDW) and Upper Circumpolar Deep Water (UCDW) (Chiswell et al., 2015). Below approximately 3500 meters in the western Pacific, the deep water is predominantly influenced by the LCDW (Zhang et al., 2022). Recent mooring observations reveal that the Yap-Mariana Junction acts as a key conduit for the LCDW to flow into the western Pacific. Furthermore, the abyssal current from the West Mariana Basin (WMB) enters the North Pacific Basin (NPB) via the Kyushu-Palau Ridge (KPR) Channel (Wang et al., 2023). The seabed topography in these critical channels is highly complex, with the deep flow fields and water mass structures displaying pronounced seasonal variability (Wang et al., 2023). The intermediate water in the study area is likely influenced by the North Pacific Intermediate Water (NPIW), whereas the surface water dynamics are predominantly controlled by the North Equatorial Current (NEC) (Figure 1).

2.2 Sample information

Core E20 was collected from a depression (12.000167°N, 140.200575°E) on the Mariana Arc at a water depth of approximately 4100 meters (Figure 1c). The 331 cm-long core displays pronounced lithological variability, comprising three distinct sedimentary units from base to top: U3 (280–331 cm), composed of brown pelagic clay/calcareous clay; U2 (10–280 cm), dominated by fragments of the giant diatom *E. rex*, forming yellow-

brown to greyish-yellow laminations with occasional grey laminations and a loose structure. This unit is further subdivided into two parts: the upper part (U2-1, 10–115 cm) contains a small amount of detrital material, and the lower part (U2-2, 115–280 cm) is characterized by a higher abundance of diatoms; U1 (0–10 cm) is a layer of brown calcareous siliceous clay (Li et al., 2021).

2.3 Analytical method

Successive samples were collected at 2 cm intervals, with the final sample extending 328–330 cm, resulting in a total of 165 subsamples used for analyses of major elements, organic carbon and nitrogen, and carbonate content. Major elements were determined using an AxiosMAX (Netherlands) X-ray fluorescence spectrometry (XRF). Sample pretreatment followed the method described by Liao et al. (2024), and the analytical results have a relative error of <5%. Loss on ignition was measured by high temperature calcination at 1,000°C for 40 minutes. The total carbon, organic carbon and nitrogen contents were analyzed using an Elementar Vario elemental analyzer (Germany). Sample pretreatment followed the method described in Luo et al. (2017), and the analytical accuracy was ±0.01%. The $CaCO_3$ content was calculated following the method of Khim et al. (2012), and the biogenic silica (opal) content was calculated following the method of Nath et al. (1989).

Clay fractions (<2 μm) were extracted according to Stoke's settling velocity principle for clay mineral composition analysis (Wan et al., 2007). A total of 17 samples were collected from core E20: two samples from U1 (2–4 cm and 6–8 cm) and fifteen samples from U3 (at 2 cm intervals between 292–330 cm). No samples were taken from U2 due to the extremely high concentration of bioclastic debris in this unit. The pretreatment of clay mineral samples followed the method described by Wan et al. (2007) and can be summarized as follows: (1) Removal of salts, approximately 8–10 g of dried sample was washed with deionized water; (2) Removal of organic matter, 20 mL of 20% hydrogen peroxide was added; (3) Removal of $CaCO_3$, dilute hydrochloric acid was added; (4) Extraction of clay fractions, the <2 μm clay fraction was extracted and prepared into oriented clay slices using the 'smearing method'. Clay mineral analysis was conducted using an X'Pert PRO X-ray diffractometer (Netherlands) with the following parameters: tube voltage of 45 kV, tube current of 40 mA, scan range of 3° to 35° (2θ), and scan speed of 1.8°/min. The relative contents of four clay minerals (illite, smectite, chlorite, and kaolinite) were calculated using the BISCAYE method (Biscaye, 1965).

The sedimentation rates of different units (U1-U3) were calculated based on the AMS^{14}C dating results from Li et al., 2021.

3 Results

3.1 Major elements composition

The average content of major elemental oxides in core E20 decreases in the following order: SiO_2 > CaO > Na_2O > Al_2O_3 > Fe_2O_3 > MgO > K_2O > TiO_2 > MnO > P_2O_5. The concentration of SiO_2 ranges from 22.03% to 81.45%, with an average of 64.60%, whereas the average concentrations of the remaining oxides are all below 10% (Supplementary Table S1).

The contents of major oxides exhibit distinct segmentation with depth (Figure 2), a pattern that aligns with changes in the brightness curve (L*) and a* values (Li et al., 2021). This segmentation correlates closely with lithological variations, showing more pronounced fluctuations in U1 and U3 (clay layers) and relatively minor variations in U2 (diatom layer). As illustrated in Figure 2, the profiles of TiO_2, Al_2O_3, Fe_2O_3, K_2O, MgO, MnO, and P_2O_5 display similar trends, with peak concentrations in U3 and the lowest concentrations in U2. The high SiO_2 values in U2 reflect the significant influence of siliceous biogenic debris. In contrast, the CaO content shows a pronounced peak in U3 and an upward trend in U1. The Na_2O profile is unique, with the highest concentrations observed in U2, likely attributable to the high pore water content in this unit.

The mean values of major oxides in core E20 and potential source areas were normalized to the upper continental crust (UCC) (Figure 3a). The results reveal distinct geochemical patterns across the sedimentary units. U1 is relatively enriched in CaO and MnO but deficient in SiO_2, Al_2O_3, K_2O, and TiO_2. U2 is characterized by relatively high concentrations of SiO_2 and Na_2O but exhibits lower concentrations of most other major oxides. In U3, the sediments are relatively enriched in Fe_2O_3, MgO, CaO, MnO, and P_2O_5 but deficient in SiO_2, Al_2O_3, and K_2O. In general, the clay-rich sections (U1 and U3) of core E20 exhibit a major oxide composition most similar to that of Mariana Trench sediments, although they are relatively enriched in CaO (Figure 3b). Compared to Mariana Arc and Mariana Trough basalts, these sections are more enriched in Na_2O, K_2O, and MnO but deficient in Fe_2O_3, MgO, and TiO_2.

Although widely reported, many *E. rex*-rich deposits often contain significant amounts of clay minerals and thus cannot be simply classified as LDMs. In typical LDM samples from core E20, SiO_2 content exceeds 60% (Figure 2). Due to potential dilution effects from calcareous or lithogenic detritus, distinguishing between LDM and DC (diatom clay) based solely on total SiO_2 or opal content is inaccurate. Based on analytical results from Site E20, we recommend using the SiO_2/Al_2O_3 ratio as the diagnostic criterion: samples with SiO_2/Al_2O_3 >10 are classified as LDM; those with ratios between 4–10 as DC; and samples with ratios <4 as pelagic clay (PC).

3.2 TOC and TN contents

The total organic carbon (TOC) content in core E20 ranges from 0.13% to 0.67%, with an average of 0.28%. U1 has an average TOC content of 0.40%, while U2 and U3 have lower averages of 0.28% and 0.24%, respectively. Within U2, the upper part (U2-1) has an average TOC content of 0.22%, whereas the lower part (U2-2) has a higher average of 0.33% and contains the highest TOC value in the core. The total nitrogen (TN) content ranges from

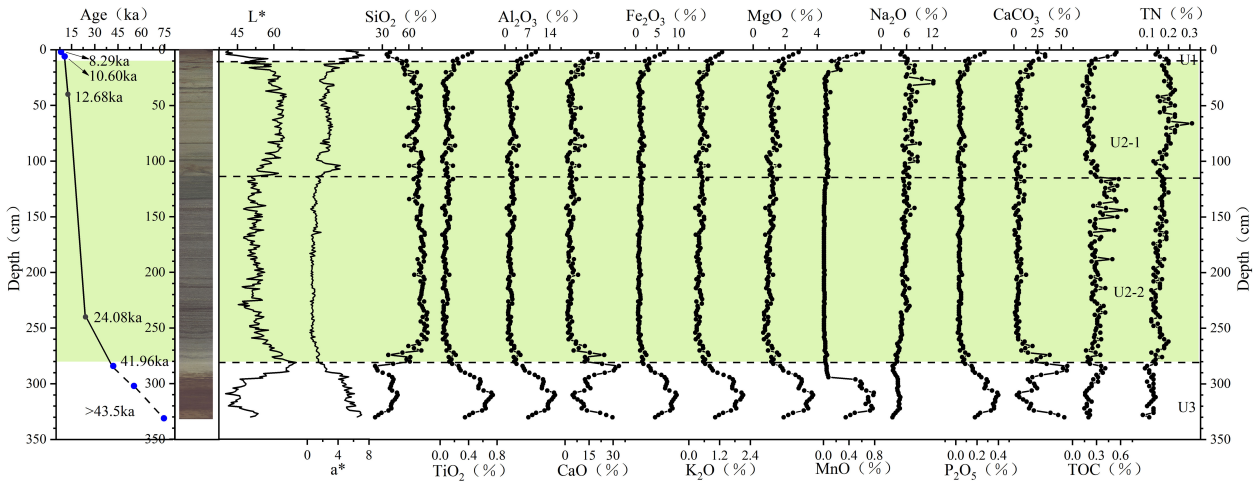

FIGURE 2
Geochemical profiles and core scan results (photo, L*, and a*) of core E20. The five blue dots represent planktonic foraminiferal ages, while the two black dots correspond to organic carbon ages. Core scan results and AMS ^{14}C ages are from Li et al. (2021). The green shaded area indicate diatom mat.

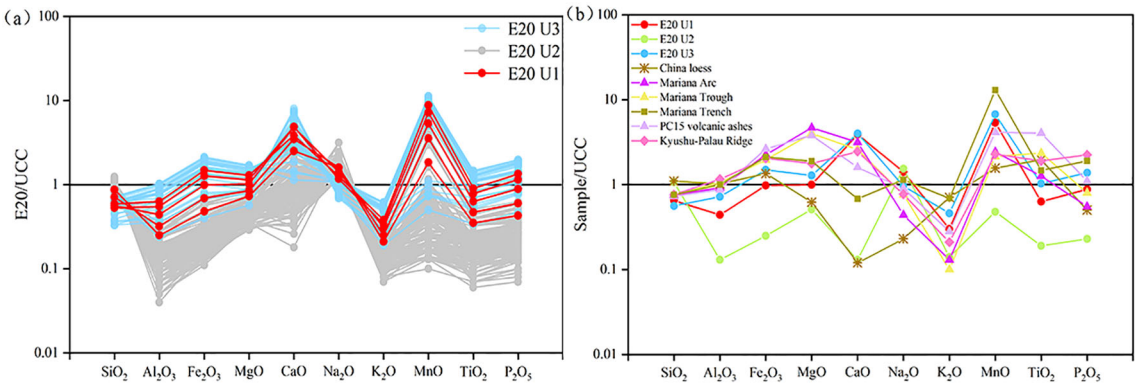

FIGURE 3
UCC (Upper Continental Crust) normalization of major oxides in core E20 **(a)** and potential source regions **(b)**. Data sources: Chinese loess (Qiao et al., 2011); Mariana Arc and Mariana Trough (Ikeda et al., 2016); Mariana Trench (Luo et al., 2018b); Kyushu-Palau Ridge (Lelikov et al., 2018; Ishizuka et al., 2011); PC15 volcanic ashes (Wang et al., 2021); UCC (Taylor and McLennan, 1985).

0.08% to 0.30%, with an average of 0.16%. U1 has a mean TN content of 0.17%, which shows an inverse relationship with TOC. U2 has an average TN content of 0.17%, with the highest value observed at 68 cm. U3 has a mean TN content of 0.12%. The TOC/TN ratio in core E20 ranges from 0.59 to 4.50, with an average of 1.82.

3.3 Carbonate contents

In U3, the average $CaCO_3$ content is 26.49%, with significant variability. In contrast, U2 has a lower average $CaCO_3$ content of 6.89%, showing minimal variation. Within U2, the lower part (U2-2) has an average $CaCO_3$ content of 6.41%, while the upper part (U2-1) has a slightly higher average of 7.62%. In U1, the $CaCO_3$ content gradually increases toward the top, with an average of 27.55%.

3.4 Clay mineral composition

The clay mineral composition of the E20 core sediments is dominated by illite, with an average content of 54%. Smectite has an average content of 19%, while chlorite and kaolinite are present in smaller amounts, averaging 15% and 13%, respectively (Supplementary Table S2).

In U3, the clay mineral content is highly variable. In contrast, the two samples from U1 show a decrease in illite content and a significant increase in smectite content compared to U3.

3.5 The age of diatom mats in core E20

No age reversal is observed in core E20 (Supplementary Table S3, Li et al., 2021). Foraminiferal ages from the 0–2 cm and 4–6 cm layers in U1 indicate a low average sedimentation rate of 1.73 cm/kyr. The sedimentation rate increases significantly between the 4–6 cm and 38–40 cm intervals, reaching 16.35 cm/kyr. This places the age of the lower boundary of U1 at 10.9 ka. Foraminiferal dating from the 282–284 cm layer (just below the lower boundary of U2) yields an age of 41.96 ka, indicating that the diatom bloom occurred after this time. Assuming a constant sedimentation rate in the LDMs section and using the two dating results (24.08 ka from the 238–240 cm interval and 12.68 ka from the 38–40 cm interval, bulk sediment), we estimate that diatom mats first appeared at 280 cm around 26.48 ka. This aligns with the earliest diatom bloom age reported by Zhai et al. (2009). Given the absence of diatoms and lower water content in U3, we assume its sedimentation rate is lower than that of U1.

4 Discussion

4.1 Glacial-interglacial cycle of carbonate content in E20

E. rex LDMs in the Western Pacific are predominantly found in deep-water basins and trenches, with their ages (from 28.6 ka to 6.76 ka) primarily determined by AMS ^{14}C dating of organic matter (Zhai et al., 2009; Luo et al., 2018b; Tang et al., 2024; Zhang et al., 2024). To our knowledge, the currently available AMS ^{14}C dating on foraminifers (*G. ruber*) in LDMs from the Western Pacific is exclusively documented in Core P38 (water depth: 3838 m) recovered from the Caroline Ridge (or southern slope of the Mariana Trench). In this core, the basal age of LDMs is approximately 46.06 ka, while foraminifers from 4–6 cm depth in the overlying DC layer (0–14 cm) yield an age of 8.87 ka. In Core E20, the AMS ^{14}C ages of foraminifers from DC layer both above and below the LDMs (Figure 2) are broadly consistent with those from corresponding lithological units in Core P38. However, no AMS ^{14}C dating on foraminifers has been conducted within the LDMs of core E20. Nevertheless, by comparing carbonate content profiles with other Western Pacific cores, we can better constrain the depositional timeframe of core E20.

Numerous sediment cores from the Western Pacific exhibit carbonate content variations that deviate from the typical 'Pacific-style cycle'—a pattern generally characterized by high values during glacial periods and low values during interglacial periods. Since MIS 6, the carbonate records predominantly display an inverse trend, with lower concentrations during glacials and higher concentrations during interglacials (Maeda et al., 2002; Yamane, 2003; Khim et al., 2012; Tachikawa et al., 2011; Sun et al., 2017; Figure 4).

Microscopic observations have revealed that the carbonate-rich layers in E20 contain abundant foraminifers and no evidence of microbial sulfate reduction related authigenic carbonates (Liu et al., 2024) was found. Assuming constant $CaCO_3$ productivity, variations in $CaCO_3$ content are primarily controlled by the dilution of detrital material (both lithogenic and siliceous biogenic debris) and the dissolution of $CaCO_3$. Sun et al. (2017) suggest that $CaCO_3$ dissolution was the dominant control in core MD06–3050 from the Benham Rise. During MIS2 and MIS4, MD06–3050 exhibits higher sedimentation rates, increased foraminiferal shell fragmentation ratios, and lower $CaCO_3$ contents compared to MIS1, MIS3, and MIS5. Core E20 and MD06–3050 are located at similar latitudes, meaning both sites are influenced by the NEC and Kuroshio Current (KC) in the upper ocean and the LCDW in the lower ocean. Additionally, both sites are distant from direct fluvial inputs and may receive eolian contributions from the Asian interior (Sun et al., 2017; Li et al., 2021). Therefore, comparing the $CaCO_3$ content of E20 and MD06–3050 provides a more accurate estimate of the age of U3 in E20.

Assuming an average sedimentation rate of 1.5 cm/kyr (slightly lower than the rate of section U1) for section U3 of core E20, the $CaCO_3$ profiles of E20 and MD06–3050 show remarkable coherence and align well with other western Pacific carbonate records (Figure 4). These findings validate the assumption that the estimated average sedimentation rate of 1.5 cm/kyr for section U3 in core E20 is reasonable. Consequently, the U3 interval spans approximately 32.7 ka, constraining the basal age of E20 to ~74.7 ka, which corresponds to the termination of MIS 5. This chronological framework indicates that sediment accumulation in core E20 initiated near the MIS 5/4 boundary, with the ~270 cm thick LDMs predominantly deposited from the onset of MIS 2 through the early Holocene.

4.2 More volcanic matter and less dust input during the diatom blooms

Provenance studies are crucial for understanding the formation mechanisms of diatom mats and associated environmental changes. The "Eolian-Silicon-Induced Bloom" hypothesis is fundamentally supported by silicon (Si) isotopic signatures in diatom mats, which suggest that the primary source of bioavailable Si is eolian dust deposition (Xiong et al., 2015; Tang et al., 2024). Additionally, mineralogical and geochemical studies indicate that non-biogenic detritus within or adjacent to the LDMs originates from a mixture of Asian eolian dust and submarine volcanic material (Xiong et al., 2010; Lai et al., 2023; Luo et al., 2018a).

Illite and chlorite are common land-derived minerals in the clay mineral composition of marine sediments. Kaolinite, on the other hand, is abundant in soils of intertropical regions with warm and humid climates, while smectite is typically derived from the weathering of volcanic materials (Chamley, 1989). In core E20, the trends in illite and chlorite contents are similar, suggesting a shared origin. In contrast, the smectite and illite contents exhibit opposing trends (Figure 5a). As illustrated in Figure 5b, the clay mineral composition of E20 reflects a mixture of eolian dust (characterized by high illite and chlorite contents) and volcanic material (characterized by high smectite content). The clay mineral composition of U3 is similar to that of sediments from the Kyushu-Palau Ridge (Seo et al., 2014), while the two samples from U1 show

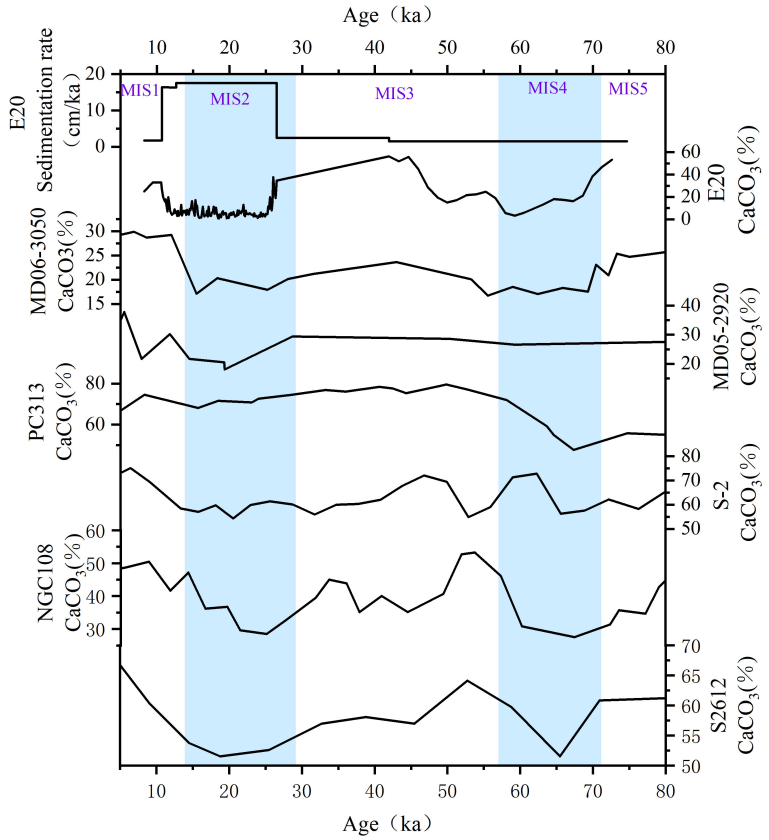

FIGURE 4
Changes in sedimentation rate and $CaCO_3$ content since MIS 5 in core E20, compared to the $CaCO_3$ curves of reference cores. Blue shaded areas indicate stadial periods. Reference cores from the Western Pacific Warm Pool include PC313 (Khim et al., 2012), MD05-2920 (Tachikawa et al., 2011), and MD06-3050 (Sun et al., 2017). Reference cores from the Shatsky Rise include S-2 (Yamane, 2003), S2612, and NGC108 (Maeda et al., 2002).

greater influence from volcanic material, with compositions resembling those of Mariana Trench sediments (Luo et al., 2018a; Lai et al., 2023).

Asian dust is characterized by higher K content and lower Fe and Mg contents compared to material from the western Pacific island arcs/ridges (Figure 3b; Qiao et al., 2011; Ikeda et al., 2016). In the K_2O/Al_2O_3-Fe_2O_3/Al_2O_3 and K_2O/Al_2O_3-MgO/Al_2O_3 correlation plots (Figure 6), the E20 samples generally align more closely with Mariana Trench sediments. The chemical index of alteration (CIA) is positively correlated with the degree of sediment

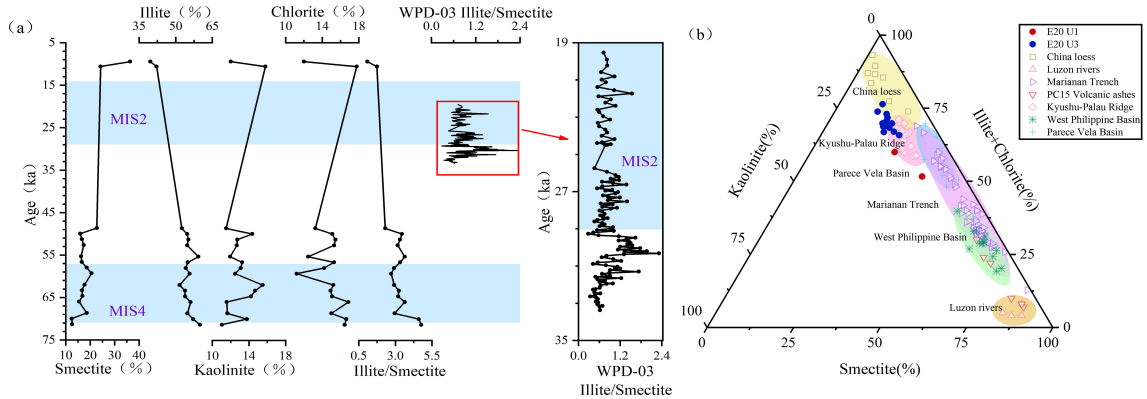

FIGURE 5
Clay mineral composition of core E20 and Illite/Smectite ratio of core WPD-03 **(a)** and potential source regions **(b)**. Blue shaded areas indicate stadial periods. Data sources: Chinese loess and West Philippine Basin (Wan et al., 2012); Luzon rivers (Liu et al., 2009); Mariana Trench (Luo et al., 2018a; Lai et al., 2023); PC15 volcanic ashes (Wang et al., 2021); Kyushu–Palau Ridge (Seo et al., 2014); Parece Vela Basin (Ming et al., 2014).

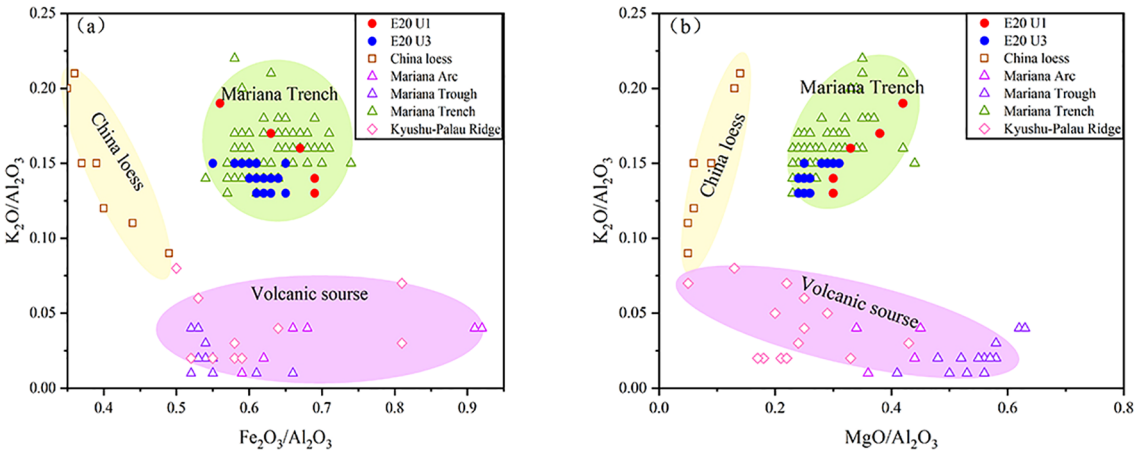

FIGURE 6
Relationships between **(a)** K_2O/Al_2O_3-Fe_2O_3/Al_2O_3 and **(b)** K_2O/Al_2O_3-MgO/Al_2O_3 in core E20 and potential source areas. Data sources: Chinese loess (Qiao et al., 2011); Mariana Arc and Mariana Trough (Ikeda et al., 2016); Mariana Trench (Luo et al., 2018b); Palau-Kyushu Ridge (Lelikov et al., 2018; Ishizuka et al., 2011).

weathering, with values ranging from 30 to 45 for fresh basalts and 45 to 55 for granite and granodiorite (Nesbitt and Young, 1982). The combination of CIA and A-CN-K diagrams is widely used to assess sediment weathering intensity and trace changes in sediment sources (Bi et al., 2015; Xiong et al., 2018). As shown in Figure 7, most U3 samples exhibit weak weathering and are similar to Mariana Trench samples, indicating the influence of local volcanic material. The U1 samples show even weaker weathering. Notably, all six samples (three in U3 and three in U1) with CIA values below 40 are located just below or above the LDMs, suggesting the presence of diatom fragments with lower Al content but higher pore water content compared to typical pelagic sediments.

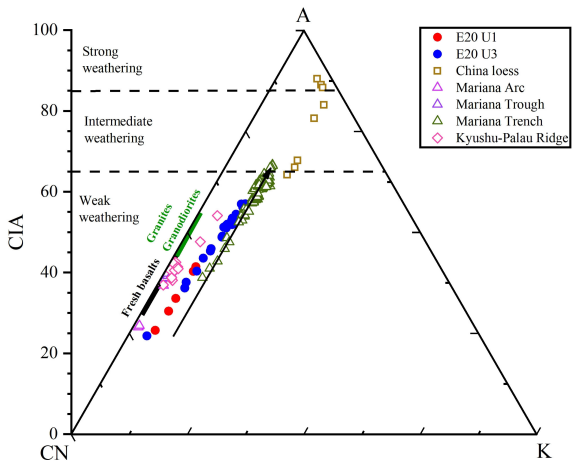

FIGURE 7
CIA-A-CN-K diagram illustrating the degree of chemical weathering. Data sources: Chinese loess (Qiao et al., 2011); Mariana Arc and Mariana Trough (Ikeda et al., 2016); Mariana Trench (Luo et al., 2018b); Kyushu–Palau Ridge (Lelikov et al., 2018; Ishizuka et al., 2011).

Clay mineralogy and geochemical signatures reveal a pronounced increase in volcanic material admixture within U1 relative to U3. In U2 (LDMs), recurrent peaks in Fe_2O_3/Al_2O_3 ratios (Figure 8a) further corroborate the syn-depositional input of volcanic-derived constituents during LDMs formation. These findings collectively demonstrate that volcanic material incorporation was pervasive throughout both the peak diatom bloom phase (LDM deposition) and its termination stage (DC formation). In core WPD-03, the LDM interval exhibits a marginally lower illite/smectite ratio compared to the underlying DC layer (Figure 5a; Xiong et al., 2013). This disparity likely reflects a proportional increase in volcanic-sourced material rather than a decline in eolian illite delivery.

Critically, the observed coupling between diatom productivity pulses and volcanic material enrichment does not necessitate a direct causative link to episodic volcanic eruptions (submarine or subaerial). Sedimentological evidence indicates that diatom mat deposition occurs over millennial-scale intervals, starkly contrasting with the short-lived, event-driven nature of volcanic eruptions. Furthermore, no robust sedimentological or tephrochronological evidence exists for large-magnitude volcanic eruptions in the western Pacific margin during the LGM.

We hypothesize that the volcanic material influx coincident with diatom blooms may instead reflect enhanced deep-current vigor during these periods. Such hydrodynamic intensification could have facilitated the lateral redistribution of weathered volcanic detritus from proximal submarine sources, ultimately concentrating these materials at the depositional site.

4.3 Source and significance of Fe in LDMs

In U2 of core E20, depleted Fe_2O_3 levels inversely correlate with SiO_2 (Supplementary Figure S1d) yet maintain positive covariation with Al_2O_3, TiO_2, and MgO (Supplementary Figures S1a–c), indicating predominantly lithogenic rather than biogenic iron

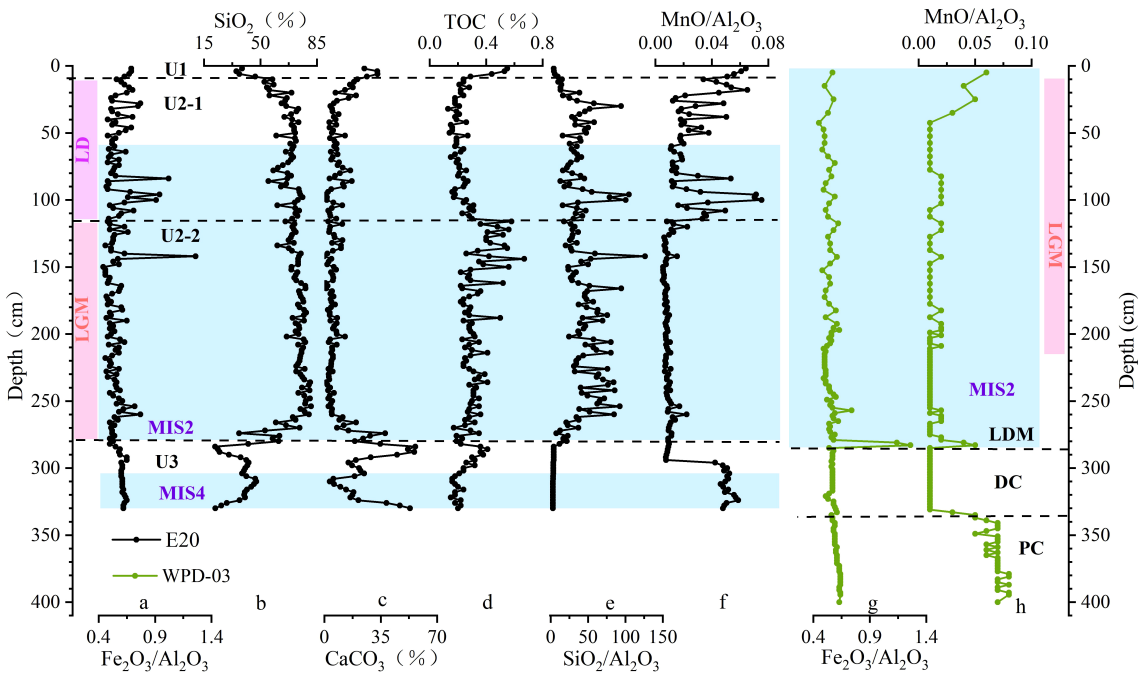

FIGURE 8
Content and ratio profiles of key parameters in core E20 **(a–f)** and core WPD-03 **(g, h)**. Data for WPD-03 are from Xiong et al. (2012). Blue shaded areas indicate glacial periods. DC, Diatomaceous clay; PC, Pelagic clay.

provenance within LDMs through detrital sediment incorporation (Xiong et al., 2022). The association of certain Fe_2O_3/Al_2O_3 peaks with moderate SiO_2 contents (Supplementary Figure S1) suggests periodic inputs of volcanic material, likely sourced from adjacent ridges or seamounts, into the sedimentary record. While iron input from eolian dust may support diatom growth and contribute to diatom mat formation (Xiong et al., 2013, 2015), it is not the primary limiting factor for diatom blooms. Instead, the iron (and possibly silicon) supplied by eolian dust should be regarded as a contributing, rather than decisive, factor in diatom productivity.

Asian eolian dust primarily consists of unreactive iron-bearing minerals, which supply only limited bioavailable iron for diatom growth (Chen et al., 2020). In the stratified, high-nitrate, low-chlorophyll (HNLC) subarctic Pacific Ocean, long-term changes in diatom productivity have been predominantly driven by variations in upwelling and stratification, with sporadic iron fertilization from volcanic ash inputs playing a secondary role (Chen et al., 2020). In the equatorial Pacific, upwelling delivers two orders of magnitude more dissolved iron than eolian dust (Winckler et al., 2016). In subtropical gyres, iron is generally not considered a limiting nutrient for primary production, as excess iron tends to accumulate once major nutrients are depleted (Moore et al., 2013).

The duration of LDMs in core E20 is significantly longer than the peak periods of typical terrestrial and marine aeolian dust accumulation since MIS2 (Figures 9a, b). Therefore, we do not believe that the diatom blooms recorded in E20 were solely triggered by nutrients such as iron (and silicon) brought by Asian inland dust.

4.4 Diatom blooms stimulated by enhanced middle-deep water upwelling?

Traditionally, the formation of *E. rex* LDMs was thought to depend on stratification (Kemp et al., 2000; Kemp and Villareal, 2013; Xiong et al., 2013, 2015). However, recent studies of diatom and radiolarian assemblages suggest that diatom blooms may not necessarily require stratified conditions. Instead, strong *E. rex* blooms during the LGM may have been driven by weak upper water stratification and the upwelling of nutrient-rich lower waters (Zhang et al., 2021). This raises the question: Why and where does middle-deep water upwelling occur?

Existing studies indicate a correlation between the distribution of *E. rex* LDMs and the bottom topography in the Western Pacific. We propose a new hypothesis for how middle-deep water upwelling may have stimulated diatom blooms (Figure 10). During the last glacial period, the Antarctic Circumpolar Current (ACC) weakened (Basak et al., 2018), but the generation of AABW may have increased (Hall et al., 2001; Hu and Piotrowski, 2018; Lynch-Stieglitz et al., 2016), leading to a faster deep Pacific overturning circulation (Figure 9h; Hu and Piotrowski, 2018) and an intensified western boundary deep inflow into the North Pacific (Figure 9e; Hall et al., 2001). In the North Pacific, the western branch of LCDW accelerates into the Philippine Sea primarily via the northern passage of the Mariana Trench (Wang et al., 2023; Figure 10). Upon encountering topographic features such as island arcs, ridges, and seamounts, the upwelling of deep water brings middle-deep nutrients to the euphotic zone and shoals the nutricline (Kemp and Villareal, 2018), stimulating the growth of buoyancy-regulating

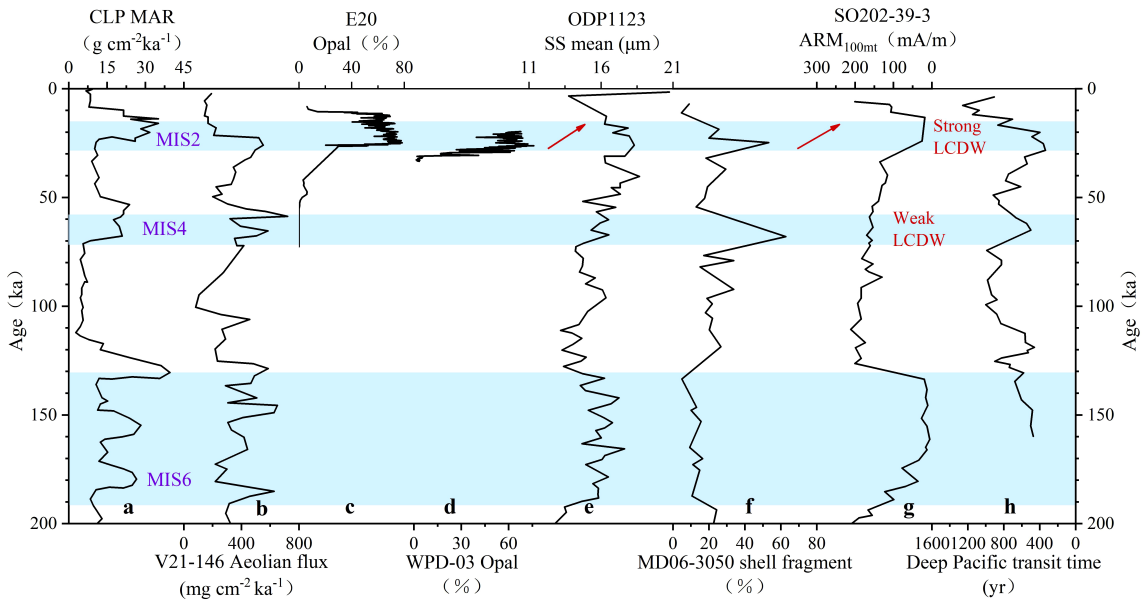

FIGURE 9
Comparative records of aeolian dust flux, biogenic opal content, and deep-current activity indicators: **(a)** Mass accumulation rate (MAR) from the Chinese Loess Plateau (Sun and An, 2005); **(b)** Eolian dust flux from core V21–146 on the Shatsky Rise (Han et al., 2002); **(c, d)** Opal content of core E20 and WPD-03 (Xiong et al., 2013); **(e)** Mean grain size of sortable silt (SS mean) of ODP 1123 (Hall et al., 2001); **(f)** Shell fragment ratio from core MD06-3050 (Sun et al., 2017); **(g)** Magnetic mineral index (ARM_{100mt}) from core SO202-39-3 (Korff et al., 2016); **(h)** Deep Pacific transit time (Hu and Plotrowskl, 2018). Blue shaded areas indicate glacial periods.

diatoms (e.g., *E. rex*) that thrive in the Deep Chlorophyll Maximum (DCM) (Kemp and Villareal, 2018). After blooming, the siliceous biogenic debris settles and drifts, eventually becoming trapped in depressions through the "funnel effect", which is intrinsically linked to the redistribution processes of diatomaceous detritus (Tang et al., 2024), thus forming *E. rex* LDMs. In the following section, we will present several lines of evidence supporting this hypothesis.

Firstly, numerous studies have consistently demonstrated the existence of biological-physical coupling phenomena in the proximity of prominent topographic features (e.g. Dower and Mackas, 1996; Sokolov and Rintoul, 2007; Wang et al., 2024; Xie et al., 2024). Sokolov and Rintoul (2007) found that most regions of elevated chlorophyll in the open Southern Ocean can be explained by upwelling of nutrients (both macronutrients and micronutrients) where the ACC interacts with topography, followed by downstream advection. In the Indonesian Seas, regions with narrow straits, steep topography and dynamic circulation with strong vertical mixing display high net community production and chlorophyll-a, suggesting that vertical nutrient transport dominates biological productivity (Xie et al., 2024). Although constrained by limited spatial resolution, the nitrate concentration profile spanning the Mariana Trench and KPR system reveals a pronounced spatial pattern: the nutricline depth in the topographically elevated western sector is consistently shallower compared to adjacent areas (Supplementary Figure S2).

Secondly, sedimentary records provide robust evidence for intensified deep current activity in the western Pacific during the last glacial period. This is supported by: (1) the dissolution of fine-grained magnetic minerals in sediments near Shatsky Rise (Figure 9g; Korff et al., 2016) and (2) enhanced carbonate dissolution in a core from Benham Rise (Figure 9f; Sun et al., 2017) during MIS 2, both of which suggest a stronger influence of southern-sourced deep water masses. Additionally, in regions with pronounced topographic variability, if the illite/smectite ratio in sedimentary records is interpreted as an indicator of deep current intensity rather than eolian dust input, the lower ratios observed in LDMs (e.g., in core WPD-03) would imply more vigorous deep current activity. Furthermore, the two-stage evolution in LDMs in core E20-from U2-2 (LGM) to U2-1 (LD), reveals a progressive decrease in TOC content and an increase in the MnO/Al_2O_3 ratio upward through the sequence. This trend likely reflects improved bottom-water oxygenation or enhanced deep-water ventilation during the deglacial period. Notably, this phased transition in sedimentation aligns closely with reconstructed variations in Southern Ocean deep water formation since the last glacial period, as evidenced by previous studies (Basak et al., 2018).

Finally, the diatom mats discovered near the Mariana Trench exhibit the most extensive temporal span, ranging from late MIS 3 (Cai, 2019) to the mid-Holocene (Zhang et al., 2024). In contrast, those found in the Philippine Sea display a relatively shorter chronological duration. This discrepancy likely suggests that the key deep-water passages adjacent to the Mariana Trench are more responsive to LCDW intrusions, exhibiting intensified mixing and upwelling processes. These dynamics facilitate the upward transport of nutrient-rich deep waters, thereby enhancing local productivity relative to other regions.

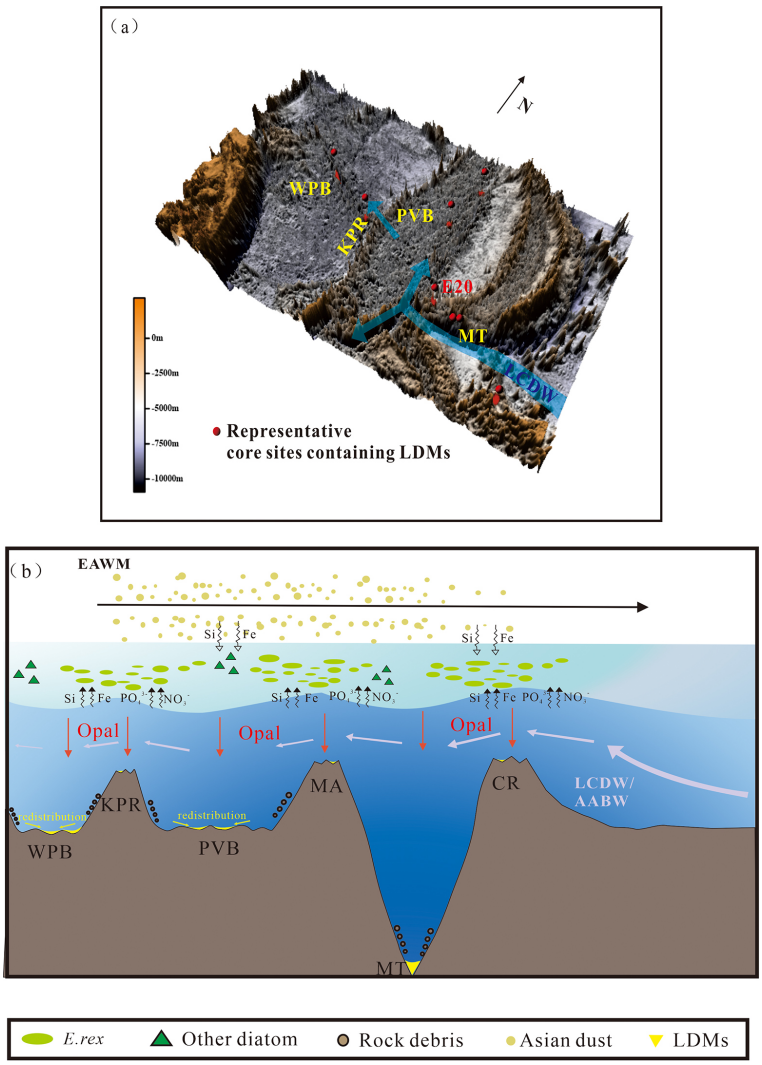

FIGURE 10
(a) Distribution of representative cores containing laminated diatom mats (LDMs) in the western Pacific, overlaid with the deep current pathways based on observational data (Wang et al., 2023); **(b)** Schematic illustration depicting the formation process of LDMs. The locations of LDM-bearing cores are derived from Luo et al. (2018a); Xiong et al. (2013); Tang et al. (2024); Shibamoto and Harada (2010); Cai (2019), and Zhang et al. (2021). WPB, West Philippine Basin; KPR, Kyushu-Palau Ridge; PVB, Parece Vela Basin; MA, Mariana Arc; MT, Mariana Trench; CR, Caroline Ridge.

The absence of *E. rex* LDMs during MIS4 in the study area may be attributed to weak LCDW. Indirect evidence from sedimentary archives near the Shatsky Rise (Korff et al., 2016) supports this: no significant magnetic mineral dissolution was observed during MIS4, in contrast to pronounced dissolution during MIS2 and MIS6 (Figure 9g; Korff et al., 2016), suggesting a weaker influence of Antarctic-sourced bottom water during MIS4. Prior to the formation of the LGM *E. rex* LDMs in Core XT47 near the Kyushu-Palau Ridge, four peaks in radiolarian abundance and opal content were recorded, possibly linked to glacial-interglacial changes (Zhang et al., 2021). Future studies of long cores, particularly those located on the rims of the Mariana Trench, will help determine whether *E. rex* LDMs formed during MIS6 and earlier glacial periods, ultimately uncovering the true mechanisms behind their formation in the low-latitude Western Pacific.

5 Conclusion

(1) Core E20 comprises both calcium-rich and silica-rich sediments. Notably, the variations in carbonate content do not align with the 'Pacific-type dissolution cycle' but instead mirror the records observed in other cores from the western Pacific, exhibiting higher concentrations during interglacial periods. Diatom blooms in core E20 predominantly occurred from the LGM to the early Holocene, leading to a substantial dilution effect on carbonate content.

(2) The lithogenic detritus in core E20 is primarily derived from volcanic sources, with a smaller component originating from eolian dust. The synchronous occurrence of volcanic material influx and diatom blooms suggests an intensification of deep-current activity, which likely facilitated the lateral transport of weathered volcanic detritus from nearby submarine sources.

(3) The input of iron from eolian dust acts as a beneficial supplement rather than a critical requirement for diatom blooms.

(4) A new hypothesis is proposed to explain how middle-deep water upwelling may have stimulated these blooms. During the last glacial period, the intensified western branch of the LCDW accelerated into the Philippine Sea, primarily through the northern passage of the Mariana Trench. When encountering topographic features such as ridges and seamounts, the upwelling of deep water transported middle-deep nutrients to the euphotic zone, promoting the growth of buoyancy-regulating diatoms. These diatoms eventually formed *E. rex* LDMs as they became trapped in depressions due to the "funnel effect."

Data availability statement

The original contributions presented in the study are included in the article/Supplementary Material. Further inquiries can be directed to the corresponding author.

Author contributions

JL: Conceptualization, Data curation, Formal Analysis, Software, Validation, Visualization, Writing – original draft, Writing – review & editing. DX: Conceptualization, Funding acquisition, Investigation, Methodology, Project administration, Resources, Supervision, Writing – review & editing. YL: Data curation, Formal Analysis, Methodology, Writing – review & editing. LY: Writing – review & editing. QG: Writing – review & editing. YB: Writing – review & editing. XH: Writing – review & editing. WZ: Writing – review & editing. SC: Writing – review & editing.

Funding

The author(s) declare that financial support was received for the research and/or publication of this article. This research was funded by the National Program on Global Change and Air-Sea Interaction (GASI-02-PAC-CJ07 and GASI-01-CNPAC-CJ01).

Acknowledgments

We thank the staff of the R/V Xiangyanghong 10 for their help in collecting samples and the reviewers for their valuable suggestions.

Conflict of interest

The authors declare that the research was conducted in the absence of any commercial or financial relationships that could be construed as a potential conflict of interest.

Correction note

A correction has been made to this article. Details can be found at: 10.3389/fmars.2025.1661159.

Generative AI statement

The author(s) declare that no Generative AI was used in the creation of this manuscript.

Publisher's note

All claims expressed in this article are solely those of the authors and do not necessarily represent those of their affiliated organizations, or those of the publisher, the editors and the reviewers. Any product that may be evaluated in this article, or claim that may be made by its manufacturer, is not guaranteed or endorsed by the publisher.

Supplementary material

The Supplementary Material for this article can be found online at: https://www.frontiersin.org/articles/10.3389/fmars.2025.1556799/full#supplementary-material

References

Basak, C., Fröllje, H., Lamy, F., Gersonde, R., Benz, V., Anderson, R. F., et al. (2018). Breakup of last glacial deep stratification in the South Pacific. *Science* 359, 900–904. doi: 10.1126/science.aao2473

Bi, L., Yang, S., Li, C., Guo, Y., Wang, Q., Liu, J. T., et al. (2015). Geochemistry of river-borne clays entering the East China Sea indicates two contrasting types of weathering and sediment transport processes. *Geochemistry Geophysics Geosystems* 16, 3034–3052. doi: 10.1002/2015GC005867

Biscaye, P. E. (1965). Mineralogy and sedimentation of recent deep-sea clay in the Atlantic Ocean and adjacent seas and oceans. *GSA Bull.* 76, 803–832. doi: 10.1130/0016-7606(1965)76[803:MASORD]2.0.CO;2

Bowman, C. L., Rand, D. S., Lisiecki, L. E., and Bova, S. C. (2023). An 800-kyr planktonic $\delta^{18}O$ stack for the West Pacific Warm Pool. *Earth System Sci. Data Discussions* 2023, 1–19. doi: 10.5194/essd-16-701-2024

Broecker, W. S., Clark, E., Lynch-Stieglitz, J., Beck, W., Stott, L. D., Hajdas, I., et al. (2000). Late glacial diatom accumulation at 9 S in the Indian Ocean. *Paleoceanography* 15, 348–352. doi: 10.1029/1999PA000439

Bradtmiller, L. I., Anderson, R. F., Fleisher, M. Q., and Burckle, L. H. (2006). Diatom productivity in the equatorial Pacific Ocean from the last glacial period to the present: A test of the silicic acid leakage hypothesis. *Paleoceanography* 21, PA4201. doi: 10.1029/2006PA001282

Cai, Y. (2019). Sedimentary diatoms records and their paleoenvironmental indications in the southern Mariana Trench and its adjacent areas. University of Xiamen, China.

Chamley, H. (1989). Clay minerals. *Clay sedimentology (Berlin Heidelberg: Springer Berlin Heidelberg)* 3-20. doi: 10.1007/978-3-642-85916-8_1

Chen, T., Liu, Q., Roberts, A., Shi, X., and Zhang, Q. (2020). A test of the relative importance of iron fertilization from aeolian dust and volcanic ash in the stratified

high-nitrate low-chlorophyll subarctic Pacific Ocean. *Quaternary Sci. Rev.* 248, 106577. doi: 10.1016/j.quascirev.2020.106577

Chiswell, S. M., Bostock, H. C., Sutton, P. J., and Williams, M. J. (2015). Physical oceanography of the deep seas around New Zealand: a review. *New Z. J. Marine Freshwater Res.* 49, 286–317. doi: 10.1080/00288330.2014.992918

Dai, M., Luo, Y. W., Achterberg, E. P., Browning, T. J., Cai, Y., Cao, Z., et al. (2023). Upper ocean biogeochemistry of the oligotrophic North Pacific Subtropical Gyre: from nutrient sources to carbon export. *Rev. Geophysics* 61, e2022RG000800. doi: 10.1029/2022RG000800

Dower, J. F., and Mackas, D. L. (1996). Seamount effects" in the zooplankton community near Cobb Seamount. *Deep Sea Res. Part I: Oceanographic Res. Papers* 43, 837–858. doi: 10.1016/0967-0637(96)00040-4

Hall, I. R., McCave, I. N., Shackleton, N. J., Weedon, G. P., and Harris, S. E. (2001). Intensified deep Pacific inflow and ventilation in Pleistocene glacial times. *Nature* 412, 809–812. doi: 10.1038/35090552

Han, Z., Liu, D., and Hovan, S. A. (2002). Lightness timescale for terrestrial sediments in the past 500,000 years. *Paleoceanography* 17, 20–1-20-7. doi: 10.1029/2001PA000731

Harrison, K. G. (2000). Role of increased marine silica input on paleo-pCO2 levels. *Paleoceanography* 15, 292–298. doi: 10.1029/1999PA000427

Hendry, K. R., Robinson, L. F., Mcmanus, J. F., and Hays, J. D. (2014). Silicon isotopes indicate enhanced carbon export efficiency in the North Atlantic during deglaciation. *Nat. Commun.* 5, 3107. doi: 10.1038/ncomms4107

Hollstein, M., Mohtadi, M., Rosenthal, Y., Prange, M., Oppo, D. W., Méndez, G. M., et al. (2018). Variations in Western Pacific Warm Pool surface and thermocline conditions over the past 110,000 years: Forcing mechanisms and implications for the glacial Walker circulation. *Quaternary Sci. Rev.* 201, 429–445. doi: 10.1016/j.quascirev.2018.10.030

Hu, D., Wu, L., Cai, W., Gupta, A. S., Ganachaud, A., Qiu, B., et al. (2015). Pacific western boundary currents and their roles in climate. *Nature* 522, 299–308. doi: 10.1038/nature14504

Hu, R., and Piotrowski, A. M. (2018). Neodymium isotope evidence for glacial-interglacial variability of deepwater transit time in the Pacific Ocean. *Nat. Commun.* 9, 1–12. doi: 10.1038/s41467-018-07079-z

Huang, Y., Sun, C., Yang, G., Yue, X., Jiang, F., Cao, W., et al. (2020). Geochemical characteristics of hadal sediment in the northern Yap Trench. *J. oceanology limnology* 38, 650–664. doi: 10.1007/s00343-019-9010-3

Ikeda, Y., Nagao, K., Ishii, T., Matsumoto, D., Stern, R. J., Kagami, H., et al. (2016). Contributions of slab fluid and sediment melt components to magmatism in the Mariana Arc–Trough system: Evidence from geochemical compositions and Sr, Nd, and noble gas isotope systematics. *Island Arc* 25, 253–273. doi: 10.1111/iar.12150

Ishizuka, O., Taylor, R. N., Yuasa, M., and Ohara, Y. (2011). Making and breaking an island arc: A new perspective from the Oligocene Kyushu-Palau arc, Philippine Sea. *Geochemistry Geophysics Geosystems* 12, Q05005. doi: 10.1029/2010GC003440

Kemp, A. E., and Baldauf, J. G. (1993). Vast Neogene laminated diatom mat deposits from the eastern equatorial Pacific Ocean. *Nature* 362, 141–144. doi: 10.1038/362141a0

Kemp, A., Grigorov, I., Pearce, R. B., and Garabato, A. N. (2010). Migration of the Antarctic Polar Front through the mid-Pleistocene transition: evidence and climatic implications. *Quaternary Sci. Rev.* 29, 1993–2009. doi: 10.1016/j.quascirev.2010.04.027

Kemp, A. E., Pearce, R. B., Grigorov, I., Rance, J., Lange, C., Quilty, P., et al. (2006). Production of giant marine diatoms and their export at oceanic frontal zones: Implications for Si and C flux from stratified oceans. *Global Biogeochemical Cycles* 20, GB4S04. doi: 10.1029/2006GB002698

Kemp, A. E., Pike, J., Pearce, R. B., and Lange, C. B. (2000). The "Fall dump"—a new perspective on the role of a "shade flora" in the annual cycle of diatom production and export flux. *Deep Sea Res. Part II: Topical Stud. Oceanography* 47, 2129–2154. doi: 10.1016/S0967-0645(00)00019-9

Kemp, A. E., and Villareal, T. A. (2013). High diatom production and export in stratified waters–A potential negative feedback to global warming. *Prog. Oceanography* 119, 4–23. doi: 10.1016/j.pocean.2013.06.004

Kemp, A. E., and Villareal, T. A. (2018). The case of the diatoms and the muddled mandalas: Time to recognize diatom adaptations to stratified waters. *Prog. Oceanography* 167, 138–149. doi: 10.1016/j.pocean.2018.08.002

Khim, B.-K., Kim, H. J., Cho, Y. S., Chi, S. B., and Yoo, C. M. (2012). Orbital variations of biogenic $CaCO_3$ and opal abundance in the western and central equatorial pacific ocean during the late quaternary. *Terrestrial Atmospheric Oceanic Sci.* 23, 107–117. doi: 10.3319/TAO.2011.07.05.01(Oc

Korff, L., von Dobeneck, T., Frederichs, T., Kasten, S., Kuhn, G., Gersonde, R., et al. (2016). Cyclic magnetite dissolution in Pleistocene sediments of the abyssal northwest Pacific Ocean: Evidence for glacial oxygen depletion and carbon trapping. *Paleoceanography* 31, 600–624. doi: 10.1002/2015PA002882

Lai, W., Liu, X., Tian, J., Wang, H., Zhang, J., Huang, J., et al. (2023). Mineralogy of sediments in the Mariana Trench controlled by environmental conditions of the West Pacific since the Last Glacial Maximum. *J. Asian Earth Sci.* 245, 105553. doi: 10.1016/j.jseaes.2023.105553

Lelikov, E., Sedin, V., and Pugachev, A. (2018). Geology and geochemistry of magmatic rocks from the southern part of the Kyushu–Palau ridge in the Philippine Sea. *Oceanology* 58, 273–289. doi: 10.1134/S000143701802008X

Li, Y., Xu, D., Zhang, Z., Jiang, K., and Liu, G. (2021). Sedimentary characteristics and environmental significance since the last glaciation recorded in core E20 in the western Pacific Ocean. *J. Marine Sci.* 39, 12–20. doi: 10.3969/j.issn.1001-909X.2021.02.002

Liao, J., Chen, J., Sun, X., Deng, Y., Wang, Y., Wang, D., et al. (2024). Controlling factors on REY enrichments in basins from the Pacific Ocean: Early diagenesis and local constraints. *Geochemistry Geophysics Geosystems* 25, e2023GC011111. doi: 10.1029/2023GC011111

Liu, X., Wang, H., and J.and Zhuang, G.-C. (2024). Microbial sulfate reduction and its role in carbon sequestration in marine sediments. *J. Earth Sci.* 35, 1378–1381. doi: 10.1007/s12583-024-1998-4

Liu, Z., Zhao, Y., Colin, C., Siringan, F. P., and Wu, Q. (2009). Chemical weathering in Luzon, Philippines from clay mineralogy and major-element geochemistry of river sediments. *Appl. Geochemistry* 24, 2195–2205. doi: 10.1016/j.apgeochem.2009.09.025

Lumpkin, R., and Speer, K. (2007). Global ocean meridional overturning. *J. Phys. Oceanography* 37, 2550–2562. doi: 10.1175/JPO3130.1

Luo, M., Algeo, T. J., Chen, L., Shi, X., and Chen, D. (2018a). Role of dust fluxes in stimulating Ethmodiscus rex giant diatom blooms in the northwestern tropical Pacific during the Last Glacial Maximum. *Palaeogeography palaeoclimatology Palaeoecol.* 511, 319–331. doi: 10.1016/j.palaeo.2018.08.017

Luo, M., Algeo, T. J., Tong, H., Gieskes, J., Chen, L., Shi, X., et al. (2018b). More reducing bottom-water redox conditions during the Last Glacial Maximum in the southern Challenger Deep (Mariana Trench, western Pacific) driven by enhanced productivity. *Deep Sea Res. Part II: Topical Stud. Oceanography* 155, 70–82. doi: 10.1016/j.dsr2.2017.01.006

Luo, M., Gieskes, J., Chen, L., Shi, X., and Chen, D. (2017). Provenances, distribution, and accumulation of organic matter in the southern Mariana Trench rim and slope: implication for carbon cycle and burial in hadal trenches. *Marine Geology* 386, 98–106. doi: 10.1016/j.margeo.2017.02.012

Lynch-Stieglitz, J., Ito, T., and Michel, E. (2016). Antarctic density stratification and the strength of the circumpolar current during the Last Glacial Maximum. *Paleoceanography* 31, 539–552. doi: 10.1002/2015PA002915

Maeda, L., Kawahata, H., and Nohara, M. (2002). Fluctuation of biogenic and abiogenic sedimentation on the Shatsky Rise in the western North Pacific during the late Quaternary. *Marine Geology* 189, 197–214. doi: 10.1016/S0025-3227(02)00405-X

Ming, J., Li, A., Huang, J., Wan, S., Meng, Q., Jiang, F., et al. (2014). Assemblage characteristics of clay minerals and its implications to evolution of eolian dust input to the Parece Vela Basin since 1.95 Ma. *Chin. J. Oceanology Limnology* 32, 174–186. doi: 10.1007/s00343-014-3066-x

Moore, C., Mills, M., Arrigo, K., Berman-Frank, I., Bopp, L., Boyd, P., et al. (2013). Processes and patterns of oceanic nutrient limitation. *Nat. Geosci.* 6, 701–710. doi: 10.1038/ngeo1765

Nath, B. N., Rao, V. P., and Becker, K. P. (1989). Geochemical evidence of terrigenous influence in deep-sea sediments up to 8 S in the Central Indian Basin. *Marine Geology* 87, 301–313. doi: 10.1016/0025-3227(89)90067-4

Nelson, D. M., Tréguer, P., Brzezinski, M. A., Leynaert, A., and Quéguiner, B. (1995). Production and dissolution of biogenic silica in the ocean: revised global estimates, comparison with regional data and relationship to biogenic sedimentation. *Global biogeochemical cycles* 9, 359–372. doi: 10.1029/95GB01070

Nesbitt, H. W., and Young, G. M. (1982). Early Proterozoic climates and plate motions inferred from major element chemistry of lutites. *Nature*, 299, 715–717. doi: 10.1038/299715a0

Qiao, Y., Hao, Q., Peng, S., Wang, Y., Li, J., and Liu, Z. (2011). Geochemical characteristics of the eolian deposits in southern China, and their implications for provenance and weathering intensity. *Palaeogeography Palaeoclimatology Palaeoecol.* 308, 513–523. doi: 10.1016/j.palaeo.2011.06.003

Romero, O., and Schmieder, F. (2006). Occurrence of thick Ethmodiscus oozes associated with a terminal Mid-Pleistocene Transition event in the oligotrophic subtropical South Atlantic. *Palaeogeography Palaeoclimatology Palaeoecol.* 235, 321–329. doi: 10.1016/j.palaeo.2005.10.026

Scott, R., and Kroenke, L. (1980). Evolution of back arc spreading and arc volcanism in the Philippine Sea: Interpretation of Leg 59 DSDP results. *Geophysical Monograph Ser.* 23, 283–291. doi: 10.1029/GM023p0283

Seo, I., Lee, Y. I., Yoo, C. M., Kim, H. J., and Hyeong, K. (2014). Sr-Nd isotope composition and clay mineral assemblages in eolian dust from the central Philippine Sea over the last 600 kyr: Implications for the transport mechanism of Asian dust. *J. Geophysical Research: Atmospheres* 119, 11492–11504. doi: 10.1002/2014JD022025

Shen, L., Chen, M., Lan, B., Qi, H., Zhang, A., Lan, D., et al. (2017). Diatom distribution as an environmental indicator in surface sediments of the West Philippine Basin. *Chin. J. Oceanology Limnology* 35, 431–443. doi: 10.1007/s00343-016-5306-8

Shibamoto, Y., and Harada, K. (2010). Silicon flux and distribution of biogenic silica in deep-sea sediments in the western North Pacific Ocean. *Deep Sea Res. Part I: Oceanographic Res. Papers* 57, 163–174. doi: 10.1016/j.dsr.2009.10.009

Sokolov, S., and Rintoul, S. R. (2007). On the relationship between fronts of the Antarctic Circumpolar Current and surface chlorophyll concentrations in the Southern Ocean. *J. Geophysical Research: Oceans* 112, C07030. doi: 10.1029/2006JC004072

Sun, H., Li, T., Chang, F., Wan, S., Xiong, Z., An, B., et al. (2017). Deep-sea carbonate preservation in the western Philippine Sea over the past 1Ma. *Quaternary Int.* 459, 101–115. doi: 10.1016/j.quaint.2017.08.041

Sun, Y., and An, Z. (2005). Late Pliocene-Pleistocene changes in mass accumulation rates of eolian deposits on the central Chinese Loess Plateau. *J. Geophysical Research: Atmospheres* 110, D23101. doi: 10.1029/2005JD006064

Tachikawa, K., Cartapanis, O., Vidal, L., Beaufort, L., Barlyaeva, T., and Bard, E. (2011). The precession phase of hydrological variability in the Western Pacific Warm Pool during the past 400 ka. *Quaternary Sci. Rev.* 30, 3716–3727. doi: 10.1016/j.quascirev.2011.09.016

Tang, H., Ye, H., Yang, W., Huang, Y., Sun, T., Ge, Y., et al. (2024). East Asian Winter Monsoon and enhanced stratification in the western Pacific promoted giant marine diatom (Ethmodiscus rex) blooms during the last deglaciation. *Quaternary Sci. Rev.* 336, 108798. doi: 10.1016/j.quascirev.2024.108798

Taylor, S. R., and McLennan, S. M. (1985). *The continental crust: Its composition and evolution* (Oxford: Blackwell Scientific Publications).

Wan, S., Li, A., Clift, P. D., and Stuut, J.-B. W. (2007). Development of the East Asian monsoon: mineralogical and sedimentologic records in the northern South China Sea since 20 Ma. *Palaeogeography Palaeoclimatology Palaeoecol.* 254, 561–582. doi: 10.1016/j.palaeo.2007.07.009

Wan, S., Yu, Z., Clift, P. D., Sun, H., Li, A., and Li, T. (2012). History of Asian eolian input to the West Philippine Sea over the last one million years. *Palaeogeography Palaeoclimatology Palaeoecol.* 326, 152–159. doi: 10.1016/j.palaeo.2012.02.015

Wang, H., Yi, L., Deng, X., and He, G. (2021). Geochemical and mineral properties of quaternary deep-sea sediments in the Central-Tropical Pacific and its response to the Mid-Pleistocene Transition. *J. Marine Sci. Eng.* 9, 1254. doi: 10.3390/jmse9111254

Wang, J., Wang, F., Lu, Y., Zhang, H., Ma, Q., Pratt, L. J., et al. (2023). Abyssal circulation from the yap-mariana junction to the northern philippine basin. *Geophysical Res. Lett.* 50, e2022GL100610. doi: 10.1029/2022GL100610

Wang, X., Li, H., Zhang, J., Chen, J., Xie, X., Xie, W, et al. (2024). Seamounts generate efficient active transport loops to nourish the twilight ecosystem. *Science Advances* 10, eadk6833. doi: 10.1126/sciadv.adk6833

Webster, P. J., Magana, V. O., Palmer, T., Shukla, J., Tomas, R., Yanai, M., et al. (1998). Monsoons: Processes, predictability, and the prospects for prediction. *J. Geophysical Research: Oceans* 103, 14451–14510. doi: 10.1029/97JC02719

Winckler, G., Anderson, R. F., Jaccard, S. L., and Marcantonio, F. (2016). Ocean dynamics, not dust, have controlled equatorial Pacific productivity over the past 500,000 years. *Proc. Natl. Acad. Sci.* 113, 6119–6124. doi: 10.1073/pnas.1600616113

Xiao, C., Wang, Y., Tian, J., Wang, X., and Xin, Y. (2020). Mineral composition and geochemical characteristics of sinking particles in the Challenger Deep, Mariana Trench: Implications for provenance and sedimentary environment. *Deep Sea Res. Part I: Oceanographic Res. Papers* 157, 103211. doi: 10.1016/j.dsr.2019.103211

Xie, T., Cao, Z., Hamzah, F., Schlosser, P., and Dai, M. (2024). Nutrient vertical flux in the Indonesian seas as constrained by non-atmospheric helium-3. *Geophysical Res. Lett.* 51, e2024GL111420. doi: 10.1029/2024GL111420

Xiong, Z., Li, T., Algeo, T., Doering, K., Frank, M., Brzezinski, M. A., et al. (2015). The silicon isotope composition of Ethmodiscus rex laminated diatom mats from the tropical West Pacific: Implications for silicate cycling during the Last Glacial Maximum. *Paleoceanography* 30, 803–823. doi: 10.1002/2015PA002793

Xiong, Z., Li, T., Algeo, T., Nan, Q., Zhai, B., and Lu, B. (2012). Paleoproductivity and paleoredox conditions during late Pleistocene accumulation of laminated diatom mats in the tropical West Pacific. *Chem. Geology* 334, 77–91. doi: 10.1016/j.chemgeo.2012.09.044

Xiong, Z., Li, T., Crosta, X., Algeo, T., Chang, F., and Zhai, B. (2013). Potential role of giant marine diatoms in sequestration of atmospheric CO_2 during the Last Glacial Maximum: $\delta^{13}C$ evidence from laminated Ethmodiscus rex mats in tropical West Pacific. *Global Planetary Change* 108, 1–14. doi: 10.1016/j.gloplacha.2013.06.003

Xiong, Z., Li, T., Zhai, Z., Wan, S., and Nan, Q. (2010). Clay Mineral Characteristics of Ethmodiscus rex Diatoms from Low-Latitude Western Pacific during the Last Glacial and Implications for Their Formatiom. *Earth Science——Journal China Univ. Geosciences* 35, 551–562. doi: 10.3799/dqkx.2010.071

Xiong, Z., Zhai, B., Algeo, T. J., Lu, Z., Li, T., Meyer, H., et al. (2022). Intensified aridity over the Indo-Pacific Warm Pool controlled by ice-sheet expansion during the Last Glacial Maximum. *Global Planetary Change* 217, 103952. doi: 10.1016/j.gloplacha.2022.103952

Xiong, Z., Li, T., Chang, F., Algeo, T. J., Clift, P. D., Bretschneider, L., et al. (2018). Rapid precipitation changes in the tropical West Pacific linked to North Atlantic climate forcing during the last deglaciation. *Quaternary Science Reviews* 197, 288–306. doi: 10.1016/j.quascirev.2018.07.040

Xu, Z., Wan, S., Colin, C., Li, T., Clift, P. D., Chang, F., et al. (2020). Enhanced terrigenous organic matter input and productivity on the western margin of the Western Pacific Warm Pool during the Quaternary sea-level lowstands: Forcing mechanisms and implications for the global carbon cycle. *Quaternary Sci. Rev.* 232, 106211. doi: 10.1016/j.quascirev.2020.106211

Xu, Z., Li, T., Clift, P. D., Lim, D., Wan, S., Chen, H, et al. (2015). Quantitative estimates of Asian dust input to the western Philippine Sea in the mid-late Quaternary and its potential significance for paleoenvironment. *Geochemistry, Geophysics, Geosystems*. 16, 3182–3196. doi: 10.1002/2015GC005929

Yamane, M. (2003). Late Quaternary variations in water mass in the Shatsky Rise area, northwest Pacific Ocean. *Marine Micropaleontology* 48, 205–223. doi: 10.1016/S0377-8398(03)00017-3

Yan, X. H., Ho, C. R., Zheng, Q., and Klemas, V. (1992). Temperature and size variabilities of the Western Pacific Warm Pool. *Science* 258, 1643–1645. doi: 10.1126/science.258.5088.1643

Yoder, J. A., Ackleson, S. G., Barber, R. T., Flament, P., and Balch, W. M. (1994). A line in the sea. *Nature* 371, 689–692. doi: 10.1038/371689a0

Zhai, B., Li, T., Chang, F., and Cao, Q. (2009). Vast laminated diatom mat deposits from the west low-latitude Pacific Ocean in the last glacial period. *Chin. Sci. Bull.* 54, 4529–4533. doi: 10.1007/s11434-009-0447-1

Zhang, H., Che, H., Xia, J., Cheng, Q., Qi, D., Cao, J., et al. (2022). Sedimentary $CaCO_3$ accumulation in the deep west Pacific Ocean. *Front. Earth Sci.* 10. doi: 10.3389/feart.2022.857260

Zhang, J., Witkowski, A., Tomczak, M., McCartney, K., He, G., and Zgłobicka, I. (2019). Diatomaceous ooze in a sedimentary core from Mariana Trench: implications for paleoceanography. *Acta Geologica Polonica*, 69, 627–643. doi: 10.24425/agp.2019.126448

Zhang, L., Hu, B., Qiu, Z., Guo, J., Ding, X., Lu, J., et al. (2021). Records of polycystine radiolaria in the diatom mats sediments from the western Philippine Sea and their environmental significance. *Earth Sci.* 46, 853–865. doi: 10.3799/dqkx.2020.341

Zhang, J., Tomczak, M., Li, C., McCartney, K., Deng, X., and He, G. (2024). Laminated diatomaceous ooze from southern Mariana Trench in Late Pleistocene and Holocene for paleoclimate and paleoceanography implication. *Quaternary Sci. Rev.* 325, 108500. doi: 10.1016/j.quascirev.2024.108500

frontiers | Frontiers in Marine Science

TYPE Correction
PUBLISHED 28 August 2025
DOI 10.3389/fmars.2025.1661159

OPEN ACCESS

EDITED AND REVIEWED BY
Xiaodong Jiang,
Guangdong University of Technology, China

*CORRESPONDENCE
Dong Xu
xudong@sio.org.cn

RECEIVED 07 July 2025
ACCEPTED 14 August 2025
PUBLISHED 28 August 2025

CITATION
Lin J, Xu D, Li Y, Ye L, Ge Q, Bian Y, Han X, Zhang W and Cheng S (2025) Correction: Giant diatom blooms driven by deep water upwelling since late MIS3? Evidence from the rim of the Mariana Trench.
Front. Mar. Sci. 12:1661159.
doi: 10.3389/fmars.2025.1661159

Correction: Giant diatom blooms driven by deep water upwelling since late MIS3? Evidence from the rim of the Mariana Trench

Junyu Lin[1,2], Dong Xu[1,2]*, Yue Li[2], Liming Ye[1,2], Qian Ge[1,2], Yeping Bian[1,2], Xibin Han[1,2], Weiyan Zhang[1,2] and Shenghui Cheng[1,2]

[1]State Key Laboratory of Submarine Geoscience, Hangzhou, China, [2]Second Institute of Oceanography, Ministry of Natural Resources, Hangzhou, China

KEYWORDS

last glacial period, Western Pacific, Mariana Trench, laminated diatom mats, *Ethmodiscus rex*

A Correction on

Giant diatom blooms driven by deep water upwelling since late MIS3? Evidence from the rim of the Mariana Trench

By Lin J, Xu D, Li Y, Ye L, Ge Q, Bian Y, Han X, Zhang W and Cheng S (2025) *Front. Mar. Sci.* 12:1556799. doi: 10.3389/fmars.2025.1556799

In the published article, there was an error in Figure 7, "CIA-A-CN-K diagram illustrating the degree of chemical weathering", as published. Figure 7 was inadvertently replaced with an earlier draft version during the production process. The corrected Figure 7 and its caption appear below.

The original version of this article has been updated.

Publisher's note

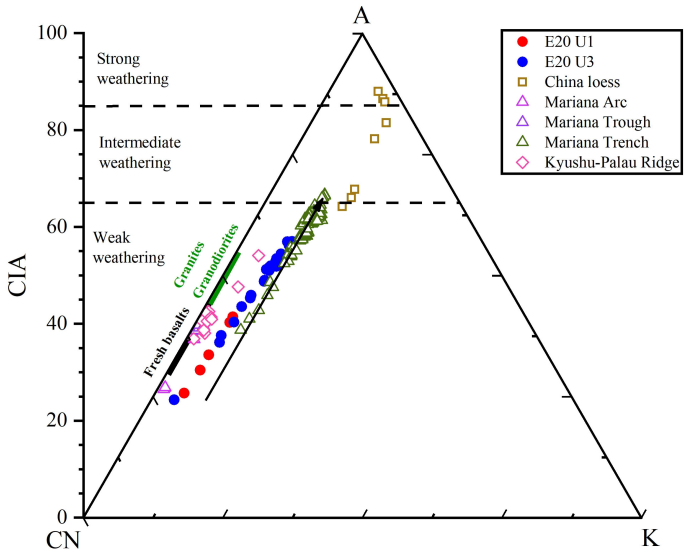

FIGURE 7
CIA-A-CN-K diagram illustrating the degree of chemical weathering. Data sources: Chinese loess (**Qiao et al., 2011**); Mariana Arc and Mariana Trough (**Ikeda et al., 2016**); Mariana Trench (**Luo et al., 2018b**); Kyushu–Palau Ridge (**Lelikov et al., 2018**; **Ishizuka et al., 2011**).

Frontiers in Marine Science

Explores ocean-based solutions for emerging global challenges

The third most-cited marine and freshwater biology journal, advancing our understanding of marine systems and addressing global challenges including overfishing, pollution, and climate change.

Discover the latest Research Topics

See more →

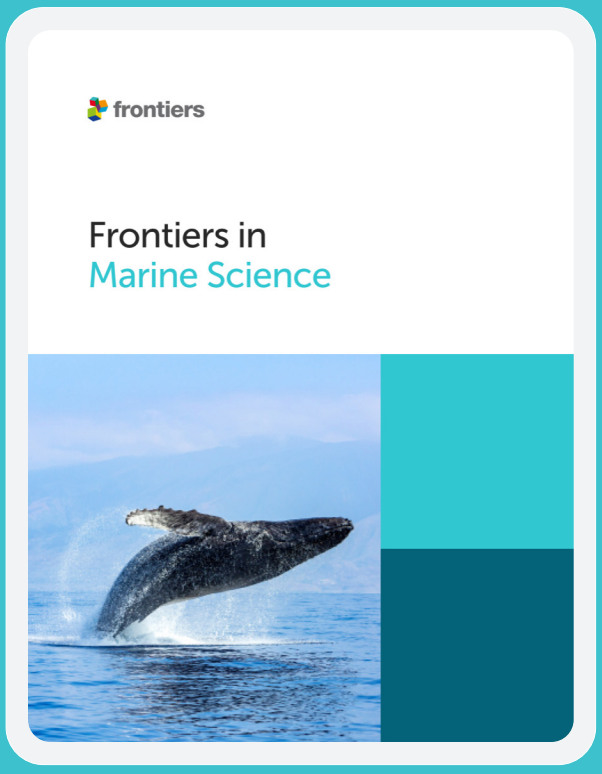

Frontiers

Avenue du Tribunal-Fédéral 34
1005 Lausanne, Switzerland
frontiersin.org

Contact us

+41 (0)21 510 17 00
frontiersin.org/about/contact